International Sorption 20
Heat Pump Conference 21

Technische
Universität
Berlin

ISHPC 2021 Proceedings

Part II - Call 2021

August 22nd - 25th 2021

Technische Universität Berlin

Campus Charlottenburg

Editor	Co-Editors
Thomas Meyer	José Corrales Walther Hüls Roland Kühn Felix Ziegler

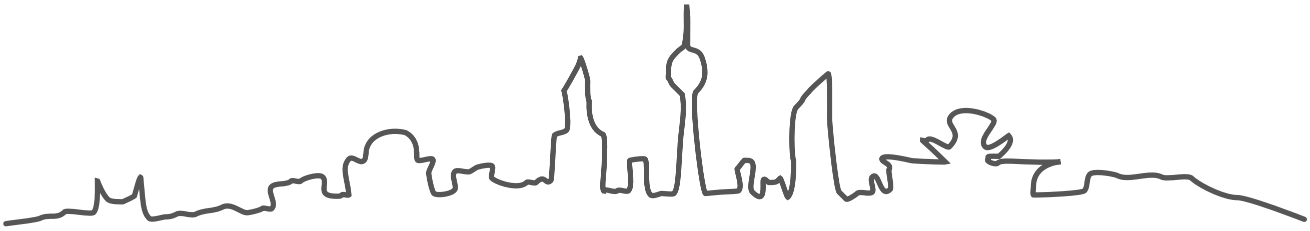

Scientific Committee

Prof. Dr. Jocelyn Bonjour
Prof. Dr. Keumnam Cho
Prof. Dr. Alberto Coronas
Prof. Dr. Robert Critoph
Prof. Dr. Carlos Infante Ferreira
Prof. Dr. Srinivas Garimella
Dr. Kyle Gluesenkamp
Prof. Dr. Gershon Grossman
Prof. Dr. Marco Guerra
Prof. Dr. Siyoung Jeong
Prof. Dr. Yong Tae Kang
Prof. Dr. Kwang J. Kim
Prof. Dr. Paul Kohlenbach
Prof. Dr. Renato M. Lazzarin
Prof. Dr. Giovanni Antonio Longo
Prof. Dr. Francis Meunier
Prof. Dr. Tetyana Morozyuk
Prof. Dr. Reinhard Radermacher
Prof. Dr. René Rieberer
Prof. Dr. Kiyoshi Saito
Dr. Lena Schnabel
Prof. Dr. Christian Schweigler
Prof. Dr. Ruzhu Wang
Prof. Dr. Felix Ziegler

Organizing Committee

Jan Albers
José Corrales
Rupert Graf
Walther Hüls
Roland Kühn
Thomas Meyer
Felix Ziegler

http://dx.doi.org/10.14279/depositonce-12278

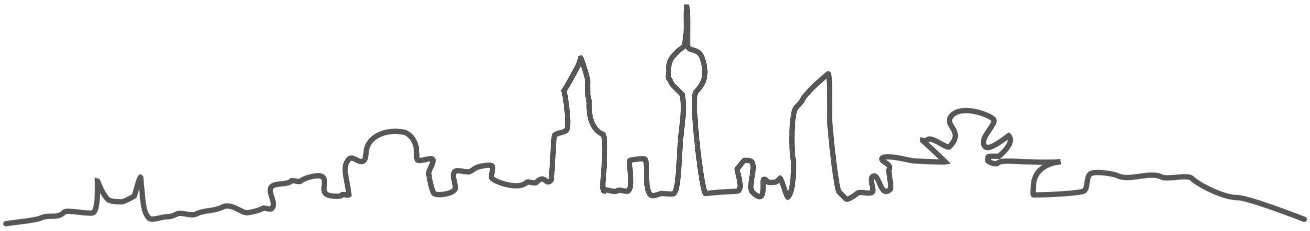

Foreword

In this second part of the proceedings to the International Sorption Heat Pump Conference 2021 all accepted contributions of the second call for papers in the year 2021 are collected. The previously accepted contributions of our first call for papers in 2020 have already been published in the first part of the proceedings in 2020. All the contributions have been peer-reviewed by the scientific committee and other invited sorption scientists.

Again, a rather general scheme is applied to sort the articles by five primary research categories:

1. Heat & Mass Transfer
2. Working Media
3. Sorption Cycles
4. Components
5. Technical Applications

In this second part of the proceedings, all papers of chapters 1 and 3 are summarized in one combined chapter due to the smaller number of submitted papers in these categories.

The ISHPC 2021 virtual conference aims to display the competitiveness of sorption heat pumps and to find ways to introduce this technology to the market as one major topic. The current transition to an energy system based on renewables changes the boundary conditions. Sorption heat pumps will have an indispensable place in this context, especially due to their potential to make use of waste heat.
We want to look at the future of sorption heat pumping devices including the newest research developments, as well as reports about pilots and mature technology.

The dissemination of insights and progress in sorption technology has been one of the major aspects of the International Sorption Heat Pump Conference. Therefore, the editorial board decided to publish this work as open access articles.

Unfortunately, the worldwide COVID-19 pandemic still prevents a safe and responsible realization of an on-site conference. For that reason, the conference is conducted completely virtually from August 22nd to August 25th 2021.
A virtual instead of an on-site conference also comes with some great opportunities. Probably, one of the most striking of these opportunities is the vast amount of greenhouse gases which are avoided by not flying around the world to attend the on-site conference in Berlin.
And we try to counteract the lack of personal contact in a virtual conference by some virtual networking lunch and coffee breaks as well as virtual social events.
We hope that despite these limitations in personal contact it will be a fruitful and enlightened ISHPC 2021 virtual conference.

We would like to thank all authors for their contributions, the reviewers for their effort, and wish all participants a lively discussion during ISHPC2021!

Berlin, August 3rd, 2021

Contents

Development of a numerical model of a liquid desiccant air-conditioning system

Mandow, Wael; Mützel, Martin; Völker, Lisa; Fleig, Daniel; Jordan, Ulrike

Institute of Thermal Engineering, University of Kassel, Kurt-Wolters-Str.3, 34125-Kassel, Germany
E-Mail: solar@uni-kassel.de

Abstract:

A TRNSYS model of a liquid desiccant air-conditioning system (LDAC system) is developed and validated with laboratory measurements. The absorber and regenerator of the investigated LDAC system are designed as tube bundle heat and mass exchangers with corrugated media as wicking fins. They are described with an ε-NTU model. The air and desiccant are in cross flow configuration. The desiccant sump of the LDAC system is modeled as two connected one-node individual tanks for the concentrated and diluted desiccant solution, respectively. An aqueous solution of lithium chloride ($LiCl-H_2O$) is used as desiccant. Temperatures and the mass fractions of the desiccant, the moisture removal rate of the air in the absorber and the water removal rate of the desiccant in the regenerator, as well as temperatures of the air and of the heating and cooling water are evaluated for steady-state and transient conditions of the system. The percentage average absolute deviation of the measured and simulated results of the absorbed moisture and regenerated water removal rates yield 4 % and 6 %, respectively.

1 Introduction

Liquid desiccant air conditioning (LDAC) systems are used for air dehumidification. The systems reach a low humidity ratio of the supply air and they are aimed to reduce electrical energy consumption if they replace vapor compression systems. In the recent years, LDAC systems are drawing more and more attention. The systems are composed essentially of an absorber, a regenerator, as well as an intermediate heat exchanger for the liquid desiccant and a desiccant sump. Whereas research focusses on the modeling of solely the absorber or the regenerator of LDAC systems, as shown e.g. in [1, 2], there are few studies about modeling and validation of the entire system. Crofoot [3] and Bouzenada et al. [4], for example, developed and validated a system model with laboratory and field measurements. The models of the absorber and the regenerator are based on efficiency correlations for the absorption and the regeneration processes. The correlations are derived from fitted curves of their own experimental data of the components. The desiccant sump is modeled as a fully mixed tank. Mohaisen et al., Zhang et al. and Yang et al. [5–7] developed different system models, however without taking into account desiccant tanks. Yang et al. [7] does not use correlations implemented into the model to describe the number of transfer units (NTU) for heat and mass transfer and the Lewis number (Le). Instead, the parameters must be provided by the user which does not allow to describe transient conditions. The ε-NTU model of the absorber and regenerator by Mohaisen et al. [5] contains efficiency correlations of the heat and mass transfer derived from fitted curves of experimental data from other studies. Kozubal et al. [8] describes a model of a desiccant sump as two individual tanks with mixing under specific conditions for system simulations. The absorber and the regenerator are described as simple fitted-curve models based on simulation data of a physical model for the absorption process and own experimental data for regeneration process. However, in [5–8] the validation of the developed system models is provided just for the absorber and/or regenerator model, not for a system model.

Other than in the LDAC models reported in literature, in this study the desiccant sump is modeled as two individual tanks with mixing under specific conditions. The NTU and therewith the efficiencies of heat and mass transfer in the absorber and regenerator are calculated from correlations according to [9], implemented into the model. The system model is validated for steady-state and transient conditions with laboratory measurements. In the following section, the investigated LDAC system is described, followed by a brief description of the ε-NTU and the sump model. Finally, the LDAC system model and its validation with experimental data is presented.

2 Experimental Set-up

The LDAC system developed by AIL Research is shown in Figure 1. It consists of an absorber, a regenerator, a desiccant sump and an intermediate heat exchanger of the concentrated and diluted desiccant solution. In the internally cooled absorber and heated regenerator, air passes along a liquid desiccant film in cross flow configuration. In the absorber, water vapor is absorbed by the concentrated aqueous LiCl-solution due to its lower water vapor pressure above the solution compared to that in the air. Enthalpy of absorption (evaporation and dilution) is released during the process and transferred to the air and liquid desiccant, as well as to the cooling water inside the absorber. The diluted desiccant solution is regenerated afterwards. The absorber and regenerator are made of corrugated fiber glass sheets as wicking fins attached to cupronickel tube bundles, Figure 2. The desiccant sump is composed of two individual tanks for diluted and concentrated desiccant. If the mean desiccant flow rate in the absorber is higher than the one in the regenerator, diluted desiccant solution is flowing into the tank with the concentrated solution. In addition, in an intermediate heat exchanger sensible heat is transferred from the concentrated to the diluted desiccant streams. Corrosion of the tube bundles is a general problem of the set up. Entrainment of the desiccant into the air is not investigated.

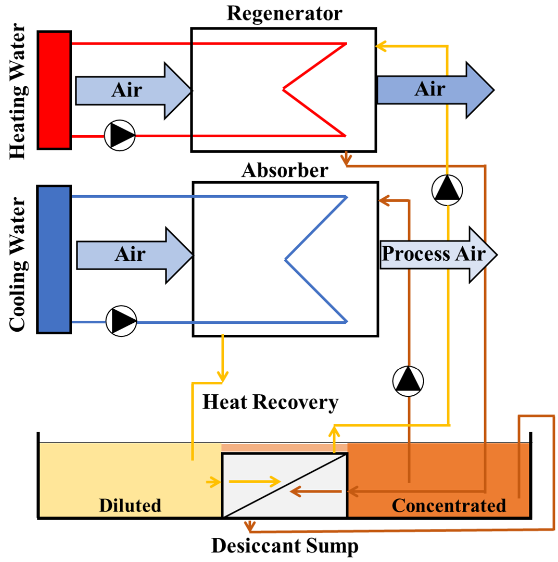

Figure 1: AIL-LDAC System, schematic diagram

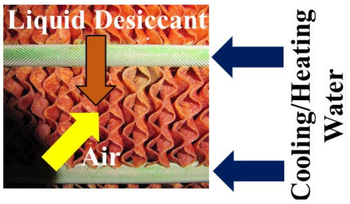

Figure 2: Heat and mass exchanger design with corrugated wicking material (fiberglass)

Table 1: Specific data of the AIL- LDAC System

	Fluid	Absorber	Regenerator
Set flow rate	Air	2000 m³/h	600 m³/h
	Desiccant	330 kg/h	230 kg/h
	Water	2000 kg/h	1000 kg/h
Temperature	Water	25 °C	60 °C
Transfer area	Fiberglass	60 m²	27 m²
	Tube bundle	2 m²	1 m²

3 Component models

3.1 Model of the absorber and the regenerator

The model of the absorber and regenerator is a single-node ε-NTU model based on efficiency correlations. The temperature and the mass fraction of the desiccant are calculated iteratively at the phase boundary. The heat of dilution and vapor pressure are implemented as nonlinear correlations of temperature and mass fraction. The heat transfer coefficients and the efficiency of the heat transfer are calculated with correlations according to [9]. The Lewis number is calculated from air properties. Finally, the mass transfer coefficient and the efficiency of the mass transfer is calculated in analogy of the heat transfer.

3.2 Component model validation

The model is validated with laboratory measurements for a wide range variation of the inlet parameters for the absorption and regeneration process. The heating and cooling water temperature and mass flow rate, the humidity ratio of the air, the air mass flow rate at absorber inlet, and the desiccant mass flow rate are varied.

Table 2: Average absolute deviations (AAD) of the outlet temperatures and percentage average absolute deviation (AAD%) of the moisture removal as well as water removal rates (component investigations)

Absorption process			Regeneration process		
Moisture removal rate $\dot{m}_v$		4 %	Water removal rate $\dot{m}_w$		6 %
T_{out}	Air	0.3 K	T_{out}	Air	1.3 K
	Cooling water	0.3 K		Heating water	0.4 K
	Desiccant	0.9 K		Desiccant*	0.9 K

*The AAD of desiccant outlet temperature of the regeneration process was evaluated for five measurements

Since the density of the liquid desiccant is only measured at the inlet of the components, the moisture and water removal rates are only evaluated at the air side. Both, the moisture and water removal rates, $\dot{m}_v$ and $\dot{m}_w$ (in g/s), respectively, are calculated from the humidity ratio ω of the air, as described by equation (1):

$$\dot{m}_{v/w} = \dot{m}_{da} \cdot |(\omega_{out} - \omega_{in})| \qquad (1)$$

With $\dot{m}_{da}$: mass flow rate of the dry air (in g/s). The average absolute deviation (AAD) and the percentage average absolute deviation (AAD%) for variable P between the experimental and the numerical results, are defined as: $AAD(P) = (1/n) \cdot \sum(P_{Sim} - P_{Exp})$ and $AAD\%(P) = (1/n) \cdot (\sum(P_{Sim} - P_{Exp}) / \sum P_{Exp})$. The AAD% of the moisture and water removal rates and the AAD for outlet temperatures for 33 nearly steady-state conditions are shown in Table 2. It yields that the simulated and experimental values for the absorption and regeneration processes agree very well. The deviations are mostly within the measurement uncertainty. The average measurement uncertainty of the moisture and water removal rates are about 13 and 12 %, respectively, for both components and system evaluations. The conditions are considered to be steady-state as soon as the deviations between the moisture and water removal rates of absorber and regenerator are below about 1 % for the simulations and about below 10 % for the measurements.

3.3 Model of the desiccant sump and heat exchanger

Each tank of the desiccant sump is described as single-node model, i.e. with homogeneous temperature and mass fraction. If the desiccant flow rate in the absorber is higher than the one in the regenerator, then part of the diluted desiccant solution flows into the other tank and is mixed with the concentrated solution. The intermediate solution counter flow heat exchanger model is a standard TRNSYS type. The overall heat transfer coefficient-area product (UA) of the intermediate heat exchanger was calculated from the experimental data and it was assumed to be equal for all simulations (UA=500 W/(m²•K)).

4 System model

4.1 TRNSYS model and inlet conditions

The TRNSYS system model consists of user defined and TRNSYS standard component models. The absorber and regenerator model (same model for both components) and the model of the desiccant sump were developed in this study. TRNSYS standard component models are used for modelling the pumps and the heat exchanger. The system model was validated for both, nearly steady-state and transient conditions. In this paper, the results of the nearly steady-state conditions are presented. The set-point inlet variables of the LDAC system measurements are shown in Table 3 The inlet variables are nearly constant for each process.

Table 3: Inlet conditions for 33 LDAC system measurements, ṁ: mass flow rate, T: Temperature and ω: humidity ratio. Index w: water and da: dry air

		Air			Desiccant	Water	
		ṁ kg/h	T °C	ω g_w/kg_{da}	ṁ kg/h	ṁ kg/h	T °C
Absorber	Reference	1200	25	12	330	2000	25
	Variation	1100-2350	20-30	5-22	188-480	0-2000	15-30
Regenerator	Variation	350				500-2000	50-80
	Reference		25	12	230	1000	60

4.2 System model validation and results

Figures 5 and 6 show results of the moisture and the water removal rates for the absorption and regeneration processes, respectively, at steady-state conditions calculated with the system model.

The average absolute deviation of the air outlet temperature in the absorber and regenerator is 0.3 and 0.6 K, respectively. The values for ADD% and AAD, as defined for the component evaluations, are shown for the system model in Table 4. The deviations are mostly within the measurement uncertainty.

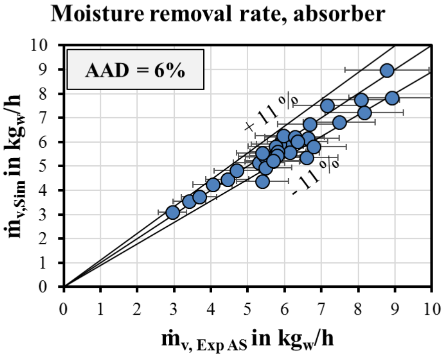

Figure 3: System model: Moisture removal rate of the air in the absorber. Experimental and simulated values

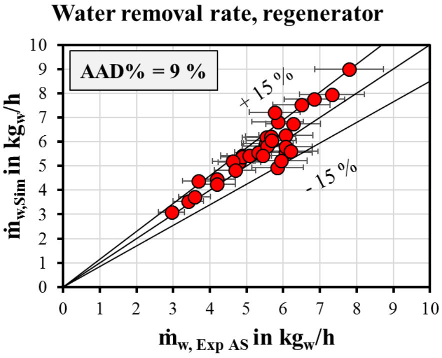

Figure 4: System model: Water removal rate of the desiccant in the regenerator. Experimental and simulated values

Table 4: Average absolute deviations (AAD) of the inlet and outlet temperatures and percentage average absolute deviation (AAD%) of the moisture and water removal rates and of the inlet mass fraction of the desiccant(ξ_{in}) (system investigations)

Absorption process			Regeneration process		
Moisture removal rate $\dot{m}_v$		6 %	Water removal rate $\dot{m}_w$		9 %
T_{out}	Air	0.3 K	T_{out}	Air	0.6 K
	Cooling water	0.2 K		Heating water	0.2 K
T_{in}	Desiccant	0.8 K	T_{in}	Desiccant	2 K
ξ_{in}		1.3 %	ξ_{in}		1.3 %
T_{out}		0.7 K	T_{out}^*		1.4 K

*The AAD of desiccant outlet temperature of the regeneration process was evaluated for five measurements

5 Conclusions

A single-node efficiency model to describe the heat and mass transfer for both, absorption and regeneration processes, as well as a single-node model of the desiccant sump is developed, validated with experimental data and implemented into TRNSYS. Correlations from literature for model parameters, like U-values and efficiencies are implemented into the model. The areas for heat transfer between cooling/heating water and the desiccant and the area for heat and mass transfer between the air and the desiccant are chosen according to the tube bundle and corrugated plate areas, respectively. The desiccant sump is modeled as two desiccant tanks, with mixing of concentrated and diluted solution in case of different mean flow rates in the absorber and regenerator. The system model is validated with laboratory measurements for a wide range variation of the constant inlet conditions, as well as for transient conditions. This paper focusses on the evaluation of steady-state conditions. Taking into account that the system model is based solely on independently evaluated parameters and on inlet conditions (of the air, as well as the heating and cooling water), the evaluation of 33 nearly steady-state conditions is in excellent agreement with the experimental results. The deviations are mostly within the measurement uncertainty.

6 Acknowledgment

The research project was financed by the German Federal Environmental Foundation (DBU) with a PhD scholarship, by the German Federal Ministry of Education and Research (BMBF) in the framework of the research project (OpenSorp, subsidy initiative storage research, code 03SF 0444) and by European Regional Development Fund (EFRE) in the framework of the research project (LDAC). The authors would like to express their sincere thanks for the support.

7 List of References

[1] Chen X, Riffat S, Bai H et al. (2020) Recent progress in liquid desiccant dehumidification and air-conditioning: A review. Energy and Built Environment 1(1): 106–130. doi: 10.1016/j.enbenv.2019.09.001

[2] Gurubalan A, Maiya MP, Geoghegan J (2019) A comprehensive review of liquid desiccant air conditioning system. Applied Energy 2019

[3] Crofoot L (2012) Experimental Evaluation and Modeling of a Solar Liquid Desiccant Air Conditioner

[4] Bouzenada S, McNevin C, Harrison S et al. (2016) Performance of a liquid desiccant air-conditioner driven by evacuated-tube, flat-plate, or hybrid solar thermal arrays. Energy and Buildings 117: 53–62. doi: 10.1016/j.enbuild.2016.02.002

[5] Mohaisen AK, Ma Z (2015) Development and modelling of a solar assisted liquid desiccant dehumidification air-conditioning system. Build. Simul. 8(2): 123–135. doi: 10.1007/s12273-014-0196-1

[6] Zhang T, Liu X, Jiang J et al. (2013) Experimental analysis of an internally-cooled liquid desiccant dehumidifier. Building and Environment 63: 1–10. doi: 10.1016/j.buildenv.2013.01.007

[7] Yang Z (2015) Development of simulation modules for liquid desiccant systems in SorpSim

[8] Kozubal E, Herrmann L, Deru M et al. (2014) Low-Flow Liquid Desiccant Air-Conditioning: Demonstrated Performance and Cost Implications

[9] (2010) VDI Heat Atlas. Springer Berlin Heidelberg, Berlin, Heidelberg

The Influence of Temperature on Marangoni Convection during Vapor Absorption

Giannetti, Niccolo[1], Fukui, Ryota[2], Fleßner, Christian[3], Meyer, Thomas[3], Saito, Kiyoshi[2]

[1] *Waseda Institute for Advanced Study, Waseda University 1-6-1 Nishiwaseda, Shinjuku-ku, Tokyo 169-8050, Japan, niccolo@aoni.waeda.jp*

[2] *Department of Applied Mechanics and Aerospace Engineering, Waseda University 3-4-1 Okubo, Shinjuku-ku, Tokyo, 169-8555, Japan*

[3] *Institute of Energy Engineering, Technische Universität Berlin, KT2, Marchstrasse 18, 10587, Berlin, Germany*

Abstract:

Although the addition of surfactant additives is a customary practice for a more compact design and higher efficiency of absorption chillers, heat amplifiers, and heat transformers, investigations conducted at high solution temperature are lacking in literature. The beneficial effect of these substances is particularly significant in terms of improved wetting and intensified absorption rate due to the triggering of the interfacial turbulence known-as Marangoni convection. However, the characterization of the latter phenomenon remains unresolved and the little knowledge available in literature is limited to low temperatures typical of chiller operation only. This study presents a preliminary experimental investigation to characterize the intensity of high-temperature Marangoni convection. Surface tension of aqueous lithium-bromide solution is measured in a temperature range of 30 to 80 °C with different mass fractions of n-octanol. The difference in the surface tension between pure aqueous lithium-bromide solution versus lithium-bromide solution containing surfactant additive decreases as the solution temperature increases. Accordingly, as the local differences in surface tension are directly related to the driving force of Marangoni convection, a lower intensity of the phenomenon is assumed at the high-temperature range of absorption heat transformers and heat amplifiers. A first visualization of the phenomenon with fluorescent uranine clearly confirms this hypothesis by showing a correspondingly lower intensity of the interfacial turbulence due to the weakened Marangoni convection at higher solution temperatures.

1 Introduction

Absorption systems present a strategic opportunity for energy recovery from low-exergy sources even though relatively bulkier and requiring higher investment costs than vapor compression systems. Within these systems, the transfer capability of the absorber is recognized as the bottleneck of their performance [1]. In fact, a particularly effective method of enhancing the internal transfer performance of absorption systems and consequently reducing size and cost is the addition of small fractions of surfactant additives. The beneficial effect of these substances is particularly obvious in terms of improved wetting and intensified absorption rate due to the triggering of the interfacial turbulence known-as Marangoni convection. Even though these additives have been known and used for decades, given the complexity of Marangoni convection, a conclusive characterization of the phenomenon remains unresolved [2]. Furthermore, the related data available in literature are limited to low temperatures typical of chiller operation only [3-4].

As temperature variations drastically affect the thermophysical properties of the absorbing solution, thus affecting the hydrodynamic and wetting behavior of the film, a comprehensive characterization should cover the whole operating range of absorption systems. Additionally, it is expected that the driving force of surfactant-induced Marangoni convection will vary along such broad range of solution temperature. Therefore, the purpose of this study is to assess the effect of Marangoni convection on the absorption phenomenon in a wide temperature range. To address this goal, a preliminary experimental investigation to characterize the intensity of high-temperature Marangoni convection is presented. Surface tension of aqueous lithium-bromide solution is measured in a temperature range of 30 to 80 °C, for two representative values (55 and 60 weight %) of the solution mass fraction, with different mass fractions of n-octanol. These data provide a first estimation of the constitutive gradients of the surface tension as a function of concentration and temperature, which are required to close numerical models for simulating Marangoni convection [5]. It is found that the difference in the surface tension between pure aqueous lithium-bromide solution versus lithium-bromide (LiBr) solution containing n-octanol decreases as the solution temperature increases. As the local differences in surface tension are directly related to the driving force of Marangoni convection, a lower intensity of the phenomenon is assumed at the high-temperature range of absorption heat transformers and heat amplifiers.

Experiments are conducted on a static liquid film for increasing temperatures of the solution. A Petri dish containing the 20 K-subcooled absorptive solution is placed in an airtight container and vapor absorption is induced by the inflow of temperature-controlled water vapor into the container. For visualization of interfacial turbulences, a fixed mass fraction of fluorescent uranine (Fluorescein disodium, $C_{20}H_{10}Na_2O_5$) is added to the absorptive solution.

2 Experimental Set-up

The experimental test sections are designed for measuring the surface tension and the constitutive relations to characterize the surface tension gradients as functions of concentration and temperature, as well as for recreating and visualizing Marangoni convection under controlled-temperature conditions.

2.1 Surface tension measurement

A solution sample of 200 ml is firstly adjusted to the desired mass fraction of lithium bromide using a densitometer. Consequently, the desired surfactant mass fraction and fluorescent uranine (1000 ppm) for fluid visualization are added using a precision micropipette. The mixture is then stirred using a magnetic stirrer before each experiment. The surface tension measurements are conducted in accordance with the pendant drop method. The solution is gradually delivered at the tip of the injection needle (placed vertically), as shown in Fig. 1, and the shape of the largest pendant drop before falling is recorded and related to the value of surface tension extracted [6]. The procedure is repeated with different mass fractions of n-octanol (0, 20, 80 ppm) and LiBr (55, 60 %) for a temperature range of 30 to 80 °C by heating and controlling the piping and the atmosphere to an arbitrary temperature using a syringe heater and a stage heater, respectively (as in Fig. 1).

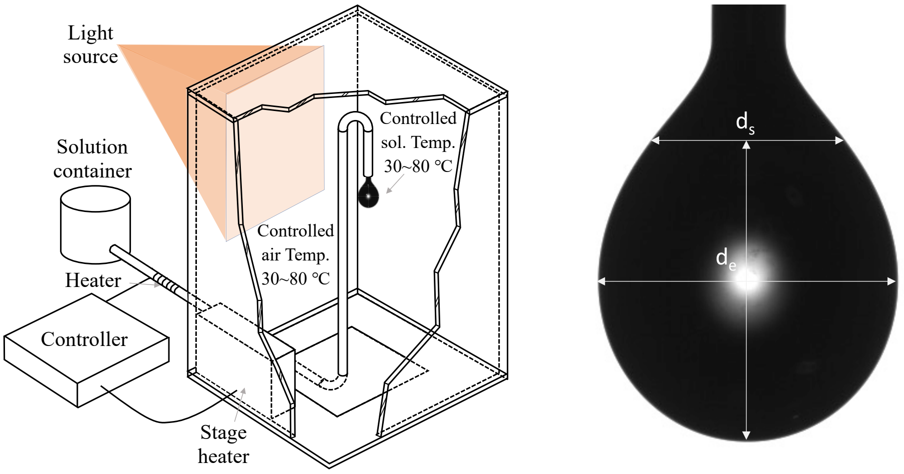

Figure 1 – Schematic diagram of the pendant drop setup (left) Photograph of pendant droplet (right).

2.2 Visualization of Marangoni convection

In order to obtain a first phenomenological characterization of the interfacial turbulence due to Marangoni convection in the target temperature range, the phenomenon is recreated and visualized in a temperature-controlled environment. The schematic diagram of the experimental setup and a photo of the solution fluorescence when irradiated with UV lights are shown in Fig. 2. The absorptive solution is prepared according to the same procedure as for the surface tension measurement.

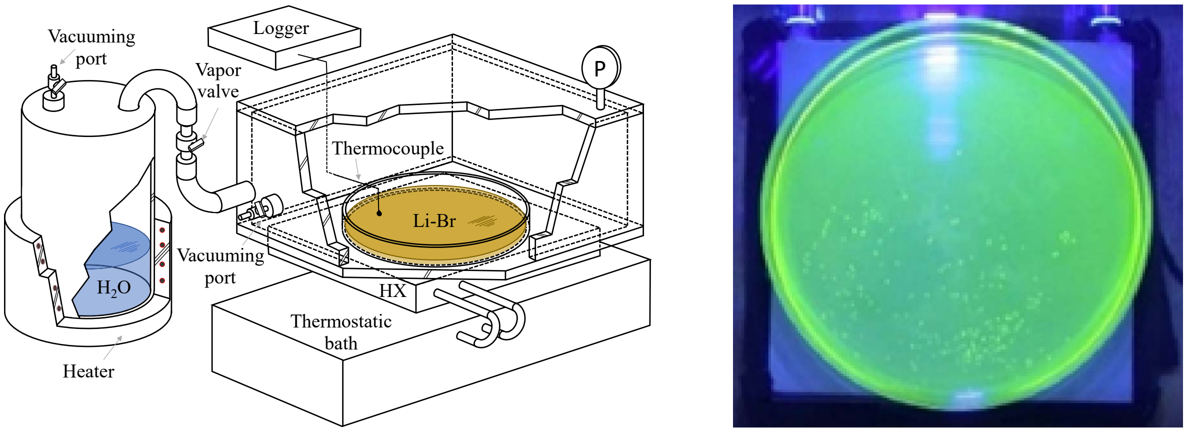

Figure 2 - Schematic diagram of the experimental setup (left-hand side) - Liquid film with fluorescent uranine (right-hand side)

As aqueous lithium-bromide solution is colorless and transparent, fluorescent uranine is added in the same mass fraction (1000 ppm) as during the surface tension measurement to enable the visualization of the interfacial turbulence triggered by Marangoni convection. Uranine is a fluorescent dye soluble in water, which isotropically emits green light when irradiated with UV light. Assuming a homogeneous distribution of the fluorescent uranine in the bulk liquid phase, this property enables a clear visualization of the film thickness variations due to Marangoni convection.

As shown in Fig. 2, a petri dish containing the lithium bromide solution is placed inside an airtight vessel, and the water vapor generated in a separate tank is delivered into the vessel. In order to commence absorption, the solution and the tank are controlled to a predetermined temperature using a thermostatic bath and a heater, respectively. Opening the vapor valve (Fig. 2) from the heated water tank initiates the experiment. In parallel, visualization of the gas-liquid interface is conducted.

3 Results

3.1 Surface tension measurement

The measured surface tension values are plotted in Fig. 3 along with the results of Iyoki and Uemura (1977) [7] for aqueous LiBr solution without additive. Fair agreement is found between these corresponding data, although larger deviations are shown at higher temperature values. It is demonstrated that the surface tension decreases at higher temperature and slightly decreases at lower LiBr mass fractions. Contrarily, measurements with n-octanol result into the opposite trend. Higher mass fractions of surfactants and higher LiBr mass fractions give a lower surface tension. When no surfactant is added, the surface tension decreases slightly with decreasing salt mass fraction and with increasing temperature. Contrarily, when the surfactant is added to the solution, the surface tension increases with decreasing salt mass fractions and decreasing temperature. This is related to the solubility of the additive. The solubility of the surfactant in the solution is reduced by increased salt mass fraction and lower temperatures, consequently the amount of surfactant concentrated at the interface is increased leading to decreased values of surface tension. The measurements carried out in this study are obtained in surfactant mass fraction conditions globally lower than the solubility limit of n-octanol in aqueous solutions [8].

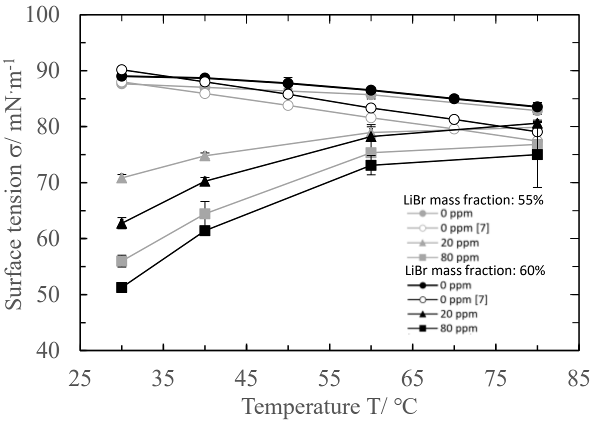

Figure 3 – Evolution of surface tension of aqueous LiBr solution with temperature for varying mass fractions of n-octanol

The relation between the absorbent surface tension gradient established at the liquid-vapor interface and induced convection onset is among the little well-established understanding of Marangoni convection. Nonetheless, [9] pointed out that the lack of data for representing the surface tension behaviour in the presence of surfactant additives hindered the full understanding of the phenomenon. Intense surface tension gradients are arising by the local differences in the surface tension between interface areas having different surfactant additive concentration. The measured data in Fig. 3 highlight that adding n-octanol to highly concentrated LiBr solution leads to a drastic decrease of surface tension at low temperatures, around 30 to 40 °C. This surface tension variation for the solution with additives decreases as the solution temperature increases, reaching the values for the solution without surfactant at approx. 80 °C. Accordingly, as the local differences in surface tension are directly related to the driving force of Marangoni convection, a lower intensity of the phenomenon is suggested at the high-temperature range of absorption heat transformers and heat amplifiers.

The measured values result from the application of Laplace equation to the pendant droplet, which is characterized in its shape (d_e and d_s, in Fig. 1) with a given digital resolution. The calculation requires the value of the gravitational acceleration g and the density difference between the liquid solution and the air within the test section as input quantities. The density of the solution is measured with a Coriolis densimeter having a sensor accuracy of ±10.0 kg/m^3. The combination of the sensor uncertainty (±0.01 mN/m, in relation to the digital resolution of the pendant droplet test section [6], and a maximum value of ±0.5 mN/m due to the sensor accuracy of the Coriolis densimeter) and the experimental uncertainty, calculated as the standard deviation of the repeated measurements from the mean value, is in the range of 1 mN/m^3 (Fig. 3). A noticeably larger standard deviation of the measurement repetitions was encountered for a 60 % mass fraction solution at 80 °C, which resulted in a maximal value of the experimental uncertainty of approx. ±5.7 mN/m.

3.2 Phenomenon visualization

The experimental observation of the phenomenon has been preliminarily conducted at a LiBr mass fraction of 55 % and additive concentration of 80 ppm, for a range of solution temperature between 30 and 60 °C. Meanwhile, the vapor temperature is set at a value 20 K higher than the equilibrium temperature determined by the concentration and temperature of the solution, specifically resulting in the temperature range from 21 to 51.7 ℃ corresponding to the vapor pressure range 2.48~13.4 kPa. The thickness of the liquid film is set to 1 mm.

A first qualitative comparison between the captured visual recordings of the phenomenon at 30 °C and 60 °C demonstrates less intense interfacial fluctuations as the solution temperature increases (Fig. 4). Brighter green shades are associated to a thicker film, whereas the thinnest film areas are approaching the blue colour of the UV light reflection of the backgound. This is thought to be due to the stronger Marangoni convection that occurs at lower temperatures, in agreement with the hypothesis formulated in section 3.1. Image processing techniques and calibration cells [10] may be investigated in conjunction with this first qualitative analysis of the visual data.

30 °C

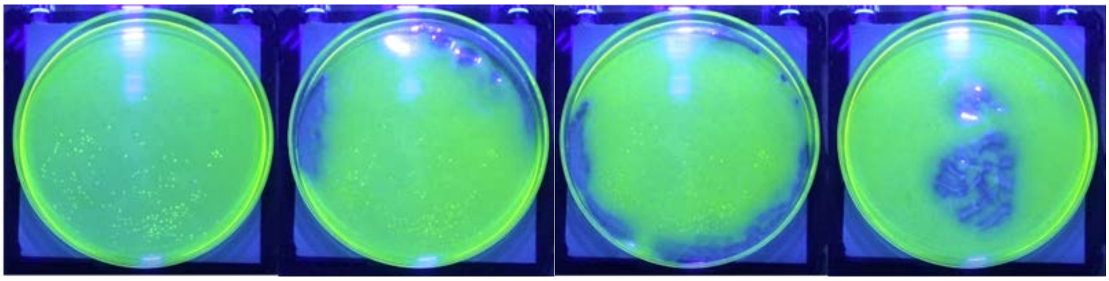

0s 10s 20s 30s

60 °C

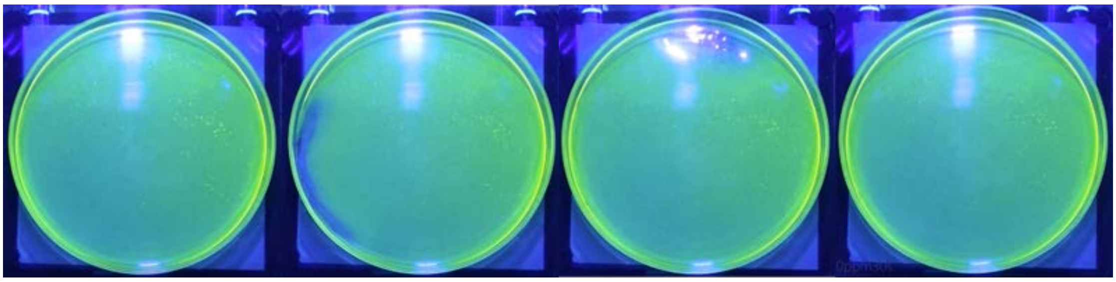

0s 10s 20s 30s

Figure 4 - Visualization results (30 ℃) - Visualization results (60 ℃)

4 Conclusions

In this study, experiments were conducted to characterize Marangoni convection in a wider range of solution temperature covering the high temperature values encountered in absorption heat amplifiers and heat transformers, which has not been assessed in previous literature. Surface tension of aqueous lithium-bromide solution was measured in a temperature range of 30 to 80 °C with different mass fractions of n-octanol. These data provide a first estimation of the constitutive relations of the surface tension as a function of concentration and temperature, which are required to close numerical models for simulating Marangoni convection.

It was found that the difference of the surface tension between pure aqueous lithium-bromide solution versus lithium-bromide solution containing surfactant additive decreases as the solution temperature increases. As the local differences in surface tension are directly related to the driving force of Marangoni convection, a lower intensity of the phenomenon is assumed at the high-temperature range of absorption heat transformers and heat amplifiers.

A first visualization of the phenomenon with fluorescent uranine clearly demonstrated that the fluctuations of the film thickness due to Marangoni convection are more intense in the low temperature range, and that this fluctuation weakened at higher solution temperatures, thus confirming this hypothesis.

Additional experimental measurements of the absorbed mass and numerical simulations are being performed to support, argue and quantify the suggested conclusions.

5 List of References

[1] Ibarra-Bahena, J.; Romero, R.J. (2014): Performance of Different Experimental Absorber Designs in Absorption Heat Pump Cycle Technologies: A Review. *Energies*, vol. 7, pp. 751-766.

[2] Matsumoto, S., Yoda, S., Nishino, K., Kawamura, H., Ueno, I., Ohnishi, M., Sakurai, M., Kawaji, M., Komiya, A. (2012): Status and outlook of Marangoni experiment on ISS. *Space Utiliz. Res. © ISAS/JAXA*, vol. 28, pp. 6-8.

[3] Nordgren, M., Setterwall, F. (1996): An experimental study of the effects of surfactant on a falling liquid film. *International Journal of Refrigeration*, vol. 19 (5), pp. 310-316.

[4] Zhang, H., Yin, D., You, S., Zheng,W., Wei, S. (2019): Experimental investigation of heat and mass transfer in a LiBr-H2O solution falling film absorber on horizontal tubes: Comprehensive effects of tube types and surfactants. *Applied Thermal Engineering*, vol. 146, pp. 203-211.

[5] Hozawa, M., Inoue, M., Sato, J., Tsukada, T., Imaishi N. (1991): Marangoni convection during steam absorption into aqueous LiBr solution with surfactant. *J. Chemical Engineering Japan*, vol. 24, pp. 209-214.

[6] https://www.asumigiken.co.jp/ Asumi Giken - 株式会社あすみ技研 (Asumi Giken Co., Ltd.). Accessed on Feb. 28th, 2021.

[7] Iyoki, S., Uemura, T. (1977): Studies on the Surface-active Agent of the Lithium Bromide-Water Absorption Refrigerating Machine. *REFRIGERATION*, vol. 52, pp. 33-39.

[8] Yaws, C.L., Hopper, J.R., Sheth, S.D., Han, M., Pike, R.W. (1998): Solubility and henry's law constant for alcohols in water. Waste Management, vol. 17(8), pp. 541-547.

[9] Nakoryakov, V.E., Grigoryeva, N.I., Bufetov, N.S., Dekhtyar, R.A. (2013): Heat and mass transfer intensification at steam absorption by surfactant additives. International Journal of Heat and Mass Transfer, vol. 51(21–22), pp. 5175-5181.

[10] Bonart, H., Marek, A., Repke, J.U. (2017): Experimental characterization of stable liquid rivulets on inclined surfaces: Influence of surface tension, viscosity and inclination angle on the interfacial area. Chemical Engineering Research and Design, vol. 125, pp. 226-232.

A Two-stage Pulsed Solid Sorption Cooling

Ghosh, Indranil[1]

[1] Cryogenic Engineering Centre, Indian Institute of Technology Kharagpur, 721302, India
E-mail: indranil@cryo.iitkgp.ac.in

Abstract:
When an adsorbent bed (with the length to diameter ratio much larger than one), is pressurized and depressurized with gas in quick succession, a temperature differential is created across the length of the column. This new compressor-driven pulsed solid sorption cooling process facilitates connecting the hot and cold ends permanently to heat sink and source respectively. This technique not only eliminates the operational difficulties of connecting a desorbing bed to a heat source and an adsorbing bed to a heat sink in alternate cycles, but it also renders an added benefit of combining multiple stages easily in a single unit. This work is about an investigation of the feasibility of multi-staging in solid sorption cooling. As proof of the concept, a dual-stage pulsed solid sorption cooler is conceptualized and fabricated. Few test runs are performed with activated carbon and nitrogen as the adsorbent adsorbate pair. The results indicate the feasibility of multi-staging in pulsed solid sorption cooling.

1 Introduction

Processes based on ‘pressure swing adsorption’ (PSA) and ‘temperature swing adsorption’ (TSA) are prevalent in chemical engineering technologies. The applications of similar concepts are also seen in the solid sorption cooling systems [1-2]. While an equivalent to PSA type in the sorption cooling is known as the ‘mechanical compressor driven’ sorption cooler [3], the TSA-based counterpart is called the ‘thermal compressor driven’ system [4]. In a thermal compressor-driven solid sorption cooler, alternative high and low pressures are created by the desorbing and adsorbing beds respectively. Similarly, in a mechanical compressor-driven system, the pressure waves are generated by the compressor, while the sorbent beds are analogous to the evaporator/condenser. The concept of solid sorption cooling has long since emerged as a potential alternative due to the benign nature of the constituents and the unique ability of the process to be effective over a wide range of temperatures [5-6]. However, in recent times, the thought of solid sorption cooling has become more meaningful in the context of global warming and growing concern about the environment [7].

While the sorption coolers are known for their environment-friendly feature, those are also tagged with low thermal performance devices. Moreover, the complex sequential operations of multiple adsorbent beds are usually done by numerous valves to thermally link them to the heat sink or the source in alternative cycles [8]. A special valve arrangement is often needed to connect the sorbent beds periodically to the heat sink/source [9].

As an alternative to this inherently intermittent process, one can take advantage of a recent development linked to quick pressurization and depressurization of a single adsorbent bed with suitable gas (as adsorbate) [10-11]. The new process and the subsequently modified forms [12-13] are essentially PSA-type systems where a mechanical compressor generates the pressure swing. The typical operating frequency being of the order of a few milli-Hertz, the process is called the pulsed solid sorption cooling [14]. In the pulsed sorption cooling process, a *temperature differential* is eventually created across the length of the adsorbent column which renders double benefits. Firstly, it enables connecting the hot end to the heat sink and the cold end to the heat source permanently, making the operational aspect very simple. Secondly, it facilitates combining multiple stages in a single unit. This manuscript describes an experimental proof of the concept towards the multi staging of pulsed solid sorption cooling.

2 Background

A brief description of a single-stage pulsed solid sorption process is presented in the following section to maintain a continuity of reading [10, 13]. Figure 1 shows the schematic of a regenerative, pulsed solid sorption cooler capable of producing continuous cooling. An adsorbent bed (1) and a regenerator (2) are placed *inline* with a valve assembly. During the pressurization cycle, the inlet valve (4) is kept open while the exit valve (7) remains closed. Under this condition, the compressed gas from the mechanical compressor (3) is allowed to enter the adsorbent column via the regenerator. Since the orifice valve (5) always remains open, the compressed gas, during this half of the cycle, finds an escape to the buffer vessel (6). At the end of the pressurization cycle, the inlet valve (4) closes and the exit valve (7) opens. The gas retracts the path followed during adsorption to leave the adsorbent bed. Desorption occurs simultaneously through the exit solenoid (7) and the orifice valve (5). The depressurization cycle ends with the closure of the exit valve. Although the proposed sorption cooler looks similar to the pulse tube cryocooler in terms of operation and appearance, they are fundamentally different in terms of the constituents, operating frequency, and the genesis of the cooling [13].

Rapid pressurization and depressurization of the adsorbent column create temperature-differential across the length of the tube. It enables combining multiple stages in a single unit.

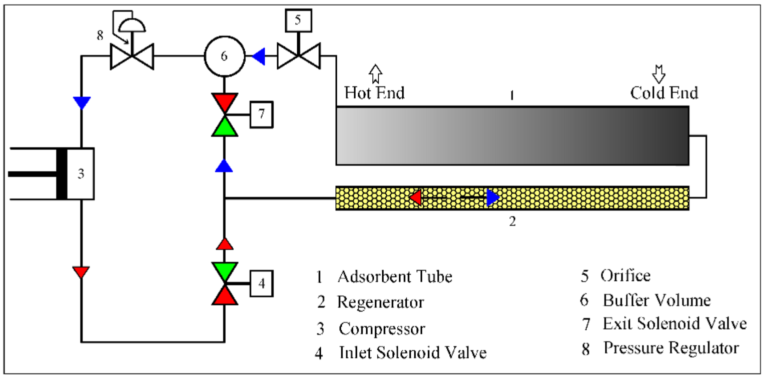

Figure 1 - Schematic of compressor-driven (single-stage) pulsed solid sorption cooling

3 Experimental Set-up

The schematic of the experimental test set up for a two-stage pulsed solid sorption cooler is shown in Figure 2. The same figure also includes a photographic view of the setup as inset.

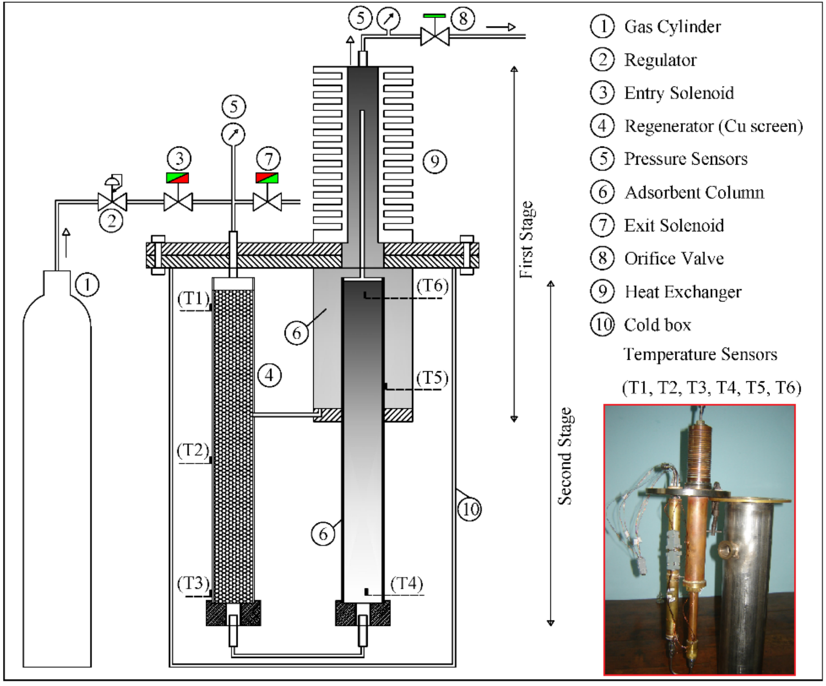

Figure 2 - Schematic of two-stage pulsed solid sorption cooling process (with a pictorial view as inset)

Although the proposed sorption cooling process should be operated ideally in a closed-loop condition taking the help of a mechanical compressor, test runs have been performed with compressed gas taken from a gas cylinder. The test setup comprises of two major arrangements, namely, (*i*) valve assembly with gas supply from high-pressure cylinder creating necessary pressure swing, and (*ii*) dual adsorbent columns which are interlinked through a metallic regenerator. The entire flow control of adsorbate (gas) is taken care of by the valve assembly comprising of a pair of solenoid-operated valves and a regulating valve. On the other hand, the adsorbent beds are essentially two tubular columns of different diameters such that the thinner one is positioned inside the thicker one. Both the tubes including the annular space between them are filled in with activated carbon (as shown in Figure 2). The adsorbent-adsorbate combination being critically important in any solid sorption cooling, activated carbon-nitrogen pair has been chosen due to practical aspects like ease of handling in the laboratory scale.

The supply of pressurized gas comes from a high-pressure cylinder (1). The gas pressure is adjusted in a regulator (2) before it enters the adsorbent beds through the *entry* valve (3) and subsequently through the regenerator (4). The regenerator is made of thin, porous copper screen cut into circular shape and dimension equal to the inner diameter of the tube used as holder. The pieces are stacked together in a single unit called the regenerator. Two pressure sensors (5), one to be found near the entry/exit side of the columns (6) and the other being located near the orifice end, dynamically monitor the system pressure. During pressurization, the inlet valve (3) is kept open, while the exit valve (7) remains closed. However, the orifice opening (8) which is essentially a regulating valve, remains open all the time. In the desorption cycle, depressurization of the adsorbent beds happens with the closure and opening of the inlet valve and exit valves, respectively. It may be highlighted that whenever pressurization or depressurization occurs, it takes place simultaneously in both the adsorbent columns. While the column with a bigger diameter tube is named the *first stage*, the smaller diameter bed is termed the *second stage*. The second stage is partly inserted within the first one. The upper part of the first stage is connected to an integral finned heat exchanger (9) exposed to ambient, whereas the lower end of the tube is housed within an enclosure, usually called 'cold box' (10). However, the cold box has not been maintained in a vacuum as done ordinarily. The flow of gas (in both halves of the cycle) as it passes through the regenerator gets distributed to each stage (as shown in Figure 2). The gas flow to the second stage occurs through the end of the regenerator, while the entry (exit) to (from) the first stage happens nearly at the middle of the regenerator.

Six resistance type (Pt-100) sensors have been used to measure temperatures at various locations schematically shown in Figure 2. While three of the temperature sensors are mounted at the exterior of the regenerator tube, the remaining temperature sensors are all located inside the activated carbon columns. While two of those three sensors measured the temperature at the top and bottom of the second stage, one sensor has been dedicated to measuring the cold-end temperature of the first stage.

A Labview program is written to open and close the solenoid valves at a pre-set interval of time. The program is duly assisted by the digital outputs of the data acquisition system and the solid-state relays (SSRs). An online data logger has been used additionally to acquire the recorded temperature-pressure data.

4 Results & Discussions

Figure 3 shows the time-temperature-pressure records of the adsorbent column. While the total cycle time is 15 s, the duration of pressurization is 5 s and that of desorption is 10 s. It may be noted that the sensors (T1, T2, T3) mounted on the exterior of the regenerator surface show comparatively less temperature variations compared to those (T4, T5, T6) located within the column filled with activated carbon. The coolest section of the adsorbent column, as anticipated, is at the lower part of the second stage (T4). The sensor T5 being colder than sensor T6 signifies that the cooling produced at the lower end of the first stage (indicated by T5) has been utilized to remove the heat generated at the top end of the second stage. The pressure variations in *Figure* 3 show that an expansion of the gas from charging pressure 2.2 MPa to 0.8 MPa at the orifice end takes place.

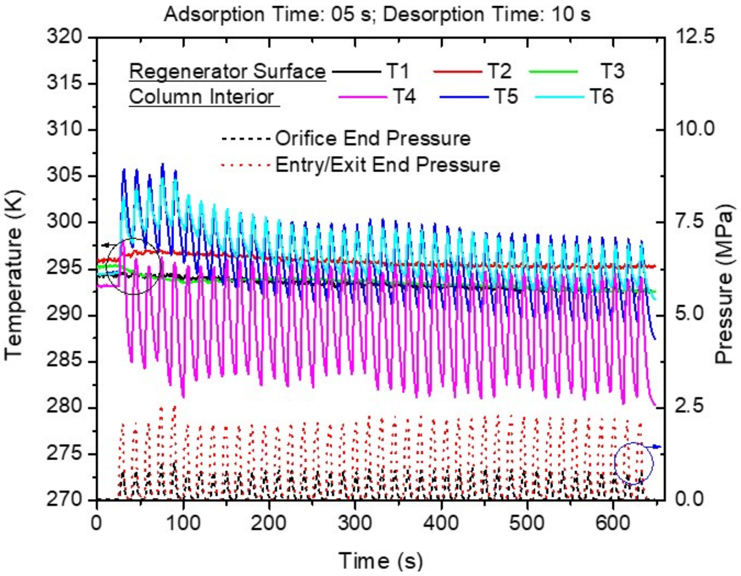

Figure 3-Time-temperature-pressure variation for 5s Adsorption - 10s Desorption cycle

Another experimental run is carried out with a different cycle time of 8 s adsorption followed by 12 s desorption. The time-temperature-pressure variations of the experimental study are shown in Figure 4. Due to the wrong adjustment of the orifice opening, initially, the difference between the charging pressure and the orifice side pressure is negligibly small. However, at the end of the test run, with the appropriate opening of the orifice valve, the charging pressure 2.1MPa could be reduced to 0.8 MPa. A quick response to this modification is discernible from the change in temperature profiles of the adsorbent beds. It is relevant to mention that the ambient temperature during both the test runs remains at 300 K ±1 K. As a whole, the temperature variations on the regenerator surface and adsorbent column interior are qualitatively similar to the earlier test run. Nevertheless, the effect of multi-staging is evident from both the experimental data.

When compared to the cold end temperature of a single-stage pulsed solid sorption cooler, tested under similar conditions (reported in Ref. [13]), the effect of multi-staging is evident. In the dual-stage cooler, the cold end of the second stage remains colder (by 3-5K) than that of a single-stage under similar operating conditions.

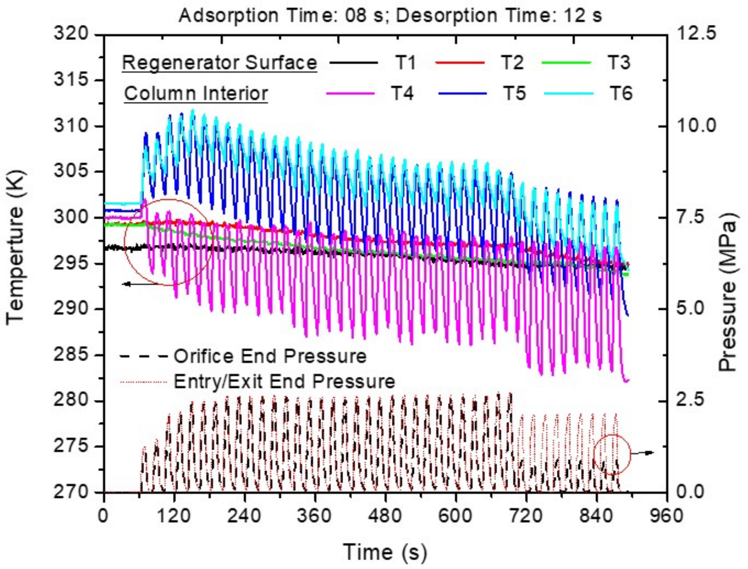

Figure 4 - Time-temperature-pressure variation for 8s Adsorption - 12s Desorption cycle

5 Conclusions

The following major conclusions are drawn from the experimental study on a pulsed solid sorption cooler:

- Differential temperature created along the length of an adsorbent column enables easy unification of multiple stages into a single unit. Stages are integrated such that the cooling produced at the cold end of the first stage is utilized to remove the heat generated at the hot end of the second stage.
- It has been observed that the hot end of the first stage initially remains warmer than the ambient and subsequently becomes colder.
- The cold end of the second stage in a two-stage cooler remains colder than that of a single-stage unit.
- The total cycle-time *vis-à-vis* adsorption and desorption cycle-times have prominent effect on two-stage solid sorption cooling.
- The pressure drop occurring between the two ends of the sorption bed is another important parameter governing the cooling production.

6 List of References

1. Ruthven D. M. (1984) Principles of Adsorption and Adsorption Processes, John-Wiley & Sons, New York.
2. Suzuki, M. (1990): Adsorption Engineering, Elsevier Science, Amsterdam.
3. Leppard, C. J. Leslie, S. (1980): Adsorption Heat Pump, US Patent No. 4,183,734.
4. Jones, J. A., Golben, .P M. (1985): Design, life-testing and future-designs of cryogenic hydride refrigeration systems. Cryogenics, vol. 25, pp. 212-219.
5. Zeigler, F. (2002): State of the art in sorption heat pumping and cooling technologies, *Int. Journal of Refrigeration*, vol. 25 (4), pp. 450-459.
6. Critoph, R.E. (1989): Activated carbon adsorption cycles for refrigeration and heat pumping, *Carbon*, vol. 27(1), pp. 63-70.
7. Meunier, F. (2001): Adsorptive cooling: A clean technology, *Clean Prod Processes*, vol. 3 (1), pp. 8-20.

8. Swain, S., Ghosh, I. (2010): Conceptual design analysis of a compressor driven sorption cooling system, *Int. Journal of Energy Research*, vol. 34 pp.1016-1026.
9. Park, J. G., Jang, K.J., Lee, P. S., Lee, J.Y. (2001): The operating characteristics of the compressor-driven metal hydride heat pump system, *Int. Journal of Hydrogen Energy*, vol. 26, pp. 701-706.
10. Koley, S., Ghosh, I. (2013): New technique for generating continuous sorption cooling in a single adsorbent column, *Applied Thermal Engineering*, vol. 55 (1-2), pp. 33-42.
11. Koley, S., Ghosh, I. (2014): Generating continuous solid sorption cooling in a single adsorbent tube - Experiment and generalised transient analysis, *Int. Journal of Heat Mass Transfer*, vol. 72, pp. 470-478.
12. Ghosh, I. (2015): On scope of improving solid sorption cooling – generating it continuously in a regenerative single adsorbent column, *Sci. and Tech. for the Built Environment*, vol. 21pp. 275-279.
13. Ghosh, I. (2016): Continuous sorption cooling in activated carbon-nitrogen using metal foam regenerator. *Proc. of 26th ICEC – ICME*, New Delhi, India
14. Ghosh, I. (2018): Comparison between Pulse Tube Cooling and Pulse Sorption Cooling. *Proc. of ICCR 2018*, Shanghai, China

Performance analysis on a hybrid liquid desiccant air conditioning system using condenser heat for regeneration

Völker, Lisa; Mandow, Wael; Fleig, Daniel; Jordan, Ulrike

University of Kassel, Institute of Thermal Engineering, Kurt-Wolters-Str.3, 34125-Kassel, Germany (solar@uni-kassel.de)

Abstract

A hybrid liquid desiccant air conditioning system consisting of a vapor compression system and a liquid desiccant system is investigated in a simulation study. The condenser and the regenerator are coupled by a water circuit. A control strategy is implemented to provide a set supply air temperature and humidity. Capacity matching of the cooling load of the air and the evaporator is reached by a stepless power control of the compressor whereas capacity matching of regenerator and condenser is realized by an auxiliary heater or cooler. In total 36 operating points with different outdoor temperatures and humidity are investigated. The evaluations yield a significant decrease of the COP of the systems as soon as auxiliary heating is necessary. For the considered operating points the COP of the system is in a range of 1.2 to 4.3.

1 Introduction

To realize dehumidification in air conditioning systems, usually the air is cooled below the dewpoint and reheated afterwards to supply air conditions. To avoid the dew point cooling for air dehumidification it is possible to use a liquid desiccant system. The combination of a liquid desiccant system and a vapor compression system (VCS) is often referred to as hybrid liquid desiccant air conditioning system (H-LDAC system). Various system configurations have been studied to combine the two systems so that cooling and heating capacity of the VCS can be used.

Abdel-Salam et al. [1] integrated a VCS into a liquid desiccant system to cool and heat the solution before entering the dehumidifier and regenerator in a numerical study. No additional sensible cooling system is used to cool the air to specified supply air conditions. The parameter study is focused on the capacity matching of evaporator and cooling load of the solution, as well as condenser and heating load for the regeneration. Abdel-Salem et al. conclude that besides an additional auxiliary condenser, at low ambient air temperatures an additional auxiliary evaporator could be necessary to achieve capacity matching. They reveal a COP in the range of 2.3-3.4. The system investigated by Dai et al. [2] numerically dissipates the latent load by only 40% by the absorber whereas the remaining latent load is handled by the evaporator. They reveal a COP of about 3.3 for defined values of the supply air and two different outdoor conditions. The possibility to use condenser heat for the regeneration is mentioned but not evaluated in detail. Thus, capacity matching is not considered. Chen et al. [3] carried out a numerical parameter study of an H-LDAC system for very hot and humid outdoor conditions. The evaporator cools the air and solution whereas the condenser heat is used to heat the solution and the air before entering the regenerator. They conclude that the energy efficiency of the systems decreases in latent load dominated conditions and reveal a COP of the system in the range of 2-4.2

The system models described in [1] to [3] evaluate stationary conditions. A system control to reach defined values of the supply air temperature and humidity and thus to realize capacity matching for various outdoor air conditions is not implemented.

This paper describes a transient simulation study of an H-LDAC system using condenser heat for an internally heated regeneration process and using an internally cooled dehumidification process. The air is dehumidified solely in the dehumidifier. The simulation tools TRNSYS and Dymola are used. A control strategy is implemented to achieve capacity matching and the defined supply air conditions. In total 36 operating points are investigated.

2 System description and Modelling

2.1 System description

Figure 1 shows the H-LDAC system which consists of a liquid desiccant system on the left and a VCS on the righthand side. A water circuit is used to transfer the condenser heat to the regenerator. Outdoor air is passed through a dehumidifier where it gets in contact with the liquid desiccant which is a LiCl-H_2O solution in this study. In the corrugated-plate dehumidifier the air is dehumidified to the defined supply air humidity ratio (x_{sup}). Afterwards the air passes through a fin and tube evaporator (direct expansion) where it is cooled to the set supply air temperature (T_{sup}). To enhance the absorption-process the dehumidifier is cooled internally. In this study it is assumed that the cooling water temperature is provided by a cooling tower. The diluted liquid desiccant solution leaving the dehumidifier flows into a tank, also referred to as sump. From here it is pumped to the regenerator where it is concentrated again by heat from the condenser and (if necessary) auxiliary heater. Before entering the regenerator, the diluted solution is pre heated in an internal heat exchanger by the solution leaving the regenerator. The water cycle transfers heat to the regeneration process and cools the condenser of the liquid desiccant system. For capacity matching of the condenser and regenerator an auxiliary heater or cooler is necessary in the water circuit after the condenser. The outdoor air flowing through the regenerator is preheated by the air leaving the regenerator in an air to air heat recovery unit.

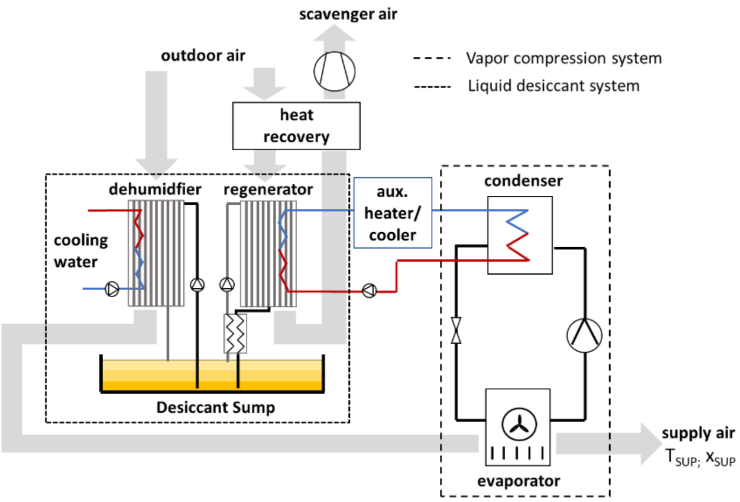

Figure 1 – Schematic diagram of H-LDAC system

2.2 Modelling of H-LDAC systems

An NTU-effectiveness model was developed in TRNSYS to describe the heat and mass transfer of the dehumidifier and regenerator [4]. The model is based on semi empirical approaches to determine the heat and mass transfer coefficients at the phase boundary of air and liquid desiccant. The overall liquid desiccant system model consists of a dehumidifier and regenerator connected to pumps and a liquid desiccant tank [5]. In this study the dehumidifier and regenerator have the same size (exchange area: 60 m²) and both components are operated with a constant air volume flow rate of 1000 m³/h and a constant solution mass flow rate of 200 kg/h. The temperature and the concentration of the solution at the dehumidifier and regenerator inlet are calculated by the model, i.e., they not given as input parameters. The water flow rate of the cooling water is constantly 0.5 kg/s.

The VCS including the control strategy is modelled in Dymola using the TIL-Suite, a library focusing on thermal components and systems. A one-stage vapor compression cycle is modelled consisting of a direct expansion evaporator (fin and tube heat exchanger), a water-cooled condenser (plate heat exchanger), a compressor, an ideal separator after the condenser and an expansion valve. R134a is used as refrigerant. Both described systems are coupled by a water circuit which serves as cooling water for the condenser and as heating water for the regenerator. The water mass flow is constantly 0.3 kg/s. Since two different simulation programs are used, the two models are linked by a co-simulation using FMI. Further components for the H-LDAC system like pumps and fans are also considered for the performance evaluation. The energy recovery coefficient of the heat recovery unit is assumed to be 0.65. The transient H-LDAC system simulations stop when a steady state condition is reached. The outdoor air temperature (T_{oa}) is varied between 24 °C and 34°C and the humidity ratio (x_{oa}) between 11 $g_{H2O}/kg_{dry,air}$ and 16 $g_{H2O}/kg_{dry,air}$.

A control strategy is implemented whereas a supply air temperature of 18°C and a humidity ratio of 8 $g_{H2O}/kg_{dry,air}$ are defined as the set supply conditions in this study. The air is dehumidified down to the set supply air humidity ratio by the dehumidifier of the liquid desiccant system. The difference of outdoor and supply air humidity ratio is defined as Δx. The hot water temperature in the regenerator serves as the essential control regulating variable for controlling the humidity in that system configuration. If the ratio of available condenser capacity $\dot{Q}_c$ and needed heating capacity for the regeneration process $\dot{Q}_{reg}$ is lower unity auxiliary heating mode is necessary. For the case that this ratio is greater unity additional cooling is essential to reach capacity matching. Additional heating is assumed to be provided by electrical energy whereas auxiliary cooling is can be realized by the cooling tower. A simplified model for the cooling tower is used assuming that the outlet water temperature is always 3 K above the wet bulb temperature of the outdoor air. In the VCS a superheat control and a stepless power control of the compressor are implemented to reach the supply air temperature. The frequency of the compressor is the control regulating variable.

2.3 Performance evaluation

The coefficient of performance (COP) of the H-LDAC system is calculated by equation 1

$$COP_{sys} = \frac{\dot{m}_{a,in,deh}(h_{a,in,deh} - h_{a,out,evap})}{P_{el,total}} \tag{1}$$

where $\dot{m}_{a,in,deh}$ is the mass flow rate and $h_{a,in,deh}$ the enthalpy of the air at the inlet of the dehumidifier and $h_{a,out,evap}$ the enthalpy at the outlet of the evaporator which corresponds to that of the supply air. $P_{el,total}$ is the sum of the electrical power of the compressor, the electrical heater (if necessary) and all pumps and fans. The VCS can be evaluated using the energy efficiency ratio (EER)

$$EER = \frac{\dot{Q}_0}{P_{el}} \tag{2}$$

where $\dot{Q}_0$ is the cooling capacity of the evaporator and P_{el} is the electrical power of the compressor.

3 Results

3.1 Performance of the H-LDAC system

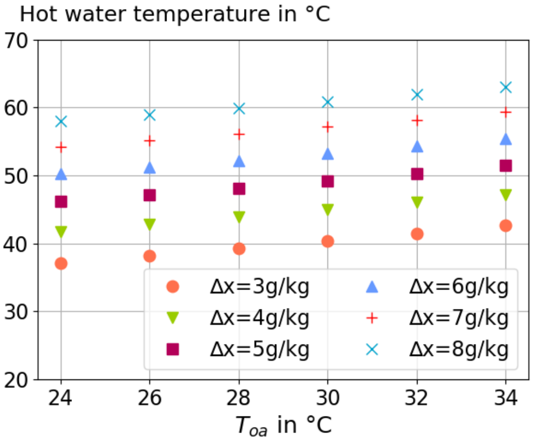

Figure 2 – Hot water temperature for the set supply air condition depending on T_{oa} and Δx

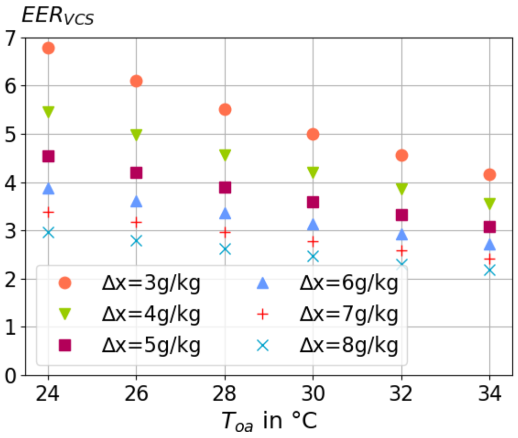

Figure 3 – EER of the VCS depending on T_{oa} and Δx

Figure 2 shows the needed hot water temperature of the regenerator to reach a humidity ratio of the supplied air of 8 g/kg for the 36 operating points. The necessary hot water temperature increases with increasing Δx. This is because the concentration of the solution in the dehumidifier is higher for a higher outdoor humidity ratio to reach a sufficient partial water vapor pressure difference at the phase boundary between the air and the solution. Moreover, the hot water temperature level rises with increasing outdoor air temperature T_{oa}. Further the cooling water temperature of the dehumidifier increases as well with increasing outdoor air temperature and humidity, again with an impact on the partial water vapor pressure. Concluding, an increase of the hot water temperature by 3-4 K yields to an increase of the dehumidification by about 1 $g_{H2O}/kg_{dry,air}$ for the considered outdoor air temperatures.

Figure 3 shows the EER of the VCS of the H-LDAC system. With increasing outdoor humidity ratio and thus increasing Δx the EER decreases. Since higher water temperatures for the regeneration are necessary the condenser temperature increases as well, whereas the evaporation temperature keeps almost constant. This leads to a higher pressure ratio and thus, more compressor power is needed. Furthermore, the cooling capacity of the evaporator increases with higher outdoor humidity ratio because more heat is released during the absorption process.

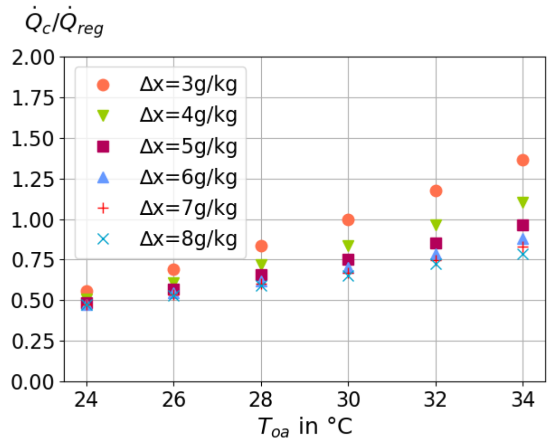

Figure 4 – Auxiliary heating and cooling capacity depending on T_{oa} and Δx

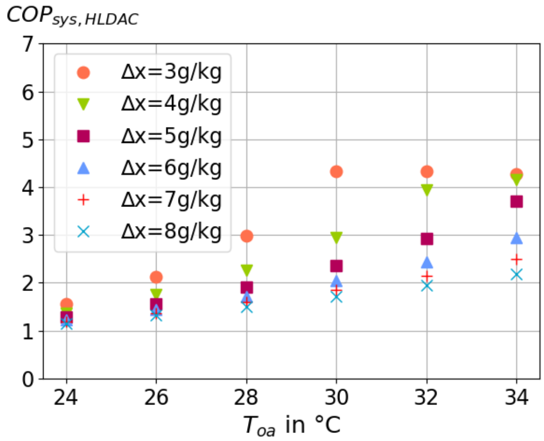

Figure 5 - COP_{sys} depending on T_{oa} and Δx

For the capacity matching of the regenerator and the condenser an auxiliary heater or cooler is necessary. Figure 4 shows the ratio of available condenser capacity $\dot{Q}_c$ and needed heating capacity for the regeneration process $\dot{Q}_{reg}$. If $\dot{Q}_c/\dot{Q}_{reg} < 1$ auxiliary heating after the condenser is necessary because the condenser capacity is not sufficient to fulfill the requirements and if $\dot{Q}_c/\dot{Q}_{reg} > 1$ auxiliary cooling is needed. It yields that with increasing outdoor air temperature the ratio increases because more cooling capacity and thus more condenser capacity is provided by the VCS. The impact of the additional electrical heating on the COP of the system is shown in Figure 5. For the outdoor air conditions which do not require additional heating after the condenser ($\dot{Q}_c/\dot{Q}_{reg} > 1$) the COP_{sys} is in a range of 4.0-4.2. As soon as auxiliary heating is mandatory, the COP_{sys} drops significantly and decreases further. With increasing Δx the COP_{sys} decreases because of the increasing electrical power of the reheater and the compressor (because higher temperatures for the regeneration process are necessary). The electrical power of the fans and pumps stays constant because the mass flows are constant.

Comparing the H-LDAC system to a conventional VCS (conv) with dew point cooling, the evaporator temperature of the H-LDAC-system ($T_{0,\ H\text{-}LDAC}$=11…15 °C) is significantly higher than for the conventional VCS ($T_{0,conv}$=6…8°C) because no dehumidification takes place in the evaporator. However, with rising outdoor humidity ratio the condenser temperature for the H-LDAC system increases significantly more than for the conventional VCS. Further depending on the outdoor air conditions the ratio of $EER_{H\text{-}LDAC}$ and EER_{conv} is in a range of 0.75 to 1.5. Comparing the total electrical power of both systems it was found that the H-LDAC system shows only energy saving potential for climatic conditions for which the ratio $\dot{Q}_c/\dot{Q}_{reg}$ is higher 0.75. The electrical savings are in a range of 5 to 40 % depending on the operating point. Detailed investigations on the comparison of the H-LDAC to a conventional VCS reference system are being carried out in further research.

4 Conclusions

An H-LDAC system model which couples the condenser of a VCS and the regenerator of a liquid desiccant system is developed and 36 operating points with different outdoor temperatures and humidity are investigated. A control strategy is implemented in the model to reach a defined supply air temperature and humidity. The air is dehumidified by the liquid desiccant system and afterwards it is cooled by the evaporator. The hot water temperature for the regeneration and the compressor frequency are identified as essential control variables for this system. Furthermore, the auxiliary cooling and heating capacity for capacity matching of the regenerator and condenser is evaluated. The COP of the system for specified outdoor air humidity ratio and temperature is quantified. The evaluations yield a significant decrease of the COP of the systems as soon as auxiliary heating is necessary. Moreover, the evaluations yield a COP of the system in a range of 1.2– 4.3 for all studied operating points.

5 Acknowledgment

The financing within the framework of the research project "LDAC-Anlagen" (WIBank, no. 20005248) by the European Regional Development Fund is gratefully acknowledged.

EUROPÄISCHE UNION:
Investition in Ihre Zukunft
Europäischer Fonds für regionale Entwicklung

6 List of References

[1] A.H. Abdel-Salam, C.J. Simonson, Capacity matching in heat-pump membrane liquid desiccant air conditioning systems, International Journal of Refrigeration 48 (2014) 166–177.

[2] Y.J. Dai, R.Z. Wang, H.F. Zhang, J.D. Yu, Use of liquid desiccant cooling to improve the performance of vapor compression air conditioning, Applied Thermal Engineering 21 (2001) 1185–1202.

[3] Y. Chen, Y. Yin, X. Zhang, Performance analysis of a hybrid air-conditioning system dehumidified by liquid desiccant with low temperature and low concentration, Energy and Buildings 77 (2014) 91–102.

[4] W. Mandow, M. Mützel, D. Fleig, A. Lowenstein, U. Jordan, Comparison of Modelled and Measured Heat and Mass Transfer in a Liquid Desiccant Air-Conditioning System, in: Eurosun, Rapperswil, Switzerland, 2018.

[5] W. Mandow, M. Mützel, D. Fleig, U. Jordan, Entwicklung eines Systemmodells einer offenen Absorptionsanlage, in: Fachforum Thermische Energiespeicherung, Meerbusch, Germany, 2019.

Adaptation of a gray-box entropy-based model of a gas-driven absorption heat pump for a new low-capacity prototype

Villa, Giorgio[1], Toppi, Tommaso[1], Aprile, Marcello[1], Motta, Mario[1]

[1] Department of Energy, Politecnico di Milano, 20156 Milan, Italy
E-mail address: giorgio.villa@polimi.it (G. Villa)

Abstract:
In this work, a gray-box model of a gas driven absorption heat pump previously used to describe the performances of a 40kW commercial unit is adapted to characterize the steady-state behavior of a new low-capacity gas driven heat pump prototype. The results show that the model is still very accurate, although the two heat pumps differ in terms of capacity and thermodynamic cycle. After modifying a few parameters, the deviation between the performances calculated by the model and the experimental ones are lower than 3%.

1 Introduction

The physical phenomena that take place in absorption heat pumps are difficult to describe with a mathematical model. In fact, an existing model that sets conservation equations on each component provides a system of non-linear equation to solve [1]. However, to perform year-round energy simulation of the building system, simplified models easier to solve are convenient. For this reason, several empirical and semi-empirical models of absorption heat pumps have been developed. A comparison of different models is shown in [2]. It concludes that the models shown in [3] and in [4] can be used to obtain relative errors between the calculated quantities and the experimental ones lower than 10%. The first one [3] calculates the COP as function of the Carnot efficiency and a set of parameters to identify experimentally. The second one [4] calculates the thermal power as a linear function dependent on ΔΔT' that is the so called characteristic temperature function. An additional very accurate model is shown in [5]. The gas-driven absorption heat pump (GHP) model consists in a gray-box model of the combustion chamber, a lumped parameter model of the flue gas heat exchanger and an entropy-based model of the ammonia-water GAX cycle. It was calibrated on a 40kW commercial unit with a gas burner nominal capacity of 28.2 kW. In this work, this model is calibrated on experimental data provided by an air-water gas driven heat pump prototype with a nominal capacity of the gas burner of 6.69 kW. In addition, the original model is based on a commercial unit designed with a different heat generator technology and a slightly different thermodynamic cycle with respect to the prototype. To do that, the model has been slightly modified with an additional parameter to identify, in order to obtain a more general model. The main goal of this work is to evaluate the accuracy of the entropy-based model also for low capacity GHP. In the following chapters, a brief presentation of the original gray-box model and the difficulties met to calibrate the model on a different GHP are described. To conclude, the results obtained by the recalibration process are shown.

2 Gray-box model description

2.1 General description of the model

The original model [5] divides the GHP in three main parts, as shown in Figure 1:

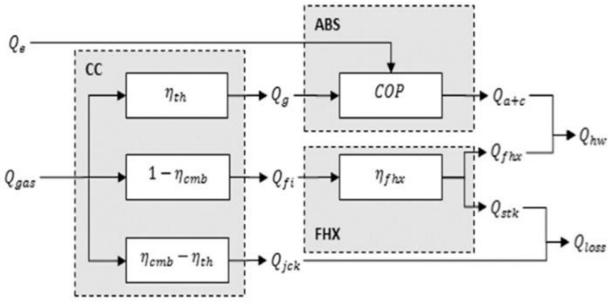

Figure 1: GHP thermodynamic cycle

- Combustion chamber (CC): in this component and in the generator, a complex mass transfer and a radiative-convective heat transfer take place. Thus, a simple integral model of the gas furnace and generator calculates the heat input to the generator (Q_g), the mass flow rate on dry gas basis ($\dot{m}_{f,dry}$), and the temperature of the gases leaving the chamber (T_{fi}). The inputs are the gas input (Q_{gas}), the combustion efficiency (η_{cmb}) and the thermal efficiency (η_{th}). The efficiencies are assumed constant and equal to 0.82 and 0.80 respectively [5].
- Flue gas heat exchanger (FHX): The model is based on the approach used for condensing coils [6]. It calculates the heat recovered from flue gases (Q_{fhx}) to heat up the inlet water. The inputs are $\dot{m}_{f,dry}$ and T_{fi}, calculated by

the combustion chamber model, and the heat exchanger UA-value in condensation ($\mathrm{UA_{wet}}$) that is identified with experimental data.

- Absorption cycle (ABS): The qualitative representation of the absorption cycle is shown in Figure 2. The diagram is specific to the heat input ($\mathrm{Q_g}$), provided by the combustion of the natural gas. In fact, α is defined as the ratio between the heat leaving the absorber ($\mathrm{Q_a}$) and the input heat at the generator ($\mathrm{Q_g}$). Then, the heat input at the evaporator divided by the heat input at the generator is (COP-1), thus the energy balance of the system, neglecting the work input at the solution pump and the heat losses, gives the heat leaving the condenser (COP-α).

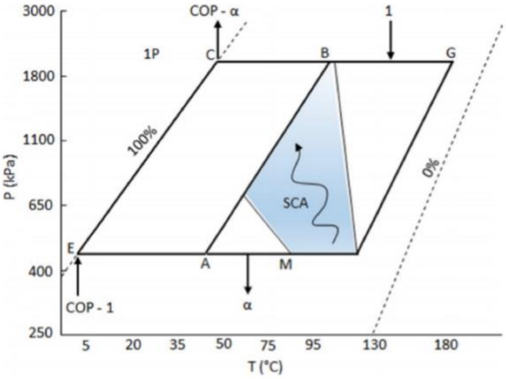

Figure 2: Absorption cycle in a P-T-x diagram – (A) rich solution leaving the absorber, (B) bubble point generator feed, (G) poor solution at the base of the generator, (M) mixing point between refrigerant vapor and solution leaving the Solution cooler absorber (SCA)

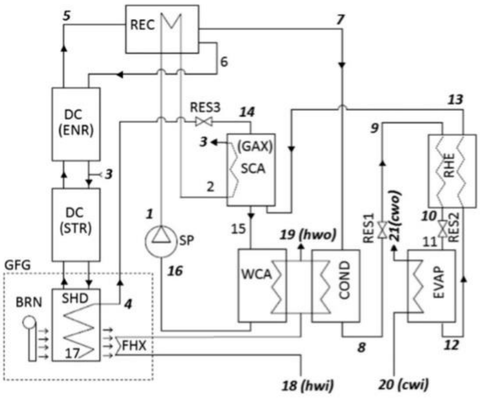

Figure 3: GHP scheme - gas burner (BRN), solution heated desorber (SHD),flue gas heat exchanger (FHX), distillation column (DC), rectifier (REC), solution cooled absorber (SCA), water cooler absorber(WCA), condenser (COND), evaporator (EVAP), refrigerant heat exchanger (RHE), restrictor (RES)

2.2 How the model works

The model is based on the entropy balance shown in (1). The goal is to calculate the outputs of the GHP using as input the inlet water mass flow rate ($\mathrm{\dot{m}_{hw}}$) and temperature ($\mathrm{T_{hwi}}$), the inlet brine mass flow rate ($\mathrm{\dot{m}_{cw}}$) and temperature ($\mathrm{T_{cwi}}$), and the heat input ($\mathrm{Q_g}$).

$$\Delta S_{IRR} + \frac{Q_g}{T_g} + \frac{Q_E}{T_E} = \frac{Q_a}{T_a} + \frac{Q_C}{T_C} \tag{1}$$

Writing the balance per unit of heat input at the generator and solving for COP, the equation (2) is obtained. COP is defined as the ratio between the heat output of the absorption cycle ($\mathrm{Q_a + Q_C}$) and the heat input ($\mathrm{Q_g}$). $\mathrm{\delta_{INT}}$ is the ratio between ΔS_{IRR} and the heat input at the generator ($\mathrm{Q_g}$).

$$COP = \frac{T_C}{T_g}\frac{T_g - T_E}{T_C - T_E} + \alpha\,\frac{T_E}{T_a}\frac{T_C - T_a}{T_C - T_E} - \delta_{INT}\frac{T_E\,T_C}{T_C - T_E} \tag{2}$$

Being an entropy-based model, the computation of the internal entropic average temperature is needed. The heat input provided by the natural gas combustion occurs at an intermediate temperature ($\mathrm{T_g}$) between (B) and (G), while the $\mathrm{Q_a}$ heat output occurs at ($\mathrm{T_a}$), between (A) and (M). It is assumed, on experimental basis, that the heat leaving the condenser ($\mathrm{Q_C}$) occurs at temperature ($\mathrm{T_C}$) that is equal to the water leaving the condenser ($\mathrm{T_{hwo}}$). The temperature ($\mathrm{T_E}$), correspondent to the heat input at the evaporator ($\mathrm{Q_E}$), should be calculated considering the refrigerant mass fraction ($\mathrm{x_r}$) and the pressure ($\mathrm{P_{low}}$). However, temperatures and pressure are unknown, thus an iterative process that involves several pre-set parameters takes place. First, the output water temperatures of the condenser ($\mathrm{T_{hwo}}$) and the evaporator ($\mathrm{T_{cwo}}$) are calculated as in (3) and (4), showing the need for an iterative solver. Then, the temperatures of the absorption cycle $\mathrm{T_E}$ and $\mathrm{T_A}$ are calculated as in (5) and (6). Experiments show that T_E can be assumed close to T_{cwo} [7]. However, below a critical value of the temperature difference $T_{hwi} - T_{cwo}$, the difference between T_E and T_{cwo} changes rapidly. For this reason, a piecewise linear interpolant has been used, as shown by equation (5). $c_{p,hw}$ and $c_{p,cw}$ are assumed constant and equal to 4.186 kJ $\mathrm{K^{-1}kg^{-1}}$and 3.6 kJ $\mathrm{K^{-1}kg^{-1}}$ respectively.

$$T_{cwo} = T_{cwi} - \frac{(COP - 1)Q_g}{\dot{m}_{cw}c_{p,cw}} \tag{3}$$

$$T_{hwo} = T_{hwi} + \frac{COP\;Q_g + Q_{fhx}}{\dot{m}_{hw}c_{p,hw}} \tag{4}$$

$$T_E = \begin{cases} T_{cwo} - e_1 - e_2\,(T_{hwi} - T_{cwo}) & (T_{hwi} - T_{cwo}) < e_0 \\ T_{cwo} - e_1 - e_0\,(e_2 - e_3) - e_3(T_{hwi} - T_{cwo}) & (T_{hwi} - T_{cwo}) \geq e_0 \end{cases} \tag{5}$$

$$T_A = T_{hwi} + a_0 \tag{6}$$

Assuming the ammonia concentration (x_r) constant and equal to 0.98 [5], the pressure P_{low} and P_{high} can be calculated as bubble point pressures at T_E and T_C respectively. Then, x_A is calculated as the equilibrium mass fraction of the liquid phase at T_A and P_A, which is equal to P_{low} minus the pressure drop through the absorber (20 kPa) [5]. At this point, T_B is calculated as the bubble point temperature at P_{high} and x_A. To conclude, T_M, T_G, and δ_{INT} are calculated as in (7), (8) and (9). Solving the system with the secant method, letting varying COP within 1 and 2, the outputs of the thermodynamic cycle can be calculated. To conclude, the Gas Utilization Efficiency (GUE) is calculated as in (10).

$$T_M = m_0 + m_1 T_E + m_2 T_A + m_3 T_B \tag{7}$$

$$T_G = g_0 + g_1 T_E + g_2 T_A + g_3 T_B \tag{8}$$

$$\delta_{INT} = (s_0 + s_1 T_A + s_2 T_B)\left(1 + \left|f_1(T_B - T_A) + f_2 * \frac{Q_g}{Q_{g,nom}}\right|^{+}\right) \tag{9}$$

$$GUE = \frac{Q_a + Q_C + Q_{fhx}}{Q_{gas}} \tag{10}$$

2.3 Parameters identification

The model uses several parameters that have to be defined (UA_{wet}, e_0, e_1, e_2, e_3, m_0, m_1, m_2, m_3, g_0, g_1, g_2, g_3, s_0, s_1, s_2, f_1, f_2, a_0, α). a_0 and α are predefined parameters equal to 7°C and 0.95 respectively, in accordance with experimental data [7]. The other parameters are set using the following identification procedures. All the parameters, except for f_1 and f_2, are identified using seven experimental test measurements at nominal gas input and constant ΔT_{hw} and ΔT_{cw}. f_1 and f_2 are identified using two additional tests at partial loads.

- UA_{wet} is calculated by means of an identification process, which minimises the root mean square error (RMSE) of the energy balance (11) , where the heat pump useful effect ($\tilde{Q}_{hw}$), the natural gas input ($\tilde{Q}_{gas}$), and the heat exchanged at the evaporator ($\tilde{Q}_e$) are experimental values. The only unknown is the heat recovered by the flue gas heat exchanger (Q_{fhx}) , which depends on UA_{wet} as in the model in [6].

$$\tilde{Q}_e = \left(\tilde{Q}_{hw} - Q_{fhx}\right) - \eta_{th}\,\tilde{Q}_{gas} \tag{11}$$

- e_0, e_1, e_2, e_3 are calculated minimizing the RMSE between the T_E, calculated with the equation (5) and the T_E indirectly measured using the refrigerant concentration (x_r) and the experimental value of P_{low}.
- m_0, m_1, m_2, m_3 are calculated minimizing the RMSE between T_M calculated by the equation (7) and T_M calculated using the energy balance of the absorber, as shown by the equation (12). T_A is calculated by equation (6), while $\dot{m}_{ps}$ and $\dot{m}_r$ are calculated by equation (13) and (14). $c_{p,sol}$ is the average equivalent specific heat of the two-phase mixture. It is assumed constant and equal to 17 kJ $K^{-1}kg^{-1}$ for the typical range of concentrations, pressures and qualities at the inlet of the absorber [5]. Δh_e is the enthalpy increase of the refrigerant in the evaporator that can be considered nearly constant and equal to 1050 kJ kg^{-1} [5]. ρ_B is the density evaluated at T_B.

$$\alpha\, Q_g = \left(\dot{m}_{ps} + \dot{m}_r\right) c_{p,sol} (T_M - T_A) \tag{12}$$

$$\dot{m}_{ps} = k\sqrt{\rho_B (P_{high} - P_{low})} \tag{13}$$

$$\dot{m}_r = \frac{Q_g (COP - 1)}{\Delta h_e} \tag{14}$$

- g_0, g_1, g_2, g_3 are calculated minimizing the RMSE between the T_G calculated by equation (8) and the T_G calculated as the bubble point temperature at P_{high} and x_G. The latter is obtained from the mass and species balance equation of the desorber system, as shown by equation (15).

$$x_G = x_A - (x_r - x_A)\frac{\dot{m}_r}{\dot{m}_{ps}} \tag{15}$$

- s_0, s_1, s_2, f_1, f_2 are calculated minimizing the RMSE between the COP calculated by equation (2) and the COP calculated with the experimental data.

The original model is based on a water-water commercial heat pump with a nominal capacity of the generator of 28.2 kW. In this work, the same model is used to calculate the performances of an air-water GHP prototype with a nominal heat capacity of the generator of 6.69 kW. Despite they use different heat sources (air and water) they are comparable because the prototype has a secondary loop that heats up the brine flow with outdoor air. Therefore, to complete the model of the air-water heat pump, the air-water heat exchanger has to be added (not considered in this paper). Moreover, the absorption cycle and the generator of the prototype are slightly different from the ones showed in figure 3. In fact, the prototype has an additional solution heat exchanger between the SCA and the SHD. Then, the commercial heat pump has a cross-tube generator, while the prototype has a fire-tube generator, which has the advantage of lower heat losses and better heat distribution. To perform the identification phase, a set of experimental data similar to the one used in [5] was measured. Moreover, two small changes among the predefined parameters, defined in the previous chapters (x_r, $c_{p,sol}$, Δh_e etc.), have been done. $Q_{gas,n}$ is 6.69 kW instead of 28.8 kW. Then, the value of k, used by equation (13), in the original model [5] was set having a deep knowledge of the restrictor RES3, shown in figure 3. However, the restrictor used in the 40 kW commercial unit is quite different from the restrictor used by the prototype. To solve this issue, two ways are available:

- Simplified k method: It is assumed that the k varies linearly with $Q_{gas,n}$. For the prototype, it is equal to 0.154.
- Advanced k method: An additional parameter (k_k) is defined and the new value of k is calculated dividing the k obtained with the simplified method by the additional parameter k_k. To define the value of k_k a minimization process of the RMSE between the experimental GUE and the GUE calculated by the model is performed, obtaining a value of k_k equal to 1.64.

Table 1 – Identified parameters for the prototype, simplified method (value1) and advanced method (value 2)

Parameter	Value 1	Value 2	Unit	Parameter	Value 1	Value 2	Unit
UA_{wet}	3.374E-3	3.600E-3	kg s^{-1}	g_0	201.595	423.996	°C
e_0	32.405	32.575	°C	g_1	0.999	3.872	-
e_1	22.501	24.187	°C	g_2	-1.707	-6.732	-
e_2	-0.572	-0.638	-	g_3	0.623	1.299	-
e_3	0.035	0.032	-	s_0	2.099E-4	7.715E-4	K^{-1}
m_0	35.186	29.666	°C	s_1	7.725E-6	-8.109E-6	K^{-2}
m_1	-0.858	-1.202	-	s_2	3.946E-6	7.541E-9	K^{-2}
m_2	1.743	2.015	-	f_1	0.023	0.016	K^{-1}
m_3	-0.290	-0.231	-	f_2	-2.163	-1.589	-

3 Results

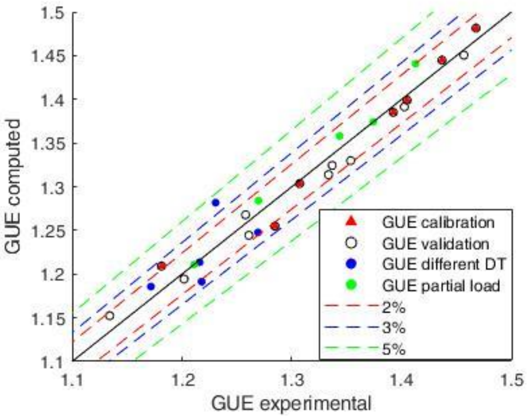

Figure 4 – Model accuracy, simplified method (k_k=1)

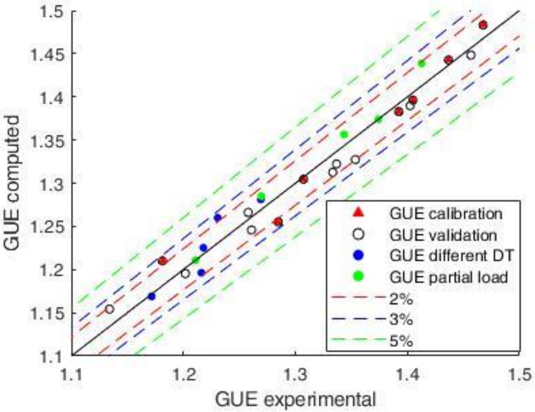

Figure 5 –Model accuracy, advanced method (k_k=1.64)

Figure 4 and figure 5 show the comparison between the GUEs calculated by the model in different conditions and the experimental GUEs in the same conditions. Figure 4 shows the results obtained using the simplified approach, while figure 5 shows the results obtained using the advanced method to define k. In both cases, several working conditions are taken into account, such as different inlet water temperatures (T_{hwi}), different outlet temperature set points (T_{hwo}), partial load, and different inlet temperatures at the evaporator (T_{cwi}).

4 Conclusions

The results show that the proposed model describes accurately the performances of the prototype, although it has a different generator, thermodynamic cycle and nominal capacity with respect to the commercial unit. The difference between the GUEs calculated by the model and the experimental ones are always lower than 3%, except for one case. Furthermore, using the advanced method, the accuracy of the model increases reaching a deviation between the experimental values and the calculated ones, usually lower than 2%.

5 List of References

[1] G. Grossman and A. Zaltash, "ABSIM-modular simulation of advanced absorption systems," *International Journal of Refrigeration,* vol. 24, pp. 531-543, 2001.

[2] F. Boudéhenn, S. Bonnot, H. Demasles and A. Lazrak, "Comparison of different modeling methods for a single effect water-litium bromide absorption chiller," in *Proceeding of EuroSun 2014*, Aix-les-Bains, France, 2014.

[3] A. Le Denn, F. Boudehenn, D. Mugnier and P. Papillon, "A simple predesign tool for solar cooling, heating and domestic hot water production systems," *Proceedings 13th Conference of International Building Performance Simulation Association,* pp. 1031-1036, 2013.

[4] A. Kühn and F. Ziegler, "Operational results of a 10kWabsorption chiller and adaptation of the characteristic equation," in *Proceeding of First International Conference on Solar Air Conditioning*, Bad-Saffelstein, Germany, 2005.

[5] M. Aprile, R. Scoccia, T. Toppi and M. Motta, "Gray-box entropy-based model of a water-source NH3-H2O gas-driven absorption heat pump," *Applied Thermal Engineering,* vol. 118, pp. 214-223, 2017.

[6] J. L. Threlkeld, Thermal Environmental Engineering, New York: Pretice-Hall, 1970.

[7] M. Aprile, R. Scoccia, T. Toppi, M. Guerra and M. Motta, "Modelling and experimental analysis of a GAX NH3-H2O gas-driven absorption heat pump," *International Journal of refrigeration,* vol. 66, pp. 145-155, 2016.

Thermodynamic analysis of a trigeneration system combined with an additional ORC cycle

Santiago, Thalyta[1], Achiles, Ana Elisa[1], Dangelo, José Vicente[1]

[1] *Department of Chemical Systems Engineering, School of Chemical Engineering, University of Campinas, 500 Albert Einstein Avenue, Building A, Campinas – São Paulo, Brazil, CEP: 13083-852. Corresponding author: dangelo@unicamp.br*

Abstract:
In this work a conventional trigeneration system combined with an additional organic Rankine cycle (ORC) was simulated and its thermodynamic performance was evaluated considering different operating conditions and working fluids. This system was defined to meet cooling, heating and power demands of a medium-sized hospital. Two configurations were considered in the analysis: P1 with the ORC place between the HRSG and the absorption chiller and P2, after the absorption chiller. Energetic analysis showed that the ORC operating with R141b after the absorption chiller produces 42% more power.

1 Introduction

A trigeneration system is a technology that uses a single primary energy source to generate power, heat and cooling more efficiently compared with conventional plants [1,2]. Al-Sulaiman *et al.* [3] presented an energetic and exergetic analyses of a biomass trigeneration system using an organic Rankine cycle (ORC). Their study demonstrated that the overall efficiency increased from 12% for electrical power to 88%. A lot of attention has been directed to the utilization of low-temperature heat sources like geothermal, solar, and waste heat energy in cogeneration and trigeneration systems [4]. ORC is a potential subsystem to be integrated into a trigeneration system to produce mechanical power because it is considered to be an effective solution for low and medium temperature heat recovery for power production [5].

In a conventional trigeneration system, power is obtained through a Brayton cycle; heating is provided by a boiler or a heat recovery steam generator (HRSG), while the cooling system uses a single-effect absorption chiller. A literature review has shown that despite this technology has been extensively studied, there are still some gaps, especially for applications involving commercial and residential sectors. In most cases, the focus has been on investigating its performance by a thermodynamics analysis or reducing cost and environmental impact. However, there are not so many studies regarding the influence of different configurations of a trigeneration system, for example, considering the inclusion of a second power plant cycle to increase its efficiency and the best location of this additional cycle.

In this paper, two different configurations of a trigeneration system are investigated, considering the inclusion of an ORC and its position in the cycle in order to improve thermodynamic efficiency:

- Configuration 1: ORC operating with R601, placed between the HRSG and the absorption chiller (P1);
- Configuration 2: ORC operating with R141b, placed after the absorption chiller (P2).

The aim of this study is to evaluate the feasibility of using a trigeneration system to meet the demands of medium-scale hospital by a thermodynamic approach considering the energetic efficiency of this system.

2 Background/Fundamentals/Experimental Set-up

2.1 System description

The trigeneration system examined in this study consists of a conventional trigeneration system, i.e., an open-type Brayton cycle, followed by a heat recovery steam generator (HRSG), a single-effect absorption chiller and a second power cycle (an ORC) located before or after the absorption cycle. The choice of an ORC is justified by: (1) the largest utility demand mapped in the hospital was electricity; (2) ORC is widely used in literature to produce power when a low or medium temperature source is available.

Organic fluids (R601 and R141b) were selected based on [6], in which they have pointed out that the best organic fluid are the ones that present a critical temperature 30-50 K above the hot source. Ammonia-water was select as the working pair refrigerant/absorbent in absorption chiller considering that this pair has been widely used in many studies as well in industrial plants. Natural gas, essentially methane, was selected as the primary energy source to be used in the Brayton cycle due to its availability, low cost, and reduced environmental impact [7].

Table 1 presents the utilities demands of the hospital studied in this work, considering daily averages and two different groups related to the seasons of the year.

Table 1 – Energy demand daily average.

Group	Electricity (kW)	Steam (kg·h^{-1})	Hot water (kg·h^{-1})	Chiller (kW)
1 (spring/summer)	1400	200	519	200
2 (autumn/winter)	1200	150	1173	150

2.2 Modeling

The following assumptions were considered for the simulation of the trigeneration system: steady-state operation; variations of potential and kinetic energies are neglected in all control volumes; pressure drops in pipelines and heat exchangers are neglected; condensers outlet streams are saturated liquid and evaporators outlet streams are saturated vapor; all equipment are adiabatic; expansion valves are isenthalpic; isentropic efficiency for compressor and turbines was fixed as 85%; based on recommended values by [8]; minimum temperature approach of 10 ºC was considered in all heat exchangers except in the evaporator where it was adopted to be 5 ºC.

The simulations were developed to provide a fixed net power of 194.6 kW (200 kW at ISO conditions) using software Aspen Hysys ® version 10 from AspenTech. The thermodynamic packages selected for the simulations were: Peng-Robinson equation of state to model Brayton and ORC cycles; Peng-Robinson-Stryjek-Vera Equation of State to model the absorption chiller and the ASME steam fluid package, considered for water. The conventional trigeneration input parameters assumed in the simulations are listed in Table 2.

Table 2 – Input parameters assumed in the simulation.

Parameter	Value
Micro turbines	
Fuel mass flow rate (kg·h^{-1})	45.15
Fuel inlet pressure in CC (kPa)	610.4
Gas exhaustion mass flow rate (kg·h^{-1})	4766
Gas turbine outlet pressure (kPa)	110
HRSG	
Outlet pressure (kPa)	588
Vapor fraction	1
Absorption refrigeration cycle	
Cooling load in spring/summer (kW)	200
Cooling load in autumn/winter (kW)	150
Low pressure in the absorber (kPa)	430
High pressure in the generator (kPa)	1243
Refrigerant mass fraction in strong solution	0.4707
Refrigerant mass fraction in weak solution	0.2607

2.3 Energetic analysis

The energetic performance was computed by means of a coefficient of performance (COP) of the system, which was defined by the ratio between the sum of all energy outputs and the input as presented in Equation (1).

$$COP = \frac{\dot{W}_{net} + \dot{Q}_h + \dot{Q}_{hw} + \dot{Q}_c}{\dot{Q}_{in}} \tag{1}$$

where the outputs are: $\dot{W}_{net}$ (net power of the system), $\dot{Q}_h$ (heat load rate provided in the heat exchanger to produce steam), $\dot{Q}_{hw}$ (heat load rate provided in the heat exchanger to produce hot water) and $\dot{Q}_c$ (cooling rate produced by the system); and the input is $\dot{Q}_{in}$, total energy rate input in the system.

3 Results

3.1 Parametric analysis

Thermodynamic performance of two different configurations of a trigeneration system was evaluated considering energetic efficiency. COP as defined by Equation (1) was examined through changing the parameters presented in Table 2. Operating variables studied were: pinch point temperature (T_{PP}) of the ORC heat exchanger (varied from 10 ºC to 60 ºC); inlet turbine pressures (varied from 1000 kPa to 3000 kPa) and inlet temperature of the ORC pump (varied from 112 kPa to 323 kPa and from 97 kPa to 282 kPa, when the working fluid used was R141b and R601 respectively). Figures 1 to 4 present the influence of the parameters studied over the electrical power and mass flow rate of the working fluid in the ORC. Table 3 presents the codes used in these figures.

Table 3 – Trigeneration code used in each configuration.

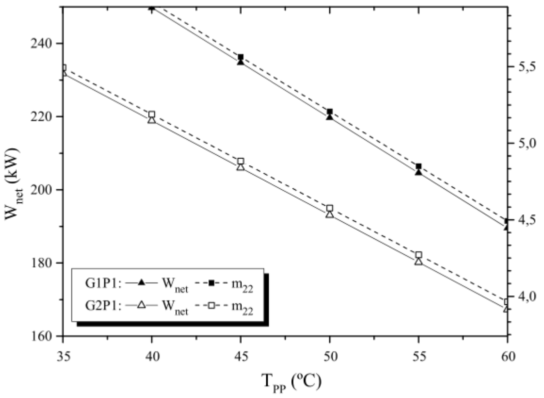

Figure 1 - Influence of ORC heat exchange pinch point temperature with R141b on the electrical power and mass flow rate.

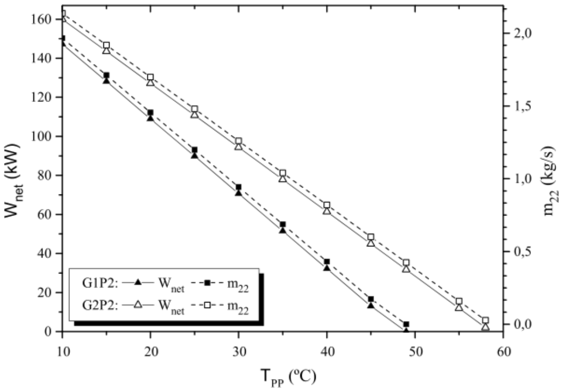

Figure 2 - Influence of ORC heat exchange pinch point temperature with R601 on the electrical power and mass flow rate.

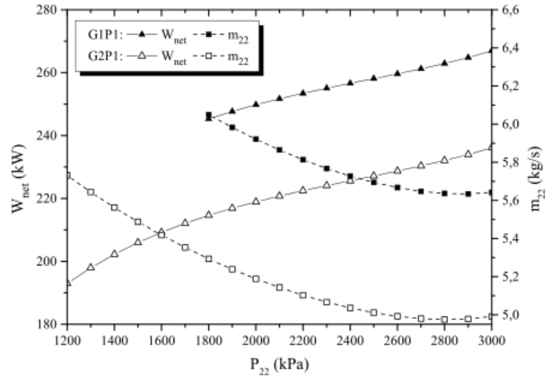

Figure 3 - Influence of ORC inlet turbine pressure with R141b on the electrical power and mass flow rate.

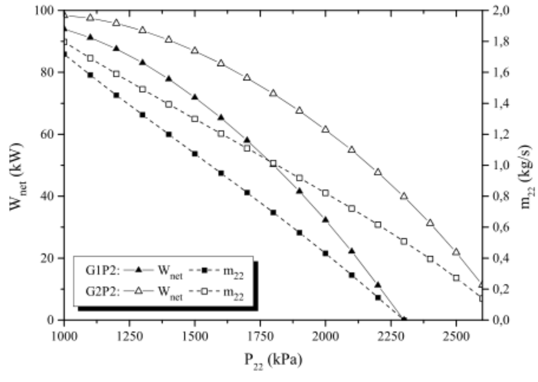

Figure 4 - Influence of ORC inlet turbine pressure with R601 on the electrical power and mass flow rate.

Regarding the influence of the pinch point temperature on ORC energetic efficiency, as the pinch point temperature increases, energetic efficiency decreases in all cases. In R601 trigeneration, energetic efficiency is greater in G2P2 than G1P2. This behavior occurs because the mass flow rate to guarantee the same pinch point is twice greater in group 2 and when R141b trigeneration was used, the energetic efficiency increases significantly. The influence of the turbine inlet pressure on ORC energetic efficiency have shown to be insensible when R141b was used for both G1P1 and G2P1 and that for R601 the increment of pressure decreases COP. Finally, the inlet temperature of the ORC pump does not influence the energetic efficiency, this is why the graphisc of the influence of this variable over the electrical power and mass flow rate were not presented in this work.

4 Conclusions

The main conclusions that can be drawn out from this study are:

- The trigeneration system was able to produce 1374.8 kW power, 200 kW heating, and 200 kW cooling. The addition of a second power plant produced an additional 307.3 kW power and 1363.1 kW of hot water with R141b, while with R601, 178.9 kW power and 940 kW of hot water;
- Considering the pinch point temperature (T_{PP}), the best performance of the ORC cycles is attained at the following operating parameters: for R141b T_{PP} = 40 ºC, and for R601 T_{PP} = 10 ºC. This difference between these two T_{PP} is due the fact that heat load in the heat exchanger of the ORC is different for each fluid, as well is the mass flow rate. These values where the minimum attained in each simulation that allowed the simulation to run properly once the outlet temperature of the exausted gases should be greater than 40 ºC;
- The energetic analysis showed that the ORC operating with R141b and positioned after the absorption cycle allows the production of about 42% more power compared to the other system, but this configuration requires a mass flow rate around 64% higher.

5 Acknowledgment

Authors acknowledge the financial support from the Coordination of Superior Level Staff Improvement (Coordenação de Aperfeiçoamento de Pessoal de Nível Superior – CAPES) through the scholarship granted.

6 List of References

[1] M. Sheykhi, M. Chahartaghi, M. M. Balakheli, B. A. Kharkeshi, S. M. Miri (2019): Energy, exergy, environmental, and economic modeling of combined cooling, heating and power system with stirling engine and absorption chiller, *Energy Conversion and Management,* vol. 180, pp 183–195.

[2] M. Jradi, S. Riffat (2014): Tri-generation systems: Energy policies, prime movers, cooling technologies, configurations and operation strategies, *Renewable and Sustainable Energy Reviews*, vol. 32, pp. 396–415.

[3] F. A. Al-Sulaiman, I. Dincer, F. Hamdullahpur (2012): Energy and exergy analyses of a biomass trigeneration system using an organic rankine cycle, *Energy*, vol. 45, pp. 975–985.

[4] M. A. Kordlar, S. M. S. Mahmoudi, F. Talati, M. Yari, M. A. H. (2019): A new flexible geothermal based cogeneration system producing power and refrigeration, part two: The influence of ambient temperature, *Renewable Energy*, vol. 134, pp. 875–887.

[5] S. Safarian, F. Aramoun (2015): Energy and exergy assessments of modified organic rankine cycles (orcs), *Energy Reports*, vol. 1, pp. 1–7.

[6] J. Hærvig, K. Sørensen, T. J. Condra (2016): Guidelines for optimal selection of working fluid for an organic rankine cycle in relation to waste heat recovery, *Energy,* vol. 96, pp. 592–602.

[7] M. Ameri, A. Behbahaninia, A. Tanha (2010):Thermodynamic analysis of a tri-generation system based on micro-gas turbine with a steam ejector refrigeration system, *Energy*, vol. 35, pp. 2203–2209

[8] A. Gimelli, R. Sannino (2018): A multi-variable multi-objective methodology for experimental data and thermodynamic analysis validation: An application to micro gas turbines, *Applied Thermal Engineering*, vol. 134, pp. 501–512.

A modified linear driving force model for adsorption heat pump and CO_2 capture applications

Rupa, Mahua Jahan[1,2], Pal, Animesh[3], Saha, Bidyut Baran[1,2]

[1]International Institute for Carbon-Neutral Energy Research (WPI-I2CNER), Kyushu University, 744 Motooka, Nishi-ku, Fukuoka 819-0395, Japan

[2]Mechanical Engineering Department, Kyushu University, 744 Motooka, Nishi-ku, Fukuoka 819-0395, Japan

[3]Department of Nuclear Engineering, University of Dhaka, Dhaka 1000, Bangladesh

*Author to whom correspondence should be addressed,
E-mail: jahanmahua@gmail.com

Abstract:

Adsorption is one of the most widely applied techniques for environmental remediation. Its application plays a crucially important role in energy conversion and environmental technologies, especially for gas-solid adsorption systems. The dynamic performance of an adsorbate/adsorbent pair has significant influences in optimizing the systems' speceific power, size as well as the total cost. This paper presents a new kinetics model that perfectly describes the dynamic behavior of different adsorbate/adsorbent pairs for a gas-solid adsorption system. The new kinetics model is established based on the theory of the linear driving force model by introducing three new parameters to this model. The main achievement of this model is that it can predict the dynamics of the system during the entire cycle thoroughly. Conclusively the modified LDF equation is validated by the experimental data of adsorption chiller and CCS (carbon dioxide capture and storage) applications of different adsorbate/adsorbent pairs.

1 Introduction

Adsorption of gases onto solid is widely utilized in different applications like separation and purification of gases, gas storage systems, adsorption-based heating and cooling systems, and energy storage systems. The basic fundamental of all these applications is they work as a batch-wise process i.e. adsorption and desorption occur alternatively and is also time-dependent [1]. So, the adsorption rate or kinetic equations are widely used to describe adsorption data at non-equilibrium conditions and are significant to investigate the basic understanding of the adsorption process that ranges from transient to the cyclic steady state.

Numerous models exist to describe the adsorption kinetics of various gasses onto different adsorbents. The main diffusion equation comes from Fick's equations [2] along with a very difficult analytical solution under a practical situation. But, the most popular model for describing the gas-solid adsorption kinetics is the linear driving force (LDF) model [3]. In the LDF model, the experimental data are fitted with the equation applying some fitting parameters [4,5]. Though, the LDF model ensures a good description of the breakthrough curves still its applicability for the adsorption system is under intensive discussion [6]. At constant temperature, the LDF model underestimates the uptake at short times and overestimates it at long times. Several authors have modified the LDF model following their needs. Sultan et al. [7] modified the LDF model by introducing a dimensionless power 'm' as a variable and this model only represents the water vapor adsorption kinetics of two polymer-based sorbents. Jribi et al. [8] investigated the kinetics of CO_2 adsorption onto AC by modifying the LDF equation with a variable mass transfer coefficient which is a function of the equilibrium and instantaneous uptakes. Sircar and Hufton analyzed [1] the relation between the LDF model and the FD (Fickian Diffusion) model, but the detailed characteristics of the local adsorption kinetic model are neglected during integrations.

Until now, clearly there is no such modification that has been carried out to overcome the drawbacks of the LDF model which perfectly derives the kinetics of all types of adsorbate/adsorbent pairs. Therefore, the main objective of this study is to present a modified LDF model with a time-based correction factor that can accurately derive the dynamic behavior of all types of adsorbate/adsorbent pairs along with the short and long-term phases of adsorption. Some significant contributions of this study are noted below:

- A modified LDF kinetics model has been introduced to predict the experimental kinetics data of a wide range of adsorption pairs.
- The proposed model fits the experimental data accurately for the initial unsaturated phase as well as the later near saturation phase.

2 Mathematical derivation of modified LDF model

The adsorption rate of the adsorbent/adsorbate pair of the LDF model can be written as:

$$\left(\frac{dw}{dt}\right) = F_0 \frac{D_s t}{R_p^{\,2}}\left(W(\infty) - W(t)\right) \tag{1}$$

By integrating equation 1, one can obtain the fractional uptake by the following form,

$$F = \frac{W(t) - W(initial)}{W(\infty) - W(initial)} = 1 - \exp\left(-F_0 \frac{D_s t}{R_p^{\,2}}\right)$$

Simplifying the above equation we obtain,

$$F = 1 - \exp\left(-t \big/ \left(R_p^2 \big/ F_0 D_s\right)\right) = 1 - \exp\left(-t/\tau\right)$$

where $\tau = R_p^2 \big/ F_0 D_s$

The LDF model is modified by taking the power of the following form

$$F = 1 - \exp\left(-\frac{t}{\tau}\right)^{at^2+bt+c} \tag{2}$$

Where a, b, and c are the fitting parameters. c is a dimensionless fitting parameter, a and b have units, s^{-2}, and s^{-1}, respectively, and these two fitting parameters are strongly related to time.

The differential equation form can be written as:

$$\frac{\partial w}{\partial t} = \left(-t/\tau\right)^{at^2+bt+c}\left(\ln\left(-t/\tau\right)\left(2at+b\right) + \left(\left(at^2+bt+c\right)/t\right)\right)\left(w(\infty) - w(t)\right) \tag{3}$$

The modified model can be integrated by using the following boundary conditions to get the instantaneous adsorption uptake as follows

(i) At $t=0$; $w(t)=w(0)$

(ii) At $t=t$; $w(t)=w(t)$

$$\int \frac{\partial w}{\left(w(\infty) - w(t)\right)} = \int e^{\left[\left(at^2+bt+c\right)\ln\left[-\frac{t}{\tau}\right]\right]}\left(\ln\left(-t/\tau\right)\left(2at+b\right) + \left(\left(at^2+bt+c\right)/t\right)\right)\partial t$$

Finally, we can write,

$$e^{\left[\left(at^2+bt+c\right)\ln\left[-\frac{t}{\tau}\right]\right]} + \ln\left(w(\infty) - w(t)\right) - \ln\left(w(\infty) - w(0)\right) = 0$$

$$\Rightarrow w(t) = w(0) + \left(w(\infty) - w(0)\right)\left(1 - \exp\left(-t/\tau\right)^{at^2+bt+c}\right) \tag{4}$$

From equation (4), we can predict the instantaneous uptake at any time.

3 Applications of modified LDF model

3.1 Adsorption chiller

3.1.1 Activated carbon fiber (A-20)/ethanol pair

Activated carbon fiber (ACF) of type A-20 is a fibrous adsorbent that has the advantages of high porosity, fast adsorption rate, and ease of handling when compared with powdered or granular adsorbents. Compared to many popular adsorbents, it has a higher pore volume and surface area. Hence the adsorption capacity of the ACF (A-20)/ ethanol pair is considerably higher than that of the ACF (A-15)/ethanol pair. El-Sharkawy et al. [9] checked the adsorption kinetics of ethanol onto ACF (A-20). The authors conducted the measurements of adsorption rates using a thermogravimetric analyzer (TGA). Experimental measurements were conducted at several adsorption temperatures within a range from 27 °C to 60 °C. At each adsorption temperature, adsorption uptake was recorded at 0.5 s intervals until the equilibrium condition was attained. Figure 1 shows the dynamic ethanol vapor adsorption onto activated carbon fiber fitted with the proposed model and LDF model. Noticeably, the proposed model provides excellent fitting with the experimental data with an RMSD value of 2.4% at the temperature of 27 °C.

The obtained diffusion time constant (D_s/R_p^2) and the proposed model's fitting parameters are furnished in Table 1.

3.1.2 RD Silica gel/water pair

In adsorption refrigeration, dehumidification, or cooling applications, silica gel/water is a widely used adsorption pair. In this section, the proposed equation is fitted with the experimental data of adsorption dynamics of water vapor onto different silica gel types, including different configurations (single or multilayers). Authors [10] measured experimental data employing the LTJ (Large Temperature Jump) method. The details of this pair and the layering configuration can be found in the reference [10]. Figure 1 shows the experimental data of adsorption dynamics of RD silica gel/water pair with different layers. The fitted proposed model with the experimental data is also plotted on the same figure. It is seen that the proposed model perfectly matches with the experimental data with RMSD values 0.2% to 0.7%. All kinetics parameters of the proposed equation are summarized in Table 1.

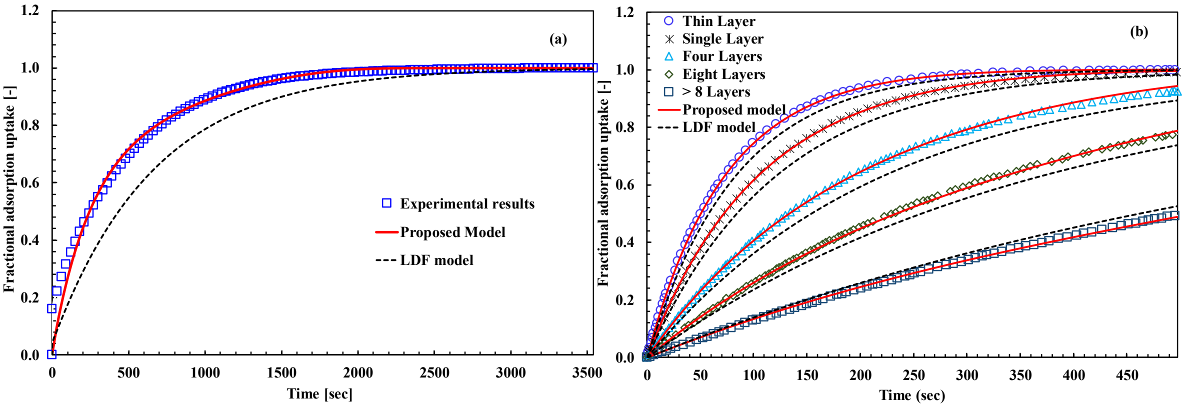

Figure 1 - Adsorption kinetics data of (a) activated carbon fiber/ethanol pair at 27 °C [9]*, (b) RD silica gel/water pair* [10] *(markers represent the experimental data, solid lines represent the proposed model, and dashed lines represent the LDF model).*

3.2 Carbon dioxide capture and storage

3.2.1 Activated carbon/CO_2 pair

Activated carbon (AC) is a widely used adsorbent for carbon dioxide capture and storage applications due to the high uptake and faster kinetics. In this section, the kinetics data of a fine commercial AC (DARCO FGD (Norit)) for CO_2 adsorption [11] has been validated with the proposed model. The breakthrough curves of the AC/CO_2 pair were measured with a temperature swing adsorption sound assisted fluidized bed rig, and the adsorption temperature ranges from 25 to 150 °C and partial pressure of CO_2 ranges from 0.05-0.20 atm. The experimental data for 5 vol% CO_2 concentration at intake temperatures of 70 and 130 °C have been fitted with the proposed model and presented in Figure 2. It can be observed that the proposed model fits well with the experimental data with an RMSD value of 1.23 and 0.89 % for 70 and 130 °C, respectively. The kinetics parameter values are presented in Table 1.

3.2.2 CB-FM/CO_2 pair

To advance our study, we also consider the CO_2 adsorption [12] in the framework of CO_2 capture and storage (CCS), whereas the adsorbent material is a composite, namely CB-FM, consists of 50 %wt carbon black (CB) and 50 %wt magnetite (FM). The kinetics of the CO_2 adsorption on CB-FM was measured in a lab-scale fixed bed reactor at the adsorption temperatures 18, 40, 70, 100, and 150 °C. The experimental data for 15 vol% CO_2 concentration at adsorption temperatures 40 and 150 °C have been presented in Figure 2, along with the proposed kinetics model. It is evident that the proposed model can accurately fit S-shape adsorption kinetics data. Kinetics fitting parameters and diffusion time constant values are furnished in Table 1.

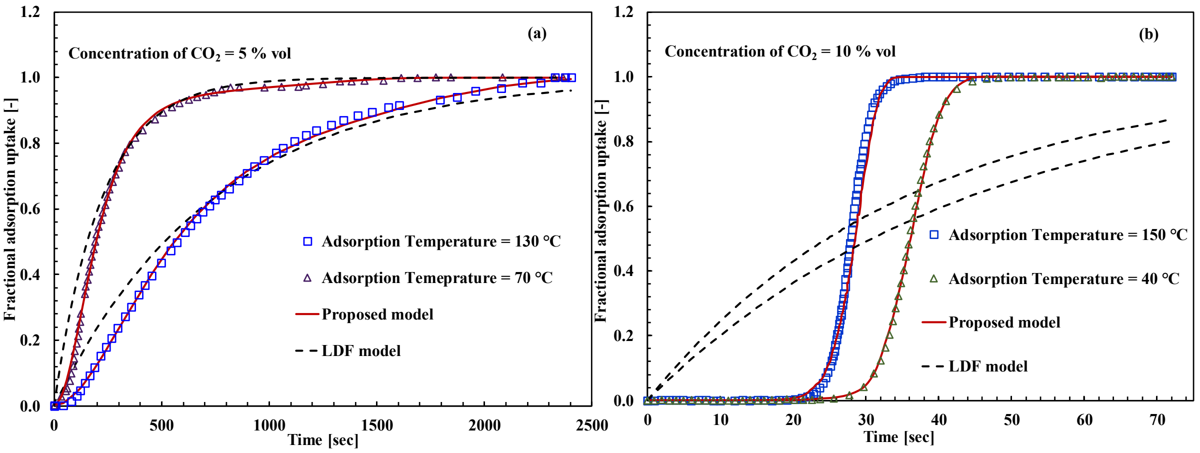

Figure 2 - Adsorption kinetics data of (a) activated carbon/CO$_2$ [11]*, (b) CB-FM/CO$_2$ pair*[12] *(markers represent the experimental data, solid lines represent the proposed model, and dashed lines represent the LDF model).*

Table 1 – Kinetics fitting parameter of studied adsorption pairs.

Adsorbent/adsorbate pair	T_{ads}[a] [°C]	Type	D_s/R_p^2 [s^{-1}]	a [s^{-2}]	b [s^{-1}]	c [-]	RMSD[b] [%] (m. LDF)	RMSD [%] (LDF)
Activated carbon fiber/ethanol	27	-	1.77E-07	1.72E-07	-3.0E-04	0.92	2.40	8.34
RD Silica gel/water	29.85	Thin layer	9.14E-04	7.02E-07	-8.6E-05	0.96	0.20	3.00
		Single layer	6.40E-04				0.60	3.66
		4 layers	3.46E-04				0.70	4.31
		8 layers	1.98E-04				0.60	3.34
		Above 8 layers	7.59E-05				0.30	2.05
Activated carbon/CO$_2$	70	-	2.69E-04	6.55E-07	-1.6E-03	1.83	1.20	8.44
	130		9.01E-05	3.05E-07	-8.5E-04	1.69	0.89	5.51
CB-FM/CO$_2$	40	-	5.56E-05	6.55E-05	-9.6E-02	3.45	0.84	26.2
	150		1.91E-05	5.55E-05	-9.6E-02	2.75	4.39	27.3

[a] adsorption

[b] modified LDF

4 Conclusions

The linear driving force (LDF) model is frequently and successfully used for the analysis of adsorption kinetics data of different systems because it is simple, analytic, and physically consistent. Yet, there are some drawbacks of this model, and based on the drawbacks, this study proposes a new modification of the LDF kinetics model. For the two most popular gas-solid adsorption systems, like, adsorption chiller and CCS applications, the modified LDF model has been validated. The proposed modified LDF model successfully predicts the adsorption kinetics of all the studied pairs better than the other models found in the literature. Moreover, for the initial phase and long-time approximation, this model is found equally good. From the RMSD value, it is observed that the modified LDF model gives a better value compared to the original LDF model. The diffusion time constant is also calculated for all studied pairs. Therefore, the proposed model leads to the accurate determination of the dynamic performance of gas-solid adsorption systems in the studied adsorbent/adsorbate pair.

5 List of References

[1] Sun, B., Chakraborty, A. (2015): Thermodynamic frameworks of adsorption kinetics modeling: Dynamic water uptakes on silica gel for adsorption cooling applications. *Energy*, vol. 84, pp. 296-302.

[2] Bhatia, S. K., Bonilla, M. R., Nicholson, D. (2011): Molecular transport in nanopores: A theoretical perspective. *Phys. Chem. Chem. Phys.*, vol.13, pp. 15350–15383.

[3] Glueckauf, E. (1955): Formula for diffusion into sphere and their application to chromatography. *Trans. Faraday Soc.*, vol. 51, pp. 1540–1551.

[4] Haerifar, M., Azizian, S. (2013): An exponential kinetic model for adsorption at solid/solution interface. *Chem. Eng. J.*, vol. 215–216, pp. 65–71.

[5] Azizian, S., Haerifar, M., Bashiri, H. (2009): Adsorption of methyl violet onto granular activated carbon: Equilibrium, kinetics and modeling. *Chem. Eng. J.*, vol. 146, pp. 36–41.

[6] Aristov,Y. I. (2020): Dynamics of adsorptive heat conversion systems: Review of basics and recent advances. *Energy*, vol. 205, pp. 117998.

[7] Sultan, M., El-Sharkawy, I. I., Miyazaki, T., Saha, B. B., Koyama, S., Maruyama, T., Maeda, S., Nakamura, T. (2016): Water vapor sorption kinetics of polymer based sorbents: Theory and experiments. *Appl. Therm. Eng.*, vol. 106, pp. 192–202.

[8] Jribi, S., Miyazaki, T., Saha, B. B., Pal, A., Younes, M.M., Koyama, S., Maalej, A. (2017): Equilibrium and kinetics of CO 2 adsorption onto activated carbon. *Int. J. Heat Mass Transf.*, vol. 108, pp. 1941–1946.

[9] El-Sharkawy, I. I., Saha, B. B., Koyama, S., Ng, K. C. (2006): A study on the kinetics of ethanol-activated carbon fiber: Theory and experiments. *Int. J. Heat Mass Transf.*, vol. 49, pp. 3104–3110.

[10] Aristov,Y. I., Glaznev, I. S., Girnik, I. S. (2012): Optimization of adsorption dynamics in adsorptive chillers: Loose grains configuration. *Energy.*, vol. 46, pp. 484–492.

[11] Raganati, F., Chirone, R., Ammendola, P. (2020): CO2 Capture by Temperature Swing Adsorption: Working Capacity As Affected by Temperature and CO2 Partial Pressure. *Ind. Eng. Chem. Res.*, vol. 59, pp. 3593–3605.

[12] Raganati, F., Alfe, M., Gargiulo, V., Chirone, R., Ammendola, P. (2019): Kinetic study and breakthrough analysis of the hybrid physical/chemical CO2 adsorption/desorption behavior of a magnetite-based sorbent. *Chem. Eng. J.*, vol. 372, pp. 526–535.

Experimental investigation of a double effect adsorption refrigeration cycle driven with low grade heat sources

Atsushi Akisawa[1], **Masahiro Kono**[2]

[1] *Tokyo University of Agriculture and Technology, 2-24-16 Nakacho, Koganei, Tokyo, 184-8588, Japan*
akisawa@cc.tuat.ac.jp
[2] *Tokyo University of Agriculture and Technology, 2-24-16 Nakacho, Koganei, Tokyo, 184-8588, Japan*

Abstract:
This study focuses on a double effect adsorption refrigeration cycle with adsorption heat recovery. It consists of two adsorbent heat exchangers, namely HTC for high temperature cycle and LTC for low temperature cycle. The adsorption heat discharged in HTC is recovered to drive the desorption process of LTC. The objective of this study is to investigate the performance of the double effect cycle experimentally in order to verify the double effect scheme for adsorption refrigeration technologies. In this study, the double effect cycle was actually set up and the experimental results showed that the scheme worked effectively, where the adsorbent of LTC could be regenerated with the hot water from HTC which was driven at 80 degC.

1. Introduction

Adsorption heat pumps are one of the technologies to utilize low grade heat sources less than 100 degC, for example, for producing refrigeration. Most of adsorption chillers are based on the single stage scheme which consists of two adsorbent heat exchangers, an evaporator and a condenser. They have the COP of approximately 0.6 for the driving heat sources of 70-80 degC. To increase the COP, the scheme of double effect cycle is useful. Generally absorption chillers adopt this scheme where the condensation heat of the refrigerant vapor is recovered and used internally in the cycle, which enhances the COP up to 1.3.

The objective of this study is to verify the double effect scheme utilizing adsorption heat internally, which is different from the scheme of double effect absorption chillers. Some studies examined adsorption cycles with the double effect scheme [1,2]. However, the heat source temperature is as high as 200 degC. In contrast, the temperature is less than 100 degC in this study. This study aims at investigating how the proposed double effect scheme works experimentally.

2. Method

2.1. Double effect adsorption cycle

The configuration of the double effect cycle is similar to that of single stage adsorption cycle, which is shown in Figure 1. It should be noted one of the adsorbent heat exchangers works as HTC (high temperature cycle) while the other as LTC (low temperature cycle). LTC is operated with the heat recovered from the absorption process of

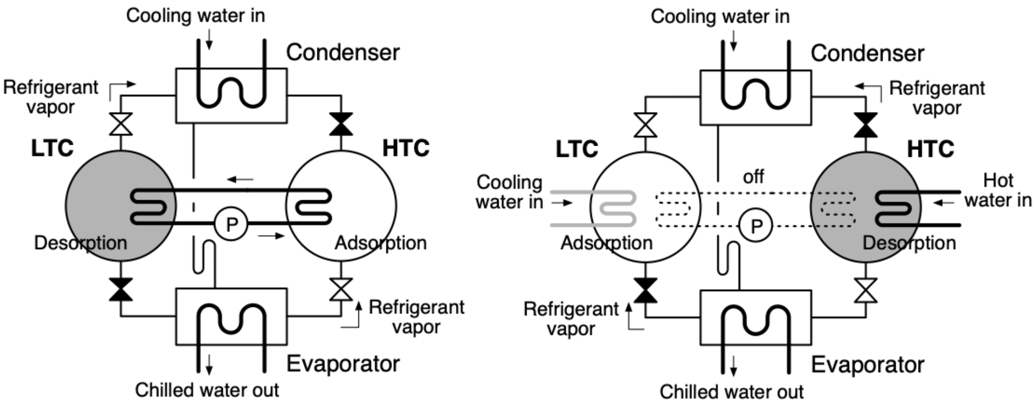

(a) Adsorption heat recovery (b) Desorption by external heat

Figure 1 - Double effect adsorption cycle with adsorption heat recovery

HTC as illustrated in Figure 1(a). A thermal fluid circulates between HTC and LTC to transfer the adsorption heat in order to drive the desorption process of LTC. HTC is the cycle to be driven with an external heat source as Figure 1(b) shows. Because the system uses external heat only for HTC but produces cooling from both HTC and LTC, the COP can be improved from that of the conventional single stage cycle.

In the conventional cycle, the same adsorbent material such as silica gel, for example, is used for two adsorbent heat exchangers. In contrast, different materials are adopted to the proposed cycle because HTC and LTC operate in different temperature range. The authors selected FAM-Z02[3] for HTC and silica gel for LTC based on a simulation study[4] and the material availability.

2.2. Experimental set-up

A small experimental rig was constructed in this study. The refrigerant is water, and the circulating fluid is also water. Silica gel of 0.21 kg and FAM-Z02 of 3 kg are packed in LTC and HTC, respectively. Experimental conditions are the following: the hot water temperature is 80 degC, the cooling water temperature is 25 degC and the chilled water inlet temperature is 12 degC. The total cycle time is 705 sec which consists of the adsorption/desorption time of 270 sec and pre-cooling/pre-heating time of 75/90 sec for HTC. The measurement error of the temperature sensors is 0.6 degC.

3. Results

3.1. Behavior of the cycle

Figure 2 shows the temperature behavior of the inlet and the outlet of the chilled water. It can be confirmed that both of HTC and LTC produce cooling, which means the desorption process of LTC performs with the recovered heat from HTC as expected. It is observed that the cooling output from LTC is decreasing in short time due to the small mass of silica gel in LTC. Consequently the result indicates that the double effect scheme works successfully even at the relatively low temperature of 80 degC.

The temperature of the circulating fluid is shown in Figure 3. When the pre-heating of LTC and the pre-cooling of HTC begin, the fluid starts circulating. Due to the time delay during the circulation, the temperature is oscillating at the beginning, but it finally stabilizes around 50 degC. Even though the temperature difference is very small between the inlet and the outlet, the fluid preferably works to cool down HTC while working to heat up LTC. It is confirmed from the fact that both HTC and LTC work to produce cooling in adsorption phase.

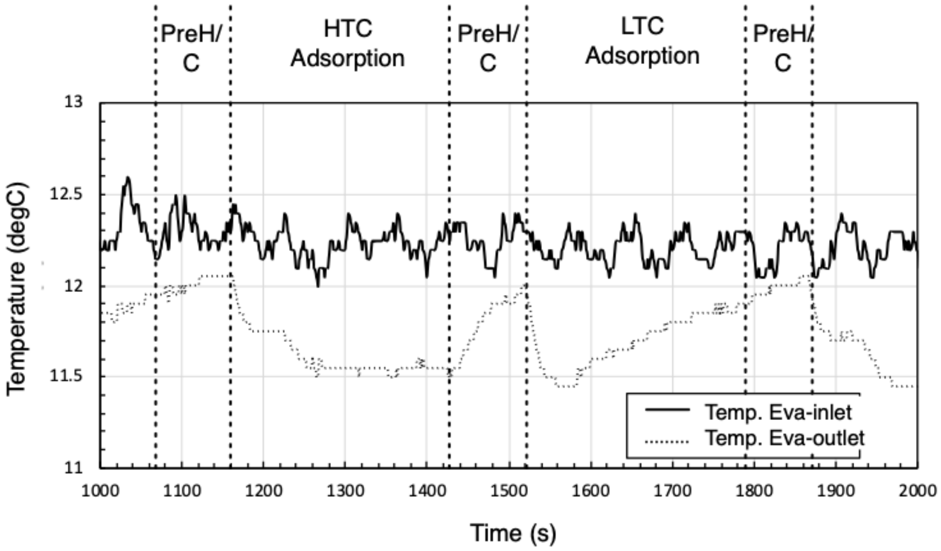

Figure 2 - Temperature of the inlet/outlet of chilled water

Table 1 – COP derived from the experiments. ( ) indicates uncertainty.

Cycle	Cooling output (kJ)	Heating input (kJ)	COP
Double effect cycle	19.97 (0.48)	206.0 (3.5)	0.0970 (0.0028)
Single stage cycle	19.97 (0.48)	445.1 (3.3)	0.0448 (0.0075)

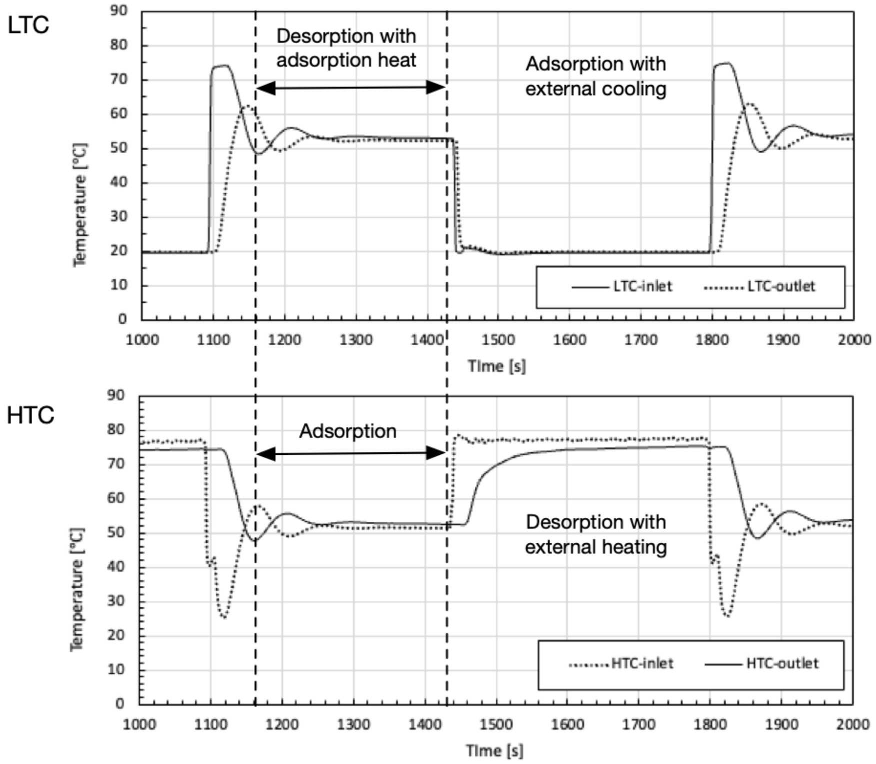

Figure 3 - Temperature of circulating fluid

3.2. COP

Table 1 shows the average COP of the experiments. The observed COP is very low because the experimental rig is small size and was not insulated well. There is no direct experiments of single stage cycle. The COP of single stage cycle is calculated taking into account the internally recovered heat as the external input. According to the result, COP increases from 0.045 to 0.10 by the double effect scheme.

4. Conclusions

This study examined the double effect adsorption cycle internally utilizing adsorption heat experimentally. Both of HTC and LTC successfully works to produce cooling with the double effect scheme at the driving heat source temperature of 80 degC. Even though the cooling power and the COP are yet small due to the small scale experiments, it has been confirmed that the double effect scheme is effective to improve the COP.

Future tasks will be optimization of the cycle time settings to maximize the cooling power and the rearrangement of silica gel mass for LTC.

5. Acknowledgment

The authors thank TANIKAWA FUND PROMOTION OF THERMAL TECHNOLOGY for the financial support to this study.

6. List of References

1. Douss, N., Meunier, F. (1989): Experimental Study of Cascading Adsorption Cycles, *Chemical Eng. Science*, vol.44 (2), pp.225-235.
2. Liu, Y., Leong, K.C. (2006): Numerical study of a novel cascading adsorption cycle, *Int. J. Refrigeration*, vol.29 (2), pp.250-259.
3. Kakiuchi, H., Shimooka, S., Iwade, M., Oshima, K., Yamazaki, M., Terada, S., Watanabe, H., Takewaki, T. (2005): Novel Water Vapor Adsorbent FAM–Z02 and its Applicability to an Adsorption Heat Pump, *Kagaku Kogaku Ronbunshu*, vol.31 (4), pp.273-277. (in Japanese)
4. Tamogami, A., Nakayama, M., Akisawa, A. (2018): Performance Analysis of Double Effect Adsorption Refrigeration Cycle with Adsorption Heat Recovery by Dynamic Simulation, *The 9th Asian Conference on Refrigeration and Air-conditioning*, Sappro, 10-13 June, 2018.

Heat Transfer and Frictional Pressure Drop Characteristics of H_2O/LiBr Solution in Plate Heat Exchanger for Triple Effect Absorption Cycle Application

Song, Joo Young[1], Park, Joon Ho[1], Kang, Yong Tae[†] (Corresponding author)

[1] Graduate school of Mechanical Engineering, Korea University, 145, Anam-ro, Seongbuk-gu, Seoul 02841, Republic of Korea

[†] Department of Mechanical Engineering, Korea University, 145 Anam-ro, Seongbuk-gu, Seoul 02841, Republic of Korea

Abstract:

In this study, single-phase H_2O/LiBr solution heat transfer and frictional pressure drop characteristics in plate heat exchangers (PHEs) for the widest range of LiBr concentration are experimentally evaluated for triple-effect H_2O/LiBr absorption chiller applications. The test PHEs are single-pass heat exchangers with 78.5° and 55.7° chevron angles for high- and low-theta PHEs respectively. Heat transfer and frictional pressure drop experiments in the PHEs were conducted with the concentration range for triple-effect absorption application from 50.21% to 64.92%, solution Reynolds number from 19.39 to 479.10, and Prandtl number from 3.63 to 24.40. All experiments were conducted within ±3% energy balance error range, and the heat transfer and pressure drop correlations developed are applicable within ±10% and ±5% error ranges, respectively.

1 Introduction

An absorption system that separates refrigerants from absorbents using heat energy multiple times in multiple generators is called a multi-effect absorption system. In 2021, a Korean manufacturer is preparing to enter the market by completing the development of a triple-effect absorption system with a coefficient of performance (COP) of 1.65 and integrated part load value (IPLV) [1] of 1.75. The H_2O/LiBr triple-effect absorption systems operate with a wider LiBr concentration range than double-effect absorption systems due to the additional refrigerant generation process.

A solution heat exchanger is essential for improving the COP of absorption systems [2]; however, studies pertaining to it are insufficient. In the development of the triple-effect absorption refrigerator, high performance and compactness of the system are required simultaneously, therefore the application of the PHE to the system is essential. Few researchers evaluated the performance of the PHEs as the solution heat exchanger, but the concentration range of the solution was not wide enough [2-4].

The objectives of this study are to evaluate the single-phase heat transfer and frictional pressure drop characteristics of the H_2O/LiBr solution in the PHE. The findings are then applied to the triple-effect H_2O/LiBr absorption cooling system; hence, experiments were performed for the widest range of LiBr concentration compared with that of other relevant studies.

2 Experiment

Figure 1(a) shows the schematics of the experimental apparatus. The experimental apparatus consisted of two solution loops; a high-temperature solution and a low-temperature solution. Both solution tanks were equipped with three heaters; one 3 kW heater and two 5 kW heaters. The temperature of hot side solution was controlled by only the heaters. The temperature of the cold-side solution was controlled by heaters, followed by the secondary fine adjustments in an auxiliary PHE. In the auxiliary PHE, the heat exchange between the cold-side solution and cooling water occurs; therefore, the cold-side solution releases additional thermal energy. Figure 1(b) shows the schematics of the test PHEs, and the specifications of the PHEs are summarized in Table 1.

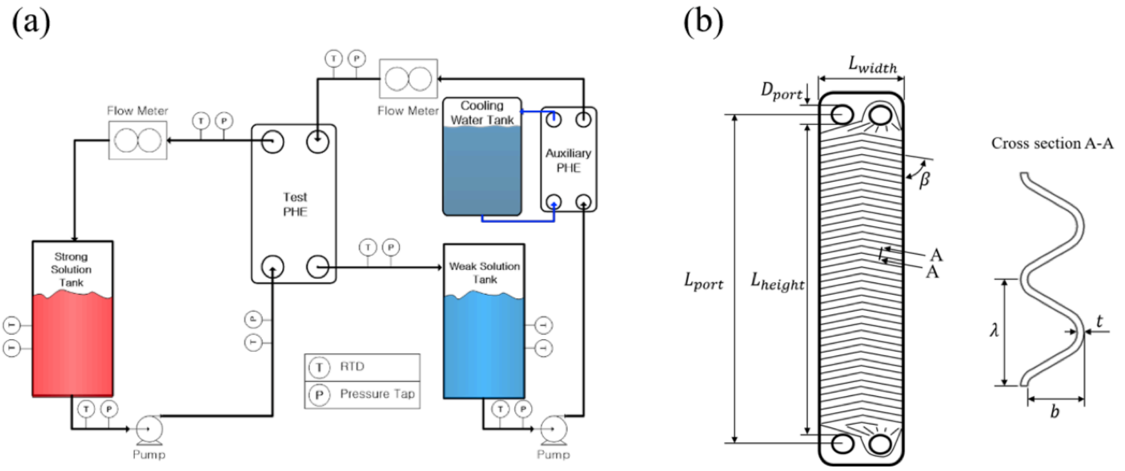

Figure 1 – Schematics of experimental apparatus(a) and test plate heat exchanger(b)

Table 1 – Geometric conditions of the test plate heat exchanger

Port to port length, m	L_{port}	0.466
Plate height, m	L_{height}	0.4315
Plate width, m	L_{width}	0.111
Plate thickness, m	t	0.0004
Corrugation depth, m	b	0.002
Corrugation length, m	λ	0.007
Port diameter, m	D_{port}	0.0345
Chevron angle, °	β	78.5 (High-theta) 55.7 (Low-theta)

RTDs and pressure sensors were installed as close as possible to the inlet and outlet of the test PHE. The hot-side solution flows from the bottom to the top, whereas the cold-side solution flows from the top to the bottom; both solutions were arranged with a single pass and a counter flow in the test PHE. The experiment was conducted for more than 20 min under steady state, and all measured data were recorded every 5s. All heaters were on/off controlled with the solution temperature, and the pumps were controlled by inverters.

The concentration of the solution was controlled by refrigerant absorption and generation. When distilled water was added to the low-temperature solution in a vacuum state, the concentration of the solution was reduced. By contrast, when steam was released from the solution by heating, the concentration of the solution increased. The concentration, which is a function of temperature and pressure, was calculated using the measured temperature and pressure of the solution in the tank. The properties of the solution were calculated using an Engineering Equation Solver (EES).

3 Results

Energy balance error refers to the difference in heat transfer rate between the hot- and cold-side solution in the PHE. In this study, heat transfer experiments were conducted within ±3% energy balance error in the high- and low-theta PHEs. Figures 2(a) and 2(b) show the Nusselt numbers with various Reynolds numbers in the high- and low-theta PHEs. As shown in Figures 2(a) and 2(b), Nusselt number increased with Reynolds number and Prandtl number. Prandtl number of the solution increased as the LiBr concentration increased and the temperature decreased. A high Prandtl number indicates a high Nusselt number within a similar Reynolds number range. The heat transfer experiments in the PHEs were conducted with the wide LiBr concentration ranging from 50.21% to

64.92% and 50.71% to 64.76%, respectively. The experimental conditions for heat transfer tests in the PHEs are summarized in Table 2. Nusselt numbers in the PHEs were obtained by the Wilson plot method [5, 6].

Based on the experimental results, the heat transfer correlations were developed for each PHE as Eqs. (1, 2).

$$\mathrm{Nu} = 0.2597\, Re^{0.677}\, Pr^{0.413} \text{ (High-theta PHE)} \tag{1}$$

$$\mathrm{Nu} = 0.2446\, Re^{0.676}\, Pr^{0.319} \text{ (Low-theta PHE)} \tag{2}$$

The correlations are applicable within ±9.87% and ±9.78% for high- and low-theta PHEs, respectively.

Table 2 – Experimental conditions (Heat transfer test)

	High-theta PHE	Low-theta PHE
LiBr Concentration, %	50.21-64.92	50.71-64.76
Inlet Solution Temperature, $^{\circ}C$	23.16-149.80	19.16-148.20
Inlet solution Flow Rate, $10^{-3}\,kg/s$	4.90-31.03	5.05-29.55
Reynolds Number	35.00-475.30	19.38-479.10
Prandtl Number	3.83-24.41	3.88-22.19

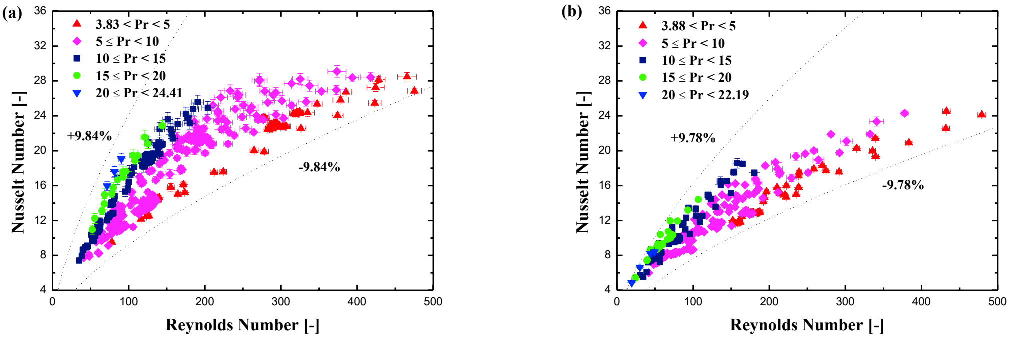

Figure 2 – Nusselt numbers with various Reynolds numbers in the high-theta PHE(a) and in the low-theta PHE(b)

Figures 3(a) and 3(b) show the friction factor with various Reynolds number in the high- and low-theta PHEs. As shown in Figures 3(a) and 3(b), the friction factors decreased as the Reynolds number increased, indicating that the frictional pressure drop increased with the flow rate. The frictional pressure drop experiments in the PHEs were conducted with the wide LiBr concentration ranging from 50.21% to 62.05% and 50.71% to 59.13%, respectively. The experimental conditions for pressure drop tests in the PHEs are summarized in Table 3.

The fanning friction factor, for convenience, is calculated using the mass flux for a single channel as shown in Eq. (3)

$$\mathrm{f} = \frac{dP_f}{4\left({L_{eff}}/{D_{hyd}}\right)\left({\rho V_{ch}{}^{2}}/{2}\right)} = \frac{dP_f}{4\left({A_{tot}}/{A_{cross}}\right)\left({G_{ch}{}^{2}}/{2\rho}\right)} \tag{3}$$

Based on the experimental results, the friction factor correlations were developed for each PHE as Eqs. (4, 5).

$$\mathrm{f} = 3.124 + 461.6/Re^{1.112} \text{ (High-theta PHE)} \tag{4}$$

$$\mathrm{f} = 2.639 + 438/Re^{1.132} \text{ (Low-theta PHE)} \tag{5}$$

The correlations are applicable within ±4.88% and ±4.85% for high- and low-theta PHEs, respectively. The form of the friction factor correlation was selected, according to Focke et al. [7].

Table 3 – Experimental conditions (Pressure drop test)

	High-theta PHE	Low-theta PHE
LiBr Concentration, %	50.21-62.05	50.71-59.13
Inlet Solution Temperature, $^{\circ}C$	133.80-149.80	130.50-148.70
Inlet solution Flow Rate, $10^{-3}\,kg/s$	5.21-30.43	5.25-28.92
Reynolds Number	52.68-536.90	57.92-580.60

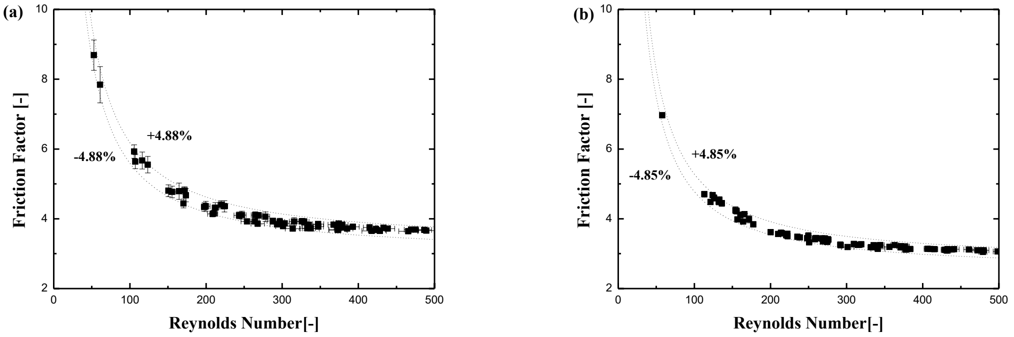

Figure 3 – Friction factor with various Reynolds number in the high-theta PHE(a) and in the low-theta PHE(b)

4 Conclusions

In this study, the heat transfer and frictional pressure drop characteristics of a H_2O/LiBr solution in the high- and low- theta PHEs were evaluated with wide LiBr concentration range for the triple-effect absorption refrigerator applications. New experimental heat transfer and frictional pressure drop correlations were developed. All experiments were carried out within $\pm 3\%$ energy balance error range.

(1) Based on the experimental results, the new heat transfer correlations were developed and were applicable within $\pm 10\%$ error range for the plate heat exchangers as $\mathrm{Nu} = 0.2597\, Re^{0.677}\, Pr^{0.413}$ and $\mathrm{Nu} = 0.2446\, Re^{0.676}\, Pr^{0.319}$ for the high- and low-theta PHEs, respectively.

(2) Based on the experimental results, the new fictional pressure drop correlations were developed and were applicable within $\pm 5\%$ error range for the plate heat exchangers as $\mathrm{f} = 3.124 + 461.6/Re^{1.112}$ and $\mathrm{f} = 2.639 + 438/Re^{1.132}$ for the high- and low-theta PHEs, respectively.

5 Acknowledgment

This work was supported by the Korea Institute of Energy Technology Evaluation and Planning (KETEP) and the Ministry of Trade, Industry & Energy (MOTIE) of the Republic of Korea (No. 10060218).

6 List of References

[1] Yu, F.W., & Chan, K.T. (2009): Environmental performance and economic analysis of all-variable speed chiller systems with load-based speed control, *Applied thermal engineering.*

[2] Song, J.Y., Lee, J.W., Kang, Y.T. (2019): Comparisons of Nu correlations for H2O/LiBr solution in plate heat exchanger for triple effect absorption chiller application, *Energy*. [4]

[3] Kim, H.J., Kim, J.H., Kim, S.S., Jeong, J.H., Kang, Y.T. (2005): Heat Transfer and Pressure Drop Characteristics of Plate Heat Exchangers for Absorption Application, *Proceedings of the SAREK Conference*.

[4] Kwon, O.K., Cha, D.A., Yun, J.H., Kim, H.S. (2009): Performance Evaluation of Plate Heat Exchanger with Chevron Angle Variations, *Transactions of the Korean Society of Mechanical Engineers B*.

[5] Wilon, E.E. (1915): A basis for rational design of heat transfer apparatus. *The Journal of American Society of Mechanical Engineers.*

[6] Fernandez-Seara, J. Uhía, F.J., Sieres, J. Campo, A. (2007): A general review of the Wilson plot method and its modifications to determine convection coefficients in heat exchange devices. *Applied Thermal Engineering.*

[7] Focke, W.W., Zachariades, J., Oliver, I. (1985): The effect of the corrugation inclination angle on the thermohydraulic performance of plate heat exchangers. *International Journal of Heat and Mass Transfer.*

Thermally driven Ice Slurry generation for Heating and Cooling Applications – TAFEis

Tillmann, Christine[1], Richter, Lutz[1], Safarik, Mathias[1], Kemmerzehl, Christian[2]

[1] Institute of Air Handling and Refrigeration, Applied Energy Engineering Department, Bertolt-Brecht-Allee 20, 01309 Dresden, Germany

[2] WEGRA Anlagenbau GmbH, Oberes Tor 106, 98630 Römhild, Germany

Abstract:
The objective of the TAFEis project (thermally driven ice slurry generation for heating and cooling applications) is the development of a thermally driven ice slurry generation plant in order to be able to generate coolant temperatures of less than 0 °C. For this purpose, various additives for the evaporator will be investigated in order to determine one which makes the direct evaporation process more efficient under given criteria. Moreover, the absorption process also has to be adapted to the target temperature in the evaporator. A successful development of such a technology opens up a variety of new fields of application by combining the advantages of the vacuum ice slurry generation technology and the absorption chiller.

1 Introduction

The TAFEis project is part of the SubSie project network. The goal of the SubSie-project is to expand the application range of refrigeration systems and heat pumps using water as a refrigerant and driven by heat. As a result, energy saving potential can be exploited in the provision of cooling and heating through waste heat utilization.

Within TAFEis, the absorption refrigeration process will be coupled with a direct evaporator. The plant configuration is intended to provide coolant temperatures below 0 °C in the form of ice slurry. This is a prerequisite for opening up new fields of application. In addition, the advantages of both technologies can be used, including waste heat recovery, pumpability of the ice, use of the ice slurry as a storage medium, the higher storage capacity of ice slurry compared to water, and therefore smaller pipe dimensions for cold distribution.

2 Project Targets and Challenges

The main objective of the TAFEis project is the development and construction of a thermally driven ice slurry generation system by using direct evaporation as well as its testing and demonstration of functionality.

The functional model to be developed will have a cooling capacity range of 15 to 25 kW or 25 to 42 kW heating capacity in heat pump mode according to the testing conditions in the ILK laboratory. This chosen capacity range allows scaling to higher capacity ranges.

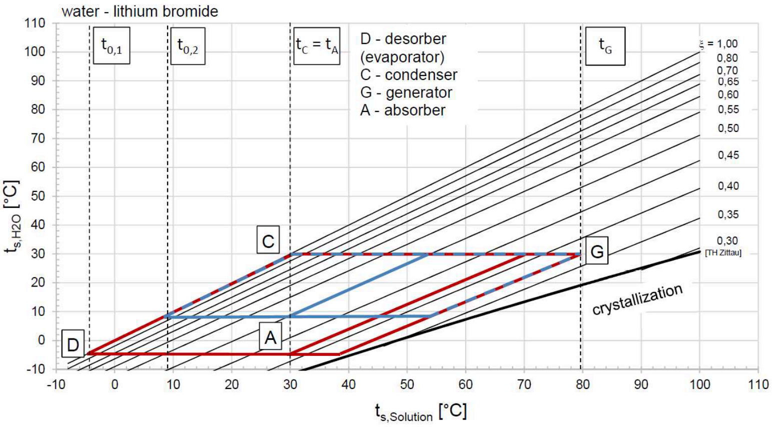

Figure 1 – Principle graph of the comparison of different evaporation temperatures and the influence on the cycle (crystallization risk)

The functional model will be used to determine the limits of the ice slurry absorption heat pump process with water lithium bromide in terms of temperatures and efficiency. These results are transferable to an operating mode as an absorption chiller with regard to the required drive and re-cooling temperatures.

The risk of crystallization in water-lithium bromide cooling systems requires special attention in thermal ice slurry generation. Figure 1 shows the Dühring diagram with the crystallization line according to [3]. The diagram shows an absorption cycle for the supply of air-conditioning refrigeration (blue) and a cycle for the supply of temperatures below 0 °C (red). It can be clearly seen that as the evaporation temperature decreases, the cycle approaches the crystallization line. The lowering of the evaporating temperature is also combined with a reduction in cooling capacity. Reducing the evaporating temperature in a water-lithium bromide absorption cycle at constant cooling capacity can be achieved either by increasing generator operating temperature or by decreasing cooling water temperature. Both lead to a further increase in the risk of crystallization, as can be seen from figure 1.

By using a direct evaporator, where ice is generated directly in the refrigerant of the evaporator, the highest possible evaporation temperature for ice generation is achieved, because an additional temperature difference for heat transfer can be avoided. The ice slurry is pumpable due to the addition of additives and can therefore be used directly as a coolant.

3 Investigation areas

To achieve coolant temperatures below 0 °C, an additive lowering the freezing point has to be added to the refrigerant in the evaporator. In a literature research, additives that are already in use in the field of ice slurry generation were analyzed. From the comparison of the data as well as own investigations, a selection of additives for further investigations was made. For these additives, thermodynamic and physical properties such as the influence on the vapor pressure of the solution, the dynamic viscosity and the pressure drop will be determined. In the following, an additive will be selected for further investigation of the determination of the system limits of the functional model that will be developed. Table 1 shows the additive selection made for the thermodynamic and physical property data investigations. The additive quantity in w% given in Table 1 refers to a freezing point depression of 5K.

Table 1 – first additive selection

additive	sum formula	[w%$_{FP\,-5\,°C}$] [1][2][3]	dyn. viscosity [cP][1][2][3]*,**	density [kg/m³][1][2][3]*,**	WHC
potassium formate	K(HCOO)	10,15	1,18	1061	1
glucose	$C_6H_{12}O_6$	30,92	3,15	1131	1
propylene glycol	$C_3H_8O_2$	15,30	1,72	1011	1
ethanol	C_2H_6O	11,12	1,60	980	1
lithium bromide	LiBr	10,45	1,60	1072	1

* at 20 °C, ** for mixtures t_{FP} = -5 °C, FP – freezing point, WHC – water hazard class

Compared to other salts such as sodium chloride or lithium bromide which are used as additives to lower the freezing point, *potassium formate* is less corrosive to steel and stainless steel. In addition, potassium formate is less viscous than other additives at the reference point of t_{FP}, which has a positive effect on the transport properties of the liquid ice. Although *glucose* has a high dynamic viscosity at the reference point (t_{FG} = -5 °C) compared to the other selected additives, it is expected that the ice slurry generated with glucose shows good rheological properties. This is due to the higher mass fraction at the same freezing point depression. [4] *Propylene glycol* exhibits low viscosity with slightly higher additive mass fraction to achieve the same freezing point depression. *Ethanol* also has low dynamic viscosity and leads to good rheological ice slurry properties. [4] The database of thermodynamic and physical properties is comprehensive. *Lithium bromide* was selected despite its high price and rather unfavorable corrosion properties because it offers favorable process engineering solutions for special applications. It is already used as a sorbent in the plant circuit. Another advantage of lithium bromide is that a good database for thermodynamic and physical properties already exists and it will therefore be used as a reference for comparisons and initial investigations. All selected additives are classified in the lowest water hazard class 1.

A potential additive should only lead to a slight vapor pressure depression. The low evaporation temperature needed for ice slurry generation already reduces the pressure already and thus the absorption capacity of the solution in the absorber. A further reduction in pressure through the additive would further reduce the absorption capacity. Therefore, studies on the saturation vapor pressure of the solution as a function of the additive will be investigated for the selected additives within the project.

In addition to the qualification of a suitable additive, another focus of the funded project, as already mentioned, is the design, construction, implementation and measurement of a functional model for thermal ice slurry generation. The basis for the functional model to be developed is a commercially available absorption refrigeration plant type Maral of the company EAW. In this plant, asymmetric plate heat exchangers are used for the main components evaporator, absorber, condenser and generator. For the evaporator, a direct evaporator will replace the plate heat exchanger. A construction design will be developed that allows a simple production engineering implementation and makes a low specific plant volume feasible. A simplified PID of a possible integration variant is shown in Figure 2.

In addition, aspects such as avoiding additive carryover, the absorber design under the given conditions and the dimensioning of the solution heat exchanger must be taken into account during the design implementation of the plant in order to develop an optimally operating system. Further points of the investigations are: the distribution of the refrigerant in the direct evaporator, the optimal integration of an agitator for homogeneous mixing of the ice slurry, the optimal ice fraction depending on the additive, avoiding the reduction of the heat and mass transfer surface due to the ice fraction, the design of the inlets and outlets to avoid blockages and the optimization of the ice slurry transport.

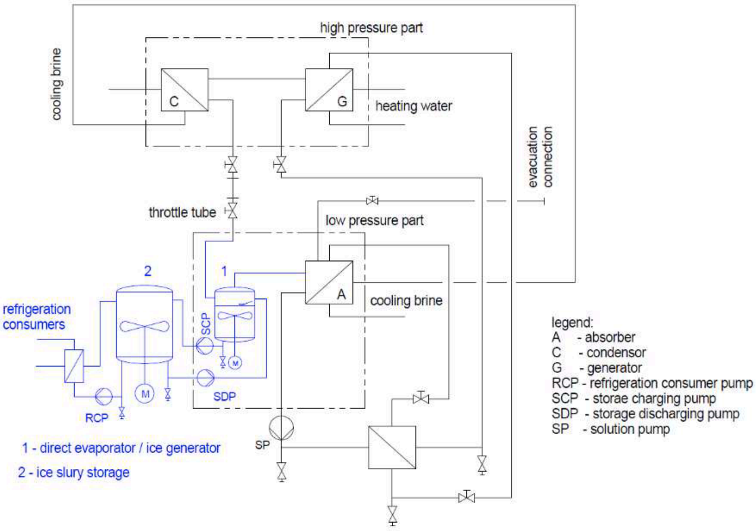

Figure 2: simplified PID of an absorption chiller with direct evaporation

4 Results

For the development of an optimally operating thermally driven ice slurry generation plant, it is necessary to analyze and evaluate the effects of using additives in the evaporator and the influence of low evaporation temperatures on the thermodynamic cycle. The study of the absorption cycle is followed by the integration of the direct evaporator into the plant and its measurement.

In the first step, a water-lithium bromide absorption cooling system was investigated at low coolant outlet temperatures. The test plant is a modified plant of the type MARAL from the company EAW. No design changes were made to the experimental plant for ice slurry generation. Lithium bromide solution with 15w% (corresponding to a freezing point tFP = -8.1 °C) was filled into the evaporator in order to be able to evaluate just the evaporation capacity at low evaporation temperatures without ice generation using different additives. The evaporator operates as a desorber and the experimental plant in a modified resorption mode. The results form the basis for dimensioning the functional model.

Results of the measurements are shown in figure 3. The absorption capacity decreases at lower temperatures and thereby lower pressures. Nevertheless, - 5 °C coolant outlet temperature and about 50% of the nominal cooling capacity of the air-conditioning chiller were achieved at only 85 °C heating water inlet temperature. As the cooling capacity decreases with decreasing coolant outlet temperature (see Figure 3, right), the absorber is oversized for this operating mode. Therefore, the logarithmic temperature difference in the absorber decreases. The absorber is sufficiently dimensioned for the application.

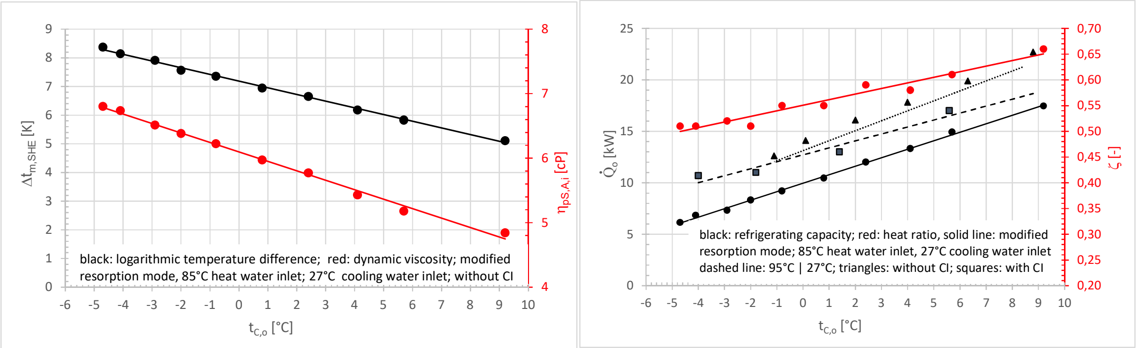

Figure 3 – left: logarithmic temperature difference of the solution heat exchanger and dynamic viscosity (poor solution absorber outlet, $\eta_{ps,A,i}$*) as a function of the coolant outlet temperature (*$t_{C,o}$*); right: cooling capacity (*$\dot{Q}_0$*) and heat ratio (*ζ*) as a function of the coolant outlet temperature*

In the left figure, it can be seen that the temperature difference in the solution heat exchanger ($t_{m,SHE}$) increases at lower coolant outlet temperatures ($t_{C,o}$). This is because the lithium bromide concentrations of the poor and rich solutions are higher at lower coolant outlet temperatures than at higher coolant outlet temperatures. Related to this, the solution has higher viscosity and lower heat capacity, which reduces the heat transfer. The solution heat exchanger has to be modified for the new operating conditions.

Figure 3, right, also shows measurements with a heating water inlet temperature of 95 °C with and without the addition of a crystallization inhibitor (CI) in the absorption solution circuit. An ionic liquid patented for this application was used as crystallization inhibitor. Without crystallization inhibitor, measurements had to be stopped at coolant outlet temperatures below ¬1 °C because crystallization occurred. With crystallization inhibitor, coolant outlet temperatures of up to ¬5 °C could be achieved. Thus, the operating range of the system can be significantly extended by using a crystallization inhibitor.

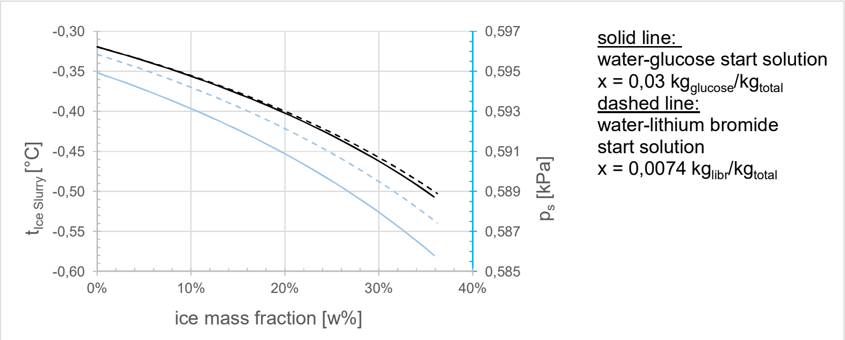

Figure 4: Ice slurry temperature ($t_{Ice\ Slurry}$*) and saturation vapor pressure (*p_s*) as a function of the ice mass fraction*

Figure 4 shows the freezing point depression and the vapor pressure depression as a function of the ice mass fraction for glucose and lithium bromide, respectively, as an additive for ice slurry generation. The difference in freezing point depression between glucose and lithium bromide is small in the freezing point range considered (black lines). The vapor pressure depression is also small for both and the effect on the absorption process is marginal (see Figure 4, blue lines). It is astonishing that at a melting point depression of 0.18 K (from ¬0.32 °C to ¬0.5 °C), the ice mass fraction in the ice slurry is already 30w%.

5 Acknowledgment

We like to thank the Federal Ministry for Economic Affairs and Energy for the funding of the development project (03EN2046A).

6 List of References

[1] Melinder, Å. (2010): Properties and other aspects of aqueous solutions used for single phase and ice slurry applications

[2] Lide, R. (2003): CRC Handbook of Chemistry and Physics, National Institute of Standards and Technology

[3] Kretzschmar, H.-J., et al. (2004): thermo physical property program, library for water/lithium bromide mixtures (TH Zittau) based on reference equations of Kim and Infante Ferreira

[4] Koffler, M. (2019): Partikelagglomeration und Partikelgrößenverteilung beim Speichern von Eisbreigemischen

Hydrothermal stress test - Investigation on zeolite 13X and Al-fumarate for their application in open heat storage application

Lina Rustam[1], Stephan Ruh[1], Philipp Hügenell[1], Sebastian-Johannes Ernst[1], , Stefan Henninger[1]

[1] Fraunhofer Institute for Solar Energy Systems ISE, Heidenhofstr. 2, 79110 Freiburg, Germany,
lina.rustam@ise.fraunhofer.de

Abstract:
This paper presents the results of an approach for accelerated ageing of the well-known adsorbents zeolite 13X, shaped in binder-free granules, and Al-fumarate and the characterisation of the degradation mechanisms. The approximation of a temperature-dependent degradation function is applied based on the approach of van't Hoff, a simplified approach of Arrhenius. Due to unknown degradation mechanisms activation energies were assumed for e.g. ligand displacement and hydrolysis.

1 Introduction

Heat storage, dehumidification and heat pumps are an important part of future development and contribute greatly to CO2 reduction. It is known from previous studies that sorption materials such as zeolites and MOFs are stable under the boundary conditions of thermally driven adsorption heat pumps and chillers. [1,2] With regard to stability, numerous studies, including stress tests, have been carried out, which include static and multi-cyclical stability studies with differently selected test parameters [2]. With regard to their applications, these results give less insight into performance over their lifetime if used as material in heat pumps or dehumidification rotors, as assumed. However, it is unclear if the materials are suitable for storage applications in open systems. Dynamic cyclization experiments on pelleted binderless 13X have already been described by Storch et al. [4]

The aim of this public funded project DEGRATEST is to develop a thermally accelerated ageing process to test the materials with regard to their durability. Knowledge of the degradation mechanism and the corresponding activation energies is necessary. Activation energies known from literature are in the range of 50 - 250 kJ/mol based on the degradation mechanism, which is mainly related to a ligand displacement for MOFS - exchange of a linker molecule, e.g. with an OH group [3]- or the bond breakage of Si-O bonds in the tetrahedral structure of zeolitic materials. The degree of degradation of the materials should be derived by subsequent characterization by N2-physisorption, PXRD and water absorption and give a conclusion about the lifetime of the materials.

2 Experimental Set-up

2.1 Materials and stress test procedure

The materials used (granulated binderfree 13X zeolite, aluminium fumarate, fluoride free MIL100(Fe)) are used without further treatment or purification. For thermal aging, the named materials are exposed to defined temperatures for a period of 11 days. Since it is known that the desorption process in particular is a major stress factor, high temperatures with low moisture content were selected as the stress temperatures [2,4,5].

With an appropriate humidity generator the samples are constantly circulated with a humidity flow of 0.08 nL/min. The humidity test corresponds to a dew point of 19°C and 27°C. Synthetic air is used as the carrier gas in order to simulate the real boundary conditions in the best possible way.

The exposure time is based on the approach of Arrhenius and is as follows

$$t_{ST} = t_{SL} \cdot e^{-\frac{Ea}{R}\cdot\left(\frac{1}{T_{SL}}-\frac{1}{T_{ST}}\right)}$$

with the accelaerated stress test time t_{ST} and temperature T_{ST}, respectivly the service life time t_{SL} and temperature T_{SL}. E_a and R represent the activation energy and the general gas constant. Figure xy shows the exposure time plotted against the activation energy for different temperatures.

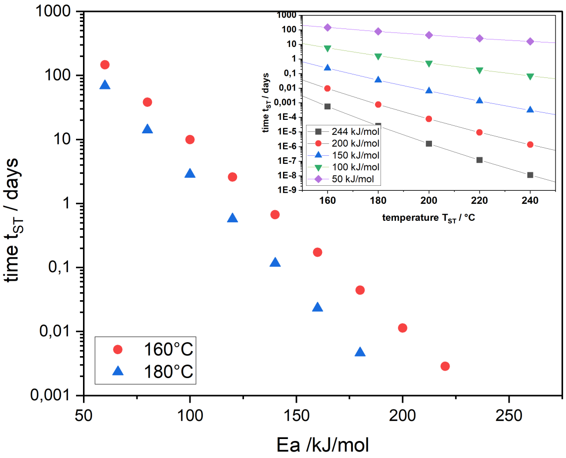

Figure 1 Time of stress test over the activation enegies related to hydrolysis reactions and ligand displacement reactions for MOFs.

2.2 Characterisation of Sorption Materials

The characterization was carried out before (untreated) and after exposure using N2 physisorption, PXRD in the angular range of 2 theta = 2.5 - 55 °. In addition, the gravimetric determination of the water absorption was carried out at 20°C for 72 hours over a relative humidity of 23% for 13X zeolite and aluminium fumarate over 44%, respectively. Al fumarate was picked

3 Results

The nitrogen isotherms with the corresponding DFT-fits over the range of the micropore volume is shown in Figure 2. For the 13X zeolite, the loading capacity decreases with increasing stress, while for the isotherms an increasing slope can be observed. With increasing stress, the adsorption capacity decreases, especially in the microporous range (p/p0 0.1) and forms a stronger hysteresis above p/p0 > 0.4, which is maximal for 180DP27.
This indicates that there is an increase in pores in the mesoporous region. The application of the pore diameter over the differentiated pore volume confirms, in accordance with the N2 isotherms (see inlet Figure 2), that a strong degradation takes place in the microporous region and is accompanied by an increase in pore diameter due to capillary condensation at p/p0 > 0.4.

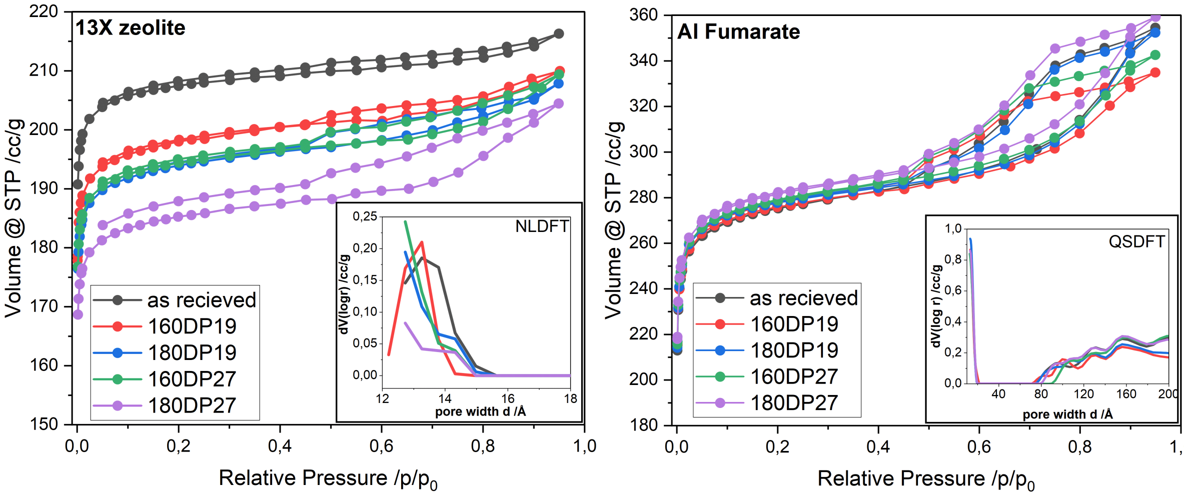

Figure 2 Nitrogen physisorption isotherms at 77 K The inlet vizualize the corresponding differential pore width.

From the isotherms it can be deduced that the moisture has a higher influence on the degradation of the 13X zeolite. The steady increase in hysteresis of the 13X zeolite with increasing load stress is striking indicating that dealumination reactions take place. The removal of aluminium from the network can lead to bimodal distributions or, as assumed here, to a collapse of the micropore structure into mesopores. Further investigations using XPS and/or IR [7] are necessary to prove dealumination. Compared to the 13X, the aluminium fumarate shows a slight increase over the entire sorption range, which tends to increase with higher stress.

From the XRD datas in Figure 3 can be seen that the crystallinity for the 13X zeolite decreases with increasing stress. The determination of the decrease in crystallinity was done by comparing the 2 theta values at 6.16° which refers the miller index (*100*).

The aluminium fumarate, on the other hand, generally shows the lowest reflex intensities for the 160DP19 stress test, although this may also be due to the load condition depending on the environmental humidity of the sample at the time of measurement. A definite statement cannot be derived from the XRD data for the aluminium fumarate.

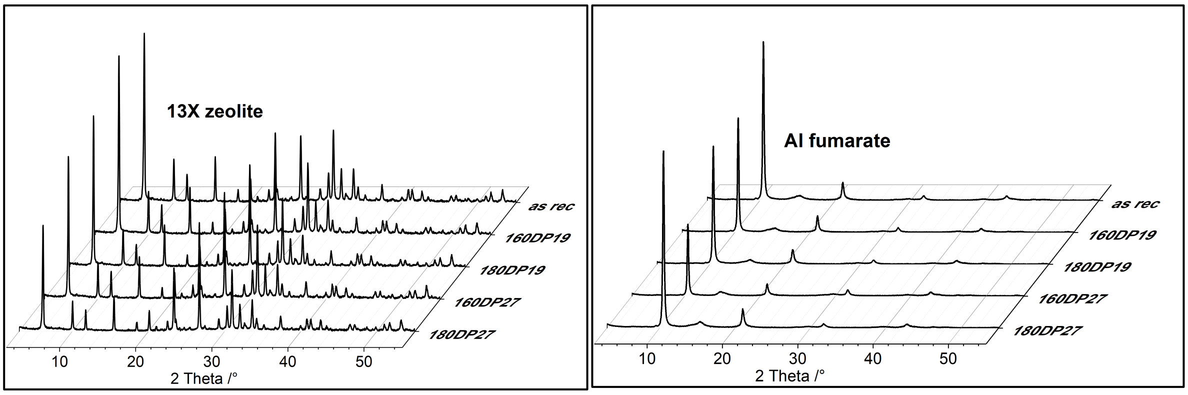

Figure 3 XRD datas of 13X zeolite and aluminium fumarate oft he as recieved and accelerated stress test samples.

In Figure 4Figure 4 the adsorption capacity of the loaded materials shows, like the previous results, a decrease for the 13X, respectively an opposite behaviour of the Al fumarate for increasing stress. For Al fumarate, the result again indicates that the hydrothermal stress partially removes synthesis residues and is responsible for the indifferent behaviour.

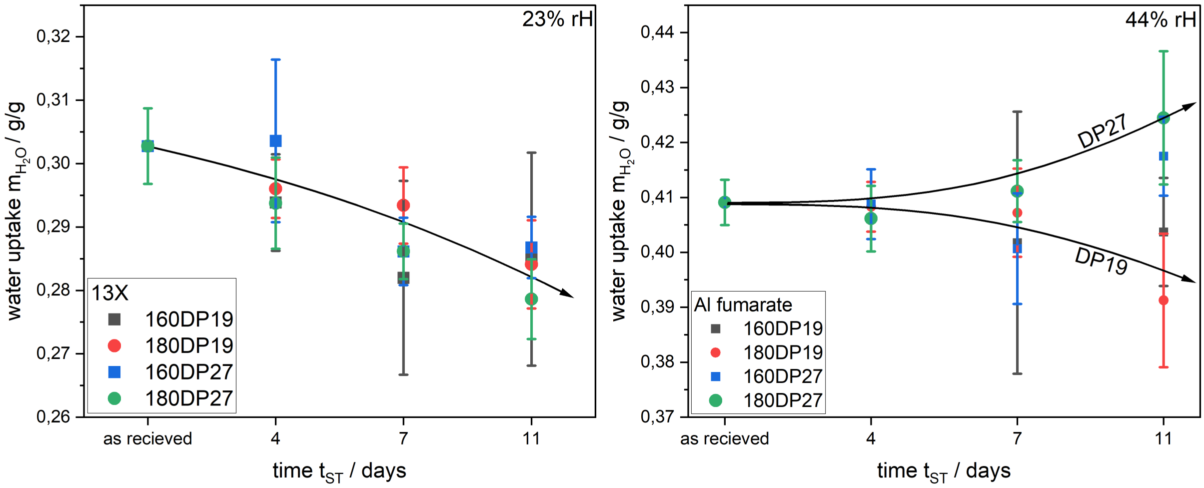

Figure 4 Gravimetric water adsorption capacity after 72 hours exposure in an dessicant at 23 % relative humidity for 13X and 44 % relative hymidity for Al fumarate.

4 Summary and Conclusions

In order to derive correlations, datas of the 13X Zeolite and Al fumarate are summarized in Table 1 Summary of the results for 13x and Al fumarate

Table 1 Summary of the results for 13x and Al fumarate

13X	S_{BET} m^2/g	V_{micro} cc/g	V_{cum} cc/g	$m_{H2O\ (rH=23\%)}$ g/g	XRD Relative
As received	863	0.35	0.36	0.303	100%
160DP19	818	0.33	0.35	0.285	106%
180DP19	799	0.32	0.35	0.284	85%
160DP27	802	0.32	0.35	0.287	86%
180DP27	763	0.30	0.33	0.279	63%
Al fumarate	S_{BET} m^2/g	V_{micro} cc/g	V_{cum} cc/g	$m_{H2O\ (rH=44\%)}$ g/g	XRD Relative
as received	1097	0.40	0.52	0.409	---
160DP19	1099	0.40	0.49	0.404	---
180DP19	1111	0.40	0.52	0.391	---

160DP27	1115	0.41	0.51	0.418	---
180DP27	1124	0.41	0.53	0.424	---

This results indicates that derivation of an accelerated stress test on MOFs, represented by the Al fumarate, seems to be generally difficult, since their synthesis routes depend on the precursors used, and preparation and purification steps also have an influence on the procedure. This has also been shown in the investigation for other MOFs, as the measurement results suggest that synthetic residues in the material are removed by the stress tests. Extensive analyses are required to confirm the presumption of synthesis residues in MOFs.

In contrast, the 13X shows a linear decrease in performance, which is reflected in all analysis methods.

It has been shown that higher humidity levels have a greater influence on degradation.

In order to get a better insight into the degradation and therefore to derive an accelerated aging process, exposure over a longer period of time is necessary. Also additional analysis.

5 Acknowledgment

The work was carried out within the project DEGRATEST, funded by the German Federal Ministry for Economic Affairs and Energy under funding reference code 03ET1615

6 List of References

[1] Henninger, S. K., Schmidt, F. & Henning, H.-M. *Appl. Therm. Eng*. 30, 1692–1702 (2010).

[2] Henninger, S. K., Hügenell, P.P.C., Munz, G., Baumgartner, M., Kummer, H., Jeremias, F. *Abschlussbericht Stabisorp-2* (2015).

[3] Low, J.J., Benin, A.I.,Jakubczak, PP., Abrahamian, J. F.; Faheem, S. A.; Willis, R. R., *J. Am. Chem. Soc*. **131**, 15834-15842 (2009)

[4] Storch G., Reichenauer G., Scheffler F., Hauer A.; *Adsorption* 14, 275-281 (2008)

[5] Fischer F., Lutz W., Buhl J.-C., Laevemann E., *J. Micro Meso* 262, 258-268 (2017),

[6] Sachse A., Grau-Atienza A., Jardim E.O., Linares N., Thommes M., Garcia-Martinez J., *Cryst. Growth Des*. 17,4289-4305 (2017)

[7] Lutz W., Rüscher C.H., Gesing Th.M., Stöcker M., Vasenkov S., Freude D. Gläser R., Berger C., *Studies in Surface Science and Catalysis* 154, 1411 – 1417 (2004)

[8] Ristic A., Fischer F. Hauer A., Zabukovec Logar N., *J. Mater. Chem. A* 6, 11521-11530 (2018)

The preparation of an aluminum composite adsorbent by anodizing technique for adsorption chiller.

Chumnanwat, Suppanat[1], Ota Shinji[1], Tanaka Tsutomu[1], Okada Hiroki[1], Kodama Akio[2], Kumita, Mikio[2]

[1] *Graduate School of Science and Technology, Kanazawa University, Kakuma-machi, Kanazawa-shi, Ishikawa, 920-1192, Japan*

[2] *Institute of Science and Engineering, Kanazawa University, Kakuma-machi, Kanazawa-shi, Ishikawa, 920-1192, Japan (kumita@se.kanazawa-u.ac.jp)*

Abstract:
The layer thickness and effective heat transfer are important parameters to enhance the adsorption rate of adsorbent and cooling and/or heating performance of adsorption refrigeration systems. The aluminum plate surface was modified into spike-type and barrier layer-type aluminum oxide films by anodizing and etching. This preparation method yields a 123 µm spike layer for the former and a 67 nm solid layer for the latter. A synthetic zeolite was used as an adsorbent coated on the modified surfaces by using 3-trimethoxysilylpropyl chloride for bonding between zeolite particles and the modified surface. The spike height and the film thickness could be generally controlled by the anodizing and etching times. The bonding strength between zeolite particles and the modified surface was determined to evaluate the benefit of the surface modification. The barrier layer-type film provided a higher strength zeolite layer on its surface. According to the adsorption dynamics investigation, the spike-type film played a role in enhancing the heat transfer in the composite.

1 Introduction

The important parameters for performance improvement of adsorption heat pumps and chillers are the adsorption rate and the heat transfer efficiency of a solid-adsorbent heat exchanger. One of the interesting configuration techniques is coating due to a thin adsorbent layer with lower heat and mass transfer resistances compared to a fixed bed [1]. However, the coating techniques still have problems with mechanical strength and thermal resistance due to the low thermal conductivity of a binder. This work focused on the surface modification for an aluminum plate before processing with coating to enhance the heat transfer efficiency and mechanical strength of the coated layer. The surface modification was conducted through anodizing and etching methods. A spike-type and barrier layer-type aluminum oxide films were created on the aluminum surface, and then they were coated with zeolite particles by the dipping method. The composites obtained were investigated experimentally for the mechanical strength of the coated layer and the water vapor adsorptivity.

2 Experimental

2.1 Surface modification of aluminum plate

An aluminum plate with a purity of 99.6% was used as a base material, and the plate was 40 mm long, 12 mm wide and 0.3 mm thick. The grease and contaminants on the surface were removed by soaking in sulfuric acid and sodium hydroxide solutions as presented in recent work [2]. The aluminum plate surface was modified into two types. The first one was a spike-type aluminum oxide film created by anodizing and etching methods consequently. A stainless plate was installed as a cathode and the aluminum plate as an anode in a 0.3 M oxalic acid bath. A direct current of 200 A/m^2 was applied to the electrodes at 21°C for anodizing. This procedure yielded a porous aluminum oxide film upon the aluminum surface. Then, the anodized aluminum was soaked into a 6 wt% phosphoric acid solution at 40°C to obtain the spike surface as represented in a scanning electron microscope (SEM) image (Figure 1a)). The second one was barrier layer-type aluminum oxide film prepared by only anodizing in a mixed solution of 0.5 M H_3BO_3 and 0.05 M $Na_2B_4O_7 \cdot 10H_2O$ at 20°C. Undergoing this process, the barrier layer-type aluminum oxide film as shown in Figure 1b grew on its surface.

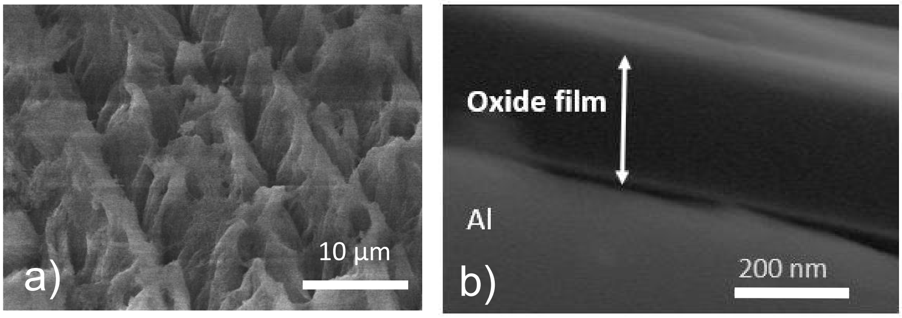

Figure 1 – SEM images of a) spike-type and b) barrier layer-type aluminum oxide films

2.2 Coating with adsorbent particles

A synthetic zeolite AQSOA-Z01 was used as an adsorbent for coating the modified aluminum surfaces. In order to facilitate the coating, silane modification was applied to the surface of the two types of aluminum samples. The silane solution of ethanol, distilled water, and 3-trimethoxysilylpropyl chloride was prepared at a volume ratio of 18:1:1. The aluminum plate was soaked with the silane solution and was dried at 80°C for 30 min. Three times the amount of zeolite particles by weight was added to the above-mentioned silane solution for the coating process. The silane-modified aluminum plate was dipped into the zeolite suspension. The thickness of zeolite layer could be controlled by the number of dipping cycles.

2.3 Water vapor adsorption

The zeolite-aluminum composites were examined for their water vapor adsorption capacities and dynamics based on the volumetric method at 30°C. The experimental apparatus and installation were presented in our previous work [3]. The adsorption dynamics were investigated in the relative pressure range of 0.09 – 0.29. This range corresponds to the operating temperatures of adsorption chiller systems: 10°C evaporation, 30°C cooling, and 80°C regeneration.

3 Results and discussion

3.1 Surface modification: Spike

Figure 2 represents the effect of anodizing and etching times on the spike height. Sample codes of A4, A6, and A8 represent the anodizing times of 4, 6, and 8 h, respectively. An increase in anodizing time leads to long spike height, and the highest spike length is 120 µm at 8 h anodizing and 2 h etching. An increase in etching time would bring about the dissolution of the spike-type aluminum oxide film. The spiked surface requires at least an etching time of 2, 2.5, and 3 h for Samples A8, A6, and A4, respectively.

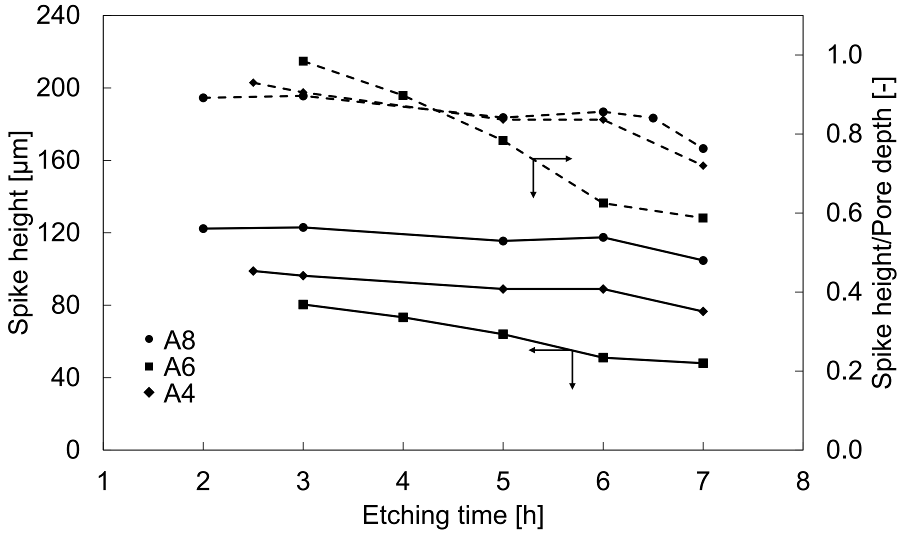

Figure 2 – Effect of anodizing and etching times on spike height

3.2 Surface modification: Oxide film

Figure 3 illustrates the effect of applied voltage and anodizing time on the thickness of barrier layer-type aluminum oxide film. An increase in anodizing time extends the oxide film growth on the aluminum surface. The aluminum oxide film thickness should be thin as possible because the oxide film retards the heat transfer between the zeolite layer and the aluminum plate.

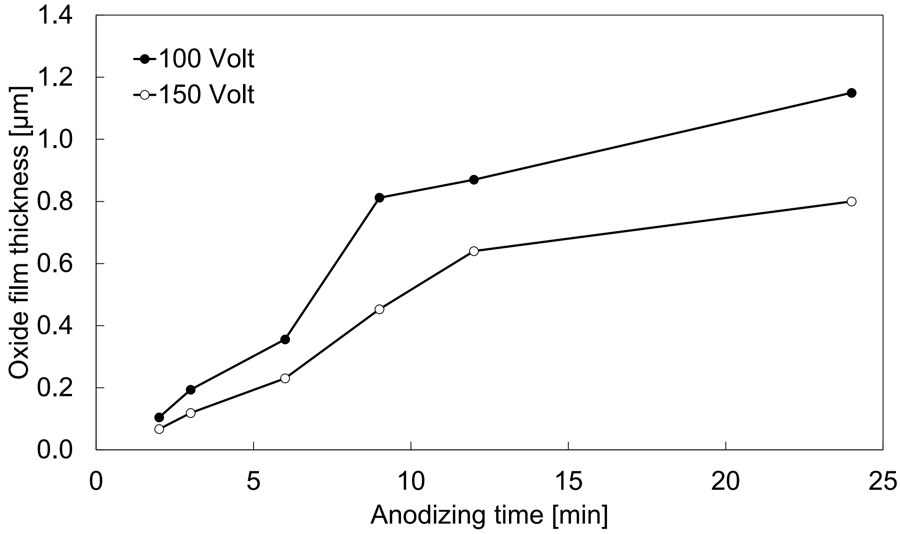

Figure 3 – Effect of applied voltage and anodizing time on aluminum oxide film thickness

3.3 Mechanical strength of zeolite layer

A peeling test was performed to determine the mechanical strength of zeolite layer on the aluminum surface through a residual ratio referred to JIS K 5400 standard (Figure 4). The residual ratio was determined from the change in the mass of zeolite before and after the peeling test. The barrier layer-type aluminum oxide film is the strongest adhesion between zeolite layer and the film surface due to the domination of hydroxyl group linkage on the plate surface when compared to the spike-type surface and original bare surface.

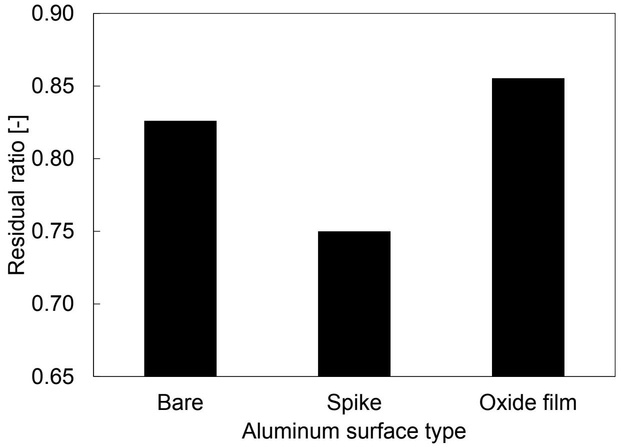

Figure 4 – The residual ratio of coated zeolite on the aluminum plate

3.4 Adsorption dynamics

Figure 5 shows the temporal changes in the adsorption ratio of water vapor and surface temperature of the composites. Samples codes of BL-25, BL-200, and S-200 represent the surface types (BL: barrier layer-type surface and S: spike-type surface) and the zeolite layer thicknesses of 25, 200, and 250 µm, respectively. As shown from Figure 5a, the adsorption ratio of Composite BL-25 reaches 0.8 of the equilibrium value within 200s meanwhile 0.66 for BL-200 and 0.69 for S-200. The thinner zeolite layer obviously promotes water vapor adsorption rate. In contrast, the thicker coated layer brings a high mass transfer resistance resulting in a slow adsorption rate. The absolute amount of water vapor adsorbed during adsorption process is 6 mg for BL-25 and 45 mg for BL-200, showing that an increase of zeolite layer thickness leads to 7.6 times the water vapor uptake larger compared between Composite BL-200 and BL-25. In the perspective of heat transfer efficiency, the spike-type surface, Composite S-200 promotes the heat transfer in the zeolite layer according to the changes in the composite surface temperature (Figure 5b) in an early stage. After that, the surface temperature rapidly decreases up to a 30°C heat-sink temperature for Composite BL-25 and gradually reduces for BL-200 and S-200. However, the adsorption rate of Composite S-200 is not enhanced due to the limitation of water vapor transfer in the zeolite layer. Whereas the thinner zeolite layer yields both rapid adsorption and heat transfer rates.

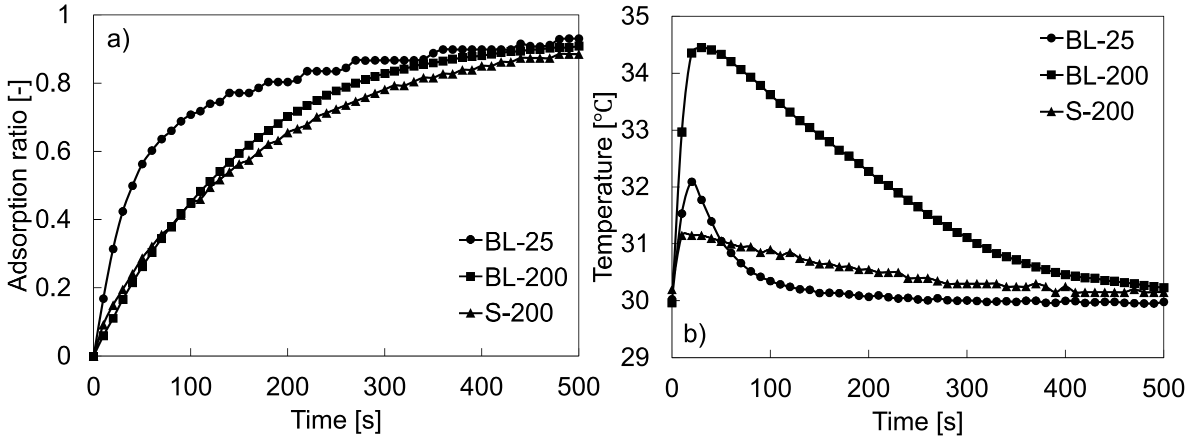

Figure 5 – a) Water vapor adsorption dynamics and b) surface temperature of zeolite coated on the aluminum plates

4 Conclusions

The surface modification method of aluminum plate would control the structure of both spike-type and barrier layer-type aluminum oxide films. The modified aluminum surfaces promote the mechanical strength of zeolite layer for the barrier layer-type film and the heat transfer efficiency for the spike-type film. The zeolite layer thickness is the parameter that impacts to the adsorption rate rather than the heat transfer efficiency.

5 Acknowledgment

This study was supported by Hosokawa Powder Technology Foundation, Japan.

6 List of References

[1] Pinheiro, JM., Salústio, S., Rocha, J., Valente, AA., Silva, CM. (2020): Adsorption heat pumps for heating applications. *Renewable and Sustainable Energy Reviews*, vol.119, p. 109528.

[2] Kumita, M., Meiwa, M., Watanabe, K., Kodama, A. (2013): Preparation of calcium chloride-anodized aluminum composite for water vapor sorption. *Applied Thermal Engineering*, vol.50(2), pp.1564–1569.

[3] Chumnanwat, S., Watanabe, Y., Taniguchi, N., Higashi, H., Kodama, A., Seto, T., Otani, Y., Kumita, M (2020): Pore structure control of anodized alumina film and sorption properties of water vapor on CaCl2-aluminum composites. *Energy*, vol.208, p.118370.

Experimental study of a thermochemical heat transformer using deposit of $CaCl_2$

Börtlein Clémentine[1], Michel Benoit[1*], Zoude Camille[2], Prud'homme Elodie[2], Gremillard Laurent[2], Clausse Marc[1]

[1] Univ Lyon, INSA Lyon, CNRS, CETHIL, UMR5008, 69621 Villeurbanne, France

[2] Univ Lyon, INSA Lyon, CNRS, MATEIS, UMR5510, 69621 Villeurbanne, France

**corresponding authors:benoit.michel@insa-lyon.fr*

Abstract:

A challenge in thermochemical heat transformers (THT) is to increase the specific heat power without compromising the temperature lift and cycle stability of the system. The objective of this study is to evaluate the potential of the salt hydrate calcium chloride ($CaCl_2$) in a 1-salt 1-stage and 2-salts 1-stage experimental THT for waste heat upgrade. The first 3 equilibrium reactions have been identified indicating large temperature lifts possible in the target operating conditions (waste heat under 100 °C upgraded till 150 °C and higher). In the 1-salt 1-stage configuration, the $CaCl_2$ packed bed produced large temperature lifts between 38.2 °C and 70.4 °C from a waste heat ranging from 82.7 °C to 98.7 °C with generally short reaction times. In the 2-salts 1-stage configuration, the same upgrade conditions lead to longer reaction times of the packed bed. A $CaCl_2$-based deposit with PVA (polyvinyl alcohol) as a binder could also achieve identical temperature lift but in a much shorter time, which is promising for achieving a higher specific power.

1 Introduction

Upgrading heat to higher temperatures is a lever for avoiding low temperature waste heat, like at the exit of an industrial process. In the industry sector which is a major energy consumer, 42% of the worldwide heat losses occur below 100 °C [1]: there is an opportunity for heat-to-heat conversion systems that can operate in these temperature ranges. Next to electrical heat pumps and absorption heat transformers, thermochemical heat transformers (THT) could avoid the issues of the afore-mentioned technologies by achieving high temperature lifts (>50 K) with a rather simple system architecture without any crystallization or corrosion issues.

In its simplest form, a THT is composed of an evaporator-condenser (E/C) and a reactor filled with reactive material (1-salt 1-stage) [2]. In the charging phase, the condenser is set to low temperature T_L and the reactor is heated at intermediate temperature (from waste heat for example) at T_m. This allows the decomposition of the reactive solid. In the discharging phase, waste heat at temperature T_m triggers the evaporation of water and the high temperature exothermic synthesis reaction occurs: T_H is collected. The difference between temperature input T_m and output T_H is called temperature lift. In order to allow a reduction of the high-pressure lift occurring in THT when high temperature lifts are sought, Goetz et al. [3] proposed a 2-salts 1-stage configuration (also called resorption heat pump). It uses the synthesis/decomposition of another reactive solid instead of the E/C. There exists a large number of solid-gas working pairs for 1-salt and 2-salts THT applications. Salt/ammonia pairs have been extensively studied for THT applications while there have been some evaluation of salt/methanol and salt/H_2O [2] with encouraging results for the latter. The solids working pair need to be compatible following the criteria listed by Michel and Clausse [4]. They identified a promising salt hydrate working pair for the upgrade of industrial waste heat: $SrBr_2$ and $CaCl_2$.

Among existing reactive solid implementation, the packed bed (or fixed bed) is the most common one. Reactive material is simply placed on a substrate or directly in contact with the heat exchanger. This solution is easily manageable and adaptable to the heat exchanger geometry, but has disadvantages such as heat and mass transfer limitations, performance degradation due to microstructure change, melting and aggregation after excess hydration… etc [5,6]. For solving these issues, an encouraging salt implementation is to use deposit of salt [7–9]. Even though used in adsorption cooling, some promising specific powers were reported as well as increased cycle stability. This innovative implementation is developed with a composite of salt and polymer binder.

In order to investigate the performance of a 2-salts THT configuration using $SrBr_2$ and $CaCl_2$ pair, for industrial waste heat upgrade (from 100 °C to 150 °C and above), a simpler THT system with one reactor was developed and instrumented. Since $SrBr_2$ has been intensively studied in literature [10], further investigation of $CaCl_2$ was the priority. The salt used for every experiments presented in this work is calcium chloride (dihydrate, Sigma

Aldrich, molar mass of 147.01 g/mol, purity higher than 99%). The study started with the characterization of $CaCl_2$ equilibrium reactions which indicate the highest temperature output possible. Then, an investigation of the salt performances (temperature lifts possible with waste heat at around 90 °C, reaction kinetics…) was performed. A reference salt implementation with a fixed bed was tested under the target operating conditions ($T_L/T_m/T_H$). The innovative implementation as a deposit was experienced at last.

2 Background/Fundamentals/Experimental Set-up

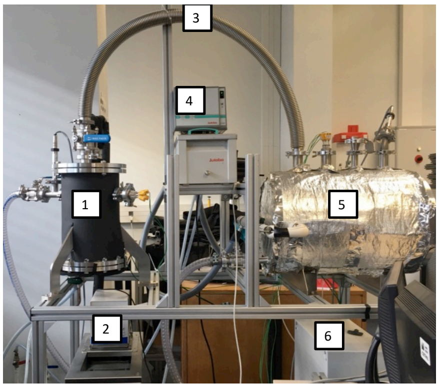

Figure 1. Picture of the test bench

The experimental setup is depicted in fig. 1. It is made of two main elements: a reactor chamber (5) and an E/C (1). The reactor is a cylinder of 380 mm outer diameter and 580 mm in length. For an easier setup, condenser and evaporator are a one and only vessel of 220 mm outer diameter and 320 mm in length. Each element has a thermal bath connected to it in order to control their temperature. The "cold" bath (2) drives the temperature using a spiral coil in the E/C's liquid water. The "hot" bath (4) drives the flow in the reactor's double skin envelope and in a plate heat exchanger (HX) contained in the reactor. This reactor heat exchanger enables the heat transfers with the reactive solid. It is custom-made with dimensions 200x200x70 mm. The salt container is placed on top of it with a thermal paste for good thermal contact between each other. The exchange between both chambers is carried out through a wide pipe (3) and a ball valve. Both chambers are fitted with a ball valve for connection with a vacuum pump during preparation of an experiment. Two pressure gauges (Keller PAA35X) are disposed on the reactor and the E/C. Moreover, 5 thermocouples (K-type) are place in the reactor. The acquisition unit (6) NI-DAQ has a 0.2 Hz acquisition frequency.

3 Results

3.1 $CaCl_2$ equilibrium reactions

Concerning $CaCl_2$ equilibrium reactions, hydration and dehydration experiments of around 100 g salt samples were conducted in the prototype with a closed reactor. A finite quantity of water vapor is introduced in the reactor, the temperature is imposed while the pressure is self-adjusting by the reactive material to reach it equilibrium. Three reactions have been identified and characterized between approximately 40 and 150 °C as can be seen in Figure 2. Comparing with the literature [11,12], these reactions could be identified to the reactions from $CaCl_2$ to $CaCl_2{\cdot}H_2O$ (equilibrium <1/0>), from $CaCl_2{\cdot}H_2O$ to $CaCl_2{\cdot}2H_2O$ (<2/1>) and from $CaCl_2{\cdot}2H_2O$ to $CaCl_2{\cdot}4H_2O$ (<4/2>). These data are ran in a custom-made program (using minimization function with differential evolution method) in order to fit our data with the typical law describing a monovariant solid/gas equilibrium reaction, the Clapeyron equation:

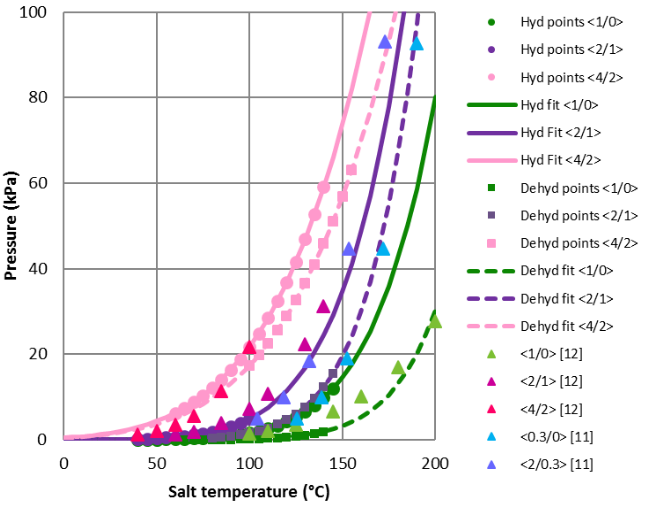

Figure 2. Hydration (hyd) and dehydration (dehyd) equilibrium curves for $CaCl_2$

$$p_{eq} = p^0 e^{-\frac{\Delta h_r^0}{RT_{eq}} + \frac{\Delta s_r^0}{R}} \tag{1}$$

where Δh_r^0 and Δs_r^0 the determined parameters which are respectively the standard enthalpy and entropy of reaction, p_{eq} and T_{eq} are the equilibrium pressure and temperature and p^0 the reference pressure (1 bar).

It is then possible to extrapolate the reactions equilibriums till 200 °C. The obtained equilibriums are in good agreement with the literature. They present an important hysteresis between the hydration and dehydration that is unfavorable to a THT system operation: higher waste heat temperature (T_m) or lower vapor pressure (hence a lower cold temperature T_L) are required for full dehydration. However, this salt is still promising of high temperature lifts and high power for the THT system.

3.2 THT performances

During the investigation of the THT prototype's performances, the heat upgrade phase has been studied in depth. Hydration experiments were conducted with waste heat temperature T_m ranging from 82.7 to 98.7 °C and upgraded to a working temperature T_H between 128.2 to 157.4 °C. The targeted reactions were the first two as identified previously (anhydrate to supposed dihydrate salt state).

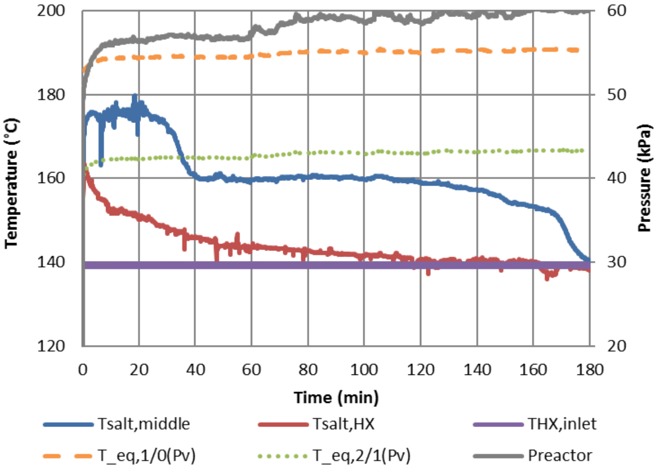

Figure 3. Temperature & pressure evolution during $CaCl_2$ hydration
(1-salt, $T_m = 87.6$ °C, $T_H = 138.0$ °C, $P_{mean} = 59.1$ kPa)

A typical hydration experiment is shown in Figure 3. The operating conditions T_m/T_H are 87.6/138.0 °C with 59.1 kPa reaction pressure. The resulting temperature lift is 50.4 °C. The reactive salt has been previously dehydrated. After the connection between the E/C and the reactor (at t=0 min), the high E/C pressure is introduced in the reactor and the reaction starts as indicated by the temperature increase both in the salt bulk and at the frontier between salt and HX. The bulk temperature rises till a plateau of approximately 175 °C. This reaction heat may be attributed to the first reaction we characterized earlier in this work (<1/0>). The equilibrium temperature corresponding to the reactor pressure is displayed along and shows the equilibrium drop necessary for the reaction to occur ($T_{eq,1/0}$ for reaction <1/0> and $T_{eq,2/1}$ for reaction <2/1>). The heat is evacuated via the heat exchanger as indicated by the frontier temperature, decreasing much quicker than in the bulk and indicating the heat transfer direction: this tendency is in line with an axial moving reaction front [13]. After 40 min, the bulk temperature decreases till a second plateau around 160 °C. The reaction occurring at this temperature is the second hydration step (<2/1>). This step is much longer and lasts from 40 to 180 min, probably due to the lower equilibrium drop and the lower heat transfer caused by the lower temperature gradient. The frontier temperature decreases slowly during that time, evacuating progressively the reaction heat. 180 min after the start of the reaction, the temperature in the bulk and at the frontier are both back to their original value: the salt is not reacting anymore.

The end of the first temperature plateau of the salt middle indicates that the first reaction is finished at this point (hypothesis of an axial moving reaction front [13]), therefore for half of the salt mass. It is thus possible to calculate the theoretical specific mean power released during half this reaction step. The temperature lifts obtained with waste heat temperature T_m are displayed in Figure 4 along with the theoretical specific mean power. Two THT configurations were tested: 1-salt 1-stage and 2-salts 1-stage and two implementations: packed bed and deposit. In the 1-salt 1-stage configuration of the THT system, the hydration of $CaCl_2$ is driven with water evaporation at the E/C. The salt is placed in the reactor as a packed bed, which is a commonly studied implementation. A variation of the initial conditions (either T_m or T_H) influence the temperature lift that can be obtained and the reaction duration. A promising trade-off between a high temperature lift and short reaction time (hence high specific mean power) was obtained for an upgrade from 80-85 °C to 145-150 °C: 170 W/kg salt were reached.

In the 2-salts 1-stage THT configuration, as the experiment dispose of only one reactor, the E/C simulates the dehydration (hydration) of the low temperature salt ($SrBr_2$) by evaporating (condensing) at the imposed pressure p_v, defined as the average pressure between the equilibrium pressure of the $SrBr_2$ at T_m (T_L) and $CaCl_2$ at T_H (T_m). Two implementations of the reactive material have been investigated. The first one is as a salt packed bed. In comparison to the 1-salt experiments, these hydrations were investigated with lower lifts but show specific mean power in the same ranges. Temperatures could effectively be upgraded with lifts ranging from 38 to 48 °C.

The second implementation used in the 2-salts 1-stage configuration was in the form of a deposit. A mix of $CaCl_2$ (91 wt%) and PVA as a binder were deposited with a thickness of around 0.5 cm on an aluminum plate and experimented using the 2-salts 1-stage protocol. Two samples were tested. It achieved an upgrade of 47 °C (see Figure 4). Compared to the reference experiment for the packed bed, the reaction is much quicker resulting in a specific mean power as high as 355 W/kg_{salt} (against 85 W/kg for its reference experiment in packed bed). However, a decrease over successive hydration/dehydration cycle is observed for this specific power. A possible explanation lies in the material aging as it can be observed on figure 5a&b. After few cycles, cracks tend to appear at the coating surface. A cross-sectional observation (Fig. 5c) make appear what could be a segregation between the salt and the binding, resulting in a drop in performances. Further investigations are needed to fully characterize and understand the phenomena involved.

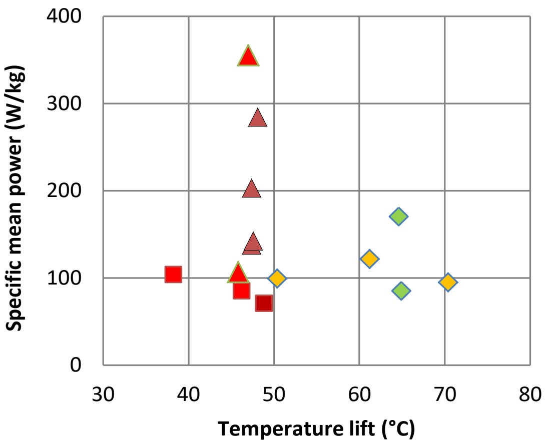

Figure 4. Temperature lift and specific mean power obtained during hydrations

◆ packed bed 1-salt, Tm [80..85°C], ◆ packed bed 1-salt, Tm [85..90°C], ■ packed bed 2-salt, Tm [90..95°C], ■ packed bed 2-salt, Tm [95..105°C], coating 2-salt, Tm [90..95°C]: coating 1 ▲ coating 2 ▲.

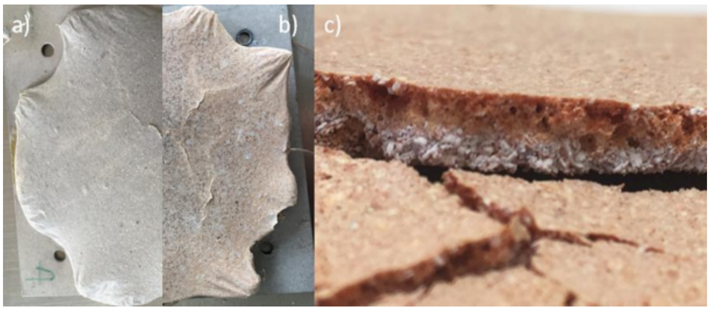

Figure 5. Picture of a PVA-deposit a) before experiment and b) after one hydration-dehydration cycle at 2/90/140 °C and c) after two cycles

4 Conclusions

In this study, the potential of $CaCl_2$ as a high temperature salt in a thermochemical heat transformer was investigated. Promising performances were achieved for waste heat upgrading from 100 °C to temperature above 150 °C. The reactions involved in this discharging phase are the first two hydration steps identified experimentally for this salt. Two reactor configurations were tested: packed bed and coating. The latter one enables a similar lift with a higher specific mean power. A next step will be to test this implementation at a larger scale and to progress in the coating formulation and behavior characterization.

5 Acknowledgment

The authors wish to thank the Institut National des Sciences Appliquées de Lyon (INSA-LYON, France) (BQR FATAL RECUP) for funding this study.

6 List of References

[1] C. Forman, I. K. Muritala, R. Pardemann, et B. Meyer, « Estimating the global waste heat potential », *Renew. Sustain. Energy Rev.*, vol. 57, p. 1568‑1579, mai 2016, doi: 10.1016/j.rser.2015.12.192.

[2] Y. Q. Yu, P. Zhang, J. Y. Wu, et R. Z. Wang, « Energy upgrading by solid–gas reaction heat transformer: A critical review », *Renew. Sustain. Energy Rev.*, vol. 12, nᵒ 5, p. 1302‑1324, juin 2008, doi: 10.1016/j.rser.2007.01.010.

[3] V. Goetz, F. Elie, et B. Spinner, « The structure and performance of single effect solid-gas chemical heat pumps », *Heat Recovery Syst. CHP*, vol. 13, nᵒ 1, p. 79‑96, janv. 1993, doi: 10.1016/0890-4332(93)90027-S.

[4] B. Michel et M. Clausse, « Design of thermochemical heat transformer for waste heat recovery: Methodology for reactive pairs screening and dynamic aspect consideration », *Energy*, vol. 211, p. 118042, nov. 2020, doi: 10.1016/j.energy.2020.118042.

[5] A. Fopah Lele, K. E. N'Tsoukpoe, T. Osterland, F. Kuznik, et W. K. L. Ruck, « Thermal conductivity measurement of thermochemical storage materials », *Appl. Therm. Eng.*, vol. 89, p. 916‑926, oct. 2015, doi: 10.1016/j.applthermaleng.2015.06.077.

[6] J. Stengler et M. Linder, « Thermal energy storage combined with a temperature boost: An underestimated feature of thermochemical systems », *Appl. Energy*, vol. 262, p. 114530, mars 2020, doi: 10.1016/j.apenergy.2020.114530.

[7] A. Freni, F. Russo, S. Vasta, M. Tokarev, Yu. I. Aristov, et G. Restuccia, « An advanced solid sorption chiller using SWS-1L », *Appl. Therm. Eng.*, vol. 27, nº 13, p. 2200‑2204, sept. 2007, doi: 10.1016/j.applthermaleng.2005.07.023.

[8] S. Bahrehmand, M. Khajehpour, W. Huttema, C. Mccague, et M. Bahrami, « The effects of graphite flake on specific cooling power of sorption chillers: An experimental study », sept. 2018.

[9] H. Kummer, G. Füldner, et S. K. Henninger, « Versatile siloxane based adsorbent coatings for fast water adsorption processes in thermally driven chillers and heat pumps », *Appl. Therm. Eng.*, vol. 85, p. 1‑8, juin 2015, doi: 10.1016/j.applthermaleng.2015.03.042.

[10] A. Fopah-Lele et J. G. Tamba, « A review on the use of SrBr2·6H2O as a potential material for low temperature energy storage systems and building applications », *Sol. Energy Mater. Sol. Cells*, vol. 164, p. 175‑187, mai 2017, doi: 10.1016/j.solmat.2017.02.018.

[11] M. Molenda, J. Stengler, M. Linder, et A. Wörner, « Reversible hydration behavior of CaCl2 at high H2O partial pressures for thermochemical energy storage », *Thermochim. Acta*, vol. 560, p. 76‑81, mai 2013, doi: 10.1016/j.tca.2013.03.020.

[12] K. E. N'Tsoukpoe *et al.*, « A review on the use of calcium chloride in applied thermal engineering », *Appl. Therm. Eng.*, vol. 75, p. 513‑531, janv. 2015, doi: 10.1016/j.applthermaleng.2014.09.047.

[13] B. Michel, P. Neveu, et N. Mazet, « Comparison of closed and open thermochemical processes, for long-term thermal energy storage applications », *Energy*, vol. 72, p. 702‑716, août 2014, doi: 10.1016/j.energy.2014.05.097.

Kinetic performance evaluation of high-ordered microporous silica in an experimental water-based adsorption heat storage system

Miksik, Frantisek[1,2], Ahmed, Youssef[1], Miyazaki, Takahiko[1,2], Kotlik, Josef[3]

[1]Department of Energy and Environmental Engineering, Faculty of Engineering Sciences, Kyushu University, Kasuga-koen 6-1, Kasuga-shi, Fukuoka 816-8580, Japan, miksik@kyudai.jp

[2]International Institute for Carbon-Neutral Energy Research, Kyushu University, 744, Motooka, Nishi Ward, Fukuoka, 819-0385, Japan

[3]Institute of Chemistry and Technology of Environmental Protection, Faculty of Chemistry, Brno University of Technology, Purkynova 464/118, Brno 612 00, Czech Republic

Abstract:

We have evaluated cooling performance of a small-scale experimental adsorption heat storage system filled with nano-tailored microporous silica adsorbent with aluminium doping. The simple adsorption bed used in this work consisted only of the filled powdered adsorption material and heat exchanger. Despite the simple design and highly unfavourable weight ratio between the adsorption material and the heat exchanger we were able reach acceptable COP of 0.5 at medium ΔT (ambient – evaporator) = 15 °C in cooling mode. The working conditions were set to charging temperature of 80 °C and ambient temperature of 30 °C, with a constant discharge time of 1 hour. The peak specific cooling power at the target cooling temperature of 15 °C was 300 W/kg while the specific cooling energy was approximately 300 kJ/kg. We have compared the experimental values with a theoretical model and evaluated the kinetic effects on the respective differences between these two values.

1 Introduction

Adsorption heat transformation processes are well known from the progressing technology of adsorption heat pumps and are actively developed across the globe. The less common adsorption heat storage builds on the same principles but works with an adjusted concept to accommodate for its own peculiarities. Arguably the most important part of both systems are the adsorption materials. Nanotailored mesoporous and microporous silica explored in our previous works offer good control over the pore size distribution and designing the shape of these materials is also possible to a certain degree. However, due to the scarce availability of these materials, the practical testing is so far highly limited and the energy applications are mostly discussed theoretically[1]. Far more common are materials such as silica gel, zeolites and zeolite-like aluminophosphates, and lately also MOFs are being increasingly mentioned in the adsorption field[2].

In this work, we show some promising results of the use of highly ordered nano-tailored microporous silica in the adsorption heat storing application inside a downscaled experimental device on industrially produced material. Our focus is practical estimation of kinetics limitations on the performance in a constant-time experiment.

2 Experimental Set-up

2.1 Material

Nano-tailored silica used in this work has been extensively studied in our previous work in terms of adsorption isotherm and physical properties[1,3] with water as working fluid. The selected material in this work shows strong and regular microporosity around the mean of 1.8 nm together with good hydrophilic properties expressed by Type IV adsorption isotherm. The increased water adsorption and hydrothermal stability is further supported by aluminium doping (~1.5 %). The summary of the basic physical properties is provided in Table 1. The material was obtained in a form of white powder and particle size ranging from 100 nm to 500 nm. To prepare the adsorption cell, we mixed the material with water to create a paste which we then poured between the fins of the exchanger to completely fill up the space. The filled exchanger was then slowly dried at 60 °C for 48 h and then another 24 h at 110 °C. The exchanger prepared for measurement is shown in Figure 1 (right).

Table 1 – Adsorbent properties

Mean pore size (DFT)	Surface area (N_2/BET)	Total pore volume (N_2)	Wall thickness (DFT/XRD)	Specific heat	Tap density
1.8 nm	602.0 m^2g^{-1}	0.33 cm^3g^{-1}	1.8 nm	0.89 $J\cdot g^{-1}K^{-1}$	0.274 cm^3g^{-1}

2.2 Method

The closed adsorption unit shown in Figure 1 (left) is typical one bed adsorption unit with one combined evaporator-condenser unit. To disregard the effect of ambient temperature fluctuations, the whole system was put into an isothermal cabinet and the temperature was kept constant above the condensation point at each step. Before the experiment we measured the heat capacities of the individual components in series of dry runs for variable temperature range. Uncertainties of the measurement shown in Figure 1 (right) were obtained through standard calibration methods. The adsorption heat was adopted from [1] and used in a form of a polynomial function:

$$\Delta H°_{st} = \int_{q_0}^{q_e} -1.079\cdot 10^6 q^5 + 1.226\cdot 10^6 q^4 - 5.333\cdot 10^5 q^3 + 1.105\cdot 10^5 q^2 - 1.100\cdot 10^4 q + 1.033\cdot 10^3\, dq \qquad \text{Eq. 1}$$

In Eq. 1 the adsorption enthalpy (heat) $\Delta H°_{st}$ (kJ/kg) is expressed as an integral of the absolute adsorption uptake specified by the residual adsorbed amount after charging q_0 (kg/kg) and adsorbed amount after discharge q_e (kg/kg). The values for residual adsorption uptake were obtained experimentally as well as theoretically based on the adsorption isotherm shown in Eq. 2. The adsorption pair-specific values q_m, C, α, ω, and σ for adsorption isotherm in the range 5 °C to 30 °C were adopted from [4] according to the Table 5 (mBET+G model's temperature dependent parameters approximation) and Eq. (39). Parameters for the regeneration temperature T_d were based on a separate high temperature experiment $q_m = 0.113$ g g^{-1}, $C = 9.085$, $\alpha = 0.150$, $\omega = 0.357$, and $\sigma = 0.043$.

$$q = q_m \frac{Cx}{1-x}\frac{1-(n+1)x^n + nx^{n+1}}{1+(C-1)x - Cx^{n+1}} + \alpha\frac{1}{2}\left[1 + erf\left(\frac{x-\omega}{\sqrt{2}\sigma}\right)\right], \qquad x = \frac{P}{P_0} \qquad \text{Eq. 2}$$

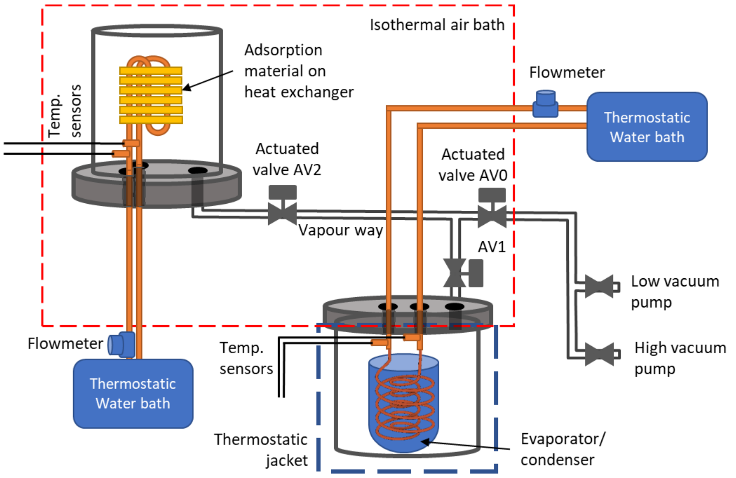

Measurement uncertainties

Temperature sensors Pt100 (thin film), DIN 1/3	±0.05 °C
Flowmeter OVAL-EG (gravimetric calibration, applicable range 0.1 – 1 L/min)	(5-50 °C) ±0.003 L/min (50-80 °C) ±0.005 L/min

Figure 1 – Adsorption system schema (left) and measurement uncertainties (right)

The performance estimations are based on the classical model evaluating the adsorption energy and evaporation energy in the perspective of the individual thermal masses of the system. The equations are summarised in the following equation set Eq. 3 to Eq. 6. The characteristics are discussed on the basis of COP and SCE.

$$COP_{cooling} = \frac{SCE}{Q_{des} + Q_{sens}}, SCE = Q_{evap} \qquad \text{Eq. 3}$$

$$Q_{des} = \int_{q_{reg}}^{q_{ads}} \Delta H°_{st}\,(q)dq \qquad \text{Eq. 4}$$

$$Q_{evap} = \left(q_{ads} - q_{reg}\right)\Delta H_{vap}(T) \qquad \text{Eq. 5}$$

$$Q_{sens} = w_{adsorber}\int_{T_s}^{T_d} c_{P,adsorber}\,(T)dT + \left(q_{ads} - q_{reg}\right)\int_{T_s}^{T_d} c_{P,w}\,(T)dT + w_{evaporator}\int_{T_c}^{Ts} c_{P,evaporator}(T)dT \qquad \text{Eq. 6}$$

The system kinetics performance is analysed based on the energy performance from the perspective of the variable discharge conditions, in here, the target cooling temperature in the range of T_c = 25 – 10 °C (ΔT = 5 – 20 °C). The ambient temperature acted as the heat sink temperature for both condensation and adsorption and was kept constant at T_s = 30 °C. Charging temperature was also kept constant for all experiments T_d = 80 °C. The summary on the experimental conditions is provided in Table 2. The adsorption and desorption time was set constant in both cases to exactly 1 hour.

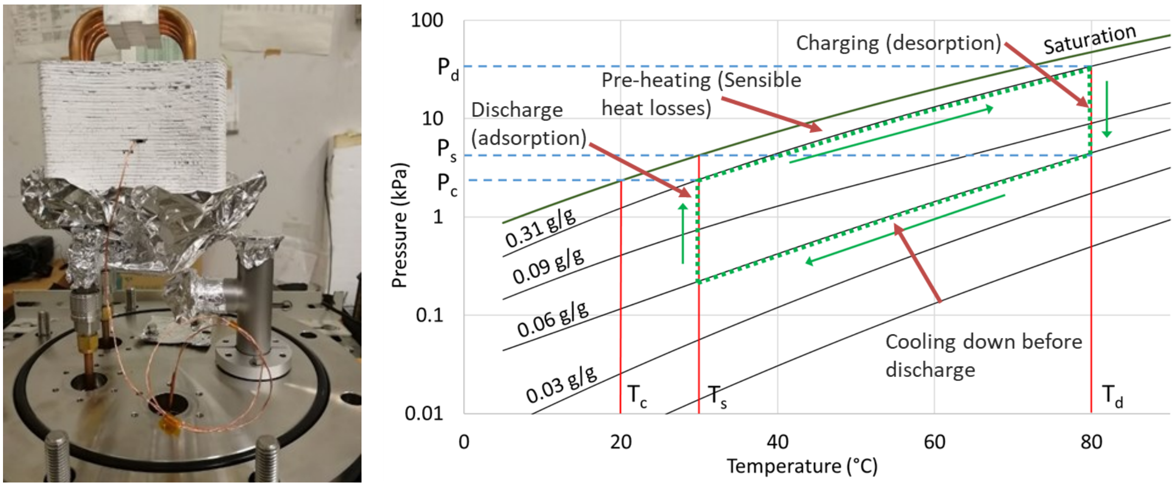

Figure 2 – Adsorption bed (left); and adsorption cycle schematics (right) (Example 30/20/80 °C)

The cycle schematic is shown in Figure 2 in a P-T diagram explaining the working conditions on an example with a target cooling temperature T_c = 20 °C. The cycle is characterized by four typical stages Discharge, Pre-heating, Charging, and Cooling down. Because we evaluate the system from the perspective of energy storage, the pre-heating energy is perceived as irreversible loss during the cooling down period.

Table 2 – Experimental settings

Adsorber unit flow	Evaporator flow	Ambient Temp.	Evaporator Temp.	Charging Temp.	Heat capacity Adsorber unit	Heat capacity Evaporator	Adsorbent amount
~0.1 L·min^{-1}	~0.1 L·min^{-1}	30 °C	10-25 °C	80 °C	889 J·K^{-1}	1842 J·K^{-1}	141.7 g

3 Results

While the set time period of 1 hour was sufficient to fully charge the system, the discharge of the system was significantly slower, and except the highest set cooling value T_c = 25 °C, it diverged from the model greatly. The actual breakthrough curves of the temperature inlet and outlet of the adsorption unit is shown in Figure 3 (right). This curve corresponds to the free non-fixed bed, when the system releases most of its energy in the beginning of the process and then slowly dissipates the energy via a slow thermal conduction through the adsorption material.

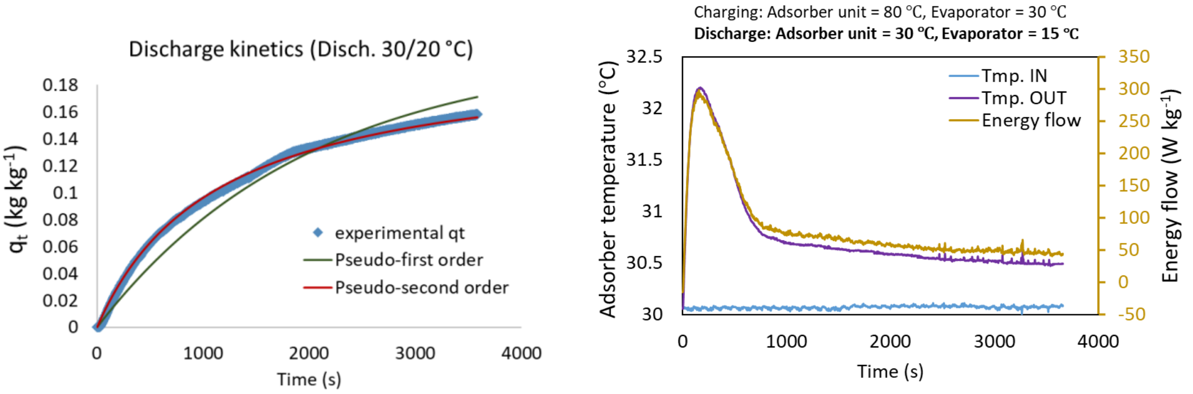

Figure 3 – Discharge kinetics at 30/20 °C mode (left) and discharge breakthrough curve of the adsorption unit at target cooling (evaporator) temperature T_c = 15 °C (right)

The specific cooling power (SCP) in the Figure 3 (right) was reaching sufficient 300 W/kg and was naturally higher at lower ΔT (T_s - T_c). For example, at target cooling temperature T_c = 25 °C, the SCP was more than double of this value. The basic analysis on the process kinetics based on first and second order kinetics in Figure 3 (left) revealed better agreement with second order kinetics, suggesting at least two co-depended processes limiting the adsorption kinetics. That would be also the logical conclusion based in the adsorption and heat transfer processes progressing next to each other. However, this well corresponding fitting was observed only at target cooling temperatures of 20 °C and 25 °C implying different dependence of the limiting factors with decreased pressure difference. The cumulative energy yields for individual settings for both model and experiment are compared in Figure 4 (left) as the specific cooling energy. We can see that for the lower target temperatures the one-hour period is insufficient in the current design and the energy flow is strongly distorted. The SCE (Specific Cooling Energy) drops from reasonable 600 kJ/kg at 25 °C to some 130 kJ/kg at 10 °C, making the material at the lower target temperature very difficult to use. As the difference increases similarly with the pressure decrease relevant to the target temperature, we can reason, that this drop in the adsorption speed and energy release is more connected to the pressure and accessibility of the material rather than the energy transport inside the heat exchanger. The theoretical model then reveals the actual limit of the material at the ambient temperature T_s = 30 °C to be T_c = 15 °C. Further decrease in the T_c temperature leads to a step decrease in the adsorption amount effectively rendering the system practically unusable.

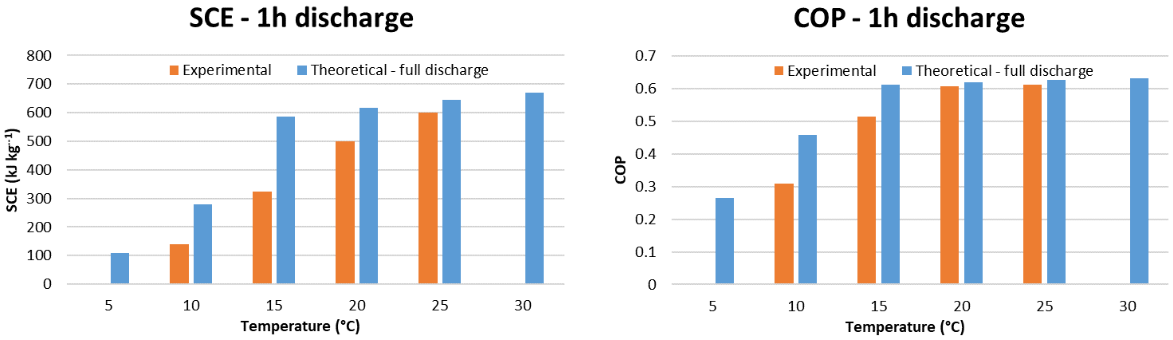

Figure 4 – Specific cooling energy (left) and COP at 1 hour discharge time (right) on the delivery temperature

The COP results show that despite the reduction in the discharge speed the COP is affected in a significantly less dramatic manner and the drop between theoretical and experimental values at T_c = 15 °C is just some 15-20 % compared to the 50 % drop of SCE. That is particularly interesting information as some of the values has to be presented in perspective of the overall performance. The key point will be to increase the energy yield without increasing the discharge time too much. We can achieve that by several different approaches based on the presented analysis addressing mostly the permeability of the bulk material. Based on the model comparison in Figure 4, we can see especially a certain potential for further enhancement in the 5 °C < ΔT < 15 °C region. The theoretical analysis furthermore revealed natural constraints of the presented material allowing us to focus on achievable improvements. In the future investigation we would like to also address the issue of regeneration temperatures of this adsorption material which seem to be promising, reaching 80 % desorption target at low T_d of 60 °C in the preliminary testing (not shown in this work).

4 Conclusions

Understanding of the limiting factors of individual systems is an important ingredient to improve the design and progress. In this work, we have performed a basic analysis of a water adsorption heat storage system with a very simple design of the adsorption bed consisting of highly ordered microporous silica. Despite its simplicity, the material produces surprisingly good values of key parameters such as COP, while others are limited by the design or the material itself, or both. The results show limiting use of the setup, however, show a potential for improvement. Through this analysis we can expect certain enhancement of the adsorption process by better layer separation allowing for increased vapour circulation through the exchanger.

5 Acknowledgment

We express our great appreciation to Taiyo Kagaku Co., Ltd. for providing us with the adsorption material for this work.

6 List of References

[1] Miksik, F. and Miyazaki, T. (2019) Material selection and properties for adsorption heat storage: perspectivity of TMPS series mesoporous silica nano-materials. *Adsorption*. 25 (6), 1137–1145.

[2] Vasta, S., Brancato, V., La Rosa, D., Palomba, V., Restuccia, G., Sapienza, A., et al. (2018) Adsorption Heat Storage: State-of-the-Art and Future Perspectives. *Nanomaterials*. 8 (7), 522.

[3] Mikšík, F., Miyazaki, T., and Inada, M. (2019) Detailed investigation on properties of novel commercial mesoporous silica materials. *Microporous and Mesoporous Materials*. 289 (August), 109644.

[4] Mikšík, F., Miyazaki, T., and Thu, K. (2020) Adsorption Isotherm Modelling of Water on Nano-Tailored Mesoporous Silica Based on Distribution Function. *Energies*. 13 (16), 4247.

Ammonia-salt sorption: testing and analysis, modelling and validation

Critoph, Robert E.[1], **Hinmers, Samuel**[2], **Atkinson, George H.** [3]

[1] *University of Warwick, School of Engineering, Library Road, Coventry, CV47AL, UK*
(R.E.Critoph@warwick.ac.uk)

Abstract:

Large temperature jump experiments are key to producing reliable data for the reversible reactions between ammonia and salt. This paper presents a detailed approach to analysing salt behaviour and measuring an accurate heat of reaction, through temperature jump and isosteric heating tests. Using a MATLAB® model, the simulated outputs can be matched to measured experimental data and model parameters obtained that characterise the salt. This method has been validated for a number of candidate high and low temperature salts and provides the basis for design of a resorption system.

1 Introduction

Faraday first noted the heating effect that occurred when ammonia adsorbed into silver chloride, as well as the cooling effect as the reaction drove the evaporation of liquid ammonia in an adjoined vessel [1]. Ammonia-salt systems using this effect have the potential for diverse applications, but to produce effective results and to develop machines, it is necessary to understand their complex behaviour. The Large Temperature Jump (LTJ) method is well explored and has been used many times since its conception by Aristov and Dawoud [2]. It is an effective tool to apply when considering ammonia-salt reactions. Salts have proven challenging due to their low thermal conductivity, tendency to agglomerate and hysteresis, but recent research has focused on conductive matrices and composites, often using Expanded Natural Graphite (ENG). The composites act as a host matrix for the salt, ensuring small crystal size to prevent agglomeration and increasing the conductivity of the now composite salt.

Work at Warwick has adapted the LTJ method to produce a simple experiment to test the composite materials and to validate a model that includes both heat transfer and reaction rate relationships. The experiment rapidly heats and cools the composite cylindrical samples whilst measuring the sample temperature (at the centre when heating externally and at the surface when heating internally) and system pressure. Using silicone oil as the thermal fluid provides a system that can heat the salts towards 200 °C and cool below 0 °C, enabling testing for wide ranging applications. While heating and cooling, the system pressure is measured and with an expansion volume in the system such that the pressure rise is small but measurable. The dynamic measurement of the LTJ experiment produces results akin to that of a working machine. Characterisation of the salt is obtained via matching experimental and simulated model outputs, providing a tool for design and understanding of the behaviour of salts.

2 Background and experimental set-up

2.1 Modelling

A finite difference model is used, currently based on a cylindrical structure in which the composite ENG with its impregnated salt is either externally heated or cooled within a tube or internally heated from a central tube. This is the geometry used in LTJ tests and also that anticipated in a full size device. Any number of radial nodes can be used. Conduction heat transfer is assumed between elements and the heat transfer between the tube wall and the adjoining node is simulated by the resistance of a static ‘gap’ layer of gaseous ammonia between the two. For each time step, the heat fluxes into and out of each element are calculated; this is ultimately what drives the adsorption or desorption. An estimated pressure rise is assumed for the time step which must be iterated to arrive at the final value. The chemical reaction rate equation below is used to determine the masses of ammoniated complexes changing from one state to another using the assumed pressure rise and current progression of the reactions taking place.

$$\frac{dX}{dt} = (1 - X)^n A \frac{p_{eq} - p}{p}$$

X is the advancement of the reaction (from zero to unity)
p is the pressure

p_{eq} is the equilibrium pressure
A and n are constants

This enables the temperature changes in the nodes to be calculated using energy balance equations. These may then be used to calculate the total mass of ammonia (gaseous or adsorbed) in the system consisting of the reactor, any void volume, and the expansion vessel. This must of course be constant and the estimated pressure rise is varied (using the MATLAB® fzero function) until this is between proscribed limits.

Composite metal-chloride salts in an LTJ experiment exhibit hysteresis, i.e. are observed to have separate equilibrium lines for adsorption and desorption, with a pseudo-equilibrium region between the lines where no reaction takes place [3]. A complication is that in general the two lines do not have the same slope and that neither slope cannot be used to calculate heats of sorption since the process is irreversible. The difference between adsorption and desorption enthalpies can be shown to be typically less than 0.1%. In this work a ‘true’ equilibrium line has been used to calculate the value. It is established by heating and cooling up and down the saturation line with minimal gas void space so that very little adsorption or desorption occurs; an isosteric temperature change (ITC) test. It is carried out very slowly (typically a 10 hour cycle) and shows good repeatability.

Matching the temperature and pressure simulations to experimental results reveals all the parameters needed to model the reaction. These are: adsorption and desorption lines, heat of sorption, fraction of salt that is accessible, radial conductivity, contact resistance and the constants A and n.

2.2 Large Temperature Jump Tests to identify reaction rates and salt behaviour

A unit cell tube-side (double pipe) LTJ reactor was used as in [5] but with improved temperature measurement as described by Hinmers et, al [4]. Tests were carried out with ammonium, barium, calcium, and manganese chlorides. Although in principle the results obtained could be applied to a configuration in which the heat source / sink was an internal tube rather than an external tube, it was decided to manufacture an LTJ apparatus using this configuration. This increased testing capability and provided further evidence in support of the model’s ability to predict reaction dynamic behaviour.

The LTJ reactor is connected to expansion vessels, and the temperature in the vessels and pressure are measured. The expansion volumes ensure a low pressure rise, akin to changes in a real system with a condenser, or the pressure drop caused by adsorption when connected to an evaporator. Temperature jumps that initiate adsorption and desorption are generated by switching between a hot and cold oil bath. The LTJ is a novel solution to understanding the salt behaviour, from which it is possible to measure the reaction onset and to observe a superheating metastate – this is key to understanding the behaviour, as gravimetric balances that do not measure the sample temperature will miss this.

The simplicity of this LTJ experimental set up is described by Hinmers et, al. [4, 5] allows it to be adapted easily in order to simulate different dimensions that might be used in real machines. The shell-side system also provides a basis for different reactor geometries. The intention is that following model validation / characterisation of behaviour, the model can be used to optimise the design of a full-size reactor (e.g. in a ‘shell-side’ configuration of a shell-and-tube reactor, the tube diameter and pitch) and that the corresponding unit cell can quickly receive a confirmatory LTJ test.

3 Results

3.1 Large Temperature Jump results

The large temperature jump test is a quick method to test composite salts, identify application and also expose a number of interesting characteristics of the material, for example, a superheating effect and return to equilibrium can be seen at the onset of reaction, Figures 1 and 2. A full cycle (desorption followed by adsorption) with ammonium chloride can be seen in Figure 1.

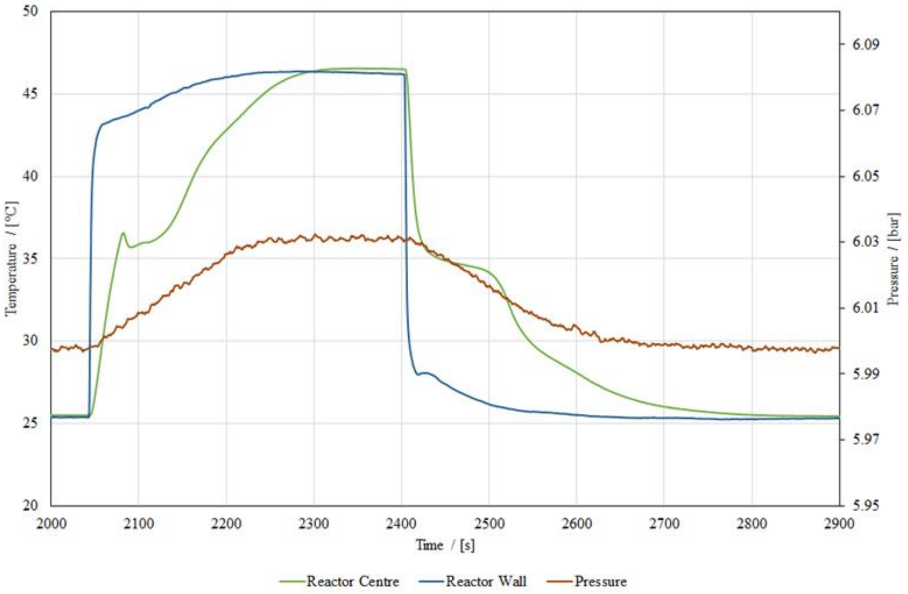

Figure 1: *Ammonium chloride LTJ cycle, with pressure in red on the right-hand scale. The cycle proceeds and some superheating effect is observed before a return to equilibrium conditions.*

Similarly, a full barium chloride cycle can be seen in Figure 2. One can see that ammonia appears to desorb at a lower temperature than barium chloride at a similar pressure. It is this characteristic that enables identification of appropriate salt pairs and optimal working conditions. Of additional note, is that there is reduced hysteresis in the ammonium sample as the difference between adsorption and desorption temperature is low. A number of results at different pressures would enable evaluation of the applicability of a salt; for example, identifying a low temperature salt, with an ability to desorb below 5°C in a heat pump application.

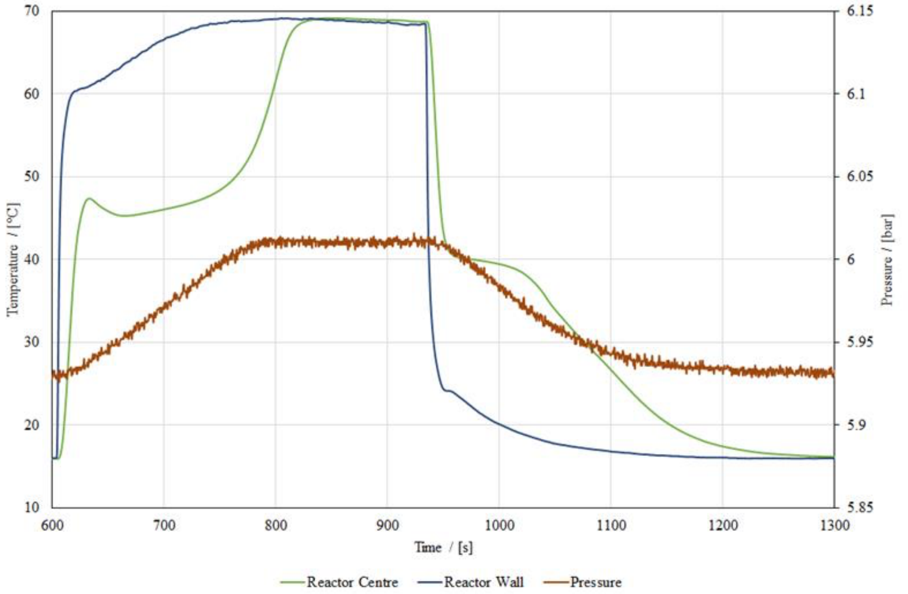

Figure 2: *Barium chloride large temperature jump cycle.*

3.2 Isosteric temperature change to derive enthalpy of reaction

To get results that were reversible and nearly free of hysteresis required high salt loading, mimimum expansion volume and the rate of temperature change to be as low as 0.05 °C/min. The orange plot in Figure 3 shows the cycle with much reduced hysteresis, and sections of the line are near to parallel, suggesting a single heat of reaction. The blue plot shows a less successful run where the reaction appeared to completely desorb. Adjusting the heating rate and the mass of salt improved the results, reducing hysteresis and producing the orange line.

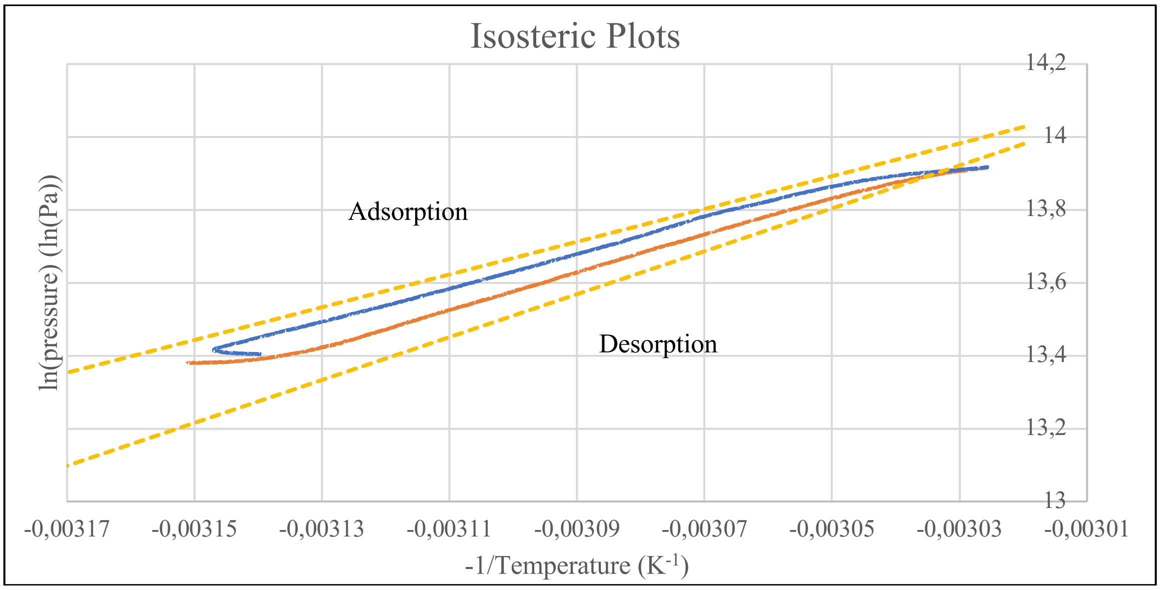

***Figure 3**: Plot of dashed equilibrium lines from the LTJ versus the reduced hysteresis lines from the ITC. The blue and orange plots (adsorption and desorption respectively) have a section that is near to parallel, from this a single heat of reaction can be estimated by taking an average of their gradients. The yellow dashed lines are the measured equilibrium lines from LTJ experiments with extensive hysteresis and inconclusive enthalpy of reaction [5].*

4 Conclusions

Large temperature jump testing is key to analysing the behaviour of ammonia-salt reactions, but a comprehensive understanding requires an accurate measure of the heat of reaction. An isosteric temperature change experiment has been developed for this purpose. Overall, large temperature jump tests at Warwick have been shown to observe the interesting behaviour of salts in real working conditions, a method has been devised to measure the heat of reaction accurately and a comprehensive understanding of salt characteristics has been developed. The use of the equilibrium sorption heats in the LTJ model has proved very successful in measuring both the heat transfer and reaction constants for a wide range of tests and is being reported elsewhere.

5 Acknowledgment

This research is funded by EPSRC as well as part funded by the Energy Research Accelerator through UKRI. As ever the authors would like to thank Charles Joyce for his manufacturing of widgets and components.

6 List of References

[1] M. Faraday, "On the condensation of several gases into liquids," *Philosophical Transactions of the Royal Society of London,* vol. 113, pp. 189-198, 1823. [Online]. Available: www.jstor.org/stable/107648.

[2] Y. I. Aristov, B. Dawoud, I. S. Glaznev, and A. Elyas, "A new methodology of studying the dynamics of water sorption/desorption under real operating conditions of adsorption heat pumps: Experiment," *International Journal of Heat and Mass Transfer,* vol. 51, no. 19-20, pp. 4966-4972, 2008, doi: 10.1016/j.ijheatmasstransfer.2007.10.042.

[3] N. Mazet, M. Amouroux, and B. Spinner, "ANALYSIS AND EXPERIMENTAL STUDY OF THE TRANSFORMATION OF A NON-ISOTHERMAL SOLID/GAS REACTING MEDIUM," *Chemical Engineering Communications,* vol. 99, no. 1, pp. 155-174, 1991/01/01 1991, doi: 10.1080/00986449108911585.

[4] S. Hinmers, R. E. Critoph, G. Atkinson, and J. Locke, "Ammonia-salt Large Temperature Jump Experimental Technique Advances " in *International Sorption Heat Pump Conference*, Berlin, 2020: TU 2020, pp. 155-158. [Online]. Available: https://core.ac.uk/download/pdf/333593318.pdf#page=160. [Online]. Available: https://core.ac.uk/download/pdf/333593318.pdf#page=160

[5] S. Hinmers and R. E. Critoph, "Modelling the Ammoniation of Barium Chloride for Chemical Heat Transformations," vol. 12, no. 23, p. 4404, 2019. [Online]. Available: https://www.mdpi.com/1996-1073/12/23/4404.

Sorption Kinetics Assessment of Microencapsulated Sorbent with Humid Air Employing Variable Separable Approach

Atif, Amim, Bukke, Kiran Naik

Sustainable Thermal Energy Systems Laboratory (STESL), Department of Mechanical Engineering, National Institute of Technology Rourkela, Odisha, India – 769008; Tel.: +919435686059; Email addresses: naikkb@nitrkl.ac.in; k.bukke@gmail.com

Abstract:

In the present study, a one-dimensional unsteady state-based analytical tool is developed using the separation of variables method for assessing the sorption kinetics of the microencapsulated sorbents with humid air. The developed analytical tool is validated with the experimental data and observed reasonable accuracy of 13%. By choosing, water uptake and energy exchange as performance parameters and EVM/$SrBr_2$40 and $SrBr_2$ as sorption materials, the variation of the performance parameters with microencapsulated sorbent radius and sorption time are analyzed. From the variation analyses, it is found that the water uptake and energy exchange capabilities of EVM/$SrBr_2$40 are high compared to $SrBr_2$. Further, it is observed that $SrBr_2$ takes more time to reach energy equilibrium with humid air in comparison with EVM/$SrBr_2$40. Moreover, it is analyzed that with an increase in microencapsulated sorbent radius, i.e. 0.01 m to 0.04 m, the energy exchange and water uptake decreases by 17% and 43% for EVM/$SrBr_2$40 and 26% and 60% for $SrBr_2$, respectively.

1 Introduction

To curb the dependency on electricity for building heating/cooling applications, utilization of low-grade energy obtained from industrial waste heat is found to be an alternative approach. But to transport the waste/unutilized heat from the industries to the user end, there is a need for thermal energy transportation devices or mobile thermal energy storage (MTES) devices. There are three types of MTES devices available, they are sensible, latent, and thermochemical based MTES devices. In these MTES devices, thermochemical is found to be better because of high energy storage density, less energy loss with time, high reliability, and seasonal energy storage aspects [1]. The thermochemical based MTES device is further classified as microencapsulated sorption and desorption based MTES devices. Among these, in the present investigation, microencapsulated sorption based thermochemical MTES device is chosen due to less hazardous, more reliable, long life, high energy efficient and eco-friendly features. Traditional microencapsulated sorbents that are available for MTES application are silica gel, metal organic frameworks, zeolite, activated carbon, molecular sieves, and natural rocks. But these have less sorption capacity, low volumetric energy storage density, high charging temperature and low thermal stability [2]. Thus, to overcome afore-mentioned material characteristic features, salt hydrate $SrBr_2$ and composite sorbent EVM/$SrBr_2$40 (EVM-expanded vermiculite as a porous matrix in which 40% of $SrBr_2$ is infused into it) are chosen as microencapsulated adsorbent materials for present investigation and analyzed its sorption kinetics behavior with humid air (Fig. 1) by developing an analytical technique using separation variable method.

From the literature, it is observed that very few research works were carried out for assessing the microencapsulated sorbents sorption kinetics experimentally and analytically [1-6]. But none of them developed the analytical tool/technique to investigate the sorption kinetics of microencapsulated sorbent material with humid air for an unsteady state-based model. Therefore, in this paper, an unsteady state based one dimensional analytical tool using variable separable method is developed for assessing the sorption kinetics of microencapsulated sorbent with humid air. Further, by choosing water uptake and energy exchange as performance parameters adsorption behavior of EVM/$SrBr_2$40 and $SrBr_2$ sorbents with humid air is analyzed by varying the sorption time and microencapsulated sorbent radius.

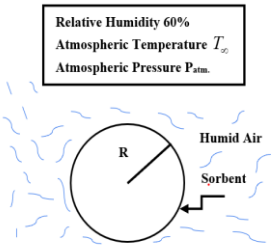

Figure 1. Schematic of microencapsulated sorbent interaction with humid air

2 Variable separable approach for sorption kinetics assessment

In this section, an analytical technique developed for assessing the thermal and sorption behaviour of thermochemical sorbents with humid air is presented in detail. For developing this analytical technique, a one-dimensional unsteady model is considered, and a single micro-encapsulated thermochemical sorbent is chosen. The assumptions made for developing this technique is as follows, a) Thermophysical properties of humid air and

sorbent are constant; b) Effect of convection inside the microencapsulated sorbent is negligible; c) Due to low temperature difference between sorbent and humid air, radiative heat transfer is neglected.
Based on the assumptions, the governing equations for assessing the sorption kinetics are formulated as,

Energy equation: $\frac{\partial^2 T(r,t)}{\partial r_s^2}+\frac{\psi(t)}{k_s}=\frac{1}{\alpha_h}\frac{\partial T(r,t)}{\partial t}$ where $\psi(t)=\rho_s h_s\left(\frac{d\omega}{dt}\right)$ (1)

Mass transfer equation: $\frac{\partial^2 \beta(r,t)}{\partial r_s^2}=\frac{1}{\alpha_m}\frac{\partial \beta(r,t)}{\partial t}$ (2)

The initial and boundary conditions chosen for developing the analytical technique are presented as,
Initial conditions: $t=0;T(r,0)=T_i;\beta(r,0)=\beta_i$ (3)

Boundary conditions: $r=0;\left.\frac{\partial T(r,t)}{\partial r}\right|_{r=0}=0;\ \left.\frac{\partial \beta(r,t)}{\partial r}\right|_{r=0}=0;$ (4a)

$r=R;\ -\mathrm{k}_s\left.\frac{\partial T(r,t)}{\partial r}\right|_{r=R}=h\left(T(r,t)-\mathrm{T}_\infty\right);\ \beta=\beta_i+\gamma=\beta_o;$ (4b)

2.1 Generalized form

a) Governing equations

The energy generation term is a function of time $\psi(t)$. So, to make the energy equation (Eq.1) in a generalised form, the $\psi(t)=\rho_s h_s\left(\frac{d\omega}{dt}\right)$ is differentiated with respect to temperature and linear relation between water uptake (ω) and temperature is chosen from Fig. A of Appendix–I. Thus, after differentiation with respect to temperature and choosing linear relation, the generalized form of energy equation from Eq. 1 is obtained as,

Energy equation: $\frac{\partial\theta}{\partial t}=\phi_h\frac{\partial^2\theta}{\partial r^2}$ where $\theta=T(r,t)-T_\infty$; $\frac{1}{\phi_h}=\frac{1}{\alpha_h}-\frac{AC_{p,s}\rho_s h_s}{k_s h_l}$ (5)

Mass transfer equation: $\frac{\partial\gamma}{\partial t}=\alpha_m\frac{\partial^2\gamma}{\partial r^2}$ where $\gamma=\beta(r,t)-\beta_o$; (6)

b) Initial and boundary conditions

Initial conditions: $t=0;\ \theta=\theta_i;\gamma=\gamma_i$ (7)

Boundary conditions: $r=0;\left.\frac{\partial\theta}{\partial r}\right|_{r=0}=0;\ \left.\frac{\partial\gamma}{\partial r}\right|_{r=0}=0;$ (8a)

$r=R;-\mathrm{k}_s\left.\frac{\partial\theta}{\partial r}\right|_{r=R}=h\theta;\ \gamma=0;$ (8b)

where, ρ_s is sorbent density (kg/m^3), k_s is sorbent thermal conductivity (W/mK), h_s is sorption enthalpy (kJ/kg) [7], $\psi(t)$ is thermo-chemical energy generation (kW/m^3), α_h is thermal diffusivity (m^2/s), α_m mass diffusivity (m^2/s) $C_{p,s}$ is sorbent specific heat capacity (kJ/kg –K), h is convection heat transfer Coefficient (W/m^2/K), h_l is vaporization enthalpy (kJ/kg), β is concentration of sorbate in sorbent ($g_{sorbate}/g_{sorbent}$), β_i initial Concentration, β_o is concentration at surface, A is a constant value: 1.078.
By applying boundary conditions for the given generalizes governing equations and solving based on variable separable method, the final temperature and concentration profiles can be obtained as

Temperature profile: $T(r,t)=T_\infty+\sum_{n=1}^{p}C_n e^{-\phi_h\lambda_n^2 t}\cos\lambda_n r$; where $C_n=\frac{\int_0^R\theta_i\cos\lambda_n r dr}{\int_0^R\cos^2\lambda_n r dr}$ (9)

'λ_n' is the eigen values and it can be plotted by intersecting the correlation – $\cot\lambda_n R=\frac{\lambda_n R}{Bi}$

Concentration profile: $\beta(r,t)=\beta_o+\sum_{n=1}^{p}D_n e^{-\alpha_m\lambda_n^2 t}\cos\lambda_n r$ where $D_n=\frac{\int_0^R\gamma_i\cos\lambda_n r dr}{\int_0^R\cos^2\lambda_n r dr}$ (10)

'λ_n' is the eigen values and it can be plotted using the correlation: $\lambda_n=\frac{(2n+1)\pi}{2R}$

Here, the energy and mass transfer is incorpotated together in energy equation through thermochemical energy generation term which contain water uptake variation with time as shown in Eq.1.

2.2 Performance parameters

a) Water uptake

The amount of water vapour absorbed by the microencapsulated sorbent is determined as water uptake and it is calculated by keeping the value of integral number from n = 1 to n = 5 in summation form of Eq. 10 and neglecting higher integral number. Then, the water uptake is formulated as,

$$\beta = \beta_o + \frac{4(\beta_i - \beta_o)}{\pi}\left(-e^{-\alpha_m \lambda_n^2 t}\left(\frac{\left(\cos\left(\frac{3\pi}{2R}\right) r\right)}{3} \right) + e^{-\alpha_m \lambda_n^2 t}\left(\frac{\left(\cos\left(\frac{5\pi}{2R}\right) r\right)}{5} \right) - .... \right) \tag{11}$$

b) Energy exchange

The energy adsorbed by the sorbent or the energy desorbed from the humid air is termed energy exchange between humid air and sorbent material. This is calculated from Eq. 12 as

Energy exchange: $$\underbrace{C_{p,s}\Delta T + h_l + h_s}_{\text{Energy Adsorbed-Sorbent}} = \underbrace{C_{p,s}\Delta T + h_s + h_l(\beta(r))}_{\text{Energy Desorbed-Humid Air}} \tag{12}$$

3. Model validation

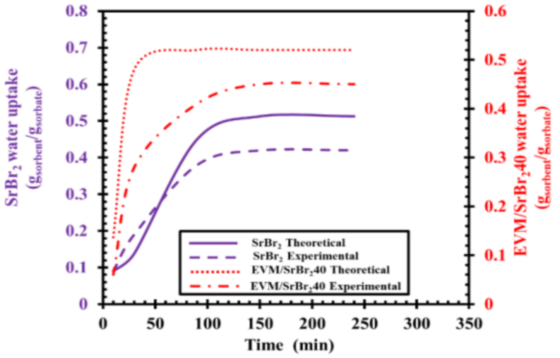

Figure 2. Validation of SrBr$_2$ and EVM/SrBr$_2$40

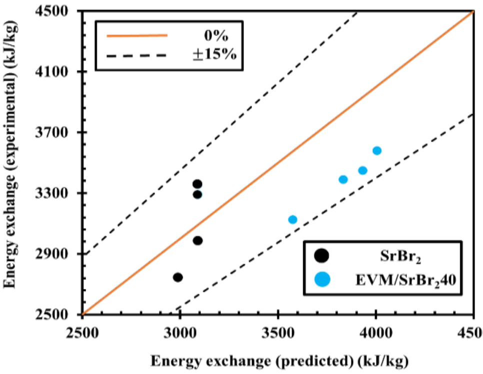

Figure 3. Energy Exchange Validation

Table 1 and Table 2 state the sorbent thermophysical propoerties and inlet condition chosen for the present investigation. To analyze the reliability of the developed analytical technique, a comparison is made in between the predicted data and experimental data available in the literature [7] by choosing EVM/SrBr$_2$40 and SrBr$_2$ as the microencapsulated composite sorbents (Fig. 2). For the developed technique validation purpose, energy exchange and water uptake are taken as performance parameters. From the validation results shown in Figs. 2 and 3, it is observed that the developed technique is reliable with a reasonable accuracy of ±13% and the deviation between experimental and analytical data is due to the assumptions chosen in the presnet invetigation. Further, from Fig. 3 it is found that for a given inlet condition (Table 2), with increase in sorption time, the water uptake increases to a certain extent for both the sorbents and later it becomes constant. This indicates that the sorption capability of the sorbent gets saturated with increase in time. Moreover, from Fig. 3 it is found that for a given inlet condition (Table 2), EVM/SrBr$_2$40 has high adsorption capability compared to SrBr$_2$. This is due to high porous matrix of EVM compared to SrBr$_2$. Further, it is analyzed that the SrBr$_2$.6H$_2$O takes 160 min to reach vapour pressure equilibrium (i.e. when sorbent reaches saturation point) with humid air whereas EVM/SrBr$_2$40 takes 110 min.

Table 1. Thermophysical properties of Sorbents [7]

Sorbents	Thermal conductivity (W/m K)	Density (kg/m^3)	Specific heat capacity (kJ/kg-K)	Sorption enthalpy (h_s)(kJ/kg)
SrBr$_2$.6H$_2$O	1.31	2386	1	814.4
EVM/SrBr$_2$.40	1.33	675	1.10	1656.7

Table 2. Inlet Condition chosen for the present investigation [7, 8]

Parameters	Radius (cm)	Ambient temperature (T_∞) in (°C)	Initial temperature (T_i) in (°C)	Initial concentration (β_i) (g/g)	Surface concentration (β_o)(g/g)	Enthalpy of vaporisation (h_l) (kJ/kg)
Values	5	35	30	0.01	0.6	2260

4 Results and discussion

For the given inlet condition (Table 2), key results obtained from the predicted data (theoretical data) based on the developed analytical model is depicted in Figs. 4 and 5. Fig. 4 shows the energy exchange variation with sorption time for EVM/$SrBr_2$40 and $SrBr_2$. From this figure, it is observed that as the sorption time increases, the energy exchange increases up to certain extent and later, it reaches almost constant. This indicates that humid air and sorbent achieves vapour pressure and energy equilibriums with humid air. Moreover, from Fig. 4 it is found that the EVM/$SrBr_2$40 has high energy exchange capability compared to $SrBr_2$ but percentage increase in energy exchange is only 24% in EVM/$SrBr_2$40 while for $SrBr_2$ it is 37.5% in 90 min of sorption time. This happens due to high energy storage density of EVM/$SrBr_2$40 composite sorbent compared to $SrBr_2$. The variation of energy exchange and water uptake with increase in sorbent radius for EVM/$SrBr_2$40 and $SrBr_2$ sorbents is shown in Fig. 5. From this figure it is found that, as the sorbent radius increases from 0.01 m to 0.04 m , the sorbent energy exchange and water uptake decreases by 17% and 43% for EVM/$SrBr_2$40 and 26% and 60% for $SrBr_2$, respectively. It happens because at the surface of the microencapsulated sorbent, there is high sensible, latent, and chemical heat interactions/exchange phenomenon with humid air compared to inner portion of the microencapsulated sorbent (i.e., towards/near to the centre of the microencapsulated sorbent). Furthermore, it is also observed from Fig. 5 that the EVM/$SrBr_2$40 has high energy exchange and water uptake profiles compared to $SrBr_2$. This states that EVM/$SrBr_2$40 composite has high energy exchange capability compared to $SrBr_2$.

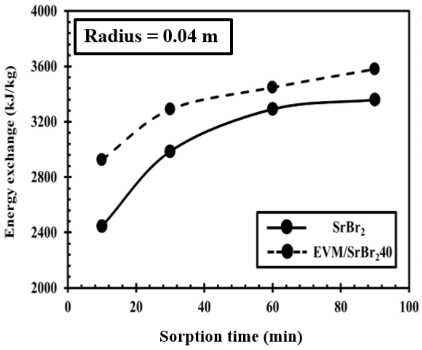

Figure 4. Energy exchange variation with time

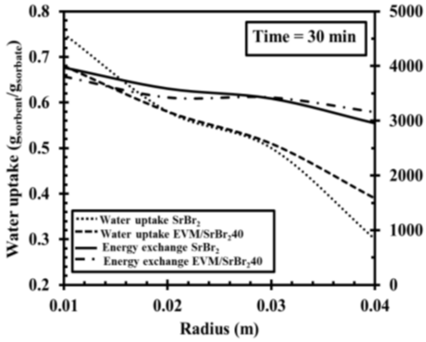

Figure 5. Water uptake and energy exchange variation with radius

5 Conclusions

Developed one dimensional unsteady state based analytical technique to predict the sorption kinetics in between the humid air and microencapsulated sorbent material. Using water uptake and energy exchange as performance parameters, the modelled analytical technique is compared with the experimental data reported in the literature and found good agreement with a maximum possible error of ±13%. Using proposed analytical technique, for a given inlet condition, the variation of sorbent water uptake and energy exchange with time and radius are predicted by choosing EVM/$SrBr_2$40 and $SrBr_2$ as sorbents. The conclusions drawn based on the results obtained from the theoretical data of the developed analytical model is observed as follows,

- In the current study, a simplified analytical model is developed for assessing the sorption kinetics of micro-encapsulated sorbents, $SrBr_2$ and EVM/$SrBr_2$40. Further, thermochemical energy generation is considered in the governing equations in a simplified approach which makes the proposed model unique compared to models reported in the literature.
- The water uptake rate of the EVM/$SrBr_2$40 found to be fast and attains saturation state at 110 min while the $SrBr_2$ has slower water uptake and took 160 min to attain the saturation state.
- This study also predicts the water uptake and energy exchange variation with radius which is unique compared to the reported literature. From the variation analysis, it is observed that for EVM/$SrBr_2$40, the water uptake decrement with radius is only 43% while for $SrBr_2$ it is about 60%. From this, it is concluded that, the smaller diameter is better for sorbent water uptake because as the sorbent diameter increases, core diameter utilization for sorption water uptake reduces, which is not favorable.
- EVM/$SrBr_2$40 energy exchange increases by 24 % while for $SrBr_2$ energy exchange increases by 37.5 % at a given sorption time of 90 min. This result concludes that the EVM/$SrBr_2$40 will have less thermal energy loss compared to $SrBr_2$. Thus, it is noticed from water uptake and energy exchange variation with microencapsulated sorbent radius analyses that the microencapsulated EVM/$SrBr_2$40 is more favorable for practical application.

Moreover, the developed analytical technique simplifies the approach for predicting the sorption and desorption kinetics of different microencapsulated sorbents interacting with humid air/water vapour.

Appendix–I

The thermo-chemical energy generation is represented as,

$$\psi(t) = \rho_s h_s \left(\frac{d\omega}{dt}\right) \tag{I.1}$$

The linear variation of water uptake with temperature is obtained as shown in figure A and it is formulated as,

$$\omega(t) = 1.0784 C_{p,s} \frac{T(r,t)}{h_l} - 16.422 \qquad \text{(I.2)}$$

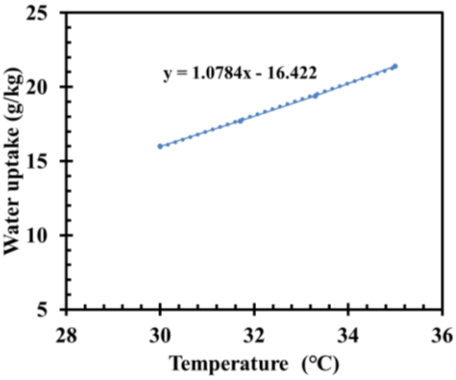

Figure A. Water uptake variation with temperature.

Further it can be simplified as,

$$\frac{\partial \omega}{\partial t} = \frac{\partial \omega}{\partial T} * \frac{\partial T}{\partial t}$$

$$= 1.0784 \frac{C_{p,s}}{h_l} \frac{\partial T(r,t)}{\partial t} \qquad \text{(I.3)}$$

After putting, the governing equation can be rewritten as,

$$\frac{\partial^2 T(r,t)}{\partial r_s^{\,2}} = \left(\frac{1}{\alpha_h} - A \right) \frac{\partial T(r,t)}{\partial t} \qquad \text{(I.4)}$$

where, $A = \frac{1.0784 C_{p,s} \rho_s h_s}{k_s h_l}$

Then, energy equation can be written in generalizes form as,

$$\frac{\partial^2 T(r,t)}{\partial r_s^{\,2}} = \frac{1}{\phi_h} \frac{\partial T(r,t)}{\partial t} \qquad \text{(I.5)}$$

where, $\frac{1}{\phi_h} = \frac{1}{\alpha_h} - A$

6 List of References

[1] P.A.J. Donkers, L.C. Sögütoglu , H.P. Huinink , H.R. Fischer , O.C.G. Adan, A review of salt hydrates for seasonal heat storage in domestic applications, *Applied Energy* 199 (2017) 45–68.

[2] Y. Zhang, R. Wang, Sorption thermal energy storage: Concept, process, applications and perspectives, *Energy Storage Materials* 27 (2020) 352–369.

[3] H. Zhang, Y. Yuan, N. Zhang, Q. Sun, and X. Cao, Core-shell microstructured nanocomposites for synergistic adjustment of environmental temperature and humidity, *Scientific Reports(2016)* 6:36974.

[4] K. Yang, Y. Shi, M. Wu, W. Wang, Y. Jin, R. Li, M. W. Shahzad, K. C. Ng and P. Wang, Hollow spherical SiO2 micro-container encapsulation of LiCl for high-performance simultaneous heat reallocation and seawater desalination, *J. Mater. Chem. A*, 2020, 8, 1887–1895.

[5] J. S. Kharbanda, S. K. Yadav, V. Soni, and A. Kumar, Modeling of heat transfer and fluid flow in epsom salt ($MgSO_4$•$7H_2O$) dissociation for thermochemical energy storage, *Journal of Energy Storage* 31 (2020) 101712.

[6] A. Shkatulov, R. Joosten, H. Fischer, and H. Huinink, Core−Shell Encapsulation of Salt Hydrates into Mesoporous Silica Shells for Thermochemical Energy Storage, *ACS Appl. Energy Mater*. 2020, 3, 6860−6869.

[7] Y.N. Zhang, R.Z. Wang, Y.J. Zhao, T.X. Li , S.B. Riffat, N.M. Wajid, Development and thermochemical characterizations of vermiculite/ $SrBr_2$ composite sorbents for low-temperature heat storage, *Energy* 115 (2016) 120-128.

[8] D. Abhishek, K. Ramakrishna and B. K. Naik, Evaluation of heat and mass transfer coefficients at beetroot-air interface during convective drying, *Interfacial Phenomena and Heat Transfer* 8 (2020) 4.

Surface tension and contact angle measurement of LiBr and Carrol solution

Jian, Zheng[1], Jesús, Castro[1], Carles, Oliet[1], and Assensi, Oliva[1]

[1]*Centre Tecnologic de Transferencia de Calor (CTTC), Universitat Politécnica de Catalunya-BarcelonaTech(UPC), C/Colom 11, Terrassa, E-08222, Spain , Tel + 34 93 739 81 92, cttc@cttc.upc.edu*

Absctract

The surface tension and contact angle play a relevant role in the heat and mass transfer for the absorption system working pairs. However, LiBr aqueous solution surface tension/contact angle studies are limited and for Carrol solution, according to the author's knowledge, there is no published information. In this work, the working pairs LiBr/H_2O and Carrol/H_2O (Carrol contains LiBr and EG (ethylene glycol) with a mass ratio at 4.5:1), with and without surfactant were measured to determine the surface tension and contact angle. The surfactant for working pair LiBr/H_2O is 2-EH (2-Ethyl-1-hexanol), while for the Carrol solution 1-Phenylethanol is employed as surfactant due to the presence of an organic component. The surface tension of different working pairs was measured with the Du Nouy ring method at different concentrations, at ambient condition, and the results show high agreement with other references for a high surfactant concentration (>100PPM) in term of LiBr/H_2O solution. In the results, for a 60% mass fraction LiBr aqueous solution, the surface tension with 2-EH could be reduced to 34.8mN·m^{-1}, while for the Carrol solution at 60% mass fraction, the surface tension with high surfactant concentration is 39mN·m^{-1}. Besides, the contact angle between working pairs and the solid base was also measured by employing a simple optical method. The solid base materials are chosen as SS (stainless steel) and PVC, both are untreated. The contact angle and surface tension show a linear relationship. Moreover, the contact angle of LiBr solution on the SS plate is higher than on the PVC plate, and for the Carrol solution, the contact angle on the SS plate is lower when compared with the LiBr solution.

1. Introduction

Enhancement methods to improve the heat and mass transfer performance for the working pairs are widely applied in the absorption system, in which reducing the surface tension or the contact angle by adding surfactants is very common. Many authors did measurements of the surface tension of the LiBr solution with different concentrations of additives. The surface tension of LiBr, LiCl solutions with additives 1-octanol and 2-EH was measured in [1], employing a drop-volume method. The results show the surface tension varies with different LiBr concentration and temperature, and the 2EH could reduce the surface tension to 35.24 mN·m^{-1} while 1-octanol could reduce it to 25.17mN·m^{-1} at 25°C. The surface tension of 60wt% LiBr solution with 2-EH was measured in [2] with the Du Nouy ring method, and the results showed the surface tension changed from 81.3 to 34.9 mN·m^{-1} with 2EH concentration at 0 - 200ppm. Besides 2-EH and 1-octanol, CTAC/CTAB (cetyltrimethyl ammonium chloride/cetyltrimethyl ammonium bromide) were also used as additives to reduce the surface tension by [3], since 1-octanol is easy to decompose at high temperature. Moreover, apart from adding additives in the liquid phase, the surfactant in the vapour phase could also play an important role to reduce the surface tension according to [4]. In which a drop volume method was employed to measure the surface tension change of water and 60wt% LiBr solution with the presence of 2-EH in the air and the results showed that the surfactants were more efficient in the vapour phase than in the liquid phase. In terms of the working pair Carrol-H_2O (proposed by [5] to reduce the crystallization risk), and the standard heat transfer additive is not operative in the LiBr/EG/water ternary fluid, thus, phenylmethylcarbinol (PMC, 1-Phenylethanol) was used as a surfactant, suggested by [6].

Besides the surface tension of the solution, the contact angle also plays an important role in the heat and mass transfer performance, and the contact angle depends not only on the liquid properties but also on the solid base surface characteristics. The contact angle of LiBr solution on different materials was measured by [7, 8] with the sessile drop method using a goniometer. The results showed that the surface tension and contact angle have a linear relationship with all the materials. In case the goniometer is not available, a simple optical method was proposed by [9] to determine the contact angle with an acceptable error without expensive equipment.

The object of this work is to present the experimental results of the surface tension of the new working pairs Carrol

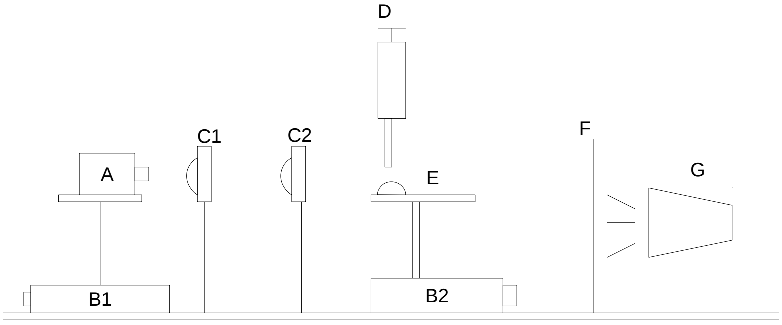

Figure 1: *Experimental set-up for the measurement of contact angle: A is camera, B1, B2 are moving stage, C1, C2 are lens, D is micro pipet, E is drop sample, F is diffuser, and G is light source*

solutions with and without additives and its contact angle with stainless steel, also, the results will be compared with the LiBr solution. In this work, the Du Nouy ring method was used to measure the surface tension of working pairs LiBr/H_2O and Carrol/H_2O with surfactant concentration 20 - 2000 ppm in the liquid phase, and the surfactants were 2-EH, 1-Phenylethanol, respectively. Besides, the contact angle of both working pairs was measured with the simplified optical method at stainless steel and PVC plates.

2. Experimental Set-up

A tensiometer with the Du Nouy ring method was used to measure the surface tension of different samples, and the tensiometer has a resolution of 0.1 $\text{mN}\cdot\text{m}^{-1}$, i.e. error 1%. For the contact angle, the measurement set-up is shown in Figure 1, and the set-up consists of camera, lens, moving stage, micro pipet and light source, etc. For the solution sample, it was prepared using a balance with resolution at 10mg, LiBr purity 99%, Ethylene glycol purity 99.5%, distilled water purity 99%, and then, a micropipette at an error of 1% is used to transport surfactant into the solution sample. The liquid samples should be prepared carefully without contamination and keep sealed before the measurement. For the Carrol solution, it should be taken into consideration that the stratification will significantly affect the final result, so the solution should be well mixed before the measurement. In terms of the solid base for the measurement of contact angle, stainless steel and PVC plate were cut from untreated raw material with a dimension of 3cm*3cm, then a 3μL droplet is introduced on the dry plate, and finally, the image is taken through the montage. The contact angle is calculated by software ImageJ.

3. Results

3.1. Surface tension measurement results

A correction of the surface tension measurement is automated with ASTMD-971 method [10], as shown in equation 1 and 2:

$$V = P * F \tag{1}$$

$$F = \sqrt{0.7250 + 0.01452 * P/C^2/(D-d) + 0.04534 - 1.679 * r/R} \tag{2}$$

where V, P, F are the real surface tension, measured surface tension and correction parameter, respectively. C is the perimeter of the platinum ring in cm, R is the diameter of the ring in cm, D and d are the density at 25°C of liquid and air, respectively, in g/mL. And r is the thickness of the wire of the ring, also in cm. Table 1 shows the results of the surface tension and compared them with other references. The surface tension of an aqueous solution is affected by many factors, such as the purity of the substance, the measurement method, the relative humidity, etc. Hence, the data from different authors won't completely agree with each other. In this work, the surface tension of pure liquid of distilled water and ethylene glycol is measured to validate the precision of measurement. And when those two working pairs are compared, due to the presence of organic compound EG, the Carrol solution has lower surface tension. Figure 2 shows the surface tension results of the LiBr solution with 2-EH and Carrol solution with 1-Phenylethanol at different concentrations. In terms of the LiBr solution, with high additive concentration, the surface tension reaches 34.5 $\text{mN}\cdot\text{m}^{-1}$, while the surface tension of Carrol solution with surfactant could be reduced

Table 1: *Surface tension results of LiBr and Carrol solution at different concentrations and compare them with other references*

Liquid type	Experimental results		Reference value	
	T[°C]	σ[mN·m]	T[°C]	σ[mN·m^{-1}]
Distilled water	21.2	72.9	20	72.4[11]
Ethylene glycol	21.2	47.3	20	47.3[12]
50%LiBr	21.2	82.9±0.2	20	88.1±0.15[1]
			24	77.6±0.4[2]
55%LiBr	22.5	86.2±0.3	28	86.42[3]
60%LiBr	21.2	91.3±0.6	25±0.2	94.3±0.5[4]
			20	94.4±0.1[1]
55%Carrol	21.3	72.5±0.2	-	-
60%Carrol	21.3	74.7±0.3	-	-

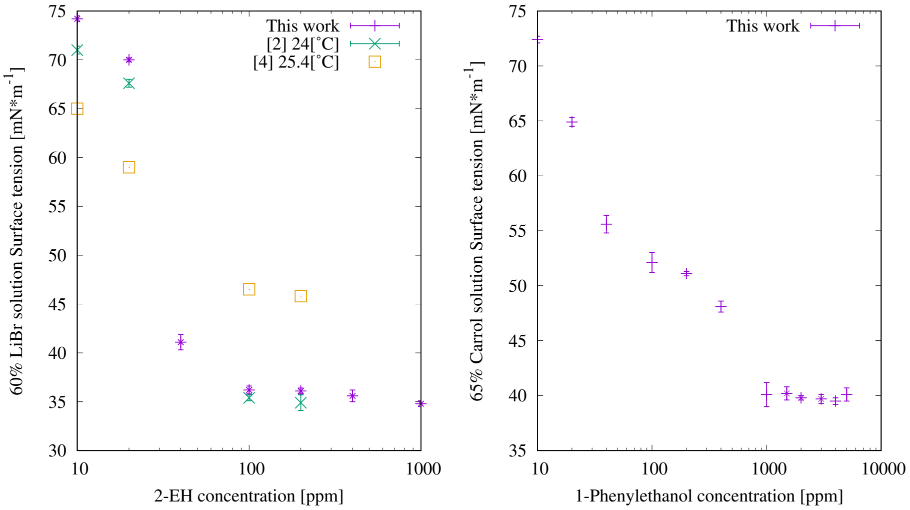

Figure 2: *Surface tension results of two working pairs with a surfactant, and measurements were made under 22.5±1°C, 35±1RH%. The left figure represents the surface tension change of 60wt% LiBr solution with 2-EH, and the right one represents the Carrol solution at 60wt% with 1-Phenylethanol.*

to 39 mN·m^{-1}. And from the result, it could be concluded that the surfactant solubility limit of 2-EH in the LiBr solution is much lower than 1-Phenylethanol in the Carrol solution. The solubility limit observed in this work is around 100 ppm, while [4] calculated the solubility limit as 27 ppm. For the Carrol solution, the solubility observed is around 1000 ppm, more research should be done to quantify the solubility limit.

Besides additive in the liquid sample, the additive in the vapour phase is also considered a key parameter to surface tension, [4] found that for LiBr solution, the effect of 2EH from the vapor side is more significant than the effect from the liquid side with a drop volume method. Further investigation could be carried out for the additive in vapor side, besides, the surface tension in the high vacuum condition, like the working condition in the absorber, is also interesting since the results may differ from the measurements in the ambient condition.

3.2. Contact angle measurement results

The contact angle results are shown in Figure 3, in which the 60% LiBr solution has a higher contact angle on SS than on the PVC plate, and the 60% Carrol solution has a lower contact angle when compared with LiBr solution. Also, Figure 3 shows the linear relationship between surface tension and contact angle. The surface roughness may be the reason for the significant deviation, in this work, the SS solid base is untreated raw material, while in [7, 8] the SS plate surface roughness R$_a$ is 0.01 μm and 287.4 nm, respectively. Besides the surface roughness, other parameters like liquid purity, droplet sample volume, minor contamination of the system could also affect the final results of the contact angle. Moreover, the contact angle of solution with surfactant is also measured, unfortunately, no reliable data was obtained by the author due to the uncertainty of surfactant concentration of the liquid droplet.

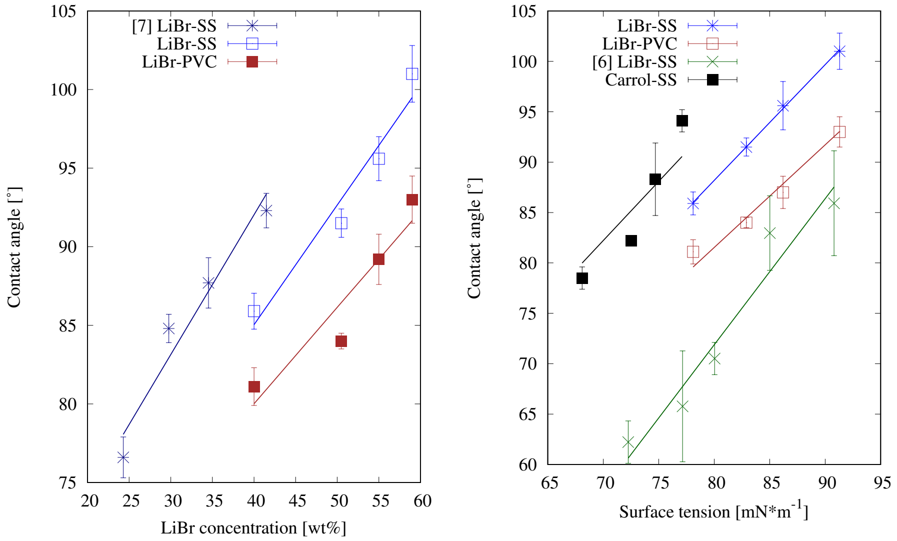

Figure 3: *Experimental results of contact angle of LiBr and Carrol solution , and the measurements were made under 22.5±1°C, 35±1RH%. The left figure represents the LiBr solution contact angle change against concentration, and the right one represents the contact angle evolution of both LiBr and Carrol solution against surface tension, and the concentration is the only variable in the measurement. No additive is added in the measurement of contact angle.*

Other characteristics like MLFT (Minimum Liquid Film Thickness) and MWR (Minimum Wettig Rate) are strongly dependent on the contact angle, and [7] obtained theoretical results with the experimental results of contact angle. Details of the relationship between MLFT/MWR and contact angle in both simulation and experiment deserve further investigation.

4. Conclusions

In this work, the surface tension of working pairs LiBr/H_2O and Carrol/H_2O is measured, for the 60% mass LiBr solution, the surface tension will change from 91.3 to 34.8 mN·m^{-1} at additive 2-EH concentration 0 - 1000 ppm. Meanwhile, in the 60% Carrol solution, the surface tension reduced from 74.7 to 39.8 mN·m^{-1} at additive 1-Phenylethanol concentration 0-5000 ppm. And the solubility limit observed of 2-EH in 60% LiBr solution is around 100 ppm, while the 1-Phenylethanol in 65% Carrol solution is around 1000ppm. In terms of contact angle, from concentration 40-60% LiBr solution, varies from 85-100° at stainless steel plate and 80-92° on a PVC plate, and for the Carrol solution on a stainless plate, the contact angle is 77-92°. For future work, the effect of additive in the vapour phase to the surface tension is interesting to investigate, other parameters like relative humidity, air temperature, additive vapor pressure, vacuum condition could also be controlled to obtain further information. In term of the contact angle, experiments of MLFT and MWR could be carried out for more details in an absorption system, especially for a falling film type absorber.

5. Acknowledgment

J. Zheng holds a China Scholarship Council Studentship with the Polytechnical University of Catalonia.
This project has received funding from SOLAR-ERA.NET Cofund 2 joint call undertaking under the European Union's Horizon 2020 research and innovation programme.
This work has been financially supported by the Ministerio de Ciencia e InnovaciÃşn, Spain (PID2020-115837RB-I00)

References

[1] Yao,W., Setterwall, F., and Bjuretröm, H. (1991): Surface Tension of Lithium Bromide Solutions with Heat-Transfer Additives. *Journal of Chemical and Engineering Data*, *vol.36(1)*, pp.96-98.

[2] Kim, K. J. and Janule, V. P. (1994): Surface tension of aqueous lithium bromide with 2-ethyl-1-hexanol. *International Communications in Heat and Mass Transfer*, *vol.21(6)*, pp.839-848.

[3] Hua Cai, W., wei Kong, W., Wang, Y., sheng Zhu, M., and lei Wang, X. (2015): Surface tension of lithium bromide aqueous solution/ammonia with additives and nano-particles.*Journal of Central South University*, *vol.22(5)*, pp.1979-1985.

[4] HYuan, Z. and Herold, K. E. (2001): Surface tension of pure water and aqueous lithium bromide with 2-ethyl-hexanol.*Applied Thermal Engineering*,*vol.21*, pp.881-897.

[5] R. Reimann (1979): Properties of the Carrol system and a machine design for solar powered, air cooled, absorption space cooling.*Technical report*.

[6] Löf, G. O. (Ed.). (1993): Active solar systems, *vol.6*, MIT Press.

[7] Martinez-Urrutia, A., Fernandez de Arroiabe, P., Ramirez, M., Martinez-Agirre, M., and Mounir Bou-Ali, M. (2018): Contact angle measurement for LiBr aqueous solutions on different surface materials used in absorption systems.*International Journal of Refrigeration*, *vol.95*, pp.182-188.

[8] Qi, R., Lu, L., Jiang, Y. (2015): Investigation on the liquid contact angle and its influence for liquid desiccant dehumidification system. *International Journal of Heat and Mass Transfer*, *vol.88*, pp.210-217.

[9] Lamour, G., Hamraoui, A., Buvailo, A., Xing, Y., Keuleyan, S., Prakash, V., Eftekhari- Bafrooei, A., and Borguet, E. (2010): Contact angle measurements using a simplified experimental setup. *Journal of Chemical Education*, *vol.87(12)*, pp.1403-1407.

[10] ASTM D97-17b (2017): Standard Test Method for Pour Point of Petroleum Products. ASTM International, West Conshohocken, PA. www.astm.org

[11] Harkins, W. D. (1952): The physical chemistry of surface films.*Reinhold.*.

[12] Adamson, A. W., Gast, A. P., et al. (1967): Physical chemistry of surfaces.,Interscience publishers New York, *vol.15*.

Performance Evaluation of an Adsorption Heat Pump Having Transitional Metal Doped Green Aluminum Fumarates as Adsorbents

Rupam, Tahmid Hasan[1,2,*] , Palash, M.L.[3] , Saha, Bidyut Baran[2,4]

[1] *Kyushu University Program for Leading Graduate School, Green Asia Education Center, Kyushu University, Kasuga-koen 6-1, Kasuga-shi, Fukuoka 816-8580, Japan*

[2] *International Institute for Carbon-Neutral Energy Research, Kyushu University, 744 Motooka, Nishi-ku, Fukuoka 819-0395, Japan*

[3] *Department of Electrical and Electronic Engineering, University of Dhaka, Dhaka-1000, Bangladesh*

[4] *Department of Mechanical Engineering, Kyushu University, 744 Motooka, Nishi-ku, Fukuoka 819-0395, Japan*

**Correspnding author email address: tahmidrupam33@gmail.com*

Abstract:

This study aims to analyze and compare the performance of transitional metal (10 % Ni and Co) doped aluminum fumarate metal organic frameworks as adsorbent materials in an adsorption-based heat pump where water is considered as the refrigerant. Porous properties of the in-situ metal doped aluminum fumarates namely the surface area and pore volume are assessed. Doping of metal resulted in a reduction of surface area and pore volume. Additionally, the water uptakes on these adsorbents were measured at 303 K and 353 K gravimetrically. It was found that, Co doped samples showed higher equilibrium uptake while the adsorption isotherm moved towards the lower pressure region. After that, adsorption cycles involving the pressure, temperature, and uptakes (P-T-q diagrams) were drawn to investigate their cyclic performances. The specific cooling effects were also calculated and compared among the associated adsorbent/adsorbate pairs. For the calculations, the adsorption, desorption, evaporator and condenser temperatures were considered as 303 K, 353 K, 288 K and 308 K respectively.

1 Introduction

Solid-gas adsorption phenomenon has been utilized in a wide range of heat transformation applications started from heating[1], cooling[2], air conditioning (HVAC)[3,4], gas separation[5], storage[6], purification[7] and lately thermal batteries[8]. Among these adsorption-based heating and cooling systems have stand out as one of the most potential technologies in the past decades because of the systems being noiseless, non-corrosive and environment friendly. Additionally, these systems can be driven by low grade heat energy (typically below 373 K heat source is required) often retracted from waste heat sources or solar thermal collectors. The heart of the adsorption-based heat pumps is considered as the adsorbent/refrigerant pair being used. Generally, for water assisted adsorption heat pump systems, silica gels and zeolites are among the popular choices for adsorbent materials which inherit lower net uptake, high release heat and a linear water uptake[9,10]. Because of the lower net uptake and thermal conductivity of silica gels, the current water-based adsorption heat pump is bulky, thermally inefficient and possess a high installation cost. Over the years, many researchers have tried to increase the uptake and thermal conductivity of the silica gels and zeolites by different approaches, yet no satisfactory outcome has emerged[11,12]. However, in recent times, development in the synthesis and modification techniques of metal organic frameworks (MOFs) have shown promise in developing the existing water-assisted adsorption chillers to its next phase. MOFs inherit higher thermal conductivity along with high surface area and tunable porosities[13]. Moreover, hydrophilic groups can be easily incorporated in MOFs structures to increase its affinity towards water. Additionally, water adsorption isotherms in MOFs usually take the shape of ‘S’ which enables the system to have a higher net uptake[14]. The net uptake is directly proportional to the specific cooling effect (SCE) which is an essential performance indicator of an adsorption chiller[15]. SCE indicates about the cooling effect produced by unit mass of the adsorbent material.

Aluminum fumarate metal organic framework has been considered as one of the most potential alternative adsorbents for next generation adsorption chillers because of its ‘S’ shaped water adsorption isotherm with a hydrophobic length around 20% RH. These conditions are vital for having a higher net uptake in the preferred pressure region between P/Ps 0.1 to 0.3 [8]. Palash et, al. [16] in their study have shown that, the transitional metals 10% Ni and 10% Co doped aluminum fumarate shows higher water uptake and also the isotherms shift towards the lower pressure region. These findings are also crucial for further development of the adsorption chiller. Therefore, this study, aims to investigate the system performances of these modified adsorbents by means of drawing adsorption cycles utilizing their respective water adsorption isotherms. Additionally, SCE is calculated for the samples considering the adsorption, desorption, evaporator and condenser temperatures as 303 K, 353 K, 288 K and 308 K respectively to show a reasonable comparison between them.

2 Experiment and mathematical models

To investigate about the porous properties of the samples, N_2 adsorption/desorption experiment were performed at 77 K. the samples were regenerated at 333 K for 3 hours before N_2 adsorption/desorption experiment. BET model was invoked to calculate the BET surface area and Non-localized density functional theory was used to measure the pore size distribution.

The water adsorption on to the samples were measured gravimetrically using the magnetic suspension adsorption measurement unit (Rubotherm of type MSB-VG-S2), supplied by MicrotracBEL, Japan. Detailed experimental procedures can be found in the literatures provided by Palash et, al.[16].

For estimating the SCE, the phase change (from vapour to liquid) of the net refrigerant uptake is considered. The SCE also accounts for the heat released by the refrigerant entering to the evaporator from the condenser. Equation (1) can be used to measure the SCE for an adsorption cooling system.

$$SCE = \left(q_{ads} - q_{des}\right)\left\{ h_{fg}(T_{evap}) - \int_{T_{evap}}^{T_{cond}} dh_f \right\} \tag{1}$$

For simplicity, the latent heat of evaporation can be considered as the cooling capacity of the adsorption chiller whilst the adsorption enthalpy can be thought of as the minimum energy requirement for driving the system.

3 Results and discussion

The results obtained from the volumetric N_2 adsorption/desorption is summarized in Table 1.

Table 1 – porous properties of the studied samples.

Sample name	BET Surface area [m^2/g]	Pore size [Å]	Pore volume [cm^3/g]
ALFC	600.3	11.93	0.32
SMOF	874.10	10.84	0.371
SMOF 10% Co	751.56	11.2	0.307
SMOF 10% Ni	745.68	11.17	0.302

**SMOF is green synthesized aluminum fumarate. ALFC is commercial aluminum fumarate produced using DMF

It is evident from Table 1, that all the studied samples are microporous in nature. The green synthesized aluminum fumarate (SMOF) has higher BET surface area compared with the DMF based commercial aluminum fumarate. The in situ doping of transitional metals on to the green synthesized aluminum fumarate results in a reduction of BET surface area. The water adsorption isotherms of the studied samples are given in Figure 1. From Figure 1(a). it can be concluded that the water uptake in the doped samples were higher than that of the parent sample. When compared, the 10% Co doped sample exhibited the highest equilibrium uptake. Moreover, the isotherms have shifted towards the lower pressure region as a result of metal doping.

Figure 1 (b), (c) and (d) illustrates the adsorption cycle drawn using the water adsorption isotherms of the SMOF, SMOF 10% Co and SMOF 10%Ni samples respectively. When drawing the adsorption cycles, the adsorption, desorption, evaporator and condenser temperatures were considered as 303 K, 353 K, 288 K and 308 K respectively as operating conditions. From the adsorption cycles, the net uptake for SMOF, SMOF 10% Co, and SMOF 10% Ni are obtained as 0.25 kg kg^{-1}, 0.26 kg kg^{-1}, 0.24 kg kg^{-1}

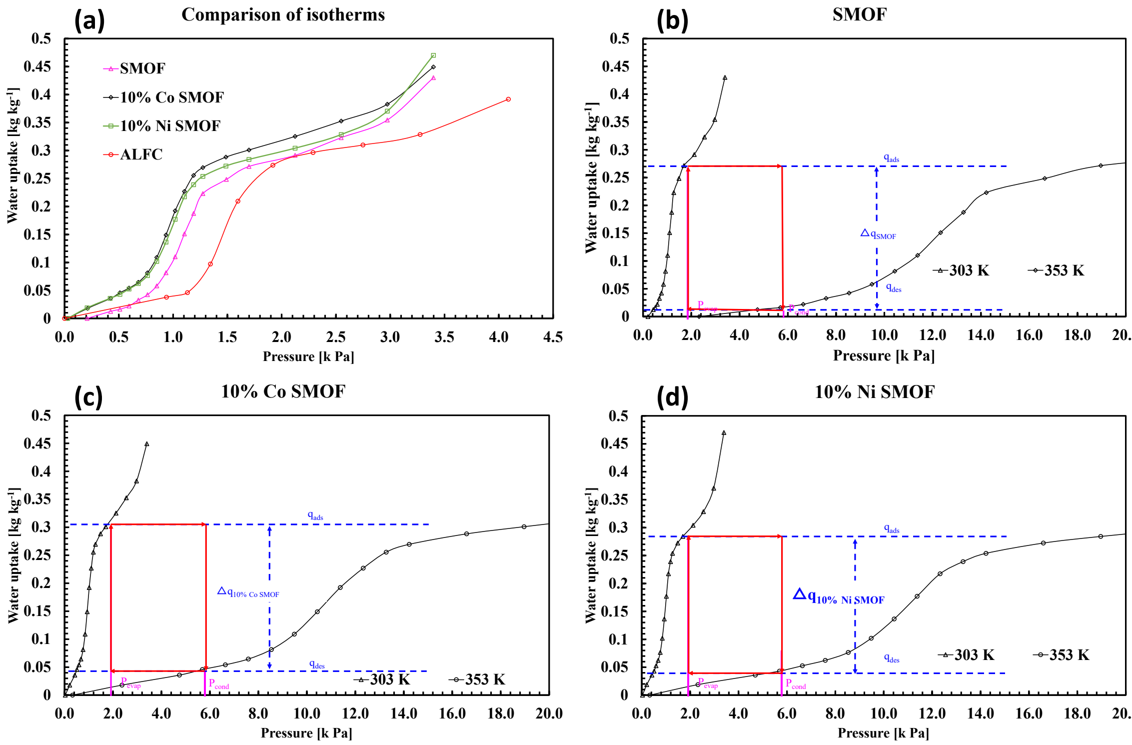

Figure 1 –(a) comparison between the water adsorption isotherms for all the samples at 303 K, Adsorption cycles (b)SMOF (c) SMOF 10 % Co (d) SMOF 10%Ni at T_{ads} = 303 K, T_{des} = 353 K, T_{evap} = 288 K, T_{cond} = 308 K

Equation (1) is used to calculate the specific cooling effect of the repetitive samples considering a cooling temperature of 288 K. Figure 2. depicts the SCE values for the assorted samples and compares them with the SCE values obtained for traditional RD silica gel.

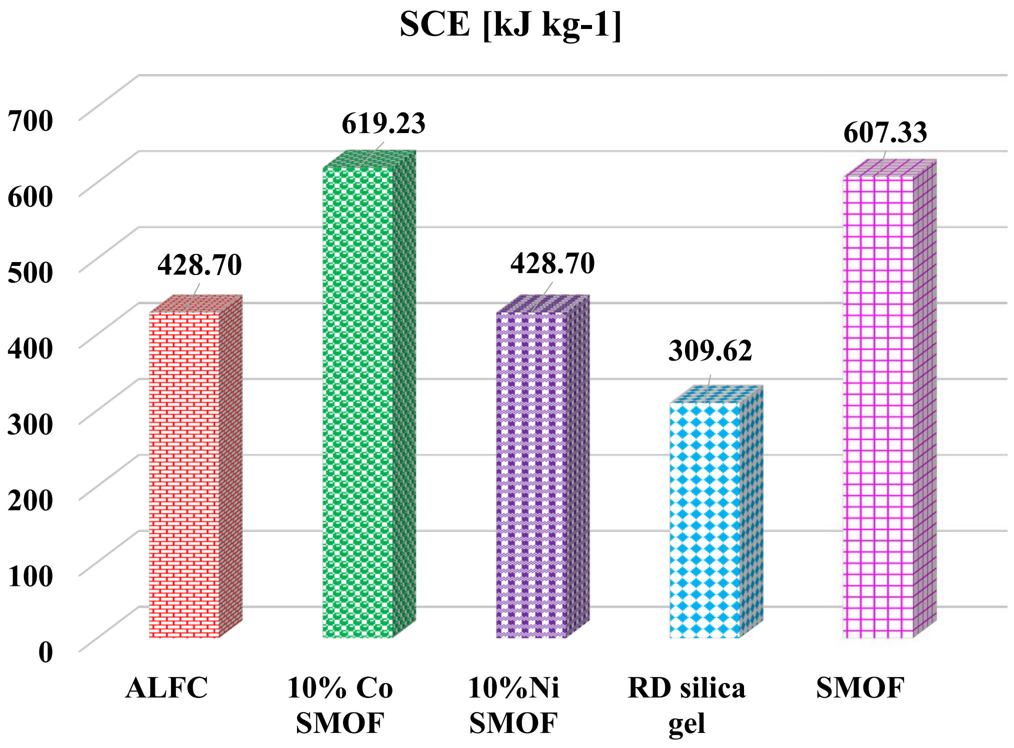

Figure 2 –Specific cooling effect of the samples at T_{ads} = 303 K, T_{des} = 353 K, T_{evap} = 288 K, T_{cond} = 308 K

From Figure 2. it can be concluded that the SMOF10% Co sample outperforms the other two samples in terms of SCE. Interesting fact is that, although SMOF 10% Ni has higher equilibrium uptake when compared with parent SMOF, due to the lower net uptake it has lower value of SCE.

4 Conclusions

Controlled transitional metal doping into aluminum fumarate MOFs can enhance their water sorption properties by introducing the mixed valance metallic ions in the structure. Though the BET surface area decreases with increased amount of transitional metals, the equilibrium water uptake increases. Moreover, the isotherm shifts towards lower pressure region ensuring a lower cooling temperature. The specific cooling effect has shown that the SMOF 10% Co has the highest value of 619 kJ kg^{-1} when compared with SMOF(607 kJ kg^{-1}) and SMOF 10% Ni(428 kJ kg^{-1}). Despite of SMOF 10% Ni having higher equilibrium uptake when compared with parent SMOF, due to the lower net uptake it has lower value of SCE. However, all the MOFs characterized in this study, showed significantly higher values of SCE when compared with the SCE values obtained with traditional RD silica gel. Therefore, it can be concluded that the MOF samples can be a feasible alternative adsorbent for the next generation water based adsorption chiller.

5 Acknowledgment

The initial author acknowledges the Japan Society for the Promotion of Science (JSPS) for financial support.

6 References

[1] A. Pal, K. Thu, S. Mitra, I.I. El-Sharkawy, B.B. Saha, H.-S. Kil, S.-H. Yoon, J. Miyawaki, Study on biomass derived activated carbons for adsorptive heat pump application, Int. J. Heat Mass Transf. 110 (2017) 7–19. https://doi.org/https://doi.org/10.1016/j.ijheatmasstransfer.2017.02.081.

[2] T.H. Rupam, M.A. Islam, A. Pal, A. Chakraborty, B.B. Saha, Thermodynamic property surfaces for various adsorbent/adsorbate pairs for cooling applications, Int. J. Heat Mass Transf. 144 (2019) 118579. https://doi.org/10.1016/j.ijheatmasstransfer.2019.118579.

[3] K. THU, N. TAKEDA, T. MIYAZAKI, B.B. SAHA, S. KOYAMA, T. MARUYAMA, S. MAEDA, T. KAWAMATA, Experimental investigation on the performance of an adsorption system using Maxsorb III + ethanol pair, Int. J. Refrig. (2018). https://doi.org/10.1016/j.ijrefrig.2018.06.009.

[4] M.L. Palash, T.H. Rupam, A. Pal, A. Chakraborty, B.B. Saha, R. Wang, Design principles for synthesizing high grade activated carbons for adsorption heat pumps, Chem. Eng. J. Adv. 6 (2021) 100086. https://doi.org/10.1016/j.ceja.2021.100086.

[5] A. Abedini, E. Crabtree, J.E. Bara, C.H. Turner, Molecular analysis of selective gas adsorption within composites of ionic polyimides and ionic liquids as gas separation membranes, Chem. Phys. 516 (2019) 71–83. https://doi.org/10.1016/j.chemphys.2018.08.039.

[6] B. Li, H.-M. Wen, Y. Yu, Y. Cui, W. Zhou, B. Chen, G. Qian, Nanospace within metal–organic frameworks for gas storage and separation, Mater. Today Nano. 2 (2018) 21–49. https://doi.org/10.1016/J.MTNANO.2018.09.003.

[7] S.J. Chen, Y. Fu, Y.X. Huang, Z.C. Tao, M. Zhu, Experimental investigation of CO2 separation by adsorption methods in natural gas purification, Appl. Energy. 179 (2016) 329–337. https://doi.org/10.1016/J.APENERGY.2016.06.146.

[8] S. Kayal, A. Chakraborty, H.W.B. Teo, Green synthesis and characterization of aluminium fumarate metal-organic framework for heat transformation applications, Mater. Lett. 221 (2018) 165–167. https://doi.org/https://doi.org/10.1016/j.matlet.2018.03.099.

[9] M.J. Kalmutzki, C.S. Diercks, O.M. Yaghi, Metal–Organic Frameworks for Water Harvesting from Air, Adv. Mater. 30 (2018) 1–26. https://doi.org/10.1002/adma.201704304.

[10] M.L. Palash, A. Pal, T.H. Rupam, B.-D. Park, B.B. Saha, Surface energy characterization of different particulate silica gels at infinite dilution, Colloids Surfaces A Physicochem. Eng. Asp. 603 (2020) 125209. https://doi.org/10.1016/j.colsurfa.2020.125209.

[11] K.A. Rocky, A. Pal, T.H. Rupam, Nasruddin, B.B. Saha, Zeolite-graphene composite adsorbents for next generation adsorption heat pumps, Microporous Mesoporous Mater. 313 (2021) 110839. https://doi.org/10.1016/j.micromeso.2020.110839.

[12] K.A. Rocky, A. Pal, T.H. Rupam, M.L. Palash, B.B. Saha, Recent advances of composite adsorbents for heat transformation applications, Therm. Sci. Eng. Prog. 23 (2021) 100900. https://doi.org/10.1016/j.tsep.2021.100900.

[13] I. Jahan, M.A. Islam, M.L. Palash, K.A. Rocky, T.H. Rupam, B.B. Saha, Experimental Study on the Influence of Metal Doping on Thermophysical Properties of Porous Aluminum Fumarate, Heat Transf. Eng. (2020) 1–15. https://doi.org/10.1080/01457632.2020.1777005.

[14] Y.I. Aristov, Challenging offers of material science for adsorption heat transformation: A review, Appl. Therm. Eng. 50 (2013) 1610–1618. https://doi.org/10.1016/J.APPLTHERMALENG.2011.09.003.

[15] T.H. Rupam, M.A. Islam, A. Pal, B.B. Saha, Adsorption thermodynamics and performance indicators of selective adsorbent/refrigerant pairs, Appl. Therm. Eng. 175 (2020) 115361. https://doi.org/10.1016/j.applthermaleng.2020.115361.

[16] M.L. Palash, I. Jahan, T. Hasan Rupam, S. Harish, B. Baran Saha, Novel Technique for Improving the Water Adsorption Isotherms of Metal-Organic Frameworks for Performance Enhancement of Adsorption Driven Chillers, Inorganica Chim. Acta. (2019) 119313. https://doi.org/10.1016/J.ICA.2019.119313.

Novel LiCl solutions for crystallization control in LiCl/H_2O absorption systems

Lin, Yao[1] (First author), Xiao, Fu[2] (Second author)

[1] *Lin Yao, Department of Building Services Engineering, The Hong Kong Polytechnic University, Kowloon, Hong Kong*

[2] *Xiao Fu, Department of Building Services Engineering, The Hong Kong Polytechnic University, Kowloon, Hong Kong. E-mail: linda.xiao@polyu.edu.hk; Tel : (+852) 27664194*

Abstract:

Alkali halides solutions have long been used in the absorption field due to their high hygroscopicity. Most absorption technologies rely on the concentration difference of alkali halides solutions during absorption. Solutions with higher concentrations are favored for their lower vapor pressure. However, the concentrated solution has a higher risk of crystallization, which will influence the fluidity and blocking flow channels in absorption devices. In this paper, two additives are introduced to modify the crystallization of LiCl solution: ethylene glycol (EG) and SiO_2 nanoparticles (SNPs). Experiments show that EG can significantly increase the solubility of LiCl, allowing the LiCl solution to work at a higher concentration. Combining EG and SNPs can further allow the LiCl solution to work at a concentration higher than the solubility by promoting the growth of LiCl fine crystal slurry with good fluidity. Both are potential alternatives in absorption devices.

1 Introduction

Absorption technologies are gaining increasing attention due to their potential in harvesting low-grade waste heat, exploiting intermittent solar energy and balancing the fluctuations in energy supply and demand. Currently, absorption technologies are widely used in liquid desiccant [1], absorption chiller [2], absorption heat pump [3] ,etc. Commonly used working pairs in the absorption field includes LiBr/H_2O, LiCl/H_2O, ammonia/H_2O, etc. For LiCl/H_2O in the absorption chillers and absorption heat pumps, the concentration is typically 35~45% and while the working concentration difference is generally lower than 6%. Once the concentration exceeds the solubility or the ambient temperature drops below the crystallization temperature, the absorption system suffers from crystallization risks. Therefore, in their real operations, both the working concentration range and the working temperature require strict control to avoid crystallization. For absorption thermal energy storage, typically, the energy storage density increases with the concentration difference. When the crystallization is allowed in the solution, is usually called “three-phase absorption thermal energys storage”, which has an even higher energy storage density since the concentration of the solution is higher than the solubility. To realize this, proper control of the crystallization is crucial[4]. However, existing studies haven’t fully address the crystallization issue for three-phase absorption thermal energy storage.

There are two possible ways to overcome the crystallization risks, both relying on using additives to modify the properties of the solution. The first is to inhibit crystallization at high concentrations and low temperatures. The second is to allow only fine and suspended crystals to grow in the solution. The solution eventually becomes crystal slurries with good fluidity. Two types of additives corresponding to these two possible ways are available in the literature, i.e. crystallization inhibitors and nucleating agents.

Wang et al. [5] summarized some commonly used crystallization inhibitors for the LiBr solution, including organic compounds, inorganic salts and ionic liquids. Organic compounds, like ethylene glycol (EG) [6] and propylene glycol (PG) [7], can reduce the crystallization temperature of LiBr/H_2O. Biermann [8] developed a novel mixed fluid called “Carrol” for absorption devices to inhibit crystallization. The mass ratio of LiBr and ethylene glycol in “Carrol” was 4.5:1. Thermodynamic properties of Carrol such as pressure-concentration-temperature equilibrium, crystallization curve, density and viscosity were also measured by Riemann [9]. Since then, “Carrol” was widely adopted in various absorption devices including absorption chillers [10] and absorption heat pumps [11]. Yoon and Kwon [12] compared the crystallization temperature of LiBr solution with and without propylene glycol. The authors found that propylene glycol can increase the crystallization concentration limit by 8% at a constant vapor pressure. Despite the enhancement of solubility, the concentration of a solution with crystallization inhibitors should still be kept below the enhanced solubility to prevent crystallization. There are very few studies on adding nucleating agents to modify solutions, but in the existing literature, they exhibited good potential for crystallization control. Itaya et al. [13] proposed a modified LiBr solution by dispersing zeolite powder into it. Zeolite assisted the formation and suspension of LiBr fine crystals. Moreover, the LiBr fine crystal slurries maintained good fluidity. However, nucleating agents cannot increase the solubility of salts. Whether the combination the crystallization inhibitors and nucleating agents can take advantage of both additives remains further investigation.

This paper presents a novel method to modify the LiCl solution by adding two types of additives. The solubility of LiCl in water increases and only fine crystal slurries with good fluidity can grow in the solution. The following parts of this paper are organized as follows. First, crystallization inhibitors and nucleating agents are selected. Then, the physical phenomena of adding additives into LiCl solution are presented. After that, the experimental results are analyzed. Conclusions about the effects of additives on LiCl crystallization are made in the end.

2 Crystallization fundamentals and selection of additives

2.1 Crystallization fundamentals

The crystallization process often consists of two major steps, nucleation and crystal growth. Figure 1 shows the state of LiCl solution near the solubility line, which is mainly dependent on the concentration of the solution. When the concentration is greater than the corresponding solubility, the solution is supersaturated. Supersaturation is the driving force of both nucleation and crystal growth. The required supersaturation degree for nucleation is greater than that for crystal growth. Therefore, as shown in Figure 1, the supersaturated solution has metastable and labile states depending on the supersaturation degree. The boundary of the metastable and labile zone is the supersolubility line. In the metastable zone, the supersaturation degree is lower, crystals can grow but nucleation cannot occur unless additional nucleation agents or external disturbances are added. In the labile zone, the supersaturation degree is higher, nucleation and growth will happen simultaneously. The boundary between the metastable and the labile zone is the super solubility curve.

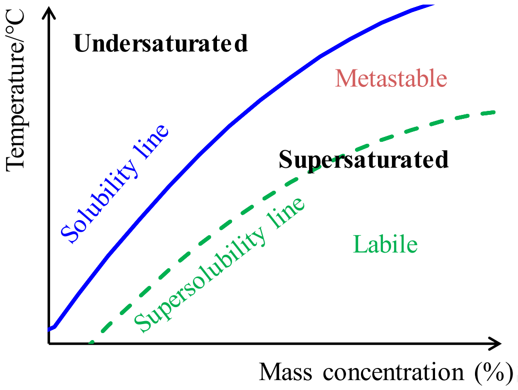

Figure 1 – Schematic illustration of the state of LiCl solution near the solubility line

Additives can be used to modify the solubility and crystallization properties of the supersaturated solution. Two types of additives were used in this study: crystallization inhibitors and nucleating agents. Crystallization inhibitors can prevent the nucleation of supersaturated LiCl solutions and therefore reduce crystallization temperature [14]. Besides, they can increase the metastable zone width of the solution and stabilize the solution at this state. Nucleating agents, on the other hand, can facilitate nucleation by providing active sites on its surfaces. Besides, it can promote the formation of fine crystals in the metastable zone.

2.2 Selection of additives

For crystallization inhibitors, EG was chosen due to its wide application in LiBr absorption. For nucleating agents, SiO_2 nanoparticles (SNPs) was selected for their large specific surface area, stable suspension in water. Besides, SNPs can be used to enhance the heat and mass transfer of LiBr falling film absorption [15].

3 Results and discussion

3.1 The effects of ethylene glycol

To examine the effect of EG on inhibiting LiCl crystallization, a total of 9 supersaturated LiCl solutions with a mass concentration of 53% were prepared. The solutions were first heated up to 95°C to dissolve LiCl. Then, EG was added to the solution. The highest mass ratio of $LiCl+H_2O$: EG is 5:1, which is comparable with the existing studies on additives[5]. After that, the solutions were placed at the ambient temperature of 25°C for 24 hours.

Figure 2 shows the crystallization phenomena of concentrated LiCl solution with different mass ratios of EG. In 9 samples, the mass ratio of LiCl+H_2O: EG increases from 40:0 to 40:8. The amount of crystals in the mixed solution decreases significantly with the increase of EG's mass ratio. Considering the poor solubility of LiCl in EG, the significant reduction in the number of crystals can be attributed to the enhanced supersolubility of LiCl in water. For LiCl solution without additives (i.e. mass ratio of LiCl+H_2O: EG=40:0), the weight of the LiCl crystal accounts for 22.5% of the total solution. For the mass ratio of LiCl solution: ethylene glycol reaches 40:8, there are no visible crystals in the solution. Therefore, the solution is in the metastable zone, and its supersolubility can reach 53%. In other samples, LiCl still crystalizes since its concentration is higher than its enhanced solubility. Therefore, the concentration of the solution should also be kept below the solubility to prevent crystallization.

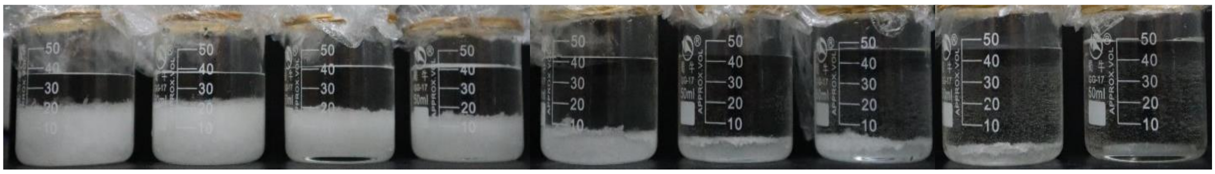

Figure 2 – Effects of EG on LiCl solubility, the mass ratio of LiCl+H_2O: EG=40:x; from left to right x=0~8

3.2 The effects of ethylene glycol+SiO_2 nanoparticles

SNPs dispersion in water was used in the experiment to achieve even dispersion of nanoparticles in LiCl solutions. However, if only SNPs are introduced, the solution crystallized at a concentration lower than the original solubility, which is harmful for system operation. Therefore, EG and SNPs were introduced into concentrated LiCl solution simultaneously to examine its crystallization phenomena.

Figure 3 (a) shows the suspension of LiCl crystals in the presence of SNPs and EG. The concentrations of 6 LiCl solutions are all 53%. The mass ratios of LiCl+H_2O: additives are all 5:1. The mass ratio of EG and SNPs in each sample is different. From left to right, the mass ratio of SNPs increases. The suspension of LiCl crystals improves with the increase of SNPs. For the mass ratio of LiCl+H_2O:EG: SiO_2=50:8.5:1.5, almost no visible separation between solid LiCl crystals and liquid solution can be observed, indicating good suspension of LiCl crystals.

Figure 3 (b) shows the deposited solid phase after pouring out the suspension LiCl crystals. For the mass ratio of LiCl+H_2O:EG: SiO_2=50:8.5:1.5, almost no LiCl is left inside the container, which further proves the good suspension of LiCl crystals. The crystalized LiCl solution becomes fine LiCl slurries with good fluidity, which reduces the risk of blocking the absorption systems. Moreover, it can be a potential working fluid for three-phase absorption thermal energy storage.

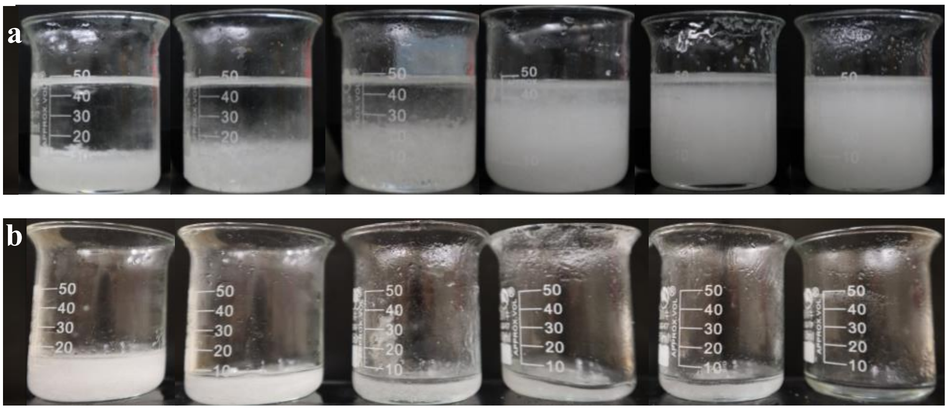

Fig. 3 Effects of SNPs and EG on LiCl crystals, mass ratio LiCl+ H_2O: EG: SiO_2=50: x: y; from left to right: x=9.75, y=0.25; x=9.5, y=0.5; x=9.25, y=0.75; x=9, y=1; x=8.75, y=1.25; x=8.5, y=1.5. (a) suspension (b) solid phase left after pouring out the liquid

In the real operation of absorption machines, the surface defects of metals can serve as nucleating agents for absorption working fluid. Crystals may grow and agglomerate on these nucleating agents, which may result in blockage or cause fluidity issues. If SNPs are introduced into the solution, crystals are more likely to grow in fine slurry, which will reduce such risks.

4 Conclusions

LiCl/H_2O is a commonly used working pair in absorption systems. Traditional LiCl solutions have high crystallization risks when the concentration is too high. This paper proposes two modified solutions for crystallization control by using additives, crystallization inhibitors and nucleating agents. These two additives with a competing mechanism allow the LiCl to function at a concentration higher than its original solubility and reduce the crystallization risks.

1. LiCl solution + EG: EG can significantly increase the solubility of LiCl. However, EG does not promote the suspension of LiCl crystals. Once the concentration of LiCl exceeds the supersolubility, crystallization will still take place. The absorption system is still vulnerable to the concentration changes in the supersaturation solution.
2. LiCl solution + EG + SNPs: Combining EG and SNPs can help the formation of fine LiCl slurries, which guarantees the fluidity of crystalized solutions. Therefore, the absorption system can withstand slight variations in concentration when the solution's concentration is high.

In general, the proposed LiCl solution + EG has higher solubility while the proposed LiCl solution + EG + SNPs has fine crystal slurries with good fluidity, making them potential alternative working fluids for absorption chillers, absorption heat pump and three-phase absorption thermal energy storage systems. However, the present experiment only focuses on the use of additives to modify the solution. Future work needs to focus more on other properties of the working fluids to access its overall performance in absorption machines.

5 Acknowledgment

The authors gratefully acknowledge the support of this research by the Science and Technology Program of Guangzhou, China (201904020027).

6 List of References

[1] Wen T, Lu L, Zhong H. Investigation on the dehumidification performance of LiCl/H2O-MWNTs nanofluid in a falling film dehumidifier. Building and Environment, 2018,139:8-16.

[2] Xie GZ, Wu QP, Fa XM, et al. A novel lithium bromide absorption chiller with enhanced absorption pressure. Applied Thermal Engineering, 2012,38:1-6.

[3] Ibarra-Bahena J, Romero RJ. Performance of Different Experimental Absorber Designs in Absorption Heat Pump Cycle Technologies: A Review. Energies, 2014,7(2):751-66.

[4] Wang L, Liu X, Yang Z, et al. Experimental study on a novel three-phase absorption thermal battery with high energy density applied to buildings. Energy, 2020,208:118311.

[5] Wang K, Abdelaziz O, Kisari P, et al. State-of-the-art review on crystallization control technologies for water/LiBr absorption heat pumps. International Journal of Refrigeration-Revue Internationale Du Froid, 2011,34(6):1325-37.

[6] Eisa MAR, Diggory PJ, Holland FA. A Study of the Operating Characteristics of an Experimental Absorption Cooler Using Water Lithium Bromide Ethylene-Glycol as a Ternary Working System. International Journal of Energy Research, 1988,12(3):459-72.

[7] Park Y, Kim JS, Lee H. Physical properties of the lithium bromide plus 1,3-propanediol plus water system. International Journal of Refrigeration-Revue Internationale Du Froid, 1997,20(5):319-25.

[8] Biermann W. Properties of the Carrol system and a machine design for solar-powered, air-cooled, absorption space cooling. Phase I and Phase II. Final report, September 1977-March 1979. Carrier Corp., Syracuse, NY (USA). Energy Systems Div.; 1981.

[9] Biermann W, Reimann R. Properties of the Carrol system and a machine design for solar-powered, air-cooled, absorption space cooling. Phase I and Phase II final report: Carrier Corporation New York; 1979.

[10] Biermann W, Reimann R, editors. Water cooled absorption chillers for solar cooling applications. Heat Pump Contractors' Program Integration Meeting; 1982.

[11] Santoyo-Gutierrez S, Siqueiros J, Heard CL, et al. An experimental integrated absorption heat pump effluent purification system. Part I: operating on water lithium bromide solutions. Applied Thermal Engineering, 1999,19(5):461-75.

[12] Yoon JI, Kwon OK. Cycle analysis of air-cooled absorption chiller using a new working solution. Energy, 1999,24(9):795-809.

[13] Itaya Y, Ichihashi N, Nagatani K, et al. Performance of absorption heat pump using fine particle slurry of LIBR crystal. HEFAT 2012, 2012.

[14] Inada T, Tomita H, Takemura F, et al. Crystallization temperature, vapor pressure, density and viscosity of lithium bromide plus lithium iodide plus ethylene glycol plus water system for absorption refrigerators for automotive use. International Journal of Refrigeration-Revue Internationale Du Froid, 2019,100:274-83.

[15] Kim H, Jeong J, Kong YT. Heat and mass transfer enhancement for falling film absorption process by SiO_2 binary nanofluids. International Journal of Refrigeration-Revue Internationale Du Froid, 2012,35(3):645-51.

Experimental evaluation of the water absorption process in a horizontal tube falling film absorber with aqueous solutions of [Emim][OAc] and different tube materials

Prieto, Juan[1], Salavera, Daniel[1], Coronas, Alberto[1]

[1] Universitat Rovira i Virgili, Mechanical Engineering Department, CREVER Group, Av. Països Catalans 26, 43007, Tarragona, Spain. Email: juan.prieto@urv.cat

Abstract:

Ionic liquids are promising absorbents for closed absorption heat pumps because of their suitable properties, such as low vapor pressure, specific solubility for the refrigerants, etc., although they also present some drawbacks as high viscosity and low mass diffusivity. As the absorber is one of the key components of the absorption heat pumps, it is interesting to experimentally study the absorption process with these new absorbents. In this study, we present the experimental evaluation of the water absorption process in a horizontal tube falling-film absorber with aqueous solutions of +1-ethyl-3-methylimidazolium acetate. Results are shown in terms of heat duty, overall heat transfer coefficient and absorption rates. In addition, the absorber performance with this mixture is experimentally obtained with two tube materials, copper and 316L stainless-steel.

1 Introduction

The water/LiBr pair has been widely used in absorption chillers. However, its performance is limited to a certain range of concentrations, due to the risk of salt crystallization. This limitation prevents it from operating at high temperatures in the absorber, so the heat has to be rejected with cooling towers. On the other hand, the risk of crystallization does not allow to produce heat at suitable temperatures when functioning as absorption heat pump (AHPs). This limitation might be overcome by using Ionic liquids (ILs) as absorbents since crystallization is avoided.

ILs represent one of the most promising fields of research in recent years. ILs are compounds with a complex molecular structure that are liquid at room temperature. The results found in the last years allow us to affirm that, although the ILs are attractive absorbents, their applicability on AHPs is conditioned by their molecular structure and associated properties, as viscosity, surface tension, and mass diffusivity.

Among all the components, the absorber plays a critical role in the overall performance of the AHPs. Both heat and mass transfers take place simultaneously in this component. The falling-film configuration is the most commonly used in the absorption chillers available on the market [1]. One of the drawbacks of falling-film exchangers is the misdistribution of the film on the exchanger surface, which affects flow uniformity at low Reynolds numbers. The non-wetted areas do not participate in the absorption process, thus decreasing the useful area of these components and consequently the absorption rates. Thermophysical properties of the mixture as viscosity and surface tension are crucial for a good surface wetting [2,3]. For this reason, when new working mixtures for AHPS are analyzed, the experimental study of the absorption process is of special importance.

In this study, we present the experimental evaluation of the water absorption process in a horizontal tube falling film absorber with aqueous solutions of 1-ethyl-3-methylimidazolium acetate [Emim][OAc]. Both, copper and 316L stainless-steel tubes are tested.

2 Methodology

2.1. Experimental set-up description

Figure 1 shows a general scheme of the set-up designed to operate in a continuous way at steady-state conditions. In order to avoid corrosion, stainless steel has been used as the main system material. The main components of the system are the absorber (ABS), the generator (GEN), the solution circuit, the water-cooling circuit, two tanks, the sensors and the data acquisition system. The system is thought to provide the inlet conditions of the different fluid streams for the absorber as it would operate in a single-effect absorption cycle.

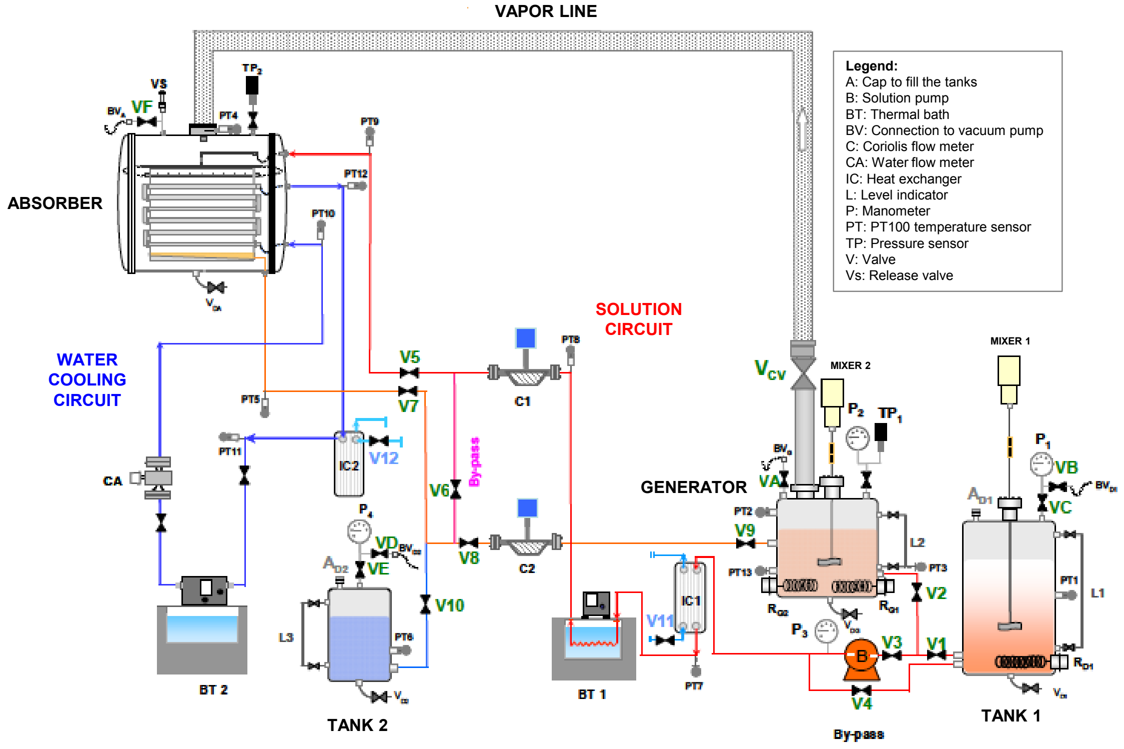

Figure 1 – General scheme of the absorber test bench (adapted from[4]).

The absorber is of the falling-film with horizontal tubes type. It is placed inside a cylindrical chamber which contains a tube bundle with one column of 6 horizontal copper/stainless-steel tubes. These tubes are perfectly aligned and connected in serial disposition. On the top of the copper/stainless-steel tubes, it is placed a solution distributor which drops the solution from the top to the bottom around the horizontal tubes. Moreover, the absorber was designed to allow the visual inspections of the falling film and the horizontal tubes wetting. For this reason, the cylindrical chamber contains two circular windows on both sides of it. The main specifications of the absorber are summarized in Table 1.

Table 1 – Main specifications of the absorber device.

Parameter	Value
Number of tubes	6
External diameter of tubes (mm)	16
Thickness of tubes (mm)	1
Tube spacing (mm)	30
Wetted length of tubes (mm)	400

Table 2 – Working ranges for the absorption study.

Experimental conditions	H_2O/[Emim][OAc]
Inlet absorbent mass fraction (%)	76.7-81.3
Inlet solution temperature (°C)	34.1-48.1
Inlet solution flow rate (kg/h)	32.0-56.0
Cooling water flow rate (l/h)	50.0-85.0
Inlet cooling water temperature (°C)	25.9-42.4

In terms of material compatibility/corrosion, we have conducted a previous corrosiveness analysis with both materials (copper and stainless-steel). We have observed that the corrosion rate for the copper in [Emim][OAc]/H_2O (60%) solution is lower than LiBr/H_2O (60 %), approximately 4 times lower after 400 h. For stainless steel SS-316, the corrosion rate is very low.

2.2. Experimental conditions

The experimental tests of the absorption process study have been performed at absorber conditions for the H_2O/[Emim][OAc] mixture. These conditions are listed in Table 2. It is important to mention that each inlet variable can be controlled independently in the test bench. This is the case of the inlet mixture temperature, concentration, and pressure. The inlet solution conditions were adjusted to keep a constant subcooling in the mixture.

2.3. Calculation of performance parameters

The vapor absorbed ($\dot{m}_v$) can be calculated from the mass balance equations, this is:

$$\dot{m}_{s,in} + \dot{m}_v = \dot{m}_{s,out} \tag{1}$$

$$\dot{m}_{s,in} \cdot w_{in} = \dot{m}_{s,out} \cdot w_{out} + \dot{m}_v \tag{2}$$

Where $\dot{m}_{s,in}$ and $\dot{m}_{s,out}$ are the inlet and the outlet solution mass flow rate, and w_{in} and w_{out} are the inlet and outlet absorbent mass fraction.

The absorber heat duty ($\dot{Q}_{abs}$) is the rejected heat rate by the cooling water in the absorber. Therefore, it can be calculated with the sensible heat equation in the water side, this is:

$$\dot{Q}_{abs}(kW) = \frac{\dot{v}_w \cdot \rho_w}{1000} \cdot c_{p,w} \cdot (T_{w,out} - T_{w,in}) \tag{3}$$

Where ρ_w and $c_{p,w}$ are the water density and specific heat capacity, both calculated the average water temperature, $\dot{v}_w$ is the volumetric water flow rate, and $T_{w,out}$ and $T_{w,in}$ are the outlet and inlet water temperatures.

At the same time, the absorber heat duty can be also calculated on the solution side, this is:

$$\dot{Q}_{abs}(kW) = \dot{m}_{s,in} \cdot h_{s,in} - \dot{m}_{s,out} \cdot h_{s,out} + \dot{m}_v \cdot h_v \tag{4}$$

Where $h_{s,in}$ and $h_{s,out}$ are the solution specific enthalpies, h_v is the latent heat of the water at the absorber vapor temperature. If steady-state conditions are reached, $\dot{Q}_{abs}$ is the only unknown variable from the previous two equations, what means that one of these equations can be used to evaluate the measurements.

The overall heat transfer coefficient (U) is calculated from the absorber heat duty ($\dot{Q}_{abs}$), the external tube area (A_t) and the logarithmic mean temperature difference (ΔT_{LM}) as:

$$U\left(\frac{kW}{m^2 \cdot {}^\circ C}\right) = \frac{\dot{Q}_{abs}}{A_t \cdot \Delta T_{LM}} \tag{5}$$

Where ΔT_{LM} is calculated as:

$$\Delta T_{LM}({}^\circ C) = \frac{(T_{s,in} - T_{w,out}) - (T_{s,out} - T_{w,in})}{\ln\left(\frac{T_{s,in} - T_{w,out}}{T_{s,out} - T_{w,in}}\right)} \tag{6}$$

3 Results

Left graph of Figure 2 shows the absorber heat duty as a function of the inlet solution temperature and the absorbent mass fraction. In this case, the higher the inlet solution temperature, the lower the absorber heat duty. This influence is caused by the lower amount of vapor absorbed by the mixture at higher temperatures.

On the other hand, right graph of Figure 2 shows the absorber heat duty as a function of the water flow rate and the inlet solution mass fraction. As it can be observed from this figure, the higher the cooling water flow rate and the higher the absorbent mass fraction, the higher the absorber heat duty. Both results are expected, since cooling water flow rate increases the overall heat transfer coefficient and the solution mass fraction increases the amount of water absorbed by the solution.

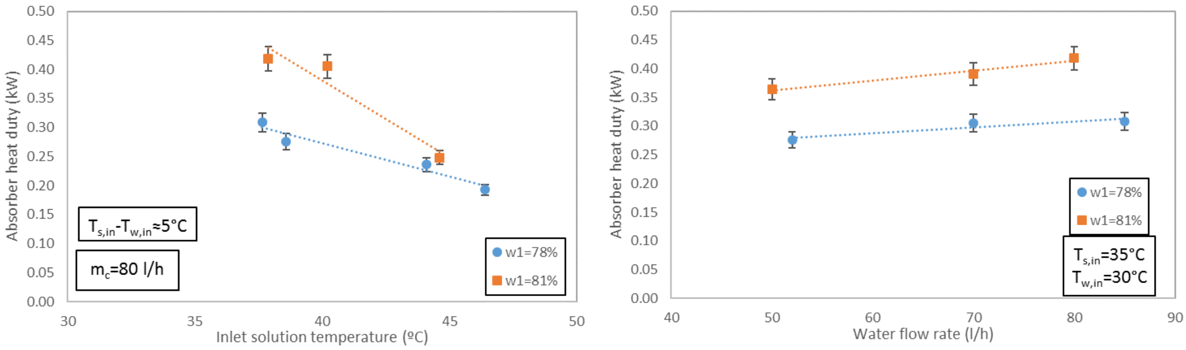

Figure 2 – Absorber heat duty as function of the inlet solution composition and the inlet solution temperature (left) and as a function of the inlet solution composition and cooling water flow rate (right).

Left graph of Figure 3 shows the overall heat transfer coefficient achieved by the absorber with stainless-steel tubes as a function of the water absorption rate. As it can be observed from this figure, values of the overall heat transfer coefficient is low (in the range of 0.2 to 0.3 kW/m$^2\cdot$K) mainly due to a bad tube wetting. In addition, the higher the water absorption rate, the lower the overall heat transfer coefficient. This effect is due to a higher outlet solution temperature because of the heat released during the absorption process.

Right graph of Figure 3 shows the absorber heat duty with the two tube materials as a function of the inlet solution temperature and the inlet water temperature difference. The absorber heat duty is influenced in the same way by both tube materials: the higher the difference of temperatures, the higher the absorber heat duty. On the other hand, the absorber heat duty achieved with the copper tubes is higher than with stainless-steel tubes (in the range of 45 % higher). This increasing is likely due to both a better wetting performance of the mixture and a higher thermal conductivity of copper that increases the overall heat transfer.

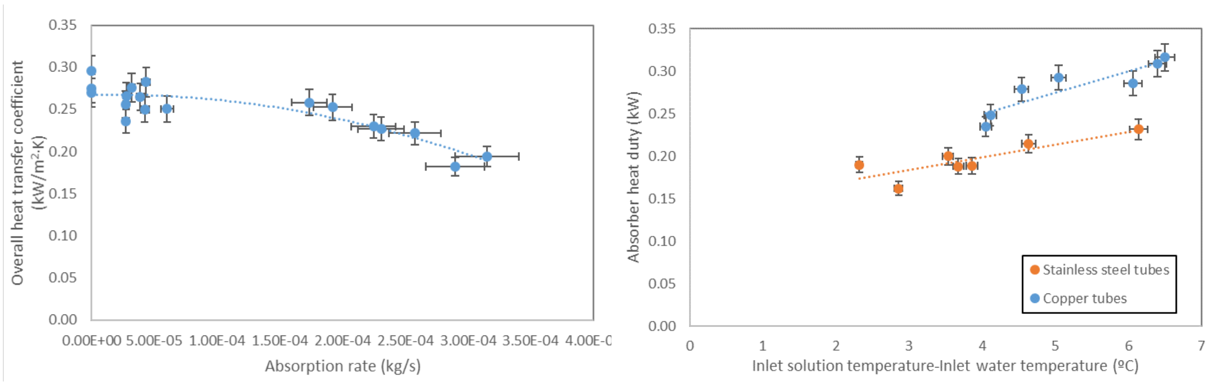

Figure 3 - Overall heat transfer coefficient as a function of the water absorption rate (left) and absorber heat duty with copper and stainless-steel tubes as a function of the inlet solution and inlet water temperature difference (right).

4 Conclusions

The experimental evaluation of the water absorption process in a horizontal tube falling film absorber with aqueous solutions of [Emim][OAc] has been performed. Both, copper and 316L stainless-steel tubes have been tested. The main conclusions of this study are:

- The effect of the inlet solution temperature, the water flow rate and the inlet solution mass fraction on the absorber heat duty have been analyzed independently. In this sense, the lower the inlet solution temperature and the higher the water flow rate and the inlet solution mass fraction, the higher the absorber heat duty.
- The absorber heat duty achieved with stainless-steel tubes is lower than the achieved with copper tubes (around 30% lower). This decreasing is likely due to the decreased wetting performance of the mixture and the lower thermal conductivity of the stainless-steel.

5 Acknowledgment

The authors want to acknowledge YTC America for their funding support for this study.

6 List of References

[1] Zhang, H., Yin, D., You, S., Zheng, W., Wei, S., 2019. Experimental investigation of heat and mass transfer in a LiBr-H_2O solution falling film absorber on horizontal tubes: Comprehensive effects of tube types and surfactants. Appl. Therm. Eng. 146, 203-211.

[2] A. Altamirano, N. Le Pierrès, B. Stutz, Review of small-capacity single-stage continuous absorption systems operating on binary working fluids for cooling: Theoretical, experimental and commercial cycles. International Journal of Refrigeration 106 (2019), 350-373.

[3] L. Hoffmann, I. Greiter, A. Wagner, V. Weiss. G Alefeld, Experimental investigation of heat transfer in a horizontal tube falling film absorber with aqueous solutions of LiBr with and without surfactants. International Journal of Refrigeration 19 (1996), 331-341.

[4] Álvarez-Bermúdez, M.E., 2013. Estudio teórico y experimental de la solución acuosa de nitratos de litio, sodio y potasio como fluido de trabajo en enfriadoras de agua de absorción con accionamiento a alta temperatura. Doctoral Thesis, Universitat Rovira i Virgili.

A preliminary analysis of the influence of mass diffusivity on the performance of ammonia/ionic liquids absorption refrigeration cycles

Rives, Ronny[1], Coronas, Alberto[1]

[1] *CREVER-Group of Applied Thermal Engineering, Mechanical Engineering Dept., Universitat Rovira i Virgili, Av. Països Catalans 26, 43007 Tarragona (Spain) (corresponding author: ronny.rives@alumni.urv.cat)*

Abstract:

Research efforts on the use of ionic liquids as absorbents for ammonia refrigerant are mainly focused on analysing the thermodynamic performance of absorption cycles. However, the unfavourable transport properties of ionic liquids, which are widely recognized as the main shortcoming for their effective implementation, are generally overlooked in these analyses. This paper is intended to illustrate how mass diffusivity can influence the performance of ammonia/ionic liquids absorption cycles. For this purpose, two ionic liquids were selected as absorbents for ammonia: [emim][BF$_4$] and [bmim][BF$_4$], the former with better mass diffusivity, while the latter with better solubility. At a fixed residence time in the absorber, the mixture with better mass diffusivity absorbed more ammonia than the other. Thus, the results highlighted the importance of considering a favourable interplay between mass diffusivity and solubility when screening ionic liquids as absorbents for ammonia.

1 Introduction

In the last two decades, ionic liquids (ILs) have been proposed as alternative absorbents for natural refrigerants in absorption refrigeration systems due to their excellent and tuneable physicochemical properties [1,2]. In particular, the main benefit of using ILs as a replacement for water in the conventional ammonia/water working pair is that the rectification process is avoided [3,4]. Most of the studies in the literature related to the use of ILs as absorbents for ammonia refrigerant are based on the thermodynamic analysis of the absorption cycle. Only thermodynamic data such as vapour-liquid equilibrium (VLE), enthalpy and density of solutions are needed. Various assumptions are made in order to simulate the absorption cycle: for example, the saturation conditions of the liquid streams exiting the absorber and the desorber [1,2,5]. Moreover, since the mixing enthalpy of the ammonia/IL solutions is usually unknown, it is estimated using different VLE models. However, VLE models can yield very different values of mixing enthalpy for ammonia/IL solutions, and consequently, the performance indicators of these absorption cycles are strongly dependent on the VLE model used [5]. Therefore, this type of cycle performance analysis should use reliable thermodynamic property data of the working fluid mixture.

In real absorption machines, the areas available for heat and mass transfer, and hence the residence time within the absorber, are limited. Thus, the transport properties, such as mass diffusivity, determine how much of the absorption potential can be utilized [6,7]. Unfortunately, IL-based solutions often show unfavourable transport properties, such as very high viscosity and low mass diffusivity. As a result, a low degree of absorption completion is frequently observed for IL-based working pairs when exiting the absorber [7,8]. Therefore, it is convenient to account for these large deviations from equilibrium when screening ILs as absorbents for ammonia.

The present study combines experimental and theoretical work to illustrate how the mass diffusivity influences the amount of ammonia absorbed by the solution in a limited residence time and, consequently, the performance of ammonia/IL absorption cycles. For this purpose, two ILs were selected as absorbents for ammonia: [emim][BF$_4$] and [bmim][BF$_4$], the former with better mass diffusivity, while the latter with better solubility. Experimental data of the ammonia absorbed in the two ILs were obtained in an absorption test loop based on the Pressure Drop Method. The absorption process was visualized with a Mach Zehnder interferometer and the ammonia concentration profiles were obtained. A non-equilibrium mass diffusion model was developed for describing the absorption processes and used for obtaining the mass diffusivity of ammonia in the two ILs. The developed model enabled to obtain the spatio-temporal profiles of ammonia concentration in the solution. For the cycle performance analysis, a model based on the mass balances in the components of a single-stage absorption refrigeration cycle was used. The ammonia concentration of the solution exiting the absorber was estimated for a given residence time using the mass diffusion model developed and compared with the saturation concentration. This paper is organized as follows. First, the development of the mass diffusion model used is described. Then, the modelling approach used for the ammonia/IL absorption cycles is addressed. Finally, the results are presented and discussed.

2 Development of the mass diffusion model

2.1 Selection of the ionic liquids used as absorbents for ammonia refrigerant

Ionic liquids: 1-ethyl-3-methylimidazolium tetrafluoroborate ([emim][BF$_4$], CAS no. 143314-16-3) and 1-butyl-3-methylimidazolium tetrafluoroborate ([bmim][BF$_4$], CAS no. 174501-65-6), which presented inverse trends of viscosities [9,10] and ammonia solubilities [11] were selected for ammonia absorption experiments. The selection of these ILs was also made considering the availability of experimental data on ammonia diffusivity from different literature sources [12,13]. Moreover, [emim][BF$_4$] has previously been investigated by our research group as a potential absorbent not only for ammonia [4] but also for 2, 2, 2-trifluoroethanol [14]. In the case of [bmim][BF$_4$], it has been observed that ammonia vapour can be almost completely desorbed at the ambient temperature (303 K) and atmospheric pressure [12].

2.2 Experimental study of the absorption process

The experimental setup consists of an absorption test loop based on the Pressure Drop Method and an optical system for visualization that used the Mach-Zehnder interferometer. The main components of the test loop were the absorption cell, which mimicked a pool-type absorber, and the cylindrical tank, which contained the ammonia vapour that fed the absorption cell during the absorption process. The temperature and pressure of the absorption cell and the cylindrical tank were continuously monitored. Moreover, the temperature of the absorption cell was controlled by a circulating bath (Huber, model Pilot One), which pumped distilled water through a copper cooling coil placed around the absorption cell. Absorption experiments lasting 15 hours were performed at infinite dilution of ammonia, at 303.15 K. A detailed explanation on the preparation and cleaning of samples and equipment can be found in [15].

The absorption cell and the cylindrical tank were connected by a valve initially closed, which kept separated the ammonia vapour (at higher pressure), and the ILs (in vacuum conditions). To start the absorption experiments, the valve was opened. Consequently, the ammonia vapour expanded into the absorption cell, and the absorption process began. As a result, temperature, pressure, and the spatial distribution of ammonia concentration in the ILs studied changed over time. In turn, the changes in concentration caused changes in the refractive index, which were shown in the form of interferograms and were visualized with the Mach-Zehnder interferometer. Optical Digital Interferometry (ODI) method in combination with the Fourier transform (FFT) technique were used to process the interferograms and extract the experimental profiles of refractive index change ($\Delta n_{exp}(z,t)$) during the absorption process. Further details on the determination of $\Delta n_{exp}(z,t)$ using the ODI and FFT methods can be found in the literature [16].

2.3 Mass diffusion model

Here, the mass diffusion of ammonia in the selected ILs was described using Fick's Second Law. In particular, the mass diffusion process was considered to occur in a semi-infinite medium, in which initially there is no ammonia. Moreover, the ammonia mass transfer flux at the vapour-liquid interface was assumed to be proportional to the difference between the saturation concentration under the equilibrium pressure and the existing concentration at the interface. Thus, the total concentration of dissolved ammonia ($\bar{x}(t)$) at any diffusion time during the absorption process in the ILs studied can be expressed as [17]:

$$\bar{x}(t)/x_{eq} = \frac{1}{k_D}\left[exp(k_D^2 t_D)\, erfc\left(k_D\sqrt{t_D}\right) - 1 + 2k_D\sqrt{\frac{t_D}{\pi}}\right] \qquad \text{Eq. (1)}$$

where $t_D = D_{12} \cdot t/z_0$ is the diffusion time, D_{12} [m^2 s^{-1}] the mass diffusivity of ammonia in the ILs, t [s] the time, z_0 [m] the height of the ammonia/IL solution in the absorption cell, $k_D = k_{12} \cdot z_0/D_{12}$ the mass-transfer Biot number, k_{12} [m s^{-1}] the mass transfer coefficient, and x_{eq} the equilibrium concentration (that is, the solubility of ammonia in the ILs at a given temperature and equilibrium pressure). Here, D_{12} and k_{12} were simultaneously determined using a non-linear least-squares minimization of the deviation between experimental ($\Delta n_{exp}(z,t)$) and calculated ($\Delta n_{cal}(z,t)$) refractive index change profiles as described in [15].

In Eq. (1), the term $\bar{x}(t)/x_{eq}$ provides a key indicator of the absorption process performance. It relates the actual concentration ($\bar{x}(t)$) at a short or limited contact time between the vapour and liquid phases to the concentration (x_{eq}) at a contact time long enough to reach the equilibrium state. Thus, the term $\bar{x}(t)/x_{eq}$ can be regarded as a type of mass effectiveness ($\varepsilon_m \equiv \bar{x}(t)/x_{eq}$) since it defines the ratio of the (actual) transferred mass to the maximum transferable mass during the absorption process. ε_m was used to illustrate the interplay between solubility and mass diffusivity and its influence on cycle performance, as described below.

3 Modelling of ammonia/IL absorption cycle

Herein, we have modelled a single-stage absorption cycle (Figure 1) using ammonia and the ILs studied as working fluids. The operating conditions correspond to those used by Yokozeki and Shiflett [1] for other ammonia/IL working pairs in absorption refrigeration cycles. The cycle modelling was based on the available VLE data and the mass balances in the components of the absorption cycle, neglecting the corresponding energy balances. Thereby, we avoid using VLE models to estimate the mixing enthalpies of the ammonia/IL solutions. The solution circulation ratio (f) was used here as the main indicator of cycle performance:

$$f = \frac{1-x[6]}{x[1]-x[6]} \qquad \text{Eq. (2)}$$

where $x[1]$ is the ammonia mass fraction of the rich solution (at the absorber outlet), and $x[6]$ is the ammonia mass fraction of the poor solution (at the generator outlet).

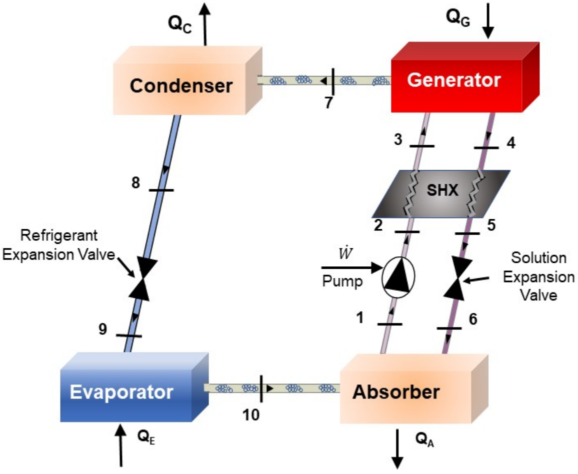

Figure 1. Schematic representation of a single-stage ammonia/IL absorption cycle

The values of $x[1]$ and $x[6]$ depend on the operating conditions and specific modelling approach used (i.e., assumptions). While $x[6]$ was determined assuming equilibrium for the solution exiting the generator, two different modelling approaches were used to calculate $x[1]$:

a) In the first approach, we assumed saturation conditions for the ammonia/IL solution exiting the absorber. Thus, $x[1] = x_{eq}$ where x_{eq} is the equilibrium ammonia mass fraction, determined at the absorber temperature (T[1] = 30 ºC) and pressure (P[1] = 6.15 bar, obtained from the vapour pressure of pure ammonia at the evaporator temperature T[1] = 10 ºC). In this case, a comparison between our results (f = 12.85) and those of Yokozeki and Shiflett [2] (f = 12.98) using the VLE data reported by the latter for the ammonia/[bmim][BF$_4$] mixture revealed excellent agreement.

b) In the second approach, we got rid of the common simplifying assumption that the solution exiting the absorber is at saturation conditions. Instead, $x[1]$ was calculated using the experimentally observed ε_m: $x[1] = \varepsilon_m \cdot x_{eq}$. Thus, the contact time between the ammonia and the ILs during our absorption experiments was considered as the residence time within the absorber.

These two modelling approaches were intended to illustrate how the interplay between mass diffusivity and solubility of ammonia in selected ILs could influence the absorption cycle performance.

4 Results and Discussion

Figure 2 shows the mass effectiveness (ε_m) as a function of the residence time within the absorber for the two ILs studied at 303.15 K. For the same residence time, ε_m was greater for the absorption process of ammonia in [emim][BF$_4$]. For a residence time of 15 hours, for instance, ε_m was on average 10.2% higher in [emim][BF$_4$] than in [bmim][BF$_4$]. Thus, we have quantitatively confirmed an intuitive fact of competing mass diffusivity and solubility contributions in the absorption process performance. For a limited residence time, the higher diffusivity caused [emim][BF$_4$] to absorb more ammonia than [bmim][BF$_4$] despite the higher solubility of ammonia in the latter.

Despite its importance, mass diffusivity is not usually considered when evaluating the thermodynamic performance of ammonia/IL absorption cycles. Maximum mass effectiveness ($\varepsilon_m = 1$) is taken for granted, and the solution exiting the absorber is assumed to be saturated. Under these assumptions, some authors [18] found that the solution circulation ratio (f) of an absorption heat pump using ammonia/[bmim][BF$_4$] (f = 29.282) was considerably more favourable than when using ammonia/[emim][BF$_4$] (f = 46.284). Similarly, we found a better solution circulation ratio for an absorption refrigerator using ammonia/[bmim][BF4] (f = 9.49) than one using ammonia/[emim][BF4] (f = 11.72). However, once we considered a limited residence time, our results revealed that the solution circulation ratio may be more favourable for the ammonia/[emim][BF4] working pair due to the better mass diffusivity.

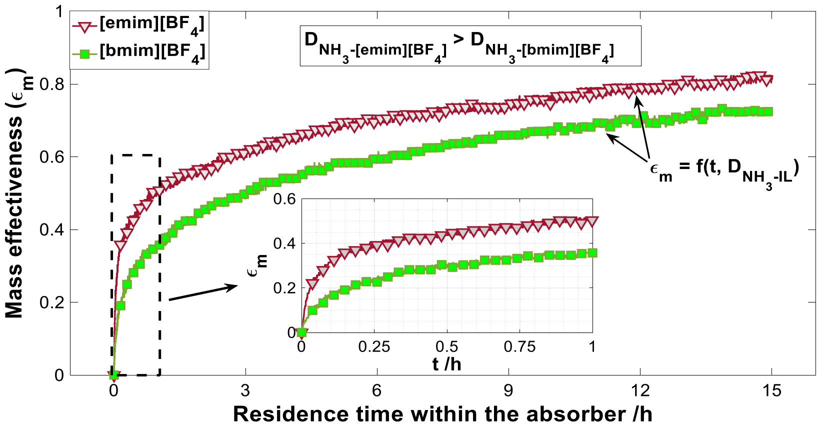

Figure 2. Mass effectiveness as a function of the residence time within the absorber during the absorption process of ammonia in ionic liquids: [emim][BF4] and [bmim][BF4], at 303.15 K.

Table 1 shows the calculated solution circulation ratio at limited residence times for the ammonia absorption processes in [emim][BF4] and [bmim][BF4] at 303.15 K. At short residence times, when ε_m was much higher for the ammonia/[emim][BF4] pair, the solution circulation ratio was considerably more favourable for this working pair than for the ammonia/[bmim][BF4] pair. For a residence time of 3 hours, ε_m for the ammonia/[emim][BF4] pair was still higher (due to the higher diffusivity), but the solution circulation ratio was found to be more favourable for the ammonia/[bmim][BF4] pair (due to the higher ammonia solubility). Despite this, the solution circulation ratio for both working pair was found to be comparable for a long residence time of 15 hours. Thus, considering the much more favourable transport properties, [emim][BF4] should be more suitable than [bmim][BF4] as an absorbent for ammonia in absorption refrigeration systems.

Table 1. Mass effectiveness (ε_m) and calculated solution circulation ratio (f) as a function of the residence time within the absorber for ammonia absorption processes in [emim][BF4] and [bmim][BF4] at 303.15 K.

Residence time/ h	**[emim][BF4]**		**[bmim][BF4]**		**$\Delta\varepsilon_m/\varepsilon_m$/%**	**Δf/ %**
	ε_m	f	ε_m	f		
0.25	0.381	30.79	0.238	39.90	60.08	-22.83
0.5	0.437	26.79	0.293	32.43	49.15	-17.39
1	0.511	22.92	0.357	26.56	43.14	-13.70
2	0.567	20.66	0.456	20.81	24.34	-0.72
3	0.610	19.20	0.498	19.07	22.49	0.68
15	0.812	14.42	0.725	13.10	12.00	10.08
∞ (equilibrium values)	1	11.70	1	9.49	0	23.30

5 Conclusions

In this study, we illustrated how the mass diffusivity affected the performance of absorption refrigeration cycles using ammonia and ionic liquids as working fluids. An intuitively obvious fact of competing mass diffusivity and solubility in the amount of ammonia absorbed for a limited residence time was quantitatively confirmed. When a limited residence time was considered, the results revealed comparable solution circulation ratio for ammonia/[emim][BF4] and ammonia/[bmim][BF4], despite the higher solubility of ammonia in [bmim][BF4]. Thus, the results highlighted the importance of considering a favourable interplay between mass diffusivity and solubility when screening ionic liquids as absorbents for ammonia.

6 Acknowledgments

The authors would like to acknowledge the financial support by the Ministry of Economy and Competitiveness of Spain and FEDER/UE under the Research project DPI2015-71306-R.

7 References

[1] A. Yokozeki, M.B. Shiflett, Vapor-liquid equilibria of ammonia + ionic liquid mixtures, Appl. Energy. 84 (2007) 1258–1273. doi:10.1016/j.apenergy.2007.02.005.

[2] A. Yokozeki, M.B. Shiflett, Ammonia solubilities in room-temperature ionic liquids, Ind. Eng. Chem. Res. 46 (2007) 1605–1610. doi:10.1021/ie061260d.

[3] A. Cera-Manjarres, Experimental determination and modelling of thermophysical properties of ammonia/ionic liquid mixtures for absorption refrigeration systems, Doctoral Thesis, Universitat Rovira i Virgili, 2015. http://hdl.handle.net/10803/404017.

[4] H.M. Ariyadi, Thermodynamic study on absorption refrigeration systems using ammonia/ionic liquid working pairs, Doctoral Thesis, Universitat Rovira i Virgili, 2016. http://hdl.handle.net/10803/396178.

[5] M. Wang, T.M. Becker, C.A.I. Ferreira, Assessment of vapor–liquid equilibrium models for ionic liquid based working pairs in absorption cycles, Int. J. Refrig. 87 (2018) 10–25. doi:10.1016/j.ijrefrig.2017.09.021.

[6] T. Meyer, U. Schulze, Experimental Data on Mutual Mass Diffusivities of Binary Mixtures of Ethanol and [EMIM][DEP], Chem. Eng. Technol. 42 (2019) 1414–1420. doi:10.1002/ceat.201900027.

[7] R. Kühn, T. Meyer, F. Ziegler, Experimental investigation of ionic liquids as substitute for lithium bromide in water absorption chillers, Energy. 205 (2020) 117990. doi:10.1016/j.energy.2020.117990.

[8] A. Kühn, M. Seiler, M. Radspieler, O. Kotenko, Ionic liquids as new absorbents for absorption chillers and heat pumps, in: A. Kühn (Ed.), Thermally Driven Heat Pumps Heating and Cooling, Deutsche Nationalbibliothek, Berlin, 2013: p. 215.

[9] J. Salgado, T. Regueira, L. Lugo, J. Vijande, J. Fernández, J. García, Density and viscosity of three (2,2,2-trifluoroethanol + 1-butyl-3-methylimidazolium) ionic liquid binary systems, J. Chem. Thermodyn. 70 (2014) 101–110. doi:10.1016/j.jct.2013.10.027.

[10] C.M.S.S. Neves, K.A. Kurnia, J.A.P. Coutinho, I.M. Marrucho, J.N.C. Lopes, M.G. Freire, L.P.N. Rebelo, Systematic study of the thermophysical properties of imidazolium-based ionic liquids with cyano-functionalized anions, J. Phys. Chem. B. 117 (2013) 10271–10283. doi:10.1021/jp405913b.

[11] G. Li, Q. Zhou, X. Zhang, L. Wang, S. Zhang, J. Li, Solubilities of ammonia in basic imidazolium ionic liquids, Fluid Phase Equilib. 297 (2010) 34–39. doi:10.1016/j.fluid.2010.06.005.

[12] J. Bedia, J. Palomar, M. Gonzalez-Miquel, F. Rodriguez, J.J. Rodriguez, Screening ionic liquids as suitable ammonia absorbents on the basis of thermodynamic and kinetic analysis, Sep. Purif. Technol. 95 (2012) 188–195. doi:10.1016/j.seppur.2012.05.006.

[13] T. Turnaoglu, M.B. Shiflett, 110th Anniversary: The First Thermodynamic and Kinetic Analysis of Ammonia in Imidazolium-Based Ionic Liquids Using a Gravimetric Microbalance, Ind. Eng. Chem. Res. 58 (2019) 4644–4655. doi:10.1021/acs.iecr.9b00274.

[14] D.S. Ayou, M.R. Currás, D. Salavera, J. García, J.C. Bruno, A. Coronas, Performance analysis of absorption heat transformer cycles using ionic liquids based on imidazolium cation as absorbents with 2,2,2-trifluoroethanol as refrigerant, Energy Convers. Manag. 84 (2014) 512–523. doi:10.1016/j.enconman.2014.04.077.

[15] R. Rives, Theoretical and Experimental Study of the Absorption Process of Ammonia in Ionic Liquids for Absorption Refrigeration Systems, Doctoral Thesis, Universitat Rovira i Virgili, 2021. http://hdl.handle.net/10803/670713.

[16] R. Rives, A. Mialdun, V. Yasnou, V. Shevtsova, A. Coronas, Experimental determination and predictive modelling of the mutual diffusion coefficients of water and ionic liquid 1-(2-hydroxyethyl)-3-methylimidazolium tetrafluoroborate, J. Mol. Liq. 296 (2019) 111931. doi:10.1016/j.molliq.2019.111931.

[17] J. Crank, The Mathematics of Diffusion, 2nd ed., Oxford University Press, Oxford, 1975.

[18] M. Wang, C.A. Infante Ferreira, Absorption heat pump cycles with NH3– ionic liquid working pairs, Appl. Energy. 204 (2017) 819–830. doi:10.1016/j.apenergy.2017.07.074.

On the effects of additives for ionic liquids in absorption chillers

Kühn, Roland[1]

[1] *Chair for Energy Conversion Technology, Technische Universität Berlin, Berlin, 10587, Germany, roland.kuehn@tu-berlin.de*

Abstract:
Ionic liquids (ILs) are an alternative to common absorbents in absorption chillers. Although the efficiency by using ILs can be comparable to state-of-the-art absorbents, the achieved power density is usually much lower. Additives are standard for lithium bromide (LiBr) water absorption chillers but are still less investigated for use with ILs. In the paper at hand the influence of the standard additive 2EHL and another additive TegoTwin4000 on the cooling capacity and efficiency of an absorption chiller with ILs will be investigated and compared to results with LiBr.

1 Introduction

Ionic liquids (IL) are an alternative to lithium bromide (LiBr) in water absorption chiller, e.g., to cope with crystallization [1,2]. However, usually cooling capacities achieved with ILs are smaller than by using LiBr [3,4]; efficiencies might be comparable, but can also be much lower, depending on the IL [3,4]. It is state of the art to use additives in LiBr-water absorption chillers to increase the cooling capacity [5] or to reduce corrosion. However, this is not yet considered in the most investigations on ILs in absorption chillers. The standard additive to improve the heat and mass transfer in the LiBr-water film is 2-ethyl-1-hexanol (2EHL) [5]. The effect of 2EHL is that the surface tension of the LiBr-water-2EHL mixture becomes very sensitive to the water concentration, inducing Marangoni convection in the film, which in turn increases the heat and mass transfer [5]. Unfortunately, the effect of 2EHL is different at least on some ILs; the surface tension is reduced but does not become sensitive to the water concentration [6]. Thus, it is not sure if 2EHL effects the cooling capacities achieved by ILs or if different additives might be necessary.

The paper at hand will investigate the influence of 2EHL and TegoTwin4000, a siloxane-based surfactant from Evonik Industries, on the cooling capacity and the COP achieved with the IL [emim][Cl] (called IL3 here). The results will be compared to LiBr solutions with a sufficient amount of 2EHL and a lower 2EHL content. First, the system setup will be described shortly before the measurement results will be discussed.

2 Experimental Set-up

The experimental data were obtained by investigating the absorbents in one dedicated absorption chiller with tube bundle heat exchangers and glass housing (Figure 1, left).

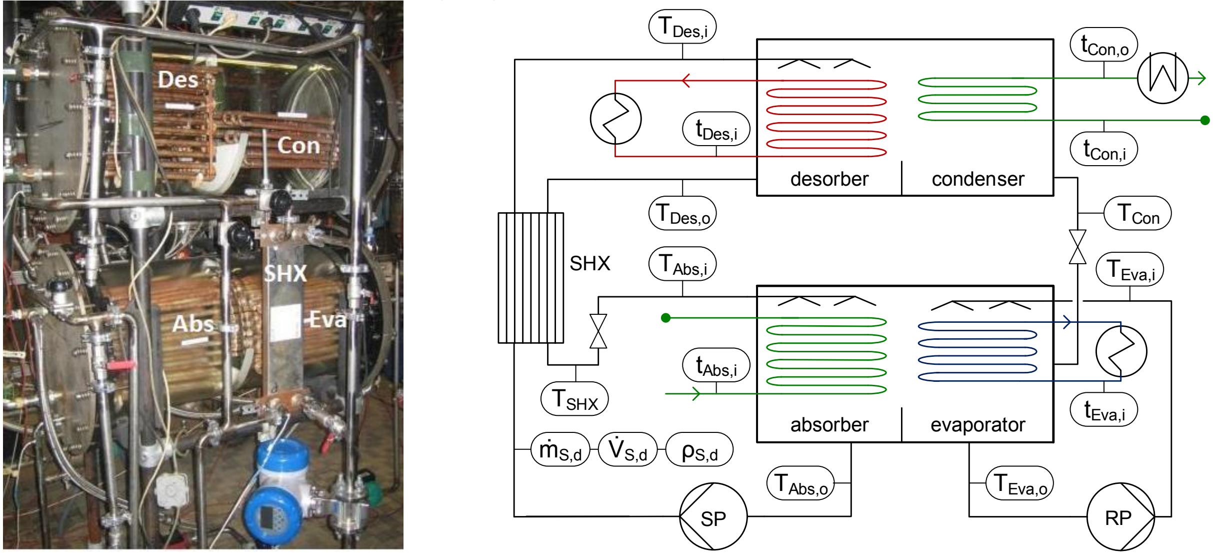

Figure 1 – Photograph (left) and simplified flow sheet (right) of the experimental absorption chiller

For the examinations in the paper at hand the measured internal and external inlet and outlet temperatures as well as the volumetric flow rate of the external circuits and the diluted solution flow rate are used (Figure 1, right). The target diluted volumetric solution flow rate was 100 l/h (systematic uncertainty of about 5 l/h). The solution flow rate can be adjusted by the solution pump, pumping the rich solution from the absorber to the desorber, or by a manual valve in the flow path from the desorber to the absorber, this flow is driven by gravity forces; in steady state both flows are dependent on each other. The details on the experimental setup as well as some experimental results without additives were published previously [7].

The investigated IL3 ([emim][Cl]) was provided from Evonik Industries and was produced in lab scale. The dynamic viscosity of IL3 is much higher than for LiBr at chiller operation conditions [7]. However, the dynamic viscosity of IL3 is even much higher than for [emim][Cl] in literature [7,8]. Thus, the results presented here might not be comparable to results with other [emim][Cl] solutions.

3 Results

Figure 2 shows the achieved cooling capacity (left) and COP (right) for operation with an aqueous IL3 solution with different additives and with aqueous LiBr solution with different 2EHL contents at 18 °C external evaporator inlet temperature and 27 °C external absorber inlet temperature for a variation of the external desorber inlet temperature. Regarding the cooling water, the condenser is connected in series after the absorber. The tests were performed in 2010/2011.

An evaluation of the experimental uncertainties was performed. The statistical uncertainties are shown directly on the data points and the maximum systematic uncertainty is shown on extra data points next to the legend in the left bottom corner. The connecting lines are just for better visualization and have no physical background.

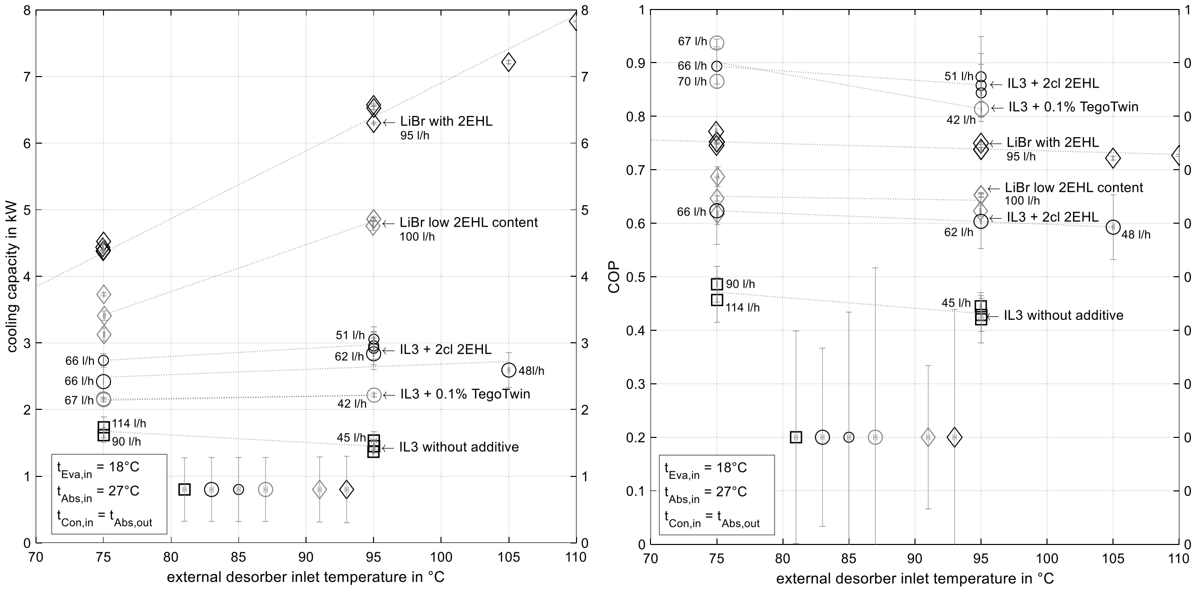

Figure 2 – cooling capacity (left) and COP(right) of IL3 and LiBr for different external desorber inlet temperatures

The **cooling capacity** achieved with the different sorbent mixtures varies over a wide range. The cooling capacities for all LiBr experiments are higher than for all IL3 experiments. The cooling capacity of **LiBr** with a sufficient amount of 2EHL (black diamonds) is highest and even approx. 40% higher than for LiBr with a low 2EHL content (grey diamonds). The low 2EHL content was reached by performing experiments over 3 months with nearly daily evacuation of the chiller and without adding new 2EHL; thus, the exact 2EHL content is unknown. The solution flow rate in all LiBr experiments was very stable over the whole desorber temperature range. A significant increase of the cooling capacity with increasing external desorber inlet temperature can be observed for all LiBr experiments; the increase is nearly linear for the experiments with sufficient 2EHL.

The achieved cooling capacity **without any additives in IL3** (black squares) is the lowest. Comparing the cooling capacity at 75°C and 95°C desorber inlet temperature, a reduced cooling capacity at higher desorber temperatures occurs. This is due to the fact, that the diluted volumetric solution flow rate significantly decreased to 45 l/h at 95°C desorber temperature. At higher volumetric flow rates, a higher cooling capacity might be possible, as it is observed at 75°C desorber inlet temperature, when increasing the solution flow rate from 90 to 114 l/h.

Unfortunately, in the most IL3 experiments the solution flow rate is limited by the gravity-driven flow path from the desorber to the absorber. Boiling in the desorber sump was observed, so that presumably cavitation in the tubes to the adsorber occurs and influences the flow rate. The boiling in the sump increased with increasing external desorber inlet temperature.

The black circles show two different days of measurements after 20 ml of **2EHL** were added to IL3. In the first test series (big black circles) a sample of the solution at 95°C desorber temperature was taken from the chiller to determine the concentration in absorber and desorber. Unfortunately, the (cold) solution became more viscous after adding 2EHL; apparently the solution properties did change. Hence, pumping of the solution at chiller startup and controlling of the solution flow rate during the tests were very complicated, and the statistical uncertainty of these data sets is much higher than for the other experiments. Despite these complications, the cooling capacity at 75°C is increased by more than 60% in comparison to the solution without additive although the solution flow rate is with 66 l/h nearly 30% lower. Now, an agitated surface on the desorber film was observed – less apparent but like in the experiments with 2EHL in LiBr solutions – which comes from the Marangoni effect. Boiling in the desorber sump was not observed anymore (or only slightly at chiller startup), but the solution flow rate could not be increased to 100 l/h. At 95°C desorber inlet temperature the solution flow rate has not decreased significantly, and the cooling capacity is increased; the solution flow rate is now higher than with pure IL3 at the same desorber temperature. At 105°C desorber inlet temperature the solution flow rate decreases and so does the cooling capacity. The cooling capacity decreases more than it does for the pure IL3 from 75°C to 95°C with a stronger decrease in solution flow rate. This might be due to a negative effect of an increasing salt concentration entering the absorber as it was observed also for other IL-refrigerant mixtures [9]. During the second test series 4 days later (small black circles), the achieved cooling capacity was slightly higher.

Afterwards, the siloxane-based surfactant **TegoTwin4000** from Evonik Industries was used as alternative to 2EHL. 70g of TegoTwin4000 were added to the IL3-2EHL-water mixture which corresponds to a concentration of approx. 1%. Unfortunately, neither stable running of the chiller nor reaching a comparable cooling capacity was possible. Thus, the amount of the additive was reduced by mixing a part of the present IL3 solution with pure IL3 without additives and filling it into the chiller again. Thus, the concentration of TegoTwin4000 was reduced to 0.1% which is the intended concentration by the manufacturer. No additional 2EHL was added so that its content is reduced to below 2ml and no significant effect of 2EHL is to be expected anymore. In fact, neither occurred problems with a high-viscous IL3 solution at chiller startup nor could an agitated film surface from the Marangoni effect be observed. Nevertheless, the reached cooling capacity with the IL3-0.1%TegoTwin4000 mixture is much higher than it is for the pure IL3-water mixture, but slightly lower than when using 2EHL only. Apparently, the mechanism of TegoTwin4000 in the mixture is different from that of 2EHL, but both have a considerable effect. At 95°C desorber inlet temperature the cooling capacity remained nearly constant, although the volumetric solution flow rate was reduced by nearly 40%. By comparing the cooling capacities and volumetric flow rates at 95°C of IL3-0.1%TegoTwin4000 to IL3-2EHL at 95°C and 105°C, it is most likely that the cooling capacity for IL3-0.1%TegoTwin4000 will remain smaller than for IL3-2EHL even when volumetric flow rates or desorber inlet temperatures would have been higher. Unfortunately, the experiments with TegoTwin4000 were not reproduced.

Observing the **COP** (Figure 2, right), an advantage of LiBr solutions is not distinct in terms of efficiency. Although IL3 without additives shows the lowest COP and cooling capacity, the COPs of IL3 with additives are comparable or even higher than for LiBr. For **LiBr** with a low 2EHL content the COP is between 0.6 and 0.7; the lower COPs correspond to the lower cooling capacities. Presumably, non-condensable gases could be present at lower cooling capacities and COPs. The COP achieved with LiBr is significantly increased with a sufficient 2EHL content. Here, the COP is less affected by an increasing desorber temperature. The COP decreases almost linearly with increasing desorber temperature of up to 110°C at constant solution flow rate.

For **IL3 without additives** the cooling capacity increased with increasing solution flow rate (from 90 to 114 l/h at 75°C), but the COP decreases. This meets expectations as solution heat exchanger losses will increase with increasing solution flow rate. The COP also decreases with increasing desorber inlet temperature. Although the decreasing COP is not totally unexpected, ones could assume a much smaller decrease, because the solution flow rate also decreased which should have a positive effect on the COP.

With **2EHL as additive** for IL3, the COP is increased significantly from below 0.5 to 0.6 in the first test series (big black circles) and is now comparable to LiBr with a low 2EHL content. The statistical uncertainty is much higher than for all other measurements due to the before mentioned difficulties in chiller control. The decrease in

COP with increasing desorber temperature is less strong for the IL3-2EHL mixture than for LiBr with a low 2EHL content when comparing it to the highest COP data points at 75°C and 95°C external desorber inlet temperature; the decrease in COP is also much less significant than for the pure IL3-water mixture, although the solution flow rate at 95°C external desorber inlet temperature is lower for IL3 without additives. As for the LiBr data with sufficient 2EHL, the decrease in COP from 75°C to 105°C is also linear for the IL3-2EHL mixture, although the solution flow rate is decreased at 105°C. Apparently, the decreased solution flow rate at 105°C has no visible positive effect on the COP here.

In the second test series of the IL3-2EHL mixture (small black circles), the COP is much higher; with above 0.9 it is higher than for all LiBr measurements. However, the solution mass flow rate of LiBr is more than double of that in the IL3 experiments, so that more heat must be transferred within the solution heat exchanger and solution heat exchanger losses might be higher for LiBr. The decrease in COP with increasing desorber temperature is comparable to the first data set. An explanation for the huge difference in COP between both test series could be a significant sub-cooling in the absorber in the first tests. The IL samples, taken in the first experiments at 95°C, showed still significant sub-cooling (SC) in the absorber, although no boiling (super-heating) in the desorber sump was observed anymore (absorber: inlet: ~10 K SC, outlet: ~14 K SC; desorber: inlet: ~5 K SC, outlet: ~2 K SC). Presumably, the sub-cooling decreased in the second test series, which would explain the much higher COPs; but unfortunately, no new samples were taken to proof this hypothesis.

Even though the cooling capacity by adding **TegoTwin4000** to IL3 is lower than by using 2EHL only, the COP by applying TegoTwin4000 is increased to comparably high values as they are for the second test series with 2EHL as additive; both additives seem to be comparably favorable for increasing the chiller efficiency. Admittedly, the one data point with a COP of above 0.9 for IL3 with TegoTwin4000 seems to be unlikely high (although physically possible). Additionally, the sum of statistical and maximum systematic uncertainty for the second test series with 2EHL and for the TegoTwin4000 experiments is approx. 0.1 higher than for the other measurements, so that the difference in COP to LiBr with 2EHL might also be smaller. The qualitative statement stays untouched, by adding either 2EHL or TegoTwin4000 to IL3, the chiller can operate as efficient as with LiBr and 2EHL. Why nevertheless cooling capacities with IL3 are higher with 2EHL than with TegoTwin4000, especially also for the first test series with much lower COPs with 2EHL, needs further investigation.

4 Conclusions

Today no one would use LiBr in absorption chillers without additives, e.g., 2EHL. The significant difference in cooling capacity and COP by using LiBr with or without 2EHL was shown here as reference experiment. Also, by applying additives to IL water solutions a significant increase in achievable cooling capacity as well as COP was discovered. Unfortunately, there were problems by achieving stable operation conditions of the chiller with IL3, especially for maintaining constant solution flow rates, regardless of using an additive or not, so that comparing all data with each other is difficult. For the examined IL3, both investigated additives achieved a significant increase in cooling capacity by about 50% with TegoTwin4000 and by more than 60% with 2EHL; the cooling capacity remained below that of LiBr. The COP for IL3 without additive and for LiBr with a low 2EHL content were between 0.4 and 0.5, and between 0.6 and 0.7, respectively. The COP by adding 2EHL to IL3 was increased to above 0.6, and in a later test series to above 0.8; COP of LiBr with 2EHL was slightly below 0.8. By using TegoTwin4000 as additive with IL3, the COP was also increased to above 0.8. Obviously, both additives improve the utilization of IL3 and then the efficiency is comparable to that of LiBr with 2EHL. However, yet it cannot be explained why the achieved cooling capacity is higher when applying 2EHL than when using TegoTwin4000, although the COPs are comparable (or even lower with 2EHL).

5 Acknowledgment

The measurements were performed in a research project together with Evonik Industries AG, project number 0327472 funded by the German Federal Ministry for Economic Affairs and Energy. Many thanks also to the other team members from TU Berlin Thomas Meyer, Annett Kühn, Oliver Buchin, José Corrales Ciganda, Falk Cudok and Maximilian Winker and all team members from Evonik Industries AG, especially to Olivier Zehnacker.

6 List of References

[1] Khamooshi, M, Parham, K, Atikol, U. (2013): Overview of ionic liquids used as working fluids in absorption cycles. *Adv Mech Eng*

[2] Seiler, M, Schneider, M-C, Kühn, A, Ziegler, F. (2010): New high-performance working pairs for absorption chillers and heat pumps. *Proc Int Symp Innov Mater Process Energy Syst*, pp. 350-360

[3] Radspieler, M, Schweigler, C (2011): Experimental investigation of ionic liquid emim EtSO4 as solvent in a single-effect cycle with adiabatic absorption and desorption. *Proc Int Sorption Heat Pump Conf*, pp. 125-134

[4] Kühn, A, Seiler, M, Radspieler, M, Kotenko, O. (2013) Ionic liquids as new absorbents for absorption chillers and heat pumps. *Therm Driven Heat Pumps Heat Cool*, pp. 215-220

[5] Kulankara, S., Herold, K.E. (2000): Theory of Heat/Mass Transfer Additives in Absorption Chillers. HVAC&R Research, vol. 6, pp. 369-380

[6] Kühn, A. (2012): Verbundprojekt: Verwendung von ionischen Flüssigkeiten in Absorptionskälteanlagen: Schlussbericht. *Technische Informationsbibliothek (TIB)*

[7] Kühn, R., Meyer, T., Ziegler, F. (2020): Experimental investigation of ionic liquids as substitute for lithium bromide in water absorption chillers. *Energy*, vol. 205, pp. 1-11

[8] Klinov, A V., Fedorov, M V., Malygin, A V., Minibaeva, LR (2014): Properties of an aqueous solution of ionic liquid [Emim][Cl] at standard atmospheric pressure. *Russ J Phys Chem A*, vol. 88, pp.1682-1688

[9] Meyer, T., Winker, M., Bergemann, S., Kühn, R., Ricart, C., Ziegler, F. (2017): Experimental investigation of an absorption refrigerator working with ionic liquids and ethanol. *TPTPR Proceedings*

Numerical and experimental evaluation of adsorption performances of SAPO-34 coated adsorber obtained by direct synthesis process

Calabrese, Luigi[1,3,4], Freni, Angelo[2], Herrmann, Ralph[3], Giuseppe E. Dino[4], Palomba, Valeria[4], Pizzanelli, Silvia[2], Frazzica, Andrea[4]

[1] *Department of Engineering, University of Messina, Contrada di Dio Sant'Agata, Messina 98166, Italy*

[2] *CNR-ICCOM, Via G. Moruzzi 1, Pisa I-56124, Italy*

[3] *Fahrenheit GmbH, Siegfriedstr. Munich, Germany*

[4] *Istituto di Tecnologie Avanzate per l'Energia "Nicola Giordano", CNR ITAE, Messina, Italy*

Abstract:

In this work, COMSOL FEM analysis and experimental testing of an SAPO-34 coated adsorber obtained by direct synthesis process is presented. Firstly, small-scale SAPO-34 specimens have been synthesised on aluminium sheets in order to assess mechanical and structural stability, as well as water adsorption capacity. Afterwards, the synthesis technique has been applied by Fahrenheit GmbH in order to prepare a real-size SAPO-34 coated HEX. A 2D time-dependent COMSOL FEM model was realized in order to simulate the heat and mass transfer processes through the coated adsorber and its preliminary validation was successfully performed. The full scale coated HEX is currently under testing at the CNR ITAE lab in order to evaluated the achievable performance and validate the numerical model.

1 Introduction

Adsorption heat pumps and chillers represent a viable solution to provide heating and cooling with reduced electricity consumption, since the working cycle is thermally driven. The core component of an adsorption cycle is the adsorber, which represents the thermal compressor, where the adsorbent material is put in contact with a heat exchanger. Two main approaches can be identified to manufacture coated adsorber: in-situ crystallization and binder-based composite coatings [1].

The former technique represents a promising technological approach for the realization of high-performance zeolite coated adsorber. Differently from the binder-based zeolite composite coatings, for which the intrinsic heterogeneity of the material is a potential applicative issue, the in-situ crystallization process allows to obtain a homogeneous, mono-material zeolite coating characterized by a high surface interaction with the substrate on which the zeolite crystals germinate [2].

However, a targeted integration of the properties, stability and homogeneity of the coating are essential prerequisites in order to maximize the subsequent performance of the coated absorber. This also represents an essential precondition for obtaining a high performance durable adsorber.

In this context, the purpose of this paper is the integration of a structural study, at material level, conducted on the coating deposited in the exchanger coupled with an experimental analysis, at system level, on the component under real operating conditions. Furthermore, finite element model analysis was applied in order to better assess the heat and mass transfer phenomena occurring during the sorption/desorption phases, thus supporting the final design of the full-scale adsorber.

2 Experimental part

2.1 Materials

Two types of coated specimens were used for the experimental campaign.

- Al6061 aluminum sheets, dimensions 50 mm x 50 mm x 0.2 mm were used for an evaluation of the mechanical and structural stability of the zeolite coatings.
- An adsorber was obtained by direct synthesis of SAPO-34 on Al6061 heat exchanger (dimensions 83 cm x 72 cm x 6,5 cm) for subsequent investigations on the component.

2.2 Characterization

X-ray diffraction (XRD) measurements were performed using CuKα radiation on Bruker D8 Advance (Bruker Billerica, MA, USA) diffractometer in the 2θ range of 5–50°. The surface morphologies of the specimens were evaluated using a focused ion dual beam/scanning electron microscope (FIB-SEM ZEISS Crossbeam 540, Oberkochen, Germany). Furthermore, energy-dispersive spectroscopy (Aztec Oxford, EDS) was applied to evaluate the coating composition. Cross-sectional images of the samples were performed embedding the samples in an epoxy thermosetting resin and measured using a 3D optical microscope (KH8700 3D digital microscope, Hirox, Tokyo, Japan). Furthermore, the water vapor adsorption isobars (P=11 mbar) of coated samples, were measured by a thermogravimetric dynamic vapor system (DVS Vacuum) (from 30 to 150°C).

3 Results and discussion

3.1 Coating morphology

Figure 1a shows a reference SEM image of the coating. The distribution of the cubic-shaped zeolite is almost regular well distributed in the aluminum substrate. The dimension of the grain is in the range 6-12 µm. The coating structure is compact and no discontinuities or macroscopic defects are identified. A thin transgranular crack evolves transversely along the right side of the figure. This can be due to the direct synthesis process during the calcination step in which there is a differentiated shrinkage between the aluminum support and the brittle zeolite coating that favors internal stresses [3]. However, the cracks are not deep and extensive and do not affect the mechanical stability of the coating which remains adhered and compact over the support surface, as demonstrated by the pull-off measurements performed on SAPO-34 coated aluminum sheets. EDS and XRD analysis (Figure 1a corner and Figure 1b, respectively) confirm the good purity of the silico-alumino-phosphate zeolite.

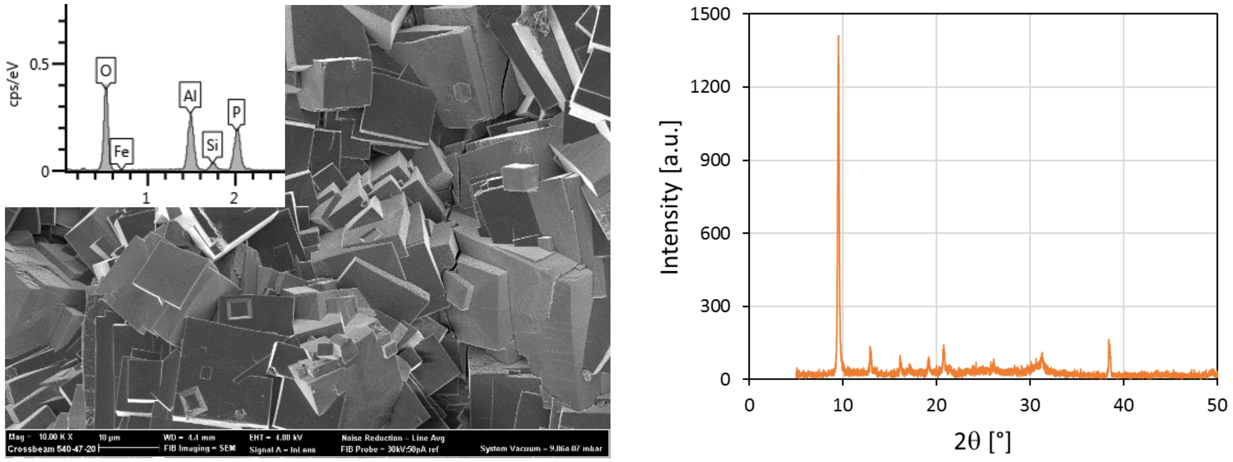

a) b)

Figure 1 – a) SEM image and related EDS b) XRD analysis on SAPO-34 coating.

3.2 Adsorption isobar

Once the morphological and mechanical features were evaluated, the sorption properties of the coating were investigated. A thermogravimetric apparatus working according to the Dynamic Vapor Sorption (DVS) principle was employed. The coated surface was cut in small pieces which were analyzed both in the DVS and by means of the SEM, in order to investigate the thickness of the aluminum support and then subtract it from the initial dry mass loaded inside the crucible of the thermogravimetric apparatus. Up to five different pieces were tested and the equilibrium data were properly post-treated to evaluate the sorption equilibrium. A slight deviation of less than 2% was obtained. Figure 2 reports the average isobar obtained. The shape of the isobar as well as the maximum uptake is in line with the one obtained from the pure zeolite produced during the in-situ crystallization process and not deposited over the aluminum substrate. This confirmed the reliability of the overall synthesis process as well as the ability of the applied post-synthesis process to completely burn out the template from the pores of the SAPO-34.

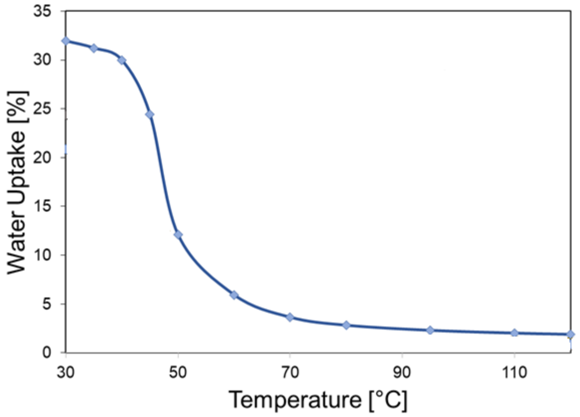

Figure 2: Adsorption isobar measured at the water vapour pressure of 11 mbar over the coated sample.

3.3 FEM modelling

In order to optimize the power density of the adsorber, a 2D time-dependent model for description of heat and mass transfer through an adsorbent media was realized by the FEM-based commercial software COMSOL Multiphysics®. In particular, the main aim of the modelling activity is to have a tool useful to optimize, according to the first prototype tested in the lab, both the HEX design as well as the thickness of the SAPO-34 deposited, in order to meet the required power density for the final prototype.

The developed tool is based on energy and mass balances and can predict pressure, temperature and water uptake distribution through an adsorbent coating in thermal contact with a flat-tube finned HEX. The model governing equations were implemented by considering the “heat transfer in porous media” and “mass transfer in porous media – adsorption sub-node” COMSOL interfaces. Water diffusion was described by Fick’s law assuming macropore diffusion control. Adsorption equilibrium was calculated by Dubinin-Polanyi Theory assuming local thermal equilibrium. HEX domain was simulated considering the “Heat transfer in solids and fluids” and “Nonisothermal fluids flow” COMSOL interfaces.

As shown in Figure 3 a and b, preliminary calibration and validation of the model was successfully performed considering a reference SAPO-34 coating on a standard flat-tube finned HEX, subjected to an adsorption step under isothermal conditions at T= 55°C. The considered reference curve is the one obtained from the analytical solution available for isothermal differential step adsorption, due to the lack of experimental data available.

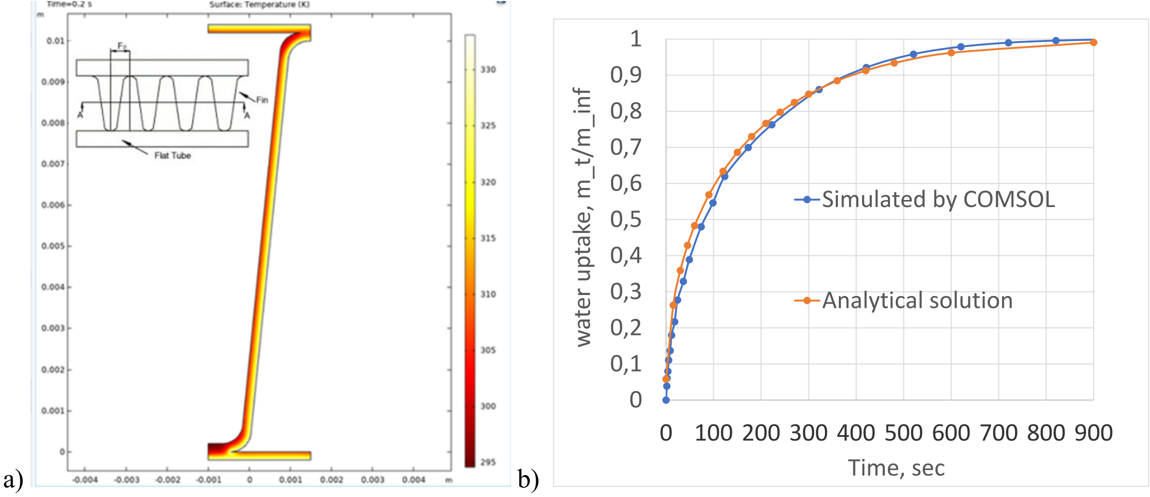

Figure 3: a) COMSOL implementation of a SAPO34 coating on a standard flat-tube finned HEX, b) water uptake evolution compared with the analytical solution (isothermal adsorption T=55°C).

SAPO-34 thermophysical parameters have been taken from literature [4, 5] and experimentally measured at CNR ITAE lab. Simulations are in progress to further refine the model and study of the effect of heat and mass transfer efficiencies and heat capacities on the performance of the adsorber manufactured by Fahrenheit.

3.4 Ongoing activities

An in-situ coated adsorber was manufactured by Fahrenheit for being tested under controlled conditions at the CNR ITAE lab, by means of an available testing rig [6].

The full characterization of the coated adsorber is currently ongoing, aiming at evaluating the achievable performance in terms of thermal COP as well as specific cooling power (SCP), under real operating conditions typical of the adsorption chiller applications. The experimental results will be then used to further validate the thermo-fluid dynamic model implemented, to the investigate optimal thickness of the coating as well as the proper design of the finned heat exchanger, for the final sizing that will be implemented in a hybrid chiller to be installed in a demo site.

4 Conclusions

In this paper, a structural characterization on SAPO-34 coated heat exchanger, was performed both at material level, and system level. Firstly, small-scale SAPO-34 specimens have been synthesized on aluminum sheets in order to assess structural, mechanical and adsorption capabilities. Afterword, a real-size SAPO-34 coated HEX obtained by direct synthesis technique has been applied by Fahrenheit GmbH. Furthermore, a simplified 2D time-dependent Comsol FEM model was performed in order to assess the heat and mass transfer phenomena occurring at the HEX interfaces. The full scale coated HEX is currently under testing at the CNR ITAE lab in order to corroborate the achievable performance of the coated HEX module.

5 Acknowledgments

This project has received funding from the European Union’s Horizon 2020 research and innovation programme under grant agreement No 814945 (SolBio-Rev).

6 List of References

[1] Caprì, A., Frazzica, A., Calabrese, L., (2020) Recent Developments in Coating Technologies for Adsorption Heat Pumps: A Review, *Coatings*. 10, 855. https://doi.org/10.3390/coatings10090855.

[2] Calabrese, L., (2018) Anticorrosion Behavior of Zeolite Coatings Obtained by In Situ Crystallization: A Critical Review., *Materials*. 12, 59. https://doi.org/10.3390/ma12010059.

[3] Calabrese, L., Bonaccorsi, L., Di Pietro, D., Proverbio, E., (2014), Effect of process parameters on behaviour of zeolite coatings obtained by hydrothermal direct synthesis on aluminium support, *Ceram. Int.* 40, 12837–12845. https://doi.org/10.1016/j.ceramint.2014.04.138.

[4] Brancato, V., Frazzica, A., (2018) Characterisation and comparative analysis of zeotype water adsorbents for heat transformation applications, *Solar Energy Materials and Solar Cells*, 180, 91-102.

[5] Freni, A., Bonaccorsi, L., Calabrese, L., Caprì, A., Frazzica, A. Sapienza, A., (2015) SAPO-34 coated adsorbent heat exchanger for adsorption chillers, Applied Thermal Engineering, 82, 1-7.

[6] Dino, G.E., Palomba, V., Nowak, E., Frazzica, A., (2021) Experimental characterization of an innovative hybrid thermal-electric chiller for industrial cooling and refrigeration application, Applied Energy, 281, 116098.

Design optimization of three-fluid desiccant contactor using genetic algorithm

Hosho, Tatsuki[1], Varela, Richard Jayson[2], Giannetti, Niccolo[3], Jeong, Jongsoo[4], Miyaoka, Yoichi[4], Saito, Kiyoshi[5]

[1] Graduate School of Fundamental Science and Engineering, Waseda University (3-4-1-58-212 Okubo, Shinjuku-ku, Tokyo, 169-8555)
[2] Research Innovation Center, Waseda University (3-4-1-58-212 Okubo, Shinjuku-ku, Tokyo, 169-8555)
[3] Waseda Institute for Advanced Study, Waseda University, 1-6-1 Nishiwaseda, Shinjuku-ku, Tokyo 169-8050, Japan
[4] Research Institute for Science and Engineering, Waseda University (3-4-1 Shinjuku-ku, Tokyo, 169-8555)
[5] Interdisciplinary Institute for Thermal Energy Conversion Engineering and Mathematics, Waseda University (3-4-1 Shinjuku-ku, Tokyo, 169-8555)

Abstract:

Liquid desiccant air conditioning technology represents a highly efficient opportunity for the control of latent loads related to the humidity contained in indoor air-streams. Above all, the integration of a third cooling/heating medium and the use of Ionic Liquid (IL) is a promising alternative for performing efficient humidity control in air conditioning. However, when compared to well-established air conditioning technologies, liquid desiccant systems are commonly bulkier and more expensive. In order to overcome this barrier to practical use, this study presents a numerical method for minimizing the size of three-fluid gas-liquid contactors, which are the bulkiest elements in the system. The structure of the gas-liquid contactor is optimized by using genetic algorithm (GA) to minimize the volume while obtaining a predetermined dehumidification effect. It is found that the volume of the three-fluid contactor can be reduced by 53%, and therefore the construction cost of the system, without compromising its capacity.

1 Introduction

At present, global environmental issues along with untenable energy provision methods are indicating the necessity of highly efficient technologies to minimize the environmental footprint of energy conversion. Air conditioning (AC) systems presently account for the largest share of energy consumption in the building sector and are now becoming a necessity for a large majority of people in the world. Given the large magnitude of latent loads during typical operation cases, proper humidity control is critical to achieve both energy saving and comfort, but conventional vapor compression air conditioners cope with this issue inefficiently. Liquid desiccant air conditioning system realizes humidity control of the process air by means of the vapor absorption phenomenon by bringing the air and the liquid desiccant solution into reciprocal contact. Unlike the vapor compression systems, as the proper control of the composition of the liquid desiccant solution drives the air to a state with lower values of the equilibrium vapor pressure, it is not necessary to lower the cooling source temperature below the dew point temperature, hence resulting in a broad margin of possible energy saving through highly efficient humidity control. However, when compared to well-established air conditioning technologies, liquid desiccant systems are commonly bulkier and more expensive. Accordingly, the development and spreading of this technology require miniaturization of the main components, especially the gas-liquid contactors, which occupy the largest portion of the system.

A gas-liquid contactor is an essential element for the system performance, where coupled heat and mass transfer occur when the air and the liquid desiccant come into contact. Gas-liquid contactors can be categorized into two main types: adiabatic gas-liquid contactors, where the air comes into contact with a pre-cooled or heated liquid desiccant solution without exchanging heat with the external environment, and internally cooled/heated gas-liquid contactors, where a more efficient dehumidification/regeneration is attempted by exchanging heat with a tertiary medium within the contactor. The structural material of the internally cooled/heated gas-liquid contactor is preferably a metal having high thermal conductivity. However, absorbing mixtures such as lithium chloride (LiCl), which is generally used as a liquid desiccant, exhibit strong corrosivity toward several metals commonly used for heat exchangers. On the other hand, Ionic liquids (IL) represent a favorable alternative option as desiccant solutions, because of their non-corrosive characteristics toward aluminum. Therefore, this research effort targets a liquid desiccant air conditioning system that combines the use of an IL and aluminum fin-tube heat exchanger as an internally cooled/heated gas-liquid contactor.

The integration within the contactor of the contemporary heat transfer through a tertiary medium already results in a reduction of the system size. However, if not properly designed such as when few design parameters are only considered, the contactor itself might be over-dimensioned. In fact, previous studies about the combination of fin-tube heat exchangers and IL are lacking in the literature. Giannetti et al. [1] created a correlation equation to predict the wet area ratio of an IL solution in a three-fluid desiccant contactor. In addition, Varela et al. [2] modeled a fin tube heat exchanger using IL and compared the analysis results with the experimental results. However, majority of the optimization studies in the literature focus on the operating conditions [3,4,5,6] and flow configuration [7] as the decision variables, and no systematic method has been developed yet for the miniaturization of the contactor. Therefore, this study presents a method for optimizing the structure of the gas-liquid contactor to minimize the volume while obtaining a predetermined dehumidification effect.

2 Calculation method

2.1 Mathematical model

Figure 1 shows a photograph of the gas-liquid contactor targeted in this study and its elemental structure. Inside the gas-liquid contactor, the liquid desiccant solution is sprayed at the top and flows vertically, the air flows horizontally through the fins, and the water flows in the tubes. These three fluids are interacting through coupled heat, matter, and momentum transfer phenomena. In addition, depending on the operating condition, the falling film of the liquid solution may experience partial wetting of the transfer surface. Therefore, it is necessary to build a model that captures these interconnected phenomena. The mathematical modeling is performed by dividing the contactor into elemental control volumes, as shown in Figure 1.

Figure 2 shows a schematic diagram of the local transport phenomena within the three fluids inside the gas-liquid contactor. In wetted areas, heat transfer occurs between air and solution, between solid walls and liquid solution, and between the solid wall and the cooling/heating medium flowing within the tubes, whereas mass transfer occurs between air and solution. In dry areas, heat transfer occurs between the air and the solid walls, and between the solid walls and the cooling/heating medium flowing within the tubes. Additionally, the possibility of direct dehumidification due to water vapor condensation on the dry areas is accounted for.

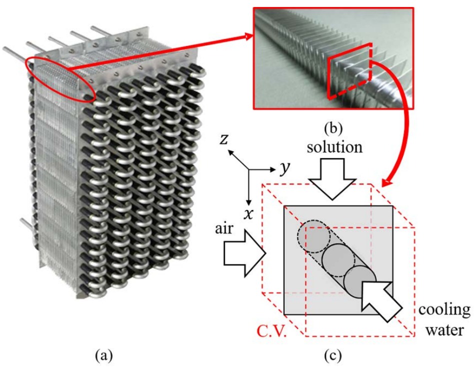

Figure 1 – Three-fluid gas-liquid contactor.

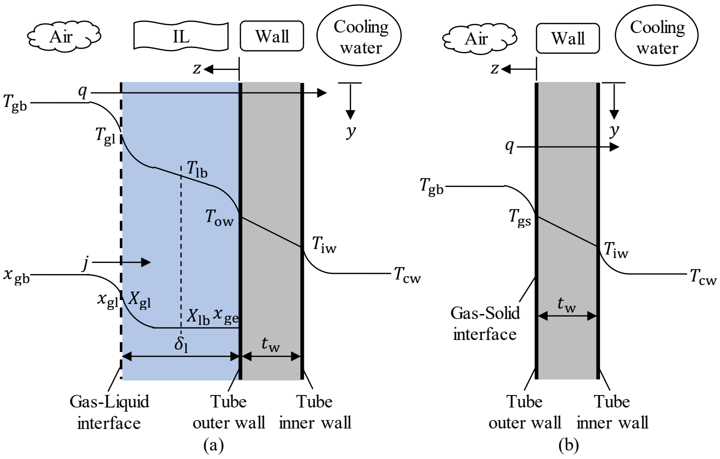

Figure 2 – Schematic diagram of the (a) heat and mass transfer on a wetted wall and (b) heat transfer on a dry wall.

The formulation of heat, mass, and momentum conservation, along with the constitutive correlations is described by Varela et al. [2], where a validation of the numerical results is also presented.

2.2 Optimization

The objective function to be optimized through the evolutionary search of genetic algorithm (GA) is the volume of the gas-liquid contactor, which is to be minimized for a given dehumidification duty. The optimization parameters are height H, width W, and depth L, which are related to the size, and $mesh\_x$ for the number of horizontal pipes, $mesh\_y$ for the number of vertical pipes, $mesh\_z$ for the number of fins, and D_o for pipe diameter, which are related to the internal structure as shown in Figure 3. Table 1 shows the search range for design each parameter determined so as not to be an unrealizable search range.

Table 1 – Search range of the design parameters

Design parameter	Search range
L	0.08~0.2 m
W	0.08~0.2 m
H	0.3~0.6 m
$mesh\_x$	10~12(2 each)
$mesh\_y$	17~30
$mesh\_z$	23~36
D_o	3~5 mm

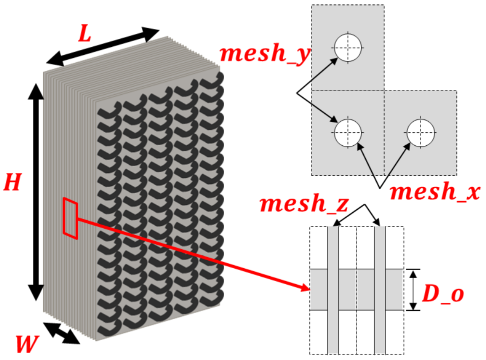

Figure 3 – Design parameters

Constraints are set to ensure that the outlet air absolute humidity is lower or equal to $10.46\,\mathrm{g/kg(D.A.)}$. Additionally, the value of the fan power and pump power are set to 1.83 W or less, to control the maximal pressure drop of the air and cooling/heating medium. These values are selected from the experiment data of the actual three-fluid liquid desiccant air conditioning experimental equipment.

Table 2 shows the external conditions set when performing the optimization calculation. The case of dehumidifying operation is investigated when external conditions representative of summer in Tokyo are assumed. As for the optimization method, in this study, continuous parameters such as size and discrete parameters such as the number of fins are mixed and optimized, the use genetic algorithm (GA) is suitable for handling variations of parameters with such different characteristics when searching for the optimal solution. The elite selection method was used for the generational change algorithm, and Kobayashi's [8] Real-Coded Ensemble Crossover (REX) was used for the crossover algorithm.

Table 2 – External/operating conditions.

Conditions	Parameter	Value
Inlet air	Temperature T_a	34 °C
	Humidity ratio x_a	$19.5\,\mathrm{g \cdot kg(D.A.)^{-1}}$
	Mass flow rate $\dot{m}_\mathrm{a}$	$0.0337881\,\mathrm{kg \cdot s^{-1}}$
Inlet solution	Temperature T_s	17.5 °C
	IL mass fraction X_IL	75 %
	Mass flow rate $\dot{m}_\mathrm{s}$	$0.06\,\mathrm{kg \cdot s^{-1}}$
Inlet cooling water	Temperature T_cw	17 °C
	Mass flow rate $\dot{m}_\mathrm{cw}$	$0.1\,\mathrm{kg \cdot s^{-1}}$

3 Results

Figure 4 shows the process of searching for a solution by GA. The volume is converging as the search progresses. Figure 5 illustrates the actual gas-liquid contactor experimentally tested in Sato et al. [9] as a benchmark for the comparison with the volume of the optimized gas-liquid contactor. Table 3 lists the geometrical characteristic of the experimental and calculated cases. It is possible to reduce the volume of the contactor by 53% compared to the original size of the contactor at the selected conditions.

The optimized contactor features a length L less than half than that of the actual contactor, which caused a significant reduction in the size of the actual contactor. On the other hand, the number of fins increased to have sufficient transfer area for achieving the same dehumidification rate. Overall, the resulting change in these two parameters results in a higher wetting rate. Also, as the number of fins increases, the fin pitch becomes narrower. Therefore, it is expected that the air flow path will be narrower and the fan power will be increased. However, by reducing the pipe diameter, and increasing the height of the contactor, the original air flow path is restored and the fan power is prevented from increasing. On the other hand, when the pipe diameter is reduced, the friction of water within the tubes is expected to increase, and the pump power would increase. However, as the pump power is relatively small compared to the fan power, the total power is balanced by a minimal variation on the fan power.

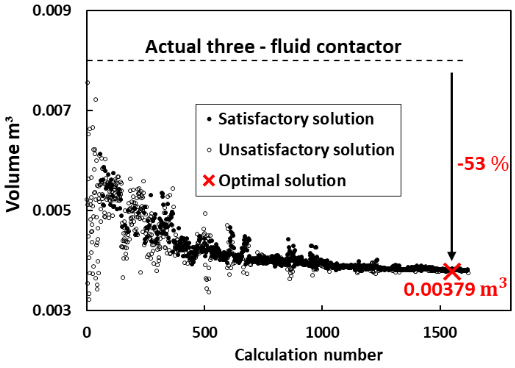

Figure 4 – Process of searching for a solution by GA.

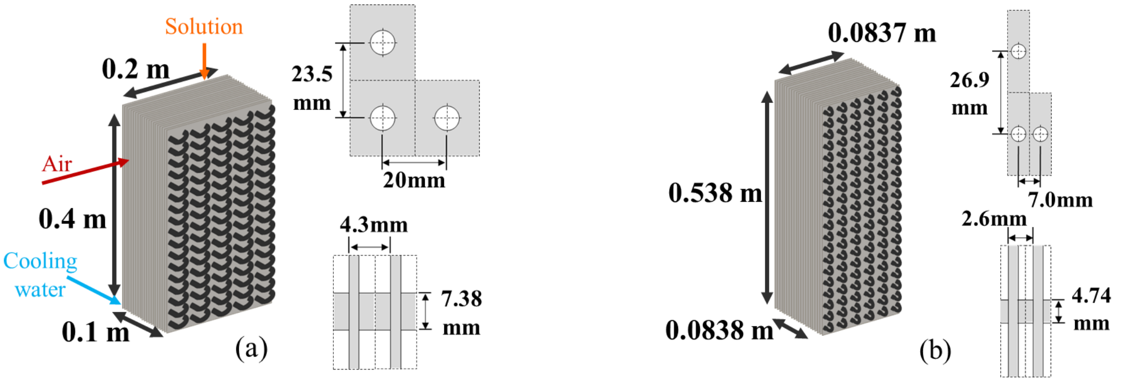

Figure 5 – (a) Actual three-fluid contactor (b) Optimized three-fluid contactor.

Table 3 – Quantitative comparison of the actual and optimized three-fluid contactor.

	Experimental contactor	Optimized contactor
Volume	0.008 m^3	0.00379 m^3
Power	1.83 W	1.83 W
Fan power	1.71 W	1.26 W
Water pump power	0.12 W	0.57 W
Wetting ratio	63 %	71 %
Tube diameter	7.38 mm	4.74 mm
Vertical tube	17	20
Horizontal tube	5	6
Fin	23	32
Vertical tube pitch	23.5 mm	26.9 mm
Horizontal tube pitch	20 mm	7.0 mm
Fin pitch	4.3 mm	2.6 mm

4 Conclusions

A design optimization method for a three-fluid IL desiccant contactor is investigated using GA for minimizing the volume of the device while achieving a given dehumidification rate. As a result, it was clarified that it is possible to realize the same dehumidification rate while reducing the contactor volume by 53 % without increasing the total power for circulating the three fluids. The results contribute to overcoming cost and size limitations for the practical application of liquid desiccant technologies not only for industrial-scale application but also for residential applications. This will lead to a less expensive and smaller liquid desiccant air conditioning system, which will facilitate highly efficient humidity control and is expected to provide both comfort and energy savings.

5 List of References

[1] Giannetti, N., Varela, R.J., Ariyadi, H., Yamaguchi, S., Saito, K., Wang, X.M., Nakayama, H., (2018): Semitheoretical Prediction of the Wetting Characteristics of Aqueous Ionic Liquid Solution on an Aluminum Finned-Tube Desiccant Contactor. *Journal of Fluids Engineering*, vol. 104(12), pp. 121109-1-121109-9.

[2] Varela, R.J., Yamaguchi, S., Giannetti, N., Saito, K., Wang, X.M., Nakayama, H., (2020): Experimental performance analysis and simulation of an internally cooled liquid desiccant air conditioning system using a novel ionic liquid. *Proceedings of the 14th IIR Gustav Lorentzen Conference*, Kyoto, Japan. IIF/IIR, 1189.

[3] Wang, X., Cai, W., Lu, J., Sun, Y., Zhao, L., (2015): Model-based optimization strategy of chiller driven liquid desiccant dehumidifier with genetic algorithm. *Energy*, vol. 82, pp. 939-948.

[4] Qi, R., Lu, L., Huang, Y., (2015): Parameter analysis and optimization of the energy and economic performance of solar-assisted liquid desiccant cooling system under different climate conditions. *Energy Conversion and Management*, vol. 106, pp. 1387-1395.

[5] Tu, M., Huang, H., Liu, Z-H., Chen, H-X., Ren, C-Q., Chen, G-J., Chen, Y-H., (2017): Factor analysis and optimization of operational parameters in a liquid desiccant air-conditioning system. *Energy*, vol. 139, pp. 767-781.

[6] Liu, X., Liu, X., Zhang, T., Xie, Y., (2018): Experimental analysis and performance optimization of a counter-flow enthalpy recovery device using liquid desiccant. *Building Services Engineering Research and Technology*, vol. 39, pp. 679-697.

[7] Zhang, L., Song, X., Zhang, X., (2018): Analysis and optimization of total heat recovery devices by using liquid desiccant as a coupling fluid in air-conditioning systems. *Energy and Buildings*, vol. 172, pp. 493-504.

[8] Kobayashi, S., (2009): The Frontiers of Real-coded Genetic Algorithms, *Transactions of the Japanese Society for Artificial Intelligence*, vol. 24(1), pp.147-162.

[9] Sato, T., Varela, R.J., Yamaguchi, S., Saito, K., Nakayama, H., Wang, X.M., (2018): Experimental study on a finned-tube internally cooled contactor for liquid desiccant air-conditioning systems with ionic liquid. *Proceedings of the 17th International Refrigeration and Air Conditioning Conference*, Indiana, USA, IIF/IIR, 2561.

Experimentation and modeling of a combined plate generator for NH_3-H_2O absorption machine

Mathilde Wirtz[1,2,*], Benoit Stutz[2], Hai Trieu Phan[1], François Boudehenn[1]

[1] *Univ. Grenoble Alpes, CEA, LITEN, DTCH. F-38000 Grenoble, France*

[2] *LOCIE, Univ. Savoie Mont Blanc, CNRS UMR5271, Savoie Technolac, 73376 Le Bourget Du Lac France*

**Corresponding author: mathilde.wirtz@cea.fr*

Abstract:

The cold production in a NH_3-H_2O absorption machine requires the use of a rectifier to remove traces of water in the ammonia vapor produced. The quantity of water to be removed mainly depends on the type of generator and its geometry. The present modelling work investigates the behavior of a flat plate falling-film combined generator, associating vapor generation and vapor purification functions, producing sufficiently pure ammonia vapor, not to require a rectifier at its output. A numerical model is developed to describe the heat and mass transfers within the combined generator. It implements correlations from the literature, balance equations and equilibrium conditions at the liquid-vapor interface. A combined generator prototype is implemented into a NH_3-H_2O absorption chiller of 5 kW cold capacity. Comparison between the experimental and numerical data shows good agreements, validating the developed model in normal ranges of operating conditions.

1 Introduction

Absorption machines are interesting for cold production compared to conventional vapor compression machines when abundant and cheap heat sources are available at medium temperature (20°C – 30°C) for heat rejection, and at high temperature (80°C - 180°C) for heating. The often-used couple NH_3-H_2O takes advantage of high-pressure operating conditions, and is favorable to internal transfers and compactness of the system. However, absorption chillers require the use of a rectifier at the generator outlet in order to eliminate water traces in the ammonia vapor produced. The heat lost by the rectification process affects the coefficient of performance of the NH_3-H_2O absorption chillers, which is lower than the one of H_2O-LiBr machines. It is all the more important as the fraction of water in the vapor at the exit of the generator is important. Combination of vapor generation and vapor purification in a single component is an interesting ideal solution, which allows reducing operating costs and at the same time avoids the need of separations bottles and pipes at the generator outlet. Flooded desorption column combining generation and rectification of NH_3 vapor as developed for example by J. Golden [1] enable this, but the compactness of such components is relatively low.

The fraction of water in the vapor at the exit of the generator mainly depends on the design of the generator used. Falling-film plate generator is a profitable configuration limiting the water fraction in the vapor produced, by taking part of the liquid-vapor equilibrium along the exchanger. They have high thermal efficiency, flexibility, reduced cost and can reach a desired efficiency by adjusting geometry [2] [3]. Their use also improves the absorption chiller compactness since no additional components are needed for phase separation. The counter-current flow configuration (ie. when the ammonia solution flows downwards while the vapor rises up from the combined generator bottom to the top) shows better performance compared to the co-current configuration [4].

The purpose of the study is to develop a new combined generator, integrating vapor generation and vapor purification functions that generates sufficiently pure ammonia vapor, not to require a rectifier at its output. This falling-film and plate exchanger is developed for a NH_3-H_2O absorption chiller of about 5 kW of cold production. The combined generator performances are evaluated through a numerical model and experiments. We investigate the impacts of different inlet parameters and validate the numerical model by comparison to the experimental data.

2 Fundamentals

2.1 Combined generator design

The combined generator is composed of two sets of vertical plates (heated and adiabatic), involving falling-film. In the upper part, the ammonia-water mixture with a high concentration of ammonia is injected into a distributor and spread over the adiabatic plates. Then, the solution flows downwards along heated and grooved plates, arranged perpendicular to the adiabatic plates. In this heated part, the heat transfer fluid (HTF) flows in counter-current mode compared to the falling-film. The vapor generated circulates from the bottom to the top of the exchanger, and interacts with the falling-film flowing along the adiabatic plates. Its partial reabsorption by the solution reduces the fraction of water it contains and thus purifies it.

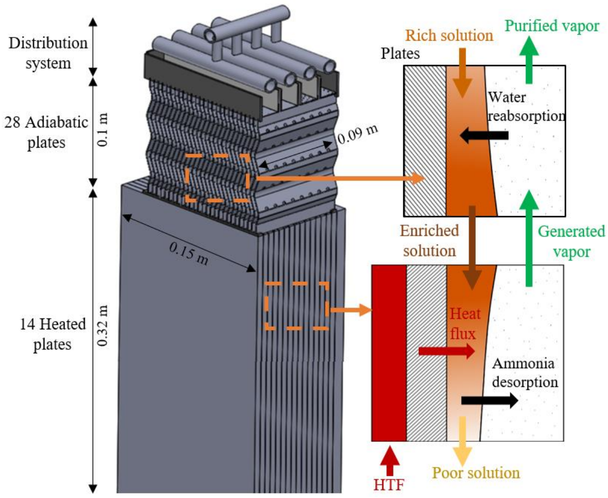

Figure 1 – Combined generator geometry and heat and mass transfers involved.

2.2 Numerical model developed

A 1-D model of NH_3-H_2O falling-film heat exchanger was developed, based on the previous work of Triché [5], to calculate the heat and mass transfers, the balance equations and equilibrium conditions at the interface between the falling-film and the vapor flow. Compared to Triché [5], we improve the robustness of the model resolution by implementing a new numerical method, allowing the simulations in both co and counter-current configurations. We can also simulate both absorption and desorption processes, which occur in the new combined generator [4].

3 Numerical model results

3.1 Nominal operating conditions

The falling-film combined generator design is presented Figure 1. The NH_3-H_2O solution flows within 4 mm thick grooves insuring negligible head losses in the vapor phase, while vapor pressure is assumed to be imposed by the saturation pressure at the condenser.

Figures 2a and 2b show the evolution of the temperature and the ammonia concentration according to the position inside the combined generator. The inlet conditions are chosen according to the operating conditions of the absorption chiller prototype, with a pressure of 12 bar. The solution enters the heat exchanger superheated (+1.5°C) compared to the saturation condition.

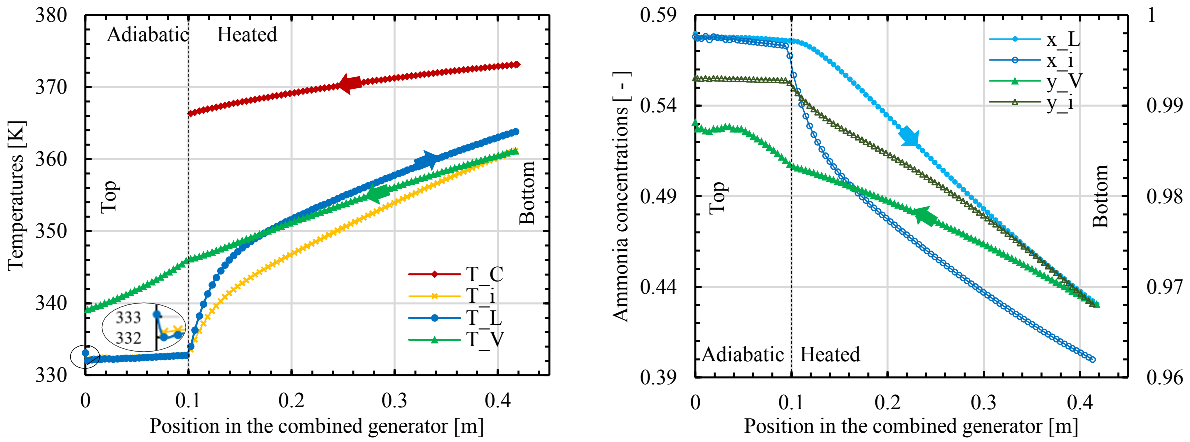

(a) Temperatures evolution

(b) Ammonia concentration evolution

Figure 2 – Temperatures and ammonia concentrations evolutions along the combined generator for nominal case.

The HTF enters at the bottom and heats the ammonia-water solution along the heated part of the combined generator. The solution falling-film is heated by the HTF at the wall, and cooled at the liquid-vapor interface because of evaporation process. At the interface, the liquid and vapor phases are at equilibrium. The interface temperature T_i depends on the pressure and on the ammonia fractions in both liquid and vapor phases x_i and y_i. The vapor flow rate is zero at the bottom, and vapor temperature at that position corresponds to the interface temperature T_i. The vapor temperature T_V along the exchanger depends on the temperature of the interface where it is generated and on the temperature of the vapor produced upstream with which it mixes. This explains the decrease of T_V from bottom to top while remaining above the interface temperature T_i. At the inlet of the combined generator, the solution is superheated, then at the outlet of the injecting flutes (see Figure 1) it undergoes a “flash” desorption, resulting in a sudden drop of the solution temperature T_L to the equilibrium temperature T_i. The solution stays in equilibrium condition until the end of the adiabatic part.

Along the heat exchanger, the solution ammonia concentration x_L decreases by desorption process with a light slope in the adiabatic section from 0.58 to 0.575 and a stronger slope in the heated section, to reach 0.43. Due to the decrease of the interface temperature from bottom to top along the vapor flow, the water fraction in the vapor flow decreases. The vapor ammonia fraction is then minimum at the bottom of the combined generator, where it is equal to the equilibrium fraction at the interface $y_V = 0.968$. Then it increases along the exchanger to reach 0.983 at the outlet of the heated part and becomes maximum at the top of the combined generator, where $y_V = 0.988$.

4 Numerical model validation

4.1 Inlet parameters

The new combined generator prototype is implemented in a NH_3-H_2O absorption chiller available in our laboratory. For the experimental set, Table 1 presents the ranges and the nominal operating conditions of the absorption chiller, with the values of the temperatures and the mass flow rates at the inlet of the external circuits and of the rich solution at the combined generator inlet.

Table 1 – Ranges and nominal operating conditions of the external circuits and the rich solution.

		Combined generator	Absorber/Condenser	Evaporator	Solution
Nominal	Temperature [°C]	95	27	18	-
	Mass flow rate [kg.h^{-1}]	1600	1230	1100	100
Range	Temperature [°C]	80 - 106	22 - 28	16 - 22	-
	Mass flow rate [kg.h^{-1}]	600 - 1800	1230	1100	80 - 115

A total number of 37 tests were led with different inlet operating conditions. The measured values of the HTF and of the rich solution temperatures (T_{CG}, T_{RS}), the mass flow rates ($\dot{m}_{CG}, \dot{m}_{RS}$), the ammonia concentration of the rich solution (x_{RS}), as well as the pressure (P) at the inlet of the combined generator are used as input values for the numerical model. The results of the simulation are then compared to the measurements.

Figure 3 compares the measurements of the heat supplied to the combined generator (Q_{CG}) with the results of the modelling. The model overestimates the heat supplied. The deviations between the experimental and the numerical values are less than 20% for 76% of the values. The experimental uncertainties are included between 2 to 7% of error. The deviation between experiment and modelling can be attributed to wettability and distribution problems. Some extreme deviations (detailed in Figure 3, between 20% and 40% of error) correspond to the following cases: high inlet rich-solution mass-flow rate ($\dot{m}_{RS} > 105$ kg.h^{-1}), high inlet HTF temperature at the absorber ($T_{abs} \geq 28$°C) and low outlet HTF temperature at the evaporator ($T_{ev} < 13$°C). At these extreme conditions, the inlet solution temperature is super-heated by more than 4°C vs. the saturation condition.

Figure 4 represents the calculated mass flow rate of the generated vapor exiting the combined generator as a function of the measured mass flow rate. The relative deviations between the experimental and the numerical values are less than 20% for 70% of the values. The numerical model overestimates the refrigerant mass flow rate produced. As for the heat supplied (Figure 3), the extreme deviations correspond to extreme inlet operating conditions of the absorption chiller.

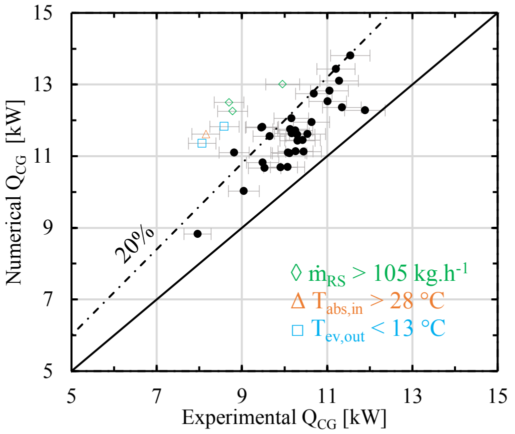

Figure 3 – Numerical heat supply at the combined generator vs. the measured heat.

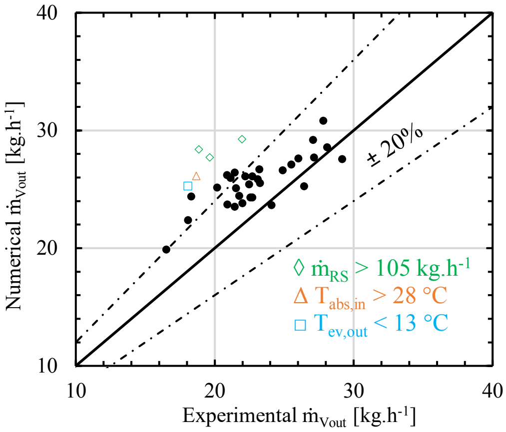

Figure 4 – Numerical mass flow rate of the generated vapor vs. the measured vapor mass flow rate.

Figure 5 compares experimental and numerical temperatures differences of the HTF, the solution and the vapor between the inlet and outlet of the combined generator. The HTF temperature decrease is included between 4°C and 15°C, and is slightly overestimated (~1°C) by the numerical model, probably because of wettability and distribution impacts. The falling-film solution temperature increases between 13°C and 30°C along the heated plates. The highest deviations appear when the HTF mass flow rate is low ($\dot{m}_{CG} < 800$ kg.h^{-1}). For the vapor, the difference of temperature is calculated between the outlet temperature of the liquid, at the bottom of the combined generator (where the generated vapor appears first) and the outlet temperature of the vapor exiting at the top of the combined generator. The vapor temperature decreases along the plates between 8°C and 30°C experimentally, and between 12°C and 23°C numerically. The highest deviations between the model and the experiments appear when the inlet operating conditions are extreme: low mass flow rate of the HTF ($\dot{m}_{CG} < 800$ kg.h^{-1}), low temperature of the absorber ($T_{abs} < 25$°C) and high temperature of the combined generator HTF ($T_{CG} > 100$ °C).

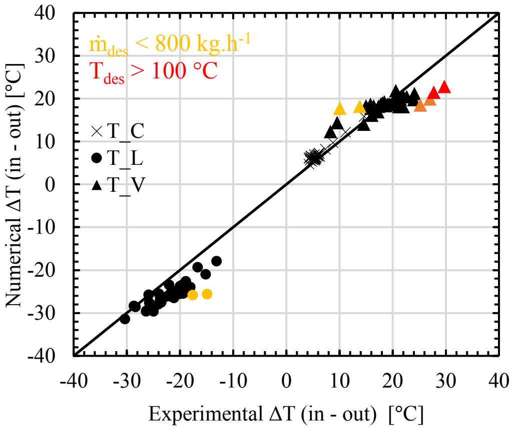

Figure 5 – Comparisons between numerical and experimental temperature differences.

5 Conclusions

Performances of a combined generator falling-film plate exchanger for NH_3-H_2O absorption chillers is studied through simulations and measurements. The results show a good agreement between the numerical and experimental data, with less than 20% of error when the inlet operating parameters are not in extreme conditions. When the combined generator replaces the boiling generator and the rectifier initially implemented in the absorption chiller, the coefficient of performance increases by +0.1, because there is no need of a rectifier. Further works are needed to analyze the experimental data in order to have a better understanding of the physical phenomena occurring in the combined generator and thereby to improve the model accuracy.

6 Acknowledgment

The authors would like to thank the Commissariat à l'Energie Atomique et aux Energies Alternatives (CEA) for supporting this work.

7 List of References

[1] Thesis of Golden J., “Ammonia-water desorption in flooded columns”, Georgia Institute of Technology, 2012.

[2] Abou Elmaaty T. M., Kabeel A. E., Mahgoub M., "Corrugated plate heat exchanger review", *Renewable and Sustainable Energy Reviews, 70* (2017) 852-860

[3] Hessami Ma. "Surface temperature and heat transfer measurements in cross corrugated plate heat exchangers", *Iran J Sci Technol; 24-3* (2000) 283-97

[4] Wirtz M., Phan H.T., Stutz B., Boudéhenn F., "Modélisation numérique d’un générateur à plaques et films tombants pour machine à absorption NH3-H2O", *Congrès Annuel de la Société Française de Thermique* 2020

[5] Triché D., Bonnot S., Perier-Muzet M., Boudéhenn F., Demasles H., Caney N., “Modeling and experimental study of an ammonia-water falling-film absorber”, *Energy Procedia 91* (2016) 857 – 867

Numerical Modeling of Heating and Cooling Sorbent beds with Fluid Heat Exchangers

Y. Garfinkel[1]**, N. Tzabar**[2]

[1] Department of Chemical Engineering, Ariel University, Ariel 40700, Israel

[2] Department of Mechanical Engineering, Ariel University, Ariel 40700, Israel

Abstract:

Research on Sorption Thermal Energy Storage (STES) is conducted in our laboratory. In this paper, we discuss the modeling of heat transfer from a fluid flow tube heat exchanger to a sorbent bed containing activated carbon and methanol. In order to calculate the heat transfer, the finite differences numerical method is selected, aiming to determine the optimum mechanical design of the heat exchanger for seasonal or daily thermal energy storage systems. The numerical model shall comply with different heat exchanger configurations, such as tube banks, inline or staggered, helical tubes, finned tubes, and more. Finally, preliminary results are presented and discussed. Future work will include further development of the model and the construction of a demonstrator, which shall validate the model.

1 Introduction

Many pieces of research are published in the field of sorption thermal energy storage [1-3]. The most common working fluids are water and methanol [1,2], where many adsorbents are considered [2,4], such as activated carbons, silica gels, zeolites, and other sophisticated materials [9].

Our research focuses on optimizing the mechanical design of the heat exchanger, for any adsorbent – adsorbate pair. Some examples are a tube bank heat exchanger [2], or a honeycomb heat exchanger [8]. The current research is based on our experience in modeling heat and mass transfer of sorption machines [5-7], and our capabilities in measuring thermal properties of sorbent beds.

2 Method

2.1 Heat transfer modeling

The numerical model aims for optimizing different fluid heat exchangers, such as tube banks, inline or staggered, helical tubes, finned tubes, and more. By calculating the radial affected area from a single tube and thruogh axisymmetry constructing a tube bank. Fig. 1. Shows two types of tube bank heat exchangers: inline and staggered. The figure also shows radial areas around every tube, which covers the majority of the entire volume. These circled areas around the tubes refer to the affected area by the tubes. The circled areas in the inline configuration equal 78% of the total rectangular area (sorbent bed) , and for the staggered configuration this ratio is 80%. Therefore, we decided to model the complex heat exchangers, which will be considered down the road of our research, by a single tube model, with a cross-section view shown in fig. 2.

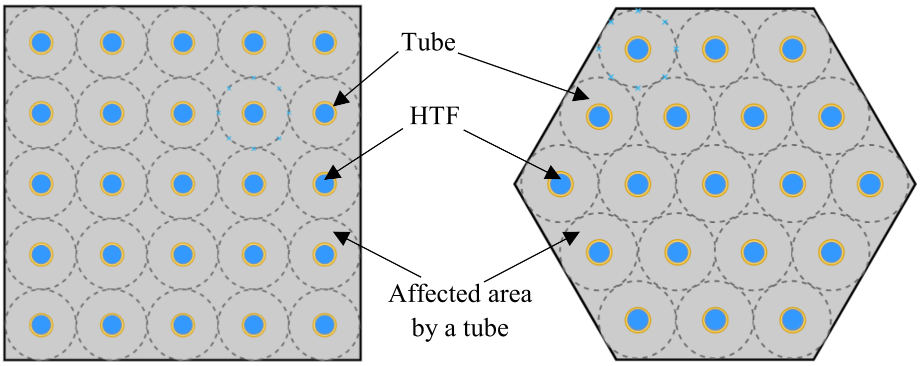

Figure 1 Inline and staggered tube banks, including the radial affected area of every tube

Aiming for the temperature distribution around a tube, in which a heat transfer fluid (HTF) flows, the following cylindrical energy balance has to be solved:

$$\rho \cdot c \cdot \frac{\partial T}{\partial t} = k \cdot \frac{1}{r} \cdot \frac{\partial}{\partial r}\left(r \cdot \frac{\partial T}{\partial r}\right) + \frac{\partial}{\partial z}\left(k \cdot \frac{\partial T}{\partial z}\right) + \dot{q}_{gen} \tag{1}$$

Where ρ is the density (kg/m^3). c is the specific heat capacity (J/kg·K). T is the temperature (K), t is time (s), k is the conductive heat transfer coefficient (W/m·K), r and z are the radius and length of the heat exchanger (m), respectively, and $\dot{q}_{gen}$ is volumetric internal heat generation (W/m^3), which for the adsorbent sections equals the adsorption and desorption heats.

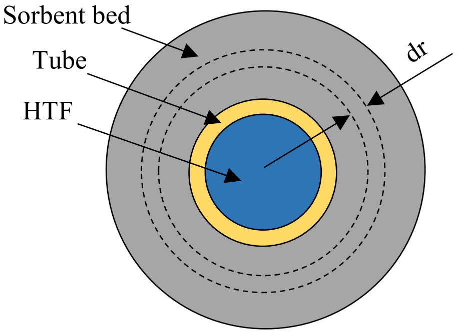

Figure 2 A cross-section view of the heat exchanger

A two-dimensional numerical heat and mass transfer model is being developed and implemented in a Matlab™ code. The model is fully parametric to comply with various design options. The current model is based on the finite differences method for predicting the temperature distribution by dividing the heat exchanger into a predefined number of elements, see fig.3. Every element acts as a lumped capacity with the ability to absorb or generate heat. The numerical energy balance for each element is:

$$T_{i,j}^{p+1} = T_{i,j}^{p} + \frac{\Delta t}{c_{i,j} \cdot \rho_{i,j} \cdot V_{i,j}} \cdot \left[\sum \frac{T_{j,i}^{p} - T_{i,j}^{p}}{R_{i,j}} + \dot{m}(h_{in} - h_{out}) + \dot{q}_{gen_{i,j}} \cdot V_{i,j}\right] \tag{2}$$

Where i & j represent the element coordinates (see figure 3.), Δt is the size of the time step (s), p is the number of time steps, V is the volume of an element (m^3), and $\dot{m}$ is the mass flow rate (kg/s), which is valid only for the HTF elements. R_{ij} is the thermal resistance between any pair of elements in contact (K/W), which consists of conduction, convection, and contact resistance. h_{in} and h_{out} are the enthalpies of the incoming and outgoing HTF flow, respectively.

The size of the time step (Δt) is determined according to the minimum ratio between the heat capacity and thermal resistances among all the elements:

$$\Delta t = \Delta \tau_{min} = \left(\frac{C_{ij}}{\Sigma\left(\frac{1}{R_{ij}}\right)}\right)_{min} \tag{3}$$

Where C is the heat capacity (J/K).

2.2 A test case

In this paper, a single test case is presented. The HTF is liquid water, flowing in a copper tube, which is surrounded by activated carbon. The edge of the heat exchanger is connected to a stainless-steel vessel. The material properties are provided in table 1 and the physical dimensions and the flow properties are provided in table 2. The Reynolds number equals 45.6, therefore the flow is laminar, the Prandtl number equals 3.42 and the Nusselt number equals 3.66. The initial temperature of the system is 300 K and the HTF enters the heat exchanger at a constant temperature, which equals 350 K.

Table 1 Material properties

	Water	Copper	Sorbent	SS316
Thermal conductivity (W/m·K)	0.645	395	0.416	54
Density (kg/m^3)	1000	8933	250.11	7833
Specific heat capacity (J/kg·K)	4182	385	2285	465

Table 2 Physical dimensions

Outer copper tube diameter (mm)	Copper tube thickness (mm)	Heat exchanger length (m)	Vessel wall thickness (mm)	Sorbent's radial thickness (mm)	Length of an element (mm)	Time step (s)	HTF flow rate (g/s)
6.35	1.2	3	4	15	30	0.0748	0.24

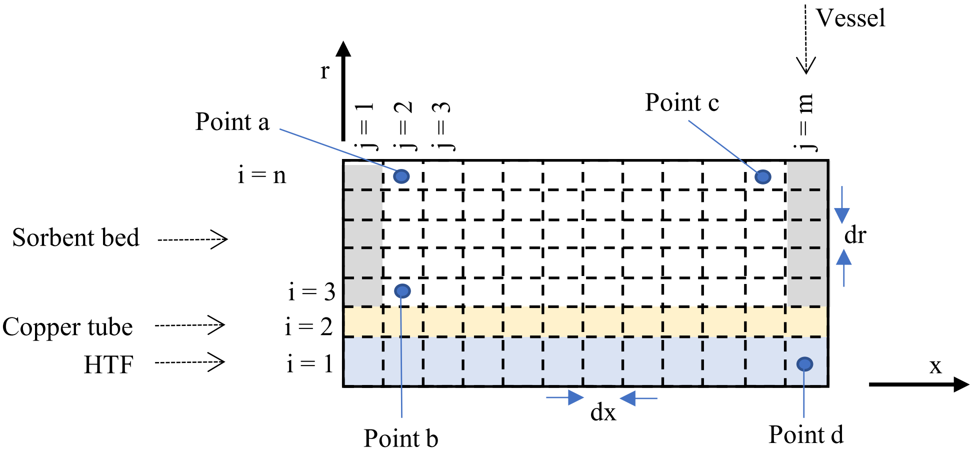

Figure 3 schematic cross-section of the heat exchanger

3 Results

Fig. 4 shows the temperatures at points a, b, c, and d (see fig.3) as a function of time. In addition, the average sorbent temperature (AST) as shown, which is calculated by:

$$AST = \frac{\sum_{i=3}^{n} \sum_{j=1}^{m-1} T_{ij} V_{ij}}{\sum_{i=3}^{n} \sum_{j=1}^{m-1} V_{ij}} \tag{4}$$

The results in fig.4 show that an *AST* of 312 K is obtained after 130 minutes, and the temperature distribution in the sorbent bed is expressed by the temperatures of points *a*, *b*, and *c*. Point *d* indicates the temperature of the HTF which leaves the heat exchanger. When this temperature reaches the inlet HTF temperature, one shall conclude that heat is no longer transferred from the HTF to the system. The calculated temperature distribution allows determining the pressure in the vessel, by the adsorption isotherms of the adsorbate-adsorbent pair. In addition, the adsorption isotherms are used to evaluate the heat of adsorption and desorption, which can be incorporated into the numerical model.

4 Conclusions

Sorption thermal energy storage systems have much potential for short terms and seasonal applications, with high energy density, relative to sensible and latent heat storage systems. Our research aims to develop a simple numerical model for describing a large range of heat exchanger configurations and to allow the optimization of the mechanical design for every application. The model is fully parametric, and is, therefore, suitable for any working pairs, any size scale, and operating conditions. Preliminary results are presented and discussed, to describe the predicted capabilities of the model in our future work.

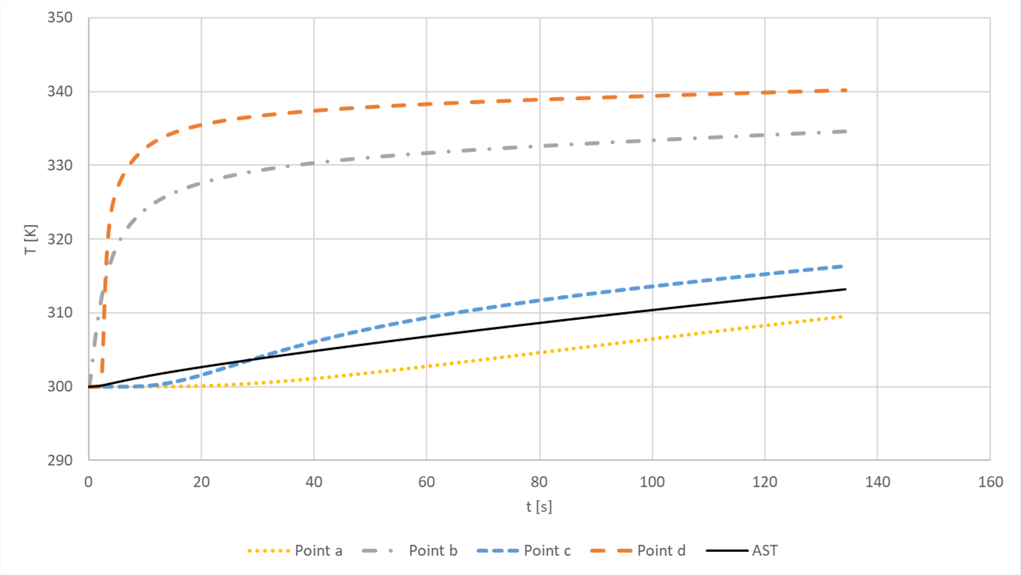

Figure 4 temperature versus time at different locations, for the discussed test case

5 Acknowledgment

The authors acknowledge the Israeli Ministry of Energy for financially supporting our research on sorption thermal energy storage.

6 List of References

[1] Jun W. Wu, S. Hadi Madani (2015): Characterizations of Activated Carbon–Methanol Adsorption Pair Including the Heat of Adsorptions, *Journal of Chemical & Engineering Data 60* (6), 1727-1731, DOI: 10.1021/je501113y

[2] L.W Wang, J.Y Wu (2003) Study of the performance of activated carbon–methanol adsorption systems concerning heat and mass transfer, Applied Thermal Engineering, Volume 23, Issue 13, Pages 1605-1617. ISSN 1359-4311, https://doi.org/10.1016/S1359-4311(03)00104-2.

[3] B. Fumey, R. Weber, L. Baldini (2019) Sorption based long-term thermal energy storage – Proces classification and analysis of performance limitations: A review, Renewable and Sustainable Energy Reviews, Volume 111, Pages 57-74, ISSN 1364-0321, https://doi.org/10.1016/j.rser.2019.05.006.

[4] M.Aydin, Sean P. Casey, Saffa Riffat, (2015) The latest advancements on thermochemical heat storage systems, Renewable and Sustainable Energy Reviews, Volume 41, Pages 356-367, ISSN 1364-0321, https://doi.org/10.1016/j.rser.2014.08.054.

[5] A.Davidesko, N.Tzabar (2021) Temperature and pressure dynamics in sorption cells, Adsorption, 27:117–128. https://doi.org/10.1007/s10450-020-00270-z

[6] A.Davidesko, N.Tzabar (2020) A numerical study on the design of sorption cells for multistage compressors, Cryogenics, Volume 108, 103074, ISSN 0011-2275, https://doi.org/10.1016/j.cryogenics.2020.103074.

[7] A.Hamersztein, N.Tzabar, (2021) A dynamic model of multi-stage sorption compressors, International Journal of Refrigeration, Volume 124, Pages 105-113, ISSN 0140-7007, https://doi.org/10.1016/j.ijrefrig.2020.12.020.

[8] Yannan Zhang, Ruzhu Wang (2020) Sorption thermal energy storage: Concept, process, applications and perspectives, Energy Storage Materials, Volume 27, Pages 352-369, ISSN 2405-8297, https://doi.org/10.1016/j.ensm.2020.02.024.

[9] Y.Ahmadi, Ki-Hyun Kim, S.Kim, M.Tabatabaei (2020) Recent advances in polyurethanes as efficient media for thermal energy storage, Energy Storage Materials, Volume 30, Pages 74-86, ISSN 2405-8297, https://doi.org/10.1016/j.ensm.2020.05.003.

Investigation on a passive adsorption heat release process using chimney effect

Zeng, Ziya[1], Zhao, Bingchen[1], Wang, Ruzhu[1,*]

[1] Institute of Refrigeration and Cryogenics, Shanghai Jiao Tong University, Shanghai 200240, China.
**Email: rzwang@sjtu.edu.cn*

Abstract:
The development of low-carbon heating technology contributes to realizing energy conservation, emission reduction and carbon neutrality. Adsorption thermal storage using open sorption bed to handle moisture water in the air was considered as one of the most promising thermal storage technology, commonly adopts air forced convection strategies to overcome the high pressure drop in the high energy density packed system, which consumes additional energy for adsorption dynamics enhancement. Herein, a passive adsorption heat release process using chimney effect was demonstrated by a proof-of-concept experiment and corresponding numerical simulation. A single channel adsorption module with different heights was established and studied. The experiment results with a short length of adsorption bed show that, a temperature lift of 2.5 °C between outlet and inlet occurs due to the adsorption heat, and with the increase of height, a larger temperature lift and more steady temperature output can be obtained. In order to further investigate the chimney effect of the adsorption heat release process, a numerical simulation is carried out. The results confirm that the temperature lift can be improved by increasing the height of adsorption channel, and further demonstrate the performance of temperature, relative humidity, and air velocity due to chimney effect.

1 Introduction

Since thermal energy accounts for a large part of the total energy consumption in modern society, it is urgent and necessary to deal with the “hard bone” by developing the low-carbon heating technology to realize the energy conservation, emission reduction and carbon neutrality around the world [1-2]. Energy storage technology can accurately regulate and match the supply and demand of thermal energy. Adsorption thermal storage, considered as one of the most promising thermal storage technology in the field of energy saving and low grade heat utilization, can realize ultra-high thermal storage density, long period, safe and controllable thermal storage process [3-4]. An adsorption thermal storage system could be designed as an open-looped adsorption process that captures water vapour and at the same time, release adsorption heat to the surrounding air.

For the active adsorption system design, which is the mainstream research for adsorption thermal storage, the pressure drop along the air transport channel is usually high to realize a higher thermal storage density [5]. Meanwhile, the high power density must be achieved by way of air forced convection to strengthen the heat and mass transfer during the adsorption heat release process, and therefore, additional energy are needed for adsorption dynamics enhancement in the system [6]. To reduce the energy consumption, in recent years, researchers pay more attention to the optimization of the air flow distribution and diffusion path. Several typical structures are developed, such as module reactors separated by diffusion paths, segmented reactors, open-adsorption pipe reactors and honeycomb-like consolidated adsorbent reactors [7-8]. However, such Active air supplying strategies achieve good performance of increasing heat and mass transfer at the expense of noise and extra energy consumption, which limit their applications in the field with strict requirements on space and weight. In this way, a passive adsorption system is much attractive and worthy.

Herein, a zero-energy-consumption adsorption heat release process using chimney effect was demonstrated by a proof-of-concept experiment and corresponding numerical simulation. To date, it is desirable but remains a great challenge to investigate the contribution of chimney effect to the performance of adsorption heat release process. Therefore, in this paper, a single channel adsorption module with different heights was experimentally established and studied, followed by a numerical simulation for further investigation of the chimney effect of the adsorption heat release process.

2 Method

2.1 Experimental Set-up

Considering that the chimney effect needs a rising channel in the same direction as gravity, a proof-of-concept module unit with a vertical air flow channel was designed and constructed. As shown in Fig. 1, the module unit consists of a cylindrical metal screen, a circular glass tube with an insulating cover, and an air flow channel between the mesh and the glass. The mesh screen with a diameter of 7 mm is used to hold adsorbents. The circular glass with two open ends acts as a side wall to form a vertical air flow channel. The module unit was placed 5 cm above the ground to allow the free convection of air. Considering the direction of buoyancy, the bottom end of the air flow channel is set as the air inlet, while the top end is set as the air outlet. Zeolite 13X with a diameter of 1.5 mm was selected as the adsorbent material. The adsorption module unit is placed inside the acrylic glass-made windshield to prevent the interference by external air convection.

Both of the temperature and humidity were measured using K-type thermocouples and high-precision hygrographs. All the measuring instruments have been calibrated. The zeolite particles are dried in the drying oven at the temperature of 150 °C over 8 hours, and then cooled to room temperature before filled into the device. During the experiment, the inlet and outlet temperature, T_i and T_o, and relative humidity, RH_i and RH_o, were real-time monitored to evaluate the performance of adsorption heat release process. The experiment began to record the data after filling adsorbents into the module unit. Three different heights of the module unit, 10 cm (Case 1), 15cm (Case 2) and 20 cm (Case 3), were introduced to test the influence of height to the performance.

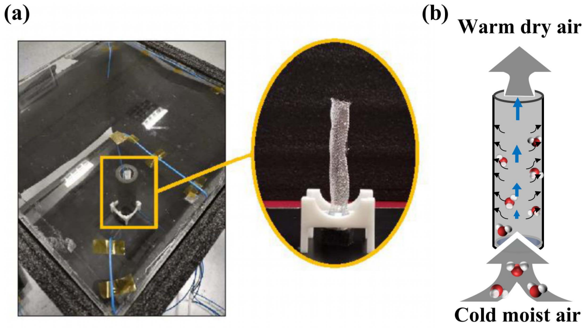

Fig. 1. (a) The experimental set-up of the adsorption module unit; (b) a schematic diagram of the chimney effect during the adsorption heat release process.

2.2 Numerical simulations

In order to further investigate the performance of chimney effect induced by adsorption heat, a numerical simulation was carried out. The non-energy-consumption heat release process of the module unit was simulated using a self-developed 2-dimenstional simulation model. A cylindrical computational domain with open boundary conditions was established to calculate the thermal behavior of the storage unit and its surrounding air. For model simplifications, the transient simulation of water adsorption of dry adsorbent was conducted at a constant ambient temperature of 15 °C and relative humidity of 80%. The side wall of the air flow channel is set to the adiabatic condition. The heat capacity of the mesh screen and glass is neglected. Some important input parameters of adsorption kinetic and thermodynamics are diffcult to test at the laboratary level. Therefore, some empirical formula and hypothesis are used in the simulation modeling.

The governing equations of the model coupling heat and mass transfer were derived from the Ref. [9].

(1) Mass balance equation

$$\frac{\partial \rho}{\partial t}+\nabla\cdot(\rho\mathbf{u})=0, \qquad \frac{\partial c}{\partial t}+\mathbf{u}\cdot\nabla c+\nabla\cdot(-D\nabla c)+\frac{1-\varepsilon_b}{\varepsilon_b}\rho_p\frac{dq}{dt}=0 \tag{1}$$

The above equations represent the overall mass balance and water vapor mass balance, respectively. ρ, c and ρ_p is the density of moist air, concentration of water vapor and the density of zeolite 13X, respectively. $\boldsymbol{u}$ is the air velocity, D is the diffusion coefficient of water vapor, ε_b is the porosity of the adsorbent, q is the adsorption capacity.

(2) Momentum balance equation

$$\rho\frac{\partial \mathbf{u}}{\partial t}+\rho(\mathbf{u}\cdot\nabla)\mathbf{u}-\nabla\cdot\left[-p+\mu\left(\nabla\mathbf{u}+(\nabla\mathbf{u})^{T}\right)-\frac{2}{3}\mu(\nabla\cdot\mathbf{u})\right]-\rho\mathbf{g}=0 \tag{2}$$

The above equation consists of the convection term, diffusion term, pressure gradient and gravity term. p, μ and g is the local pressure, the viscosity coefficient of moist air and the gravity coefficient, respectively.

(3) Energy balance equation

$$\rho c_p\frac{\partial T}{\partial t}+\rho c_p\mathbf{u}\cdot\nabla T+\nabla\cdot(-k\nabla T)-(1-\varepsilon_b)\rho_p\frac{dq}{dt}\Delta H=0 \tag{3}$$

The terms from left to right on the left side of the equation are the total heat capacity, heat convection, thermal conductivity and the released adsorption heat, respectively. c_p is the specific heat capacity of the gas or zeolite 13X, and k is the thermal conductivity.

(4) Sorption kinetics model

$$\frac{dq}{dt}=k_{LDF}\left(q_{eq}-q\right) \tag{4}$$

This equation is a generally employed LDF (linear driven force) model, where k_{LDF} is the kinetics coefficient, and q_{eq} is the equilibrium sorption capacity.

(5) Isotherms model

$$q_{eq}=\frac{q_{\max}\left(bp_v\right)^{1/n}}{1+\left(bp_v\right)^{1/n}} \tag{5}$$

The water isotherm of the adsorbent is calculated by Langmuir–Freundlich model, where p_v is the local water vapor pressure, q_{max} is the maximum adsorption capacity of the adsorbent material.
The characteristic properties of Zeolite 13X, including adsorption kinetics and thermophysical properties, together with the moist air environment were employed based on Ref. [4].

3 Results

3.1 proof-of-concept experiments

Fig. 2 shows the evolution of the temperature characteristic and the temperature lift (ΔT) calculated by T_o-T_i. For Case 1, ΔT reached its maximum with the release of adsorption heat during the initial adsorption stage. With the weakening of the adsorption driven force and reduction of the adsorption heat, T_i gradually decreases and this indicates the decline of output thermal power capacity. The maximum temperature lift of Case 1 is 2.5 °C. Case 2 also performs a similar phenomenon.

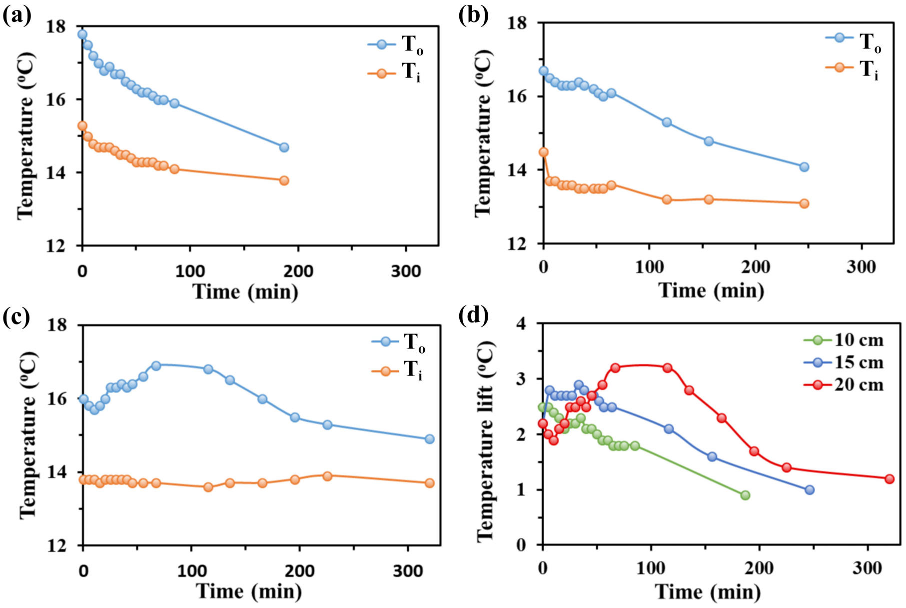

Fig. 2. The evolution of the temperature characteristic for (a) Case 1; (b) Case 2; (c) Case 3; and (d) the temperature lift comparison of three cases.

For Case 3, the result shows a different trend, experiencing an initial adsorption stage of decreasing first and then rising. It is also found that a temperature plateau of ΔT appears as the height of the module unit increases to 20 cm, which indicates a more steady heat release process. This can be explained that, with longer height, the beginning heating-up stage will lasts for a longer time because more adsorption heat released should be used to warm up the upper adsorption bed and walls. Besides, the amount of adsorbents increases with the height, thus extending the thermal power time. The maximum ΔT of Case 3 reaches 3.2 °C.

3.2 Numerical simulations

Fig. 3 shows the temperature and velocity field of air within the computation domain and the evolution of outlet temperature, *RH* and velocity characteristics of the outlet air. The chimney effect induced by released adsorption heat is demonstrated and clearly shown in Fig. 3(a). The blue arrows with different dimension and direction represent the local air velocity. Due to some model simplifications and assumptions, the simulation value of temperature lift is higher than the experiment results. However, the trend of the temperature lift increased with the height of the module unit is still consistent with the experiment. RH_o decreases sharply at the beginning as the adsorption starts, followed by a slow rise because of the decline of adsorption capacity. The velocity of air flow shows a similar curve with the temperature characteristic, which indicates that the cause of chimney effect in the adsorption process is the temperature difference induced by the released adsorption heat. The air velocity of natural convection is small, which makes it difficult to correctly measure the air velocity by experimental methods. Through the numerical simulations, the performance of temperature, relative humidity, and air velocity due to chimney effect is clearly demonstrated. Besides, the correlation between temperature and velocity of air provide a valuable reference for further experiments.

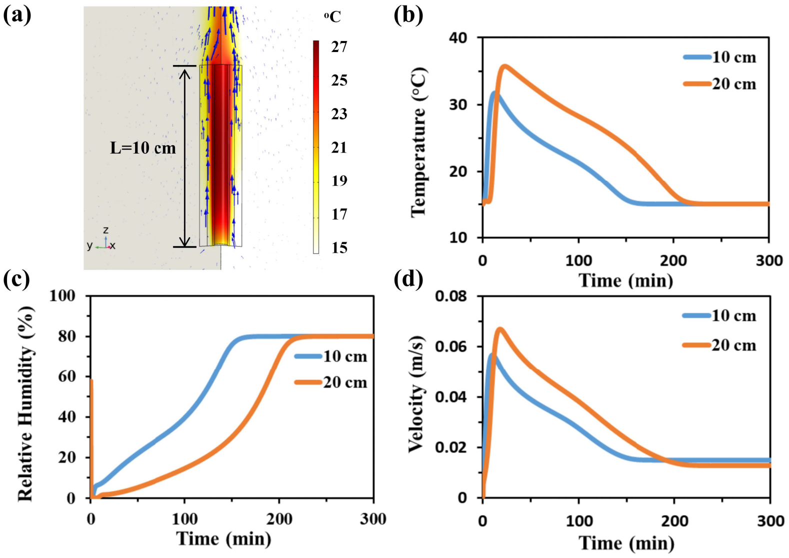

Fig. 3. (a) The temperature and velocity field of air within the computation domain; (b) the evolution of temperature, *RH,* and velocity characteristics of the outlet air.

4 Conclusions

Herein, a zero-energy-consumption adsorption heat release process using chimney effect was demonstrated by a proof-of-concept experiment and corresponding numerical simulation. The experiment results with a 10-cm length of adsorption bed show that, a significant temperature lift of 2.5 °C is observed and with the increase of height, a larger temperature lift and more steady temperature output can be obtained. The simulation results indicate that, by adjusting the height of natural convection adsorption bed, the temperature lift could be adjusted. The performance of temperature, relative humidity, and air velocity due to chimney effect is clearly demonstrated. In a further study, we might focus on the strategies to obtain an optimized performance of a large temperature lift and stable output. The temperature lift could be improved by increasing the height of adsorption channel. The air volume could also be regulated through the cross-section size of adsorption bed and flow channel. The natural convection performance of adsorption heating could be further improved by selecting superior adsorption materials. In this way, the actual heating demand of a practical adsorption thermal storage system, which is 15~20 °C to be heated to 30~35 °C, can be achieved through the passive adsorption heat release process.

5 Acknowledgment

This work was also a part supported by the Foundation for Innovative Research Groups of the National Natural Science Foundation of China (Grant No. 51521004).

6 List of References

[1] Nejat, P., Jomehzadeh, F., Taheri, M. M., Gohari, M., Abd. Majid, M. Z. (2015): A global review of energy consumption, CO 2 emissions and policy in the residential sector (with an overview of the top ten CO 2 emitting countries). *Renewable and Sustainable Energy Reviews*, vol. 43, pp. 843.

[2] Chen, X., Gao, H., Tang, Z., Dong, W., Li, A., Wang, G. (2020): Optimization strategies of composite phase change materials for thermal energy storage, transfer, conversion and utilization. *Energy & Environmental Science*, vol. 13, pp. 4498.

[3] Zhang, H., Baeyens, J., Cáceres, G., Degrève, J., Lv, Y. (2016): Thermal energy storage: Recent developments and practical aspects. *Progress in Energy and Combustion Science*, vol. 53, pp. 1.

[4] Zhang, Y., Dong, H., Wang, R., Feng, P. (2020): Air humidity assisted sorption thermal battery governed by reaction wave model. *Energy Storage Materials*, vol. 27, pp. 9.

[5] Yeboah, S. K., Darkwa, J. (2016): A critical review of thermal enhancement of packed beds for water vapour adsorption. *Renewable and Sustainable Energy Reviews*, vol. 58, pp. 1500.

[6] Baghapour, B., Rouhani, M., Sharafian, A., Kalhori, S. B., Bahrami, M. (2018): A pressure drop study for packed bed adsorption thermal energy storage. *Applied Thermal Engineering*, vol. 138, pp. 731.

[7] Liu, H. Z., Nagano, K., Togawa, J. (2015): A composite material made of mesoporous siliceous shale impregnated with lithium chloride for an open sorption thermal energy storage system. *Solar Energy*, vol. 111, pp. 186.

[8] Zhang, Y., Wang, R. (2020): Sorption thermal energy storage: Concept, process, applications and perspectives. *Energy Storage Materials*, vol. 27, pp. 352.

[9] Gaeini, M., Zondag, H. A., Rindt, C. C. M. (2016): Effect of kinetics on the thermal performance of a sorption heat storage reactor. *Applied Thermal Engineering*, vol. 102, pp. 520.

Investigation of Vapor Flow in Compact Plate Heat Exchangers Operating as Falling Film Evaporator or Absorber

Thomas Lex, Christian Schweigler

CENERGIE - Center for Energy-Efficient Buildings and Districts
Munich University of Applied Sciences, Department of Building Services Engineering
Lothstr. 34, 80335 Munich, Germany
thomas.lex@hm.edu

Abstract:

The investment costs and compactness of absorption heat pumps are largely determined by their heat exchangers. According to the state-of-the-art, tube bundle heat exchanger are commonly used in large capacity heat pumps and chillers. Aiming at implementation of compact units, the utilization of falling film plate heat exchangers as main components of the absorption heat pump, i.e. evaporator, absorber, condenser or generator, is investigated in the present study. Emphasis is placed on the analytical calculation of the pressure drop in the channels of the heat exchangers. For a conventional plate heat exchanger configuration operating at a saturation temperature of 10 °C, a reduction of the thermal duty up to 25 % due to pressure losses in the vapor flow has been found. In order to alleviate the negative influence of the pressure drop, an innovative concept is presented, where the vapor enters or leaves the heat exchanger through an opening orthogonal to the plates.

Keywords: plate heat exchanger, absorption heat pump, pressure drop, falling film evaporator

1 Introduction

Absorption heat pumps [1] using the working pair water/lithium bromide (H_2O/LiBr) operate at very low pressure conditions. Adding small portions of LiBr to the refrigerant in the evaporator expands the operational range of the absorption heat pump down to -10 °C, which corresponds to a saturation pressure in the evaporator of approximately 0.3 kPa. As under these conditions fluid temperatures at vapor-liquid equilibrium vary largely with pressure, the pressure drop in the evaporator is a decisive factor for the performance of the whole system. Whereas in conventional H_2O/LiBr-heat pumps the falling film heat exchangers are formed by tube bundles, a plate heat exchanger (PHE) is the object of interest in the present work. The pressure resistance in the channels of the PHE is determined by analytical calculations and the effect on the performance of the system is analyzed. Afterwards, an innovative design of the falling film evaporator is presented, which enables the vapor to leave the evaporator through an opening orthogonal to the plates. This configuration shall avoid the entrainment of droplets by the refrigerant vapor and offers reduced pressure resistance along the flow path of the vapor.

2 Analytical model for the pressure drop in a plate-type evaporator

The analytical calculation of the pressure drop is conducted for a typical falling film plate heat exchanger operating as an evaporator. Its schematic is presented in Figure 1. The liquid refrigerant enters the evaporator on the top and flows down along the plates driven by gravity. The interaction of the vapor flow with the falling film is neglected. Only the situation of the vapor phase is modelled.

The falling film on the secondary-side of the heat exchanger receives heat from the counter-flowing primary-side heat transfer medium, resulting in evaporation of a certain portion of the liquid film. In a conventional falling film plate evaporator, the vapor follows the channels formed by adjacent plates and leaves the heat exchanger block via the lateral cross-section. In general, the pressure drop of the vapor during its passage Δp contains both the pressure change caused by friction Δp_{fric} and the dynamic pressure drop Δp_{dyn} resulting from acceleration of the vapor flow with decreasing density [2, 3].

$$\Delta p = \Delta p_{fric} + \Delta p_{dyn}. = \frac{1}{2}\,\zeta\,\rho_v\,\bar{v}^2 + \rho_v(v_{out}^2 - v_{in}^2) \tag{1}$$

Considering a rectangular cross-section of the channels, the pressure loss coefficient ζ is determined with the length of the channel l, the hydraulic diameter d_h, the friction factor λ and a correction factor k_{rec}.

$$\zeta = k_{rec}\,\lambda\,\frac{l}{d_h} \tag{2}$$

The friction factor λ depends on the present flow regime, i.e. laminar or turbulent flow, and is calculated by established correlations [3]. The correction factor k_{rec} [2] depends on the aspect ratio of the channel a_0/b_0 and on the flow regime. Considering a narrow channel, where $a_0 \gg b_0$, the correction factor for a laminar flow is $k_{rec,lam} = 1.5$ and that of a turbulent regime is $k_{rec,tur} = 1.1$.

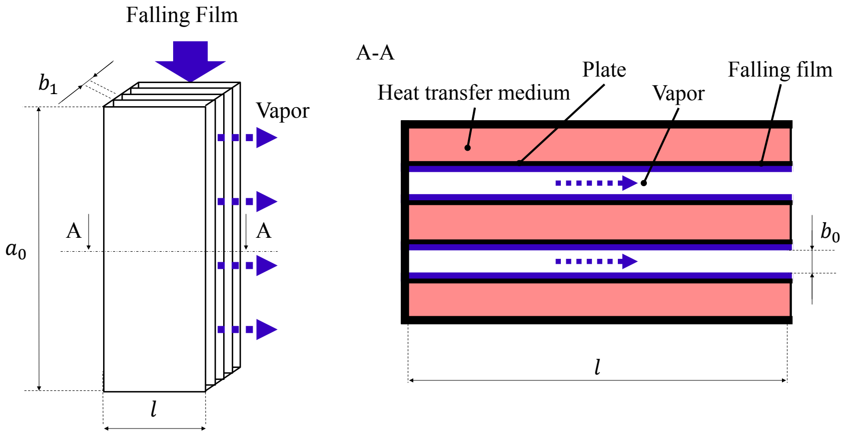

Figure 1 – Schematic of the falling film plate evaporator

Neglecting the transfer of sensible heat in the evaporator, the vapor mass flow can be determined as follows.

$$\dot{m}_{V,tot} = \frac{\dot{Q}}{\Delta h_{evap}} \tag{3}$$

Δh_{evap} denotes the enthalpy change from evaporator inlet to outlet, taking into account the throttling loss at the inlet to the evaporator. The heat, which is transferred from the heat transfer medium to the refrigerant, is calculated with the heat transfer area of the evaporator A, its heat transfer coefficient U and the logarithmic mean temperature difference $LMTD$.

$$\dot{Q} = U\ A\ LMTD \tag{4}$$

To take into account that the vapor mass flow increases along the length of the channel l, the plate is divided into n elements, according to Figure 2. For each element, the vapor mass flow $\dot{m}_i$, velocity v_i, friction factor λ_i, correction factor $k_{rec,i}$, pressure loss coefficient ζ_i and finally the pressure drop Δp_i are determined. The total pressure drop of the evaporator is obtained by the sum of the resistances within each element.

$$\Delta p_{tot} = \sum \Delta p_i \tag{5}$$

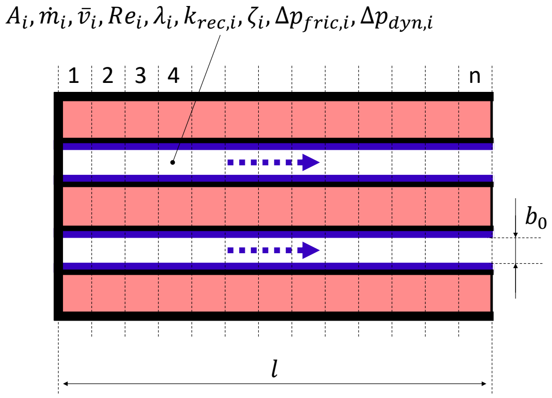

Figure 2 – Discretization of the evaporator

Assuming vapor-liquid equilibrium during evaporation, the saturation temperature of the boiling refrigerant will vary along the flow channel depending on the determined pressure profile. Figure 3 shows the temperature distribution in the evaporator with the saturation temperature of the refrigerant T_{sat}, the inlet temperature of the heat transfer medium $T_{Ch,in}$ and the profile of its outlet temperature $T_{Ch,out}$. The pressure drop in the evaporator leads to a decrease of the saturation temperature along the vapor flow channel. Consequently, the driving temperature difference of the evaporation process and finally the transferred heat is diminished by $\Delta\dot{Q}$. Similar to the calculation of the total pressure drop in the evaporator, the heat transfer area A is divided into finite elements A_i to quantify $\Delta\dot{Q}$. In order to determine its value, the trapezoidal technique was applied as follows.

$$\Delta\dot{Q}_i = U\,A_i\,\tfrac{1}{2}\left(\Delta T_{S,i} + \Delta T_{S,i+1}\right) \tag{6}$$

Summing up $\Delta\dot{Q}_i$, the total reduction of the heat transfer rate can be expressed as:

$$\Delta\dot{Q} = \sum \Delta\dot{Q}_i \tag{7}$$

The total heat transfer rate results from the heat transfer in each section, according to equation (4), taking into account the losses$\Delta\dot{Q}_i$.

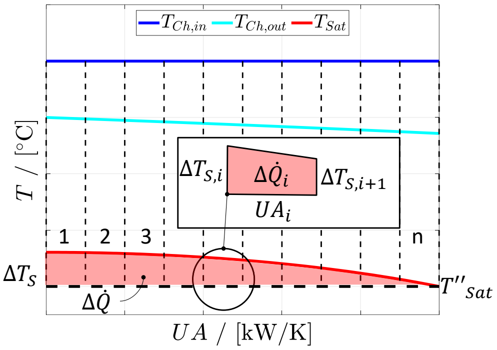

Figure 3 – Temperature distribution in the evaporator

It is obvious that the reduction of the heat transfer leads to a lower vapor mass flow and therefore decreases the vapor velocity in the channel. This effect is taken into account by modifying the vapor mass flow in each section by the amount $\Delta\dot{m}_i$.

$$\dot{m}_{i+1} = \dot{m}_i - \Delta\dot{m}_i = \dot{m}_i - \frac{\Delta\dot{Q}_i}{h_{evap}} \tag{8}$$

Consequently, an iterative method has to be applied to calculate the pressure drop in the falling film evaporator analytically.

3 Pressure drop and heat rate in a plate-type evaporator

The results of the analytical calculation are presented in Figure 4. To properly assess the results of the investigation, the pressure drop is expressed as a fraction of the saturation pressure p_{Sat} and the reduction of the transferred heat as a fraction of the total heat transfer rate $\dot{Q}$. The calculations are conducted for three different saturation temperatures and a gap size of $b_0 = 4\,mm$ between the two liquid films, covering the walls of the channel within the heat exchanger. Increasing the gap size further would decrease the pressure drop, yet limitations set by the manufacturing process are to be obeyed. The heat exchanger plates are assumed to be flat. Resorting to data of typical applications, for the heat transfer coefficient $U = 2\,kW\,/\,(m^2\,K)$ and for the driving temperature difference $LMTD = 2.5\,K$ have been assumed.

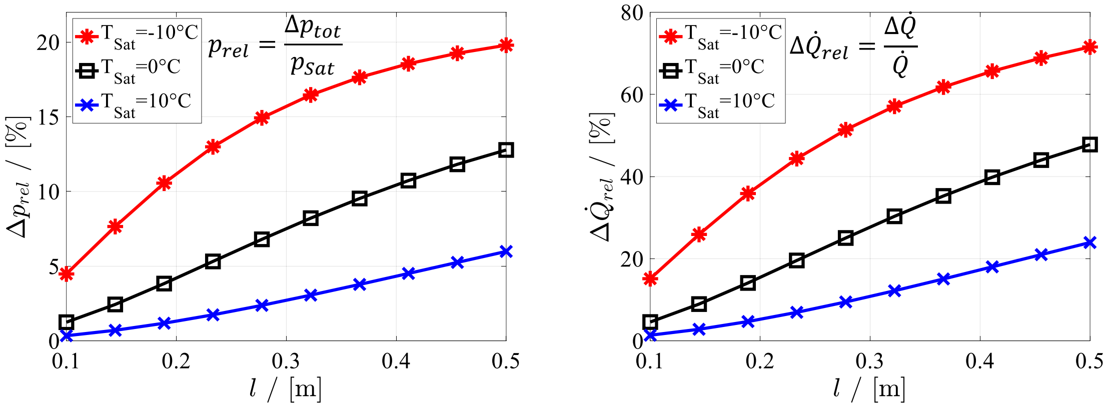

Figure 4 – Results of the analytical calculations: Relative pressure drop vs length of the evaporator (left); relative reduction of the transferred heat vs length of the evaporator (right)

Analyzing the graphs above, the importance of an optimum heat exchanger design in terms of flow resistance, especially at low operating pressures, becomes obvious. At a saturation temperature of 10 °C, the relative pressure drop does not exceed 6 %, equivalent to an increase of the saturation temperature by less than 0.9 K. Due to a higher vapor velocity in the channel, the frictional pressure drop increases considerably at lower saturation temperatures. Regarding a saturation temperature of -10 °C, the relative pressure drop amounts to 20 % at a channel length of 0.5 m. In this chase, the saturation temperature is increased by approximately 2.3 K. While the reduction of the transferred heat remains rather low at a saturation temperature of 10 °C, a huge relevance is found at lower saturation temperatures. For a length of 0.2 m and a saturation temperature of -10 °C, the heat rate drops by about 38 %, resulting in an increase of the required heat transfer area by about 60 %.

4 Geometric concept for an innovative falling film evaporator

In previous investigations [4–6], experiments were conducted to assess the performance of a falling film plate heat exchanger as shown in Figure 1. As a common result, all experiments have revealed the problem of droplet entrainment in the vapor flow. Yet, this phenomenon is not covered by the analytical calculation of the single-phase vapor flow. In order to overcome this issue, an innovative configuration for falling film heat exchangers for sorption heat pump cycles is proposed, where openings in the heat exchanger plates are provided, allowing the separation of the liquid and the gaseous phase. As shown in Figure 5, the vapor leaves the apparatus orthogonally.

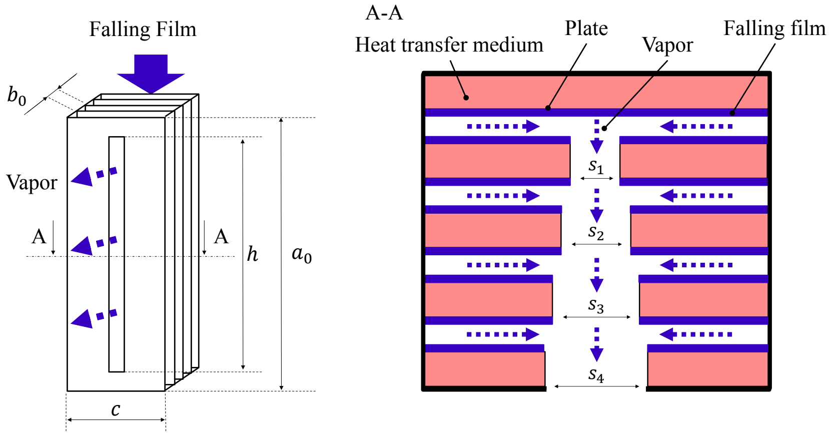

Figure 5 – Schematic of the innovative falling film evaporator – vapor leaves the evaporator orthogonally to the plates

Deviating from the basic geometry shown in Figure 5, shape, position and size of the openings may vary from plate to plate in order to achieve an optimum design of the heat exchanger stack with regard to the following criteria:

- Reduction of the length of the flow path parallel to the heat exchanger plates in order to limit the pressure drop
- Merging vapor flows require a larger size of the openings towards the vapor outlet of the stack.
- Alternating positions of the openings induce a change of the flow direction and allow for enhanced droplet retention

In the next steps, a more detailed design taking into account the flow behavior of the falling film and the requirements set by the secondary-side heat transfer will be elaborated.

5 Conclusion

This paper has highlighted the relevance of the pressure drop for the design of plate heat exchangers in absorption heat pumps at low operating pressures. With help of analytical calculations, the pressure drop of a falling film plate evaporator has been determined at three different saturation temperatures. Due to a higher velocity of the vapor, the flow resistance increased and therefore, the heat transfer rate decreased considerably at lower saturation temperatures. In order to overcome these limitations, an innovative falling film plate-type evaporator has been presented, where the vapor leaves the apparatus orthogonally to the heat exchanger stack and therefore the vapor flow path is shortened.

6 References

[1] K. E. Herold, R. Radermacher, and S. A. Klein, *Absorption Chillers and Heat Pumps, Second Edition,* 2nd ed. Bosa Roca, US: CRC Press, 2016.

[2] I. E. Idel'Chik, *Handbook of hydraulic resistance,* 4th ed. Redding, CT: Begell House, 2008.

[3] V. D. Ingenieure, *VDI-Wärmeatlas: Reference work,* 11th ed. Berlin, Heidelberg: Springer Vieweg, 2013.

[4] S. Natzer, F. Menhart, A. Linbrunner, M. Riepl, and C. Schweigler, "Absorptionskältemaschine auf Basis kompakter Plattenapparate (Absorption chiller based on compact plate heat exchangers)," 2015. [Online]. Available: https://doi.org/10.2314/GBV:837314992

[5] E. Estiot, S. Natzer, and C. Schweigler, "Heat Exchanger Development for Compact Water/LiBr Absorption Systems," *Proceedings of the 22nd IIR International Congress of Refrigeration*, 2007. [Online]. Available: https://iifiir.org/

[6] E. Estiot, S. Natzer, M. Harm, C. Kren, and S. Schweigler, "Heat Exchanger Development for Compact Water/LiBr Sorption Systems," in *Proceedings of the ASME Advanced Energy Systems Division - 2006: Presented at 2006 ASME International Mechanical Engineering Congress and Exposition, November 5-10, 2006, Chicago, Illinois, USA*, Chicago, Illinois, USA, 2007, pp. 175–187.

Vertical tube evaporator for a flue gas-condensing heat pump

Hermann, Tina[1], Pacher, Manfred[1], Sturm, Christoph[1], Glöckner, Dominik[2], Bauer, Marco[2], Schweigler, Christian[1]

[1] *CENERGIE - Center for Energy-Efficient Buildings and Districts*
Munich University of Applied Sciences, Lothstr. 34, 80335 Munich, Germany
tina.hermann@hm.edu

[2] *SCHERDEL Energietechnik GmbH, Scherdelstraße 2, 95615 Marktredwitz*

Abstract:

When integrating an absorption heat pump (AHP) with a biomass boiler, the evaporator of the heat pump provides a low-temperature heat sink for heat extraction from the flue gas of the boiler at temperatures below the dew point of the flue gas. An AHP unit is developed that aims at reduced electrical energy input and intends to forgo the use of a solution and a refrigerant pump. For this reason, the evaporator has been designed as a vertical falling film evaporator with shell side evaporation of refrigerant and tube side cooling of the flue gas. Evaporator tubes with a structured surface are used to sustain complete wetting for lowest amounts of refrigerant. Wetting behavior and heat transfer characteristics for mass flow rates per unit wetted perimeter down to 27 kg/(m h) have been experimentally investigated. Experiments with low amount of refrigerant result in a mean value of the overall heat transfer coefficient (HTC) up to 4.1 kW/(m^2 K), with a decrease down to 3.4 kW/(m^2K) when the amount of refrigerant is increased by a factor of 4. This corresponds to correlations from literature that indicate a significant increase of the HTC with decreasing film thickness. The complete evaporation of the supplied amount of refrigerant over a tube length of 1.4 m has been achieved.

Keywords: absorption heat pump, water-lithium bromide, falling film evaporation

1 Introduction

Heat recovery of biomass fired boilers reduces flue gas losses and increases the boiler efficiency. The integration of heat pumps in flue gas condensation systems is particularly useful to provide low cooling temperatures and to ensure cooling the flue gas down to temperatures below the dew point. In comparison to electrically driven compression heat pumps, heat input is the dominant driver for the operation of AHPs. To reduce the electrical consumption to a minimum, the AHP cycle can even be operated without a refrigerant and without a solution pump. For the intended application of flue gas heat recovery of a biomass fired boiler by means of an AHP, the operation of the heat pump cycle can be almost completely based on renewable energy. In previous studies [1], the concept for the AHP cycle, operated with lowest input of electrical energy has been developed and considers a vertical tube falling film evaporator with complete evaporation of the refrigerant along the tube length. To match this requirement, it is decisive to obtain a completely wetted tube surface for smallest amount of refrigerant. In the evaporator, heat is transferred from the flue gas to the evaporating refrigerant. Aiming at lowest pressure losses on the side of evaporation and appropriate flow velocity on the flue gas side, the falling film evaporator has been designed with flue gas directed downstream in a vertical tube bundle and shell side evaporation of the refrigerant. An experimental setup has been erected to particularly investigate the heat transfer of the evaporator and subsequently derive a construction of the evaporator unit for the flue gas-driven AHP. This research paper focuses on the experimental investigations of the wetting behavior and the heat transfer of the evaporator.

2 Falling Film Evaporation

2.1 Experimental setup

The experimental setup serves for investigating the falling film evaporation of water as refrigerant with low film thickness on the outer surface of vertical tubes with structured surface. The setup has already been presented previously [1] and includes an evaporator section consisting of four vertical tubes with a tube length of 4 x 1.4 m and a condensing heat exchanger coil. The feed tray system has been improved stepwise and finally provides even distribution of 2.4 g/s refrigerant flow on the evaporator tubes. This corresponds to a mass flow rate per unit wetted perimeter of 27 kg/(m h) on the top end of the tubes. With regard to the targeted application, the evaporator is operated at the saturation pressure of about 26 mbar, corresponding to an equilibrium temperature of about 21 °C.

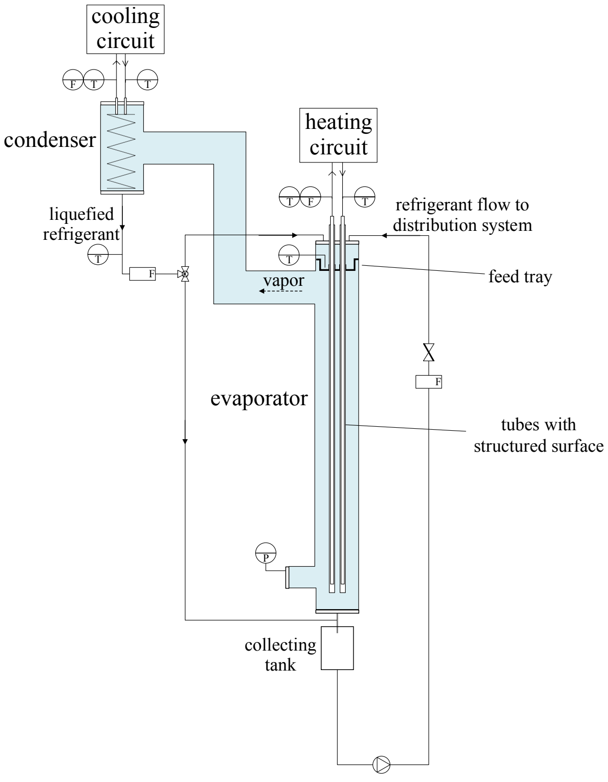

Figure 1: Experimental setup of falling film evaporator [2]

A hydronic circuit supplies heat input to the evaporator test rig. For the evaporator tubes, a concentric configuration has been chosen. The heating medium enters at the top, flows downwards inside the center tube, is reverted at the bottom end and flows upwards in the outer annular gap. Thereby, heat is transferred across the outer tube wall to the evaporating refrigerant film. The refrigerant is distributed at the top end of the evaporator tubes, flows downwards and evaporates. The vapor is liquefied in the condenser and can either return directly back to the feed tray or is led to the refrigerant collecting tank underneath the evaporator. From the collecting tank an adjustable amount of refrigerant can be pumped into the feed tray. The vacuum housing is composed of glass components allowing for visual inspection and evaluation of the tube wetting.

2.2 Fundamentals

A reference value for the falling film evaporation HTC as a function of the Reynolds number is obtained by correlations from literature [3]. Yet, validity is claimed for a pressure range down to 50 mbar only. According to equation (1) the Reynolds number is determined by the mass flow rate of refrigerant per unit circumference Γ in kg $m^{-1}s^{-1}$ and dynamic viscosity μ.

$$Re = \frac{\Gamma}{\mu} \tag{1}$$

The Nusselt number for a laminar flow is calculated by equation (2) and the heat transfer coefficient HTC subsequently results from equation (3), with the thermal conductivity λ, kinematic viscosity ν and gravitational constant g.

$$Nu_{lam} = 0.9\, Re^{-\frac{1}{3}} \tag{2}$$

$$Nu_{lam} = \frac{\mathrm{HTC}}{\lambda}\left(\frac{\nu^2}{g}\right)^{\frac{1}{3}} \tag{3}$$

Figure 2 shows the calculated values for the falling film evaporation HTC depending on the specific mass flow rate per wetted perimeter at a saturation pressure of 26 mbar, 50 mbar and 100 mbar.

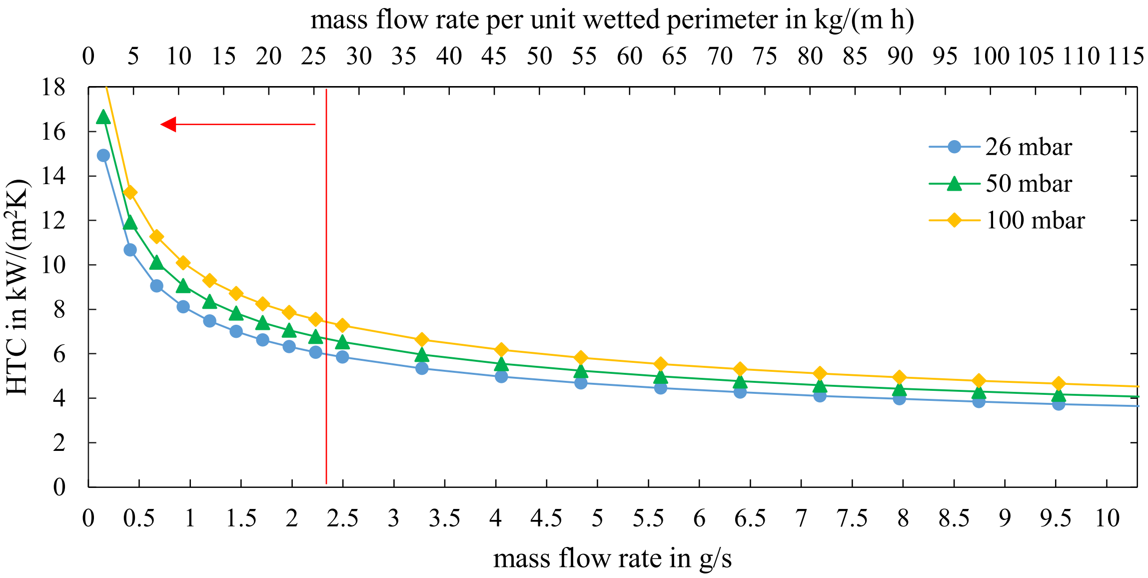

Figure 2: HTC of falling film evaporation as function of the mass flow rate

At saturation pressure of 26 mbar and an initial mass flow rate of 2.4 g/s the HTC increases from about 6 kW/(m^{2}K) to 15 kW/(m^{2}K).

According to the state of the art, horizontal tube bundle evaporators are designed for specific refrigerant flow per wetted tube length of about 150 kg/(m h) for both sides of the tube, corresponding to a refrigerant mass flow rate in the test rig of 6.7 g/s. In this conventional constellation of a horizontal tube bundle, the supplied refrigerant flow is only partly evaporated. The dominating amount is collected in the sump of the apparatus and recirculated to the refrigerant distribution at the top of the heat exchanger. Although the above cited correlation (eq. (2), (3)) refers to falling film evaporation at a vertical wall, it gives a clear indication for an increase of the HTC when the evaporator is operated with lower refrigerant mass flow rate. For lower amount of refrigerant a pronounced increase of the HTC is found, when the specific refrigerant flow is lowered by a factor of 5 compared to the conventional design.

For the intended design of a falling film evaporator without recirculation, it has to be taken into account that the film thickness is reduced along the flow path of the falling film. In the best case, dry out is reached at the bottom end of the tube. Consequently, the wetting situation changes along the vertical tube and an increase of the local HTC coefficient may be expected as expressed by the graphs shown in Figure 2. As a result, in the chosen experimental configuration, the analysis of the heat transfer experiment can only yield a mean value of the HTC, which represents an average of the local heat transfer characteristics given by the change of the thickness of the falling liquid film.

3 Results and discussion

The evaluation of the measured data determines the overall heat transfer coefficient by the energy balance, the driving temperature difference from heating fluid to refrigerant evaporation and the active heat transfer area. The heat transfer area of the tubes with structured surface refers to the outer diameter. The heat flow of the heating medium is determined by heating medium volume flow and inlet and outlet temperatures. Based on the evaporation capacity and the evaporation enthalpy, the quantity of the evaporated refrigerant mass flow can be estimated.

The experimental results for the overall HTC and the ratio of evaporated refrigerant mass flow to initial refrigerant mass flow with respect to the heating medium volume flow are shown in Figure 3. The obtained results can be compared to literature data for subatmospheric evaporation of water at enhanced surfaces. For capillary assisted evaporation of water at low pressure at finned horizontal tubes highest values of the overall HTC up to 7.0 kW/m^{2}K for thinnest film thickness have been found [4] [5]. For the vertical tube arrangement presented in the current study, even higher external HTC values can be expected due to complete wetting of the outer tube surface.

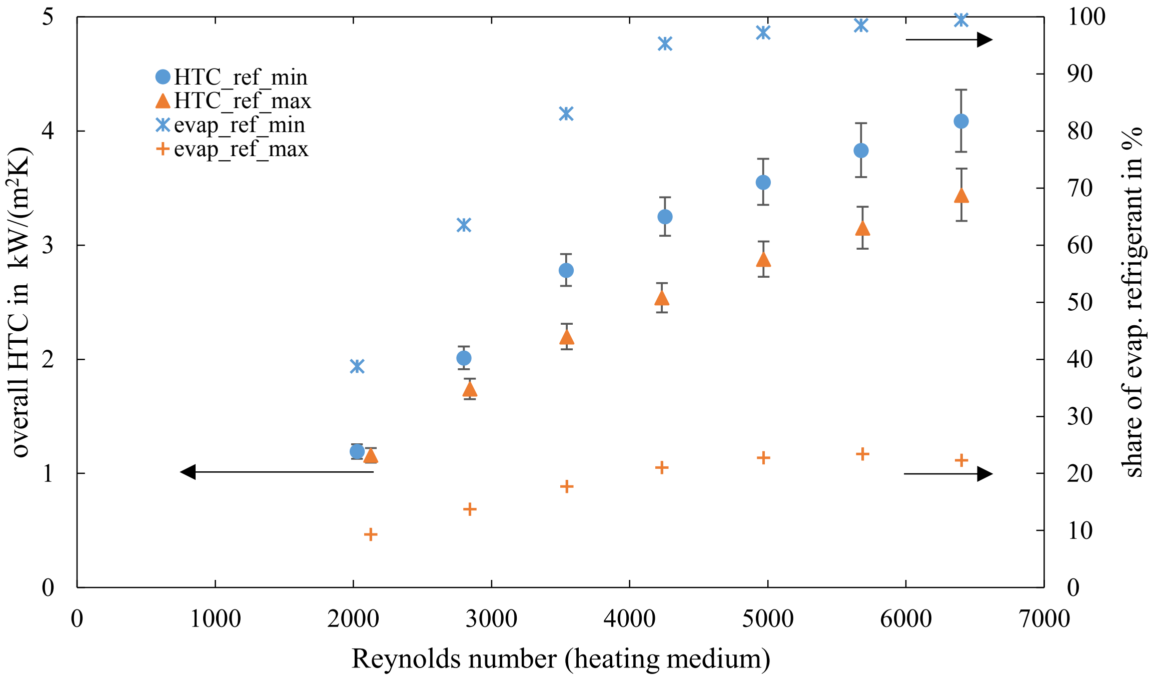

Figure 3: Overall HTC and ratio of evaporated refrigerant mass flow to supplied refrigerant mass flow over the Reynolds number of the heating medium, p_{sat}=26 mbar, values for minimal amount of refrigerant (ref_min) 2.4 g/s and maximal amount of refrigerant (ref_max) 10 g/s, LMTD=3.2-4.5 K

The increasing values of the overall HTC with increasing Reynolds number indicate that the tube-side heat transfer represents the dominating heat transfer resistance for the examined flow range. Furthermore, operation with low refrigerant mass flow leads to higher values of the overall HTC. For a supplied amount of 2.4 g/s, the refrigerant is almost completely evaporated and values of the overall HTC up to 4.1 kW/(m^{2}K) are found. Visually, the tube surface has been completely wetted throughout all measurements. The values of the overall HTC obtained with a refrigerant flow rate of 2.4 g/s are up to 20 % higher, compared to the values with the maximal amount of 10 g/s. Due to the enhanced inner geometry of the evaporator tubes, no established correlations are available for the evaluation of the internal HTC, allowing for determination of the external HTC for falling film evaporation. Therefore, the Wilson plot method has been applied to estimate the external HTC. By that means, the information about the impact of the increasing volume flow of the primary side heating medium is used for determination of the secondary side HTC. For the experiments with high refrigerant mass flow rate per unit wetted perimeter, a rather constant film thickness along the evaporator tubes may be assumed. Thus, even for changing heat rate, a constant value of the external HTC is to be expected, representing a precondition for the application of the Wilson plot method. The evaluation of the measured data results in an external HTC for evaporation about 5.0 to 6.3 kW/(m^{2}K) for high mass flow rates of refrigerant per unit perimeter. For low amounts of refrigerant mass flow with minimal film thickness, almost complete evaporation of the supplied refrigerant is reached and the analysis yields an increase of the film side HTC by a factor of 2.5. Since the estimation provided by the Wilson plot method contains a considerable uncertainty, further measurements shall be conducted for confirmation and more detailed characterization of the impact of different operating parameters. Yet, the order of magnitude of the obtained values for the falling film HTC conforms to the predictions given by the correlations above.

4 Conclusions

In this study, the heat transfer characteristics and the wetting behavior of a falling film evaporator with vertical tubes with structured surface have been investigated. Even for smallest amounts of refrigerant per unit wetted perimeter of 27 kg/(m h) complete wetting over the whole length of 1.4 m has been achieved. The measured values of the overall HTC are higher for lower mass flow rates of refrigerant conforming to correlations from literature that indicate the dependency of the film side HTC from the refrigerant mass flow rate and thus film thickness. For the application as flue gas condensing heat exchanger of an absorption heat pump, the wettability and the heat transfer characteristics are promising.

5 List of References

[1] T. Hermann, J. Geier-Pippig, C. Schweigler (2019): Sorption heat pump for flue gas condensation of biomass-fired boilers. *Proceedings of the 25th IIR International Congress of Refrigeration: Montréal , Canada, 2019.*

[2] T. Hermann, L. Dürndorfer, D. Glöckner, M. Bauer, C. Schweigler (2020): Vertical tube evaporator and thermosiphon desorber for a flue gas-condensing heat pump. *ISHPC 2021 Proceedings online pre-conference 2020.*

[3] Schnabel, G. (2013): M3 Wärmeübergang an senkrechten Rieselfilmen. *VDI-Wärmeatlas. (11th ed.).* Springer-Verlag, Berlin Heidelberg, page 1475-1482.

[4] F. Lanzerath, J. Seiler, M. Erdogan, H. Schreiber, M. Steinhilber, A. Bardow (2016): The impact of filling level resolved: Capillary-assisted evaporation of water for adsorption heat pumps. *Applied Thermal Engineering,* vol. 102, Pages 513-519

[5] Seiler, J., Volmer, R., Krakau, D., Pöhls, J., Ossenkopp, F., Schnabel, L., Bardow, A. (2020): Capillary-Assisted Evaporation of Water from Finned Tubes. *Applied Thermal Engineering*, vol.165, 114620.

Dehumidification behavior of a crossflow type heat exchanger coated with aluminophosphate zeolite regenerated by a direct hot water heating.

Sunhor, Seng[1], Osaka, Yugo[2], Tsujiguchi, Takuya[2], Kodama, Akio[2]

[1] Graduate School of Natural Science and Engineering, Kanazawa University
[2] Faculty of Mechanical Engineering, Institute of Science and Engineering, Kanazawa University, Kakumamachi, Kanazawa, Ishikawa 920-1192, Japan
**Corresponding author. Email: akodama@se.kanazawa-u.ac.jp (Akio Kodama)*

Abstract:
A crossflow type heat exchanger coated with aluminophosphate zeolite was tested for desiccant dehumidification. This adsorber has unique features, for example, the coated adsorbent can be directly heated by hot water and adsorption heat can be removed by evaporative cooling using the remained hot water. In special, evaporative cooling can accelerate the dehumidification performance. In this paper, a possibility of such thermal swing operation, which is a combination of direct hot water heating and evaporative cooling was experimentally confirmed. Then the influence of the adsorption / regeneration cycle time on the dehumidification amount was investigated. The result showed that time averaged dehumidification amount or dehumidification amount per unit time become larger at a shorter cycle time 120 s. But, the minimum humidity is obtained at a longer cycle time. This means that adsorption time and regeneration time should be controlled independently.

1 Introduction

Nowadays, air conditioning system is an essential technology for our life. However, the conventional vapor compression type refrigeration system consumes a large amount of electricity. This is one of the major concerns for worldwide energy consumption. To overcome this issue, alternative air-conditioning technologies such as desiccant cooling process were proposed [1] [2]. Desiccant coated heat exchanger DCHE is more interesting since the dehumidification performance can be enhanced by direct heating and direct cooling of the coated adsorbent [3]. A low-grade thermal energy such as waste heat can be used for regenerating the coated desiccant. Simultaneously, DCHE requests a cold medium in order to make the difference of thermal swing larger. But, cold medium is not obtained as easy as hot water. In this study, a crossflow type heat exchanger coated with aluminophosphate zeolite was tested. Although this type of DCHE is normally regenerated by hot air and cooled by ambient air [4], this study apply direct hot water heating and evaporative cooling using the remaining hot water to DCHE. At the beginning of this study, a possibility of such thermal swing operation was experimentally confirmed. Then influence of the adsorption / regeneration cycle time was investigated.

2 Experimental Set-up

2.1 Apparatus description

A Schematic diagram of the experimental apparatus is shown in Figure 1. This consists of crossflow heat exchanger type adsorber (CF-DCHE), air control boxes, hot water tank, heater, flowmeter, air separators, etc. CF-DCHE locates between rectangular acryl ducts with 230 mm x 230 mm x 75 mm length and thickness of 10 mm to supply well develop air. Dimension of the tested crossflow heat exchanger type adsorber coated with aluminophosphate zeolite was 200 mm of width, 200 mm of length, and 198 mm of height with 46 paths of the primary flow channel and 47 paths of the secondary flow channel. The fin height, fin pitch, and wall thickness were 1.43 mm, 2.83 mm, and 0.1 mm, respectively. The total effective surface area of the heat exchanger was 9.1 m^2. Aluminophosphate zeolite (1-8 mol% of iron and had a pore diameter 0.73mm, Mitsubishi Chemical Holding group) coated on the wall surface of the primary flow channel and its corrugated fins. The weight of the aluminophosphate zeolite layer per unit coated area approximated 61.6 g/m^2.

2.2 Experimental condition

Airflow velocity is calculated using the effective cross-sectional area of the heat exchanger. Two air control boxes are used as process air (PA) and cooling air (CA). At the beginning of the experiment, PA is continuously supplied to CF-DCHE for regenerating the adsorbent until the inlet and outlet of PA have the same absolute humidity. In the desorption process, hot water is directly sprayed to the secondary flow channel of the adsorber, simultaneously desorption inlet air is supplied to the primary flow channel from the left side of the heat exchanger as shown in Figure 2b. In the adsorption process, process inlet air flows through the heat exchanger from the opposite side. Concurrently the cooling air introduces to the secondary flow channel to remove the heat of adsorption as presented in Figure 2a. All experiments were carried out at constant hot water temperature (T_{HW}) 75 °C and flow rate (F_{HW}) 0.5 L/min. Process air and cooling air were set to the same absolute humidity of 16 g/kg-dry air (DA) and velocity of 1.0 m/s, respectively. Cycle time varied from 60 s to 300 s. The experimental condition is summarized in Table 1.

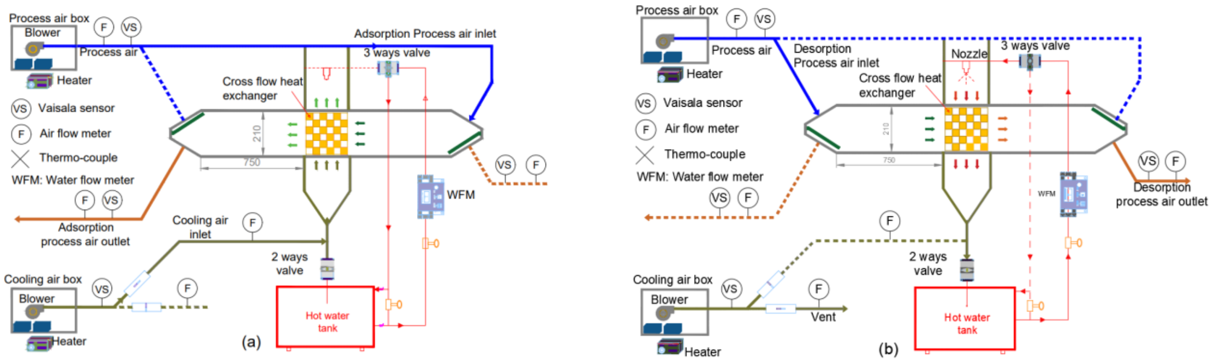

Figure 1 - Schematic diagram of the experimental apparatus (a) adsorption step (b) desorption step

Table 1 – Experimental condition.

	Temperature [°C]	Air velocity [m/s]	Absolute humidity [g/kg-DA]	Cycle time [s]
Regeneration step				60, 120, 180, 300
Process air	30	1.0	16	
Hot water	75	-	-	
Adsorption step				
Process air	30	1.0	16	
Cooling air	30	1.0	16	

2.3 Performance indexes and error analysis

The important index is the difference in air humidity between the process air inlet and outlet. AS [g/kg-DA] for the adsorption step and DS [g/kg-DA] for the desorption step are defined by the following equations.

$$AS = AS_{in} - AS_{out} \quad \text{eq. 1}$$

$$DS = AS_{out} - DS_{out} \quad \text{eq. 2}$$

In the cycle operation, time averaged humidity difference AS_{avg} for adsorption step and DS_{avg} for desorption step is defined by eq. (3) and (4), respectively.

$$AS_{avg} = \int_0^t (AS_{in} - AS_{out})dt/t \quad \text{eq. 3}$$

$$DS_{avg} = \int_0^t (DS_{out} - DS_{in})dt/t \quad \text{eq. 4}$$

Where t is cycle time.

The accuracy of measurement results depends mainly on the error caused by the sensors and instruments. In order to minimize the measuring error induced by the sensors, all the sensors are calibrated in the initial step. In addition, each testing is repeated at less three times, aiming to eliminate the deviation caused by a single experiment. The error of sensors and measurement are calculated by using roots of sum square [5]. As a result, the maximum error of absolute humidity was 4.3 % and the maximum error of temperature was approximately 1 °C. In addition, the maximum error between adsorption amount and desorpton amount in each experiment were 5.2 %.

3 Results and Discussion

Figure 2(a) and (b) respectively illustrated the time profiles of outlet air humidity and temperature at different cycle times. At the beginning of desorption step, during approximately 15 s, the outlet air humidity DS was lower than that of inlet air. It was caused by the remaining process air of the previous adsorption step inside the piping system. After that, desorption outlet humidity quickly increased to the maximum value within 40 s, and then it gradually dropped until the end of cycle time. While the time variation time of desorption outlet air temperature was relatively simple. This means that heat could be transferred from hot water to the desorption air, ensuing in the gradual increase of temperature in the desorption step. As soon as the adsorption process started, adsorption outlet air humidity once increased at the beginning because of a large amount of the residual heat in the CF-DCHE heated during the previous desorption step. Then the adsorption outlet air humidity rapidly dropped to the minimum point. After that, its humidity backed to the inlet air humidity as the adsorption amount approaches saturation. Similarly, the adsorption outlet air temperature once increased at the beginning stage of the adsorption step due to released heat from the CF-DCHE. After the evaporative cooling developed, adsorption outlet air temperature fell below the adsorption inlet air temperature.

At the shorter cycle time up to 180 s, adsorption/desorption of the coated adsorbent seems to be incomplete since the desorption outlet air humidity was higher than the inlet one, and adsorption outlet air humidity was lower than the inlet humidity. Further, the adsorption minimum humidity produced at a long cycle time lower than those produced at a short cycle time. e.g., at the cycle time 60 s, the minimum value was 11.0 g/kg-DA, whereas 9.9 g/kg-DA was obtained at cycle time 300 s.

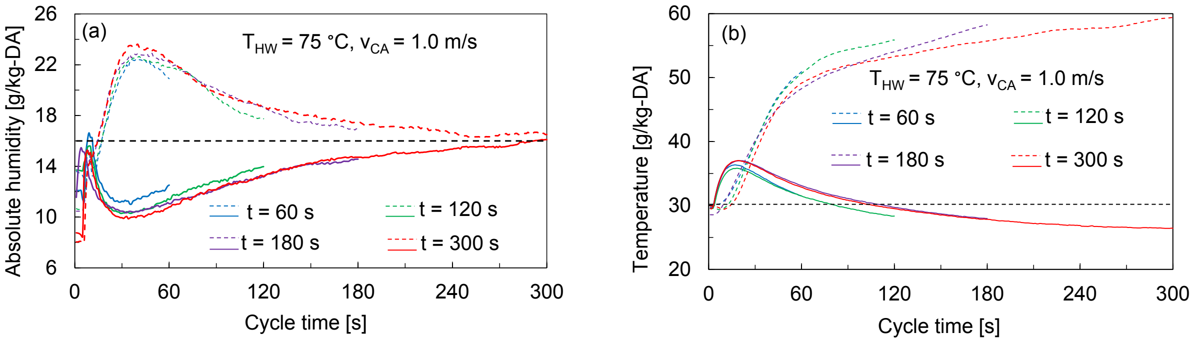

Figure 2 – Effecte of cycel time on (a) outlet air humidity (b) outlet air temperature.

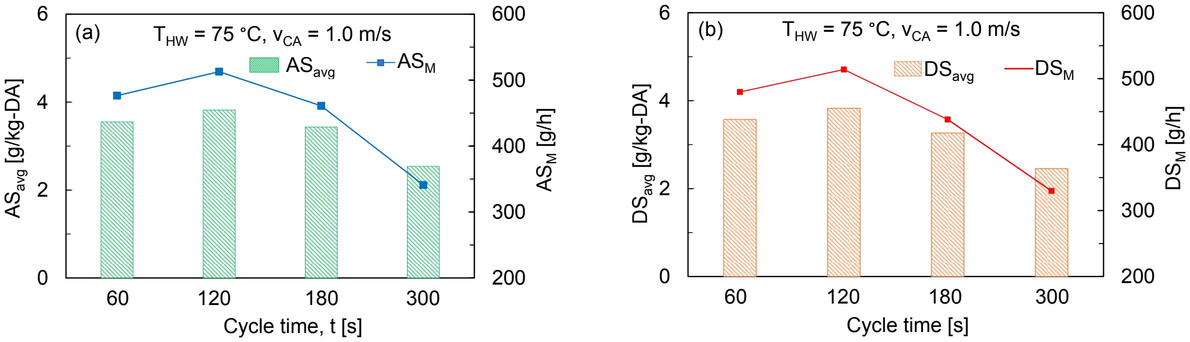

Figure 3 – Effect of cycle time on (a) adsorption amount (b) desorption amount.

Figure 3(a) showed the influence of cycle time on time averaged adsorption amount (AS_{avg}) and adsorption amount per hour (AS_M). It can be found that the largest AS_{avg} and AS_M appeared at cycle time 120 s. As the measurement error was mainly coused during a short time period at the bigining of the adsorption or desorption step, the result at the short cycle time of 60 s tended to be affected significantly. Of course, the impact of cycle time on the time averaged desorption amount (DS_{avg}) and desorption amount per hour (DS_M) were completely same as adsorption amount as indicated in Figure 3(b).

4 Conclusions

In this study, a cross flow type desiccant heat exchanger CF-DCHE coated with aluminophosphate zeolite was tested for effective dehumidification. The most important feature of this study was the thermal swing adsorption combining direct hot water heating and evaporative cooling using the remaining hot water. At first, the possibility of such a thermal swing operation was experimentally confirmed. Then the influence of the adsorption/regeneration cycle time was investigated as a significant operating parameter. The result proved that time average dehumidification amount or dehumidification amount per unit time became larger at a shorter cycle time of 120 s. But the minimum humidity can be obtained at a longer cycle time. This means that adsorption time and regeneration time should be controlled independently.

5 List of References

[1] Jani, D.B., Mishra, M., Sahoo, P.K. (2016), "Solid desiccant air conditioning - A state of the art review," *Reneable and Sustainable Energy Reviews, vol 60,* pp. 1451-1469.

[2] Pe´rez-Lombard, L., Ortiz, J., Piout, C. (2008), "A review on building energy consumption information," *Energy and Building, vol 40,* pp. 394-398.

[3] Virekh, M., Kumja, M., Bui, D.T., Chua, K.J. (2018), "Recent developments in solid desiccant coated heat exchanger - A review," *Apply Energy, vol 299, pp 778-803.*

[4] Kubota, M., Hanaoka, N., Matsuda, H., kodama, A. (2017), "Dehumidificaiton behavior of cross-flow heat exchanger type adsorber coated with aluminophosphate zeolite for desiccant humidify control system," *Applied Thermal Engineering, vol 122,* pp. 618-625.

[5] Robert, J.M. (1988), "Describing the uncertainties in experimental results," *Experimental Thermal and Fluid Science, vol 1,* pp. 3-17.

Asymmetric Plate Heat Exchanger for Absorption Refrigerating Plants

Richter, Lutz[1], Tillmann, Christine[1], Safarik, Mathias[1], Kemmerzehl, Christian[2]

[1] Institut für Luft- und Kältetechnik Dresden - 01309 Dresden - Bertolt-Brecht-Allee 20
[2] EAW Energieanlagenbau Westenfeld - 98630 Römhild - Oberes Tor 106

Abstract:

Asymmetric plate heat exchangers for water-lithium bromide absorption refrigerating plants were developed by ILK and EAW. The heat exchangers have different channel heights for two different media streams, liquid side and steam side. Also the plate design has been adapted to specific conditions. Optimum flow and thus heat transfer conditions of the media and favorable plate wetting are achieved. After the development of heat exchangers absorption refrigerating plants with different capacities were built which use only machine-made plate heat exchangers as heat and mass exchangers. This created a completely new generation of absorption refrigeration systems which represents for water-lithium bromide a world first. The systems are extremely compact. The size reduction is on average 40%. The manufacturing costs have been reduced. The new plants can also be used as absorption heat pumps, heat transformers or as resorption refrigeration systems for cold temperatures below 0°C.

1 Introduction

Higher costs and larger construction volumes of absorption refrigerating plants make their use more difficult compared to compression refrigeration systems. However absorption refrigerating plants have energetic and ecological potential within energy compound systems as the coupled generation of electrical, heating and cooling energy or the conversion of waste heat into cooling energy. Additional the natural refrigerant water is used in water-lithium bromide absorption refrigerating plants.

Currently all manufacturers on the world market use straight or spiral tube bundles made of copper or stainless steel as heat and mass exchangers in the water-lithium bromide absorption refrigerating plants except for the solution heat exchanger. Therefore constantly rising copper prices impair the profitability of absorption systems despite various system optimizations and system improvements in recent years. Plate heat exchangers are considerably more compact and more cost-effective than tube bundle heat exchangers.

Water-lithium bromide absorption refrigerating plants work in a vacuum (10 ... 100 mbar-a). The pressure losses esp. of the vapor flows need to be small in the plant because the absolute pressure differences are very small. Due to the high specific volume of water vapor large flow cross-sections are necessary. Large flow cross-sections are not good for a compact system design. The specific volume of water vapor is, for example, 1000 to 2500 times higher in comparison to the refrigerant vapor of R134a depending on the saturation temperature. Against it the external media in absorption refrigerating plants, heating water, cooling water and chilled water, require smaller flow dimensions for a good heat transfer.

Therefore conventional plate heat exchangers which have the same channel heights on both media sides cannot be used in water-lithium bromide absorption refrigerating plants. Different channel heights are required. But asymmetric plate heat exchangers that meet the special requirements for use in water-lithium bromide absorption refrigerating plants did not exist up to now.

The flow conditions need to be adapted on both sides in asymmetric plate heat exchangers. The heat exchangers should have different channel heights for the two media flows, liquid on one side and steam on the other. That leads to better heat transfer conditions.

The development target was therefore to develop new asymmetric plate heat exchangers with different optimal channels heights for the product and media side as well as with plate stampings which are adapted to the conditions of water-lithium bromide absorption refrigerating plants and improve the flow conditions and the plate wetting. This type of plate heat exchanger can be used as absorber, generator, evaporator and condenser in water-lithium bromide absorption refrigerating plants.

With the successful development of asymmetric plate heat exchangers water-lithium bromide absorption refrigerating plants can be built much more compact and cost-effective.

2 Development of Asymmetric Plate Heat Exchanger

Two types of asymmetric plate heat exchangers with different sizes have been developed. The two types have areas of 0,035 m^2/plate and 0,203 m^2/plate, for the respective application in small and medium scale absorption refrigerating plants. Both types are used to manufacture absorption chillers. Plants with a nominal cooling capacity of up to 30 kW with the smaller types and over 50 kW with the larger types. An increase in the number of plates per heat exchanger should enable the capacity range to be extended to 400 kW per system in the near future. In order to use more plates per heat exchanger, solutions regarding the material stability, dimensional stability, compressive strength, plate fixation and soldering procedure must be found. A competent cooperation partner as heat exchanger manufacturer is involved in the previous and further development.

The plate heat exchangers are copper-soldered and open to the outside on the product side (fall film side) at the top, bottom and partly lateral on the steam side. The falling film is applied by a distribution device above the open channels. The external medium flows through the heat exchanger on the medium side in closed channels horizontally (cross-flow). The mean channel heights of the heat exchangers are on the product side (B channels) with 3.5 and 7.0 mm around twice as high as those on the media sides (A channels, 1.7 and 3.3 mm) and that with a thin plate thickness.

Calculations of a numerical flow simulation helped to evaluate a homogeneous, well-developed channel flow of the external medium (flow with water and 35 vol% ethylene glycol, 20 ° C) (see Figure 1). Different barriers and dimple arrangements on the plate were taken in the calculations for the test models. A preferred variant was selected for the construction of the test models. The evaluation criteria were the avoidance of excessive local flow velocities (red), the reduction of flow shadows behind the stampings (blue) and the avoidance of bypass flows on the plate. A homogeneous media distribution was aspired.

Figure 2 shows a picture of the larger asymmetric plate heat exchanger and a partial section of the product channels that are open to the outside. The media side can be designed with one or more passes.

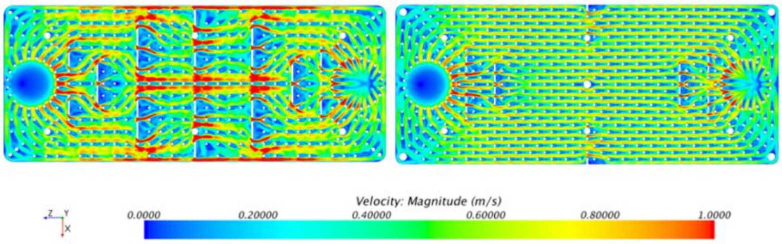

Figure 1 – Two examples of a flow simulation for an optimal plate design (design flow rate)

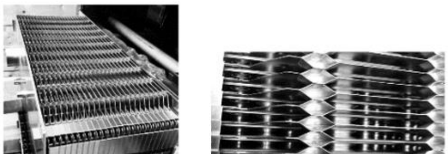

Figure 2 – Picture of the larger asymmetric plate heat exchanger and a partial section of the open product channels

3 Results of Measurement

3.1 Measurement of Plate Heat Exchanger

At first, test models were measured under vacuum conditions in the functions of the evaporator, condenser, desorber and absorber. The heat transfer coefficients for the heat exchangers were calculated with measurement data. Pressure losses on the media side were measured and the liquid distribution on the product side and the inert gas removal were investigated.

The plate heat exchangers have low external pressure losses. This is important to limit electricity consumption in the thermally driven refrigeration or heat pump systems. During the measurements the dependencies of the heat transfer coefficient on the falling film strength and the flow velocity of the external medium (see Figure 3) were investigated. In addition the inlet temperatures of the external media and the solution as well as the solution concentrations were varied. Moreover the absorption efficiency for the absorber, the quotient of the real concentration enrichment in the solution to the maximum possible saturation state, was also investigated depending on the falling film strength.

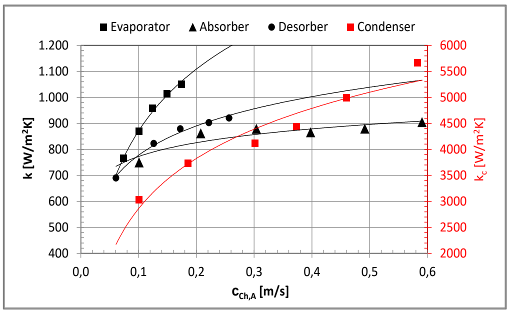

k – heat transfer coefficient [W/m²K]
t - temperature [°C]
$\dot{Q}$ – thermal capacity [kW]
ζ - heat ratio [-]

c – condenser
Ch – channel
ChB – chilled brine
ChW – chilled water
CW – cooling water
HW – heating water
i – inlet
o – outlet
o - evaporator

Figure 3 – Heat transfer coefficients depending on the flow velocity of the external medium in the A - channel for evaporation, condensation, absorption and desorption

The heat transfer coefficient increases with increasing falling film strength. But the absorption efficiency in the absorber decreases because more heat is extracted from a larger solution mass flow and the surface of the falling film which absorbs the refrigerant vapor remains the same.

The subcooling of the incoming solution in the absorber and desorber has an influence on the heat transfer coefficient. Higher subcooling is beneficial in the absorber and disadvantageous in the generator. This confirms the need for a sufficiently dimensioned and well-functioning solution heat exchanger within an absorption refrigerating plant.

The developed asymmetric plate heat exchangers worked very satisfactorily in the functions of evaporator, absorber, condenser and generator as well as in the corresponding functional units. The targets were achieved for the average k values of the heat exchangers. The venting of the A channels (external medium) is ensured by the medium flow. The inert gas removal from the condenser and absorber is ensured even while the plant is in operation. Only small suction volume flows are required for this. The pressure losses of the external media are low. A good liquid distribution is guaranteed. The fall film strength in the B-channel of the plate heat exchanger should be > 40 g/ms. The flow velocity of the external medium in the A channel should be > 0.4 m/s. Adequate protection against corrosion can be ensured by corrosion inhibition. This is associated with a long service life for the devices.

3.2 Use of the Asymmetric Plate Heat Exchangers in Absorption Refrigerating Plants

After the successful development of the asymmetric plate heat exchangers the new plate heat exchangers were integrated into a series of absorption refrigerating plants. A completely new generation of water-lithium bromide absorption refrigerating plants type Maral from EAW was created. This means that, worldwide for the first time, a water-lithium bromide absorption chiller is made exclusively with plate-heat exchangers. The smaller plants have 15, 30 and 65 kW refrigerating capacity at the nominal point and have been successfully tested and measured. Absorption refrigerating plants with a refrigerating capacity of up to 400 kW can be built with the larger plate heat exchangers and with a higher number of plates. Figure 1 contains picture of the absorption refrigerating plant with a nominal refrigerating capacity of 30 kW with and without housing.

Nomograms were created for the absorption refrigerating plants from which the achievable refrigerating capacity depending on the temperatures of the cooling brine inlet, heating water inlet and chilled water outlet can be quickly taken. The systems can be used as absorption refrigerating plants as well as resorption refrigeration systems, heat pumps and heat transformers.

The absorption refrigerating plants can be used very well in district heating networks or in waste heat recovery systems also in systems with require a high degree of heating water cooling down (low required return temperature) (see Figure 2). Cooling downs of the heating water of 25 K and higher and heating water return temperatures of 55°C and below are possible. Of course the refrigerating capacity is reduced compared to the nominal condition.

Figure 3 shows that the new absorption refrigerating plants can also be used to generate cold below 0°C. The cold generation below 0°C and the thermal generation of liquid ice are the next challenges of the new systems.

Figure 1 – Water-lithium bromide absorption refrigerating plant with 30 kW nominal cooling capacity with and without housing

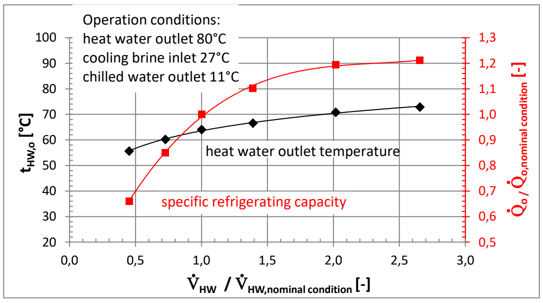

Figure 2 – Heating water outlet temperature and refrigerating capacity depending on the change in heating water volume flow (measurement of absorption chiller with 15 kW nominal cooling capacity)

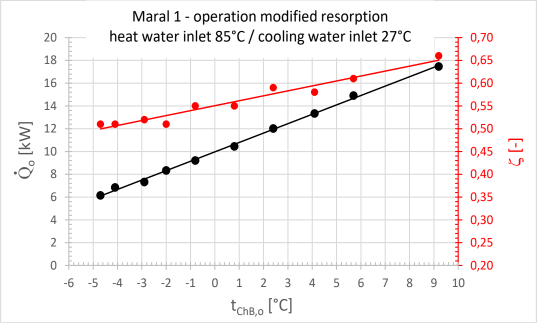

Figure 3 – Refrigerating capacity and EER$_{th}$ (ζ) of the absorption chiller type Maral 1 in resorption mode depending on the chilled brine outlet temperature for inlet temperatures 85°C heat and 27°C cooling water

4 Conclusions

The results of the development of asymmetric plate heat exchangers for water-lithium bromide absorption refrigerating plants can be assessed as very positive. In terms of design and channel height the plate heat exchangers are unique on the world market and can be used as generator, condenser, evaporator and absorber with the refrigerant water. Compared to the use of tube bundle heat exchangers the completely new series of absorption refrigerating plants from EAW reduces the costs of the absorption refrigeration systems while at the same time improving the system compactness (reduction of the construction volume to around 60%). Industrial property rights to the solutions developed have been registered [1] [2]. The developed asymmetric plate heat exchangers can also be requested at EAW for other applications such as heat transfer between water vapor and liquid.

5 Acknowledgment

We thank the Federal Ministry for Economic Affairs and Energy for funding of the successful development project (MF 150159) and for the follow-up project to further development of larger heat exchangers (49MF200050).

6 List of References

[1] Kemmerzehl, C., Otto, M. Richter, L., Safarik, M. (2018): Wasser-Lithiumbromid-Absorptionskälteanlage, *Patent DE 102018 00 2201*

[2] Kemmerzehl, C., Otto, M. Richter, L., Safarik, M. (2019): Water-Lithium Bromide-Absorption Cooling System, *European Patent EP 3 543 626 B1*

Data Driven AI and ML Tools for Exit Parameters Prediction of Hollow Fiber Membrane Liquid Desiccant Dehumidifier

Pedisetti, Kumar Sai Tejes, Bukke, Kiran Naik

Sustainable Thermal Energy Systems Laboratory (STESL), Department of Mechanical Engineering, National Institute of Technology Rourkela, Odisha, India – 769008; Tel.: +919435686059; Email addresses: naikkb@nitrkl.ac.in; k.bukke@gmail.com

Abstract:

In this paper, the application of data-driven tools for exit parameters prediction of hollow fiber membrane liquid desiccant dehumidifier (HFLDD) is investigated for the first time. Although HFLDD is widely investigated both numerically and experimentally, the application of data-driven tools has not yet investigated for HFLDD. To fill this gap, three data-driven models ANN-AI, ANFIS-AI, and KNN-ML tools were applied using thirty-four experimental datasets. The air outlet enthalpy, air outlet specific humidity, and desiccant outlet enthalpy were considered as outputs and air temperature, air specific humidity, desiccant concentration, desiccant temperature, airflow rate, and desiccant flow rate are taken as inputs. The results indicate that the ANFIS-AI tool gives the best performance in predicting all the targeted output parameters with R^2 values of 0.991, 0.996, and 0.98 for air outlet enthalpy, air outlet specific humidity, and desiccant outlet enthalpy, respectively. Further, the KNN-ML tool performance was observed to be weak for predicting the HFLDD exit parameters among the three AI and ML tools but the error predictions of the KNN-ML tool are found to be in the acceptable range for the HFLDD exit parameters prediction purposes. This study also suggests that data-driven tools such as ANN-AI, ANFIS-AI, and KNN-ML tools can be implemented with confidence for predicting the exit parameters of any energy exchanging or heat and mass transfer driven devices.

1 Introduction

For improving the indoor air quality, removing air borne pollutants and enhancing the moisture removal process, in recent years, direct contact based liquid desiccant dehumidification system became prominent. But due to carry over issues, indirect contact based LDD came into existence. The indirect contact LDD is divided into two types, they are flat plate and hollow fibre membrane based LDD. Among these, hollow fibre membrane is chosen in the present investigation instead of flat plate membrane because of high energy and mass exchange efficacy, low pressure drops, ease in manufacturing and large-scale utilization features. The hollow fibre membrane based liquid desiccant dehumidifier (HFLDD) shown in Fig. 1 consists a bundle of 200 PVDF polymer based hollow fibre membrane tubes with 1.2 mm diameter, 300 mm module length and 150 μm thickness each whereas shell diameter is 40 mm. The specific surface area of the HFLDD is 750 m^2/m^3. Lithium chloride (LiCl) is chosen as the liquid desiccant in the present study. This HFLDD is a shell and tube type configuration in which shell side, ambient air is made to flow and in tube side LiCl solution is forced to flow in counter flow direction. While flowing in counter flow direction, ambient air and liquid desiccant comes in indirect contact through hollow fibre membrane. At that instance, due to hydrophobic nature of membrane and due to vapour pressure difference between these two fluids, water vapour allowed to flow through the membrane from ambient air to liquid desiccant i.e., liquid desiccant vapour absorption occurs. Thus, conversion of strong liquid desiccant to weak liquid desiccant takes place and the dehumidified air is obtained at the exit of the HFLDD. From the literature, it is observed that for performance prediction of thermal systems, usually ANN-AI and ANFIS-AI based data driven tools were often reported [1–4]. Further, several researchers, investigated the HFLDD performance experimentally and numerically [5–10]. But to the best of authors' knowledge, none of them reported the implementation of ANN-AI, ANFIS-AI and KNN -ML tools for predicting the exit parameters of the HFLDD. Therefore, in the present investigation afore-mentioned AI tools are chosen to predict the HFLDD exit parameters.

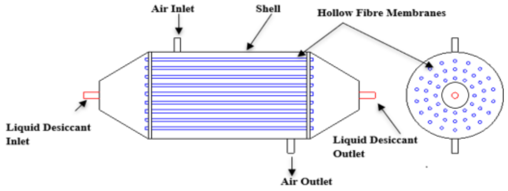

Figure 1 – Schematic of HFLDD

2 AI and ML Tools Methodologies

In the present investigation, and ANN-AI, ANFIS-AI and KNN-ML based data driven tools are chosen to predict the exit parametersthe exit parameters such as air enthalpy, air specific humidity and desiccant enthalpy for the given inlet parameters such as air and desiccant mass flow rates, air and desiccant enthalpies, desiccant concentration, and air specific humidity. The methodology to implement the afore-mentioned data driven AI and ML tools is elaborated in detail as follows,

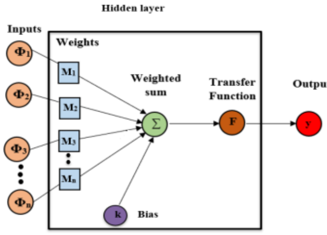

Figure 2 – Framework for MLP based ANN-AI tool

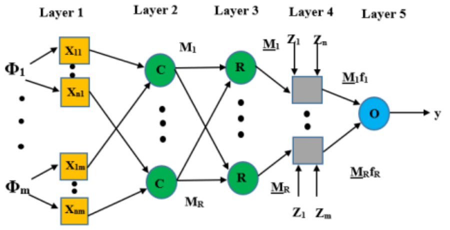

Figure 3 – Framework for ANFIS-AI tool

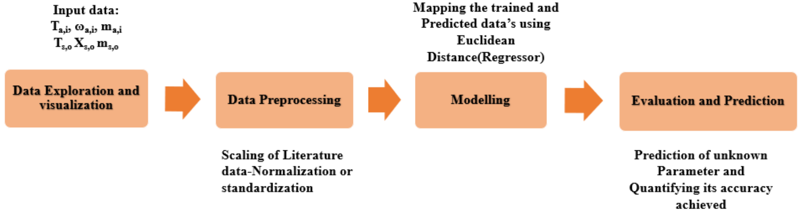

Figure 4 – Framework for KNN-ML tool

2.1 ANN-AI Tool

Classical artificial neural network based artificial intelligence (ANN-AI) tool is generally implemented in predicting the output parameters of thermal systems from the multiple inlet parameters. To establish the neural network for predicting the output parameters from the given multiple input parameters, multilayer perceptron (MLP) network with the Levenberg-Marquardt backpropagation method is observed to be best approach in the ANN-AI tool [2, 4]. Therefore, in this investigation, by choosing above-mentioned method, a neural network is framed based on no. of hidden layers, neurons, input and output layers as well as by forming the neurons and layers through the connecting weights (Fig. 2). A neural network with φ_1 input, one hidden layer consisting of weights (M_i), and bias (k), and one linear output (y) provides an approximation as depicted in Eq. 1. To predict the given outputs in terms of provided multiple inputs (φ_i), summation of weighted inputs and transfer function are considered (Fig. 1 and Eq. 1). Governing equation to predict output parameters is given as,

$$y = f(\forall) = f[\sum_{i=1}^{n} \varphi_i M_i + k] \tag{1}$$

where φ, M and k represent input, weight, and bias.

2.2 ANFIS-AI Tool

Adaptive neuro-fuzzy interference system based artificial intelligence (ANFIS-AI) tool is basically a rule-based fuzzy logic which is framed based on five layers, fuzzification, multiplication, normalization, de-fuzzification and summation. The framework for developing the ANFIS-AI tool is presented in Fig. 3. Governing functions for each layer to predict output parameters in terms of input parameters is presented as,

Fuzzification layer ($O_{1,ij}$): $\mu_{ij}(\varphi_i)$ for i = 1,m, j=1,n (2)

where μ_{ij} denotes the jth membership function of the input φ_i.

Multiplication layer ($O_{2,i}$): In this layer, the output represents weighting factor (firing strength) of the rule k. The output M_k is the product of all its inputs and it is denoted as,

$O_{2,i} = \Pi\mu_{ik}(\varphi_i)$ for i =1, m, k=1,R (3)

Normalization layer ($O_{3,k}$): The output of each node k in this layer represents the normalized weighting factor M_k of the kth rule and it is depicted as,

$$O_{3,k} = \frac{M_k}{\sum_k M_k} \quad \text{for K=1, R} \tag{4}$$

Defuzzification layer ($O_{4,k}$): Each node of this layer gives a weighted output of the first order Sugeno-type fuzzy if-then rule and it is designated as,

$$O_{4,k} = M_k f_k ; f_k = \sum_j P_{ki} + r_k \quad \text{for I = 1, m; k = 1, R} \tag{5}$$

where f_k represents the output of the kth rule. p_{ki} and r_k are the consequent parameters

Summation layer ($O_{5,k}$): This single–node layer illustrates the overall output y of the network as the sum of all weighted outputs of the rules. It is given as,

$$O_{5,k} = \sum_k M_k f_k \quad \text{for k=1, R} \tag{6}$$

ANFIS requires sets of training data of the input/output pair ($\varphi_1,\varphi_2,\dots,\varphi_m/y$) to attain the target system, which needs to be modelled. ANFIS can model the inputs (φ_1, $\varphi_2,\dots$, φ_m) and output relationship by the rule base, membership functions, and the correlated parameters emulating the specified training datasets.

2.3 KNN-ML Tool

K-nearest neighbour-based machine learning (KNN-ML) tool usually compares the given tuples (input and output parameters) with trained tuples for determining the nearest point. The overall structure of this ML tool involves data exploration and visualization of input parameters, data preprocessing, mapping, evaluation, and prediction of output parameters. The detailed framework for KNN-ML tool is presented schematically in Fig. 4. Governing equation for predicting the output parameter depending on input parameter is defined as

Euclidean distance (λ_{ED}): $\sqrt{(\varphi_1-y_1)^2+(\varphi_2-y_2)^2+\dots\dots\dots\dots+(\varphi_n-y_n)^2}$ (7)

where φ_1, φ_2……. φ_n is observed input data and y_1, y_2…….. y_n is predicted data

2.4 Error Prediction Criterions

For validating whether the predicted data obtained based on KNN-ML, ANFIS-AI and ANN-AI tools are reliable for performance prediction of hollow fibre membrane based liquid desiccant dehumidification system, following error prediction criterions are chosen for validation purpose,

Mean absolute error (MAE) = $\frac{1}{K}\sum_{i=1}^{K}|\psi_i-\psi_i|$ (8)

Root mean square error (RMSE) = $\sqrt{\frac{\sum_{i=1}^{K}(\psi_i-\psi_i)^2}{K}}$ (9)

Mean absolute percentage error (MAPE) = $\frac{1}{K}\sum_{i=1}^{K}\frac{(\psi_i-\psi_i)}{\psi_i}*100$ (10)

Coefficient of determination (R^2) = $1-\frac{\sum_{i=1}^{K}(\psi_i-\psi_i)^2}{\sum_{i=1}^{K}(\psi_i-\overline{\psi_i})^2}$ (11)

where $\psi_i,\psi_i,\overline{\psi_i}$ and K are experimental data, predicted value, mean value of experimental data and number of samples.

3 Results and Discussion

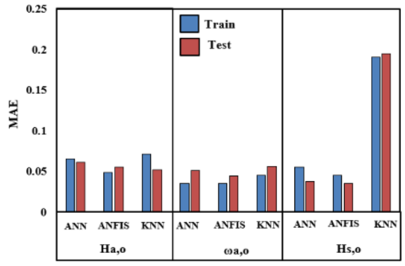

Figure 5 – MAE of $H_{a,o}$, $\omega_{a,o}$ and $H_{s,o}$ for ANN-AI, ANFIS-AI and KNN-ML tools

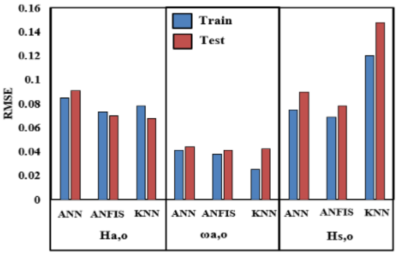

Figure 6 – RMSE of $H_{a,o}$, $\omega_{a,o}$ and $H_{s,o}$ for ANN-AI, ANFIS-AI and KNN-ML tools

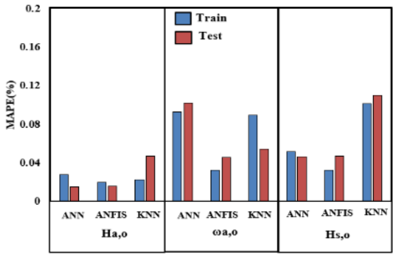

Figure 7 – MAPE of $H_{a,o}$, $\omega_{a,o}$ and $H_{s,o}$ for ANN-AI, ANFIS-AI and KNN-ML tools

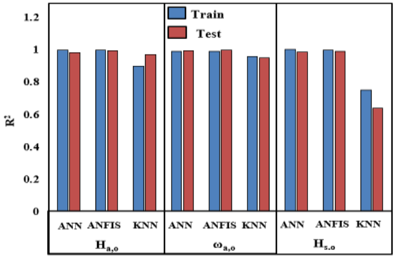

Figure 8 – R^2 of $H_{a,o}$, $\omega_{a,o}$ and $H_{s,o}$ for ANN-AI, ANFIS-AI and KNN-ML tools

In this section, the error prediction criterions (MAE, RMSE, MAPE and R^2) achieved for the three output parameters (air enthalpy ($H_{a,o}$), air specific humidity ($\omega_{a,o}$) and desiccant enthalpy ($H_{s,o}$)) from the given six inlet parameters (air flow rate, air enthalpy, air specific humidity, desiccant enthalpy, and desiccant concentration) of the HFLDD based on ANN-AI, ANFIS-AI and KNN-ML tools is presented in Figs. 5–8. To predict the output parameters, thirty-four experimental data sets are chosen from the reported literature [5]. In this study, 70% of datasets are used for training and rest of them are used for testing/validating the accuracy of the proposed tools. The HFLDD operating range taken for the present investigation is presented in Table 1. The optimal hyper parameters obtained for predicting the HFLDD exit parameters based on afore-mentioned AI and ML tools are summarized in Table 2. For the given operating range presented in Table 1, the best optimal hyper parameters are achieved after performing the tuning process in between the inlet and exit parameters and by obtaining accurate MAE, RMSE, MAPE and R^2 error predictions for the above-mentioned AI and ML tools. Moreover, it is also found that beyond the specified optimal hyper parameters of the ANN-AI, ANFIS-AI and KNN-ML tools such as no. of neurons, clusters, hidden layers Euclidean points etc., the error prediction criterions found to be similar. Also, while training the datasets no overfitting is observed. Further, the weights and bias coefficents of the ANFIS-AI, and ANN-AI tools are adjusted based on the obtained mean squared error (MSE) value during the first trail run. If the value is greater than 0.20, then the weight and bias coefficients are adjusted in such a way that it can reconcile the difference between the actual and predicted data for subsequent outcomes.

Table 1 – Input, experimental data and corresponding ranges [5].

Parameter	Mass flowrate of air kg/hr	Temperature of air (°C)	Specific humidity of air (g_{wv}/kg_{da})	Mass flow rate of desiccant (kg/hr)	Temperature of desiccant (°C)	Desiccant concentration ($kg_{LiCl}/kg_{sol.}$)
Range	5.3-10.19	25-35	9-24	6.36-15.65	25-27	0.31-0.35

Table 2 – Hyper Parameters for AI and ML tool for exit Parameters.

Model	ANN	ANFIS	KNN
Hyper Parameters for $H_{a,o}$, $\omega_{a,o}$ and $H_{s,o}$	Number of neurons in Hidden layer: 6 Number of hidden layers: 1 Type of transfer function: logsig Number of neurons: 6	Number of clusters: 4	Euclidean distance calculation Ranks {1,2,3} considered

The performance of the chosen AI and ML tools for the prediction of air enthalpy, air specific humidity and desiccant enthalpy is determined in Figs. 5–8. As it is observed from Figs. 5–8, the ANFIS-AI tool found to be superior compared to ANN-AI and KNN-ML tools for predicting the exit parameters with an MAE, RMSE, MAPE and R^2 of 0.049, 0.038, 0.19 and 0.99, respectively. Further KNN-ML and ANN-AI tools has high training time requirement compared to ANFIS-AI model. Although, the KNN-ML and ANN-AI tools showed the least performance compared to ANFIS-AI tool but the MAE, RMSE, MAPE and R^2 are within the acceptable range. This suggests that all the above-mentioned tools perform well for the HFLDD exit parameters prediction purpose but while comparing the three tools the ANFIS-AI tool found to be the better data driven tool. Further, it is also found that KNN-ML has least accuracy followed by ANN-AI tool and ANFIS-AI tool for the predicted output parameters.

4 Conclusions

In this study, the HFLDD exit parameters are predicted and analysed for the given operating range and inlet conditions using data driven models such as ANN-AI, ANFIS-AI and KNN-ML tools. Thirty-four experimental datasets of HFLDD reported in the literature is collected to train and test the three AI and ML tools. The air temperature, air specific humidity, desiccant concentration, desiccant temperature, air flow rate and desiccant flow rate are considered as input parameters, while air outlet enthalpy, air outlet specific humidity and desiccant outlet enthalpy are determined as outputs of abovementioned AI and ML tools. By tuning to optimal hyper parameters, the capability of the three AI and ML tools are assessed using error prediction criterions such as MAE, RMSE, MAPE and R^2. From the error prediction criterion analyses, it is found that among the three AI and ML tools, ANFIS-AI tool gives the superior performance compared to other ANN-AI and KNN-ML tools. Moreover, the ANFIS-AI tool achieved best reliability with the MAE, RMSE, MAPE and R^2 values of 0.049, 0.038, 0.19 and 0.99, respectively. Further, it is also found that the exit parameters predicted based on ANN-AI, ANFIS-AI and KNN-ML tools has good agreement with the experimental data. Thus, from the error prediction analysis, it is found that for a given range of inlet parameters, the three AI and ML tools can be implemented for predicting the HFLDD exit parameters. Furthermore, present investigation also demonstrates that data driven tools such as ANN-AI, ANFIS-AI and KNN-ML are robust tools for assessing the HFLDD. In addition, this study opens the gateway for researchers to implement above-mentioned AI and ML tools for analysing the energy exchanging or heat and mass transfer driven systems.

5 Acknowledgements

This work is carried as a part of the on-going technology development project entitled “Development of Novel Multipurpose Liquid Desiccant Drying/Desalination System Using Hydrophobic Membrane as an Energy Exchanger”. This project is supported by the Science & Engineering Research Board (SERB), Department of Science and Technology, Government of India, Project Number No. SR/20/ME/018.

6 List of References

[1] Naik, B.K., Chinthala, M., Patel, S. and Ramesh, P., 2021. Performance assessment of waste heat/solar driven membrane-based simultaneous desalination and liquid desiccant regeneration system using a thermal model and KNN machine learning tool. *Desalination*, *505*, p.114980.

[2] Khayet, M. and Cojocaru, C., 2013. Artificial neural network model for desalination by sweeping gas membrane distillation. *Desalination*, *308*, pp.102-110.

[3] Al Aani, S., Bonny, T., Hasan, S.W. and Hilal, N., 2019. Can machine language and artificial intelligence revolutionize process automation for water treatment and desalination? *Desalination*, *458*, pp.84-96.

[4] Faegh, M., Behnam, P., Shafii, M.B. and Khiadani, M., 2021. Development of artificial neural networks for performance prediction of a heat pump assisted humidification-dehumidification desalination system. *Desalination*, *508*, p.115052.

[5] Zhang, L.Z., 2011. An analytical solution to heat and mass transfer in hollow fiber membrane contactors for liquid desiccant air dehumidification. *Journal of heat transfer*, *133*(9).

[6] Zhang, L.Z., Huang, S.M. and Pei, L.X., 2012. Conjugate heat and mass transfer in a crossflow hollow fiber membrane contactor for liquid desiccant air dehumidification. *International journal of heat and mass transfer*, *55*(25-26), pp.8061-8072.

[7] Naik, B.K. and Muthukumar, P., 2020. Parametric and Performance Investigations on Novel Multipurpose Liquid Desiccant Drying/Desalination System. *Heat Transfer Engineering*, pp.1-17.

[8] Naik, B.K., Singh, B., Dutta, N., Subbiah, S. and Muthukumar, P., 2020. Fluid to liquid membrane energy exchanger for simultaneous liquid desiccant regeneration and desalination applications–Theoretical and experimental analyses. *Energy Conversion and Management*, *204*, p.112291.

[9] Yang, B., Yuan, W., He, X. and Ren, K., 2016. Air dehumidification by hollow fibre membrane with chilled water for spacecraft applications. *Indoor and Built Environment*, *25*(5), pp.758-771.

[10] Zhang, L.Z. and Huang, S.M., 2011. Coupled heat and mass transfer in a counter flow hollow fiber membrane module for air humidification. *International Journal of Heat and Mass Transfer*, *54*(5-6), pp.1055-1063.

Performance Evaluation of Desiccant Coated Energy Exchanger Based on Buckingham π Theorem

Priyadarshi, Gaurav, Bukke, Kiran Naik

Sustainable Thermal Energy Systems Laboratory (STESL), Department of Mechanical Engineering, National Institute of Technology Rourkela, Odisha, India – 769008; Tel.: +919435686059; Email addresses: naikkb@nitrkl.ac.in; k.bukke@gmail.com

Abstract:

In the present study, the Buckingham π theorem based thermal model is developed to predict the energy and mass exchange performance of the desiccant coated energy exchanger (DCEE). Dimesional analysis is a path for the simplification of a physical problem via dimensional homogeinity to decrease the number of related variables. Therefore, by implementing Buckingham π theorem, deducement of 25 independent parameters for energy exchange and 11 independent parameters for mass exchange into 5 and 3 dimensionless terms is carried out, repectively. The developed model is validated with the experimental data available in the literature and found reliable for DCEE performance assessment with a maximum possible error of ±14.7%. Using the developed model, the effect of inlet parameters such as cycle time, desiccant temperature, process air mass flow rate, and process air inlet specific humidity on the performance parameters are assessed and the obtained results are discussed in detail.

1 Introduction

In the present scenario, enhancing thermal comfort as well as decreasing the energy consumption in the indoor environment became a crucial factor for air conditioning buildings. There are several conventional air conditioning systems available for providing the required thermal comfort in the indoor spaces of a building. Among that, desiccant coated energy exchanger (DCEE) based air conditioning system gained more attention compared to the conventional air-conditioning systems because of in-expensive, eco-friendly, ease in the utilization of low-grade energy sources, and low maintenance features. Therefore, this study emphasizes the DCEE performance and its energy exchange phenomenon in accordance with the thermal comfort/process air moisture removal aspect. The operating principle involved in DCEE is the adsorption of vapour by coated desiccant on the fin-tube surface, thereby reducing the latent load in the process air. Here, the thermal-driven mass exchange is the driving force for the adsorption of moisture/water vapour by the DCEE. In this energy exchanger, initially, the process air is forced to flow onto the DCEE, where the coated desiccant adsorbs the water vapour present in the ambient air and attains a saturation state (Fig. 1). During this water vapour adsorption process (dehumidification process), adsorption heat is generated, and it is removed by passing cooling water through the coated fin-tube. When the DCEE reaches saturation state, the hot water generated using non – renewable source (low-grade heat sources) is passed through the coated fin-tube and the process air is passed across the DCEE simultaneously. Thus, regeneration of desiccant takes place. Then, cold water and process air are passed through the tube and across the DCEE, respectively, for simultaneous dehumidification and cooling of process air and this adsorption-desorption (dehumidification-regeneration) cycle continues.

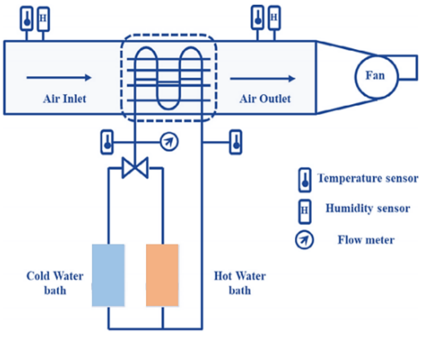

Figure 1. Schematic of DCEE.

Several efforts have been made to analyse the adsorption dynamics of the DCEE [1–4]. But the complex nature of the adsorption dynamics, complications involved in developed thermal/numerical models reported in the literature, difficulties in assessing the multidimensional energy exchange phenomenon and barriers associated in solving the energy and mass exchange occurrence at the air and coated desiccant fin-tube interface during the unsteady process, makes the researchers look for alternative approaches [4–8]. Thus, in this paper, Buckingham π theorem based thermal model which depends on dimensional analysis in compliance with homogeneity of the dimension is explored for analysing the DCEE performance and energy exchange phenomenon in a simplified yet effective approach. Further, this model explores the potentiality of dimensional interpretation of operating parameters with exit parameters.

2 Thermal model

A thermal model based on Buckingham π theorem is developed to predict the performance and exit parameters of the DCEE for the given operating parameters. The assumptions made to simplify the developed model are, a)

Thermophysical properties of process air, desiccant and water remain constant within the considered operating range; b) Fluid flow is uniform and fully developed; c) Heat and mass transfer coefficients at the air-desiccant interface of entire DCEE is constant with variation in time; d) Energy and mass exchange phenomenon occurring in the control volume will be same for entire DCEE; and e) The temperature lift of the desiccant and water is assumed to be almost equivalent with respect to each ohter but not constant [6]. Based on the above-mentioned assumptions, the energy and mass balance governing equations as well as initial and boundary conditions for a control volume of desiccant, water and process air are defined in Table 1. Further, to simplify the assessment of DCEE exit parameters and to implement the Buckingham π theorem, governing equations, initial conditions, and boundary conditions are converted into non-dimensional forms and they are listed in Table 1.

Table 1. Governing equations for assessing the DCEE exit parameters [4,5].

MASS BALANCE	**GOVERNING EQUATIONS**	**DIMENSIONLESS PARAMETERS**
AIR	$\rho_a \frac{\partial X_a}{\partial t} + \rho_a u_a \frac{\partial X_a}{\partial x} = \frac{1}{l_a} K_y (X_d - X_a)$; $\frac{\partial \psi_a}{\partial t} + u_a \frac{\partial \psi_a}{\partial x} = B_1(\psi_d - \psi_a)$	$b = \frac{dY_d}{dX_d}$; $B_1 = \frac{K_y}{l_a \rho_a}$;
DESICCANT	$\frac{\partial Y_d}{\partial t} = \frac{1}{\delta_d \rho_d} K_y (X_a - X_d)$; $\frac{dY_d}{dX_d}\frac{\partial X_d}{\partial t} = \frac{1}{\delta_d \rho_d} K_y (X_a - X_d)$; $\frac{\partial \psi_d}{\partial t} = B_2(\psi_a - \psi_d)$	$B_2 = \frac{K_y}{b \delta_d \rho_d}$ $\psi_a = \frac{X_{ai} - X_{ao}}{X_{ai} - X_{d}}$; $\psi_d = \frac{X_{di} - X_{do}}{X_{di} - X_{ai}}$
INITIAL/ BOUNDARY CONDITIONS	$X_a(x,t)\|_{x=0} = X_{a,i}$; $X_a(x,t)\|_{t=0} = (X_{a,i} - X_{d,i}) e^{\frac{-K_y x}{l_a \rho_a u_a}} + X_{d,i}$; $X_d(x,t)\|_{t=0} = X_{d,i}$	$\psi_a \|_{x=0} = 0$; $\psi_a \|_{t=0} = e \frac{-B_1 x}{u_a}$ $\psi_d \|_{t=0} = 0$
ENERGY BALANCE	**GOVERNING EQUATIONS**	**DIMENSIONLESS PARAMETERS**
AIR	$\rho_a A_a C_{pa} \left(\frac{\partial T_a}{\partial t} + u_a \frac{\partial T_a}{\partial x} \right) = h_a c (T_d - T_a) + K_y c C_{pv} (X_d - X_a)(T_d - T_a)$; $\frac{\partial \Phi_a}{\partial t} + u_a \frac{\partial \Phi_a}{\partial x} = R_1 + R_2$	$\Phi_a = \frac{T_{ai} - T_{ao}}{T_{ai} - T_{di}}$; $R_1 = \frac{h_a c}{\rho_a A_a C_{pa}}$ $R_2 = \frac{K_y c C_{pv} (X_d - X_a)}{\rho_a A_a C_{pa}}$
WATER	$\rho_w A_w C_{pw} \left(\frac{\partial T_w}{\partial t} + u_w \frac{\partial T_w}{\partial x} \right) = h_w c (T_d - T_w)$; $\frac{\partial \Phi_w}{\partial t} + u_w \frac{\partial \Phi_w}{\partial x} = R_3$	$\Phi_w = \frac{T_{wi} - T_{wo}}{T_{wi} - T_{di}}$; $R_3 = \frac{h_w c}{\rho_w A_w C_{pw}}$
DESICCANT	$\rho_d A_d C_{pd} \frac{\partial T_d}{\partial t} + \frac{k_t}{a_s} \frac{\partial T_d}{\partial x} = -h_a c (T_d - T_a) - K_y c C_{pv} (X_d - X_a)(T_d - T_a) - h_w c\ (T_d - T_w)$ $\frac{\partial \Phi_d}{\partial t} + P_1 \frac{\partial \Phi_d}{\partial x} = -G_1 - G_2 - G_3 \xi$	$P_1 = \frac{k_t}{\rho_d A_d C_{pd} a_s}$; $G_1 = \frac{h_a c}{\rho_d A_d C_{pd}}$ $G_2 = \frac{K_y c C_{pv} (X_d - X_a)}{\rho_d A_d C_{pd}}$ $G_3 = \frac{h_w c}{\rho_d A_d C_{pw}}$; $\Phi_d = \frac{T_{di} - T_{do}}{T_{di} - T_{ai}}$ $\xi = \frac{T_d - T_w}{T_d - T_a}$
INITIAL/ BOUNDARY CONDITION	$T_a(x,t)\|_{x=0} = T_{a,i}$; $T_a(x,t)\|_{t=0} = (T_{a,i} - T_{d,i}) e^{\frac{-h_a x}{\rho_a A_a C_{pa} u_a}} + T_{d,i}$; $T_w(x,t)\|_{t=0} = T_{w,i}$ $T_d(x,t)\|_{t=0} = T_{d,i}$	$\phi_a \|_{x=0} = 0$; $\phi_a \|_{t=0} = e \frac{-R_1 x}{u_a}$ $\phi_w \|_{t=0} = 0$; $\phi_d \|_{t=0} = 0$

2.1 Implementation of Buckingham π theorem

To predict the DCEE performance, the non-dimensional form of governing equations provided in Table 1 is further simplified by incorporating the Buckingham π theorem. Usually, this theorem depends on correlating the independent parameters with the dependent parameters (fundamental dimensions) in a non-dimensional form. The main criteria for applying the Buckingham π theorem is the existence of dimensional homogeneity. The advantages of this theorem are the given set of dimensionless parameters can be extracted from the given variables even from those equations not having a particular form, a group of dimensionless quantities can be used to characterize a physical phenomenon without analysing the original dimensional variables and besides, it decreases the number of parameters requiring individual attention while conducting the experiments. Thus, by using this theorem, 25 independent variables such as distance from air inlet (x), time (t), air and desiccant density (ρ_a and ρ_d), air, water, and desiccant temperatures (T_a, T_d, and T_w), convective water and air heat transfer coefficients (h_a and h_w), mass transfer coefficient at the air-desiccant interface (K_y), air, water, water vapour, and desiccant specific heat capacities (C_{pa}, C_{pd}, C_{pv}, C_{pd}), air and water velocities (u_a and u_w), perimeter of overall flow passage (c), area of cross-section for DCEE (A_a), area of cross-section for water passage (A_w), area of cross-section for desiccant passage (A_d), perimeter of water flow passage (c_w), humidity ratio of desiccant and air (X_a and X_d), specific surface area (a_s), and thermal conductivity of copper (k_t) are correlated with the dependent parameters such as air, water and desiccant temperature difference ratios (ϕ_a, ϕ_w and ϕ_d) for developing the energy balance correlations of air, water and desiccant. The Further, 11 independent variables such as desiccant thickness (δ_d), slope of isotherm b

(dY_d/dX_d) where Y is water content, a_s, x, t, ρ_a, ρ_d, u_a, X_a, X_d, and K_y are correlated with the dependent parameters such as air/desiccant dimensionless humidity difference ratios (Ψ_a, and Ψ_d) for developing the mass balance correlations. The developed correlations for dimensionless ϕ_a, ϕ_w, ϕ_d, Ψ_a, and Ψ_d in π terms using Buckingham π theorem are presented in Table 2 and the dimensions of the energy exchanger are shown in Table 3. The desiccant layer thickness is 95 µm the density of the desiccant coating is 120 g/m^2 [7].

Table 2. Correlations for dimensionless ϕ_a, ϕ_w, ϕ_d, Ψ_a, and Ψ_d in π terms.

Dimensionless corelation: $\phi = a\pi_1^b \pi_2^c \pi_3^d \pi_4^e \pi_5^f$; $\psi = a\pi_1^b \pi_2^c \pi_3^d$			
ψ_a	$\pi_1 = b\frac{\delta_d \rho_d}{l_a \rho_a}$	$\pi_2 = \frac{xNTU_{m,a-d}}{b\delta_d}$	$\pi_3 = \frac{NTU_{m,a-d} t \dot{m}_a}{b\delta_d A_a \rho_d}$
ψ_d	$\pi_1 = b\frac{\delta_d \rho_d}{l_a \rho_a}$	$\pi_2 = \frac{xNTU_{m,a-d}}{b\delta_d}$	$\pi_3 = \frac{NTU_{m,a-d} t \dot{m}_a}{b\delta_d A_a \rho_d}$
Φ_a	$\pi_1 = NTU_{m,a-d}\frac{cx}{A_a}\frac{C_{pv}}{C_{pa}}(X_d - X_a)$	$\pi_2 = NTU_{m,a-d}\frac{\dot{m}_a ct}{\rho_a A_a^2}\frac{C_{pv}}{C_{pa}}(X_d - X_a)$	$\pi_3 = \frac{Le}{X_d - X_a}$
Φ_w	$\pi_1 = NTU_{t,w-d}\frac{cx}{A_w}$	$\pi_2 = NTU_{t,w-d}\frac{ct}{A_w}$	
Φ_d	$\pi_1 = NTU_{m,a-d} cC_{pv} u_w a_s \frac{\rho_d}{k_d}(X_d - X_a)$	$\pi_2 = NTU_{m,a-d}\frac{C_{pv}}{C_{pa}}\frac{ct\dot{m}_a}{\rho_d A_d^2}$	$\pi_3 = \frac{NTU_{t,w-d}}{NTU_{m,a-d}}\frac{\dot{m}_w}{\dot{m}_a}\frac{C_{pw}}{C_{pv}}\frac{A_a}{A_w(X_d - X_a)}$
	$\pi_4 = \frac{Le}{X_d - X_a}$	$\pi_5 = \frac{T_d - T_w}{T_d - T_a}$	

Table 3. Dimensions of energy exchanger [7].

Parameters	Length (l)	Width (w)	Height (h)	Fin thickness	Fin pitch	Inner tube dia (d_i)	Outer tube dia (d_o)	No. of tube pass (N_f)
Values	200 mm	150 mm	22 mm	0.12 mm	1.6 mm	9.5 mm	10.5 mm	6

2.2 Performance parameters

The performance parameters such as transient moisture removal (TMR) and energy exchange between coated desiccant and process air (Q_e) are chosen to assess the DCEE performance.

Transient moisture removal (TMR): ΔX_a (g_{wv}/kg_{da}) (1)

where $\Delta X_a = X_{a,i} - X_{a,o}$ indicates dehumidification and $\Delta X_a = X_{a,o} - X_{a,i}$ indicates regeneration.

Energy exchange (Q_e): $\dot{m}_a (h_{a,i} - h_{a,o})$ (W) = $\dot{m}_a (h_{a,o} - h_{a,i})$ (W) (2)

where $h_a = C_{pa}T_a + X_a(1.86T_a + 2501)$; $\Delta h_a = h_{a,i} - h_{a,o}$ indicates dehumidification and $\Delta h_a = h_{a,o} - h_{a,i}$ indicates regeneration.

3 Results and discussion

3.1 Model validation

The developed correlations for dimensionless ϕ_a, ϕ_w, ϕ_d, Ψ_a, and Ψ_d based on Buckingham π theorem model are validated with the experimental data available in the literature [1,2] and observed good compliance with a maximum possible error of ±14.7% as shown in Figure 2. Thus, this indicates that the developed Buckingham π theorem based model can be applied with confidence for predicting the DCEE performance.

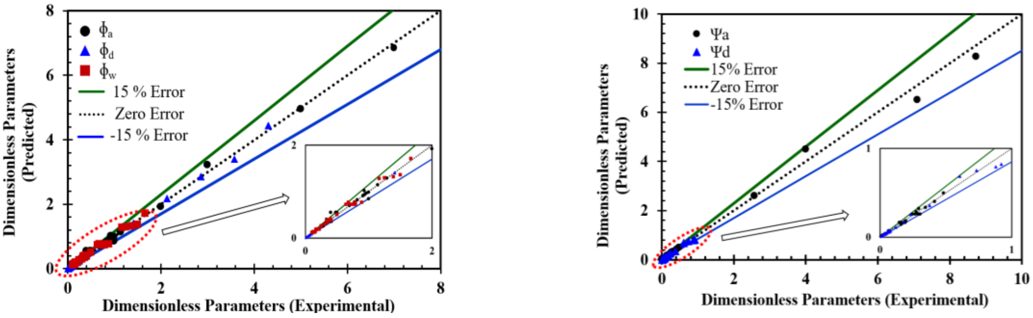

a. *Validation of predicted data with experimental data.*

b. *Validation of predicted data with experimental data.*

Figure 2. Validation of predicted dimensionless air, desiccant and water temperature difference ratios and air and desiccant humidity difference ratios with experimental data [1,2].

3.2 Performance parameters evaluation with different operating parameters

Table 3. Inlet conditions chosen for the present study.

Parameter	$\dot{m}_a$ (kg/hr)	$T_{a,i}$ (°C)	$X_{a,i}$ (kg_{da}/kg_{wv})	$\dot{m}_w$ (L/min)	$T_{hw,i}$ (°C)	$T_{cw,i}$ (°C)	t (s)
`Range	27.5	30	0.0215	2.5-2.7	50	30	600

Using the developed model, for a given inlet condition and operating range (Table 3), theoretically analyzed the thermal performance of the DCEE by varying cycle time (t), process air mass flow rate ($\dot{m}_a$), process air inlet specific humidity ($X_{a,i}$) and desiccant inlet temperature ($T_{d,i}$) with TMR and Q_e as shown in Fig. 3. The DCEE dimensions and thermophysical properties of coated desiccant, water and air chosen in the present study are taken from Vivekh et al. [1]. From Fig. 3a, it is observed that with the increase in ‘t’ from 0 to 600 s and 600 to 1200 s, TMR and Q_e decreases linearly by 46% and 45% during dehumidification and decreases linearly by 87% and 52% during the regeneration process, respectively. This happens because during dehumidification/regeneration, as the ‘t’ increases, the vapour pressure difference between the process air and coated desiccant decreases and reaches vapour and energy equilibrium condition. As a result, in dehumidification/regeneration, the TMR and Q_e show a decreasing trend. As the ‘$\dot{m}_a$’ increases from 0.043 kg/s to 0.087 kg/s, the TMR and Q_e increases linearly by 54% and 37% during dehumidification and increases constantly by 72% and 57% during regeneration, as indicated in Fig. 3b. It happens due to an increase in energy and mass interactions between coated desiccant with process air. In Fig. 3c, it is found that with the increase in ‘$X_{a,i}$’ from 0.0145 kg_{da}/kg_{wv} to 0.0215 kg_{da}/kg_{wv}, the TMR and Q_e increase steeply by 95% and 80% during dehumidification and decreases abruptly by 92% and 30% during regeneration process, respectively. This is because as the ‘$X_{a,i}$’ increases, moisture content present in the process air increases. Therefore, during the dehumidification process, high moisture adsorption occurs, whereas during regeneration, low moisture desorption takes place. Consequently, both TMR and Q_e increase during the dehumidification process and decreases during the regeneration process. With the increase in ‘$T_{d,i}$’ from 10 °C to 36 °C, the TMR and Q_e decrease straightforward by 87% for the dehumidification process whereas for the regeneration process with an increase in ‘$T_{d,i}$’ from 41 °C to 81 °C, the TMR and Q_e increases drastically by 78% and 88%, respectively as shown in Fig. 3d. It happens because as the ‘$T_{d,i}$’ increases, desiccant vapour pressure increases since the temperature is directly proportional to vapour pressure. Subsequently, the vapour pressure difference between process air and coated desiccant decreases during dehumidification and increases during regeneration, respectively. Thus, TMR and Q_e show linear decreasing/increasing trend during the dehumidification/regeneration process, respectively.

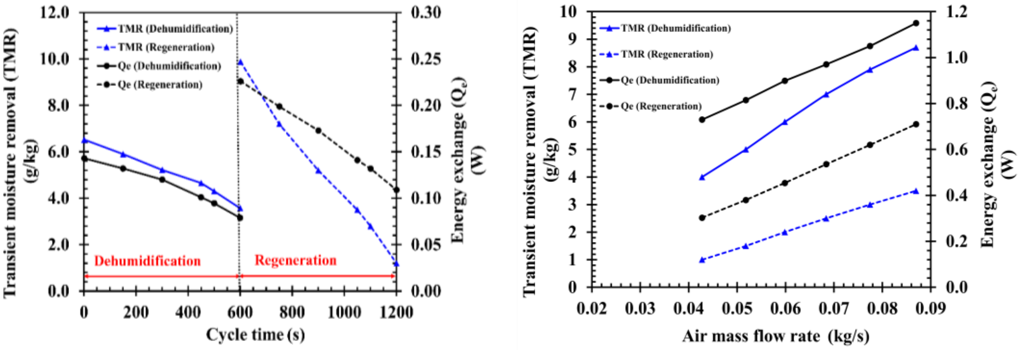

(a) *Variation of TMR and Q_e with t*   (b) *Variation of TMR and Q_e with $\dot{m}_a$*

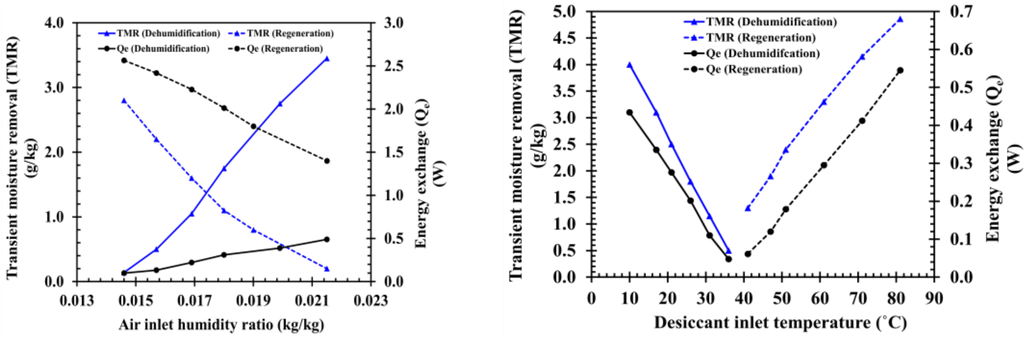

(c) *Variation of TMR and Q_e with $X_{a,i}$*   (d) *Variation of TMR and Q_e with $T_{d,i}$*

Figure 3. Variation of TMR and Q_e with t, $\dot{m}_a$, $X_{a,i}$ and $T_{d,i}$.

4 Conclusions

The feasibility of incorporating Buckingham π theorem to predict the DCEE performance is assessed in detail by developing a thermal model based on the aforementioned theorem. Several correlations for the dimensionless parameters are developed in terms of π. The proposed model has been validated with the data reported in the literature and found in good agreement. Thus, this signifies that Buckingham π theorem is well suited for predicting the energy and mass exchange phenomenon occurring across the DCEE. Based on the developed model, choosing transient moisture removal (TMR) and energy exchange (Q_e) as performance parameters, the energy and mass exchange characteristics of the DCEE is analysed by varying the cycle time (t), process air mass flow rate ($\dot{m}_a$), desiccant inlet temperature ($T_{d,i}$) and process air inlet specific humidity ($X_{a,i}$). The developed model based on Buckingham π theorem can be used as a reference tool for the design and performance prediction of DCEE in a simplified way. Further, one can quickly estimate the DCEE performance compared to computational/numerical models. Moreover, the developed model is very compatible/well-suited/accordant in nature due to which this approach can be stretched in near future to different sorption devices (thermochemical energy storage, Ad/Ab-sorber , liquid desiccant energy exchanger etc.).

5 Acknowledgment

This work is carried out as a part of the ongoing technology development project entitled, “Design and Development of Helical Threaded Desiccant Coated Heat Exchanger for HVAC Application”. This project is supported by the National Institute of Technology Rourkela, Project Number No. NITR/ES/2020/M/1597.

6 List of References

[1] Vivekh, P., Bui, D.T., Islam, M.R., Zaw, K. and Chua, K.J., 2020. Experimental performance evaluation of desiccant coated heat exchangers from a combined first and second law of thermodynamics perspective. Energy Conversion and Management, vol. 207, pp.112518.

[2] Liang, C.P., Ture, F., Dai, Y.J., Wang, R.Z. and Ge, T.S., 2021. Experimental investigation on performance of desiccant coated microchannel heat exchangers under condensation conditions. *Energy and Buildings*, vol. 231, pp.110622.

[3] Vivekh, P., Islam, M.R. and Chua, K.J., 2020. Experimental performance evaluation of a composite superabsorbent polymer coated heat exchanger-based air dehumidification system. *Applied Energy*, vol. 260, pp.114256.

[4] Hua, L.J., Sun, X.Y., Jiang, Y., Ge, T.S. and Wang, R.Z., 2020. Graphic general solutions for desiccant coated heat exchangers based on dimensional analysis. *International Journal of Heat and Mass Transfer*, vol. 154, pp.119654.

[5] Amani, M. and Bahrami, M., 2021. Greenhouse dehumidification by zeolite-based desiccant coated heat exchanger. *Applied Thermal Engineering*, vol. 183, pp.116178.

[6] Jagirdar, M. and Lee, P.S., 2018. Mathematical modeling and performance evaluation of a desiccant coated fin-tube heat exchanger. *Applied energy*, vol. 212, pp.401-415.

[7] Hua, L.J., Ge, T.S. and Wang, R.Z., 2020. A mathematical model to predict the performance of desiccant coated evaporators and condensers. *International Journal of Refrigeration,* vol. 109, pp.188-207.

[8] Ciulla, G., D’Amico, A. and Brano, V.L., 2017. Evaluation of building heating loads with dimensional analysis: Application of the Buckingham π theorem. *Energy and Buildings,* vol. 154, pp.479-490.

Experimental results and thermoeconomic analysis of an absorption heat transformer operating in a petrol refinery

Martinez-Urrutia, Asier[1], Ramirez, Miguel[1], Corrales, Jose[2], Cudok, Falk[2], Evron, Yigal[3], Pérez-Ortiz, Alberto[4], Ataç, Deren[5]

[1] *Tecnalia, Energy and Environment Division, Área Anardi, 5 Azpeitia, Guipuzkoa 20730. Spain.*

Corresponding author: asier.martinez@tecnalia.com

[2] *Tech. Univ. Berlin, Institute of Energy Conversion Eng., KT2, Marchstraße 18, Berlin, 10587, Germany.*

[3] *Technion-Israel Institute of Technology, Faculty of Mech. Engineering, Technion, Haifa, 32000, Israel.*

[4] *Aiguasol Enginyería, Roger de Llúria, 29. 3º 2ª, 08009 Barcelona, Spain.*

[5] *Tüpras, Güney Mah. Petrol Cad. No:25/1 41780, Körfez/ Kocaeli. Turkey.*

Abstract:

Industry sector demands a quarter of the total energy demand in Europe. Around 70% of its demand is related to thermal purposes; and it is estimated that 20-50 % of the energy used in industrial processes is wasted and rejected. About 300 TWh per year are rejected from these industrial processes. Nevertheless, this waste-heat presents temperatures below 150 °C, not being, in most cases, technically neither economically viable its recover or reuse. Absorption Heat Transformers (AHT) are presenting as an interesting opportunity for this purpose, being able to increase the temperature of approximately 50 % of the waste energy by up to over 50 K. The objective of the Indus3Es Project is to develop an AHT solution for the industry, currently being demonstrated in real environment at the Izmit petrochemical facilities of Tüpras and representing the first identified AHT deployments in Turkey. The aim of this paper is to present the development of the AHT and the integration and the monitored results of the development under the project, including the technoeconomical analysis of the installation.

1 Introduction

The Absorption Heat Transformers (AHT) represent a real opportunity for the recovery and revalorization of low-temperature waste-heat. Current energy frameworks require the evaluation of all options to save thermal energy and recover heat, and new efforts and developments are made to make the AHT a real alternative in the short-medium term. To achieve this goal, there has been an increase in AHT related studies in the last decade, mainly addressing the process temperature requirements in industries such as paper (during and lamination processes), chemical and petrochemical (distillation and purification processes) and food and beverage (drying, sterilization, fermentation and mold and bacteria processes) [1–4]. These works present installations with capacities between 100 kW and 5 MW, and agree that AHTs presents attractive payback periods, between 2 and 5 years, depending mainly on their capacity. Furthermore, over the past years some market installations by manufacturers Thermax and Johnson Controls – Hitachi, offering AHTs between 0.5 and 10 MW, have been documented in their respective websites.

The main objective of the Indus3Es Project (Horizon 2020 Project No. 680738) is to develop a single stage AHT, an economically viable solution for industry, appropriate for existing plants and adaptable to various industrial processes. The developed system is being under demonstration in a real environment at the Izmit facilities of Tüpras, the main petrochemical industry in Turkey, enabling to analyze integration aspects, as well as operational and business-related issues. This work presents the development of the AHT as well as its integration and monitored results and economic analysis under the Indus3Es Project. The paper firstly presents the developed system description, describing both, the AHT developed and the installation. Then the results obtained are compared with those expected from designing and extrapolation from lab-scale. Finally, techno-economic analysis and conclusions are summarized.

2 Developed system description

Single effect heat transformer has the same main components installed in a single effect absorption chiller working in reverse: it consists primarily of one condenser, one evaporator one absorber and one generator. The difference with absorption chiller is that the absorber and evaporator now operate at high pressure and the condenser and generator at low pressure. The AHT works at three temperature levels: low exergy waste heat from industrial process activates the heat transformer at the intermediate temperature level and higher temperature stream is obtained in the absorber external circuit, up to 50 K above waste heat temperature level. Half of the activation energy must be rejected at ambient temperature. New developments in absorption chillers were adapted to the developed AHT; additionally, innovative developments are included in the 200 kW prototype project.

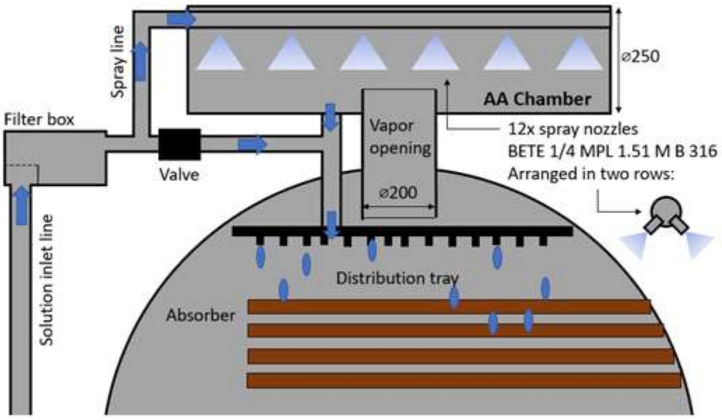

Figure 1 – Adiabatic absorption chamber and distribution system design.

On one hand, a dedicated adiabatic absorption chamber with atomizing spray nozzles distribution system is installed before the solution enters the distribution tray in the absorber. To optimize adiabatic absorption, the solution must have enough residence time, but an increase in the contact area of the solution and vapor can also accelerate this process. This can be done by atomizing the solution into-small droplets. This dedicated adiabatic absorption chamber can be bypassed and essentially cut-off from the system by a controlled valve. It was designed this way for future research purposes to help isolate the adiabatic absorption chamber and analyze its contribution.

In addition, the system includes an innovative motor-less non-condensable (NC) gases purge system solution. The installation of the purge system will provide valuable data to characterize this new concept for the first time, giving additional value to the machine developed during the project. Finally, a control strategy which prevents the cycle from moving into risky operational conditions was developed. The advanced control system ensures safe operation of the AHT, minimizing the risk of crystallization while it optimizes the performance characteristics. The Characteristic Equation Method has been used for the definition of the control system, which implied modifications from model already used in absorption chillers [5].

2.1 Installation and design

The AHT system has been installed at the power plant of the petrochemical facilities of Tüpras in Izmit (Turkey). In particular, the waste-heat source for the activation of the AHT system comes from the oily condensate flash steam tank. In order to recover the heat from the oily condensate flash steam, demineralized water sent to the boilers is first preheated by this waste source which is at about 100 °C (waste heat stream). The remaining of the waste-heat is used for thermal activation of the AHT (generator and evaporator circuits), that upgrades heat to up to 140 °C (absorber circuit). This upgraded stream heats up the demin-water circuit to 135 °C (final revalorized stream) before it is sent to the boilers. The temperature of the water stream to be revalorized, referred as supply header demineralized water, and considered constant throughout the year and equal to 65 °C.

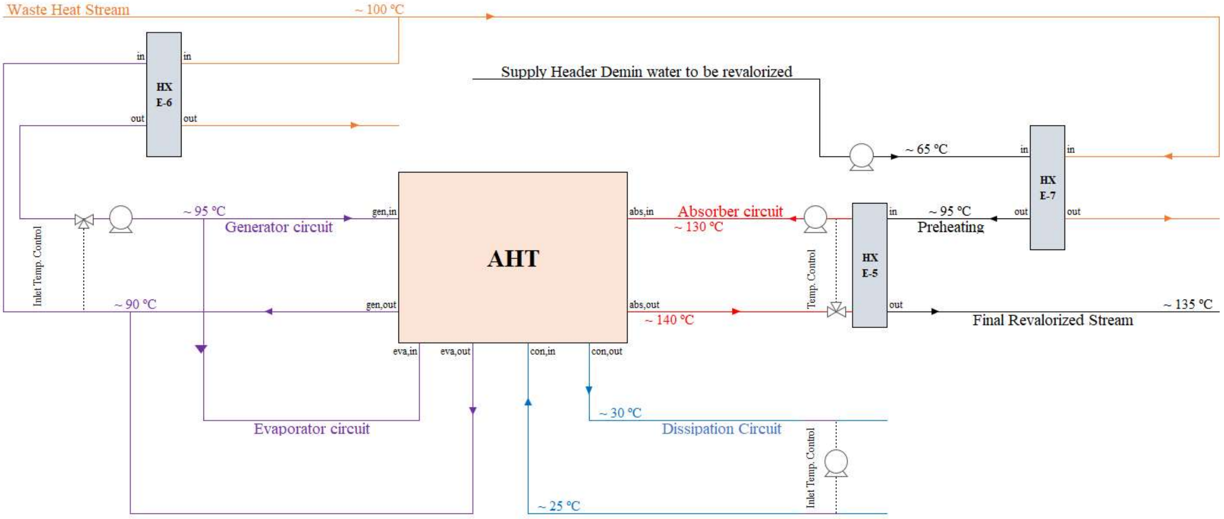

Figure 2 - Schematic diagram of an AHT and external installation.

Waste-heat stream from the tank is also used to preheat the supply header demineralized water from approximately 65 to 95 °C (preheating circuit). The temperature of the supply header demineralized water temperature is boosted to 135 °C with the heat supplied by the absorber of the AHT. In resume, these were the temperatures considered during designing phase. Figure 2 presents the conceptual diagram of the AHT pilot plant, which is mainly composed by six different system circuits: waste-heat stream, generator and evaporator, dissipation condenser, absorber and supply header demineralized water. The addition of 30 % by volume of glycol to the external absorber, evaporator and generator circuits was considered to minimize freezing risks in the installation during non-operational time periods (e.g. maintenance repairs, system failures, etc.). With this percentage of glycol by volume, the freezing point and specific heat decreases to –13.7 °C and 3.8 kJ/(kg·K) respectively.

2.2 Absorption Heat Transformer design

The final design of the equipment installed in Tüpras was based on the characterization of a lab-scale prototype [6]. The Characteristic Equation obtained from the prototype was used to scale up the AHT. The characteristic temperature difference ($\Delta\Delta t$) is an indicator of the heat transfer potential of the AHT and depends on the mean external temperatures of the AHT components and R Dühring factor, about 1.15 for LiBr aqueous solution. The average temperatures and the driving temperature difference of the Indus3Es demonstrator functioning nominal point are: t_{abs} ~ 135.0 ºC; t_{gen} ~ 97.5 ºC; t_{eva} ~ 97.5 ºC; t_{con} ~ 27.5 ºC and $\Delta\Delta t$ ~ 30 K. Near this installation design point, the heat fluxes obtained at the laboratory-scale AHT's absorber, generator, evaporator and condenser were about 4682 $W \cdot m^{-2}$ – 4468 $W \cdot m^{-2}$ – 7891 $W \cdot m^{-2}$ and 6929 $W \cdot m^{-2}$ respectively. This data was then used for the prototype design extrapolation, resulting in design capable to revalorize 200 kW at nominal temperature conditions, with following design specifications: Q_{abs} ~ 198 kW; Q_{gen} ~ 208 kW; Q_{eva} ~ 233 kW; Q_{con} ~ 229 kW; Coefficient of Performance (COP) of about 0.45 and a gross temperature lift (GTL) of about 45 K.

3 Performance analysis

From November 2019 to June 2020, the AHT has been working with different sets of conditions, with the objective of characterize the AHT performance under a wide range of conditions. The testing conditions were defined by the external temperatures, and are listed below:

- $\Delta\Delta t$ ~ 40 K (t_{abs}; t_{gen}; t_{con} = ~115; 85; 20 ºC);
- $\Delta\Delta t$ ~ 50 K (t_{abs}; t_{gen}; t_{con} = ~115; 85; 15 ºC);
- $\Delta\Delta t$ ~ 45 K (t_{abs}; t_{gen}; t_{con} = ~120; 85; 20 ºC);
- $\Delta\Delta t$ ~ 40 K (t_{abs}; t_{gen}; t_{con} = ~120; 90; 30 ºC);
- $\Delta\Delta t$ ~ 45 K (t_{abs}; t_{gen}; t_{con} = ~125; 90; 20 ºC).

Where $\Delta\Delta t = R \cdot (t_{eva} - t_{con}) - (t_{abs} - t_{gen})$ and R ~ 1.15.

As shown in the Figure 3, the capacities obtained by the demonstrator in the absorber working with no-use of the adiabatic absorption vessel lied between 218 and 245 kW under the range of temperatures and near to testing conditions mentioned above. Although the AHT was designed for revalorizing about 200 kW for $\Delta\Delta t$ value of about 30 K, in the tests performed the dissipation stream was about 10 K colder than the design value, resulting then in driving temperature differences ($\Delta\Delta t$) in the AHT between approximately 40 and 50 K. The lab-scales prototype was not tested under these conditions, but the adjusted Characteristic Equation model has been used for

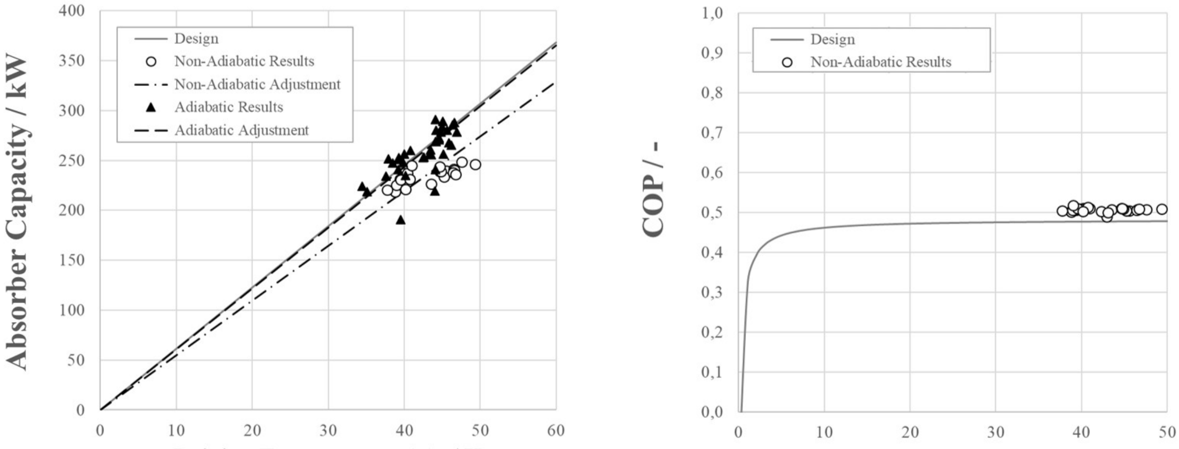

Figure 3 – Indus3Es AHT's absorber capacity and COP under Non-adiabatic(○) and Adiabatic(▲) modes from November 2019 to June 2020 in the installation in Tüpras.

comparing the results obtained by both AHTs. It was observed that the capacities in each component are lower than those expected by the design. Even though the capacity obtained is lower, the COP of the AHT is maintained in values near to 0.5. Two main reasons have been considered for the lower performance comparing to the expected one: on one side, the dissipation temperature in the condenser was lower than expected. While the nominal dissipation temperature was 25 °C, the one in the demonstrator in the dates of this tests was between 15 and 20 °C in most of the cases. There are scientific evidences that the lower the pressure of the lower pressure vessel, the influence of the NC gases could be increased, which would result in the decrease of the performance [7]. On the other hand, the solution flow rate in these tests was 13 % lower than the one defined from the design phase. During the design phase, the flow rate was set in order to have the same specific flow rate along the tube´s length. Because of cavitation risk, the solution flow rate was set to about 2600 $kg \cdot h^{-1}$, representing a decrease of the 13 %. During the second test campaign the AHT was set to work under adiabatic mode. The solution was sent to the installed adiabatic-absorption-vessel. Using the adiabatic absorption vessel (AAV), the performance of the AHT, was significantly improved, comparing to the previous tests. It is estimated that the revalorization capacity of the AHT using the AAV is about 12 % higher comparing to the non-adiabatic mode. The main advantage of the use of the AAV is the increase of the temperature entering to the absorber´s tube bundle. With higher temperature at the first row of the tubes, higher temperature energy could be transferred to the external circuit. During the tests performed, it was estimated that the 13 % of the absorption rate occurs in the AAV, increasing in about 20 K the entering solution temperature.

4 Economic and environmental analysis

According to the environmental impact assessment made, the scenario with the AHT strongly contributes to the avoidance of environmental impacts. Considering that the saved energy would be obtained from natural gas the Indus3Es system will prevent the emission of 10335 tons of CO_2 equivalents during 20 years, operating 8760 hours per year. Considering the costs of the prototype and installation developed in the project investment would be recovered in between 10 – 11 years. However, as result of an internal analysis, the ready-to-market system implementation would be about 420000 €, i.e. about 1500 €/kW revalorized by the AHT (preheating included). Results show that during the sixth year after the implementation of the market Indus3Es, the initial investment would be completely recovered. The internal rate of return and the net present value would be 16 % and 1023285 € respectively. At the end of the 20 years life cycle, more than 1.7 million euros would be saved thanks to the Indus3Es implementation. Considering 600 kW prototype the payback period would be reduced to 3 years, and to 2 years in case 1.2 MW AHT is considered.

5 Conclusions

- This work presents the results of the AHT installation performed in the Indus3Es Project. The system has been installed in a process petrochemical plant, by developing a fully stand-alone system which would help to reduce the CO_2 emissions in the plant.
- This system could work in two main different operation modes: non-adiabatic and adiabatic absorption modes. This did allow the consortium to make an estimation of the improvement of the AHT performance by the addition of an adiabatic absorption vessel, where nozzle-based distribution system was considered:
  - Working under non-adiabatic mode, presented a deviation of 12 % from the design value. The main reasons for this deviation are that, in one hand, lower dissipation temperature was available in the condenser, increasing the effect of the NC gases. In the other hand, lower solution flow-rates were set because of cavitation of the solution pump.
  - The implementation of the adiabatic absorption vessel could be a very successful improvement added to the system. It is remarked that during the tests under this operation mode not fully and long-time stationary operation could set, but promising results were observed. The temperature of the solution entering to the absorber increases in about 20 K by the AAV, and it was observed that the capacities by the implementation of the AAV could increase the design capacities about the 12 %.

6 Acknowledgment

This work has been developed under the project "Indus3Es: Industrial Energy and Environmental Efficiency" funded by the Horizon 2020 framework of the European Union, Project No. 680738. http://www.indus3es.eu/.

7 List of References

[1] Parham, K., Khamooshi, M., Tematio, D. B. K., Yari, M., & Atikol, U. (2014). Absorption heat transformers– a comprehensive review. *Renewable and Sustainable Energy Reviews*, 34, 430-452.

[2] Donnellan, P., Cronin, K., & Byrne, E. (2015). Recycling waste heat energy using vapour absorption heat transformers: a review. *Renewable and Sustainable Energy Reviews*, 42, 1290-1304.

[3] Rivera, W., Best, R., Cardoso, M. J., & Romero, R. J. (2015). A review of absorption heat transformers. *Applied Thermal Engineering*, 91, 654-670.

[4] Cudok, F., Giannetti, N., Ciganda, J. L. C., Aoyama, J., Babu, P., Coronas, A., ... & Ziegler, F. (2021). Absorption heat transformer-state-of-the-art of industrial applications. *Renewable and Sustainable Energy Revie*ws, 141, 110757.

[5] Cudok, F., & Ziegler, F. (2015). Absorption heat converter and the characteristic equation method. *In 24th International Congress of Refrigeration ICR-2015*. Yokohama (Japan); Paper 764 E2-Fr-2.

[6] Cudok, F., Ciganda, J. C., Kononenko, N., & Drescher, E. (2017). Experimental results of an absorption heat transformer. *In 12th IEA Heat Pump Conference*. Rotterdam (Netherlands); Abstract O.4.4.2. p. 101 – 102.

[7] Metzner, D., Corrales Ciganda, J. (2019) Einfluss von nicht-kondensiarbaren Gasen auf den thermodynamischen Prozess in Absorptionswaermetransformator. Paper S.04, Tagungsband der DKV-Jahrestagung.

Directly Biomass-fired Absorption Heat Pump – Concept and Test Results

KAUSCHE Manuel, HELM Martin, RIEPL Manuel

Bavarian Centre for Applied Energy Research (ZAE Bayern)
Walther-Meissner-Strasse 6, D-85748 Garching, Germany
Manuel.Kausche@ZAE-Bayern.de +49 89 329442-90

Abstract:

This paper is an updated version of paper number #57 from the online pre-conference ISHPC2020.

The development and design of a flexible two-stage absorption heat pump system comprising a directly biomass-fired desorber is presented. A nominal heating capacity of 100 kW is provided with a biomass utilization efficiency $BUE_{heat} \approx 2$ what in this context is the supplied heat referred to the lower heating value of the ligneous biomass input. For this purpose, the integrated sorption process replaces valuable renewable biomass energy with thermally upgraded heat from any additional low-temperature source. A steady-state simulation-study with input and output parameters close to reality was conducted. The results lead to an optimized design and partition of heat exchanger area and fluid circuits. The subsequent engineered system-unit allows for several operation-modes, such as double effect and double lift. The chosen design temperatures fit to common ambient heat-sources, new and old buildings and industrial processes, as the heat-input can be lowered to 4 °C and the output can reach 90 °C. Additionally, the system directly provides cold from biomass-combustion with a $BUE_{cold} \approx 1.1$. Based on the simulations, a pilot-plant was manufactured and commissioned in a test-rig. The operation under laboratory conditions showed economically and ecologically sound results, which makes the concept viable for a commercialized realization. Thus, there is need of further development by optimizing the interaction of combustion and system control and reducing heat losses by simplifying the system-setup.

1 Introduction

Completive to wind and solar, biomass represents one of the most important renewable energy resources and already contributes substantially to a climate-neutral energy supply. Although there is further development perspective, for instance regarding residual and waste materials, respecting the available state of the art, the economic potential is limited and almost fully tapped. Therefore, highly efficient usage is eminent.

Beside the use of the energy stored in ligneous biomass for electricity generation, it was particularly the heat supply from district heating stations and smaller scaled boiler, which covered the heat demand in Germany by 10.7% in the year 2016 [1]. For nominal conditions, heat units reach a biomass utilisation efficiency of approximately $BUE_{heat} \approx 0.9$. By application of innovative flue gas condensation, this value rises to $BUE_{heat} \approx 1.1$ [2]. A thermally driven, two-stage heat pump process enables an even better utilisation of the exergy from the biomass. Starting with a simple Proof of Concept in the joint German-Finish SET-plan research project “Solar Heating and Cooling for Northern and Central Europe” [3], the development of the directly biomass-fired absorption heat pump here was continued in cooperation with a biomass boiler manufacturer. The research project focused on an economic and reliable heat pump design and performance tests under lab conditions. This paper describes the basic sorption process design and results of the simulation of the research. The test rig setup as well as defined key figures for testing are shown. Finally, the most important measurement results for nominal operation are presented.

2 Fundamentals and experimental setup

The combination of a biomass combustion and sorption process offers a quite efficient way for low temperature heat supply with a certain share of ambient heat and minimal consumption of electricity. Multi-staging reduces the biomass input significantly. Nevertheless, its pros and cons have to be carefully balanced regarding economic feasibility as well as a simple, robust and reliable system design.

2.1 Advantages of a two-stage heating and cooling system with biomass-combustion

The benefits of multi-stage absorption heat pumps have been theoretically investigated sufficiently and are well known. For instance, Ziegler [4] has shown, that using the driving energy in a cascade leads to a significant higher efficiency. Coming along with that, the feasibility is limited by the necessarily rising temperatures of the driving energy source and of the working fluids. The fluid used in the apparatus presented in this essay is aqueous lithium bromide (H_2O/LiBr) with water as refrigerant. It has a common upper range for application temperatures between 150 °C and 170 °C, regarding rising corrosivity. Carrying out a multistage concept therefore is limited by economical acceptable variety and uncomplicated availability of construction materials. Moreover, an increasing quantity of stages rises the complexity and expense for heat exchangers, piping valves and instruments.

As the refrigerant H_2O limits the evaporation temperature to 1 °C to avoid internal freezing, ambient heat-sources seem to be limited for H_2O/LiBr-heat-pumps. In fact, the potential of ambient heat-sources delivering temperatures higher than 8 °C, such as groundwater, wastewater or geothermal probes is notable. Here it also has to be considered, that in rural areas, where biomass as fuel is more common and available than in cities, these kind of ambient heat-sources also are more probable. Additionally, in current research projects reliable and sufficiently efficient evaporator-systems for modified refrigerants are investigated. Presuming successful research, ambient heat sources delivering energy with temperatures below the freezing point of water could be integrated.

Respecting these constraints, a two-stage concept was chosen for the system presented here as a good compromise of performance, cost and complexity. Regarding the heat ratio ζ as the quotient of net energy and driving energy, the increase in efficiency is evident: Modern absorption single stage heat pumps enable a $\zeta_{SE} \approx 1.8$, relating to the generation of heat. A two-stage type enables values up to $\zeta_{DE} \approx 2.4$.

Commercial two-stage units typically range in capacities of a megawatt. Beside directly gas- and oil-fired systems, an implementation of steam-driven or pressurised hot water is economically justifiable in this higher capacity class. In general, one falls back to single stage hot-water-driven absorption heat pumps for lower capacities. To replace fossil energy sources in smaller systems, the attention has to be turned to waste heat, solar heat or on the best storable, locally available fuel biomass for directly driving absorption heat pumps. Ligneous biomass here succeeds as standardised fuel and its combustion is technically mature.

Without the detour of the initial generation of hot water, a directly biomass-fired two-stage heat pump in the medium capacity range is viable, respecting an increase of efficiency (ζ_{DE} / ζ_{SE}) up to 33%. The additional expenses by purchasing an absorption heat pump (AHP) are even more accommodated for the two-stage system: A rough estimate shows that the capital investment in the biomass direct-fired, two-stage absorption heat pump (bioSHC-system) is nearly the same as for a single stage AHP connected to a biomass-fired boiler.

Additionally, the efficiency of the combustion unit concerning the provided fuel is equal for both systems. The common exhaust temperature for wood firing at nominal operating conditions is set to 160°C or higher, which enables to use most of the smokestacks installed in buildings. Concerning the maximum working-fluid temperatures, the exhaust temperature of the two-stage heat pump-system is similar.

The bioSHC-system theoretically reaches a biomass utilisation efficiency up to $BUE_{heat} \approx 2$ referred to the lower heating value (LHV) of the fuel and the heat from an ambient low temperature reservoir included. With halve of the conventional fuel input providing the same amount of useable heat, emissions (dust, CO2, etc.) may be reduced in the same scale. The following section implicates, that the multi-stage structure induces further advantages regarding variety of operation modes.

2.2 Implemented modes of operation

The bioSHC-system has been developed based on the analysis of appropriate ambient heat sources for absorption heat pumps, so the goal was to utilize the lowest possible temperature of the refrigerant.

Substantially the system consists of three main subsystems - a directly biomass-fired second-stage desorber plus condenser, a single effect absorption heat pump and a pre-fabricated hydraulic-system, which helps for an easy implementation and interaction in buildings and their control systems.

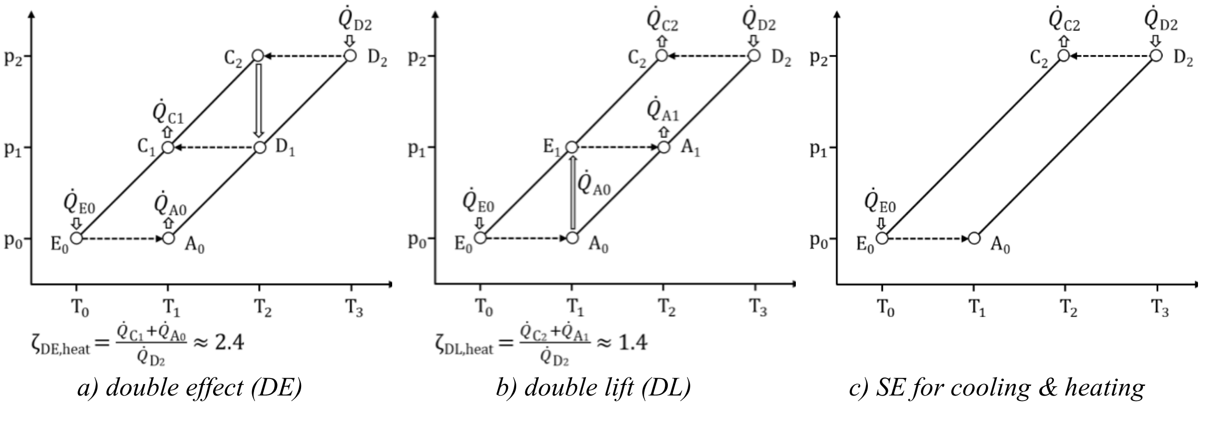

a) double effect (DE) *b) double lift (DL)* *c) SE for cooling & heating*

Figure 1 – schematic diagram of the three main operating modes of the bioSHC-system

The guideline for engineering was the double effect mode (DE). For this operation mode, the realised concept requires six main heat exchangers. The lower four exchangers evaporator (E_0), absorber (A_0), condenser (C_1) and desorber (D_1) are realised as tube bundles in two vessels and form a separate entity, that could be operated as a single stage or single effect-system (SE). A high-temperature-desorber (HTD or D_2) and a second condenser (C_2) are added for building a double effect system (DE). The second desorber D_2 herein is the innovative core piece. It is a directly biomass-fired desorber with a driving capacity of about 50 kW and a combustion power of 55 kW. The cascade of energy-use from the combustion is carried out by coupling C_2 and D_1 via an external heat carrier. In Figure 1a) this external heat transport is displayed as a double line arrow between these main components. The connecting, continuous lines follow the logarithmic depiction of the pressure curve (ordinate) for constant salt concentrations depending on equilibrium-solution-temperatures (abscissa). Dashed lines represent the vapour flow of the refrigerant between the components. Therefore, the resulting four temperature- and three pressure-levels of the bioSHC-system are visible. These levels are quite similar for the three suggested modes of operation. Comparing Figure 1a) and Figure 1b) it can be seen, that the external circuit between C_2 and D_1 allows an additional mode for an efficient and very high temperature-lift, by lifting the heat $\dot{Q}_{E0}$ coupled into the evaporator E_0 two times. This double lift-mode (DL) requires the condenser C_1 to operate as a second evaporator (E_1) and the D_1 as another absorber (A_1) at a higher pressure-level. A further operation mode named “single effect for cooling and heating” is also possible within the bioSHC-system. Figure 1c) shows that in this case, cooling and higher temperatures as in common single effect AHP can be provided at the same time without the need of a middle pressure stage.

3 Results

3.1 Modelling of the heating and cooling system

The shown system-concept was modelled in a component-based simulation on physical property data and balances of mass, sorbent and energy. The steady-state simulation-study with the Engineering Equation Solver (EES) leads to an optimum of heat-and-mass-transfer-area by variation of temperature spread as well as different internal and external hydraulics. The main results of theoretical capability, heat ratio, design temperatures and the biomass utilisation efficiency for the double effect and double lift mode at nominal conditions are given in table 1.

Table 1 – Key figures of the bioSHC-System

Key figure	Abbreviation and/or Equation	Unit	Efficiency mode *double effect mode*	Temperature-lift mode *double lift mode*
chilled water	T_{cold} (supply | return)	°C	4 | 8	4 | 8
heating water	T_{heat} (supply | return)	°C	41 | 31	90 | 70[(a)]
temperature lift	$T_{lift} = T_{heat\ supply} - T_{cold\ supply}$	K	37	86
nominal capacity	$\dot{Q}_{heat}$ | $\dot{Q}_{cold}$	kW	111 | 62	66 | 16
$\zeta^{(b)}_{heat\|cold}$	$\dot{Q}_{heat} \cdot \dot{Q}_{HTD}^{-1}$ | $\dot{Q}_{cold} \cdot \dot{Q}_{HTD}^{-1}$	-	2.22 | 1.23	1.31 | 0.3
$BUE^{(c)}_{heat\|cold}$	$\dot{Q}_{heat} \cdot (\dot{m}_{fuel} \cdot LHV)^{-1}$	-	1.99	1.18
	$\dot{Q}_{cold} \cdot (\dot{m}_{fuel} \cdot LHV)^{-1}$	-	1.10	0.27

(a) Max. 85 °C feasible *(b) Heat Ratio* *(c) Biomass Utilisation Efficiency; Reference lower heating value (LHV)*

As boundary conditions, the maximum allowable salt-concentration and temperature of the solution, external and internal temperatures, realistic heat transfer rates and heat-exchanger-efficiency were set. In addition, the wetting of the tube bundles and therefore the solution- and refrigerant-circuits have been considered based on measurements.

The key figures in table 1 are gained from the series flow-model, which is the required continuous flow of the aqueous lithium bromide fluid passing the HTD first and the desorber D_1 second for regeneration.

Considering that the design-point in practice may not always perfectly match, for example in external conditions, the system has to be resilient especially to changing supply-temperatures of the fluid-circuits. A variation of temperatures and their spread in the cold- or cooling-water shows a low sensitivity regarding the cooling-performance and ζ. As the temperature T_{cold} is varied from 3 °C to 6 °C as well as the temperature-spreads from 3 K up to 10 K, the cooling-capacity and ζ change merely 2% regarding to the nominal conditions. The temperature-variation of T_{heat} from 38 °C to 44 °C and a change in temperature-spreads from 5 K up to 12 K show the same results.

3.2 Developed plant and test-rig setup

As mentioned before, the innovative core piece of the system is the desorber HTD. It was drafted based on an existing combustion chamber geometry. The layout as a pool-desorber with natural circulation enables a homogenous allocation of temperature and solution-concentration. The design of the heat exchanger on the solution-side was based on extensive research.

In the zone of the combustion-chamber a heat flux up to 80 $kW \cdot m^{-2}$ may appear, which will not cause critical wall-temperatures above 180 °C due to best heat transfer resulting from flow-boiling, following evaluations from Riepl [5][6]. Nevertheless, the design of the desorber HTD seems very similar to any standard wood-chip-boiler with flue-tubes, except the built-in components supporting natural convection and vapour flow and the mounted high-temperature-condenser. Therefore, it was fabricated with the conventional methods of a boiler manufacturer. Due to the effective remodelling, the HTD can be produced with similar costs regarding to a commercially available hot-water boiler of the same combustion capacity.

(1) Biomass-fired desorber HTD
(2) Absorption heat pump (AHP)
(3) Storage, supply and scale for biomass-fuel
(4) Control and hydraulic system

Figure 2 – Picture of the system-setup integrated in a HIL-laboratory environment

The single stage absorption heat pump unit (AHP) has been realised for a perfect match to the high-temperature-desorber HTD. As shown in Figure 2 the entire installation of the components was assembled in a laboratory. With the aid of a hardware-in-the-loop-test-rig (HIL), measuring of the bioSHC-system was carried out close to reality.

3.3 Test results

Operational measurements of the bioSHC-system show very good agreement with the simulated process parameters as given in Table 1. Solely the heat and cold output as well as fuel efficiency is lower than expected due to the high ambient heat losses of the HTD setup. In the laboratory tests of the double effect mode, a fuel-related efficiency for heat supply of $BUE_{heat} = 1.7$ could be shown. The heat ratio achieved a very good value of $\zeta_{heat} = 2.21$. Further data from measurements including absolute uncertainties (referred to a 1-σ probability) are given in Table 2.

Table 2 – Measured performance of the bioSHC-System at nominal conditions

Key figure	Unit	Efficiency mode *double effect mode*	Uncertainty (abs.)	Temperature-lift mode *double lift mode*	Uncertainty (abs.)
T_{cold}	°C	5.6 | 9.0	±0.10	5.7 | 8.0	±0.10
T_{heat}	°C	39.9 | 31.3	±0.19	90.2 | 80.0	±0.3
T_{lift}	K	34.4	±0.19	84.5	±0.3
$\dot{Q}_{heat} \mid \dot{Q}_{cold}$	kW	95.7 | 52.3	±3.9 | ±2.1	57.9 | 13.2	±2.6 | ±1.5
$\zeta^{(a)}{}_{heat\|cold}$	-	2.21 | 1.21	±0.12 | ±0.01	1.30 | 0.30	±0.03 | ±0.02
$BUE^{(b)}{}_{heat\|cold}$	-	1.70 | 0.93	±0.07 | ±0.04	1.03 | 0.23	±0.05 | ±0.01

(a) Heat Ratio *(b) Biomass Utilisation Efficiency; Reference lower heating value (LHV)*

The low electrical energy demand of about 1 % of the usable heat $\dot{Q}_{heat}$ is to be emphasised. Emissions (dust, CO) could be kept low and amounted to only about 54 % of the emissions of conventional systems related to the same heat output. The system has potential for optimisation in terms of efficiency. By omitting all installations, sensors and actuators which are not relevant for real-life operation mandatory for scientific purposes, thermal losses could be reduced enormously. In combination with an improved combustion control, another 15% of additional heat output could be provided in the double effect mode.

4 Conclusions and outlook

The presented directly biomass-fired absorption heat pump system nearly doubles the heat-output compared to conventional biomass boilers, fired with ligneous biomass. This was proven by laboratory measurements. Essential precondition is a sufficiently available low temperature heat reservoir (e.g. geothermal probes), feeding the implemented sorption heat pump process. The modular design of the three main components allows for switching between operation modes such as single effect, double effect, double lift or the "single effect for cooling & heating". Thus, a high biomass utilisation efficiency and/or high temperature lift for solely or simultaneous heating and cooling is obtained.

In addition, the system can directly and highly efficient convert biomass energy into useable cold for cooling purposes. Furthermore, the overall very low electricity consumption relieves the electrical grids. The chosen design temperatures fit the requirements of new building-standards but are also appropriate to old buildings. This enables prospective numerous applications in real buildings or industrial processes.

The combination of biomass-combustion and heat pump technology offers further applications such as extracting heat from flue gas by utilisation of condensing. Referring to Hermann [2], cooling the flue gas of a wood chips fired desorber down to 25°C, the gained sensible and latent heat may reduce the required ambient low temperature heat source by 18% in double effect setup and 70 % in double lift setup respectively.

5 Acknowledgment

This research was supported by the German Federal Ministry for Economic Affairs and Energy (BMWi, FKZ 03KB127). We also greatly thank HDG Bavaria GmbH for additional financial support. The authors furthermore thank our colleagues from HDG Bavaria GmbH, especially W. Aich, who provided insight and assisting expertise.

6 List of References

[1] Pelkmans, L. (2018): Germany – 2018 update, Bioenergy policies and status implementation. *Country Reports. IEA Bioenergy: 09 2018,* p. 8

[2] Hermann, T., Geier-Pippig, J., Schweigler, C. (2019): Sorption heat pump for flue gas condensation of biomass-fired boilers. *25th IIR International Congress of Refrigeration, Montréal*

[3] Sipilä, K. Reda, F. Pasonen, R. Löf, A. Viot, M. Pischow, K. Helm, M. Möckl, M. Menhart, F. Kausche, M. Osgyan, P. Streib, G. (2017): Solar heating and cooling in Northern and Central Europe. *VTT Technology 287. ISBN 978-951-38-8510-6. VTT Technical Research Centre of Finland Ltd, Finland,* pp. 69 - 77.

[4] Ziegler, F. (1997): Sorptionswärmepumpen. *Forschungsberichte des Deutschen Kälte und Klimatechnischen Vereins, 1997 (Nr. 57). ISBN 978-3-932715-60-0,* pp. 7, 16, 209

[5] Riepl, M. (2020): Naturumlaufaustreiber für mehrstufige Absorptionswärmepumpen. *Thesis (under preparation), to be submitted at TUM Department of Mechanical Engineering, Technische Universität München, Munich.*

[6] Riepl, M. (2020): Heat Transfer and Flow Characteristics in Thermosiphon Generators of Multi-Stage LiBr/Water-Absorption Heat Pumps. *ISHPC 2021 proceedings – online pre-conference 2020, DOI: 10.14279/depositonce-10430.2, Berlin,* pp.119-123.

Absorption Chiller Control for 100% Turndown

Anand Gopalakrishnan[1] and Makar Ellen[1]

[1]*Energy Concepts Company, 627 Ridgely Ave, Annapolis, MD 21402, USA.*

Abstract:
The Absorption Refrigeration Cycle Turbine Inlet Chiller (ARCTIC) system can chill the inlet air of a combustion turbine to maintain optimum performance at all ambient temperatures. However, to optimize performance and yet avoid bell-mouth icing, the inlet air temperature has to be maintained within a narrow range throughout the year. These considerations require strict control of the chiller performance over a wide range of ambient conditions and down to 100% turndown. This paper summarizes the controls strategy and presents field performance data for a 600RT chiller for a Solar Turbines Mars 100 turbine.

1 Introduction

Ambient conditions greatly affect combustion turbine performance. For a MARS 100 turbine, power output drops nearly 17% as ambient temperature increases from 7°C to 35°C. Turbine efficiency also degrades by 4% on hot days with corresponding increase in carbon emissions. The Absorption Refrigeration Cycle Turbine Inlet Chiller (ARCTIC) system, shown in Fig. 1, uses exhaust heat–powered absorption refrigeration to provide inlet air chilling to the turbine. With ammonia as the refrigerant, the ARCTIC can optimize turbine performance by maintaining inlet air temperature at 7.2°C even on the hot days. The ARCTIC system is comprised of five major assemblies: Turbine Inlet Air Coil (TIAC); Heat Recovery Vapor Generator (HRVG); Condenser; Cooler; and the ARCTIC skid (containing rectifier, absorber, SHX, RHX, and pumps). The Condenser and Cooler are dry air-cooled compared to the evaporatively cooled ARCTIC presented by Anand et al. [1]. The TIAC is also chilled by an intermediate chilled water loop compared to direct refrigerant chilling [1].

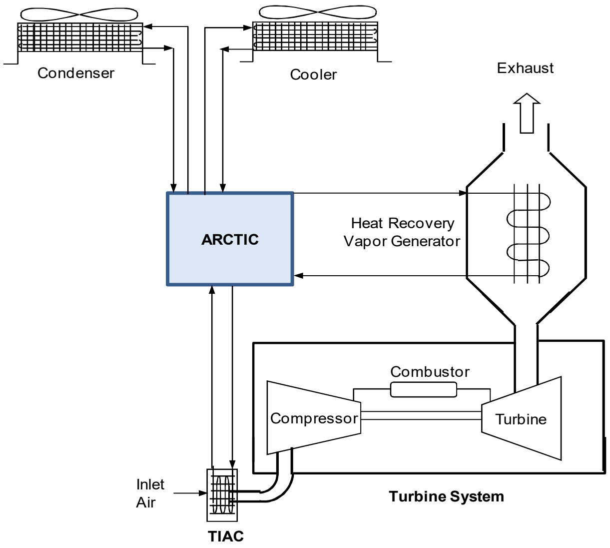

Figure 1. ARCTIC System Diagram

Economics and chiller performance guarantees require maintaining the inlet air temperature below a specified maximum temperature throughout the year. With ammonia as the refrigerant, the ARCTIC can provide very low chilling temperatures. However, two external factors limit the minimum inlet air temperature. First, some turbines such as the GE LM6000 have an optimum inlet air temperature [2]. Chilling the air below this temperature will in fact degrade turbine performance. Second, adiabatic flow acceleration of the cold saturated air in the turbine bell-mouth results in a further drop in air temperature based on the concept of stagnation enthalpy. This can lead to icing conditions in the bell-mouth [3,4,5]. The ice can break off and be ingested by the turbine causing severe damage and subsequent failure.

Thus, the inlet air temperature must be maintained within a narrow range with the upper limit set by economics and performance guarantees and the lower limit set by turbine characteristics and icing considerations. These specified inlet air temperature conditions must be met even as the ambient temperature varies from over 35°C (95°F) to below 8.9°C (48°F), as the humidity varies from 100% to below 20%, and correspondingly as the chilling load varies from 100% down to zero percent load. These considerations require strict control of the chilled air temperature over a wide range of operating conditions.

2 Controls Summary

A simplified schematic of the major components and controls is shown in Figure 2. The system is designed to operate completely automatically with no need for operator attendance. The ARCTIC senses when the gas turbine starts and automatically comes ON. When the gas turbine shuts down, ARCTIC automatically shuts down after a short cool-down period. When the ARCTIC System is operating, the several controls become active. The various controls set points for these controls were obtained by detailed simulation of ARCTIC performance over a wide range of ambient conditions. These parameters can be adjusted remotely, if needed, based on actual performance with varying ambient or plant operating conditions.

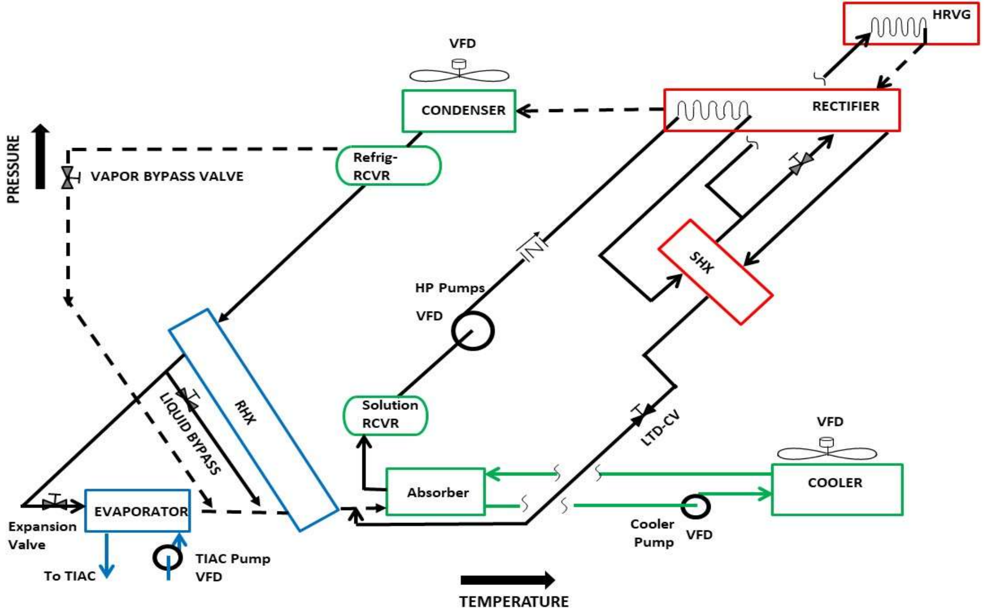

Figure 2. Schematic of ARCTIC Components and Controls on Pressure, Temperature Coordinates

A. Solution pumps- VFD controls speed of solution pumps to accommodate startup sequence and changes in load and ambient temperatures.

B. Rectifier level control (LTD-CV) - This is a motor operated valve which uses Rectifier level as a control parameter to control letdown flow. This control occurs in a standard industrial stand-alone electronic module.

C. Refrigerant flow control-expansion valve controls superheat at the exit of the evaporator. This control occurs in a standard industrial stand-alone electronic module.

D. Condenser fan speed- VFD speed logic is stand-alone in Condenser control panel and controls to high side pressure set point. A set point of 14.8 Bar (200 psig) is provided by the ARCTIC PLC.

E. Cooler fan speed- The cooler fan VFD controls coolant temperature at the outlet of the coolers. There are two Cooler bays having independent temperature measurement and fan speed control. The outlet temperature setpoint is 41.4°C (106.5°F).

F. TIAC loop controls- Maintaining desired turbine inlet air temperature is critical. Detailed TIAC coil model and loop analysis was performed to develop and specify these controls [6,7,8]. These controls can be considered as stand-alone controls except for the specification of the Evaporator chilling temperature.

G. Cooler water circulating pump speed - controlled to maintain desired low side pressures and thereby the Evaporator temperature. Desired LP pressure setpoint changes with ambient temperature. Pump speed is adjusted according to low side pressure (LP)- lower speed to increase LP pressure for cooler ambients.

H. Vapor bypass control valve - Its primary function is to compensate for the low refrigeration duty of the TIAC on cooler days. Its normal control function is to open to a fixed position, proportional to the ambient wet bulb temperature – more open on colder ambient temperature. The valve opening varies linearly from 0% open at ambient wet bulb (WB) of 24.4°C (76°F) to 45% open at WB of 7.2°C (45°F), and remains at 45% open at lower ambient temperatures.

I. Liquid bypass control valve - during low loads, part of the refrigerant liquid is bypassed from the high side to the low side. Its primary function is to compensate for mismatch between the relatively fixed heat input to ARCTIC from the HRVG, and the highly variable refrigeration load of the TIAC coil. On cooler days the refrigerant flow into the Evaporator is much lower than the refrigerant flow out of the rectifier; the liquid and vapor bypasses makes up for the difference. The liquid bypass valve normally keeps the refrigerant receiver level at a specified set point. The level set point varies linearly with ambient WB.

On colder days, the vapor bypass ensures enough vapor flow to the absorbers enabling proper flow regimes in the absorbers and adequate loading of the Coolers; whereas the liquid bypass ensures enough condenser load and turndown control.

3 Field Performance

Since commissioning at the end of summer 2020, the ARCTIC has provided inlet air chilling over a range of ambient conditions. Typically, the inlet air/TIAC air leaving dry bulb (LDB) is maintained at 7.2°C (45°F). On cooler days, if the inlet air temperature drops to 5.6°C (42°F) the chilled water pump turns OFF automatically to prevent further chilling and bell-mouth icing. On colder days, the ARCTIC continues operating till the ambient temperature drops below 1.7°C (35°F) and then turns OFF. The chiller turns back ON when the 8-hr average inlet air temperature exceeds 10°C (50°F).

Figure 3 shows ARCTIC performance in the chilling mode on a cooler day when many of the controls are active. Ambient dry bulb (EDB) temperature was initially about 6.7°C (44°F) and the WB was 5°C. The chiller was operating with minimal chilling load and the inlet air temperature is nearly same as ambient temperature. Around 1:28 AM the inlet air temperature dropped below 5.6°C (42°F). The TIAC pump turned OFF in order to stop chilling the air due to icing concerns. The ambient temperature dropped to a minimum of 3.5°C (38°F). The chiller kept operating overnight. The inlet air temperature varied between 3.5°C and 7.7°C, the lower temperature being actual ambient temperature without any chilling. The minimum chilling load was zero, i.e. the chiller operated with 100% turn down. Only the HRVG heat input had to be rejected by the Condenser and Coolers with the loads being regulated by the vapor and liquid bypasses. Due to the reduced loads the fan speeds decreased, with the Condenser fans nearing zero speed and Cooler fan speeds dropping to 15 Hz.

With the morning sun rise, the ambient temperature started increasing. The TIAC pump turned back on at minimum speed when the inlet air temperature reached 7.5°C at 8:42 AM. The ambient EDB peaked at 21.7°C (71°F) around 3:00 PM with a maximum WB of only 12°C. The maximum chilling load for this mild day was 447 kW (127 RT). With higher EDB and TIAC load the Condenser and Cooler loads and fan speeds increased and the vapor and liquid bypasses decreased.

The Evaporator chilling temperature varies with low side pressure (LP) which is directly controlled by cooler pump speed. However, in an absorption system the pressure is also dependent on solution temperature and concentration which are controlled by refrigerant level and cooler fan speed. There is an interdependence between these controls and the TIAC pump speed as shown in the performance data.

4 Conclusions

This article presents initial operating data of the Absorption Refrigeration Cycle Turbine Inlet Chiller (ARCTIC) system providing inlet air chilling for a MARS 100 turbine. A key feature of the ARCTIC is the controls strategy. The controls help maintain the inlet air temperature at desired setpoint to maximize turbine capacity and efficiency during most of the hot/warm days, accommodates 100% turndown, helps maintain performance guarantees, and in avoiding TIAC operation in icing conditions.

5 List of References

[1] Erickson, D. C., G. Anand, E. Makar (2015): Absorption Refrigeration Cycle Turbine Inlet Conditioning. *Int. Journal of Air-Conditioning and Refrigeration*, vol. 23, No. 01.

[2] Buecker, B., and Mieckowski, C. M (2012): Turbine Inlet Air Cooling Cutting Edge Technology. *Power Engineering*, Vol. 116, # 4.

[3] Stewart, W. E. (2001): Condensation and icing in gas turbine systems: Inlet air temperature and humidity limits. *ASHRAE Transactions* vol. 107(1), pp. 887-891.

[4] Stewart, W. E. (1999): *Design guide: Combustion turbine inlet air cooling systems*. ASHRAE.

[5] Maas, D. M., and McCown, N. M. (2007): Turbine Inlet Ice Related Failures and Predicting Inlet Ice Formation. ASME. Turbo Expo: Power for Land, Sea, and Air, *Volume 4: Turbo Expo 2007, Parts A and B*:1, pp. 531-1543.

[6] Anand, G. and Makar, E. (2021): Modified Chilled Coil Model Development and Application to Turbine Inlet Air Cooling. *Int. Journal of Air-Conditioning and Refrigeration*, Vol 29, No. 1, 2150006-1–10.

[7] Anand, G. and Makar, E. (2021): Chilled Coil Performance Control and Application to Turbine Inlet Air Cooling. *Int. Journal of Air-Conditioning and Refrigeration*, Vol 29, No. 2, 2150016-1–8.

[8] Anand, G. and Makar, E. (2021): Chilled Coil Control and Field Performance Verification for Turbine Inlet Air Chilling. *Int. Journal of Air-Conditioning and Refrigeration*, Vol 29, No. 2, 2150019-1–10.

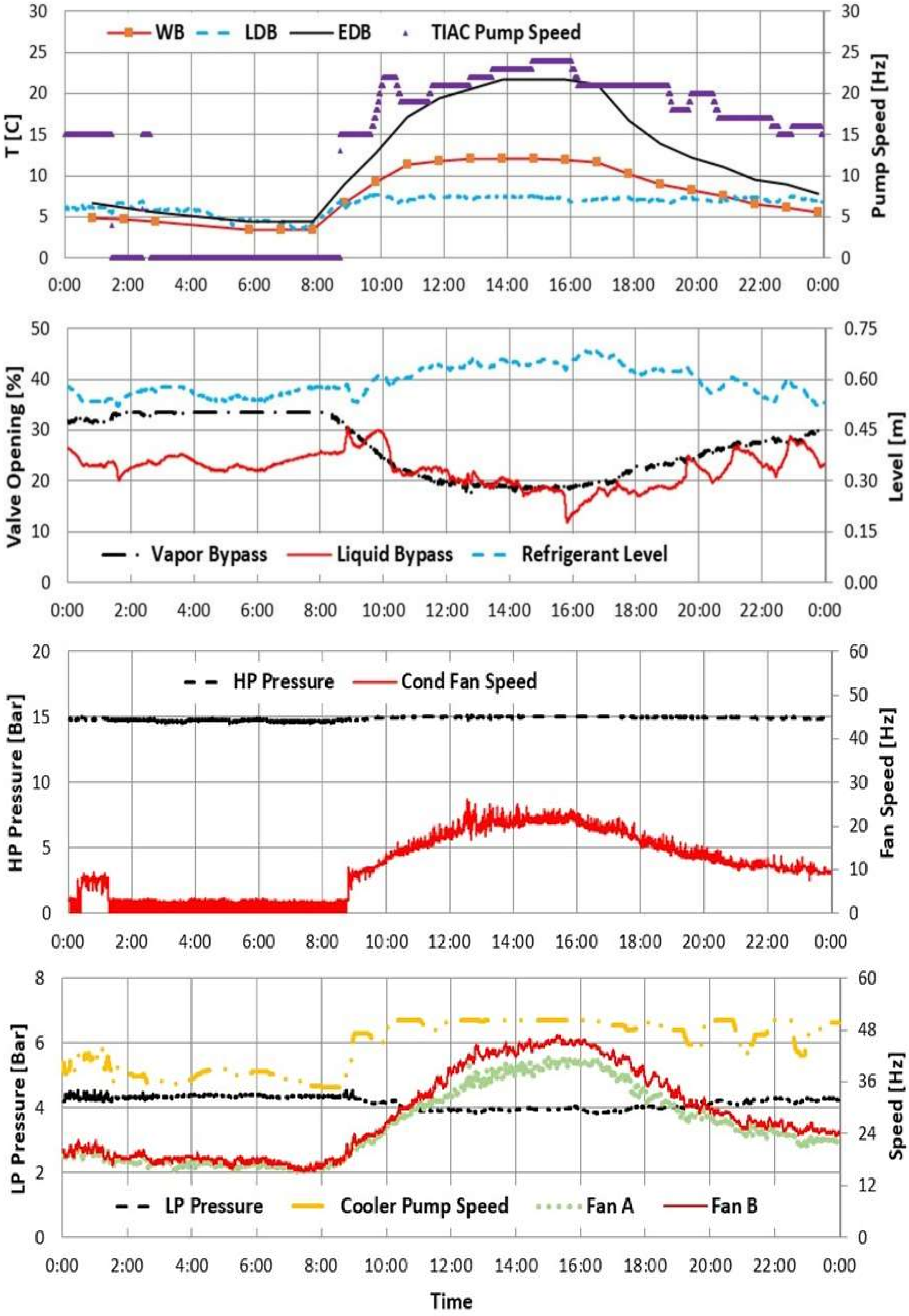

Figure 3 – ARCTIC Cold Day Performance and Control

Experimental Investigation on Thermal Management of the Mobile Devices Based on Moisture Sorption-Desorption Process

H.R. Liu, B.J. Li, C.X. Wang, R.Z. Wang*

Institute of Refrigeration and Cryogenics, Shanghai Jiao Tong University, Shanghai 200240, China.
**Correspondence author: rzwang@sjtu.edu.cn*

Abstract:

The continuous improving performance of the mobile devices urges a larger capacity of heat dissipation, while its improvement is encountering a bottleneck due to the inherent property of the natural convection and radiation. Fortunately, the recent development of a novel passive cooling strategy, moisture sorption-desorption process, offers new opportunities for enhancing heat dissipation by involving the mass transfer process. In this paper, we demonstrate the practice of the moisture sorption-desorption cycles on a state-of-art commercial smartphone. About 1.7 g MIL-101(Cr) is coated on the back surface of the smartphone, and different benchmarks, including the graphics-intensive gaming applications are tested. The experimental results show that an extra 0.6 W heat dissipation capacity can be achieved, which accounts for about 10% of the total value. Furthermore, a maximum 25% performance improvement in gaming benchmarks is obtained, strongly proving the effectiveness of the proposed cooling method.

1 Introduction

Thermal management has been one of the major challenges for electronic devices [1]. And for mobile devices, since using fans is usually not a viable solution [2], its heat dissipation capacity is hard to improve due to the inherent property of natural convection and radiation. Currently, there are mainly two directions to improve the heat dissipation of the mobile devices: improve the temperature uniformity of the exterior surfaces and energy storage technology. Limited by the user experience, the temperature of devices surface (skin temperature) should be controlled under a certain threshold [3] (generally 45 °C), thus the only way to improve the heat transfer at the devices boundary is to improve the temperature uniformity, and the heat dissipation capacity will reach its upper boundary once the distribution of the surface temperature is uniformed. Materials with high thermal conductivity, such as graphene films [4], cubic boron nitride (c-BN) [5], and isotopically purified diamond [6], can help to improve the temperature uniformity and has become a hot topic in the thermal management of electronics [7]. Ultra-thin heat pipes [8] and vapor chambers [9] can also achieve an equivalent high thermal conductivity and be considered in mobile devices. On the other hand, the intermittent use of mobile devices offers the opportunity to use energy storage technology such as phase change materials (PCMs) [10] to temporarily improve the power consumption. But the heat transfer at the devices boundary is still limited by natural convection and radiation.

Recently, with the development of solid desiccant materials, a novel passive cooling strategy, moisture sorption-desorption process, has been widely discussed. Researches have shown its successful use in the field of electronics [11], photovoltaic panels [12], and battery thermal management [13]. In general, when the device is operating, the solid desiccant materials will absorb the waste heat and generate the desorption process, and the desiccant will capture the moisture from the air when the device is idle (cooled). The abovementioned desorption process intrinsically enhances the heat transfer rate by involving the mass transfer process, providing tremendous potential in helping the mobile devices breaking the heat dissipation boundary caused by the threshold of the skin temperature. In this paper, we demonstrate the practice of the moisture sorption-desorption cycles on a state-of-art commercial smartphone. The experimental set-up and results will be discussed below.

2 Experimental Set-up

The schematic illustration of the desiccant coating and the direction of heat and mass transfer are shown in *Figure 1 (a)*. In particular, about 1.7 g (containing ~20 wt % binder) MIL-101(Cr) powder is coated on a 50μm-thick copper substrate. This copper substrate is then pasted on the back surface of the mobile devices by thermal interface materials (TIMs). In our experiment, four such cooper substrates with MOF coating, with a total area of 63cm^2, are attached to a state-of-art commercial smartphone (Mi 10 Ultra), as shown in *Figure 1 (d)*. The water sorption isotherms of MIL-101(Cr) measured at 25 °C are shown in *Figure 1 (b)*, indicating the water uptake of about 1.05 g/g in a typical ambient condition (25°C, 60%). The experimental condition is shown in *Figure 1 (c)*, the mass change is obtained by a precision electronic balance with a resolution of 10 mg. Three thermocouples (K-type) are attached at the back surface of the smartphone (shown in *Figure 1 (d)*) and are connected to a data logger. These thermocouples from top to bottom are denoted as T_{skin}-*2*, T_{skin}-*1*, and T_{skin}-*3*, respectively. Besides, the temperature distribution of the back surface is recorded by an infrared camera. Furthermore, the temperature of the system-on-chip (SoC), the frames per second (FPS), and the power consumption of the smartphone are measured by its internal sensors and be further recorded by a commercial software called PerfDog. Before experiments, the smartphone with MOF coating is initially exposed to the environmental condition at 25 °C and RH 60% until reaching both temperature and mass equilibria. All experiments are conducted at an environment-controlled chamber with the swings of temperature and RH below 0.5 °C and 2%.

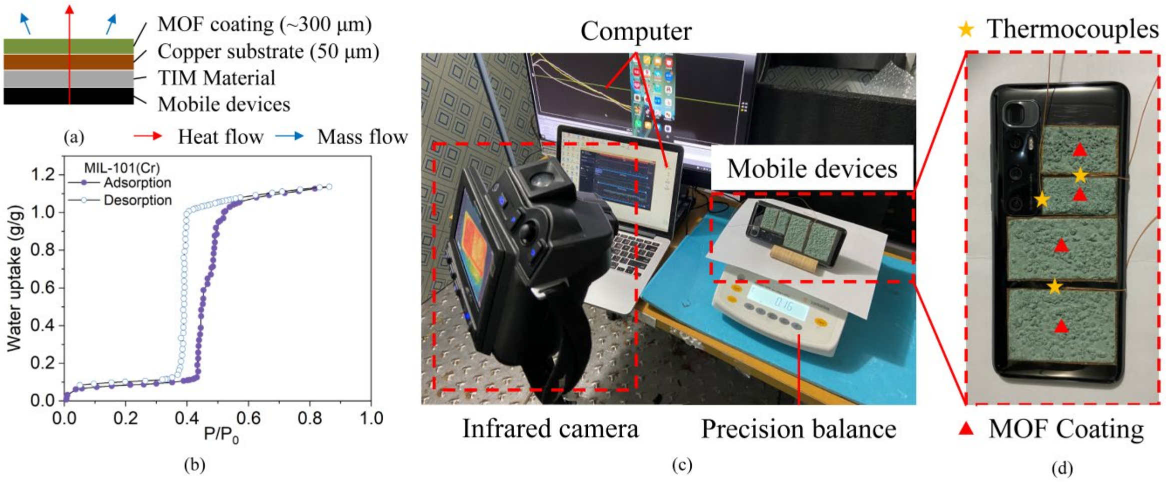

Figure 1 Experimental set-up and property of MIL-101(Cr)

3 Results

A professional benchmark (AnTuTu) and a popular graphics-intensive gaming application (Genshin Impact) are considered to validate the effectiveness of the proposed cooling strategy. In particular, three test scenarios are employed on the platform (Mi 10 Ultra) with MIUI 12.0.13 system, including 55-min AnTuTu (6 continuous cycles), 65-min Genshin, and 95-min Genshin, as shown in *Figure 2.* For comparison, the same tests are run on both the device with bare surface and the device with MOF coating. The temperature, performance, and power consumption of the devices are shown in *Figure 2*.

Due to the feedback control strategy already existed in commercial smartphones, such as dynamic power management (DPM) and dynamic voltage-frequency scaling (DVFS) [14], the extra heat dissipation caused by MOF coating is reflected in the increase of power consumption and performance, instead of the decrease of the temperature discussed in previous researches [11-13]. In order to eliminate the influence of different initial conditions and corresponding DVFS strategy, only the performance at steady state (the gray shadow in *Figure 2*) is taken into account. As shown in *Figure 2 (a, d, g)*, the skin temperature of the devices with the MOF coating is almost the same as it of the baseline, while the SoC temperature with the MOF coating has a little increase due to the improvement of the power consumption. Besides, the power consumption of three test scenarios and their frequency distribution are shown in *Figure 2 (b, e, h).* Compared with the baseline situation, the average power consumption (measured by the current and voltage sensors at the battery of the smartphone) is increased by about 0.57 W, 0.61 W, and 0.6 W, respectively. Furthermore, the performance of three scenarios, evaluated by normalized score (for AnTuTu) and FPS (for Genshin), are presented in *Figure 2 (c, f, i)*, showing an average 9%, 25%, and 19% performance improvement compared with the baseline situation.

The mass change measured by electronic balance and the corresponding transient cooling power is shown in *Figure 2 (j)* and *(h)* respectively. The average improved power consumption due to the moisture evaporation is 0.556 W, 0.629 W, and 0.563 W respectively in our three test scenarios. Although similar, the power consumption improvement evaluated by mass change rate has a little difference with it evaluated by the power consumption of smartphone battery obtained by PerfDog software due to the heat capacitance and deviation caused by curve fitting and measurement accuracy. Besides, the maximum mass change of the desiccant coating is about 1.22 g obtained in the 95-min Genshin test scenario. Considering about 1.7 g (containing ~20 wt % binder) MIL-101(Cr) powder is coated, the overall water uptake of the desiccant coating is 0.72 $g_{water}/g_{coating}$. Furthermore, in the scenario of 95-min Genshin, the moisture contained in the desiccant coating is used up in the first 87 minutes (seen in *Figure 2 (j)*), resulting in a sudden decrease in the power consumption and performance (seen in *Figure 2 (h, j)*). At the stage of 87-95 min, the average power consumption is about 5.8W, showing little deterioration compared with the baseline situation. As a result, although the complete-desorption desiccant coating will bring extra thermal resistance [11], it has an ignorable negative impact due to complicated heat transfer and temperature control systems in practical mobile devices.

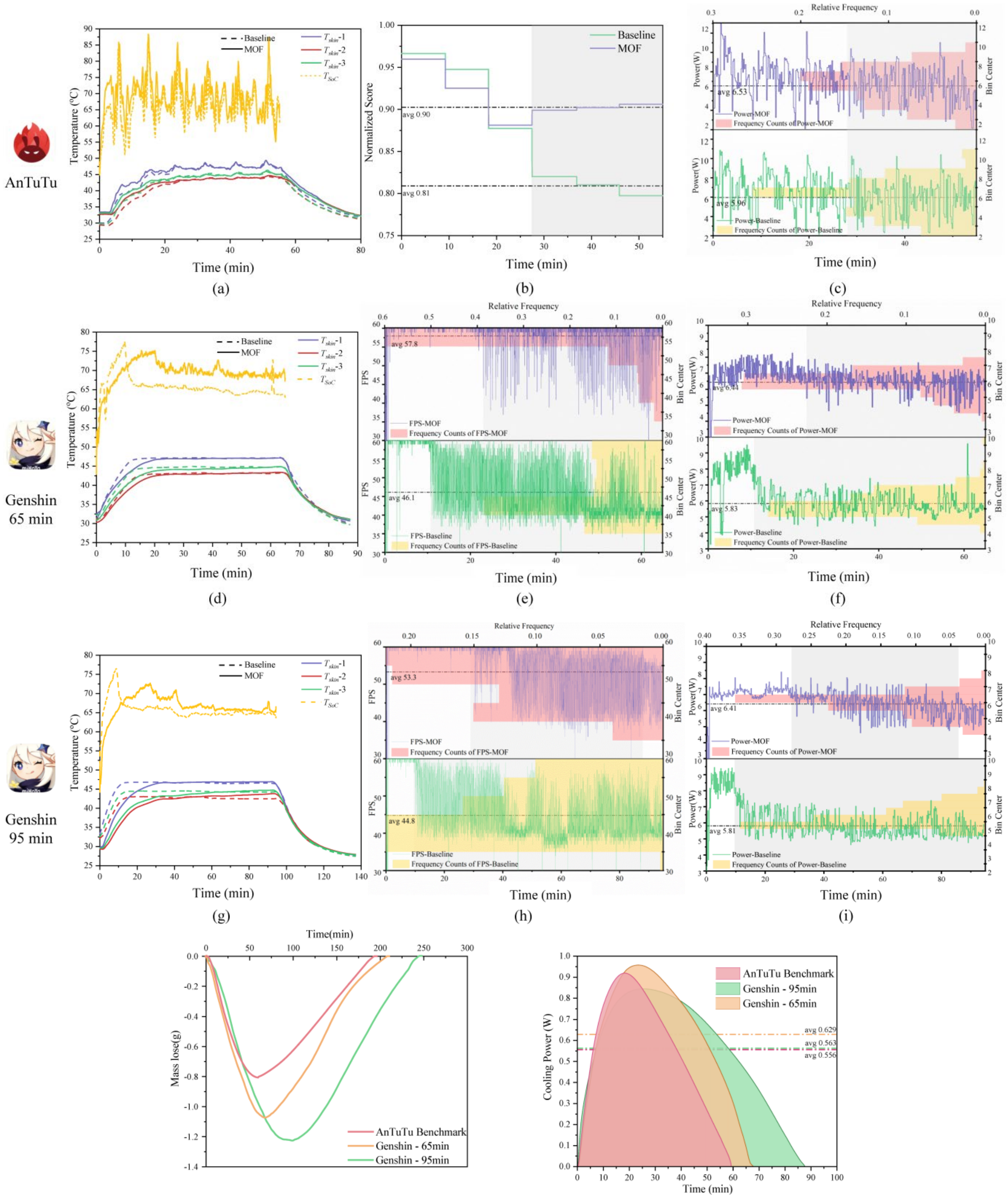

(a) (b) (c)

(d) (e) (f)

(g) (h) (i)

(j) (k)

Figure 2 - The temperature (a, d, g), performance (b, e, h), power consumption of the smartphone (c, f, i), mass change (j) and the transient cooling power derived from the desorption rate (k)

4 Conclusions

In this paper, we demonstrate the practical use of the moisture sorption-desorption process on mobile devices. The results show that an ultra-thin MIL-101(Cr) coating can achieve an extra 0.6 W heat dissipation capacity, namely a 10% improvement of the start-of-art smartphone. In our test scenarios, this improvement can lead to a maximum 25% performance increase (measured by FPS) when running the graphics-intensive gaming applications. The moisture sorption-desorption process can break through the limitation of heat dissipation capacity caused by natural convection and radiation, providing new opportunities for the cooling of mobile devices.

5 List of References

[1] van Erp R, Soleimanzadeh R, Nela L, et al. Co-designing electronics with microfluidics for more sustainable cooling[J]. Nature, 2020, 585(7824): 211-216.

[2] Bhat G, Singla G, Unver A K, et al. Algorithmic optimization of thermal and power management for heterogeneous mobile platforms[J]. IEEE Transactions on Very Large Scale Integration (VLSI) Systems, 2017, 26(3): 544-557.

[3] Chiriac V, Molloy S, Anderson J, et al. A figure of merit for mobile device thermal management[C]//2016 15th IEEE Intersociety Conference on Thermal and Thermomechanical Phenomena in Electronic Systems (ITherm). IEEE, 2016: 1393-1397.

[4] Kim K S, Zhao Y, Jang H, et al. Large-scale pattern growth of graphene films for stretchable transparent electrodes[J]. Nature, 2009, 457(7230): 706-710.

[5] Tian Y, Xu B, Yu D, et al. Ultrahard nanotwinned cubic boron nitride[J]. Nature, 2013, 493(7432): 385-388.

[6] Wei L, Kuo P K, Thomas R L, et al. Thermal conductivity of isotopically modified single crystal diamond[J]. Physical Review Letters, 1993, 70(24): 3764.

[7] Moore A L, Shi L. Emerging challenges and materials for thermal management of electronics[J]. Materials today, 2014, 17(4): 163-174.

[8] Tang H, Tang Y, Wan Z, et al. Review of applications and developments of ultra-thin micro heat pipes for electronic cooling[J]. Applied energy, 2018, 223: 383-400.

[9] Huang G, Liu W, Luo Y, et al. A novel ultra-thin vapor chamber for heat dissipation in ultra-thin portable electronic devices[J]. Applied Thermal Engineering, 2020, 167: 114726.

[10] Wu S, Li T, Tong Z, et al. High‐performance thermally conductive phase change composites by large‐size oriented graphite sheets for scalable thermal energy harvesting[J]. Advanced Materials, 2019, 31(49): 1905099.

[11] Wang C, Hua L, Yan H, et al. A thermal management strategy for electronic devices based on moisture sorption-desorption processes[J]. Joule, 2020, 4(2): 435-447.

[12] Li R, Shi Y, Wu M, et al. Photovoltaic panel cooling by atmospheric water sorption–evaporation cycle[J]. Nature Sustainability, 2020, 3(8): 636-643.

[13] Xu J, Chao J, Li T, et al. Near-Zero-Energy Smart Battery Thermal Management Enabled by Sorption Energy Harvesting from Air[J]. ACS Central Science, 2020, 6(9): 1542-1554.

[14] Prakash A, Amrouch H, Shafique M, et al. Improving mobile gaming performance through cooperative CPU-GPU thermal management[C]//2016 53nd ACM/EDAC/IEEE Design Automation Conference (DAC). IEEE, 2016: 1-6.

Thermodynamic and economic analysis of an improved absorption refrigeration system for the LNG precooling process to recover the flue gas and jacket water

Bai, Yin[1,2], Lu, Ding[1,2], Liu, Zijian[1,2], Sun, Shoujun[1,2], Gong, Maoqiong[1,2,*]

[1] *Key Laboratory of Cryogenics, Technical Institute of Physics and Chemistry, Chinese Academy of Sciences, Beijing 100190, China*

[2] *University of Chinese Academy of Sciences, Beijing 100049, China,*

**Corresponding author, Tel & Fax: +86-010-82543728, E-mail: gongmq@mail.ipc.ac.cn*

Abstract: The absorption refrigeration system is a waste heat recovery technology, which could be applied in the precooling process of LNG (liquified natural gas) stations to reduce energy consumption. In order to improve energy utilization efficiency and cooling capacity, this paper proposes an improved absorption system with high-temperature and low-temperature generators introduced, where both the high-temperature flue gas and low-temperature jacket water are recovered, respectively. By flowing part of the solution to the low-temperature generator, the system could recover low-grade heat sources, and the split ratio is optimized by the heat capacity of the two sources. Given the specific heat sources from the LNG plant with daily natural gas production of 30,000 m^3, simulation result shows that the proposed system could achieve cooling energy of 333.7 kW with the optimal split ratio of 0.6, which is 70% higher than that of the single-effect system. Economic analysis shows that adopting the proposed system to replace the compression system for the precooling process could save 432,710 CNY per year. The payback period is 1.9 years, which is 0.1 and 2 years shorter than that of the single-effect and single-effect/double-lift (SE/DL) absorption systems, respectively, indicating its promising perspective in the application.

1 Introduction

Liquefied Natural Gas station consumes a large amount of energy during the precooling and liquefication process. For some LNG stations far away from the electric grid, the gas engine is adopted to produce the required power, where an amount of heat is discharged to the atmosphere directly via flue gas, jacket water, etc. Some studies pointed out that the heat-driven absorption refrigeration system (ARS) is a proper way to replace the compression refrigeration cycles in the precooling process of LNG [1], which could produce great energy-saving benefits. Paul et al. analyzed the potential replacement of propane chillers with the absorption system in the precooling process. It is found that the system could save 1.9 MW of electric consumption from a 9 MW power generation process [2]. Mehdi et al. introduced a new process configuration for the LNG process, where the vapor compression cycle was replaced with an ammonia-water absorption refrigeration system. The numerical results showed that the power consumption of the station could be reduced by 31% [3]. He et al. studied an absorption refrigeration system using zeotropic R134a+R23 refrigerant for the precooling process. By utilizing exhaust engine heat with a temperature of 145 ℃, the absorption system obtained the evaporation temperature of -30 ℃ with a theoretical COP of 0.47 [4]. However, most of the systems mentioned above are single-effect systems driven by high-temperature flue gas, which are not suitable for recovering multiple heat sources with different grades.

It should be noted that recovering multiple heat sources of different temperatures is vital to increasing energy utilization efficiency. In order to improve the efficiency of the direct-fired absorption system, Lu et al. proposed a novel system where the heat from the combustor and flue gas is utilized in the generator and intermediate evaporator, respectively [5]. Wang et al. introduced a mix-effect absorption system for air-conditioning, where the waste heat in the flue gas and jacket water is recovered [6]. Yan et al. studied a novel system that combined the double-lift and single-effect (SE/DL) system to obtain a large temperature utilization span of the exhaust gas [7]. The study pointed out that the SE/DL system could be applied to the multiple heat sources recovery, but such work was not specifically analyzed. In addition, the double-lift vapor exchange (VX) systems with two generators are proposed to recover low-grade heat sources, while few researches paid attention to recovering two kinds of heat sources. Aiming at improving energy efficiency and cooling capacity, this paper proposes an improved VX absorption refrigeration system to recover the high-temperature flue gas and low-temperature jacket water. Given the specific data of heat sources from an LNG station with daily production of 30000 m^3, the operation parameters of the proposed system are optimized. Compared with the compression system, single-effect system, and SE/DL system, economic analysis is carried out to show the application potential of the proposed system.

2 System description

LNG stations usually contain two cooling processes: the main cooling and precooling process. Conventional LNG station uses the compression system to precool the natural gas and refrigerant of the main cooling process, which is shown in Figure 1. This paper proposes an improved VX absorption refrigeration system to replace the compression system for the precooling process in LNG, which could recover the waste heat from the flue gas and jacket water to increase energy efficiency. The electrical power demand is about 600 kW/h for an LNG plant with daily natural gas production of 30000 m^3 in the Ordos in China. The parameters of the waste heat, including the flue gas and jacket water, from the ICE Jenbacher JGS312, are shown in Table 1. The absorption and condensation temperature of the absorption system is set as 31°C, determined by the air temperature in summer. The cooling temperature of the precooling process is required to be -15°C. For the single-effect system driven by flue gas, the generation temperature usually varies from 120~170 °C. Therefore, the temperature of the generator driven by flue gas is set as 165 °C in this paper. The temperature of the generator driven by the jacket water is set as 85 °C. The working conditions are summarized in Table 2.

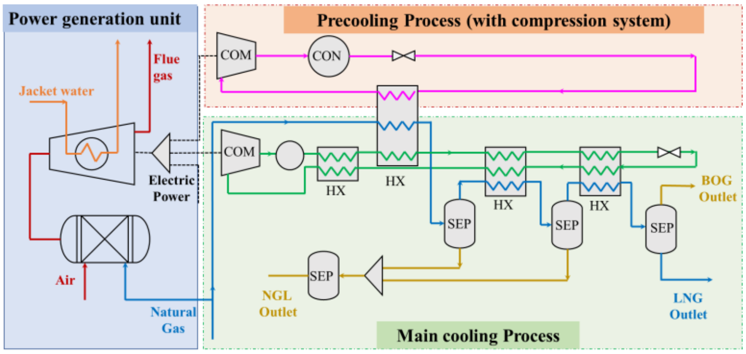

Figure 1 –Schematic diagram of the LNG process

Table 1 –Parameters of the waste heat from flue gas and jacket water.

Waste heat source	Mass flow (kg/h)	Discharged temperature ℃
Waste flue gas	3387	454~
Jacket water	22656	90~74

Table 2 – Baseline working conditions of the absorption system.

Item	Temperature /℃
Generation temperature of HTG	165
Generation temperature of LTG	85
Absorption and condensation temperature	31
Evaporation temperature	-15

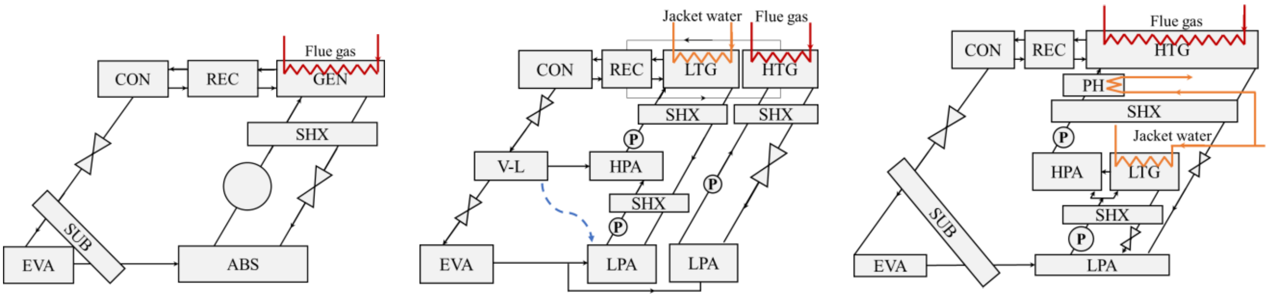

GEN:generator; REC:rectifier; CON:conderser; EVA:evaporator; SUB:subcooler; ABS:absorber; SHX:solution heat exchanger; HPA:high-pressure absorber; LPA:low-pressure absorber; P:pump

a) Single -effect system *b) Single -effect/double-lift system* *c) Improved Vaper exchange system*

Figure 2 –Different types of the absorption refrigeration system

Figure 2 shows the three types of absorption systems, including the single-effect system, the SE/DL absorption system, and the proposed system. The single-effect system has one generator, and it could not make sufficient use of the low-grade heat sources. Therefore, only flue gas is recovered for the single-effect system. The SE/DL system and the proposed system have two generators (HTG and LTG) where the flue gas and jacket water is recovered, respectively. For the proposed system, waste heat carried by the jacket water is recovered in the LTG and the pre-heater (PH). Some major assumption of the work are given as follows:

1) The system runs in a steady state. Heat losses to the surroundings and pressure drops along the pipelines are neglected.
2) The refrigerant leaving the condenser, and the solution leaving the generators and absorbers are saturated.
3) The subcooling degree of the SUB is 5 ℃. The pinch temperature of the solution heat exchanger is 5 ℃, and the pinch temperature of the flue gas and jacket water to the solution is 20℃ and 5℃, respectively.

The COP and exergy efficiency are two significant parameters to evaluate the thermodynamic performance, which is given as follow:

$$COP = \frac{Q_{\mathrm{e}}}{Q_{\mathrm{HTG}} + Q_{\mathrm{LTG}} + Q_{\mathrm{PH}}} \tag{1}$$

$$\eta_{\mathrm{ex}} = \frac{E_{\mathrm{e}}}{\Delta E_{\mathrm{flue}} + \Delta E_{\mathrm{jacket\ water}} + E_{\mathrm{pump}}} \tag{2}$$

Where Q_{e} and E_{e} are the cooling capacity and cooling exergy of the system. Q_{HTG}, Q_{LTG}, and Q_{PH} are the heat load of the HTG, LTG, and PH. $\triangle E_{\mathrm{flue}}$ and $\triangle E_{\mathrm{jacket\ water}}$ are the inlet and outlet exergy differences of the flue gas and jacket water. E_{pump} is the electric consumption of the pumps.

3 Results

3.1 Influence of the split ratio

For the proposed system, part of the solution from the LPA enters the LTG to recover the low-grade heat from the jacket water. Therefore, the split ratio of the solution entering the LTG is a significant parameter affecting the system performance. As the split ratio rises, more solution enters the LTG with more ammonia vapor generated, which would be absorbed by the HPA to produce the richer solution. As shown in Figure 3, the concentration of the rich solution increase from 0.43 to 0.91 as the split ratio increase within the range of 0 to 0.99. The intermediate pressure corresponds to the saturated pressure of the rich solution produced in the HPA, and thus the intermediate pressure increases from 0.24 MPa to 1.09 MPa as the split ratio increases from 0 to 0.99. When the split ratio is 0, there is no solution enters the intermediate pressure stage. The intermediate pressure is equal to the evaporation pressure, and the system works like a single-effect system.

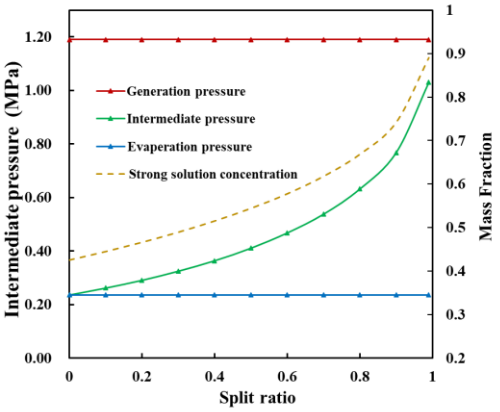

Figure 3 – the influence of split ratio on the intermediate pressure and solution concentration

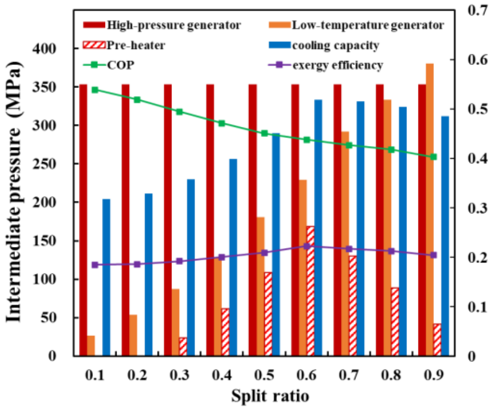

Figure 4 – the influence of the split ratio on the system performance

As shown in Figure 4, the COP decreases from 0.56 to 0.4 as the split ratio increases. In contrast, the exergy efficiency increase from 0.18 to 0.22 at first, resulting from the low-grade waste heat recovered from the jacket water. For the given heat sources from the LNG plant, the optimal value of the split ratio is determined by the maximum cooling energy that the system could produce. Figure 4 shows the heat load of the two generators, preheater, and evaporator under different split ratios. When the split ratio is 0.1, a small part of the heat from jacket water is recovered in the LTG. Moreover, the rich solution entering the PH reach over 90°C after being heated by the SHX, causing the PH to be unable to recover waste heat from the jacket water. As a result, the cooling capacity is low when the split ratio is 0.1, although the system has a relatively high COP. As the split ratio increases, more energy is recovered in the LT-GEN, and the concentration of the rich solution increases. When the split ratio is 0.3, the PH begins to recover the surplus waste heat from the jacket water. When the split ratio is higher than 0.6, the heat from the flue gas and jacket water is recovered completely. After that, the cooling energy decreases as the split ratio increase, resulting from the COP decrease. As shown in Figure 4, the optimal value of the split ratio is 0.6, and the maximum cooling capacity of 333.7 kW is obtained.

3.2 Energy and economic analysis

In this part, the performance of the proposed system with the optimal split ratio of 0.60 is analyzed. The system performance is compared with the single-effect system and the SE/DL system. As shown in Table 3, the proposed system and SE/DL system could recover around 422 kW heat from the low-grade jacket water. The COP of the single-effect system is higher, but the cooling capacity is about 60% of that of the proposed system. The DL/SE system obtains a slightly higher cooling capacity than the proposed system, but it combines the single-effect and double-lift systems, and the configuration is more complex.

Table 3 – The comparison results between the absorption systems

System Description	Input energy of the flue gas (kW)	Input energy of the jacket water (kW)	Cooling Capacity (kW)	COP
Single-effect system	353.12	0	197.71	0.56
Improved VX system	353.12	422.64	333.70	0.43
SE/DL system	353.12	422.64	335.02	0.43

To carry out the economic analysis, the cooling cost of the systems are defined as follow:

$$C_{\mathrm{s}}=C_{\mathrm{ec}}+C_{\mathrm{nc}}=C_{\mathrm{ec}}+EI+B+R \tag{3}$$

where the system cost includes the energy cost (C_{ec}) and non-energy cost (C_{nc}), the non-energy cost of the system comprises equipment investment *EI*, the auxiliary fees *B*, and the operation and maintenance cost R [8] (where B and R are totally about 19% of EI).

For the LNG station with daily natural gas production of 30000 m³, the cooling energy requirement of the precooling process is around 300kW. Conventional LNG stations adopt vapor compression refrigeration systems for precooling process, and the investment cost of a compression system per unit of cooling capacity is about 1,200 CNY/kW (1 CNY = 0.1473USD). Therefore, the initial investment for the compression system with a cooling capacity of 300kW is about 360,000 CNY. The compression system needs electric energy from the combustion engine consuming additional natural gas. Assuming that the COP of the compression system is about 2, and the power generation efficiency of the internal combustion engine is 0.39, the compression system will consume 332,854 Nm³ of natural gas per year. If the single-effect absorption refrigeration system is adopted to replace the compression system, the system could produce cooling energy of 197kW by recovering the flue gas. However, it requires additional natural gas burnt to supply more driving heat for the single-effect absorption system, in order to meet the cooling capacity requirement. Considering the investment cost per unit cooling capacity of the single-effect absorption system is about 2,500CNY/kW, the initial investment of the single-effect absorption system is about 650,000CNY. The price of wellhead natural gas in China is about 1.3 CNY/Nm³, and the single-effect system consumes 159,175 Nm³ of natural gas, saving about 225.782 CNY per year.

For the improved VX system, only a generator, absorber, pump, and preheater is add, which causes about a 30% increment in the initial investment than the single-effect system. The SE/DL system combines the single-effect and double-lift system, having a more complex configuration. Therefore, the initial investment is increased accordingly, which is about 1750,000 CNY. However, the proposed and the SE/DL system could produce cooling energy to meet the requirement of the precooling process by recovering the low-grade heat from the jacket water, meaning that there is no additional natural gas consumption. The economic analysis results are shown in Table 4. Compared with the compression system, the proposed system saves 432,710 CNY per year, and the payback period is 1.91 years, which is 2 years shorter than that of the SE/DL system. It indicates that the proposed system could produce energy and economic benefits with a promising prospect in the application.

Table 4 – The economic analysis of the different systems

System description	Initial investment cost / CNY	Annual energy cost / CNY	Annual operation cost / CNY	Payback period /year
Cmopression system	360,000	432,710	68,400	/
Single-effect system	750,000	206,928	142,500	2.05
Improved VX system	1000,000	/	190,000	1.91
SE/DL system	1750,000	/	332,500	3.98

4 Conclusions

This paper proposes an improved VX absorption refrigeration system for the LNG precooling process to improve energy efficiency. By recovering the high-temperature flue gas and low-temperature jacket water, the system could obtain a significant increase in the cooling capacity. Simulation result shows that the COP of the system decreases from 0.56 to 0.4 as the split ratio of the solution entering LTG increases. In contrast, the exergy efficiency increase from 0.18 to 0.22 at first, resulting from the low-grade waste heat recovered from the jacket water. Given the specific heat sources from the ICE, the optimal value of the split ratio is 0.60 with maximum cooling energy of 333.70 kW obtained, which is 1.68 times of the single-effect system. Economic analysis shows that it could save 432,710 CNY per year by adopting the proposed absorption system to replace the compression system for the precooling process. The payback period of the proposed system is 1.91 years, which is 2 years shorter than that of the SE/DL system.

5 Acknowledgment

The authors would like to thank the support of the National Science Fund for Distinguished Young Scholars (No. 51625603), and also thanks Taian Huaneng Refrigeration Corporation and Jereh Energy Services Corporation for the data support.

6 List of References

[1] Ansarinas Ab H , Mehrpooya M . Advanced exergoeconomic analysis of a novel process for production of LNG by using a single effect absorption refrigeration cycle[J]. *Applied Thermal Engineering*, 2017, 114:719-732.

[2] Kalinowski P , Hwang Y , Radermacher R , et al. Application of waste heat powered absorption refrigeration system to the LNG recovery process[J]. *International Journal of Refrigeration*, 2009, 32(4):687-694.

[3] Mehrpooya M , Omidi M , Vatani A . Novel mixed fluid cascade natural gas liquefaction process configuration using absorption refrigeration system[J]. *Applied Thermal Engineering*, 2016, 98:591-604.

[4] He Y , Li R , Chen G , et al. A potential auto-cascade absorption refrigeration system for pre-cooling of LNG liquefaction[J]. *Journal of Natural Gas Science & Engineering*, 2015, 24:425-430.

[5] Lu D, Chen G, Gong M , et al. Thermodynamic and economic analysis of a gas-fired absorption heat pump for district heating with cascade recovery of flue gas waste heat. *Energy Conversion and Management,* 2019, 185:87-100.

[6] Wang J , Wu J . Investigation of a mixed effect absorption chiller powered by jacket water and exhaust gas waste heat of internal combustion engine. *International Journal of Refrigeration*, 2015, 50:193-206.

[7] Yan X, Chen G, Hong D, et al. A novel absorption refrigeration cycle for heat sources with large temperature change. *Applied Thermal Engineering,* 2013, 52(1):179-186.

[8] Li Y , An H , Li W , et al. Thermodynamic, energy consumption and economic analyses of the novel cogeneration heating system based on condensed waste heat recovery[J]. *Energy Conversion & Management*, 2018, 177:671-681.

Preliminary assessment of a polygeneration system based on a concentrated photovoltaic thermal (CPVT) solar collectors

Castro, Jesús[1*], Rigola, Joaquim[1], Kizildag, Deniz[1], Oliet, Carles[1]

[1] *Heat and Mass Transfer Technological Center (CTTC), Universitat Politècnica de Catalunya BarcelonaTech (UPC), C/ Colom, 11, Terrassa, E-08222, Spain*

[*]*Corresponding author: tel. +34 93 739 8736, e-mail: cttc@cttc.upc.edu*

Abstract:

ECOSun project has as main objective a cost reduction of electricity and heat co-generation via a Concentrated Photovoltaic/Thermal (CPV-T) system by applying low-cost materials and advanced industrial manufacturing methods. In the CPV-T system, the solar radiation is captured in parabolic through concentrator based on a novel support structure fabricated by injection moulding and focused on a Co-Generation Absorber Module (CAM), where special c-SiPV-cells are operated under concentration. In this work, a preliminary assessment of the energy produced by a polygeneration system (in summer conditions) based on this technology coupled with an absorption chiller is carried out based on system simulations. The calculations are performed using NEST numerical platform, which allows the linking between the different components (solar collectors, pump, valves, heat exchangers, etc.), with high flexibility in the configurations. The simulations give information on the principal performance indicators of the systems, e.g. solar fraction, collectors' efficiency, PV modules' efficiency, and thermal and electrical COP of the absorption chiller. The simulations also estimate the electrical expenses of the auxiliary components (pumps, fans, etc.). From the cases simulated, the electrical expenses resulted in up to 25% of the electricity produced.

1 Introduction

Concentrated hybrid PhotoVoltaic/Thermal (CPV-T) solar collector is an option of interest due to its flexibility, manufacturability and high efficiency [1]. The main objective of the ECOSun project is a radical cost reduction of electricity and heat co-generation via a CPV-T system by applying low-cost materials and advanced industrial manufacturing methods. In this new hybrid solar collector, the solar radiation is captured in parabolic through concentrator based on a novel support structure fabricated by injection moulding and focused on a Co-Generation Absorber Module (CAM), where special c-SiPV-cells are operated under concentration. The heat dissipated through the cells is transferred into a heat transfer fluid (HTF) and - in combination with the generated electricity -, it can be used for various applications, such as solar cooling or heating, significantly increasing system efficiency. In this work, a preliminary assessment of the energy produced by polygeneration system (for heating, cooling and power generation) based on this technology coupled with an absorption chiller is carried out, based on system simulations with fast calculation models, to allow seasonal simulations. In the simulation, a transient model of an absorption chiller is used see reference [2] for further details. This model incorporates heat & mass transfer empirical information as well as for the pressure drop in the heat exchangers. This approach allows scalability studies, as the input data for the chiller are geometrical data of the machine (distances, surfaces, and volumes), the nº tubes of the heat exchangers, the mass of the refrigerant, absorbent, and solid parts, thermophysical properties, and characteristics of pumps and valves. Therefore, an ad-hoc experimental test campaign of the absorption machine simulated has not been necessary. This model allows estimating electrical expenses of the auxiliary components, data which is of interest in the ECOSUN project. These features are not usual in other transient models found in the literature [3-5]. The present work presents calculations of the overall performance indicators of a case study: a polygeneration system (30 kW of maximum cooling capacity) in Barcelona for a 1-week simulation (July) and full summer season performance. The model used for the CPVT is described and, the control strategy is also explained. The cooling load is estimated by a function depending on the hour and month. The summer season results indicate that about 25% of the electrical energy produced is used for the auxiliary components.

2 System description

Figure 1**¡Error! No se encuentra el origen de la referencia.** shows a scheme of the system object of analysis. It consists of three main parts: i) energy capture systems, i. e., hybrid collector field, and hot water tank; ii) absorption chiller subsystem (in this case direct air-cooled without cooling tower); iii) cooling load subsystem.

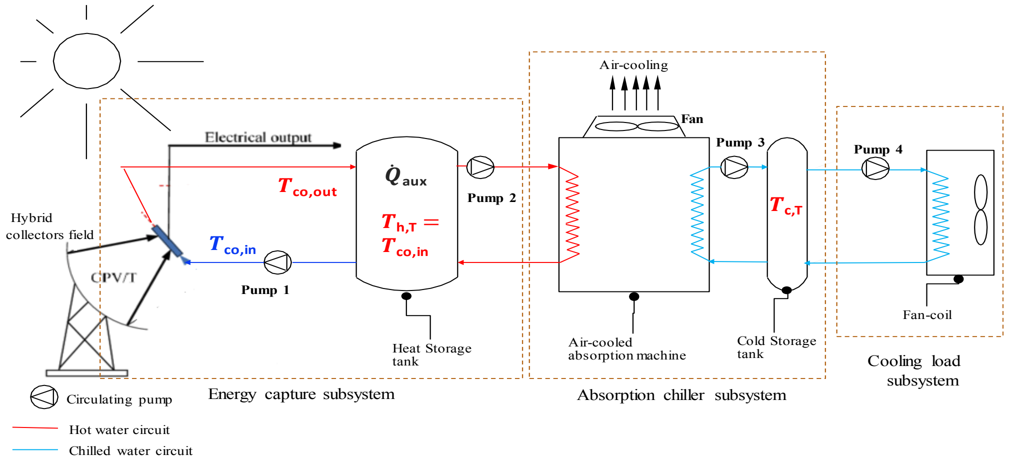

Figure 1 – Polygeneration system studied with the principal control signals, consisting in three parts: i) energy capture systems; ii) absorption chiller subsystem; iii) cooling load subsystem

2.1 Mathematical model

Energy capture system

For the CPVT collector, a simple model is employed [7], i. e. A steady-state efficiency curve is used to calculate the instantaneous overall efficiency (thermal+electrical, η) applied to the incoming solar energy (see eq.1):

$$\eta = a_0 + a_1 \Delta T/G + a_2 \Delta T/G^2 \quad (1)$$

Where ΔT is the temperature difference between the collector inlet and ambient temperature, and G is the direct normal irradiance. For calculating the electrical efficiency of the PV module (η_{el}), another steady-state efficiency curve is applied (see eq. 2):

$$\eta_{el} = b_0 + b_1 T_{cell} \quad (2)$$

Where T_{cell} is the PV module temperature. Therefore the thermal efficiency (η_{th}) is obtained by extracting eq. 2 from eq. 1 ($\eta_{th}=\eta-\eta_{el}$). In this way, an estimated value of the collector outlet ($T_{co,\,out}$*) is calculated using η_{th}:

$$T^*_{co,out} = T_{co,in} + \eta_{th} \cdot G \cdot A/\dot{m}C_P \quad (3)$$

Where $T_{co,\,in}$ is the collectors' inlet temperature, A is the solar collector area, and $\dot{m}, C_P$ are the mass flow and the heat capacity of the heat carrier fluid, respectively. The definitive outlet temperature of the solar collector stream ($T_{co,\,out}$) is calculated through a delay response function with a time characteristic (τ) to take into account thermal inertia effects. The PV module temperature (T_{cell}) is calculated using an overall heat transfer coefficient (U_{cell}):

$$T_{cell} = \left(T_{co,in} + T_{co,out}\right)/2 + \dot{q}/U_{cell} \quad (4)$$

Where $\dot{q}$ is the captured solar radiation by unit area. For the storage tanks, an overall energy balance is performed assuming a complete mixing of the liquid, i. e. no stratification effects are taken into account. The auxiliar heat for the hot water tank is introduced as an internal heat source.

Cooling load

The cooling load is simulated using cooling load profile that depends on the hour and month of the year [6]. The cold water tank is modelled in a similar way as to the hot water tank. In this case, there is no auxiliary internal heat, as the cooling load is introduced by a secondary stream, as indicated in Figure 1.

Absorption chiller

A lumped parametric transient model based on mass, momentum and energy balances applied to the internal components of the absorption machine has been used (see reference [2] for details). Transient models achieve higher prediction capabilities in comparison to steady-state modelling [8, 9]. The model depends on heat and mass transfer coefficients obtained through fundamental empirical correlations. The model has been extended to estimate pressure drops in the secondary streams [10, 11], so the pumping power required. The thermal and mass accumulation in each of the components is considered in the transient calculation. Indeed, the model is helpful to obtain detailed information on the overtime evolution of the solar cooling system, which will depend on the control strategy applied. It allows anticipating possible failure operations: crystallization, cavitation, etc.

2.2 Control strategy addressed

Energy capture system

The solar collector is activated/deactivated (pump 1) through a differential temperature controller between the input and output. Moreover, an overheating protection system based on the disconnection of the solar tracker is applied. This switch is activated by a two-step controller that limits the temperature of the PV cell to 120ºC. In addition to this, the maximum temperature of the hot water tank is limited to 96ºC (deactivating pump 1). On the other hand, the backup heat source is activated for temperatures lower than 75ºC in the hot water tank.

Cooling load

For this part of the system, pump 4 is activated if the cold water temperature is under 13ºC, i.e. the cold water has enough low temperature to attend the cooling load.

Absorption chiller

The generator pump is activated for temperatures over 75ºC in the hot water tank (activation of pump 2). On the other hand, the chilled water pump (pump3) is activated when the temperature of the cold water tank is over 8ºC. The time when the cold water tank is over 13ºC (outside limits) is considered fail time. There are also two emergency controls in the absorption chiller: i) first, crystallization prevention: in this case, the temperature difference between generator and absorber (activation on the fan and pump 3), and between evaporator and condenser (deactivation of pump 2 and fan) is maintained under 40ºC; ii) second, freezing prevention: the temperature of the evaporator is maintained over 2.5ºC (deactivation of pump 2 and activation of pump 3).

3 Results

3.1 Description of the case study

The case studied consists of a solar cooling plant with power generation located in Barcelona. The meteorological data has been obtained using MeteoNorm software. Table 1 summarizes the principal data of the case. The data for the absorption chiller is obtained from a prototype under development [2] (for a 10 kW machine, then it was scaled to 30 kW). It has to be remarked the efficiency curves of the hybrid collectors are estimations at the present stage of the project. The overall performance curve has been extracted from a commercial parabolic trough collector [12], and the electrical efficiency has been estimated [13].

Table 1 – Main data of the case study

Concept	Data	Units
Solar collector area	30; 90	[m^2]
Maximum capacity of the absorption chiller	10; 30	[kW]
Collector's transient response (τ)	1200	[s]
Collector's overall efficiency parameter (a0)	0.683	[-]
Collector's overall efficiency parameter (a1)	-0.28	[$Wm^{-2}C^{-1}$]
Collector's overall efficiency parameter (a2)	-0.0011	[$Wm^{-2}C^{-2}$]
Collector's electrical efficiency parameter (b0)	0.18	[-]
Collector's electrical efficiency parameter (b1)	-0.00072	[C^{-1}]
Hot tank volume	1500-4500; 7500-22500	[l]
Cold tank volume	1000; 3000	[l]
Back-up heat source	35; 105	[kW]
Heat transfer coefficient PV cell – carrier fluid (U)	60	[$Wm^{-2}C^{-1}$]
Maximum electrical consumption of auxiliary components	496, 1488	[W]
Maximum cooling load	12; 36	[kW]

3.2 Performance indicators

Table 2 shows the principal integrated performance indicators of the system, from left to right (starting at the 5_{th} column): thermal COP of the absorption chiller (COP_{th}), electrical COP of the chiller (COP_{el}), i.e. the cooling capacity divided by the electrical consumption of auxiliary components, overall efficiency of the hybrid collector (η), PV modules' performance (η_{el}, in %), PV modules' net performance (net η_{el}, discounting the electrical consumption of the auxiliary, in %), the solar fraction, and finally the fail time, i.e. the time the pump4 is not activated. Cases 1-4 are based on a 1-week simulation, while cases 5-6 on a complete summer season.

It can be observed that cases 1 and 3 and cases 2 and 4 show similar results as they are scaled. Moreover, cases 2 and 4, which have higher hot water tank capability if compared with cases 1 and 3, respectively, show better results of the performance of PV modules, overall efficiency and solar fraction. This better result is because the higher storage capacities of the hot water tank imply that the PV is working at lower temperatures. After all, for cases 2 and 4, the overheating protection system is much less activated due to the lower working temperatures at the hot water tank. Moreover, in the cases with higher storage capacity, the maximum temperature control of the hot water tank neither is achieved. Therefore it is not necessary to disconnect pump 1 of the collector loop, increasing solar fraction and the overall efficiency of the hybrid collector. Another interesting result is the higher COP_{el} for the cases with lower hot water tank capacity due to the overheating protection system is activated more frequently. Parallelly, the machine's performance is more irregular due to the activation of the emergency control, so the fail time is also higher. It is also important to remark that for the cases simulated, up to 25% of the power produced is used for the auxiliary components (pumps and fans).

Table 2 – Main performance indicators of the cases studied.

Nº Case	Col. area (m^2)	Hot tank capacity (l)	Max. chiller capacity (kw)	COP_{th} (-)	COP_{el} (-)	η (-)	η_{el} (%)	Net η_{el} (%)	Solar Frac. (-)	Fail time (%)
1	30	1500	10	0.727	15.8	0.587	12.9	10.2	0.745	11.9
2	30	7500	10	0.744	14.1	0.657	13.6	10.7	0.681	10.8
3	90	4500	30	0.731	16.1	0.599	12.9	10.1	0.741	10.8
4	90	22500	30	0.749	14.1	0.657	13.6	10.7	0.684	11.1
5	90	4500	30	0.656	12.4	0.515	12.9	9.6	0.772	1.8
6	90	22500	30	0.660	12.1	0.561	13.0	9.8	0.847	1.3

3.3 Detailed assessment

Figure 2 shows temperature, cooling capacity, power produced and power consumption profiles for a 1-week simulation (July). Two options are considered: i) low capacity hot water tank (table 2, option 3, left pictures); ii) high capacity tank (table 2, option 4, right pictures). It can be observed that for the case of a low capacity hot water tank, the overheating protection system for the PV module is often activated, and, as consequence, the maximum temperature achieved is about 120ºC. This fact leads to a limitation of the energy captured and the power produced, leading to an overall decreased performance of the PV module, as observed in Table 2.

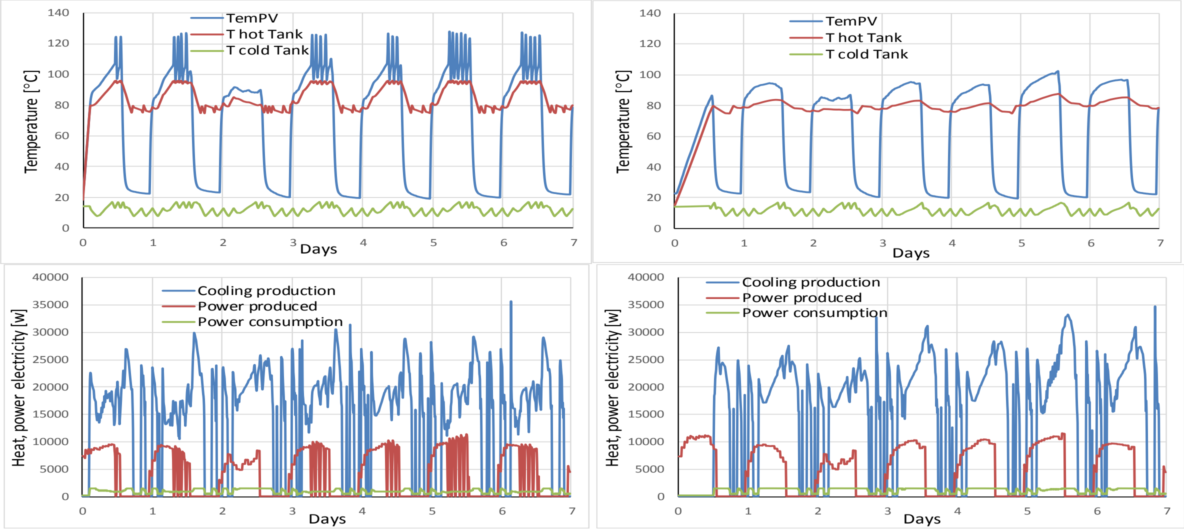

Figure 2 – 1-week simulation. Up: temperature profiles of hot, cold water tanks, and PV module. Low: cooling production, power produced and auxiliary power consumption (left 4500 l, right 22500 l of hot water tank)

4 Conclusions

A transient model plant of a complete polygeneration system for heating, cooling, and power production has been developed. The system studied couples a new CPVT hybrid solar collector together with a direct air-cooled absorption chiller. It has been possible to perform a preliminary assessment of the whole system based on an estimated efficiency of the new CPVT solar collector. The summer seasonal performance indicators for a case with a 30 kW of absorption machine in Barcelona (4500 -22500 l of hot water tank) are: a seasonal COP_{th} of the absorption chiller about 0.66, a COP_{el} about 11, and efficiency of the PV module about 13%, with a solar fraction of in the range of 0.77-0.85, and a collector efficiency ranged at 0.52-0.56. Based on the same simulation, it has been estimated that about 25% of the power produced has to be used for the auxiliary components. When a detailed analysis is performed, it can be observed that low capacity storages of the hot water tank lead to a decrease in the efficiency of the PV module because it works at a higher temperature.

5 Acknowledgment

This project has received funding from SOLAR-ERA.NET Cofund 2 joint call undertaking under the European Union's Horizon 2020 research and innovation programme.

6 List of References

[1] Sharaf, O. Z., Orhan, M. F. (2015). Concentrated photovoltaic thermal (CPVT) solar collector systems: Part I – Fundamentals, design considerations and current technologies. Renewable and Sustainable Energy Reviews. Volume 50, 1500-1565.

[2] Castro, J., Farnos, J., Papakokkinos, G., Zheng, J. and Oliet, C. (2020). Transient model for the development of an air-cooled LiBr-H_2O absorption chiller based on heat and mass transfer empirical correlations. International Journal of Refrigeration 120, 406-419.

[3] Kohlenbach, P., Ziegler, F. (2008). A dynamic simulation model for transient absorption chiller performance. Part I: The model. International Journal of Refrigeration 31, 217-225.

[4] Evola, G., Le Pierres, N., Boudehenn, F., Papillon, P. (2013). Proposal and validation of a model for the dynamic simulation of a solar-assisted single stage LiBr-water absorption chiller. International Journal of Refrigeration 36, 1015-1028.

[5] Marc, O., Sinama, F., Praene, J., Lucas, F. (2015). Dynamic modelling and experimental validation elements of a 30kw LiBr-H_2O single effect absorption chiller for solar application. Applied Thermal Engineering 90, 980-993.

[6] Red Eléctrica de España; Proyecto INDEL: Atlas de la Demanda Eléctrica Española (1997).

[7] Jonas, D., Theis, D. and Frey, G. (2018). Implementation and Experimental Validation of a Photovoltaic-Thermal (PVT) Collector Model in TRNSYS. ISES EuroSun Conference – 12th International Conference on Solar Energy for Buildings and Industry.

[8] Z. Yang, X. Tang, M. Qu, O. Abdelaziz, K. Gluesenkamp (2014). Development of updated absorption simulation software (absim), in: Proceedings of the International Sorption Heat Pump Conference.

[9] J. Castro, A. Oliva, C. D. Pérez-Segarra, J. Cadafalch (2007), Evaluation of a Small Capacity, Hot Water Driven, Air-Cooled H_2O-LiBr Absorption Machine, International Journal of Heat Ventilation Air Conditioning and Refrigeration Research 13 (1) 59-75.

[10] S. W. Churchill, Friction-factor equation spans all fluid-flow regimes, Chemical Engineering 84(24) (1977) 91--92.

[11] N.H. Kim, J.H. Yun, R.L. Webb, Heat Transfer and Friction Correlations for Wavy Plate Fin-and-Tube Heat Exchangers, Journal of Heat Transfer - Transactions of ASME 119(3) (1997) 560—567.

[12] NEP Solar AG. Technical Data for the PolyTrough 1800.

[13] Graz University of Technology. Internal communication (2021).

Techno-economic feasibility analysis of liquid desiccant technology for automotive painting

Giampieri, Alessandro[1], Ma, Zhiwei[1], Ling-Chin, Janie[1], Smallbone, Andrew[1], Roskilly, Anthony Paul[1]

[1] *Department of Engineering, Durham University, Durham, DH1 3LE, United Kingdom*

* *Corresponding author. Email: alessandro.giampieri@durham.ac.uk*

Abstract:

Automotive manufacturers are continuously striving to reduce the energy consumption of their production process due to economic, environmental, and policy compliance reasons. This study investigated the integration of the liquid desiccant technology into the conventional air management system for painting operation. The technology was appealing for its ability to control humidity, work independently as a dehumidifier and a regenerator, and store energy in a thermo-chemical form. In addition, waste heat sources available in the paint shop can be used for the regeneration of the liquid desiccant solution. Techno-economic assessment analysis of this novel process was conducted in the study for two different outdoor air conditions. Economic savings in terms of electricity and fuel consumption were achieved, resulting in a payback period of approximately 6 years and important benefits over the technology lifetime.

1 Introduction

Among all facilities in an automotive manufacturing plant, the paint shop is the largest energy consumer [1], in which air management systems that supply air to paint booths use up energy most significantly. As these systems are crucial for temperature and humidity control to ensure the quality of the final painting product [2], any ineffective control would result in paint defects and therefore require additional costs for reworking. This is particularly important for water-based paints, as both evaporation and film formation processes are influenced by the water content in the paint, which is in turn affected by the temperature and humidity of the surrounding air [3]. In such a scenario, the liquid desiccant technology could be appealing due to its temperature and humidity control characteristics [4], ability to store thermal energy in thermo-chemical form [5], and be flexible, i.e. dehumidifiers and regenerators can be located in different locations [6]. Figure 1a shows the conventional air management for painting operation, which is comprised of two air supply units, one that supplies outdoor air to the painting booth (ASU), while the other supplies recirculated air (ARU), and Figure 1b shows the possible integration of the liquid desiccant technology into the 100% outdoor air ASU.

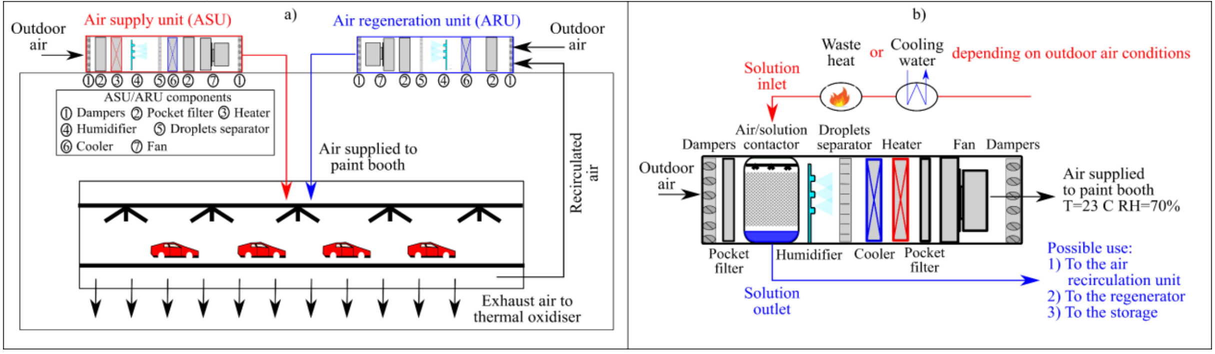

Figure 1 – (a) Conventional air handling management for automotive painting and (b) the potential integration of liquid desiccant technology into air supply unit with 100% outdoor air.

2 Background/Fundamentals/Experimental Set-up

The methodology included two main blocks for the performance and the economic analysis. The performance analysis was based on the development of correlations to include in the energy and mass balance equations of the liquid desiccant process [7]. Based on the analysis of experimental results [8-14] and correlations available in the literature [13-20], Eq.(1) was developed for the prediction of the moisture effectiveness, ε_ω, and enthalpy effectiveness, ε_h, of dehumidifiers and regenerators [21] with cellulose structured packing:

$$\varepsilon_{\omega,h} = C_1 * \left(\frac{m_{sol}}{m_a}\right)^{C_2} * \left(\frac{T_{K,sol}}{T_{K,a}}\right)^{C_3} * \left(\frac{h_{eq,sol}}{h_a}\right)^{C_4} * \left(\frac{\omega_{eq,sol}}{\omega_a}\right)^{C_5} * t^{C_6} * \left(\frac{a_e}{a_p}\right)^{C_7} \tag{1}$$

where $C_1,\dots, C_7$ are the fitting constants, m_{sol} and m_a are the mass flow rate (kg/s) of the desiccant solution and the air, $T_{K,sol}$ and $T_{K,a}$ are the inlet temperature of the desiccant solution and the air (in Kelvin), h_a and $h_{eq,sol}$ are the enthalpy of the inlet air and the air in equilibrium with the desiccant solution (kJ/kg), ω_a and $\omega_{eq,sol}$ are the moisture content of the inlet air and the air in equilibrium with the desiccant solution (kg_{H2O}/kg_{air}), t is the contact time between air and solution (s), a_e and a_p are the effective and the surface area to volume ratio of the packing material (m^2/m^3). The calculation of t and a_e are described in [22] and [23, 24], respectively. The values of $C_1,\dots, C_7$ for the moisture and enthalpy effectiveness of the dehumidification and regeneration process are reported in Table 1.

Table 1 – Fitting constants in the developed empirical correlations.

		C_1	C_2	C_3	C_4	C_5	C_6	C_7
Dehumidification	ε_ω	0.6665	0.0589	9.8644	−1.6592	0.6278	0.1716	0.1620
	ε_h	0.5397	0.108	13.1312	−2.1748	0.9327	0.1617	−0.0222
Regeneration	ε_ω	1.5236	0.3267	5.727	−1.198	−0.0775	0.2493	0.4979
	ε_h	0.8892	0.2979	−0.002	0.6514	−1.103	0.1516	0.0718

For the economic analysis, the main capital expenses (CAPEX) and operating expenses (OPEX) associated with the operation of the technology were estimated. For the CAPEX, the liquid desiccant system [25], the cost of the desiccant salt [26], cooling towers and vapour compression chillers [27] were considered, while for the OPEX, temperature and humidity control equipment [27], solution pumping [28], air blowing over the wetted packing material [29], humidifier [30] and heat rejection system [27]. The following assumptions were also considered: the paint shop is operating 250 days per year, 22.5 hours per day, while the electricity and natural gas cost were assumed as £0.11/kWh and £0.023/kWh, respectively. In addition, a carbon price of £16/ton_{CO2}e was considered [31], while the annual emission of air pollutants was calculated based on [32, 33].

To study the air handling unit operation for painting, a psychrometric chart-based strategy was developed, as shown in Figure 2, together with the flow chart used to simulate the operation of the integrated liquid desiccant air handling unit, which, depending on outdoor air conditions, can be varied to supply the temperature and humidity demand for optimal painting (T = 23 ± 2 °C, RH = 70 ± 2%).

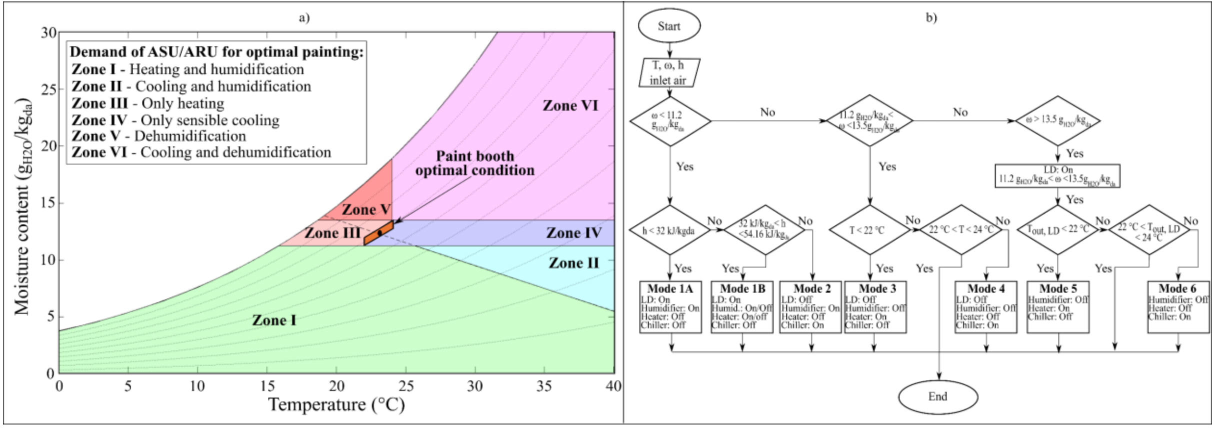

Figure 2 – a) Psychrometric-chart based analysis of air handing unit operation for painting process and b) flow chart of the simulation for analysis of integrated liquid desiccant air handling units.

3 Results

3.1 Cold climates

Figure 3 shows the schematic diagram of the technology and the simulated performance in July 2017 for Newcastle upon Tyne [34]. The ASU can operate (while the ARU operates conventionally), according to outdoor air conditions, in one of three operating modes: i) humidification operating mode (Zone 1 of Figure 2a): the solution is heated by low-grade heat and used in the ASU to heat and humidify the outdoor air (becoming cooler). Further air humidification or heating might be required after the process. Water is added to the solution to stabilise its concentration. The second air-solution contactor located outside the ASU is not used in humidification mode; ii) dehumidification operating mode (Zones 5 and 6 of Figure 2a): the solution is used in the ASU to remove the moisture from the air. The regenerator is located next to the ASU on the rooftop of the paint shop. Heat rejection is required to cool the solution before the ASU. Due to the low dehumidification demand in July in the UK, the dehumidification process can operate with a lower m_{sol}/m_a ratio compared to humidification mode; iii) the solution is stored when the outdoor air condition is in Zone 3 of Figure 2a. The outdoor air is directly heated in the ASU and supplied to the paint booth. The desiccant solution was selected as 25% wt. $CaCl_2$ [35] because of its capability to perform both humidification and dehumidification for the outdoor air conditions at Newcastle and its low cost. The flow rate of air supplied to the paint booth is 50,000 m^3/h.

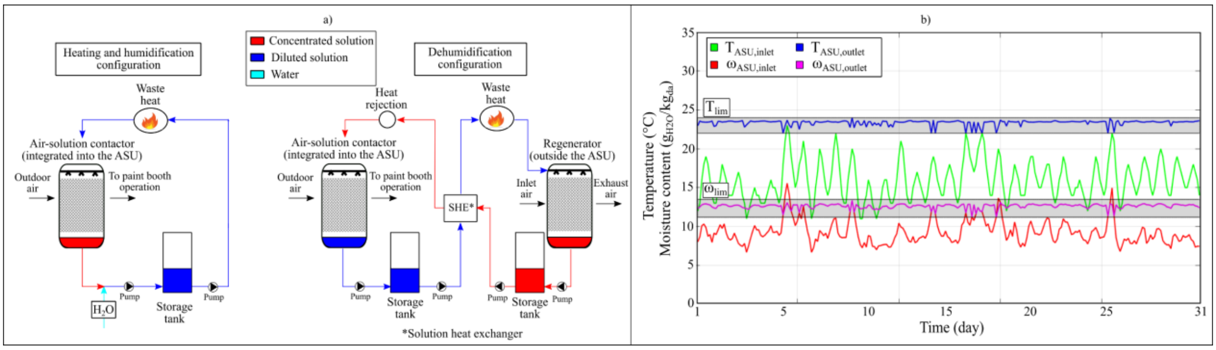

Figure 3 – a) Schematic diagram of the desiccant cycle for automotive painting application in cold climates and b) simulated performance for July 2017.

It is clear from Figure 3 that the technology would be able to perform both dehumidification during the warmest days and heating and humidification at night or during colder days, as in winter. Figure 4 compares the monthly energy costs of the conventional and novel liquid desiccant technology for the automotive painting application in Newcastle (characterised by mild summers, which limits the achievable savings for dehumidification/cooling), showing that significant savings can be obtained in the period November–April (about 60%).

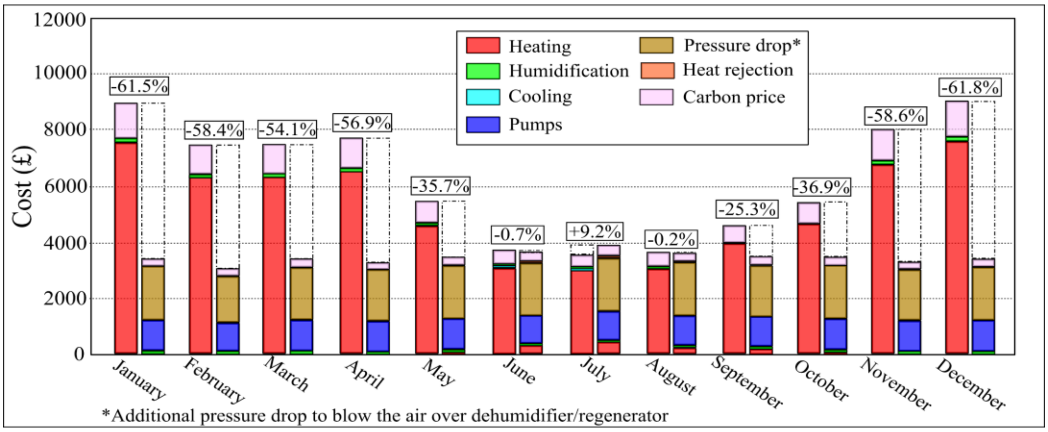

Figure 4 – Comparison of the economic performance of conventional (left) and liquid desiccant (right) process.

3.2 Hot and humid climates

For hot and humid climates (such as Singapore [34]), the liquid desiccant cycle, as illustrated in Figure 5 (together with the performance of the temperature and humidity control in the ASU/ARU simulated for January 2018), is composed of two dehumidifiers (one for ASU and one for ARU operation, respectively), one regenerator, two storage tanks, one solution heat exchanger, two cooling towers and one solution heater for regeneration. In the ASU, the concentrated solution can reduce the high humidity of outdoor air, decreasing its concentration. Thereafter the air requires additional humidification and cooling provided by the humidifier (stand-alone or in combination with an electrical chiller) to reach the temperature and humidity demand for optimal painting. After being cooled in cooling tower 2, the diluted solution is sent to the ARU where its dehumidification ability is enough to remove the moisture from the recirculated air, decreasing its concentration further. Additional air humidification and cooling are also required in the ARU after the liquid desiccant process. After the ARU, the solution is heated by waste heat and then sent to the regenerator (located close to the ASU and ARU) where it desorbs the moisture, increasing its concentration before being cooled (in cooling tower 1) and sent back to the

ASU. The desiccant solution was selected as 38% wt. $CaCl_2$ [35] due to the higher dehumidification demand in Singapore. Simulations were also carried out with LiCl as the desiccant solution. Although such a solution showed a higher dehumidification ability, its high cost curtailed the economic benefits of the technology. The flow rate of air supplied to the paint booth is 50,000 m^3/h.

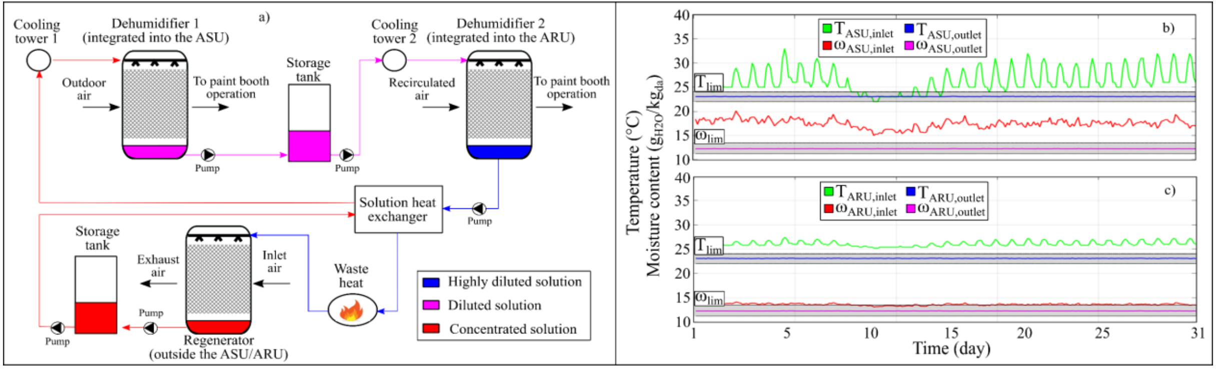

Figure 5 – a) Schematic diagram of the desiccant cycle for automotive painting application in Singapore and simulated performance for temperature and humidity control of b) ASU and c) ARU in January 2018.

It is clear from Figure 5 that the desiccant solution would be able to perform the temperature and humidity control of both the outdoor and the recirculated air for painting operation. Figure 6 compares the monthly energy costs of the conventional and liquid desiccant technology for painting application in Singapore (characterised by little variation in temperature and humidity throughout the year), showing that monthly savings between 18.3% and 38.9% can be obtained.

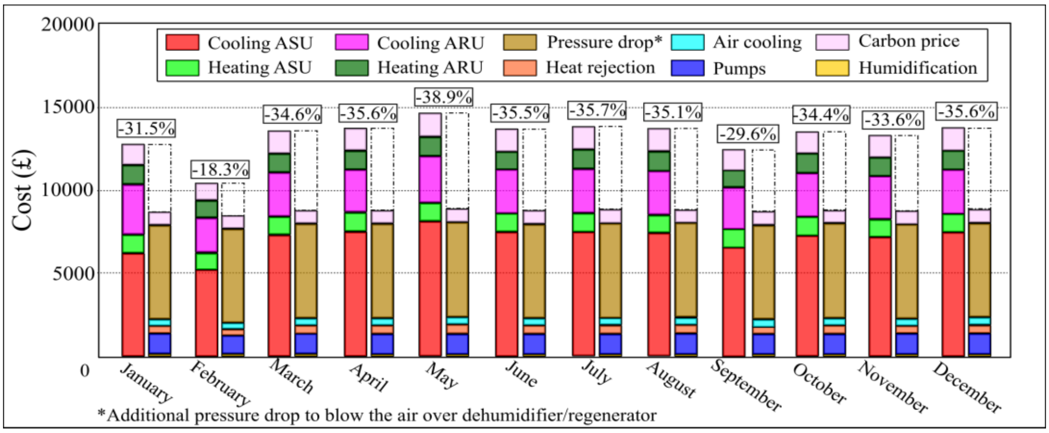

Figure 6 – Comparison of the economic performance of conventional (left) and liquid desiccant (right) process.

4 Conclusions

The results of the techno-economic analysis are illustrated in Table 2, showing a payback period of about 6 years for both climates and a promising economic performance over the technology lifetime. The energy consumption for auxiliary components of the liquid desiccant technology (solution pumping, air blowing through the packing material and heat rejection) currently hinders its economic benefits. Future research should focus on reducing this energy consumption by investigating alternative configurations of the technology, i.e. low-flow liquid desiccant systems, or alternative desiccant solutions.

Table 2 – Results of the techno-economic analysis.

	Economic parameter				
Location	CAPEX LD (£)	Payback (y)	LCOSE (£/kWh)	NPV (£)	IRR (%)
Newcastle	185,575	6.15	24.55	212,101	15.3
Singapore	278,363	5.74	97.61	358,119	16.61

5 Acknowledgment

This project was funded through the Engineering and Physical Science Research Council (EPSRC) of the United Kingdom (EP/T022981/1), “DEcarbonisation of Low TemperAture Process Heat Industry, DELTA PHI”.

6 List of References

1. Giampieri, A., et al., *A review of the current automotive manufacturing practice from an energy perspective.* Applied Energy, 2020. **261**: p. 114074.
2. *Air humidity in paint booths - Sustainable solutions for correct application of paints*. 2017, CAREL SpA.
3. Jones, F.N., M.E. Nichols, and S.P. Pappas, *Organic coatings: science and technology*. 2017: John Wiley & Sons.
4. Mei, L. and Y. Dai, *A technical review on use of liquid-desiccant dehumidification for air-conditioning application.* Renewable and Sustainable Energy Reviews, 2008. **12**(3): p. 662-689.
5. Kessling, W., E. Laevemann, and M. Peltzer, *Energy storage in open cycle liquid desiccant cooling systems.* International journal of refrigeration, 1998. **21**(2): p. 150-156.
6. Geyer, P., et al., *Hybrid thermo-chemical district networks–Principles and technology.* Applied Energy, 2017. **186**: p. 480-491.
7. Bassuoni, M., *A simple analytical method to estimate all exit parameters of a cross-flow air dehumidifier using liquid desiccant.* Journal of advanced research, 2014. **5**(2): p. 175-182.
8. Chung, T.-W., T.K. Ghosh, and A.L. Hines, *Comparison between random and structured packings for dehumidification of air by lithium chloride solutions in a packed column and their heat and mass transfer correlations.* Industrial & engineering chemistry research, 1996. **35**(1): p. 192-198.
9. Chen, Y., X. Zhang, and Y. Yin, *Experimental and theoretical analysis of liquid desiccant dehumidification process based on an advanced hybrid air-conditioning system.* Applied Thermal Engineering, 2016. **98**: p. 387-399.
10. Tang, C., K. Vafai, and D. Zhang, *Mass transfer performance of the LiCl solution dehumidification process.* International Communications in Heat and Mass Transfer, 2017. **85**: p. 139-146.
11. Xie, Y., T. Zhang, and X. Liu, *Performance investigation of a counter-flow heat pump driven liquid desiccant dehumidification system.* Energy, 2016. **115**: p. 446-457.
12. Varela, R.J., et al., *General correlations for the heat and mass transfer coefficients in an air-solution contactor of a liquid desiccant system and an experimental case application.* International Journal of Heat and Mass Transfer, 2018. **120**: p. 851-860.
13. Liu, X., X. Yi, and Y. Jiang, *Mass transfer performance comparison of two commonly used liquid desiccants: LiBr and LiCl aqueous solutions.* Energy Conversion and management, 2011. **52**(1): p. 180-190.
14. Wang, L., et al., *An experimental study on the dehumidification performance of a counter flow liquid desiccant dehumidifier.* International Journal of Refrigeration, 2016. **70**: p. 289-301.
15. Chung, T.-W., *Predictions of moisture removal efficiencies for packed-bed dehumidification systems.* Gas separation & purification, 1994. **8**(4): p. 265-268.
16. Martin, V. and D.Y. Goswami, *Effectiveness of heat and mass transfer processes in a packed bed liquid desiccant dehumidifier/regenerator.* Hvac&R Research, 2000. **6**(1): p. 21-39.
17. Abdul-Wahab, S., Y. Zurigat, and M. Abu-Arabi, *Predictions of moisture removal rate and dehumidification effectiveness for structured liquid desiccant air dehumidifier.* Energy, 2004. **29**(1): p. 19-34.
18. Liu, X., et al., *Experimental study on mass transfer performances of cross flow dehumidifier using liquid desiccant.* Energy Conversion and Management, 2006. **47**(15-16): p. 2682-2692.
19. Moon, C., P. Bansal, and S. Jain, *New mass transfer performance data of a cross-flow liquid desiccant dehumidification system.* International journal of refrigeration, 2009. **32**(3): p. 524-533.
20. Gao, W., et al., *Experimental investigation on the heat and mass transfer between air and liquid desiccant in a cross-flow dehumidifier.* Renewable Energy, 2012. **37**(1): p. 117-123.
21. Wen, T. and L. Lu, *A review of correlations and enhancement approaches for heat and mass transfer in liquid desiccant dehumidification system.* Applied Energy, 2019. **239**: p. 757-784.
22. Dong, C., et al., *Comparative performance study on liquid desiccant dehumidification with different packing types for built environment.* Science and Technology for the Built Environment, 2017. **23**(1): p. 116-126.
23. Brunazzi, E., et al., *Interfacial area of mellapak packing: Absorption of 1, 1, 1-trichloroethane by Genosorb 300.* Chemical Engineering & Technology: Industrial Chemistry-Plant Equipment-Process Engineering-Biotechnology, 1995. **18**(4): p. 248-255.
24. Kabeel, A., et al., *Dynamic behaviour simulation of a liquid desiccant dehumidification system.* Energy, 2018. **144**: p. 456-471.
25. Giampieri, A., et al., *Techno-economic analysis of the thermal energy saving options for high-voltage direct current interconnectors.* Applied Energy, 2019. **247**: p. 60-77.

26. Giampieri, A., et al., *Thermodynamics and economics of liquid desiccants for heating, ventilation and air-conditioning–An overview.* Applied Energy, 2018. **220**: p. 455-479.
27. Lucas, K., et al., *Ableitung von Kostenfunktionen für Komponenten der rationellen Energienutzung. Stiftung Industrieforschung Forschungsvorhaben.* Institut für Energie-und Umwelttech-nik eV, Duisburg-Rheinhausen, 2002. **5**.
28. *Liquid Desiccant Engineering Reference Guide, Kathabar Dehumidification Systems Inc*.
29. Liu, X.-H., Y. Jiang, and K.-Y. Qu, *Analytical solution of combined heat and mass transfer performance in a cross-flow packed bed liquid desiccant air dehumidifier.* International Journal of Heat and Mass Transfer, 2008. **51**(17-18): p. 4563-4572.
30. Lazzarin, R. and L. Nalini, *Air Humidification: Technical, Health and Energy Aspects*. 2004: Carel.
31. Rooney, M., et al., *The Future of Carbon Pricing: Implementing an independent carbon tax with dividends in the UK.* Policy Exchange, 2018.
32. Abdel-Salam, A.H., G. Ge, and C.J. Simonson, *Thermo-economic performance of a solar membrane liquid desiccant air conditioning system.* Solar Energy, 2014. **102**: p. 56-73.
33. *Greenhouse gas reporting: conversion factors*. 2019 [cited 2020 08 September]; Available from: https://www.gov.uk/government/publications/greenhouse-gas-reporting-conversion-factors-2019.
34. *World Weather Online*. [cited 2021 12 April]; Available from: https://www.worldweatheronline.com/.
35. Conde, M.R., *Properties of aqueous solutions of lithium and calcium chlorides: formulations for use in air conditioning equipment design.* International Journal of Thermal Sciences, 2004. **43**(4): p. 367-382.

Development of a compact ammonia-water Gas Absorption Heat Pump

Pistocchini, Lorenzo[1], Storoni, Andrea[1], Toppi, Tommaso[1], Aprile, Marcello[1], Motta, Mario[1]

[1] *Department of Energy, Politecnico di Milano, Via La Masa 34, 20156 Milano, Italy,*
lorenzo.pistocchini@polimi.it

Abstract:

Costs and size reduction is crucial to assure a large market penetration of Gas Absorption Heat Pumps (GHP) and the resulting cut in CO2 emissions. Such target has driven this work, focused on the development of a small rated ammonia-water GHP, mainly built of components derived from large series production, whose manufacturers actively collaborate to the project. In particular, all heat exchangers except the desorber are fusion-bonded plate heat exchangers. The outcome is an 8 kW GHP prototype, whose diaphragm pump and generator have been specifically designed to reduce the appliance size to the dimensions of a domestic condensing boiler.

We investigated the effectiveness of different configurations of the refrigerant circuit, and the benefits of adapting the flow rate of refrigerant and solution to different operating conditions.

We achieved a remarkable Seasonal Gas Utilization Efficiency (SGUE) of 1.58 on a net calorific value basis, according to standard EN 12309-6:2014.

1 Introduction

Gas Absorption Heat Pumps (GHP) can play a major role in reducing the CO2 emissions for space heating and domestic hot water production in existing buildings: they can replace gas boilers, while operating efficiently even with a high-temperature heat distribution system (radiators) and if air sourced [1]. Moreover, running on natural gas, they can handle the peaks of the demand exploiting the large capacity of existing gas and future hydrogen networks, without impacting on the electrical grid.

Absorption is a mature technology, but not in the heating sector and, more specifically, not in the residential field. Just one manufacturer of ammonia-water heat pumps is on the market, an Italian company which has demonstrated their feasibility and reliability by means of thousands “light commercial” installations. On the other hand, such market area does not have a suitable scale to boost GHPs industrialization and achieve the required cost reduction. Ammonia itself has been inherently a further limit to industrialization, as it requires steel components and rules out most of the available products normally applied in the refrigeration, which are either made of copper alloys or have unsuitable sizes being intended for industrial plants. As a result, the heat exchangers of the ammonia circuit have been so far realized in-house by the few manufacturers engaged in the development of this technology.

The scientific community can support the industry by focusing the research on practical features actually needed for absorption heat pumps large deployment, i.e. operational flexibility, long term reliability, low cost and small footprint.

In this perspective the present project aims at developing a reliable, compact, cost effective air-source ammonia-water GHP with a large modulation range. This research started from a modelling and simulation activity as the base of components sizing and design process, alternate with an extensive experimental work, until the present version of GHP prototype, which meets the project targets. In this paper we present (where not prevented by IP protection issues) the specific features of such prototype and how the final design has been selected. Then the energy performances of the prototype, measured by an accredited laboratory in accordance to the relevant international standard are reported.

2 Experimental Set-up

The subject of our development is an 8 kW air-source heat pump, with an intermediate water-glycol solution circuit between the evaporator and the outdoor heat exchanger. Despite the need of an additional heat exchanger, which may slightly reduce the efficiency, such layout has several advantages. At first it is more flexible since it enables different defrosting modes and simplifies the manufacturing of the air-side heat exchanger, allowing for the use of standard components (e.g. copper tubes). Moreover, a separate air-to-brine heat exchanger can be installed outdoor, while keeping the rest of the GHP indoor, with benefits in terms of heat loss reduction. The results presented in this work refer to the development of the sealed circuit, with a controlled brine flow used as heat source.

Our prototype is based on a single effect absorption refrigeration cycle and comprises variable expansion valves, both on the solution and refrigerant side. These are shown in the outline of prototype's circuit in Figure 1 (EV1 and EV2), together with the main components of the GHP: CONdenser, EVAporator, ABSorber, GENerator, RECtifier, Solution Pump (PSO), Ammonia Storage Vessel (ASV, shown in different points of the circuit), Flue gas heat recovery unit (FHX), Solution Heat Exchanger (SHX), Refrigerant Heat Exchanger (RHX).

Single effect cycle requires the smallest number of heat exchangers and is less affected than more advanced cycles as the GAX cycle [2] by part load and high temperature lift operation, both frequent conditions for heating applications. Moreover, the lower efficiency of single effect cycle has been compensated designing a very effective Solution Heat Exchanger (SHX).

The high effectiveness and compactness of the SHX and all the heat exchangers (except the generator) is achieved by using Plate Heat Exchangers (PHEs). Indeed, a quite recent manufacturing process - the fusion–bonding technology - makes it possible to produce 100% stainless steel PHEs, ensuring corrosion resistance and pressure-temperature ratings suitable for GHPs. Moreover, this novel method of brazing the plates can boost the industrialization of GHPs. The identification of optimal design of PHEs as components of compact GHPs is critical, since very long thermal lengths are needed to maximize the performances, and the large difference in flow rate between ammonia-water solution and heating water (or water-glycol solution) requires asymmetric PHEs. Such features can be achieved by a specific development either of plates design or of the heat exchanger as a whole, as done by previous research activities [3]. Our approach has been different, aiming at finding a suitable compromise between standard components (i.e. the plates already developed by PHE manufacturer) and custom channels configurations, which maximize series flow in most critical units (SHX and ABS) with neglectable effects of the co-current flow along the turning plates, and allows a strongly asymmetrical flow in the two sides.

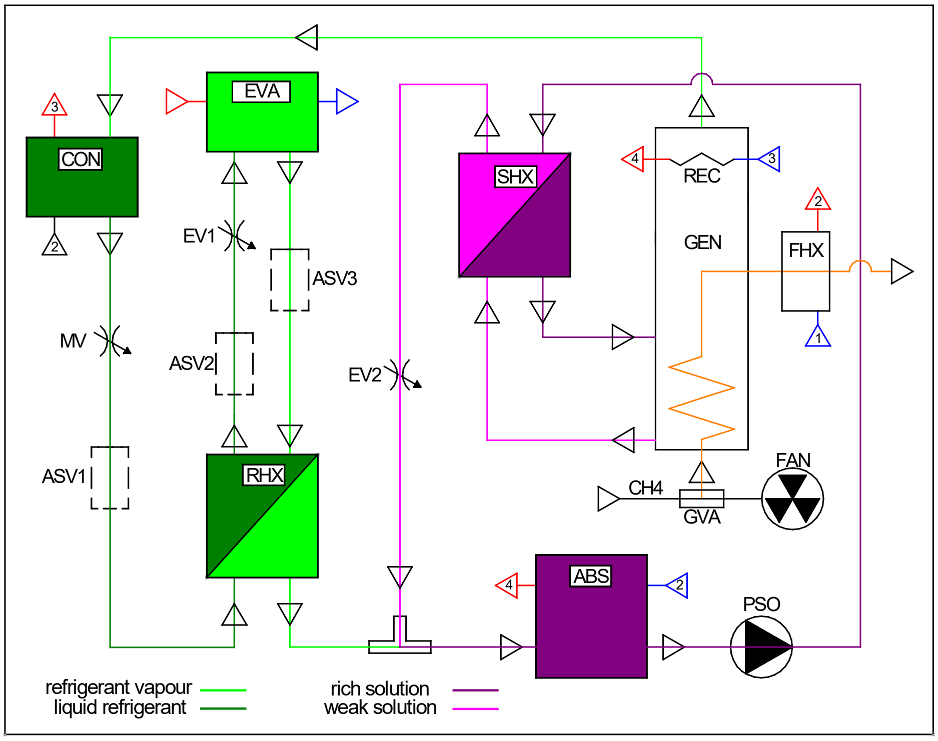

Figure 1 - Outline of GHP circuitry implementing the single effect absorption cycle.
Heating water first crosses the Flue gas heat recovery unit (FHX), then it is splitted in two equivalent parallel streams, one crossing in series the CONdenser and RECtifier, the second through the ABSorber.

We have been supplied with, and could investigate, heat exchanger prototypes, not commercially available and customized on the basis of our findings and requirements. This is an added value of the present work compared to previous research on the use of PHE in ammonia-water absorption [4-5].

The use of variable expansion valves on the solution side of the circuit, poor solution between the SHX and ABS, makes it possible to adapt the thermodynamic cycle to the operating conditions, which results in high performances over the entire range of modulation and thermal lift.

Additionally, it allows the reduction of the generator temperature at nominal power (by increasing the solution flow rate), so extending the capacity range and the durability of the GHP. Crucial is the control strategy and the choice of the control parameters, since the response time of certain physical quantities to changes in flow rate is up to some minutes. We have provided also for the use of an electronic variable expansion valve in the refrigerant circuit, to investigate different configurations of such circuit - with three different positions of the ammonia storage vessel - as well as to further optimize the AHP operation in different working conditions.

3 Results

The main findings of this work can be summarized as follows:

- The last prototype results very compact, as can be appreciated in Figure 2: the dimensions of the sealed circuit of the GHP, i.e. except for the air to brine heat exchanger, are comparable to those of a standard domestic condensing boiler. In particular, the height of nearly 850 mm is a remarkable outcome, achieved thanks to a brand-new design of generator's boiler and water cooled rectifier, for which patent applications are pending. The ammonia charge is well below 2 kg.
- Three different configurations of refrigerant circuit have been explored and compared: one is the state of the art, currently implemented in commercial GHPs, and based on fixed orifice restrictors and a passive concentration control system, placed downstream the evaporator (ASV3 in Figure 1). ASV3 is equipped with a calibrated liquid drain, whose flow rate depends on the head of liquid refrigerant, so the amount of stored ammonia in ASV3 depends on a dynamic equilibrium between inlet and outlet of liquid refrigerant. For example, stored ammonia increases in case of flooded evaporator, up to a new thermodynamic equilibrium related to the reduction of solution concentration, which promotes evaporation and thus the reduction of liquid feed from the evaporator.

  The other configurations are based on a variable electronic expansion valve (we successfully tested both a solenoid valve and a proportional needle valve), similarly to most recent ammonia-water prototypes [4-6].

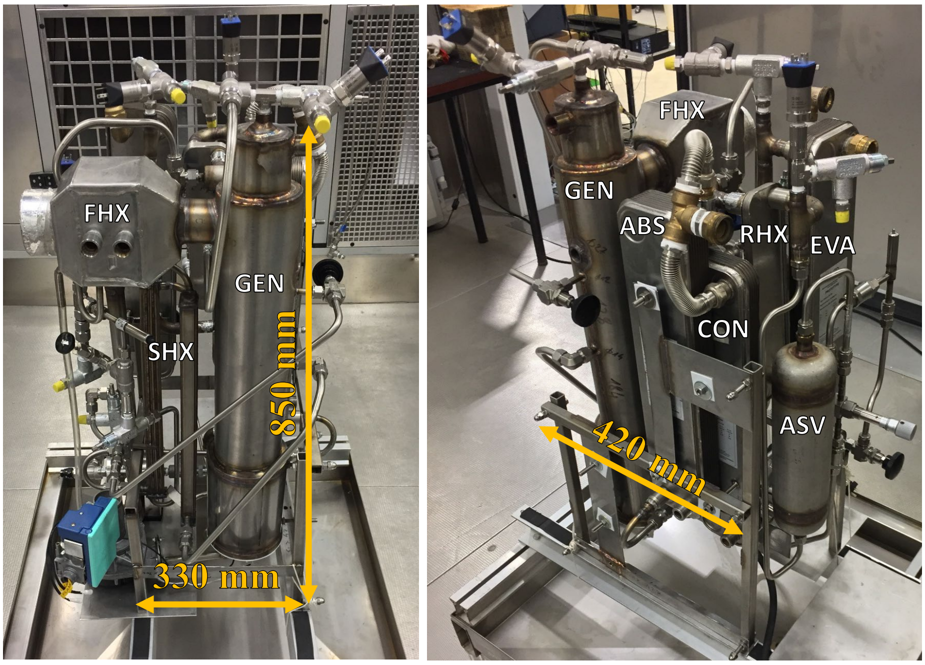

Figure 2 – View of two sides of GHP sealed circuit, showing its main components and overall dimensions

We investigated the effectiveness of placing the ammonia storage vessel just upstream or downstream the RHX (ASV1 and ASV2 in Figure 1), at an intermediate pressure in the cycle. The ASV, at least under most operating conditions, is partially filled by a two-phase solution (mostly refrigerant). As saturated liquid is drawn from the bottom of ASV, the first configuration provides the maximum efficiency, since the pressure in ASV rises until it nullifies the flash in the first restrictor (MV), so heat recovery in the RHX is maximum. The second configuration provides better valve control, since the liquid refrigerant entering the variable valve (EV1) is kept nearly at saturation. Despite the cost of variable valves, their use allows greater flexibility in sealed circuit layout, which is crucial to reduce the overall dimensions.

- The prototype, with the "efficient" configuration of the refrigerant circuit, i.e. the ASV in position 1 upstream the RHX, has been tested in the working conditions defined by the EN 12309-6:2014 [7] for high temperature application and average heating season. The results of the testing campaign, carried out in an accredited laboratory, are reported in Table 1 and provides us with the third and main outcome of our work.

  It is pointed out that the prototype has been tested with a water-glycol flow temperature lower than the required air temperature, to simulate the effect of the indirect water-glycol circuit:
  water-glycol Tin = air Dry Bulb Temp – 2 K.

  The Seasonal Gas Utilization Efficiency (SGUE) resulting from the testing campaign and calculated in compliance to EN 12309-6:2014, is 1.58 on a net calorific value basis. This is a very satisfactory result, which is mainly due to the high effectiveness of SHX, the optimized operation of refrigerant circuit, and the possibility of reducing the solution flow rate in part load conditions.

Table 1 – Gas Utilization Efficiency of GHP prototype in working conditions as per EN 12309-6:2014 - high temperature application and average heating season. Experimental data are reported in italics.

Load	**Heating Power**		**Air DBT**	**Water-glycol Tin**	**Water Tin**		**Water Tout**		**Gas Power (lhv)**	**GUE***
	kW		°C	°C	°C	°C	°C	°C	kW	
100%	8.00	*7.96*	-10	*-12.1*	42	*42.0*	55	*54.8*	*6.112*	***1.30***
88%	7.04	*7.19*	-7	*-9.1*	40	*40.0*	52	*52.3*	*5.137*	***1.40***
54%	4.32	*4.33*	2	*-0.1*	33	*33.0*	42	*41.9*	*2.714*	***1.60***
35%	2.80	*2.70*	7	*5.1*	29	*29.0*	36	*36.2*	*1.636*	***1.65***
15%	1.20	*1.21*	12	*10.0*	25	*25.0*	30	*29.8*	*0.734*	***1.65***

* based on lower heating value of methane

4 Conclusions

A five year-long numerical and experimental activity has led to the realization of a compact 8 kW rated ammonia-water Gas Absorption Heat Pump prototype. The development has been based on the wide use of custom multipass stainless steel plate heat exchangers and variable expansion valves, both in the refrigerant and solution circuits.
Flow control has led to remarkable prototype performances, as the Seasonal Gas Utilization Efficiency of 1.58 for high temperature application in average climate.
Thanks to a novel design of the direct fired desorber and a water cooled rectifier, which are the subject of patent applications, the generator height has been shortened and the overall dimensions of the sealed circuit are comparable to those of a standard domestic condensing boiler.
The reliability of expansion valves has been ascertained, while the next developments concern the implementation of the indirect water-glycol circuit, the automatic control of GHP and a further reduction in the size of solution pump and all the heat exchangers.

5 List of References

[1] Scoccia, R., Toppi, T., Aprile, M., Motta, M. (2018): Absorption and compression heat pump systems for space heating and DHW in European buildings: Energy, environmental and economic analysis. *Journal of Building Engineering*, vol.16, pp. 94-105

[2] Phillips, BA. (1990): Development of a High-Efficiency, Gas-Fired, Absorption Heat Pump for Residential and Small-Commercial Applications: Phase I Final Report: Analysis of Advanced cycles and Selection of the Preferred Cycle. ORNL/Sub/86-24610/1

[3] Garimella, S., Keinath, CM., Delahanty, JC., Hoysall, DC., Staedter, MA., Goyal, A., Garrabrant, MA. (2016): Development and demonstration of a compact ammonia–water absorption heat pump prototype with microscale features for space-conditioning applications. *Applied Thermal Engineering*, vol. 102, pp 557-564

[4] Jiménez-García, JC., Rivera, W. (2019): Parametric analysis on the experimental performance of an ammonia/water absorption cooling system built with plate heat exchangers. *Applied Thermal Engineering*, vol. 148, pp. 87-95

[5] Boudéhenn, F., Bonnot, S., Demasles, H., Lefrançois, F., Perier-Muzet, M., Triché, D. (2016): Development and Performances Overview of Ammonia-water Absorption Chillers with Cooling Capacities from 5 to 100 kW. *Energy Procedia*, vol. 91, pp. 707-716

[6] Garrabrant, M., Stout, R., Blaylock, M., Keinath, C. (2017): Residential and Commercial Capacity Absorption Heat Pumps for Space and Domestic Water Heating Applications. *12th IEA Heat Pump Conference*, Rotterdam, Netherlands

[7] EN 12309-6:2014 Gas-fired sorption appliances for heating and/or cooling with a net heat input not exceeding 70 kW. Calculation of seasonal performances.

Design and Testing of a Carbon-Ammonia Gas-Fired Heat Pump

Metcalf, Steven[1*], Rivero-Pacho, Ángeles[1], Critoph, Robert[1]

[1] *School of Engineering, University of Warwick, Coventry, UK*
* Corresponding author: steven.metcalf@warwick.ac.uk

Abstract:
This work presents the design and testing of a proof of concept carbon-ammonia gas-fired heat pump which is being developed as a domestic gas boiler replacement. The target gas utilisation efficiency (GUE, the ratio of heat output to gross calorific value of gas input) is 1.2 with a heating power of 10 kW. The system uses two beds with heat and mass recovery. It is tested here with electrical heat input to focus on the development of the adsorption system, and the target COP (the ratio of heat output to high temperature heat input) is around 1.375 in order to meet the GUE target. The sorption generators are an aluminium finned, stainless steel tube design with monolithic carbon pressed between the fins.

Testing revealed that the rate of adsorption and desorption (especially adsorption) was slower than measured during large temperature jump tests on individual tube modules and the power output of the machine was limited to between 5.9 to 7.7 kW. The long cycle times, coupled with some fluid leakage in water control valves, resulted in a maximum COP of 1.27 which would correspond to a GUE of 1.12. The slow rate of adsorption and desorption was linked to blockage of the ammonia flow passages in the beds by activated carbon powder. Work is ongoing to reconstruct the beds with the blockage removed and to design low-leakage ceramic disc valves for the water circuit.

1 Introduction

Fossil fuel boilers providing space heating and domestic hot water production are responsible for a significant proportion of global CO_2 emissions. Whilst the ultimate aim may be to replace them with electric heat pumps operating on renewably generated electricity, in many countries this would require a significant upgrade or even total replacement of the electrical grid in order to meet the demand created. In the interim period gas-fired heat pumps offer a more efficient alternative to gas boilers. Longer term they may even become renewable with the introduction of hydrogen or biogas into gas grids, and would reduce the amount of renewable gas that would need to be generated.

Several companies, universities and research establishments are developing gas-fired heat pumps with the aim of replacing domestic gas boilers [1-5] and the state-of-the-art is reviewed in the recent IEA Annex 43 report on 'Fuel Driven Sorption Heat Pumps' [6]. Systems using water as a refrigerant [1, 2] must operate with evaporating temperatures above 0°C which precludes the use of an air-source, necessitating a solar assisted or ground source for the evaporator at higher capital cost. Systems using ammonia refrigerant can operate with an air-source at lower cost and with a wider range of applicability. Ammonia-water absorption systems have a typical GUE of around 1.4-1.5 [3, 4]. Ammonia-salt adsorption systems are under development [5] with similar target GUE to the absorption systems, but the salt reactions are sensitive to the temperature conditions and reaction rates can limit the power density, adversely affecting the size and capital cost of the system.

The system developed in this work uses activated carbon-ammonia in a two-bed adsorption cycle with heat and mass recovery between the beds. The target GUE is 1.2, which although lower than typical ammonia-water absorption or ammonia-salt adsorption systems, it is expected that the system will be more compact and have a lower capital cost. The power density is limited purely by heat transfer in the activated carbon and not by mass transfer or reaction rate - the 10 kW system has a total bed volume of less than 15 litres.

2 Background/Fundamentals/Experimental Set-up

2.1 System and Test Setup

The proof of concept system is shown in Figure 1 prior to application of thermal insulation. The high temperature heat input is provided by a circulator bath providing pressurised (liquid) water at 10 bar and up to 170°C.

This decision was taken in order to focus on the development of the adsorption system and separate out the task of developing a high temperature gas burner.

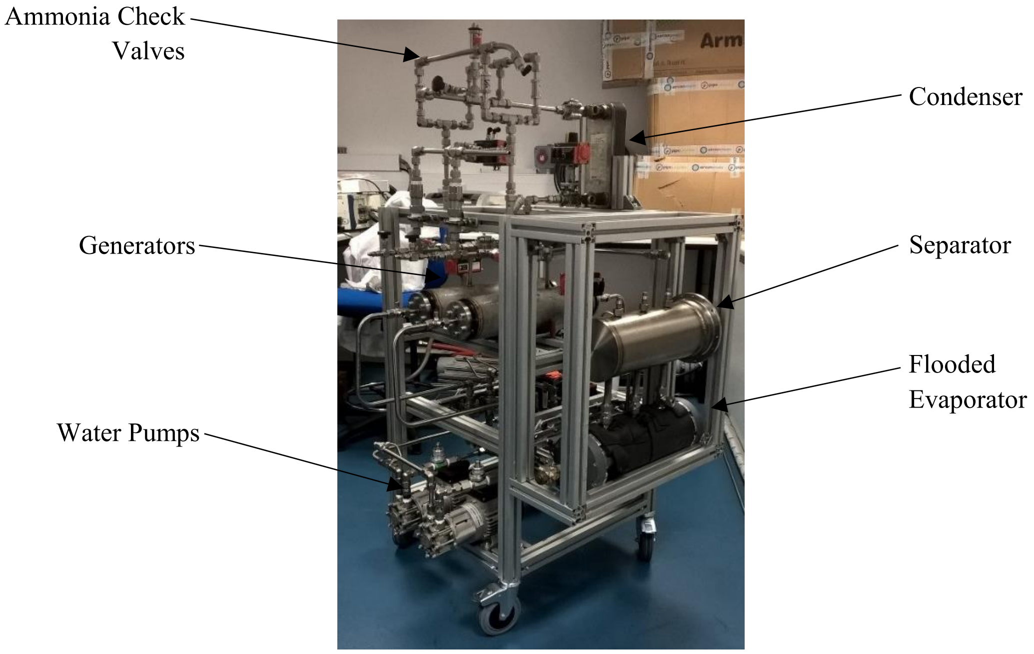

Figure 1 - Proof of concept carbon-ammonia heat pump (prior to insulation)

The evaporator is a flooded shell and tube type and its heat source is provided by a glycol circulator bath. The condenser and the cooler for rejecting the heat of adsorption are plate type heat exchangers, both of which are water cooled by two further circulator baths. The ammonia flow between the generators and the condenser and evaporator is controlled by check valves. Liquid ammonia from the condenser is collected in a 0.5 litre receiver and is dropped into the evaporator 2-4 times per cycle by closing a ball valve between the condenser and receiver and opening a solenoid valve between the receiver and evaporator. Mass recovery is accomplished by opening a pneumatically operated ball valve which links the two generators. The total ammonia charge is 1.4 kg.

The water flow to the generators is controlled by pneumatically operated ball valves. 12 valves are used, but are linked in 3 sets of 4 valves by a crank mechanism in order to reduce the number of actuators. The flow rate of water from the high temperature bath and to the condenser and cooler are measured by Coriolis mass flow meters (accuracy ±0.1%) and the inlet and outlet temperatures measured by PT100 sensors (accuracy ±0.05°C) in order to accurately calculate the COP.

The condenser heat output, cooler heat output and high temperature heat input are calculated, respectively, as:

$$\dot{Q}_{\mathrm{cond}} = \dot{m}_{\mathrm{w,cond}}(h_{\mathrm{w,cond\ out}} - h_{\mathrm{w,cond\ in}}) \tag{1}$$

$$\dot{Q}_{\mathrm{cooler}} = \dot{m}_{\mathrm{w,coooler}}(h_{\mathrm{w,cooler\ out}} - h_{\mathrm{w,cooler\ in}}) \tag{2}$$

$$\dot{Q}_{\mathrm{HT}} = \dot{m}_{\mathrm{w,HT}}(h_{\mathrm{w,HT\ in}} - h_{\mathrm{w,HT\ out}}) \tag{3}$$

The enthalpy values are calculated from a high-order polynomial fit to data from tables for saturated water based on the measured inlet and outlet temperatures. The COP is then calculated as:

$$\mathrm{COP} = \frac{\int^{\mathrm{cycle}}(\dot{Q}_{\mathrm{cond}}+\dot{Q}_{\mathrm{cooler}})dt}{\int^{\mathrm{cycle}}\dot{Q}_{\mathrm{HT}}dt} \tag{4}$$

2.2 Generator Design

The generators are an aluminium finned, stainless steel tube design as shown in Figure 2. The tube modules have hexagonal fins (so that they may be closely packed within the generators) with an across the flats dimension of 25 mm. The aluminium fins are 0.2 mm thick and the carbon layers between them are 3 mm thick. The stainless steel tube is 10 mm outer diameter and 7.5 mm inner diameter

Figure 2 – Generator tube module (19 tubes per generator)

The fins are stamped from sheet using a steel punch and die, which creates the hexagonal outer profile as well as a 7 mm central hole. The central hole is then formed into a collar with the same inner diameter as the tube diameter in order to create a larger contact area between the fin and tube. The tube is then placed inside a hexagonal split mould and a fin slid down the tube by a plunger. 1.7 g of activated carbon and a lignin based binder [7] is then poured into the mould and pressed with a force of 20 kN in a hydraulic press. This compacts the carbon and creates good contact between the fin and carbon. It also has the effect of squeezing the fin collar into tight contact with the tube. 125 such layers are built up until the laminate is 400 mm in length.

19 such tubes are welded inside a 140 mm diameter shell in a hexagonal close packed arrangement to form each generator. The volume of each generator is approximately 7 litres. Further details on the system and generator design can be found in [8].

3 Results

3.1 Heat Recovery Cycles

Table 1 shows the results for various test conditions and cycle times for cycles with heat recovery only (no mass recovery). The maximum COP achieved was 1.25 (row 1 of the table). The predicted COP under these conditions from simulation models and large temperature jump tests on individual tube modules is 1.35. The predicted cycle time from large temperature jump tests on single tube modules is around 240 seconds – in the region of 2 times shorter than those required during testing of the full-size system. The condensing temperatures, T_{cond}, and evaporating temperatures, T_{evap}, given in the table are the minimum and maximum values of the saturation temperature corresponding to the pressure in the components during the cycle (since adsorption is an unsteady, batch process the condensing and evaporating temperatures and pressures do not have fixed values). The heating power and high temperature heat input are cycle averages calculated from equations 1-3.

Table 1 – Test results with heat recovery cycles (no mass recovery).

T_{HT} [°C]	T_{evap} [°C]	T_{cond} [°C]	Cycle time [s]	Heating Power [W] ±55 W	High Temp (HT) Heat Input [W] ±55 W	COP ±0.02
160	6 – 15	37 – 41	552	6614	5295	1.25
160	6 – 15	37 – 41	612	5899	4722	1.25
140	5 – 10	36 – 40	342	7599	6277	1.21
140	5 – 10	36 – 40	462	7089	5751	1.23
140	-6 – -1	34 – 39	342	6531	5724	1.14
140	-6 – -1	34 – 39	462	6119	5273	1.16
160	-6 – -1	34 – 39	342	7721	6752	1.14
160	-6 – -1	34 – 39	462	7177	6186	1.16

Coriolis mass flow meters were placed on the ammonia flow to each generator in order to determine the cause of the poor performance. It was discovered that the rate of adsorption and desorption was significantly lower than expected, with adsorption being particularly slow. Figure 3 shows the progress of completion of adsorption and desorption during an extended duration test (determined from integration of the flow rate measured by the Coriolis mass flow meters on the ammonia). It can be seen that 90% completion takes 300 seconds for desorption, whilst adsorption takes 550 seconds (percentage completion is the percentage of the final amount of adsorption or desorption during the cycle). From large temperature jump experiments on tube modules, this time should be as low as 120 seconds. Upon cutting open the shell of one of the generators it was discovered that the ammonia flow passages between the tube modules had become blocked by carbon powder. Only the 3 outer tubes at the top of the generator had a clear ammonia path to the inlet/outlet port. This blockage affects both adsorption and desorption, but is more pronounced during adsorption due to the lower gas density and lower available driving pressure difference.

The long cycle times reduce the heating power output which causes heat losses to become more significant, lowering the COP. From an overall energy balance on the system heat losses were calculated at 100-200 W. Without this heat loss the COP could be as high as 1.27-1.3 (conditions as per row 1, Table 1), but this does not explain the entire reason for the low COP. It was discovered that during one half of the cycle one or more of the water control valves was leaking between the hot and cold streams, resulting in an average loss of around 500 W over the cycle. If this loss is removed from the high temperature heat input and the heating output then the COP would increase to 1.275. Combining the effects of external heat loss and valve leakage, the COP could be as high as 1.33. The additional difference with the model prediction of 1.35 can be attributed to extraneous thermal mass in the real system not considered in the model.

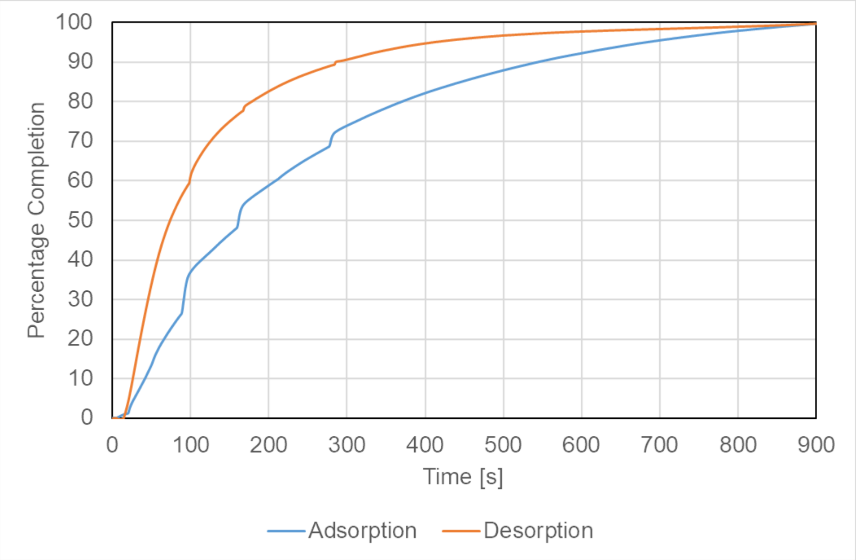

Figure 3 – Percentage completion of adsorption and desorption

3.2 Mass Recovery Cycles

Table 2 shows the effect of mass recovery on the cycle for the same conditions as row 1 of Table 1. The COP increased from 1.25 to 1.27, which is in line with model predictions of an increase from 1.35 to 1.37.

Table 2 – Effect of mass recovery

Mass Recovery?	Heating Power [W] ±55 W	High Temp (HT) Heat Input [W] ±55 W	COP ±0.02	Ammonia mass change per cycle per generator [g]
No	6614	5295	1.25	363
Yes	6740	5312	1.27	443

High temperature gas burner testing has determined that it is possible to achieve a gross burner efficiency of 80% and to recover an additional 10% of the gross gas input from the flue gas to the load. The predicted GUE under the test conditions of row 1 of Table 1 is therefore $(0.8 \times 1.269) + 0.1 \cong 1.12$

4 Conclusions

Testing of the proof of concept system has revealed that the COP and power output is lower than predicted due to blockage of the ammonia passages in the generators by carbon powder. The COP was further reduced by leakage of water control valves. Heat output was between 5.9 and 7.7 kW, compared to the target of 10 kW, and the maximum COP achieved was 1.27 compared to the target of 1.37.

5 Acknowledgments

This work was supported by the UK EPSRC grants ‘i-STUTE’ EP/K011847/1 and ‘4S-DHW’ EP/N021304/1 and by the UK government department BEIS grant LCHTIF1021 ‘Gas Adsorption Heat Pump’.

6 List of References

[1] Wittstadt, U., Füldner, G., Vasta; S., Volmer, R., Bendix, P., Schnabel, L., Mittelbach, W, Adsorption Heat Pumps and Chillers – Recent Developments for Materials and Components, *12th IEA Heat Pump Conference*, 2017

[2] Füldner, G., ADOSO – Gas Adsorption Heat Pump with a Crystalline Zeolite Heat Exchanger and a Novel Evaporator-condenser Device, German Federal Ministry of Economic Affairs and Energy (BMWi) Project. URL: https://www.ise.fraunhofer.de/en/research-projects/adoso.html

[3] Aprile M, Scoccia R, Toppi T, Guerra M, Motta M. Modelling and experimental analysis of a GAX NH3-H2O gas-driven absorption heat pump. *Int J Refrig*. 2016;66:145–55

[4] Garrabrant, M., Stout, R., Blaylock, M., Keinath, C., Residential and Commercial Capacity Absorption Heat Pumps for Space and Domestic Water Heating Applications, 12th IEA Heat Pump Conference, 2017.

[5] Blackman C, Bales C, Thorin E. Experimental Evaluation and Concept Demonstration of a Novel Modular Gas-Driven Sorption Heat Pump, *12th IEA Heat Pump Conference*, 2017.

[6] Albers, A., Aprile, M., Blackman, C., et. al., Fuel Driven Sorption Heat Pumps, IEA Annex 43 Final Report, *Heat Pump Centre*, ISBN 978-91-89167-50-6, 2020.

[7] A.M. Rivero-Pacho, R.E. Critoph, S.J. Metcalf, Modelling and development of a generator for a domestic gas-fired carbon-ammonia adsorption heat pump, Renewable Energy, 110, pp. 180-185, 2017.

[8] S.J. Metcalf, A.M. Rivero-Pacho, R.E. Critoph, Design and Large Temperature Jump Testing of a Modular Finned-Tube Carbon–Ammonia Adsorption Generator for Gas-Fired Heat Pumps, *Energies*, 2021, 14(11), 3332.

Experimental Study on A Novel Heat-Driven Multifunctional Air Treatment System

Liu, Feng[1,2], Dai, Yuze[1,2], Sui, Jun[1,2]

[1] *Institute of Engineering Thermophysics, Chinese Academy of Sciences, Beijing 100190, China (liufeng@iet.cn)*

[2] *University of Chinese Academy of Sciences, Beijing 100049, China*

Abstract:
Hot and humid air with a high marine aerosol content, which is known as 3-high air and is ubiquitous in tropical coastal areas and islands, deteriorates living environments and severely damages human health. A novel type of heat-driven multifunctional air treatment system (MATS) is constructed and tested in this study to treat 3-high air. The test results show that the integrated prototype has a fresh air treatment capacity of 6000 m^3/h, where the fresh air state is 90% RH@30°C. Air processing using the heat-driven multifunctional air treatment system produces a supply air state of 50% RH@18°C and decreases the aerosol content by over 90%. The system coefficient of performance is 0.4. Test results show that the proposed method/prototype is especially suitable for tropical islands with prominent energy supply shortages and problems associated with 3-high air.

1 Introduction

The numerous islands in tropical oceanic areas are characterized by hot and humid outdoor air with a high marine aerosol content, which is known as 3-high air. Hot and humid air has been reported to be one of the main precipitating factors for rheumatism and rheumatoid arthritis [1].The metal corrosion rate starts to increase beyond a critical air humidity and doubles for a temperature increase of 10 °C. The emergence of high concentrations of marine aerosols with NaCl as the main constituent [2] has transformed the main form of metal corrosion from chemical to electrochemical, while increasing the corrosion rate by more than 10 times, as well as intensifying damage to metals and metal products [3]. Thus, effective treatment of 3-high air is necessary in coastal areas and islands to improve the comfort of personnel and ensure personnel health, reduce the corrosion rate of metal materials and products, and improve the reliability and safety of equipment [4].

In response to the threat of the 3-high air, most of the previous research and current applications focus on passive anti-corrosion, that is, the use of metal surface treatment and heavy protection means to reduce the risk of corrosion by reducing the contact between the equipment and the 3-high air. Considering the limitation of passive anti-corroison, attention is increasingly being focused on active mthods to process 3-high air of which absorption cycles can fully exploit waste heat and renewable energy heat to deal with 3-high air [5]. Numerous dehumidification systems have been implemented in conjunction with heat pumps because of the very good energy supply-demand relationship between a vapour compression heat pump and a liquid desiccant air conditioning system [6, 7].

A 3-high air treatment method for combined cooling, dehumidification, and aerosol removal with low-grade waste heat was proposed by our team ir previous work [8]. The innovation of this work lies in the use of a one-step method to achieve cooling, dehumidification and aerosol removal, and a two-step method to regenerate the solution. The process mainly relies on low-grade heat and a small amount of electricity, with a simple structure and energy-saving operation. The work in this study is used to evaluate the performance of the equipment integrated with this process.

2 Experimental Set-up

2.1 Description of the set-up

The heat-driven multifunctional air treatment system (MATS) typically consists of a multifunctional air treatment process, a solution regeneration process, a solution heat exchanger, as well as several pumps, valves, and pipes. As core of the multifunctional air treatment process, an air washer module of compact packing structure is used to trap NaCl, wash the fresh 3-high air (fresh air) while dehumidifying it with cold and concentrated working aqueous solution. During the solution regeneration process, with the help of external low-grade heat and cold sources, the water and NaCl in the diluted solution are separated from the circulation system, so that the absorption capacity of the working solution can be restored and a new cycle can be started. A LiCl aqueous solution is used as the working solution for its excellent moisture absorption capacity and the common ion effect with NaCl.

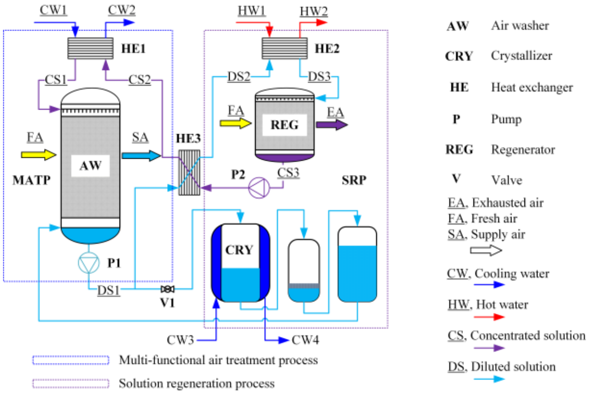

Figure 1 - Diagram of proposed MATS

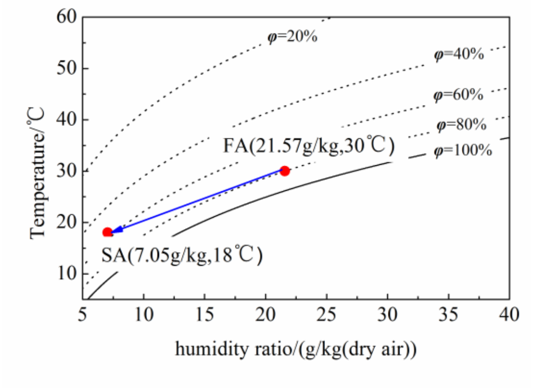

Figure 2 - Psychrometric chart showing air state before and after processing under design condition

2.2 System performance

The coefficient of performance (*COP*) is used to evaluate the performance of the MATS.

$$\mathrm{COP_S}=\frac{Q_\mathrm{R}}{Q_\mathrm{S}}=\frac{\Delta H_\mathrm{air}}{\rho_\mathrm{CW}V_\mathrm{CW1}(T_\mathrm{CW2}-T_\mathrm{CW1})+\rho_\mathrm{CW}V_\mathrm{CW3}(T_\mathrm{CW4}-T_\mathrm{CW3})+\rho_\mathrm{HW}V_\mathrm{HW1}(T_\mathrm{HW1}-T_\mathrm{HW2})} \tag{1}.$$

$$\mathrm{COP_H}=\frac{Q_\mathrm{R}}{Q_\mathrm{H}}=\frac{\Delta H_\mathrm{air}}{\rho_\mathrm{HW}V_\mathrm{HW1}(T_\mathrm{HW1}-T_\mathrm{HW2})} \tag{2}$$

$$\mathrm{COP_C}=\frac{Q_\mathrm{R}}{Q_\mathrm{C}}=\frac{\Delta H_\mathrm{air}}{\rho_\mathrm{CW}V_\mathrm{CW1}(T_\mathrm{CW2}-T_\mathrm{CW1})+\rho_\mathrm{CW}V_\mathrm{CW3}(T_\mathrm{CW4}-T_\mathrm{CW3})} \tag{3}$$

The marine aerosol removal rate is used to evaluate the ability of MATS to remove marine aerosols and is defined as

$$R_\mathrm{MATS}=\frac{c_\mathrm{A1}-c_\mathrm{A2}}{c_\mathrm{A1}}=1-\frac{c_\mathrm{A2}}{c_\mathrm{A1}} \tag{4},$$

where c_A1 and c_A2 are the marine aerosol concentrations of the fresh and supply air, respectively.

2.3 Uncertainty

Table 1 Specifications and precision of measurement instruments

Parameter	Device	Type	Accuracy	Operational range
Water/ solution temperature	Thermometer	PT-100	±0.3 °C	0~120 °C
Water/ solution volume flowrate	Flowmeter	Turbine flowmeter	±0.5 %	2~30 m^3/h
Air temperature	Thermometer	Thermocouple	±0.2 °C	-10~40 °C
Air humidity	Humidity sensor	/	±2%	0~100%
Air flow velocity	Anemometer	CTV210	±3%	0~30 m/s
Marine aerosol concentration	Electronic analytical balance	ME204	±0.2 mg	0~220 g

3 Results

3.1 Preliminary test under design condition

The auxiliary system is used to test the completed MATS, in which cooling water is from an electric chiller and hot water from a boiler. The system is considered to have reached a stable state when the deviation in the temperature and humidity of the supply air does not exceed 1% within 15 minutes, after which the main parameters of the system are recorded under this condition. Preliminary test results for the 3-high air processed by the MATS system are shown in Table 2 and 3.

Table 2 Design and test values for MATS

Item	Unit	Design value	Test value
Fresh air temperature, T_{FA}	°C	30	29.9
Fresh air relative humidity, φ_{FA}	%	90	90.7
Fresh air volume flowrate, V_{FA}	m^3/h	6000	6020
Supply air temperature, T_{SA}	°C	18	18.0
Supply air relative humidity, φ_{SA}	%	50	50.1
Cooling water temperature, T_{CW}	°C	7/12	10/17
Heating water temperature, T_{HW}	°C	60/50	55/45
COP_S	-	0.42	0.40

Table 3 Marine aerosol removal by MATS system

Air type	marine aerosol concentration/ (mg/m^3)	marine aerosol removal rate, R_{MATS}/%
Fresh air at 6000 m^3/h	2.40	97.0
Supply air at 6000 m^3/h	0.07	

The fresh air parameters are set to the system design parameters. Processing reduces the supply air temperature from 29.9°C to 18°C and the humidity from 90.7% to 50.1%, which meets the design requirements. The system COP of 0.40 is slightly lower than the design value.

Table 3 shows that the marine aerosol concentrations for 6000 m^3/h of fresh air is 2.40 mg/m^3. Processing reduces the marine aerosol concentration in the supply air to corresponding value of 0.07 mg/m^3. The corresponding marine aerosol removal rate of 97.0% is higher than the design value of 70%.

Thus, the results of the preliminary test performed under design conditions show the effect of cooling, dehumidification, and marine aerosol removal for 3-high air.

3.2 Test under off-design condition

The system performance was tested under different working conditions by carrying out preliminary tests to determine the system performance under the existing supporting conditions and changing the fresh air temperatures, as well as the fresh air humidity.

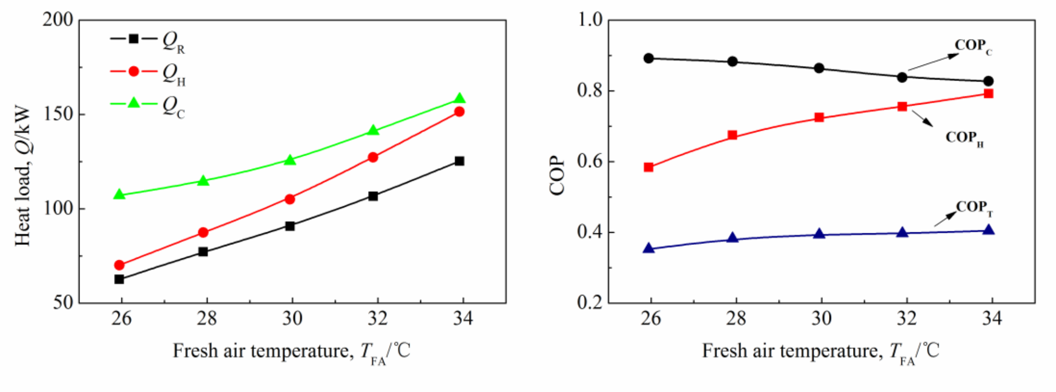

Figure 3 - Heat load and COP versus fresh air temperature

Figure 3 shows how the heat load and the COPs vary with the fresh air temperature. Under this off-design condition, the fresh air temperature changes, whereas the state of the supply air is set to a temperature of 18 °C and 50% humidity. *Figure 3*(a) shows that the decrease in the fresh air temperature causes the refrigeration capacity, the heat consumption and the cold energy consumption to all decrease; this result is obtained mainly because the decrease in fresh air temperature reduces the enthalpy difference between the fresh air and the supply air, reduces the cold energy consumption during the absorption process, and also reduces the heat consumption during the regeneration process. However, *Figure 3*(b) shows that the refrigeration COP remains at approximately 1.0 mainly because the refrigeration capacity of the fresh air is provided by the cooling water, whereas the total COP is maintained at approximately 0.4, which is slightly lower than the design value. The test results show that the system can run stably for different fresh air temperatures.

Figure 4 shows how the refrigeration capacity, heat consumption, cold energy consumption, and COPs vary with the fresh air humidity. Under this off-design condition, the fresh air humidity changes, whereas the state of the supply air is set to a temperature of 18 °C and 50% humidity.Figure 4(a) shows that the decrease in the fresh air humidity causes the refrigeration capacity, the heat consumption and the cold energy consumption to all decrease; this result is obtained mainly because the decrease in fresh air humidity reduces the latent heat load of the fresh air, reduces the cold energy consumption during the absorption process, and reduces the heat consumption during the regeneration process. However, Figure 4(b) shows that the refrigeration COP remains at approximately 1.1 mainly because the refrigeration capacity of the fresh air is provided by the cooling water, whereas the total COP is maintained at approximately 0.4. The test results show that the system can run stably for different fresh air humidities below 90%.

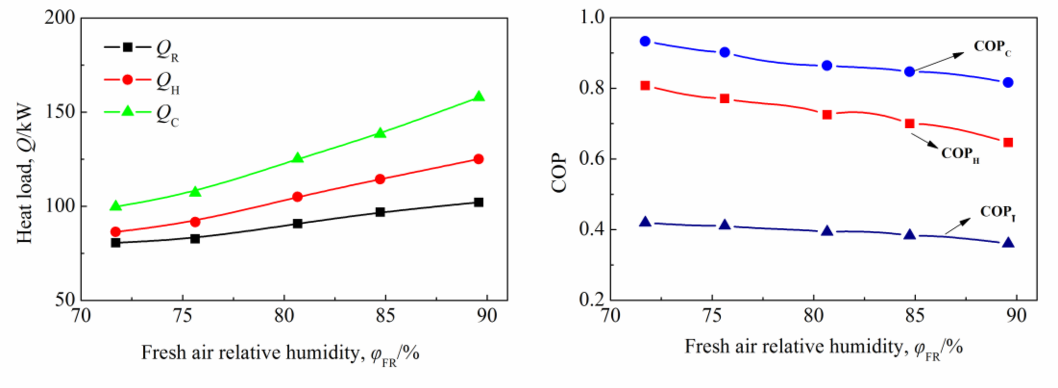

Figure 4 - Heat load and COP versus fresh air humidity

4 Conclusions

A novel type of heat-driven MATS with capacity of 6000 m^3/h was constructed and tested in this study to treat 3-high air. Preliminary test results show that the fresh air treatment capacity of the MATS is 6020 m^3/h, and the fresh air state is 90% RH@30°C. Processing air using the integrated prototype results in a supply air state of 50% RH@18°C and decreases the air aerosol content by more than 90%. The system COP is 0.40. The integrated method can feasibly be driven by waste heat for air cooling, dehumidification, and aerosol removal to effectively solve problems associated with 3-high air in coastal areas and islands, providing clean air at a suitable temperature, humidity and low aerosol content indoors and improving human comfort in living environments. The test results also show that the MATS system adapts well to variable working conditions, maintaining relatively stable performance. The method and the device developed in this study are expected to solve the problems associated with 3-high air for islands, while achieving energy savings and emission reduction and providing support for building a low-carbon, green, active anti-corrosion, and sustainable island energy system.

5 Acknowledgment

The authors acknowledge the support of the National Natural Science Foundation of China (Grant No. 51806213), and the Beijing Key Laboratory of Distributed Combined Cooling Heating and Power Systems.

6 List of References

1. W. R. Patberg and J. J. Rasker, *J Rheumatol*, 2004, **31**, 1327-1334.
2. H. Grythe, J. Ström, R. Krejci, P. Quinn and A. Stohl, *Atmos Chem Phys*, 2014, **14**, 1277 – 1297.
3. P. R. Roberge, R. D. Klassen and P. W. Haberecht, *Mater Design*, 2002, **23**, 321-330.
4. B. J. A. Duncan J R, *Marine salts contribution to atmospheric corrosion*, ASTM International, 1987.
5. R. Qi, C. Dong and L.-Z. Zhang, *Energ Buildings*, 2020, **215**, 109897.
6. S. Yamaguchi, J. Jeong, K. Saito, H. Miyauchi and M. Harada, *Appl Therm Eng*, 2011, **31**, 3741-3747.
7. Z. Li, X. Liu, Y. Jiang and X. Chen, *Energ Buildings*, 2005, **37**, 587-593.
8. Y. Dai, F. Liu, J. Sui, D. Wang, W. Han and H. Jin, *Appl Energy*, 2020, **275**, 115365.

Field test results of an adsorption off-grid vaccine refrigerator for temperate climates

Kühn, Roland[1*], Göller, Christoph[1], Mähne, Kilian[1], Römer, Julia[1], Schrecker, Stefan[1]

[1] *Coolar UG (haftungsbeschränkt), Wolfener Str. 32-34/Haus C, 12681 Berlin, roland@coolar.co*

Abstract:

In many regions, sufficient vaccination is only possible with off-grid cooling technologies. The state-of-the-art technology for the last mile of vaccine supply chains are photovoltaic solar direct drive refrigerators. As an alternative, various concepts for refrigerators based on the adsorption refrigeration technology were developed for this use-case in the past thirty years. Previously, Coolar presented a novel concept for such an adsorption refrigerator. Field test results of the latest prototype for temperate climates (32°C) are presented here.

1 Introduction

Nearly a billion people worldwide have no access to electricity [1] and many more have no reliable access. For many of these people a sufficient medical care is not guaranteed since many medicines require cooling in a temperature range between 2°C and 8°C and this is largely realized with electricity driven refrigerators. According to [2], every us dollar that is invested in effective child vaccination yields USD 16 of economic benefit through prevention of disease and even up to USD 44, taking the increased productivity and the generally improved state of health into account. However, in 2014 98% of the off-grid utilities in developing regions had either outdated (23%), improper (41%) or non-functioning (14%) or not any (20%) refrigeration solutions [3]. As a result, 78% of vaccines are exposed to the risk of inadequate or excessive cooling [3]. With insufficient cooling, the vaccines slowly lose effectiveness, while freezing immediately spoils the vaccines.

There are various off-grid technologies available. Absorption refrigeration was the previous standard technology for off-grid vaccine cooling before photovoltaic driven refrigerators became widely available. However, today, the WHO recommends using vaccine refrigerators without electrical energy storage and only such that operate without relying on fossil fuels [4]. As a result, currently so-called SDD refrigerators ("solar direct drive"), which use ice storages in the refrigerator to store the cold instead of storing electrical energy in batteries, are the primary solution deployed for cooling vaccines off-grid. A drawback of this more robust technology is that the compressors are connected directly to the photovoltaic system. Therefore, the cooling system is only able to provide cooling as long as there is sufficient solar irradiation available. Due to the necessary minimum starting current of the compressor and the weak yield of energy of the PV system from diffusive irradiation, the operation of SDD refrigerators is very prone to disruptions from cloudy weather conditions. Even if clouds occur only for a short time the compressor might stop and might not start again, resulting in an insufficient loading of the cold storage [5] which causes that the desired storage temperatures cannot be maintained overnight. Depending on the model of refrigerator, ice storages might also become too cold so that the vaccines spoil from accidental freezing [4]. Thus, the complex dimensioning of the necessary photovoltaic system plays a crucial role [4]. As an alternative, there were approaches to realize the cooling using solar thermal energy driven adsorption refrigeration systems. Most of the concepts developed over the last 30 years produce either cool water at night [6] or, at best, ice [6,7]. There is no temperature control and methanol is used as the refrigerant [6,7]. Unfortunately, the cold room is often heated by the condensed water during regeneration at daytime in these previous concepts [7]. Thus, the intervention of the user is always required, having to either manually transfer the goods to chilled or the ice [7] into a cool box. In addition, so far only solar thermal collectors which are filled directly with the sorption medium have been proposed [6,7]. These must be connected vacuum-tight to the cooling unit, which greatly limits the flexibility to place the refrigerator and makes the system difficult to install and prone to leakages. Sufficient ice production for cooling has so far only been achieved at ambient temperatures well below 30 °C [6,7].

Coolar UG developed various prototypes for vaccine refrigerators based on adsorption refrigeration technology, all of which cool the cold room and items stored inside directly and do not require intervention from the user, use water as refrigerant and just need a simple solar thermal heated water circuit to drive the system. As a result, the vacuum system can be kept very compact, enabling the heat supply to be placed more flexibly in relation to the location of the refrigerator and making the system easier to install and less prone to critical leakages. In addition, a good antifreeze-protection for vaccines can be achieved, due to use of water as the refrigerant. The paper at hand analyses field test results of the latest prototype for temperate climates (32°C ambient temperature). The focus is on maintaining the storage temperature of 2 to 8 °C.

2 Experimental set-up

In the Coolar adsorption refrigerator the refrigerant water and the adsorbent silica gel are used. The adsorption refrigeration cycle is comprised of an evaporator, an adsorber, a condenser and some valves, as it is shown in a simplified schematic in Figure 1 (left). The water evaporates inside the evaporator and provides cooling. The water vapor then flows through a check valve into the adsorber where it is adsorbed onto silica gel. The heat of adsorption is rejected by natural circulation though the tubes within the adsorber and a convector located above the adsorber. For regeneration hot water is provided through the very same tubes within the adsorber by using a standard solar thermal system. A thermal expansion valve closes the connection to the convector at 50°C water temperature to prevent additional heat losses. The desorbed water vapor then flows through a check valve into the condenser where it is condensed. The liquid water then flows back into the evaporator, driven by gravity and pressure differences. The refrigerator is a one chamber system, so that at day-time hot water is provided and regeneration is performed and when the sun is not shining cooling is provided.

The refrigerator is equipped with a 40-liter cold storage around the evaporator on all walls of the cold room. The cold storage is filled with a paraffin as phase change material (PCM) with a melting region around 5°C (Rubitherm RT 5HC). A detailed system description with schematics of the former, but comparable prototype, was published before [8]. Figure 1 shows the system setup of the field test. Due to the Corona pandemic the field test that was originally planned to be set in Kenya had to take place in Germany and was performed in August 2020 in Berlin. On the left-hand side the top-loader refrigerator with the cased elevated convectors can be seen. On the right-hand side is the flat plate solar thermal collector with 2m² surface area and an inclination angle of 45°; its orientation is to SSE. The small PV panels above provide electricity for the off-grid data acquisition system.

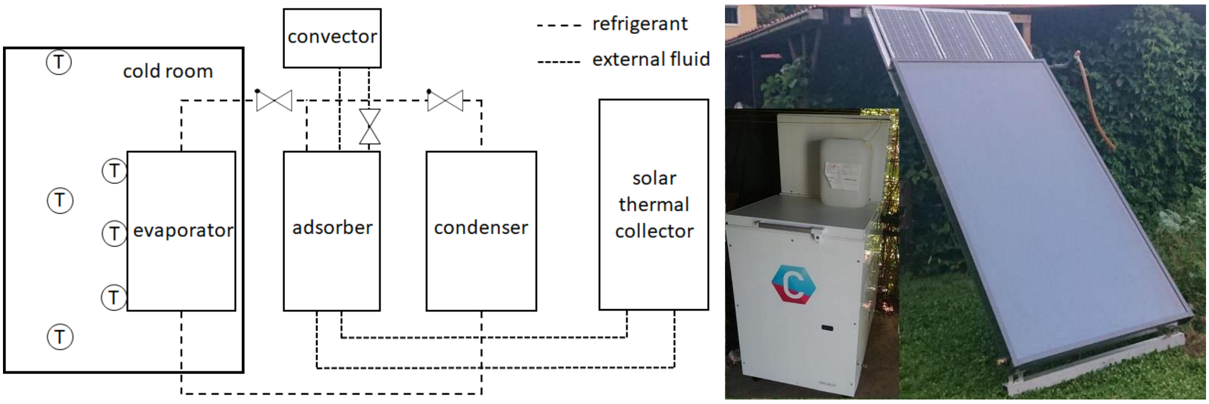

Figure 1 – simplified schematic of the refrigerator (left) and installation of the field test equipment (right)

The refrigerator is equipped with various digital temperature sensors of type Dallas DS18B20 and three pressure sensors. Externally, the temperature of the water entering and leaving the adsorber is measured. The cold room and evaporator temperature is measured by three temperatures sensors each, located on the outside wall of the evaporator and in the compartment in equal vertical spacing above each other [9]. For measuring the ambient temperature two sensors are used.

3 Field test results

Figure 2 shows the temperature evolution of the adsorber inlet, ambient, cold room and evaporator temperature over six days. Additionally, the global solar irradiation on a horizontal area [10] is shown. The green dashed horizontal lines mark the temperature limit between 2 and 8°C for the cold room. The cold storage of the refrigerator was filled with PCM on the 18th of August.

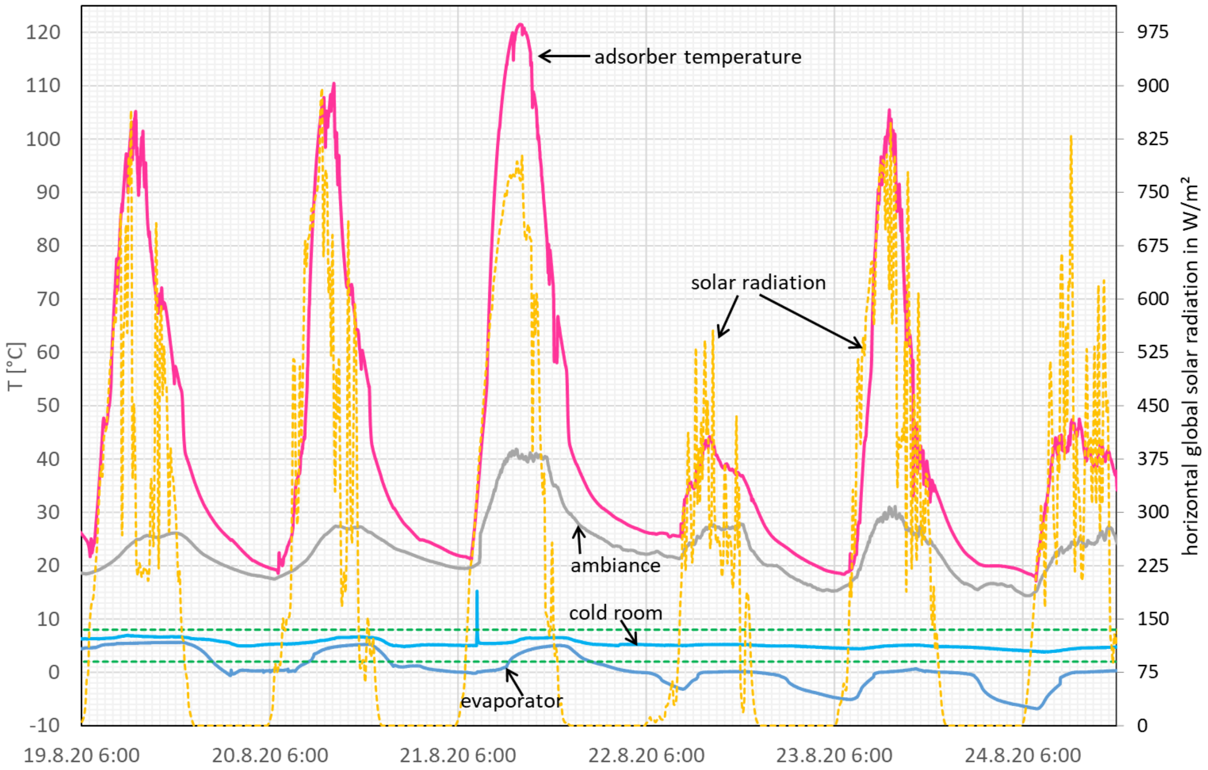

Figure 2 – temperature profiles and solar irradiation [10] in autonomous operation

Approximately one hour after sunrise (yellow dashed line), the temperature in the solar collector and thus, in the adsorber rises (red line). The cool-down of the adsorber is slower than the warm-up. On the first two days a maximum adsorber temperature of above 100°C is reached, although the solar irradiation is strongly fluctuating due to cloudy conditions. With unclouded weather conditions on day three an adsorber temperature of above 120°C is reached. On the cloudy days 4 and 6 the heat from the solar collector is also dissipated from the convectors of the adsorber, because the 50°C water temperature threshold is not reached to close the thermal valve. The ambient temperature (grey line) is qualitatively proportional to the hot water temperature and is below 30°C, except on the third day. The cold room temperature (light blue line) stays within the temperature limit between 2 and 8°C for the whole time. In the morning of the third day a temperature peak can be observed, which is a consequence of the refrigerator cabinet being opened during the test period. On the colder and less sunny days the cold room temperature decreases slightly. This results from the decreasing evaporator temperature (blue line) and the decreasing daily mean ambient temperatures.

In contrast to the cold room temperature, the evaporator temperature fluctuates significantly. When the adsorber temperature is high, water vapor is desorbed from the adsorber and flows to the condenser, the evaporator temperature increases, because no water vapor can flow from the evaporator to the adsorber. When the adsorber cools down, cooling is enabled and the evaporator temperature decreases. Adsorption already starts at an adsorber temperature of above 40°C. This is the case whenever the slight bend above 40°C in the adsorber inlet temperature evolution can be observed; then cool-down becomes slower due to the additional heat of adsorption which must be rejected. The cold room temperature follows the evaporator temperature in a damped manner. As observed on the first day, the evaporator temperature decreases to slightly below 0°C and then jumps back to 0°C when ice is formed in the evaporator. The evaporator temperature stays at 0°C for the whole adsorption period because more ice is formed in the evaporator. When adsorption stops again at around 9 a.m. on the 20th, the evaporator temperature increases. At 11.30 a.m. a small jump in temperature occurs, when adsorber temperature and pressure is high and water is recirculated from the condenser to the evaporator due to the pressure difference between the two. On the 21st of August, the mean evaporator temperature stays above 0°C, but obviously ice is also formed as the evaporator temperature stays nearly constant even during the first hours of regeneration. Then again, a temperature jump occurs and subsequently the evaporator temperature rises faster. From the 22nd onwards, sub-cooled ice is formed in the evaporator during adsorption – evaporator temperature decreases significantly below 0°C – and 0°C cold ice remains even during regeneration throughout the day. Supposedly, the whole water in the evaporator is frozen during night. Nevertheless, the temperature in the cold room stays above the 2°C limit, due to the insulating nature of the PCM around the evaporator.

From the evaporator temperatures observed during this field test, it becomes clear that under temperate climate conditions and with the significantly lower ambient temperatures at night, the sole fact that water is used as the refrigerant does not completely guarantee that the vaccines in the cold room will not freeze. As user interaction and the use of thermal expansion valves for cold room temperature control is prohibited for WHO pre-qualified devices, additional measures must be undertaken to either assure a proper temperature difference between evaporator and cold room, as has been done here with the PCM, or/and to prevent the ice from sub-cooling. The sub-cooling of ice can be prevented or reduced by having more water in the evaporator so that it is harder to freeze the entire water that is available. Thus, the evaporator design must be changed.

4 Conclusions

An off-grid solar thermal driven adsorption refrigerator for cooling vaccines was successfully built and installed at a test location near Berlin. During the field test in August 2020 a sufficient hot water temperature for regenerating the adsorption cycle with a standard flat-plate solar thermal collector could be shown. During the test, the cold room temperature stayed within the given temperature limits between 2 and 8°C. This was possible thanks to using a cold storage filled with PCM, preventing the cold room from becoming too warm at day, when no cooling is provided, and from becoming too cold at night, when sub-cooled ice is formed in the evaporator and ambient temperature is significantly lower. To improve the freeze protection of the refrigerator, the evaporator design can be changed to have either more water in the evaporator or to improve the insulating effect of the PCM by changing the thickness of the cold storage adjacent to the cold room.

5 Acknowledgment

The authors wish to thank the Dubai Expo 2020 Expo Live Program and their grant management team for supporting the prototyping and field-testing efforts that led to the results shown here.

We also thank the German Federal Ministry of Education and Research and the EU joint program "Eurostars-2" for supporting further research into solar thermal driven adsorption refrigerators for hot climate zones.

6 List of References

[1] International Energy Agency (2018): World Energy Outlook 2018, vol.1.

[2] McCarney S., Robertson, J., Arnaud, J., Lorenson, K., Lloyd, J. (2013): Using solar-powered refrigeration for vaccine storage where other sources of reliable electricity are inadequate or costly. *Vaccine*, vol.31 (51), pp.6050-6057.

[3] World Health Organization/UNICEF (2017): Solar direct-drive vaccine refrigerators: evidence brief.

[4] Pedersen, P., Katic, I, Markussen, W.B. Jensen, J.K., Cording, C., Moeller, H. (2019): Direct drive solar coolers, *Refrigeration Science and Technology Proceedings*, pp.3468-3475

[5] Nwamba, K.J. (2008): The design and evaluation of a solar-powered adsorption refrigerator for African conditions. *Magisterial Thesis Dissertation, Tshwane University of Technology.*

[6] Boubakri, A., Arsalane, M., Yous, B., Ali-Moussa, L., Pons, M., Meunier, F., Guilleminot, J.J. (1992): Experimental study of adsorptive solar-powered ice makers in Agadir (Morocco) - 1. Performance in actual site. *Renewable Energy*, vol.2(1), pp.7-13

[7] Saha, B.B, Akisawa, A, Kashiwagi, T. (2001): Solar/waste heat driven two-stage adsorption chiller: the prototype. *Renewable Energy*, vol.23, pp.93-101.

[8] Kühn, R., Mähne, K., Düwel, K., Göller, C., Römer, J. (2019): First field test results of a solar thermal off-grid refrigerator for vaccines. *Refrigeration Science and Technology Proceedings*, pp. 3484-3492

[9] Kühn, R., Göller, C., Goerdten, P., Mähne, K., Römer, J. (2020), Schrecker, S.: Performance evaluation of a double-lift concept for an adsorption refrigerator for high ambient temperatures. *International Sorption Heat Pump Conference 2021 Proceedings – online pre-conference 2020*, pp. 69-73

[10] HTW Berlin (2020): Weather data of HTW Berlin. *http://wetter.htw-berlin.de/SolarCalendar*

Compressor-assisted heat transformer for waste-heat powered district heating applications

Toppi, Tommaso[1], Aprile, Marcello[1], Gianluca Abrami[1], Mario Motta[1]

[1]*Department of Energy, Politecnico di Milano, via Lambruschini 4, 20156 Milano, Italy, tommaso.toppi@polimi.it*

Abstract:

The recovery of low-temperature waste heat can be promoted by upgrading its temperature. Heat transformers are capable to increase the temperature of a heat stream with a minor contribution of electrical energy. However, the lifting capability of heat transformers are limited by the operating conditions and often insufficient to meet the temperature required by many applications. To overcome this limitation, in this paper a compressor assisted heat transformer is numerically investigated, targeting the application in medium and high temperature district heating networks. Using waste heat at 50 and 60 °C and heat rejection temperature at 0 °C and -10 °C, it is possible to upgrade heat up to 120 °C with an electrical COP always above 4, a thermal COP of about 0.5 and an upper pressure below 40 bar.

1 Introduction

District heating is often considered a key option in the process of the decarbonization of the heating sector, thanks to its capability to both establish energy communities characterized by high renewable penetration and to match availability of waste heat with heating demand, usually not geographically close. However, while high and medium temperature waste heat can be easily recovered in district heating, it also finds other applications either directly in the industry or for electricity generation with ORC. On the contrary, low grade waste heat is harder to be recovered, so finding a way to reuse it in a district heating network would represent an interesting option both from the economic and the environmental point of view. This would also benefit by the fact that often low-temperature waste heat is generated relatively close to the urban areas, as in the case of water-cooled datacenter [1]. One option to couple low-grade heat with district heating is the use of low-temperature networks, which could allow direct recovery. However, many existing networks operate at higher temperature and would benefit by an increase of the waste heat temperature. The option normally considered is the use of a vapor compression heat pump to upgrade the heat to the required temperature. However, the potential of this option is limited by the efficiency reduction at high thermal lifts, which leads to high electricity consumption. A second opportunity is the use of a heat transformer, which faces limitations in terms of working range, i.e. its thermal lift cannot go beyond a certain level.

A compressor assisted heat transformer (CHT) merges in a single cycle the features of the two solution, exploiting the capability of a heat transformer to upgrade low temperature heat and the flexibility provided by the compressor to extend the working range. This solution has been investigated by [2] with the purpose of recovering very low heat ($T \approx 15$ °C), rejecting heat toward a low temperature environment ($T < -10$ °C) and providing heat for low temperature heating ($T \approx 45$ °C). The compression assisted heat transformer proved to require lower electrical input than a water source heat pump operating at the same conditions. However, the explored working condition represent a niche in the heating sector, due to the very low ambient and water temperature, which are favorable for the cycle performance and allow the use of very low temperature waste heat. Thus, in this work, more challenging conditions are investigated, exploring the capability of a CHT to provide efficient heat in hard-to-decarbonize networks, i.e., high (up to 120 °C) or medium temperature (80 °C), starting from a driving temperature of about 50-60 °C. This temperature range also covers a fraction of the industrial heat demand, extending the applicability of the explored solution.

2 Cycle layout and modelling approach

2.1 Cycle layout

Two options are available when adding a compressor to a single stage heat transformer. In the former, the compressor is installed between the generator (GEN) and the condenser (COND) allowing the condensation pressure to be higher than the generation pressure. Alternatively, as depicted in Figure 1, the compressor can be installed between the evaporator (EVA) and the absorber (ABS), allowing the generation pressure to be lower than the condensation pressure. In both cases the use of the compressor extends the working range of the heat transformer, enabling the use of heat sources (for GEN and EVA) at lower temperatures or heat sinks (for COND and ABS) at higher temperatures.

For the present work, the second option has been selected because it allows to use a smaller compressor, given that the specific volume of the vapor is smaller due to the higher pressure. This is beneficial for the dimensions of the compressor, especially when a volumetric machine (e.g., a membrane compressor) is used.

Two internal heat exchangers are used for heat recovery purposes: the refrigerant heat exchanger (RHE) and the solution heat exchanger (SHX).

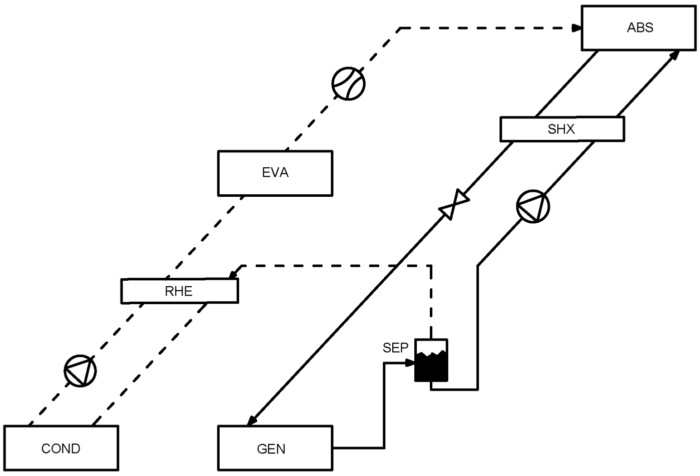

Figure 1 – Layout of the cycle

2.2 Modelling approach

It was assumed that counter-current heat exchangers are used for the heat transformer. For what concerns the generator, a phase separator is added at the solution outlet and a tray column is used to assure a high ammonia mass fraction in the vapor. In the absorber, vapor and poor solution are adiabatically mixed at the inlet of the heat exchanger.

The cycle was numerically modelled using STACY, a tool described in [3], which provides a mathematical framework for steady-state calculation of absorption cycles. The tool is based on a modular approach and support the calculation for each component of the energy, mass and species balances. Additionally, the system of equations is completed with pressure and heat transfer conditions. In particular, the following were assumed within this study:

- Pressure losses are negligible in the pipes and in all heat exchangers but the absorbers where a fixed value of 20 kPa is assumed [4, 5].
- Heat losses are negligible.
- Throttling is isenthalpic.
- The efficiency of the internal heat exchangers (SHX and RHE) is 0.85

The conditions at the absorber, condenser and evaporator were set based on the following assumptions:

- in the generator, a minimum pinch of 5 °C is set between heat source fluid and solution outlet [4].
- at the absorber, a fixed subcooling of 1 °C at the solution outlet and minimum temperature difference of 5 °C is imposed along the heat exchanger [6];
- at the condenser, a fixed subcooling of 1 °C is set at the refrigerant outlet and the minimum temperature difference of 3 °C is imposed between refrigerant and cooling water [6];
- in the evaporator, the minimum temperature difference between the heat source fluid and the refrigerant is 3°C and the refrigerant leaves the heat exchanger with a vapor quality of 0.95 [7].

The mass flow rate of the external circuits was adjusted to maintain fixed temperature differences:

- generator and evaporator are connected in series and the overall temperature difference between generator inlet and evaporator outlet is 10 °C;
- a temperature difference of 30 °C is set between inlet and outlet of the absorber;
- a temperature difference of 5 °C is set between inlet and outlet of the condenser.

The cycle performances are evaluated based on the electric COP, defined as in eq. 1, which provides the ratio between the heating capacity released at high temperature and the electric power needed to run the compressor and the refrigerant and solution pumps. The electric power is calculated assuming an efficiency of the electric motors of 0.9 and isentropic efficiencies for pumps and compressor of 0.8 and 0.7, respectively.

Moreover, the thermal COP, defined in Eq. 2, expresses the ratio between the heating capacity at high temperature and the heating power at intermediate temperature provided to the cycle. It is worth mentioning that the COP_{th} is not strictly the share of the driving heat, which is upgraded to a higher temperature, as in the balance it must be taken into account the contribution of the compressor.

$$COP_{el} = \frac{Q_{ABS}}{W_{COMP} + W_{P\ REF} + W_{P\ SOL}} \tag{1}$$

$$COP_{th} = \frac{Q_{ABS}}{Q_{GEN} + Q_{EVAP}} \tag{2}$$

3 Results and discussion

In this section the cycle performances, calculated numerically for various operating conditions, are presented. The operating conditions are identified with the inlet temperature of the intermediate ($T_{M\ in}$) and the low ($T_{C\ in}$) temperature circuits, which represent the temperatures of the available waste heat and of the available sink for the heat rejection, respectively. For what concerns the absorber, the outlet temperature ($T_{H\ out}$) is used as reference, since it is the temperature of the upgraded heat.

3.1 Influence of the high pressure

The outlet pressure of the compressor (P_{out}) can be freely fixed, provided that it is above a minimum value which allows the cycle operation. Thus, the first analysis which has been carried out is on the impact of this quantity on the cycle performances. Figure 2 reports the variation of the COP_{th} and the COP_{el} with the compressor outlet pressure, for various $T_{H\ out}$. The calculations have been done using -10 °C as the $T_{C\ in}$ and 50 °C as $T_{M\ in}$. The results show that as P_{out} increases, the COP_{el} experiences a maximum before decreasing. In fact, at low pressure, the cycle is close to cut-off conditions and the heat duty at the absorber is very low, as can be deduced looking at the trends of COP_{th}. Then, as the value of COP_{th} becomes practically constant with P_{out}, the additional power required to run the compressor does not translate into an increase of the heat duty at the absorber.

Worth to be noticed is that P_{out} which maximizes the COP_{el} is always below 40 bars, even when $T_{H\ out}$ is 120 °C.

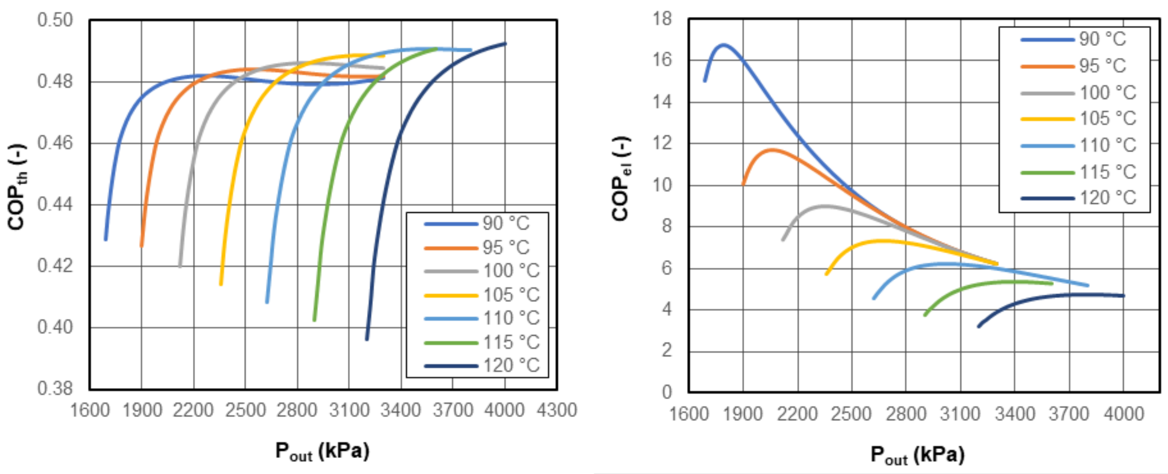

Figure 2 – COP_{th} and COP_{el} vs. Pout for $T_{H\ out}$ from 90 to 120 °C, with $T_{C\ in}$ = -10 °C and $T_{M\ in}$ = 50 °C.

3.2 Heat transformer performances

A second analysis of the cycle performances is carried out comparing four different cases, obtained through the combination of two values of $T_{C\,in}$ (0 °C and -10 °C) and two $T_{M\,in}$ (50 °C and 60 °C). The results presented in Figure 3 provide the COP_{th} and the COP_{el} as function of $T_{H\,out}$. Given the impact of P_{out} on the cycle performances, the results in Figure 3 have been obtained using for each condition the value of P_{out} which maximizes the COP_{el}. This choice can be justified considering that in the present work the use of waste heat of relatively low value is explored. Under these conditions, the minimization of the electrical input is more important than the maximization of the heat recovery. Moreover, the choice of a P_{out} optimized for the COP_{el} has little influence on the COP_{th}. In fact, as observed in Figure 2, if sufficiently far from the cut-off condition, the variation of COP_{th} with P_{out} is very limited.

The two conditions at 60 °C (orange and grey lines) begin at are higher values of $T_{H\,out}$ than the conditions at 50 °C because at low $T_{H\,out}$ the compressor is not needed and a traditional heat transformer can be used.

The results reported in figure 3 confirm that the use of a compressor allows the heat transformer to operate over the entire range of absorber outlet temperature, even in the least favorable conditions, i.e. with $T_{C\,in}$ = 0 °C and $T_{M\,in}$ = 50 °C as the low and intermediate temperature circuits. Moreover, it appears that $T_{M\,in}$ has a larger impact on the COP_{el} than $T_{C\,in}$. In fact, starting from the 0 °C and 60 °C condition, a higher COP_{el} is obtained increasing the $T_{M\,in}$ from 50 to 60 °C rather than decreasing the $T_{C\,in}$ from 0 to -10 °C.

The upper pressure of the cycle resulted below 40 bars for all the working conditions presented in Figure 3 except with $T_{C\,in}$ = 0 °C and $T_{M\,in}$ = 50 °C when $T_{H\,out}$ goes above 110 °C, when the limits move to 46 bars.

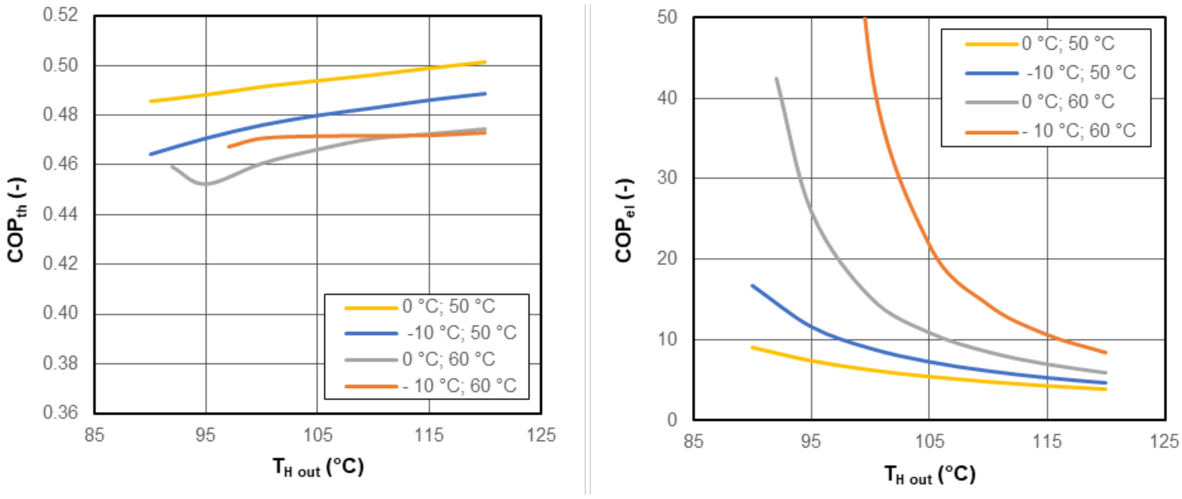

Figure 3 – COP_{th} and COP_{el} vs. absorber outlet temperatures for four combination cold and intermediate circuits temperatures.

4 Conclusions

The numerical calculation of the performances of the compression assisted heat transformer proved that it represents a suitable solution for powering district heating networks at temperatures up to 120 °C. In particular it has been observed that:

- for a given working condition the compressor outlet temperature can be adjusted to maximize the electrical COP, with minor impact on the thermal COP;
- the thermal COP is between 0.45 and 0.50 for all the investigated conditions;
- the use of a compressor increases the working range of the heat transformer allowing thermal lift which cannot be achieved with a traditional heat transformer;
- the electrical COP is well above 10 for most of the high temperature range, when the temperature of the waste heat is 60 °C.

5 List of References

[1] Ebrahimi K., Jones G.F., Fleischer A.S. (2014): A review of data center cooling technology, operating conditions and the corresponding low-grade waste heat recovery opportunities. *Renewable and Sustainable Energy Reviews*, vol. 31, pp. 622-638.

[2] Wang J., Wang B., Li X., Wu W., Shi W. (2018): Performance analysis on compression-assisted absorption heat transformer: a new low-temperature heating system with higher heating capacity under lower ambient temperature. *Applied Thermal Engineering*, vol. 134, pp. 419-427.

[3] Aprile, M., Toppi, T, Garone, S., Motta, M. (2018): STACY–A mathematical modelling framework for steady-state simulation of absorption cycles. *International Journal of Refrigeration*, vol. 88, pp. 129-140.

[4] Xu, Z.Y., Wang, R.Z. (2018): Comparison of absorption refrigeration cycles for efficient air-cooled solar cooling. *Solar Energy Energy*, vol. 172, pp. 14–23.

[5] Toppi, T., Aprile, M., Guerra, M., Motta, M. (2017). Performance assessment of a double-lift absorption prototype for low temperature refrigeration driven by low–grade heat. *Energy*, vol. 125, pp. 287–296.

[6] Toppi, T., Aprile, M., Guerra, M., Motta, M. (2016). Numerical investigation on semi–GAX NH3 -H2O absorption cycles. *International Journal of Refrigeration*, vol. 66, pp. 169–180.

[7] Garone, S., Toppi, T., Guerra, M., & Motta, M. (2017). A water-ammonia heat transformer to upgrade low-temperature waste heat. *Applied Thermal Engineering*, vol. *127*, pp. 748-757.

Optimization of Vapor Compression-Absorption Cascade Refrigeration Systems

Mussati, Sergio[1,a], **Morosuk, Tatiana**[2,b], **Mussati, Miguel**[1,c]

[1] INGAR Instituto de Desarrollo y Diseño (CONICET-UTN), Avellaneda 3657, 3000, Santa Fe, Argentina
[2] Institute for Energy Engineering, Technische Universität Berlin, Marchstr. 18, 10587 Berlin, Germany
[a] mussati@santafe-conicet.gov.ar; [b] tetyana.morozyuk@tu-berlin.de; [c] mmussati@santafe-conicet.gov.ar

Abstract:

This paper focuses on the optimization of a vapor compression-absorption cascade refrigeration system (VCACRS). The absorption cycle consists of a series flow double-effect system using saturated steam as the hot source and H_2O-LiBr as the refrigerant-absorbent pair. The compression cycle is a conventional one but considering the possibility to use one of two candidate working fluids: R717 or R134a. A binary variable is used to mathematically model the selection of the working fluid in the compression cycle, resulting in a mixed-integer nonlinear mathematical programming (MINLP) model, which is implemented in the GAMS environment and solved using an optimization algorithm based on the generalized reduced gradient (GRG) method. The minimization of the total annual cost (TAC) – which accounts for capital investment and operating expenditures – is proposed as the objective function. The refrigeration temperature and capacity are the only parameters of the model (fixed values) and the mass flow rate, pressure, temperature and composition of all process streams are simultaneously optimized (decision variables). Also, the model is implemented in such a way that allows to systematically remove the high-pressure condenser and the two solution heat exchangers – these three components can be optionally selected or removed as appropriate. As a result, an optimal structure, optimal component sizes, and optimal operating conditions of the cascade system are obtained. A novel system reported in the literature involving a different VCACRS configuration operated with H_2O-LiBr in the absorption cycle and R717 in the compression cycle is used as a reference case for comparison purposes in order to elucidate which of the two systems is preferred when the total investment cost is considered. The comparison of the results shows that the optimal solution obtained from the superstructure-based model is much less costly than the reference case and represents the main implication of the obtained optimized system. In fact, it was found that TAC is by around 37% lower with respect to the reference case. Also, the high-pressure condenser is removed from the optimal solution. The optimal refrigerant selected by the model in the compression cycle is R134a. If R134a is replaced by R717, the TAC is still by around 2% lower with respect to the reference case.

1 Introduction

This work is a continuation of the work presented in [1]. In that paper, a nonlinear programming (NLP) model was proposed, the total heat transfer area of the system (THTA) was minimized without considering the associated costs, and no selection of the refrigerant in the compression cycle was considered. In this work, it is proposed to extend the NLP model to a MINLP model, minimize the total annual cost (TAC), and select the refrigerant fluid in the compression cycle. On the other hand, this work differs from other studies in that simultaneous optimization is applied, taking into account, not only the operating conditions and equipment sizes, but also the configuration (structure) of the process. Given the refrigeration capacity (100 kW) and temperature (−30.0 ºC), the optimization problem consists in determining the structure and operating conditions that lead to the minimum TAC by applying a deterministic optimization algorithm. The aim of this work is to optimize a vapor compression-absorption cascade refrigeration system using a superstructure-based optimization model which embeds several candidate configurations and compare the obtained solution (Fig. 1a) with a solution corresponding to other system (Fig. 1b) reported in the literature [2] which is considered as a novel and attractive system. To the best of the author's knowledge, no studies focusing on such comparison is found.

2 Mathematical Modelling Aspects

The optimization mathematical model involves the mass and energy balances in all process components, the calculation of the heat transfer areas (HTA) required by them, and the electrical power required by the compressor. Methodological aspects, characteristics on how the superstructure is represented and the main model constraints can be found in [1]. Correlations reported in [3] are used to estimate the physicochemical properties of the H_2O-LiBr solution streams and those reported in [4] to estimate the properties of the working fluid in the compression cycle. Clevand [4] proposed correlations for several refrigerants using the same functional dependence on temperature for all of them. Interestingly, these correlations are effectively used in this work for selecting the most convenient fluid – between R717 and R134a in this case – through binary variables 0/1. The model allows selecting/removing the high-temperature condenser (HTC) – by placing a splitter (SPLT) prior to it – and the high- and low-temperature solution heat exchangers (HTSHE and LTSHE, respectively) considering their effectiveness (η_{HTSHE} and η_{LTSHE}) as optimization variables, which are bounded between 0 and 100%. When $\eta_{SHE} = 0$ no heat is exchanged and, consequently, the associated HTA is zero.

The total annual cost (TAC) is expressed in Eq. (1) and it accounts for the annualized capital expenditure (annCAPEX) and operating expenditure (OPEX):

$$\mathrm{TAC} = \mathrm{annCAPEX} + \mathrm{OPEX} \tag{1}$$

where the annCAPEX is calculated by Eq. (2). The equations used to calculate the purchased costs of the system components k (Z_k) are reported in [5] and expressed in Eq. (2). The parameter CRF refers to the capital recovery factor. The OPEX is calculated by Eq. (3) and it considers the costs associated to the demand of steam S, cooling water CW, and electricity E. The parameters C_s, C_E, and C_{CW} are, respectively. the specific cost of steam (0.017 $\$\cdot kg^{-1}$), electrical power (0.06 $\$\cdot kWh^{-1}$) and cooling water ($1.0\times10{-}4$ $\$\cdot kg^{-1}$) while t refers to the total operating time (7000 $h\cdot yr.^{-1}$).

$$\mathrm{annCAPEX} = \mathrm{CRF}\cdot\sum_{k} Z_k \tag{2}$$

$$\mathrm{OPEX} = \left[C_S\cdot\left(\dot{m}_{32}+\dot{m}_{36}\right)\cdot 3600 + C_E\cdot\dot{W}_{COMP} + C_{CW}\left(\dot{m}_{28}+\dot{m}_{34}\right)\cdot 3600\right]\cdot t \tag{3}$$

As a series flow double-effect system using H2O-LiBr is considered, 130 ºC is assumed as the temperature level of the heat source driving the absorption cycle. It should be mentioned that the reference case works with hot water at 75ºC. The efficiencies of the compressors are model parameters (80%). Cooling water at 25ºC is assumed in the absorber and absorption cycle condenser. A value of 0.095 $\$\cdot yr.^{-1}$ is considered for CRF. The values of the overall heat transfer coefficients ($kW\cdot m^{-2}\cdot K^{-1}$) for the evaporator, absorber, condenser, generator, condenser-evaporator, and heat exchangers are, respectively, 1.50, 0.70, 2.50, 1.50, 0.55, and 1.00. And, as a first approximation, no maintenance costs are considered.

3 Results

The optimal solution obtained by the proposed MINLP model (Fig. 1a) – hereinafter referred to as TAC-OS – is compared to the reference case taken from [2] and presented as a novel system in the literature (Fig. 1b) – hereinafter referred to as RC –. The optimal solution selected R134a as refrigerant in the compression cycle whereas R717 was considered in [2]. As shown, the system in [2] includes an additional absorber (high-temperature absorber HTABS) and an additional compressor (COMP2) in between the two single effects, which are both not present in the configuration schematized in Fig. 1a. By solving the proposed MINLP model, the HTC is removed from the optimal solution, and the refrigerant R134a is selected to operate the compression cycle. According to Table 1, the minimum TAC value obtained in TAC-OS is 48753.6 $\$\cdot yr.^{-1}$, of which 89% corresponds to OPEX (43477.8 $\$\cdot yr.^{-1}$). The costs associated to the consumption of steam and cooling water are almost similar (17313.4 $\$\cdot yr.^{-1}$ and 17941.5 $\$\cdot yr.^{-1}$, respectively), which together represent by around 81% of OPEX and 72% of TAC. Regarding annCAPEX, COMP1 is the system component that contributes the most to it (32%), followed by COND/EVAP and LTABS (26% and 20%, respectively). Table 1 shows that the TAC value obtained in TAC-OS is by 37% lower than that obtained in RC solution (48753.6 vs. 77541.7 $\$\cdot yr.^{-1}$). This is due to a significant reduction in OPEX by around 39% – from 71148.1 to 43477.8 $\$\cdot yr.^{-1}$ – since the annCAPEX in TAC-OS is 17% lesser than in RC (5275.8 vs. 6393.6 $\$\cdot yr.^{-1}$). Although the heating utility is assumed costless in RC only, the high OPEX in RC is due to the high requirements of cooling water in HTC, LTABS and HTABS and of electrical power in COMP1 and COMP2, which are by around 200% and more than 105% higher than in TAC-OS (54202.6 vs. 17941.5 $\$\cdot yr.^{-1}$, and 16945.4 vs. 8222.8 $\$\cdot yr.^{-1}$). Although THTA required in RC is by 52% lower than in TAC-OS (Table 2), the inclusion of the compressor COMP2 in RC leads to an annCAPEX value that is 17% higher than in TAC-OS (Table 1). In addition, as shown in Fig. 1b, the electrical power required by COMP2 in RC is 7.1 kW, resulting in an increase in the electricity cost of 2986.7 $\$\cdot yr.^{-1}$ (Table 1). Also, since the heat rejected in RC is by 133% higher than that in TAC-OS, the cooling water requirement in RC is tripled with respect to TAC-OS (Table 2), resulting in an increase of 36261.1 \$·yr.$^{-1}$ in the cooling water cost (54202.6 vs. 17941.5 \$·yr.$^{-1}$). The operating pressures in the absorption cycle in TAC-OS are higher than those in RC, contrary to what happens with the compression cycle. HTG and LTG operate at 43.17 and 4.89 kPa, respectively, in TAC-OS and at 5.63 and 2.00 kPa, respectively, in RC. Regarding the compression cycles, COMP1 compresses the refrigerant R134a from 85.13 to 349.89 kPa in TAC-OS and refrigerant R717 from 119.40 to 636.80 kPa in RC, but TAC-OS requires a refrigerant flow rate significantly higher than RC (0.518 kg/s of R134a vs. 0.085 kg/s of R717). The type of refrigerant strongly affects the operating conditions.

*Figure 1 – Comparison between the optimal solution TAC-OS (**a**) and the reference case RC (**b**)*

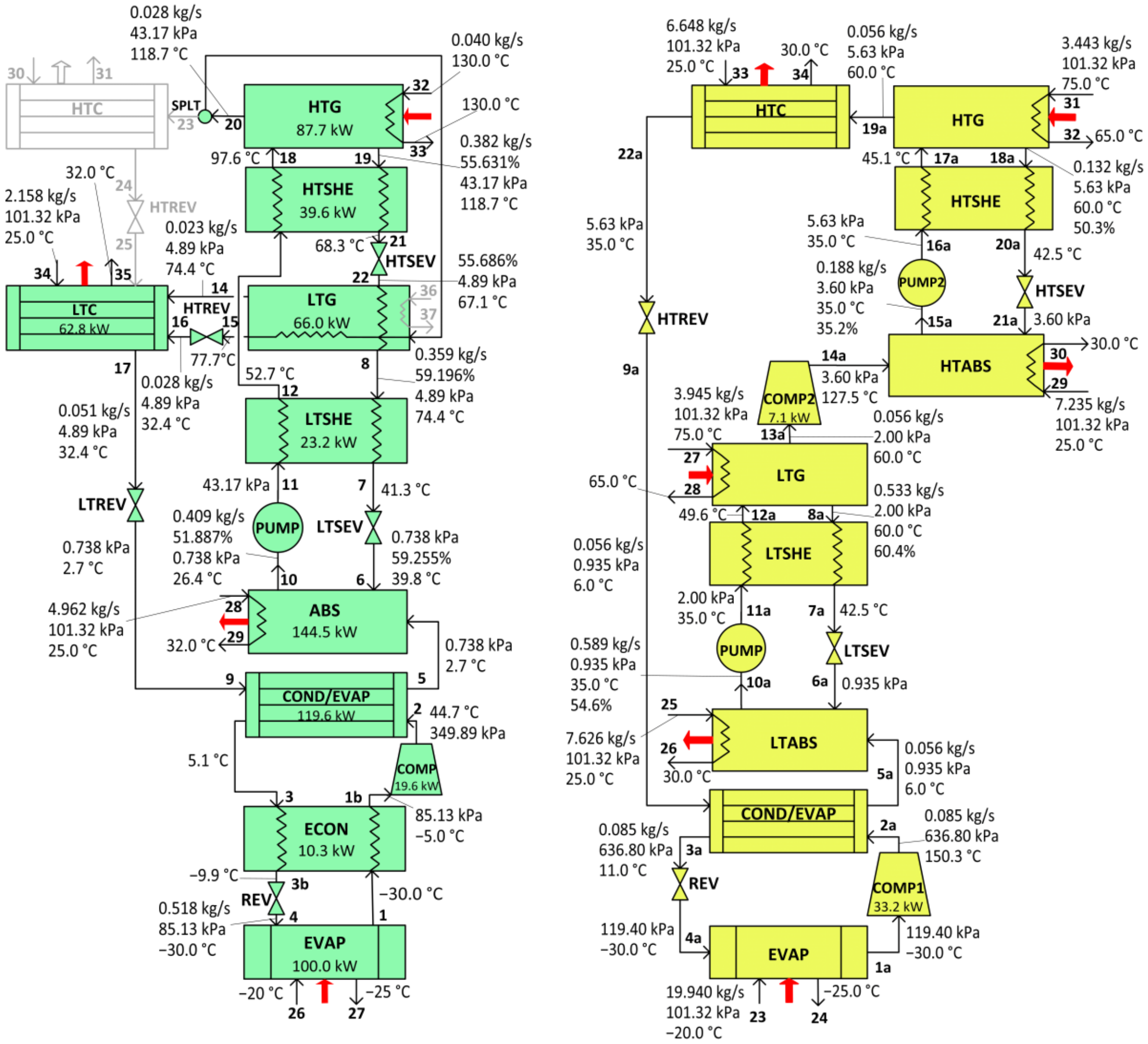

Table 1 – Comparison of cost-items between RC, TAC-OS (R134a), and TAC-SOS (R717) solutions.

Cost item	RC [2]	TAC-OS	TAC-SubOS
TAC (\$·yr.$^{-1}$)	**77541.7**	**48753.6**	**49718.0**
AnnCAPEX (\$·yr.$^{-1}$)	**6393.6**	**5275.8**	**5261.2**
EVAP	204.9	205.4	205.4
COND/EVAP	935.8	1403.8	1365.8
LTABS	572.5	1052.3	1061.1
LTSHE	102.7	79.1	79.6
LTG	326.2	318.2	320.3
HTSHE	43.3	108. 5	109.2
HTG	277.8	189.4	189.5
HTABS	554.7	–	–

	HTC	155.1	−	−
	LTC	0	189.2	190.6
	ECON	0	47.4	26.5
	COMP1	1927.1	1682.5	1712.9
	COMP2	1293.4	−	-
OPEX (\$·yr.$^{-1}$)		**71148.1**	**43477.8**	**44456.7**
Hot water		0	0	0
Steam		0	17313.4	17502.2
Cooling water		54202.6	17941.5	18145.2
	LTC	−	5438.3	5501.2
	LTABS	19217.5	12503.6	12644.0
	HTABS	18232.2	−	−
	HTC	16752.9	−	−
Electricity		16945.4	8222.8	8809.3
	COMP1	13958.7	8222.8	8809.3
	COMP2	2986.7	−	−

Table 2 – Comparison of results between RC, TAC-OS (R134a), and TAC-SOS (R717) solutions.

Variable	RC [2]	TAC-OS	TAC-SubOS
Total heat transfer area (m^2)	109.24	165.68	165.71
Heating utility (kW)	309.5 [a]	87.7 [b]	88.7 [b]
Cooling utility (kW)	450.5 [c]	207.3 [d]	209.7 [d]
Electrical power (kW)	40.3	19.6	21.0
Cooling water (kg·s^{-1})	21.509	7.120	7.205
Hot water (kg·s^{-1})	7.388	0	0
Steam (kg·s^{-1})	0	0.040	0.041

[a] includes HTG and LTG; [b] includes HTG; [c] includes HTC, HTABS and LTABS; [d] includes LTC and ABS

The same optimization problem is solved considering the R717 refrigerant by setting the binary variable to zero i.e. $y_{R134a}=0$. The obtained optimal solution is hereinafter referred to as TAC-SubOS. It represents a sub-optimal solution with respect to TAC-OS (R134a) because this imposition decreases the original degrees of freedom of the optimization problem. The main results are listed in the fourth column of Tables 1 and 2. The comparison of results shows that the TAC value in TAC-SubOS (R717) is still significantly lower than that in RC and slightly higher than that in TAC-OS (R134a). Finally, it should be mentioned that despite the correlations used in this work to calculate the physicochemical properties of streams are widely accepted in the literature, sensitivity and uncertainty analyses should be performed in order to explore and quantify the impact of possible errors in input data on the calculated model output. This issue will be deeply investigated and discussed in a next work.

4 Conclusions

A deterministic mixed-integer nonlinear mathematical programming (MINLP) model has been successfully applied to cost optimization of vapor compression-absorption cascade refrigeration systems. The selection of the refrigerant to operate the compression cycle − R717 or R134a − as well as the selection/removal of the high-temperature condenser and the two LiBr solution heat exchangers were treated as discrete decisions. A reference case reported in the literature involving a different VCACRS configuration operated with hot water and H_2O-LiBr pair in the absorption cycle and R717 in the compression cycle, is used for comparison purposes. The comparison of the results shows that the optimal solution obtained from the superstructure-based model is much less costly than the reference case and represents the main implication of the obtained optimized system. By solving the proposed MINLP model, it was found that TAC is by around 37% lower with respect to the reference case, the high-temperature condenser is removed from the optimal solution, and R134a refrigerant is selected in the compression cycle. If R134a is replaced by R717, the TAC value is still by around 2% lower with respect to the reference case. Although the heating utility is assumed costless in the reference case, the inclusion of an additional compressor increases both the electricity cost (OPEX) and the associated investment (CAPEX), resulting in a higher TAC compared to the optimization results presented in this paper.

5 List of References

[1] Mussati, S.F., Cignitti, S., Mansouri, S.S., Gernaey, K.V., Morosuk, T., Mussati, M.C. (2018): Configuration optimization of series flow double-effect water-lithium bromide absorption refrigeration systems by cost minimization. *Energy Conservation and Management*, vol.158, pp.359-372.

[2] Jain, V., Sachdeva, G., Kachhwaha, S.S. (2018): Comparative performance study and advanced exergy analysis of novel vapor compression-absorption integrated refrigeration system. *Energy Conversion and Management*, vol.172, pp.81-97.

[3] American Society of Heating, Refrigerating and Air-Conditioning Engineers (1989): *ASHRAE Handbook: Fundamentals*; ASHRAE: Atlanta, GA, USA. ISBN 978-0-910110-57-0.

[4] Cleland, A. (1986): Computer subroutines for rapid evaluation of refrigerant thermodynamic properties. *Int. Journal of Refrigeration,* vol.9(6), pp.345-352.

[5] Jing, Y., Li, Z., Liu, L., Lu, S. (2018): Exergoeconomic Assessment of Solar Absorption and Absorption-Compression Hybrid Refrigeration in Building Cooling. *Entropy*, vol.20(130), pp.1-22.

Feasibility and performance analysis of a novel resorption-compression cascade coupled system for residential heating in cold climate condition

Jia, Teng[1, 2], **Dou, Pengbo**[1, 2], **Dai, Yanjun**[1, 2, *]

[1] *School of Mechanical Engineering, Shanghai Jiao Tong University, Shanghai 200240, China*

[2] *Engineering Research Center of Solar Power and Refrigeration, MOE, China*

[*] *Corresponding author. Email: yjdai@sjtu.edu.cn*

Abstract:

Here we present a novel cascade hybrid heat pump system by combing the advantages of absorption-resorption heat pump (ARHP) (low heat source temperature need) and vapor compression heat pump (VCHP) (strong ambient temperature adaptability). The calculation results indicate that under the condition of T_e = -35 °C, T_c = 15 °C, the system can be driven by heat source above 90 °C with primary energy ratio (*PER*) higher than 0.95, and simultaneously produce 22% more heat than the single VCHP system under the same condition. When T_c increases to 30 °C, the feasible T_h can be down to 69 °C which can be fulfilled by solar heat. When solar fraction is over 45%, *PER* is constantly greater than that of the reference VCHP system within the whole heating ambient temperature range. The system can be applied in extreme cold climate condition for high efficient heating.

1 Introduction

Absorption heat pumps (AHPs) are inferior to vapor compression heat pumps (VCHPs) in low temperature adaptability despite that VCHPs suffer a lot from the declining of heating capacity with the decreasing of ambient temperature and the consequent insufficiency to the users' requirements and larger electricity consumption [1]. However, thermally activated AHPs are advantageous at higher primary energy ratio (*PER*) when driven by low grade heat sources. Hybrid heat pumps, such as compression-absorption cascade heat pump (CACHP) is promising in achieving low evaporation temperature and reduce electricity consumption [2]. Many researches have been done on CACHPs which show excellent primary energy saving effect compared with equivalent VCHP systems [3, 4]. For heating application, CACHPs with evaporation-condenser configuration can be integrated with different kinds of heat sources (devices) such as waste heat [5, 6], geothermal energy and regional boilers [6]. The cascade arrangement can enhance cold climate condition adaptability, reduce heat source temperature demand, produce more heat and save primary energy [7]. However, due to high working pressure demanded by applicable condensation (heat supply) temperature, generation (heat source) temperature is still high and the generator cannot efficiently utilize low grade heat source such as solar heat within a wide temperature range and with low temperature. Moreover, evaporation temperature of the AHP subsystem cannot be too low in order to efficiently utilize low temperature heat source and simultaneously ensure satisfactory coefficient of performance (COP). Moreover, evaporation temperature of VCHP subsystem must be sufficiently high to guarantee COP of the VCHP subsystem, thus weakening the adaptability to cold climate condition.

Absorption-resorption heat pump (ARHP) cycle can be developed based on AHP cycle by substituting the condenser and evaporator with a high pressure absorber (HPA) and a low pressure generator (LPG). According to refs. [8, 9], by adjusting the working pressures (high pressure and low pressure) and solution concentration condition, the cycle can reduce heat source temperature demand and guarantee the heat supply temperature by the phase transition temperature slip of the two components in NH_3-H_2O solution in HPA and LPG. Therefore, this paper tries to develop a novel resorption-compression heat pump system by cascade coupling the ARHP cycle and VCHP cycle by referring to configurations of the above mentioned CACHPs. The novel system is expected to further lift cold climate condition adaptability, reduce heat source demand and lift the ability of being integrated with heat sources with lower temperature for high efficiency heating. Feasibility and the specific performance are investigated in this work.

2 Fundamentals of the novel cascade system

2.1 Cycle description

The detailed configuration of the resorption-compression cascade hybrid system is shown in Figure 1. The system consists of two subsystems: a thermally activated ARHP subsystem at high temperature side for heat source integration and a VCHP subsystem at low temperature side (temperature of each state point is lower than that of any state point in the ARHP subsystems) for cold climate condition adaptation. NH_3-H_2O and R410A are utilized as the working fluid in the ARHP and VCHP subsystem, respectively. The two subsystems are connected through the configuration of LPG-CON (condenser). The condensation heat (Q_{con}) is no longer directly used for heating, but to drive the ARHP subsystem for possible heat output multiplication.

As reported in ref. [8], the ARHP can work efficiently when heat source temperature at the LPG side is above 0 °C. Therefore, the condensation temperature (T_{c}) can be substantially lower in the novel system than that in traditional VCHP system and the evaporation temperature (T_{e}) can be much lower. Moreover, benefitting from the ARHP subsystem, the cascade system can efficiently utilize low grade (temperature) heat sources for heating. For the ARHP subsystem, due to the low pressure and temperature in LPG, the generated vapor can be treated as pure refrigerant due to the high enough ammonia mass fraction. Therefore, a rectifier above HPG (high pressure generator) is required for refrigerant purification to guarantee species balance inside the ARHP rather than lift absorption efficiency in HPA. The high pressure generation process is driven by the sensible heat recovered by the coils and the external heat sources like solar heat, industrial waste heat, and of course, gas combustion.

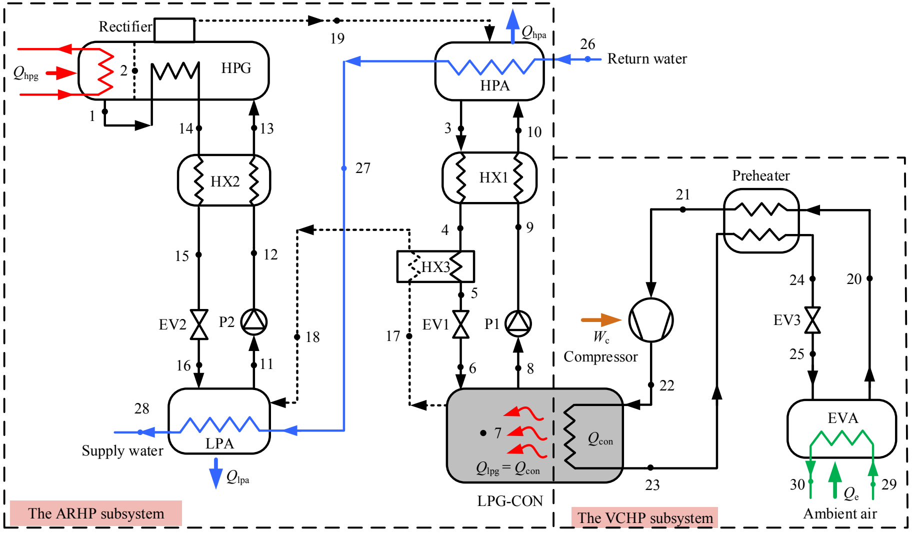

Figure 1 - Schematic diagram of the proposed resorption-compression cascade heating system

2.2 Thermodynamic models and evaluation criteria

Thermodynamic models of the ARHP subsystem and VCHP subsystem was reported in ref. [8] and ref. [10], respectively, and will not be repeated here. The performance evaluation indices are given as follows:

(1) **Primary energy ratio (PER)** is used to evaluate performance of the hybrid system and the heating PER here is defined as the ratio of the heating capacity produced in LPA (low pressure absorber), HPA to the primary energy consumption by the compressor and solution pump, given as

$$\mathrm{PER} = \frac{Q_{\mathrm{hpa}} + Q_{\mathrm{lpa}}}{\left(\frac{Q_{\mathrm{hpg}}}{\eta_{\mathrm{b}}} + \frac{\sum W_{\mathrm{p}}}{\eta_{\mathrm{e}}} + \frac{W_{\mathrm{cp}}}{\eta_{\mathrm{e}}} \right)} \tag{1}$$

where η_{b} is boiler efficiency, which is typically 0.7 for coal boilers and 0.9 for gas boilers. η_{e} is the electricity generation efficiency, with an average of 0.33 for coal-fired power plants [11]. W_{p} and W_{cp} are the power of the compressor and the solution heat pumps and the calculation expressions can be found in ref. [8] and ref. [10].

(2) Heating capacity of the cascade system can be lifted based on the VCHP subsystem with the same primary energy consumption and the relative increase (**heating capacity lift ratio, *HCLR***) can be calculated by

$$HCLR = \frac{Q_{\mathrm{hpa}} + Q_{\mathrm{lpa}} - Q_{\mathrm{con}}}{Q_{\mathrm{con}}} \tag{2}$$

It is worth noting that the condensation temperature for calculating Q_{con} is from the VCHP-only heating system, which is different from that for the current cascade system.

(3) Solar fraction (f) is defined as the ratio of the heat provided by solar collectors (Q_{sc}) to the HPG to the total heat needed for the high pressure generation process, written as

$$f = \frac{Q_{\text{sc}}}{Q_{\text{hpg}}} \tag{3}$$

3 Results

3.1 Matching of the two sub-cycles

Figure 2 depicts the pressure ratio of VCHP subsystem. Given the single-stage pressure ratio (Pr) of 6.0, the minimum evaporation temperature ($T_{\text{e,min}}$) corresponding to condensation temperature (T_{c}) of 15 °C, 20 °C, 25 °C, 30 °C are -35 °C (actually lower), -32.5 °C, -29 °C and -26 °C, respectively. On the one hand, in order to guarantee high COP of ARHP subsystem, higher T_{c} is better despite the fact that condensation heat of VCHP subsystem is not directly used for heating. When ambient air temperature (T_{a}) is higher than 20 °C (T_{e} is higher than 15 °C), space heating is no longer needed. Therefore, considering the actual heating needs, 15 °C and 30 °C can be chosen as the lower and upper limit of T_{c} for the current cascade hybrid system. According to ref. [8], maximum COP of ARHP subsystem can be achieved when high and low working pressure (P_{H} and P_{L}) conditions are 1550 kPa/580 kPa and 1550 kPa/940 kPa, respectively. The base-case and the corresponding working conditions are listed in Table 1.

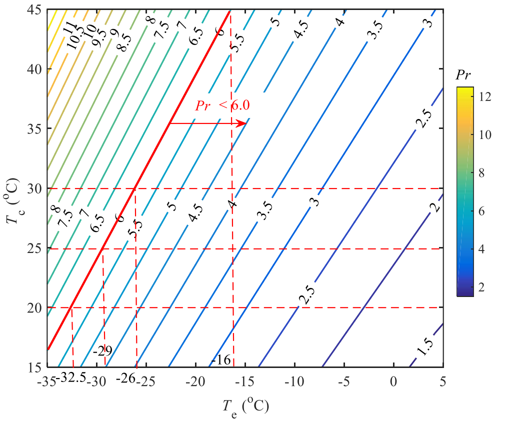

Figure 2 - Pressure ratio (Pr) of the VCHP subsystem

Table 1 - Working conditions of the base-case

Case	Case 1	Case 2
P_{H} (kPa)	1550	1550
P_{L} (kPa)	580	940
T_{c} (°C)	15	30
T_{e} range (°C)	-35~15	-26~15

3.2 *PER* of the cascade system (base-case)

The system is mainly designed for building floor heating with a return water temperature of 30 °C and supply water temperature above 40 °C. PER of the cascade system under the above two base-cases are illustrated in Figure 3. It can be seen that when T_{c} values are 15 °C and 30 °C, solution temperature at the outlet of high pressure generator (HPG) (T_1) can be as low as 85 °C and 64 °C, respectively, with a PER value higher than 0.95 at the $T_{\text{e,min}}$ of -35 °C and -26 °C. Given a minimum temperature difference of 5 °C between heat source and solution stream arranged in cross-counter flow in HPG, the heat source temperature (T_{h}) for the two base-cases are 90 °C and 69 °C, respectively. For given T_{e}, PER ascends firstly with the increasing of T_1 and then slightly descends and the change trend of PER is quite gentle with the changing of T_1. Although there exists an optimum T_{h} for maximum PER under given working conditions, chasing maximum PER by adjusting T_{h} is not necessary in actual operation.

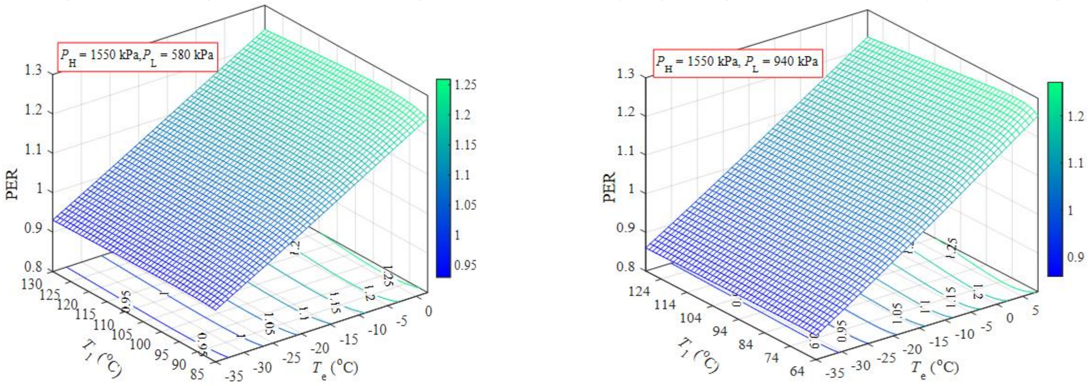

(a) T_{c} = 15 °C (b) T_{c} = 30 °C

Figure 3 - PER of the cascade coupled hybrid system

3.3 Heating capacity lift ratio

In this paper, the temperature difference between state point 1 and the heat source into the generator (arranged in counter-flow) is properly assumed to be 5 °C. In order to examine the heat production characteristics of the current hybrid system compared to the single VCHP heating system with the same primary energy consumption, heating capacity lift ratio (*HCLR*) is investigated and illustrated in Figure 4. It can be seen that when T_h = 90 °C (T_l = 85 °C), T_c = 15 °C and T_e varies from -35 °C to 5 °C, the maximum *HCLR* of 22% can be achieved when T_e = -35 °C. When T_e is within the range from -35 °C to -15.5 °C, *HCLR* is above 0, revealing that the current system can output more heat than the reference VCHP system. For the base-case of T_c = 30 °C, considering single-stage compression process, T_e value when *HCLR* is positive locates in a narrow range from -26 °C to -21 °C with the maximum value of 5%. From this point, it should be better to keep the T_c value as small as possible in the proper range to guarantee the excellent heating capacity lift performance of the cascade hybrid system in extreme cold climate condition. It is worth noting that the results were obtained with gas furnace acting as the heat source for the ARHP subsystem, i.e. the solar fraction (*f*) is 0%. When integrated with solar heat, the cascade hybrid system can show better heating capacity lift (primary energy saving) performance.

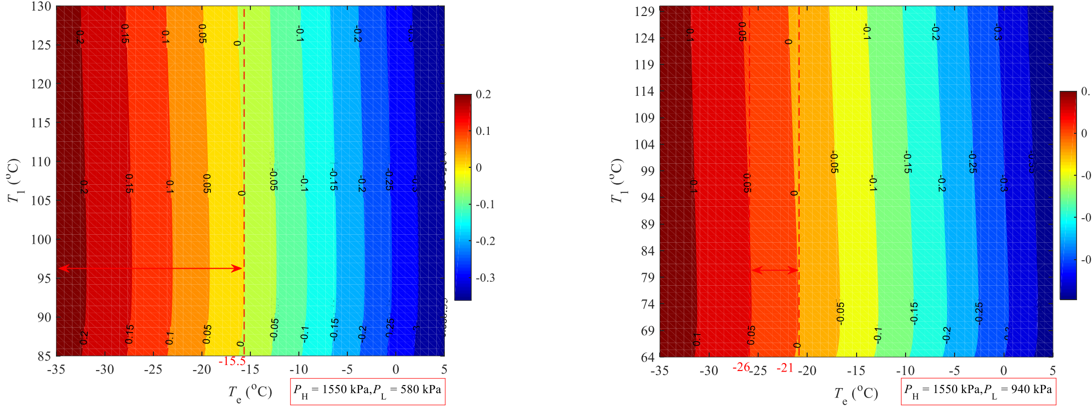

(a) T_c = 15 °C (b) T_c = 30 °C

Figure 4 - Heating capacity lift ratio (HCLR) of the cascade coupled hybrid system

3.4 Possible solar contribution

To investigate nonrenewable primary energy saving performance of the cascade hybrid system, possible solar contribution is explored and the results are depicted in Figure 5 by assuming a condition where solar heat temperature (T_f) is 90 °C and T_c is 15 °C. It can be seen that when f = 0, PER of the cascade hybrid system is higher than that of single VCHP system when T_a is in the range from -30 °C to -9 °C, which can also be concluded from Figure 4(a). For f values of 10%, 20%, 30% and 40%, the above ranges are (-30 °C, -4 °C), (-30 °C, 2 °C), (-30 °C, 7 °C) and (-30 °C, 12.5 °C), respectively. It can also be seen in Figure 5 that when f is above 45%, PER of the current system is constantly greater than that of the reference VCHP system in the whole heating T_a range from -30 °C to 15 °C. Actually, for a single VCHP system with the same heat supply temperature, when T_a is below -10.7 °C, the pressure ratio is unsatisfactory and above 6.0. The hybrid system can guarantee the needed heat supply temperature by the phase transition temperature slip in HPA by adjusting the working pressure and solution concentration values.

4 Conclusions

This paper proposed and theoretically investigated a novel resorption-compression hybrid system by cascade coupling an ARHP subsystem and VCHP subsystem for high efficient building floor heatingin extreme cold climate condition. The main results are:

(1) The hybrid system could efficiently utilize heat source as low as 90 °C for heating application when the evaporation temperature is above -35 °C with primary energy ratio greater than 0.95. When the condensation temperature is lifted to 30 °C, temperature need of the heat source can be pulled down to 69 °C.

(2) Heating capacity of the hybrid system could be 22% higher than that of the reference VCHP system with the same heat supply temperature and nonrenewable primary energy consumption. When ambient temperature increases, the heating capacity lift ratio descends slightly and the advantage in this aspect will fade away.

(3) Primary energy ratio of the hybrid system can be improved by lifting solar fraction. When solar fraction is above 45%, PER of the current cascade hybrid system is constantly greater than that of the reference VCHP system in the whole heating ambient temperature range from -30 °C to 15 °C.

5 Acknowledgment

This paper is supported by the key project of the National Natural Science Foundation of China under the contract No. 51736006.

6 List of References

[1] Zhang, L., Jiang, Y.Q., Dong, J.K., Yao, Y. (2018): Advances in vapor compression air source heat pump system in cold regions: A review. *Renewable and Sustainable Energy Reviews*, vol.81, pp.353-365.

[2] Xu, Y.J., Jiang, N., Wang, Q., Chen, G.M. (2016): Comparative study on the energy performance of two different absorption-compression refrigeration cycles driven by low-grade heat. *Applied Thermal Engineering*, vol.106, pp.33-41.

[3] Cimsit, C., Ozturk, I.T. (2012): Analysis of compression-absorption cascade refrigeration cycles. *Applied Thermal Engineering*, vol.40, pp.311-317.

[4] Salhi, K., Korichi, M., Ramadan, K.M. (2018): Thermodynamic and thermo-economic analysis of compression-absorption cascade refrigeration system using low-GWP HFO refrigerant powered by geothermal energy. *Int. Journal of Refrigeration*, vol.94, pp.214-229.

[5] Garimella, S., Brown, A.M., Nagavarapu, A.K. (2011): Waste heat driven absorption/vapor-compression cascade refrigeration system for megawatt scale, high-flux, low-temperature cooling. *Int. Journal of Refrigeration*, vol.34, pp.1776-1785.

[6] Ji, Q., Han, Z.W., Zhang, X.P., Sun, X.Q., et. al. (2021): Study on the heating performance of absorption-compression hybrid heat pump in severe cold regions. Applied Thermal Engineering, vol.185, article.116419.

[7] Farshi, L.G., Khalili, S., Mosaffa, A.H. (2018): Thermodynamic analysis of a cascaded compression-Absorption heat pump and comparison with three classes of conventional heat pumps for the waste heat recovery. *Applied Thermal Engineering*, vol.128, pp.282-296.

[8] Jia, T., Dai Y.J. (2018): Development of a novel unbalanced ammonia-water absorption-resorption heat pump cycle for space heating. *Energy*, vol.161, pp.251-265.

[9] Du, K., Yang, S.W., Zhang, S.Q. (1991): Experimental analysis and research of an aqua ammonia absorption-resorption heat pump. *Journal of Engineering Thermophysics*, vol.3(12), pp.229-233. (in Chinese)

[10] Jia, T., Dou P.B., Chu, P., Dai, Y.J. (2020): Proposal and performance analysis of a novel solar-assisted resorption-subcooled compression hybrid heat pump system for space heating in cold climate condition. *Renewable Energy*, vol.150, pp.1136-1150.

[11] Wu, W., Li, X., You, T., Wang, B.L., Shi W.X. (2015): Combining ground source absorption heat pump with ground source electrical heat pump for thermal balance, higher efficiency and better economy in cold regions. *Renewable Energy*, vol.84, pp.74-88.

List of Authors

Gong, M.	Thermodynamic and economic analysis of an improved absorption refrigeration system for the LNG precooling process to recover the flue gas and jacket water (#107)	171
GREMILLARD, L.	Experimental study of a thermochemical heat transformer using deposit of CaCl2 (#97)	55
Helm, M.	Directly Biomass-fired Absorption Heat Pump – Concept and Test Results (#81)	158
Henninger, S.	Hydrothermal stress test - Investigation on zeolite 13X and Al-fumarate for their application in open heat storage application (#93)	47
Hermann, T.	Vertical tube evaporator for a flue gas-condensing absorption heat pump (#92)	130
Herrmann, R.	Numerical and experimental evaluation of adsorption performances of SAPO-34 coated adsorber obtained by direct synthesis process (#133)	102
Hinmers, S.	Ammonia-salt sorption: testing and analysis, modelling and validation (#100)	65
Hosho, T.	Design optimization of three-fluid desiccant contactor using genetic algorithm (#85)	106
Hügenell, P.	Hydrothermal stress test - Investigation on zeolite 13X and Al-fumarate for their application in open heat storage application (#93)	47
Jahan Mahua, R.	A modified linear driving force model for adsorption heat pump and CO2 capture applications (#110)	30
Jeong, J.	Design optimization of three-fluid desiccant contactor using genetic algorithm (#85)	106
Jia, T.	Feasibility and performance analysis of a novel resorption-compression cascade coupled system for residential heating in cold climate condition (#135)	215
Joonho, P.	Heat Transfer and Frictional Pressure Drop Characteristics of H2O/LiBr Solution in Plate Heat Exchanger for Triple Effect Absorption Cycle Application (#116)	38
Jordan, U.	Development of a numerical model of a liquid desiccant air-conditioning system (#82)	1
Jordan, U.	Performance analysis on a hybrid liquid desiccant air conditioning system using condenser heat for regeneration (#98)	16
Kang, Y.	Heat Transfer and Frictional Pressure Drop Characteristics of H2O/LiBr Solution in Plate Heat Exchanger for Triple Effect Absorption Cycle Application (#116)	38
Kausche, M.	Directly Biomass-fired Absorption Heat Pump – Concept and Test Results (#81)	158
Kemmerzehl, C.	Asymmetric Plate Heat Exchanger for Absorption Refrigerating Plants (#104)	139
Kemmerzehl, C.	Thermally driven Ice Slurry generation for Heating and Cooling Applications - TAFEis (#118)	42
Kiran Naik, B.	Sorption Kinetics Assessment of Microencapsulated Sorbent with Humid Air Employing Variable Separable Approach (#106)	69
Kiran Naik, B.	Data Driven AI and ML Tools for Exit Parameters Prediction of Hollow Fiber Membrane Liquid Desiccant Dehumidifier (#112)	143
Kiran Naik, B.	Performance Evaluation of Desiccant Coated Energy Exchanger Based on Buckingham π-Theorem (#119)	148
Kizildag, D.	Preliminary assessment of a polygeneration system based on a concentrated photovoltaic thermal (CPVT) solar collectors (#113)	176

Kodama, A.	The preparation of an aluminum composite adsorbent by anodizing technique for adsorption chiller (#96)	51
Kodama, A.	Dehumidification behavior of a crossflow type heat exchanger coated with aluminophosphate zeolite regenerated by a direct hot water heating. (#101)	135
KONO, M.	Experimental investigation of a double effect adsorption refrigeration cycle driven with low grade heat sources (#114)	35
Kotlik, J.	Kinetic performance evaluation of high-ordered microporous silica in an experimental water-based adsorption heat storage system (#99)	60
Kühn, R.	Field test results of an adsorption off-grid vaccine refrigerator for temperate climates (#127)	201
Kühn, R.	On the effects of additives for ionic liquids in absorption chillers (#131)	97
Kumar Sai Tejes, P.	Data Driven AI and ML Tools for Exit Parameters Prediction of Hollow Fiber Membrane Liquid Desiccant Dehumidifier (#112)	143
Kumita, M.	The preparation of an aluminum composite adsorbent by anodizing technique for adsorption chiller (#96)	51
Lex, T.	Investigation of Vapor Flow in Compact Plate Heat Exchangers Operating as Falling Film Evaporator or Absorber (#91)	125
Li, B.	Experimental Investigation on Thermal Management of the Mobile Devices Based on Moisture Sorption-Desorption Process (#94)	167
Lin, Y.	Novel LiCl solutions for crystallization control in LiCl/H2O absorption systems (#123)	84
Ling-Chin, J.	Techno-economic feasibility analysis of liquid desiccant technology for automotive painting (#115)	181
Liu, F.	Experimental Study On A Novel Heat-Driven Multifunctional Air Treatment System (#122)	197
Liu, H.	Experimental Investigation on Thermal Management of the Mobile Devices Based on Moisture Sorption-Desorption Process (#94)	167
Liu, Z.	Thermodynamic and economic analysis of an improved absorption refrigeration system for the LNG precooling process to recover the flue gas and jacket water (#107)	171
Lu, D.	Thermodynamic and economic analysis of an improved absorption refrigeration system for the LNG precooling process to recover the flue gas and jacket water (#107)	171
Ma, Z.	Techno-economic feasibility analysis of liquid desiccant technology for automotive painting (#115)	181
Mähne, K.	Field test results of an adsorption off-grid vaccine refrigerator for temperate climates (#127)	201
Makar, E.	Absorption Chiller Control for 100% Turndown (#88)	163
Mandow, W.	Development of a numerical model of a liquid desiccant air-conditioning system (#82)	1
Mandow, W.	Performance analysis on a hybrid liquid desiccant air conditioning system using condenser heat for regeneration (#98)	16
Martinez-Urrutia, A.	Experimental results and thermoeconomic analysis of an absorption heat transformer operating in a petrol refinery (#72)	153
Metcalf, S.	Design and Testing of a Carbon-Ammonia Gas-Fired Heat Pump (#121)	192
Meyer, T.	The Influence of Temperature on Marangoni Convection during Vapor Absorption (#84)	6
MICHEL, B.	Experimental study of a thermochemical heat transformer using deposit of CaCl2 (#97)	55